

MATERIALS  
RESEARCH  
SOCIETY  
SYMPOSIUM PROCEEDINGS

VOLUME 367

# Fractal Aspects of Materials



EDITORS

Fereydoon Family  
Paul Meakin  
Bernard Sapoval  
Richard Wool

19950731 000

DECLASSIFICATION STATEMENT A

Approved for public release  
Distribution Unlimited

## Fractal Aspects of Materials

|                     |                                     |
|---------------------|-------------------------------------|
| Accession For       |                                     |
| NTIS CRA&I          | <input checked="" type="checkbox"/> |
| DTIC TAB            | <input type="checkbox"/>            |
| Unannounced         | <input type="checkbox"/>            |
| Justification ..... |                                     |
| By .....            |                                     |
| Distribution/       |                                     |
| Availability Codes  |                                     |
| Dist                | Avail and/or<br>Special             |
| A-1                 |                                     |

---

MATERIALS RESEARCH SOCIETY SYMPOSIUM PROCEEDINGS VOLUME 367

---

## **Fractal Aspects of Materials**

Symposium held November 28–December 1, 1994, Boston, Massachusetts, U.S.A.

EDITORS:

**Fereydoon Family**

Emory University  
Atlanta, Georgia, U.S.A.

**Paul Meakin**

University of Oslo  
Oslo, Norway

**Bernard Sapoval**

Ecole Polytechnique  
Palaiseau, France

**Richard Wool**

University of Delaware  
Newark, Delaware, U.S.A.



---

MATERIALS RESEARCH SOCIETY  
Pittsburgh, Pennsylvania

This work was supported in part by the Office of Naval Research under Grant Number N00014-95-1-0141. The United States Government has a royalty-free license throughout the world in all copyrightable material contained herein.

Single article reprints from this publication are available through  
University Microfilms Inc., 300 North Zeeb Road, Ann Arbor, Michigan 48106

CODEN: MRSPDH

Copyright 1995 by Materials Research Society.  
All rights reserved.

This book has been registered with Copyright Clearance Center, Inc. For further information, please contact the Copyright Clearance Center, Salem, Massachusetts.

Published by:

Materials Research Society  
9800 McKnight Road  
Pittsburgh, Pennsylvania 15237  
Telephone (412) 367-3003  
Fax (412) 367-4373

Library of Congress Cataloging in Publication Data

Fractal aspects of materials : symposium held November 28–December 1, 1994, Boston, Massachusetts, U.S.A. / edited by Fereydoon Family, Paul Meakin, Bernard Sapoval, Richard Wool

p. cm.—(Materials Research Society symposium proceedings, ISSN 0272-9172 ; v. 367)

Includes bibliographical references and index.

ISBN 1-55899-268-5 (hardcover : acid-free paper)

1. Materials—Surface—Congresses. 2. Fractals—Congresses. I. Family, Fereydoon II. Meakin, Paul III. Sapoval, Bernard IV. Wool, Richard V. Series: Materials Research Society symposium proceedings ; v. 367.

TA418.7.F73 1995  
620.1'1299—dc20

95-17185  
CIP

Manufactured in the United States of America



## Contents

|  |      |
|--|------|
| PREFACE . . . . .  | xi   |
| DEDICATION . . . . .                                       | xiii |
| MATERIALS RESEARCH SOCIETY SYMPOSIUM PROCEEDINGS . . . . . | xiv  |

### PART I: DIFFUSIVE INSTABILITY IN MATERIALS GROWTH

|   |    |
|---|----|
| *THE DIFFUSIVE INSTABILITY IN GROWTH: DLA, DENDRITIC GROWTH,<br>AND SOLIDIFICATION . . . . .  | 3  |
| Leonard M. Sander   |    |
| *DENDRITIC GROWTH IN TERRESTRIAL AND MICROGRAVITY<br>CONDITIONS . . . . .   | 13 |
| M.E. Glicksman, M.B. Koss, L.T. Bushnell, J.C. Lacombe, and E.A. Winsa  |    |
| *DIFFUSION-LIMITED AGGREGATION AS BRANCHED GROWTH . . . . .   | 23 |
| Thomas C. Halsey  |    |
| *SINGULAR INTERFACIAL HYDRODYNAMICS AND THE DIELECTRIC<br>BREAKDOWN MODEL . . . . .   | 33 |
| H.G.E. Hentschel  |    |
| WAVELET BASED STRUCTURAL ANALYSIS OF ELECTROLESS DEPOSITS<br>IN THE DIFFUSION LIMITED REGIME . . . . .  | 43 |
| A. Arneodo, F. Argoul, A. Kuhn, and J.F. Muzy   |    |
| A THEORY FOR GROWING INTERFACES IN LAPLACIAN FIELDS: A<br>MANY-BODY FORMULATION AND STATISTICAL ANALYSIS . . . . .                                      | 53 |
| Raphael Blumenfeld  |    |
| FROM FACETS TO FRACTALS—GROWTH MORPHOLOGIES IN MOLECULAR<br>CRYSTALS OF CARBON TETRABROMIDE (CBr <sub>4</sub> ) AND FULLERENE C <sub>60</sub> . . . . . | 61 |
| Rong-Fu Xiao  |    |
| REAL SPACE RENORMALIZATION GROUP FOR SELF ORGANIZED<br>CRITICALITY IN SANDPILE MODELS . . . . .   | 67 |
| S. Zapperi, A. Vespignani, and L. Pietronero  |    |
| THE GEOMETRY OF DLA: DIFFERENT ASPECTS OF THE<br>DEPARTURE FROM SELF-SIMILARITY . . . . .   | 73 |
| B.B. Mandelbrot, A. Vespignani, and H. Kaufman  |    |

### PART II: FRACTURE AND BREAKDOWN OF MATERIALS

|  |     |
|--|-----|
| *FRACTAL PROPERTIES OF FRACTURE SURFACES: ROUGHNESS<br>INDICES AND RELEVANT LENGTHSCALES . . . . . | 83  |
| Elisabeth Bouchaud   |     |
| *SPATIAL AND TEMPORAL PROBES OF DEFORMATION AND FRACTURE<br>AT INTERFACES . . . . .                | 95  |
| J.T. Dickinson, S.C. Langford, and Louis Scudiero  |     |
| NATURE OF ENVIRONMENTALLY ASSISTED FRACTURES IN<br>POLYCRYSTALS . . . . .                          | 107 |
| Leonardo Golubović and Anatoli Perefera  |     |

\*Invited Paper

|  |     |
|--|-----|
| DISCRIMINATION OF SURFACE TEXTURES USING FRACTAL METHODS . . . . .   | 113 |
| Jill P. Card, J.M. Hyde, and T. Giversen   |     |
| COMPUTER SIMULATION OF BENDING PLASTIC DEFORMATION AND CREATION OF DISLOCATIONS IN COPPER THIN FILMS . . . . .                         | 119 |
| H. Tsukahara, Y. Niwa, T. Takayama, and Masao Doyama   |     |
| MICROSTRUCTURAL FRACTAL DIMENSION OF AISI 316L STEEL . . . . .   | 125 |
| M. Hinojosa, R. Rodríguez, and U. Ortiz  |     |
| RUPTURE OF RANDOM FUSE NETWORKS: DUCTILE TO BRITTLE CROSSOVER . . . . .  | 131 |
| Rafael F. Angulo and Ernesto Medina  |     |
| FRACTURE CHARACTERISTICS OF IRON-COPPER SINTERED COMPACTS . . . . .  | 137 |
| Kamran Tabeshfar   |     |
| THE INFLUENCE OF CRYSTALLOGRAPHIC ORIENTATION OF THE CRACK PLANE AND CRACK FRONT ON THE FRACTURE OF TUNGSTEN SINGLE CRYSTALS . . . . . | 141 |
| V. Glebovsky, H. Fishmeister, J. Riedle, V. Semenov, and P. Gumbsch  |     |

### PART III: SURFACES AND INTERFACES

|  |     |
|--|-----|
| *CRITICAL CLUSTER SIZE: ISLAND MORPHOLOGY AND SIZE DISTRIBUTION IN SUBMONOLAYER EPITAXIAL GROWTH . . . . . | 149 |
| Jacques G. Amar and Fereydoon Family   |     |
| *DYNAMIC SCALING IN ELECTROCHEMICAL DEPOSITION . . . . .   | 159 |
| Hiroshi Iwasaki, Atsushi Iwamoto, Koichi Sudoh, and Tatsuo Yoshinobu                                       |     |
| *2-D AND 3-D ELECTROCONVECTION, EXPERIMENTS AND MODELS . . . . .   | 169 |
| V. Fleury and J.-N. Chazalviel   |     |
| PULSED ELECTRODEPOSITION OF TREE-LIKE COPPER AGGREGATES . . . . .  | 177 |
| Y. Huttel, E. Chassaing, M. Rosso, and B. Sapoval  |     |
| RECENT PROGRESS IN ELECTROCHEMICAL DEPOSITION WITHOUT SUPPORTING ELECTROLYTE . . . . .                     | 183 |
| V. Fleury, M. Rosso, and J.-N. Chazalviel  |     |
| FORMATION OF SELF-AFFINE SURFACE DURING THE GROWTH OF NICKEL THIN FILMS . . . . .                          | 195 |
| M.V.H. Rao, V. Srinivas, B.K. Mathur, and K.L. Chopra  |     |

### PART IV: DISORDERED MATERIALS: PERCOLATION AND POROUS MEDIA

|   |     |
|---|-----|
| *FRACTALS IN POROUS MEDIA: FROM PORE TO FIELD SCALE . . . . .   | 203 |
| Muhammad Sahimi, Hossein Rassamdana, and Alireza Mehrabi  |     |
| *FRACTAL STRUCTURE OF A POROUS CROSS-LINKED POLYMER RESIN AND DYNAMICAL BEHAVIOR OF ADSORBED SOLVENTS . . . . . | 215 |
| J.-P. Korb and C. Chachaty  |     |

\*Invited Paper

|  |     |
|--|-----|
| NON-LINEAR RESPONSE OF SELF-SIMILAR ELECTRODES AND<br>ACTIVE MEMBRANES .....                               | 225 |
| B. Sapoval   |     |
| NEW SCALING FOR AC PROPERTIES OF PERCOLATING COMPOSITE<br>MATERIALS .....                                  | 231 |
| F. Brouers and A.K. Sarychev   |     |
| SCALAR TRANSPORT BY DIFFUSION AND RANDOM ADVECTION .....   | 237 |
| Mariela Araujo   |     |
| DAMPING AND SPATIAL DISTRIBUTION OF PERCOLATION FRACTONS .....   | 243 |
| S. Russ and B. Sapoval   |     |
| FEM BASED SIMULATION OF PERCOLATION FEATURES OF<br>DISORDERED HETEROGENEOUS MEDIA ELASTIC PROPERTIES ..... | 249 |
| S.A. Timan and V.G. Oshman   |     |
| SCALING OF TRANSPORT PROPERTIES OF RESERVOIR MATERIAL<br>AT LOW SATURATIONS OF A WETTING PHASE .....       | 255 |
| Y. Carolina Araujo, Pedro G. Toledo, and Hada Y. Gonzalez  |     |

#### PART V: KINETIC ROUGHENING

|   |     |
|---|-----|
| *STEP-EDGE BARRIERS, RE-ENTRANT OSCILLATIONS, AND<br>UNSTABLE EPITAXIAL GROWTH .....  | 263 |
| Dimitri D. Vvedensky and Pavel Šmilauer   |     |
| *FILM GROWTH: CONTROL OF SURFACE MORPHOLOGY FROM<br>MONODISPERSE NANOPARTICLES THROUGH FRACTALS TO FLAT<br>EPITAXIAL HETEROSTRUCTURES .....                   | 273 |
| R. Stanley Williams, William M. Tong, and Tue T. Ngo  |     |
| *WHEN INTERFACE GETS ROUGH... ..  | 283 |
| Toh-Ming Lu, Hong-Ning Yang, and Gwo-Ching Wang   |     |
| INFLUENCE OF IMPURITIES ON MECHANISMS OF GROWTH IN<br>MOVPE GaAs .....  | 293 |
| S. Nayak, J.M. Redwing, J.W. Huang, M.G. Lagally, and T.F. Kuech  |     |
| ROUGHENING BY ION BOMBARDMENT: A STOCHASTIC<br>CONTINUUM EQUATION .....   | 299 |
| R. Cuerno and A.-L. Barabási  |     |
| TEMPERATURE DEPENDENCE OF SURFACE MORPHOLOGY OF<br>SILICON GROWN ON CaF <sub>2</sub> /Si BY ELECTRON BEAM ASSISTED<br>MBE .....                               | 305 |
| P.O. Pettersson, R.J. Miles, and T.C. McGill  |     |
| VARIATIONS OF INTERFACIAL ROUGHNESS WITH EPILAYER<br>THICKNESS AND SCALING BEHAVIOR IN Si <sub>1-x</sub> Ge <sub>x</sub> GROWN<br>ON Si(100) SUBSTRATES ..... | 311 |
| Z.H. Ming, S. Huang, Y.L. Soo, Y.H. Kao, T. Carns, and<br>K.L. Wang   |     |
| STRUCTURAL CHARACTERISATION OF IRON-COPPER MULTILAYERS<br>USING TRANSMISSION ELECTRON MICROSCOPY .....  | 317 |
| S.J. Lloyd, R.E. Somekh, R.E. Dunin-Borkowski, and W.M. Stobbs  |     |

\*Invited Paper

|  |     |
|--|-----|
| MORPHOLOGICAL EVOLUTION WITH LAYER THICKNESS IN<br>SINGLE CRYSTAL $\text{CeO}_2$ (110)/Si(100) . . . . .                   | 323 |
| Tomoyasu Inoue, Yasuhiro Yamamoto, Masataka Satoh, and Tetsu Ohsuna  |     |
| SCALING ANALYSIS OF $\alpha$ - AND <i>poly</i> -Si SURFACE ROUGHNESS<br>BY ATOMIC FORCE MICROSCOPY . . . . .               | 329 |
| T. Yoshinobu, A. Iwamoto, K. Sudoh, and H. Iwasaki   |     |
| <br><b>PART VI: GLASSY MATERIALS SLOW<br/>RELAXATION AND AGING</b>   |     |
| *GLASS TRANSITION SINGULARITIES AND SLOW RELAXATION . . . . .  | 337 |
| T. Odagaki, J. Matsui, and Y. Hiwatari   |     |
| *AGING AND GLASSY DYNAMICS IN COMPLEX SYSTEMS: SOME<br>THEORETICAL IDEAS . . . . .   | 347 |
| Jean-Philippe Bouchaud   |     |
| *SLOW RELAXATION IN POLYMERIC GLASSES BY TWO-<br>DIMENSIONAL NMR . . . . .   | 355 |
| Alan A. Jones, P.T. Inglefield, Y.H. Chin, and C. Zhang  |     |
| CHARACTERIZING FRACTAL AND HIERARCHICAL MORPHOLOGIES<br>BEYOND THE FRACTAL DIMENSION . . . . .                             | 367 |
| Raphael Blumenfeld and Robin C. Ball   |     |
| CONCENTRATION INFLUENCE ON DIFFUSION LIMITED CLUSTER<br>AGGREGATION . . . . .  | 373 |
| St.C. Pencea and M. Dumitrascu   |     |
| LASER SCANNING OF NATURAL AND ARTIFICIAL SNOW PACKS . . . . .  | 379 |
| Kazuhiko Itagaki, G.E. Lemieux, and Nina Ji  |     |
| ELASTIC AND LATTICE DYNAMICAL PROPERTIES OF METALS<br>STUDIED BY N-BODY POTENTIAL . . . . .                                | 385 |
| Yoshiaki Kogure, O. Kouchi, and M. Doyama  |     |
| MICROSTRUCTURAL CHANGES OF WELDED Zn-Al ALLOY . . . . .  | 391 |
| Yao Hua Zhu  |     |
| FRACTURE AND FRACTALS IN GLASSES . . . . .   | 397 |
| Elena A. Chechetkina   |     |
| <br><b>PART VII: COMPLEX MATERIALS</b>   |     |
| *COOPERATIVE STRATEGIES AND GENOME CYBERNETICS IN<br>FORMATION OF COMPLEX BACTERIAL PATTERNS . . . . .                     | 405 |
| Eshel Ben-Jacob, Ofer Shochet, Inon Cohen, Adam Tenenbaum,<br>Andras Czirók, and Tamas Vicsek                              |     |
| OPTICAL PROPERTIES OF FRACTAL NANOCOMPOSITES . . . . .   | 417 |
| V.A. Markel, E.B. Stechel, W. Kim, R. Armstrong, and<br>Vladimir Shalaev   |     |
| NON UNIVERSAL SCALING LAW EXPONENTS IN THE $\text{ac}$ DIELECTRIC<br>RESPONSE OF POLYMER-CARBON BLACK COMPOSITES . . . . . | 423 |
| P. Hakizabera, R. Deltour, and F. Brouers  |     |

\*Invited Paper

|   |     |
|---|-----|
| TWO-LENGTH-SCALE STRUCTURE IN SOME COMPUTER-GENERATED<br>AGGREGATES GROWN BY DIFFUSION-LIMITED AGGREGATION . . . . .        | 429 |
| Paul W. Schmidt, Giuseppe Pipitone, M.A. Floriano, E. Caponetti,<br>and R. Triolo   |     |
| KINETIC AND EQUILIBRIUM CLUSTER-SIZE DISTRIBUTIONS<br>OF ANTIBODY-ANTIGEN-INDUCED COLLOIDAL AGGREGATION . . . . .           | 435 |
| Derin A. Sherman and Richard J. Cohen   |     |
| PROPERTIES OF CONDUCTING POLYMER INTERCONNECTS . . . . .  | 441 |
| Corrine L. Curtis, Grace M. Credo, Jason E. Ritchie, and<br>Michael J. Sailor   |     |
| STRUCTURE FACTOR SCALING IN FRACTAL AGGREGATION OF<br>COLLOIDAL CLUSTERS . . . . .  | 447 |
| Guillermo Ramírez-Santiago and Agustín E. González  |     |
| HOT CORROSION MECHANISM OF SILICON NITRIDE BASED<br>CERAMICS EXPOSED TO COAL SLAG CONTAINING POTASSIUM<br>SULFATE . . . . . | 453 |
| Z.B. Yu, W.H. Li, and N.F. Li   |     |

#### PART VIII: GRANULAR MATERIALS

|  |     |
|--|-----|
| *THE SCIENTIST IN THE SANDBOX: COMPLEXITY AND DYNAMICS<br>IN GRANULAR FLOW . . . . . | 461 |
| R.P. Behringer   |     |
| *SEDIMENTATION TO FORM ROUGH, QUASI-ONE-DIMENSIONAL<br>INTERFACES . . . . .          | 471 |
| James V. Maher and M. Levent Kurnaz  |     |
| *DYNAMICS OF GRANULAR MATERIALS: FLOWS, RELAXATION, AND<br>CONVECTION . . . . .      | 483 |
| Daniel C. Hong, Su Yue, and Douglas A. Kurtze  |     |
| DIRECT OBSERVATION OF SIZE SEGREGATION: CONVECTION<br>AND ARCHING EFFECT . . . . .   | 491 |
| J. Duran, T. Mazozi, E. Clement, and J. Rajchenbach                                  |     |
| INTERACTION LAWS AND THE DETACHMENT EFFECT IN<br>GRANULAR MEDIA . . . . .            | 495 |
| S. Luding, E. Clément, A. Blumen, J. Rajchenbach, and J. Duran                       |     |
| ID EXCITED GRANULAR MEDIA: CLUSTERING AND EQUATION<br>OF STATE . . . . .             | 501 |
| D.R.M. Williams and F.C. MacKintosh  |     |
| REVERSIBLE AXIAL SEGREGATION IN ROTATING GRANULAR<br>MEDIA . . . . .                 | 507 |
| K.M. Hill, L. Yarusso, and J. Kakalios   |     |
| MIXING OF A GRANULAR MATERIAL IN A BIDIMENSIONAL<br>ROTATING DRUM . . . . .          | 513 |
| Eric Clement, Jean Rajchenbach, and Jacques Duran                                    |     |
| SUPERSONIC RUPTURE PULSES IN AN EARTHQUAKE MODEL . . . . .                           | 519 |
| Michael Leibig   |     |

\*Invited Paper

---

|   |     |
|---|-----|
| EXPERIMENTS IN MODEL GRANULAR MEDIA: A STUDY OF GRAVITY FLOWS . . . . . | 525 |
| J. Rajchenbach, E. Clement, and J. Duran                                |     |
| AUTHOR INDEX . . . . .  | 529 |
| SUBJECT INDEX . . . . .   | 531 |

## Preface

Fractal concepts have profoundly influenced our understanding of complex structures and dynamical processes in a wide range of natural and industrial phenomena. Some of the most significant and far reaching contributions of fractals have been in the field of materials science and engineering. This has been clearly demonstrated over the past decade by the ever increasing successes of the *Symposium on Fractal Aspects of Materials* that began during the 1984 Fall MRS Meeting in Boston. To celebrate this milestone, we decided to highlight several of the important contributions at the 1994 Fall MRS Meeting and publish the proceedings as a comprehensive record of these achievements. In particular, the 1994 meeting was organized around a number of interdisciplinary topics that would emphasize some of the most recent applications of fractal concepts in materials science and engineering, as well as reviews of some of the well-established contributions. The topics discussed in this symposium included: diffusive instability in materials growth, fracture and breakdown of materials, surfaces and interfaces, disordered materials, percolation and porous media, kinetic roughening in thin film and epitaxial growth, glassy materials, aging, fatigue and slow relaxations, complex materials, and granular materials. The papers included in this volume are organized roughly in the order that they were presented in the eight sessions mentioned above.

We would like to thank all of our colleagues who helped us in the organization of this extremely successful meeting. We would like to particularly thank those whose papers appear in this volume and the referees of the papers. One person who should be especially thanked for his generous and continued support and encouragement is Dr. Michael F. Shlesinger. Without his scientific contributions the field of fractals and these symposia would have been far less memorable, and without his financial support through a grant from the Office of Naval Research, this meeting would not have been possible. We are grateful to the staff of the Materials Research Society for their considerable help before, during and after the meeting. We would also like to thank Connie Copeland of Emory University for her expert assistance with the preparation of the manuscript.

Fereydoon Family  
Paul Meakin  
Bernard Sapoval  
Richard Wool

May 1995

## Dedication



**Benoit B. Mandelbrot**

The occasion of this symposium was doubly momentous because it coincided not only with the 10th anniversary of the beginning of the *Fractal Aspects of Materials Symposium* at the Fall Materials Research Society meeting in Boston, but also the 70th birthday of the founder of these symposia, and the person who is responsible for the creation and development of the field of fractals, **Benoit B. Mandelbrot**, IBM Fellow and Professor of Mathematics at Yale. Considering the impact that fractals have had in materials science and engineering, it is with great pleasure that we dedicate this volume to Benoit Mandelbrot on the occasion of his 70th birthday and wish him continued success and many more fruitful and active years.

Fereydoon Family  
Paul Meakin  
Bernard Sapoval  
Richard Wool



---

MATERIALS RESEARCH SOCIETY SYMPOSIUM PROCEEDINGS

---

- Volume 336—Amorphous Silicon Technology—1994, E.A. Schiff, A. Matsuda, M. Hack, M.J. Powell, A. Madan, 1994, ISBN: 1-55899-236-7
- Volume 337—Advanced Metallization for Devices and Circuits—Science, Technology, and Manufacturability III, S.P. Murarka, K.N. Tu, A. Katz, K. Maex, 1994, ISBN: 1-55899-237-5
- Volume 338—Materials Reliability in Microelectronics IV, P. Børgesen, W. Filter, J.E. Sanchez, Jr., K.P. Rodbell, J.C. Coburn, 1994, ISBN: 1-55899-238-3
- Volume 339—Diamond, SiC and Nitride-Wide-Bandgap Semiconductors, C.H. Carter, Jr., G. Gildenblat, S. Nakamura, R.J. Nemanich, 1994, ISBN: 1-55899-239-1
- Volume 340—Compound Semiconductor Epitaxy, C.W. Tu, L.A. Kolodziejski, V.R. McCrary, 1994, ISBN: 1-55899-240-5
- Volume 341—Epitaxial Oxide Thin Films and Heterostructures, D.K. Fork, J.M. Phillips, R. Ramesh, R.M. Wolf, 1994, ISBN: 1-55899-241-3
- Volume 342—Rapid Thermal and Integrated Processing III, J.J. Wortman, J.C. Gelpey, M.L. Green, S.R.J. Brueck, F. Roozeboom, 1994, ISBN: 1-55899-242-1
- Volume 343—Polycrystalline Thin Films—Structure, Texture, Properties and Applications, M. Parker, K. Barmak, R. Sinclair, D.A. Smith, J. Floro, 1994, ISBN: 1-55899-243-X
- Volume 344—Materials and Processes for Environmental Protection, C. Adkins, P.N. Gadgil, L.M. Quick, K.E. Voss, 1994, ISBN: 1-55899-244-8
- Volume 345—Flat Panel Display Materials, J. Batey, A. Chiang, P. Holloway, 1994, ISBN: 1-55899-245-6
- Volume 346—Better Ceramics Through Chemistry VI, C. Sanchez, M.L. Mecartney, C.J. Brinker, A. Cheetham, 1994, ISBN: 1-55899-246-4
- Volume 347—Microwave Processing of Materials IV, M.F. Iskander, R.J. Lauf, W.H. Sutton, 1994, ISBN: 1-55899-247-2
- Volume 348—Scintillator and Phosphor Materials, M.J. Weber, P. Lecoq, R.C. Ruchti, C. Woody, W.M. Yen, R.-Y. Zhu, 1994, ISBN: 1-55899-248-0
- Volume 349—Novel Forms of Carbon II, C.L. Renschler, D. Cox, J. Pouch, Y. Achiba, 1994, ISBN: 1-55899-249-9
- Volume 350—Intermetallic Matrix Composites III, J.A. Graves, R.R. Bowman, J.J. Lewandowski, 1994, ISBN: 1-55899-250-2
- Volume 351—Molecularly Designed Ultrafine/Nanostructured Materials, K.E. Gonsalves, G.-M. Chow, T.D. Xiao, R.C. Cammarata, 1994, ISBN: 1-55899-251-0
- Volume 352—Materials Issues in Art and Archaeology IV, P.B. Vandiver, J.R. Druzik, J.L. Galvan Madrid, I.C. Freestone, G.S. Wheeler, 1995, ISBN: 1-55899-252-9
- Volume 353—Scientific Basis for Nuclear Waste Management XVIII, T. Murakami, R.C. Ewing, 1995, ISBN: 1-55899-253-7
- Volume 354—Beam-Solid Interactions for Materials Synthesis and Characterization, D.E. Luzzi, T.F. Heinz, M. Iwaki, D.C. Jacobson, 1995, ISBN: 1-55899-255-3
- Volume 355—Evolution of Thin-Film and Surface Structure and Morphology, B.G. Demczyk, E.D. Williams, E. Garfunkel, B.M. Clemens, J.E. Cuomo, 1995, ISBN: 1-55899-256-1
- Volume 356—Thin Films: Stresses and Mechanical Properties V, S.P. Baker, P. Børgesen, P.H. Townsend, C.A. Ross, C.A. Volkert, 1995, ISBN: 1-55899-257-X
- Volume 357—Structure and Properties of Interfaces in Ceramics, D.A. Bonnell, U. Chowdhry, M. Rühle, 1995, ISBN: 1-55899-258-8

---

## MATERIALS RESEARCH SOCIETY SYMPOSIUM PROCEEDINGS

---

- Volume 358—Microcrystalline and Nanocrystalline Semiconductors, R.W. Collins, C.C. Tsai, M. Hirose, F. Koch, L. Brus, 1995, ISBN: 1-55899-259-6
- Volume 359—Science and Technology of Fullerene Materials, P. Bernier, D.S. Bethune, L.Y. Chiang, T.W. Ebbesen, R.M. Metzger, J.W. Mintmire, 1995, ISBN: 1-55899-260-X
- Volume 360—Materials for Smart Systems, E.P. George, S. Takahashi, S. Trolrier-McKinstry, K. Uchino, M. Wun-Fogle, 1995, ISBN: 1-55899-261-8
- Volume 361—Ferroelectric Thin Films IV, S.B. Desu, B.A. Tuttle, R. Ramesh, T. Shiosaki, 1995, ISBN: 1-55899-262-6
- Volume 362—Grain-Size and Mechanical Properties—Fundamentals and Applications, N.J. Grant, R.W. Armstrong, M.A. Otooni, T.N. Baker, K. Ishizaki, 1995, ISBN: 1-55899-263-4
- Volume 363—Chemical Vapor Deposition of Refractory Metals and Ceramics III, W.Y. Lee, B.M. Gallois, M.A. Pickering, 1995, ISBN: 1-55899-264-2
- Volume 364—High-Temperature Ordered Intermetallic Alloys VI, J. Horton, I. Baker, S. Hanada, R.D. Noebe, D. Schwartz, 1995, ISBN: 1-55899-265-0
- Volume 365—Ceramic Matrix Composites—Advanced High-Temperature Structural Materials, R.A. Lowden, J.R. Hellmann, M.K. Ferber, S.G. DiPietro, K.K. Chawla, 1995, ISBN: 1-55899-266-9
- Volume 366—Dynamics in Small Confining Systems II, J.M. Drake, S.M. Troian, J. Klafter, R. Kopelman, 1995, ISBN: 1-55899-267-7
- Volume 367—Fractal Aspects of Materials, F. Family, B. Sapoval, P. Meakin, R. Wool, 1995, ISBN: 1-55899-268-5
- Volume 368—Synthesis and Properties of Advanced Catalytic Materials, E. Iglesia, P. Lednor, D. Nagaki, L. Thompson, 1995, ISBN: 1-55899-270-7
- Volume 369—Solid State Ionics IV, G-A. Nazri, J-M. Tarascon, M. Schreiber, 1995, ISBN: 1-55899-271-5
- Volume 370—Microstructure of Cement Based Systems/Bonding and Interfaces in Cementitious Materials, S. Diamond, S. Mindess, F.P. Glasser, L.W. Roberts, J.P. Skalny, L.D. Wakeley, 1995, ISBN: 1-55899-272-3
- Volume 371—Advances in Porous Materials, S. Komarneni, D.M. Smith, J.S. Beck, 1995, ISBN: 1-55899-273-1
- Volume 372—Hollow and Solid Spheres and Microspheres—Science and Technology Associated with their Fabrication and Application, M. Berg, T. Bernat, D.L. Wilcox, Sr., J.K. Cochran, Jr., D. Kellerman, 1995, ISBN: 1-55899-274-X
- Volume 373—Microstructure of Irradiated Materials, I.M. Robertson, L.E. Rehn, S.J. Zinkle, W.J. Pythian, 1995, ISBN: 1-55899-275-8
- Volume 374—Materials for Optical Limiting, R. Crane, K. Lewis, E.V. Stryland, M. Khoshnevisan, 1995, ISBN: 1-55899-276-6
- Volume 375—Applications of Synchrotron Radiation Techniques to Materials Science II, L.J. Terminello, N.D. Shinn, G.E. Ice, K.L. D'Amico, D.L. Perry, 1995, ISBN: 1-55899-277-4
- Volume 376—Neutron Scattering in Materials Science II, D.A. Neumann, T.P. Russell, B.J. Wuensch, 1995, ISBN: 1-55899-278-2

*Prior Materials Research Society Symposium Proceedings  
available by contacting Materials Research Society*

---

## PART I

---

### **Diffusive Instability in Materials Growth**

## THE DIFFUSIVE INSTABILITY IN GROWTH: DLA, DENDRITIC GROWTH, AND SOLIDIFICATION

LEONARD M. SANDER

H.M. Randall Laboratory of Physics, The University of Michigan, Ann Arbor, MI 48109-1120

### ABSTRACT

We give an overview of the influence of the diffusive instability in forming various growth morphologies. We review dendritic growth of crystals, and discuss the DLA model as an approach to the disordered, fractal case. We consider various systems which are reasonably well described by DLA including island shapes in surface growth

### INTRODUCTION

In the formation of natural objects the rate-limiting step is often diffusion. For example, in rapid thermal crystallization, latent heat must diffuse away from the growing surface. In crystallization from the melt, dissolved atoms diffuse to the surface. There are many cases of this sort which are of interest in materials science: the growth of islands on a surface in a molecular-beam epitaxy experiment is limited by the arrival of adatoms at the step edges. In electrochemical deposition can in some cases be diffusion limited. Another example is given in Figure 1.



Figure 1. A diffusion-limited pattern of growth in the crystallization of  $\text{GeSe}_2$  from an amorphous film on a surface [1]. This deposit is polycrystalline and fractal.

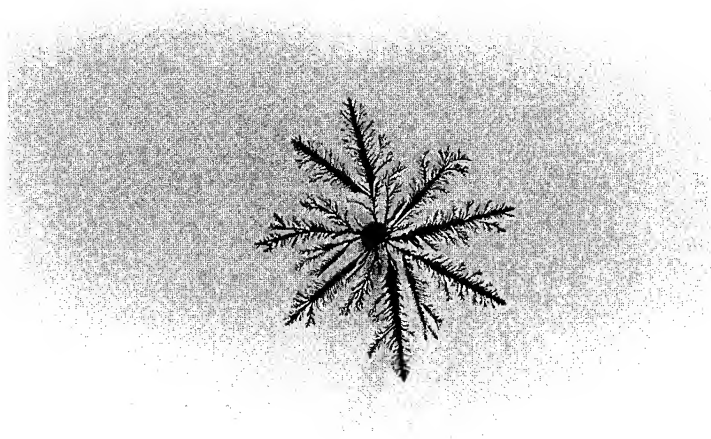


Figure 2. Zn deposit grown in electrodeposition in a flat cell [2]. This pattern is dendritic: note the fixed angle of the sidebranches with respect to the main branches.

The most interesting feature of diffusion-limited growth is that it gives rise to remarkable morphologies which tend to be ramified and complex in the way shown in Figures 1 and 2. There are two types of morphology which are often encountered, and which we will concentrate on here.

(i) If some underlying symmetry, such as the crystal symmetry, persists in growth, as in Figure 2, the pattern is *dendritic*. The most famous dendritic pattern is a snowflake.

(ii) If all apparent symmetry is lost, the pattern can nevertheless exhibit a more subtle symmetry, that of self-similarity. This is a *fractal* pattern as in Figure 1.

The key to understanding these patterns is to realize that diffusion-limited growth is generically linearly unstable for flat growing surfaces. The patterns formed during growth are complicated and subtle because non-linearities determine them completely. Physicists, physical chemists, and materials scientists have devoted considerable effort to deciphering these morphologies in the last few decades. This paper is intended to give a brief overview of the principles which underlie our current understanding. Many of the articles in this volume give an account of the ongoing activity in this area. For more comprehensive reviews the reader should consult [3-6]. These principles are very general and have applications far beyond materials science: for example, in recent years cosmologists have considered diffusive instabilities in the quark-hadron phase transition [7] and many workers have discussed how to understand growth of bacterial colonies using the ideas we will discuss here [8].

#### The Stefan problem and the diffusive growth instability

The fundamental reason for the complex shapes is that diffusion-limited growth exhibits a growth instability. We will discuss here the classic linear stability analysis of this case given by Mullins and Sekerka [9]. First we state the problem of diffusion-limited growth in continuum terms; this is known as the Stefan problem (see [3-6]). To fix our ideas, consider crystallization from a solution. Atoms in solution with density  $u(\mathbf{r}, t)$  diffuse until they reach the crystal, where they deposit. Then we have:

$$D\nabla^2 u = \partial u / \partial t \quad (1)$$

$$\partial u / \partial n \propto v_n. \quad (2)$$

That is,  $u$  should obey the diffusion equation;  $D$  is the diffusion constant. The normal growth velocity of the interface is proportional, on the average, to the flux onto the surface,  $\partial u / \partial n$ . It is useful to estimate the size of the term  $\partial u / \partial t$  by noting that if there is a typical velocity of growth,  $v$ , then  $\partial u / \partial t \sim v \partial u / \partial x$ . Now:

$$|\nabla^2 u| \approx (1/l) |\partial u / \partial x|$$

where  $l = D/v$ , the diffusion length, sets the scale for the diffusion field. In practical cases  $l$  is sometimes very much larger than the other scales in the problem, so that the right hand member of (1) can be neglected. In this case Eq. (1) reduces to the Laplace equation,

$$\nabla^2 u = 0 \quad (1')$$

and we can imagine that we are to solve an electrostatics problem and advance the surface proportional to the electric field at each point. This is called the *quasi-static* regime.

The remaining equation necessary to describe the Stefan problem is a boundary condition on the field,  $u$ , at the interface of the growing object, and far away. The latter value gives the overall scale to the problem. The most usual form adopted for the boundary condition on the interface is:

$$u_s = d_0 \kappa \quad (3)$$

where  $d_0$  is a length related to the surface tension, and  $\kappa$  is the curvature of the surface. In fact, it is necessary have some cutoff such as surface tension in the problem.

We ask then, a simple question: why do Equations (1-3) not simply describe a smooth surface which advances in time? In fact, if we start with a flat surface it does advance in time (with  $v \sim t^{-1/2}$ ) but this solution is not stable. The calculation of the spectrum of the instability is given in the standard references [3-6]. It is sufficient for our purposes to reason qualitatively. Suppose we start with a flat surface with a small bump (see Figure 3) and thus small curvature everywhere. Consider the electrostatic interpretation above. We are asked to find the potential,  $u$ , near a grounded conductor with a bump, and then advance the different parts of the surface a speed proportional to  $\partial u / \partial n|_s$ , the surface electric field. Now the field is largest near the bump, as is known in elementary electrostatics: this is the principle of the lightning rod. Thus the bump develops in time faster than the rest of the surface and get even sharper. In order to stabilize the growth other effects such as surface tension in fluid flow or crystal growth are necessary. And, clearly, these effects cannot stabilize large-scale instabilities. On some scale the surface must deform.

It is now known through the work of many groups [4, 5] that these equations in themselves cannot give rise to an *ordered* dendrite because each tip undergoes *tipsplitting*: many tipsplittings are visible in Fig. 1. In fact, the surface tension, and thus the parameter  $d_0$ , must be taken to be a function of the angle between the surface and, say, crystal axes in order to stabilize a tip. With anisotropy snowflake patterns resembling the tip of each branch of Figure 2 are the solutions to Equations (1) - (3). We will discuss this in more detail in the next section.

In the non-linear regime the instabilities and tipsplittings proliferate and mix. The result is usually fractal growth, at least in the quasi-static regime. This is considered in more detail in the third section.

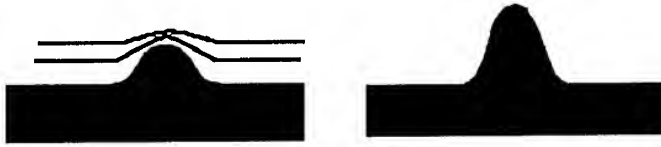


Figure 3. The Mullins-Sekerka instability. In the left hand picture equipotential lines are shown. Since they are crowded above the bump, it gets sharper.

## DENDRITIC GROWTH

The most commonly quoted experimental studies of orderly dendritic growth are those of the group of Glicksman [10] for thermal crystallization. In such growth each dendritic tip (e.g. the tips of the branches in Fig. 2) is approximately parabolic and translates in time with constant shape. Behind the tip the crystal sheds sidebranches. Many groups in the 1980's worked on understanding the shape of the tip and how it arises [3-5]. I will give here a brief overview of the current state of the problem.

We have seen that there is no stable plane solution of Equations (1-3). However, the experimental observations indicate that there is a non-trivial solution to the problem which is stable in a moving frame. In order to see this more clearly we can transcribe Eq. (1) into a reference frame moving with velocity,  $v$  in direction  $z$ :

$$\nabla^2 u + (1/l) \partial u / \partial z = \partial u / \partial t = 0. \quad (4)$$

Here, the last equality is the assumption of a fixed translating shape.

Now it is clearly reasonable to try to separate Equation 4 in parabolic coordinates. This was done by Ivantsov [11] who showed that a parabolic shape was a solution of Eq. (2) (3), (4) provided  $d_0$  in Eq. (3) is taken to be 0, that is, in the absence of surface tension. Since surface tension is, in some sense, a small perturbation on the problem, this seems a reasonable first step. The Ivantsov solution obeys a scaling law:

$$\rho/l = \rho v/D = f(\Delta) \sim \Delta^2 \quad (5)$$

where  $\rho$  is the radius of curvature of the parabolic tip, and  $\Delta$  the undercooling, i.e. the difference between the melting temperature and the temperature far from the crystal. The last result is for small  $\Delta$  and two dimensions. This law is reasonably well satisfied for real growing crystals.

However, crystals grow with a fixed  $v$  and  $\rho$ , whereas Eq. (5) only determines their product. Another scaling law originated in work by Langer [5]; for a simple argument, see the article by Pomeau and Ben-Amar in [3]. It takes the surface tension into account in an approximate way, and shows that:

$$\rho^2 v = \text{constant} = 2Dd_0/\sigma^* \quad (6)$$

The constant,  $\sigma^*$ , is expected to be of order unity, but in experiments it turns out to be quite small, of order 0.02. The origin of this small number is the subject of much work. In the view of this author, the most convincing candidate theory for explaining the solution to this

*velocity selection* problem is the microscopic solvability theory expounded in [3-5] which depends on crystalline anisotropy, as alluded to above.

On the experimental side, precise verifications of the scaling laws have been elusive, though there is no doubt that they are qualitatively correct. One reason for this is that thermal crystallization experiments are not purely diffusion-limited: thermal convection is inevitable. Glicksman, Koss, and Winsa [12, and also this conference] have performed a remarkable experiment in microgravity (in a space shuttle) which eliminates some of these effects. Analysis of this very recent data should settle many of the remaining problems with the theory.

## FRACTAL GROWTH AND DLA

In the absence of anisotropy, and in the quasi-static regime, nothing controls the proliferation of tip splittings, and, probably no steady state is possible. Instead a dynamic scaling structure arises which is very close to being a self-similar fractal. Many experimental patterns (e.g. Fig. 1) have this property: the pattern in Fig. 1 has a fractal dimension of approximately 1.7 [1].

The best-known examples such fractal patterns in diffusion-limited growth come from the body of numerical evidence surrounding the diffusion-limited aggregation (DLA) model of Witten and Sander [6, 13-14]. In this very simple computer model, we launch a random walker and allow it to wander until it attaches to a growing cluster. Then we launch another walker, and so on. DLA is a noisy version of the Stefan model. Eq. (1) governs the probability density for finding a walker, and for the slow growth of the computer simulations we should use Eq. (1'). The finite size of the walkers serves as a cutoff (albeit not of the form of surface tension). However, instead of equation (2), we have the condition that the *probability* of growth of a point is given by  $\partial u / \partial n$ . The patterns seem to be self-similar fractals with fractal dimension of 1.7 in two dimensions and strongly resemble Figure 1: see Figure 4. This is a rather small cluster with about 2000 particles.

After more than a decade of work on the DLA model, we are still far from a complete understanding of this kind of fractal growth. The model is surprisingly difficult to deal with. The remaining questions about the model are of two types: (1) Are the observed numerically generated patterns really self-similar fractals? (2) Can we understand how the model gives fractals (without doing simulations)?

### Numerical studies of DLA

Though it is clear that the pattern of Figure (4) and larger ones of the same type are approximately self-similar, it is far from clear whether there are deviations from this simple behavior. For example, Mandelbrot and collaborators [15] have discovered a remarkable fact about very large two-dimensional DLA clusters by doing simulations up to 40,000,000 particles. They rescale and then coarse-grain images of the clusters (by surrounding every cluster point by a finite neighborhood) and find that the larger clusters seem to fill space. If this is correct DLA clusters are not self-similar. In some sense the number of major branches grows with mass, and the cluster becomes more finely divided. This may be a cross-over effect, but if it is asymptotically true, it is a severe challenge for theory.

There is a very long-standing question of just how homogeneous DLA clusters are. For example, some authors [16] claim that DLA is self-affine, and not self-similar. Hegger and Grassberger [17] have returned to this problem recently and find evidence that the previous results came from a slow crossover, and that very large clusters are locally self-similar. This result is still controversial. What is clear from these two examples, and many others in the literature is that the DLA model exhibits a variety of subtle crossover effects, and is not as simple as we originally thought.



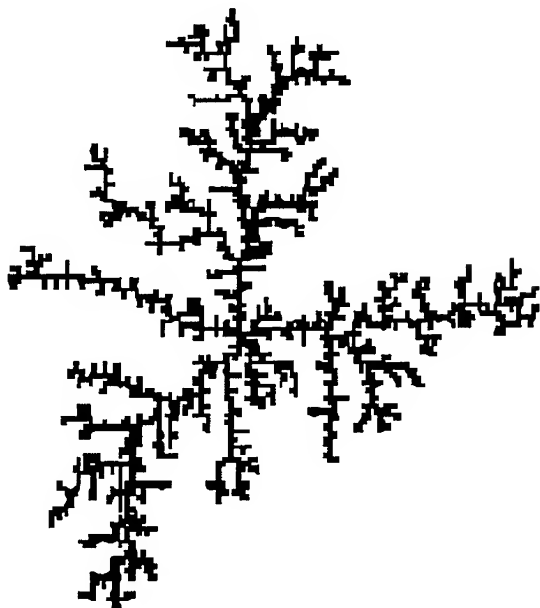


Figure 4. A small DLA cluster

#### Theory of DLA

After more a decade of frustration in formulating a theory for DLA, several groups now seem to have made substantial progress [18-20]. In my opinion, the most promising avenue is that of Halsey and co-workers [18, and also this conference] who focus on the tip-splitting event as the fundamental building block of a theory. Based on this, Halsey gives a renormalization treatment of branching processes which gives many of the observed features of DLA clusters, and which could answer some of the long-standing questions in the field.

#### **EXPERIMENTAL MANIFESTATIONS OF FRACTAL GROWTH**

DLA-like patterns occur quite commonly in nature [3, 6, 14]. When do we expect to see such behavior? We believe that the following qualitative picture is consistent the present evidence. First, we must be in a situation with diffusion length long compared to the size of the deposit. Also, since some kind of anisotropy is necessary to stabilize diffusive growth into a steady-state pattern, and suppress tip-splitting, anisotropy must either be absent, or too small to overcome the averaging effects of extrinsic noise present in the experiment. If that is the case tipsplittings proliferate and produce fractals. For example, suppose the crystal is polycrystalline, with no long-range correlation for the crystalline axes. This is the case [1] of the deposit of Figure 1: it is the formation of a polycrystalline deposit of GeSe<sub>2</sub> when an amorphous film rapidly crystallizes. In this case we observe well-defined DLA-like growths with fractal dimension  $\approx 1.67$ .

### Electrochemical deposition

Electrochemical deposition of metals is a special case of crystallization which has been studied in detail in recent years in the context of DLA. Suppose we consider an experiment in which metal is deposited on a cathode from an electrolytic solution, and the motion of the ions in solution is limited by diffusion. In this case we are dealing with an almost literal realization of the DLA model provided the electric field in the solution is not important for the motion of the ions over most of the bulk. This is the case in the experiments of Brady and Ball [21] who considered the electrodeposition of copper from  $\text{CuSO}_4$  and found fractal deposits.

In another set of experiments using flat electrochemical cells [22-25] the driving force for the motion of the ions is the electric field. The ions follow field lines on large scales. We can reinterpret  $u$  to be the electrostatic potential which obeys the Laplace equation for a conductor taken to be an equipotential and note that the deposit grows when an ohmic current arrives at the surface. Thus we seem to be back in the same situation as before, and in some cases DLA-like deposits were observed. However, this experiment is very complicated and there are many parasitic effects which complicate the interpretation. For example, the dendritic deposit of Fig. 2 was grown in the same cells under slightly different conditions. However, in recent years two French groups [26, 27, and also this conference] have done very careful work on this problem and seem to have sorted out many of the remaining difficulties.

### Island growth and diffusive instabilities in MBE experiments

In a deposition experiment to grow a thin film nucleation and island growth are the first step toward formation of a new layer. For low enough temperatures (for which the limiting step in island growth is adatom diffusion) islands form with the characteristic fractal morphology -- indeed this is one of the most beautiful examples of DLA in nature [28]. Rapid kink diffusion along the edge of the island serves as a smoothing process, as in any diffusive instability [6]. For larger coverages, and even for multilayer step flow growth Bales and Zangwill showed [29] that the diffusive instability of step edges persists provided the growth of a terrace is fed from only the bottom: this would occur in the presence of step edge barriers of the Ehrlich-Schwoebel type [30, 31]. Several groups have worked out the kinetics of the island size distribution [32-35, and this conference] in the subsequent development using these ingredients. The theories assume a given critical nucleus size for forming an island and then, with more or less detail, random diffusion and attachment, and are reasonably successful in describing the phenomenon.

Our group at Michigan has been interested in a novel effect in MBE growth [36-38] which is caused by a diffusive instability of a completely different type from the one we have considered so far. This is a *mounding* instability and it arises from the same physical effect as the step-edge instability discussed in the previous paragraph, namely the Ehrlich-Schwoebel barrier. We find in this case that a singular surface (i.e., a low index crystal face) is *unstable*, but that a vicinal surface with a miscut above a certain value is *stable* except for very small statistical roughening, and that the two cases are distinguished by a critical slope which depends on the growth conditions. In the unstable case the surface develops mounds which we identified experimentally and which occur in several different systems [39].

The physical reason for this is easy to understand in the limit of large barrier. When an atom lands on a terrace, it can only diffuse to attach to a step on the same level. This gives the in-plane diffusive instability for oncoming steps, but it also means that nucleation is favored on the tops of existing islands, and mounds form.

## SUMMARY

This brief overview of the diffusive instability is not intended to be a comprehensive review. Rather it is a personal view of a very large and exciting area and an introduction to some of the work that is included in this conference. I hope that, as such, it will be useful to readers.

This work was supported by NSF grant DMR 94-20335.

## REFERENCES

1. G. Radnoczi, T. Vicsek, L.M. Sander and D. Grier, Phys. Rev. A **35** Rapid Communications, 4012 (1987)
2. D. Grier, E. Ben-Jacob, R. Clarke and L.M. Sander, Phys. Rev. Lett. **56**, 1264 (1986).
3. *Solids Far From Equilibrium: Growth, Morphology and Defects*, C. Godereche, ed. (Cambridge University Press, 1991), articles by Caroli, Caroli, and Roulet, Pomeau and Ben-Amar, and Sander.
4. D. Kessler, J. Koplik, and H. Levine, Adv. in Phys., **37**, 255 (1988)
5. J.S. Langer, Rev. Mod. Phys. **52**, 1 (1980).
6. L.M. Sander, Nature **322**, 789 (1986).
7. F. Adams, K. Freese, and J. Langer, Phys. Rev. D **47**, 4303-8 (1993)
8. E. Ben-Jacob, O. Shochet, A. Tenenbaum, I. Cohen, A. Czirok, and T. Vicsek, Fractals **2**, 15 (1994).
9. W.W. Mullins and R. Sekerka, J. Appl. Phys. **28**, 333 (1957); J. Appl. Phys. **33**, 323 (1963)
10. See M. Glicksman and S. Marsh in *Handbook of Crystal Growth*, D. Hurler, ed. (Elsevier, 1993) **1**, p 1077.
11. G. Ivantsov, Dokl. Acad. Nauk. SSSR **58**, 56 (1947).
12. M. Glicksman, M. Koss, E. A. Winsa, Phys. Rev. Lett. **73**, 573 (1994)
13. T. A. Witten, and L. M. Sander, Phys. Rev. Lett. **47**, 1400 (1981); Phys. Rev. B **27**, 5686 (1983).
14. P. Meakin, in *Phase Transitions and Critical Phenomena*, **12**, C. Domb and J. Lebowitz, eds, (Academic, 1988).
15. B. Mandelbrot, Physica A **191**, 95 (1992)
16. P. Meakin and T. Vicsek, Phys. Rev. A **32**, 685 (1985)
17. R. Hegger and P. Grassberger Phys. Rev. Lett. **73**, 1672 (1994)
18. T. Halsey, Phys. Rev. Lett. **72**, 1228 (1994)
19. L. Pietronero, A. Erzan, and C. Evertsz, Phys. Rev. Lett. **61**, 861 (1988)
20. R. Barker, and R.C. Ball, Phys. Rev. A **42**, 6289 (1990)
21. R. Brady, R. and R. C. Ball, Nature **309**, 225 (1984)
22. M. Matsushita, M. Sano, M., Y. Hayakawa, H. Honjo, H., and Y. Sawada, Phys. Rev. Lett. **52**, 286 (1984).
23. D. Grier, E. Ben-Jacob, R. Clarke and L.M. Sander Phys. Rev. Lett. **56**, 1264 (1986).
24. Y. Sawada, A. Dougherty, J. Gollub, Phys. Rev. Lett. **56**, 1260 (1986)
25. J. Kaufman, C. Baker, A. Nazzari, A., M. Flickner, O. Melroy, and A. Kapitulnik, Phys. Rev. Lett. **56**, 1932 (1986)
26. A. Kuhn, F. Argoul, Phys. Rev. E **49**, 4298 (1994); A. Kuhn, A and F. Argoul, Fractals; **1**, 451-9; (1993)
27. V. Fleury, J.-N. Chazalviel, and M. Rosso, Phys. Rev. E **48**, 1279 (1993); V. Fleury, J.-N. Chazalviel, M. Rosso, and B. Sapoval, J. Electroanal. Chem. and Interfac. Electrochem. **290**, 249 (1990)
28. R.Q. Hwang, J. Schroder, C. Gunther, and R. J. Behm, Phys. Rev. Lett. **67**, 3279 (1991)

29. G. S. Bales and A. Zangwill, Phys. Rev. B **41**, 5500 (1991)
30. G. Ehrlich and F.G. Hudda, J. Chem. Phys., **44**, 1039 (1966)
31. R. L. Schwoebel R.L. and E. J. Shipsey J. Appl. Phys., **37**, 3682 (1966)
32. J.G. Amar, F. Family and P-M Lam in *Mechanisms of Thin Film Evolution*, MRS Proceedings **317**, 167 (1994)
33. M.C. Bartelt and J. W. Evans, Phys. Rev. B **46**, 12675 (1992)
34. L-H Tang, J. de Physique I **3**, 935 (1993)
35. C. Ratsch, A. Zangwill, P. Smilauer, and D.D. Vvedensky, Phys. Rev. Lett. **72**, 3194 (1994)
36. M.D. Johnson, C. Orme, A. W. Hunt, D. Graff, J. Sudijono, L. M. Sander, and B. G. Orr, Phys. Rev. Lett. **72**, 116 (1994)
37. A. W. Hunt, C. Orme, D. R. M. Williams, B. G. Orr, and L. M. Sander to appear in *Scale invariance, interfaces and non-equilibrium dynamics*, Proceedings of NATO ASI, Cambridge UK June 20-30, 1994
38. A.W. Hunt, C. Orme, D.R.M. Williams, B.G.Orr and L.M. Sander. Europhys. Lett. **27**, 611 (1994)
39. H-J Ernst, F. Fabre, R. Folkerts, R., and J. Lapujoulade, Phys. Rev. Lett., **72**, 112, (1994)

## DENDRITIC GROWTH IN TERRESTRIAL AND MICROGRAVITY CONDITIONS

M.E. GLICKSMAN\*, M.B. KOSS\*, L.T. BUSHNELL\*, J.C. LACOMBE\*  
AND E.A. WINSA\*\*

\*Materials Engineering Department, Rensselaer Polytechnic Institute, Troy, NY 12180-3590

\*\*Space Experiments Division, NASA Lewis Research Center, Cleveland, OH 44135.

### ABSTRACT

Dendritic growth is the most ubiquitous form of crystal growth encountered when metals and alloys solidify under low thermal gradients. The growth of thermal dendrites in pure melts is generally acknowledged to be controlled by the diffusive transport of latent heat from the moving crystal-melt interface into its supercooled melt. However, this formulation is incomplete, and the physics of an additional *selection* rule, coupled to the transport solution, is necessary to predict uniquely the dendrite tip velocity and radius of curvature as a function of the supercooling. Unfortunately, experimental confirmation or evidence is ambiguous, because dendritic growth can be severely complicated by buoyancy induced convection. Recent experiments performed in the microgravity environment of the space shuttle Columbia (STS-62) quantitatively show that convection alters tip velocities and radii of curvature of succinonitrile (SCN) dendrites. In addition, these data can be used to evaluate how well the Ivantsov diffusion solution, coupled to a scaling constant, matches the dendritic growth data under microgravity conditions.

### INTRODUCTION

The growth of dendrites is the ubiquitous mode of solidification encountered when metals and alloys solidify under low thermal gradients, as in most casting and welding processes. Furthermore, in engineering materials, the details of the dendritic morphology is directly related to various material responses, such as hot cracking, toughness, and corrosion. Although, the effects of the initial dendritic microstructure can be modified by subsequent heat treatments, the final material properties are generally dependent on the details of the original dendritic microstructure. Dendritic growth is also of interest as an archetype problem in morphogenesis where a complex pattern evolves from simple starting conditions, such as in a structureless liquid. Thus both the physical understanding and mathematical description (particularly of the dendrite's tip velocity,  $V$ , and radius of curvature,  $R$ , as a function of the supercooling,  $\Delta T$ ) of how dendritic patterns emerge during the growth process are of fundamental interest to both scientists and engineers.

A number of theories of dendritic crystal growth, based on various transport mechanisms, physical assumptions, and mathematical approximations, have been developed over the last forty years (see the review by one of the authors [1]). Concurrently, a great deal of experimental work growing, photographing, and measuring dendrites has been performed. Succinonitrile (SCN: the chemical formula for which is  $\text{NC}-(\text{CH}_2)_2-\text{CN}$ ) because of its conveniently low melting temperature, optical transparency, and well-characterized thermophysical properties [2,3] has been used as a model dendritic growth system in many of these experiments.

Unfortunately, as Glicksman and Huang showed [4], gravity induced convection dominates dendritic growth in the lower supercooling range, which confounds the analysis based on diffusive heat transfer. There has been some analysis estimating the effects of natural or forced convection on dendritic growth [5-7], but such analysis is coupled to yet unproven elements of dendritic growth theory, and, consequently can not provide an independent test of theory. In the higher supercooling range the morphological structure becomes too small, and grows too fast, which makes accurate experimental calculation unfeasible at this time.

To date, the large body of experimental evidence gathered on SCN and other suitable test materials, neither serves to confirm or deny dendritic growth theories. The experimental situation, simply stated, was that there appeared to be too narrow a range of supercoolings in any crystal-melt system thus far studied terrestrially that remains *both* free of convection effects, and permits the accurate determination of the dendrite tip radius of curvature.

Thus, a low-gravity dendritic growth experiment was proposed to measure definitively the kinetics and morphology of dendritic growth, and to measure the effects of natural convection on dendritic growth. Such a test requires that a single, clearly defined experimental parameter, viz., the supercooling, fully determine the resulting steady-state dendritic growth velocity,  $V$ , and tip size,  $R$ . NASA's Microgravity Science and Application Division supported the development of a critical microgravity space flight experiment to evaluate dendritic growth theories [8-10]. Designated the Isothermal Dendritic Growth Experiment (IDGE), the first flight, manifested on the United States Microgravity Payload-2 (USMP-2) mission, was launched and operated on the Space Transportation System-62 (STS-62) on March 4 - 14, 1994. The IDGE enabled the acquisition of accurate dendritic growth speed and morphology data under diffusion-controlled conditions, while greatly reducing buoyancy-induced convective heat transport through the reduction of gravity [11].

In this paper we briefly outline theories of dendritic crystal growth based on heat diffusion for the purpose of highlighting the still open questions of what constitutes the operating dynamical state that controls the scaling laws among growth speed, microstructural lengthscales, and supercooling. Following that we will describe the chief operating features and data reduction capabilities of the IDGE. We will conclude with a discussion of the up-to-date results from the first flight of the IDGE.

## BACKGROUND ON DENDRITIC GROWTH

The growth of dendrites in pure melts is generally acknowledged to be fundamentally rate controlled by the transport of latent heat from the moving crystal-melt interface as it advances into its supercooled melt. At the resolution of dendritic growth experiments, this growth is continuous.

A mathematical solution to the dendritic heat diffusion problem was first analyzed by Ivantsov [12], who modeled the dendrite as a paraboloidal body of revolution, growing at a constant velocity,  $V$ . The resultant thermal diffusion field can be expressed mathematically and exactly in paraboloidal coordinates moving with the dendritic tip,

$$\Delta \Theta = \text{Pe} \, e^{\text{Pe}} \text{Ei}(\text{Pe}) = \text{Iv}(\text{Pe}). \quad (1)$$

In this formulation,  $\text{Iv}(\text{Pe})$  is identified as the Ivantsov function, where

$$\Delta\Theta = \frac{\Delta T}{(l/c_p)}, \quad (2)$$

is the non-dimensional scaled supercooling,  $Pe$  is the growth Péclet number,

$$Pe = \frac{VR}{2\alpha} \equiv Iv^{-1}(\Delta\Theta), \quad (3)$$

and  $Ei(Pe)$  is the first exponential integral function. In these equations,  $\Delta T$  is the applied supercooling,  $l$  is the molar latent heat,  $c_p$  is the constant pressure molar specific heat,  $V$  is the dendrite tip velocity,  $R$  is the dendrite tip paraboloidal radius of curvature,  $\alpha$  is the thermal diffusivity of the melt phase, and  $Iv^{-1}(\Delta\Theta)$  is a formal representation of the inverse of the Ivantsov function, which can not be expressed in terms of known functions.

This diffusion solution is, however, incomplete, insofar as it specifies the tip growth Péclet number,  $VR/2\alpha$ , as a function of the supercooling, and not the explicit dynamic operating state,  $V$ , and  $R$ , explicitly. The Péclet number obtained from the Ivantsov solution for each specified supercooling, yields instead an infinite manifold of  $V$ , and  $R$ , ordered pairs  $(V, R)$ , that satisfy the diffusion solution at that particular value of  $\Delta T$ . The driving force alone does not completely describe the operating state. However, experimentally, one finds that unique, steady, operating states  $(V_{exp}, R_{exp})$  are observed at any specified supercooling,  $\Delta T$ . Considerable theoretical efforts within the physics community have been directed to answering the question as to whether and under what conditions a second equation or length scale exists, which, when combined with the Ivantsov diffusion solution, selects the unique (i.e., observed) dynamic operating state [1,13-16].

This effort has in a large part been shaped by the observations that for several materials undergoing unconstrained dendritic growth,  $VR^2$ , is constant or very weakly varying as a function of the supercooling. Two of the candidates for the additional crystal growth physics that provide the second crucial equation are the solid-melt interfacial energy, the temperature fluctuations in the melt, or both. Furthermore, the scaling equation derived from these additional physical considerations may be based on several different dynamical considerations, such as morphological stability, microscopic solvability, shape anisotropy, noise amplification, trapped waves, etc. Although the underlying mechanisms, or even the physics, for these "theories of the second length scale" might in fact be quite different, their results are often encapsulated with a scaling constant

$$\sigma^* = \frac{2\alpha d_o}{VR^2}. \quad (4)$$

Here,  $\sigma^*$  is usually referred to as the stability, selection, or scaling constant, and  $d_o$  is the capillary lengthscale, a material parameter defined as,

$$d_o = \frac{T_m \gamma_c}{l^2}, \quad (5)$$

where  $T_m$  is the equilibrium temperature of the crystal-melt interface energy. Solving eqn. 3 and 4 for  $V$  and  $R$  yields,

$$V = \frac{2\alpha\sigma^* \text{Iv}^{-2}(\Delta T)}{d_o}, \quad (6)$$

and,

$$R = \frac{d_o}{\sigma^* \text{Iv}^{-1}(\Delta T)}, \quad (7)$$

where now,  $V$  and  $R$  are unique and independent functions of the supercooling.

## IDGE FLIGHT APPARATUS AND PROCEDURES

The techniques for accomplishing simultaneous kinetic and morphological measurements for SCN dendrites are well established [2,3]. However, the constraints of an autonomous, or tele-operational, microgravity experiment require extensive modifications of established ground-based laboratory techniques [9,10,17]. This is most evident in the design and construction of the flight growth chamber, which is physically and metaphorically central to the operation of the IDGE apparatus.

### Growth Chamber

In order to withstand the 5 g<sub>o</sub> launch acceleration, and the other rigors of space flight, a delicate all glass laboratory growth chamber was replaced with a more rugged combination of glass and metal. The flight chamber provides an unobstructed view of the growing dendrites through four windows, set perpendicularly, which allow for stereographic correction. This type of chamber requires that the dendrites grow within the field of view of the windows. This requirement is accomplished by providing a thin capillary injector tube, called the stinger. Dendritic growth is initiated by energizing thermoelectric coolers attached to one end of the stinger. The other end of the stinger, where the dendrite emerges in the center of the chamber, is notched, much like the tip of a fountain pen. This helps isolate the leading dendrite and reduces the time needed until the leading dendrite is isothermal and has achieved steady state.

Two stable thermistors (the second thermistor is redundant) monitor the temperature inside the chamber. The phase change volume expansion and the thermal expansion of the melt are compensated by a stainless steel bellows which prevents stray vapor cavities from forming and overpressuring the growth chamber. The growth chamber is sealed under vacuum, and the external pressure is transmitted through the bellows from the thermostatic bath is sufficient to prevent any free surface formation due to cavitation. The attachment of all components, joints and seals used in the growth chamber that come in contact with SCN, employs autogenous electron beam welds. This joining method preserves the purity of the SCN from contamination by avoiding the introduction of any solder, fluxes, elastomers, or other alloying components that could contaminate the SCN [17].

The growth chamber is mounted inside a temperature controlled tank or thermostat inside



an Experiment Apparatus Container (EAC). Also inside the EAC is, the modified shadowgraphic optic and photographic system, the dendrite growth detection system utilizing optic ram chips, and the control electronics. The inner pressurized vessel of the EAC is controlled in an atmosphere of moist nitrogen at 15 psia and 25 C. The temperature control tank is filled with a mixture of ethylene glycol and water in a proportion such that its index of refraction matches that of molten SCN. Index matching enhances the capability of the optic system. Two heaters (one redundant) and a rotating propeller permit temperature control to the desired level (within 2 mK of the set point) both temporally and spatially. All control, including data acquisition is performed by on-board computers.

#### Flight Experiment Procedure

The IDGE flight experiment was divided into 60 operational cycles. The first cycle, the warm up cycle, consists of bringing the system up to the operational temperature where all system components are checked and initialized. Also, the purity of the SCN test specimen was confirmed by examining the flatness of the melting plateau. The second cycle measured the liquidus temperature of the SCN as a calibration point from which all subsequent supercoolings are measured. The remaining cycles were dendritic growth cycles where dendrites are grown and photographed at varying supercoolings.

For each dendritic growth cycle, the thermostatic bath is heated to over 3 K above the SCN melting temperature. The bath is maintained at this elevated temperature until the SCN inside the chamber reaches, and becomes stable, at this temperature. This insures that all the SCN in the chamber is melted. The bath temperature is then reduced to the temperature that will produce the desired supercooling in the SCN. After the SCN has cooled and stabilized at the prescribed supercooling, thermoelectric coolers initiate solidification at the capped end of the stinger. The solidifying SCN grows down the inside wall of the stinger until it emerges from the stinger in the center of the growth chamber, which is still spatially uniform at the prescribed supercooling.

#### Velocity and Radius Measurements

Typically, the dendrite undergoes a short transient growth phase until it achieves a steady-state growth velocity, which is maintained until the dendrite starts to interact with the growth chamber walls. When the dendrite is auto-detected as it emerges from the stinger, the 35mm photographic timing sequence, and the SSTV image capture and transmission sequence, start concurrently. For each image, 35mm photonegative or SSTV image, the position of the dendrite tip, and the associated time is recorded. We calculate the dendritic velocity by calculating the slope of the displacement-time curve from the steady-state regime of the growth cycle. The velocity is then adjusted by stereographic and magnification factors. This yields velocity measurements accurate to better than 2%.

The overall experimental task of measuring the size and shape of steady-state dendritic crystals tips is not a trivial one. This is evidenced by noting that the typical experimental uncertainty encountered in laboratory-based tip radii measurements is typically +/- 10%. The details of our methods are described elsewhere [18,19]. In summary, we digitize the image, locate the solid-liquid interface, which is reduced to a list of ordered pairs that define the dendrite edge. We then regress

the data describing the dendrite edge profile to an equation for the model of a dendrite, from which it is straightforward to calculate the radius of curvature at the tip. We believe that our tip radii data are accurate to within 5% at supercoolings up to 1.0 K.

## EXPERIMENTAL RESULTS AND DISCUSSION

The Isothermal Dendritic Growth Experiment (IDGE), as one of four experiments comprising the second United States Microgravity Payload Mission (USMP-2), was launched on March 4, 1994, to a low-Earth circular orbit of approximately 163 nautical miles in the payload bay of the space shuttle Columbia (STS-62). The IDGE, operated for over 9 days at an ambient quasi-static acceleration environment of approximately  $0.7 \mu g$ .

### Velocity and Radius Data

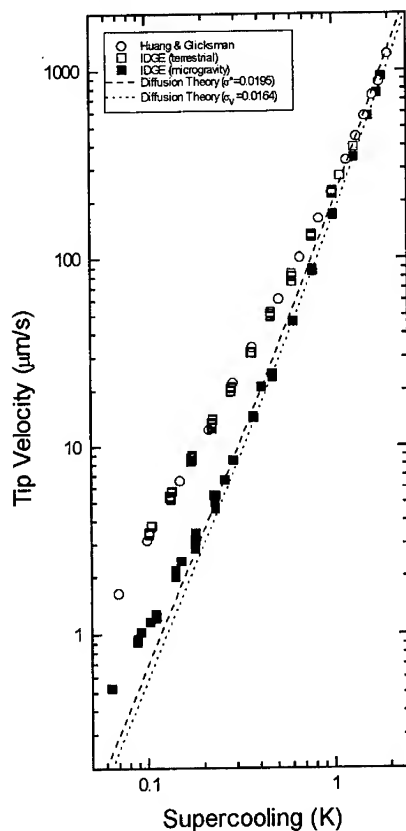


Figure 1. Steady-state dendrite tip velocity versus supercooling in both terrestrial and microgravity conditions.

Fig. 1 contains a plot of three sets of dendritic growth data: 1) IDGE velocities measured terrestrially with the flight instrument, using the same SCN sample that was flown; 2) the terrestrial data set of Huang/Glicksman [3]; and 3) the on-orbit velocity data from USMP-2. In addition, we show as the dashed curve, a theoretical velocity calculation generated from eqn. 6, using the scaling constant  $\sigma^*=0.0195$ , which happens to be the experimentally determined value of the scaling law at large supercoolings in both microgravity and terrestrial gravity. We show as the dotted curve, a theoretical velocity calculation, also generated from eqn. 6, this time using the scaling constant as an adjustable parameter,  $\sigma_v$ , to fit the microgravity velocity measurements over the upper range of these experiments where diffusion-limited growth seems justified.

The two ground-based data sets are in close agreement over the entire supercooling range. Thus, the differences between these two data sets, arising from different chamber size and shape, different SCN specimen, and different eulerian angles of the [100] growth direction with respect to gravity (restricted here to within 45 degrees of the stinger axis), have little effect on the velocity data. In addition, fig. 1 shows dramatic differences,

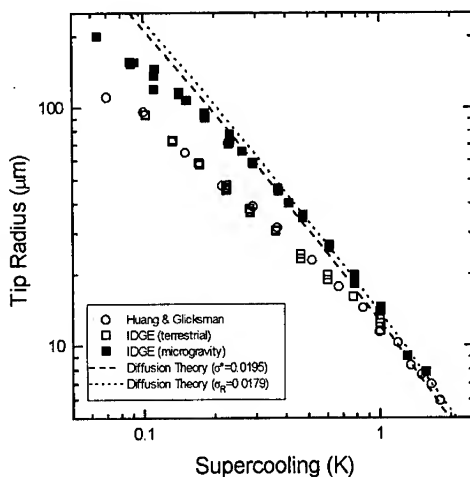


Figure 2. Steady-state dendrite tip radius of curvature versus supercooling in both terrestrial and microgravity conditions.

$\mu g_0$  has a significant, and eventually dominant, effect on dendritic growth. Thus, even in microgravity, at sufficiently low supercoolings, convection effects substantially alter the growth velocity from what is expected by heat diffusion alone.

The velocity calculations with  $\sigma_v$  are in excellent agreement with the microgravity data over range of supercoolings from 0.47 K to 1.7 K. Thus, these velocity data show that this supercooling range is where one must test dendritic growth theories describing diffusion limited heat flow as the driving force of solidification. In this supercooling range, however, a 15% difference between  $\sigma^*$  and  $\sigma_v$  clearly demonstrates that the Ivantsov function combined with a scaling rule, *is not correct*.

Fig. 2 also contains a plot of three sets of dendritic growth data: 1) IDGE radii measured terrestrially with the flight instrument, using the same SCN sample that was flown; 2) the terrestrial data set of Huang/Glicksman; and 3) the on-orbit radii data from USMP-2. Similar to the discussion in fig. 1, we show as the dashed curve, a theoretical radii calculation generated from the eqn. 7, using the scaling constant  $\sigma^* = 0.0195$ , and a dotted curve, the theoretical velocity calculation with  $\sigma_R$  as the adjustable scaling constant fit to the microgravity radii measurements over the supercooling range from 0.47 K to 1.57 K. The discussion of the radii results parallels that of the velocity data except that here the difference is between  $\sigma^*$  and  $\sigma_R$ , and is only just over 8%. The differences between  $\sigma_v$  and  $\sigma_R$  as compared to  $\sigma^*$  are a matter of definition. This is clear if you substitute eqns. 6 and 7 into eqn. 4, which yields,

$$\sigma^* = \frac{\sigma_R^2}{\sigma_v} = 0.0195. \quad (8)$$

particularly at the lower supercoolings, between terrestrial and microgravity conditions. At about 1.7 K there appears to be a small reduction in the growth velocity under microgravity conditions as compared to terrestrial conditions. This reduction in velocity is clear at 1.3 K, where the velocity measured in microgravity is approximately 30% lower than the terrestrial data. Clearly, these particular results show that there are substantial convective effects, at 1  $g_0$ , even at the higher supercoolings.

One can also see, in fig. 1, that using one adjustable parameter,  $\sigma_v$ , with the Ivantsov diffusion solution, can not fit the microgravity velocity measurements over the entire range of supercooling. We believe that at supercoolings of approximately 0.47 K and below, the quasi-static residual microgravity level of approximately 0.7

### Péclet Number and $\sigma^*$ Data

The failure of Ivantsov's solution, combined with a scaling rule, to describe the diffusion limited growth regime becomes apparent from the plot of the Péclet number data. Fig. 3, as in Figs. 1 and 2, shows three sets of dendritic growth data: 1) IDGE Péclet number measured terrestrially with the flight instrument; 2) the terrestrial data set of Huang/Glicksman; and 3) the on-orbit Péclet number data from USMP-2. The dashed curve is the theoretical Péclet number calculated from eqn. 1. This theory line uses *no* adjustable parameters. The two measured terrestrial data sets are in close agreement. The microgravity measured data set is dramatically reduced from the terrestrial data, and the microgravity data is slightly, but clearly and systematically lower than the Ivantsov curve in the diffusion limited regime.

Since without microgravity experimentation, it was not possible to decouple the Ivantsov and scaling rule components of dendritic growth theory, this is to our knowledge, the first clear evidence that the Ivantsov formulation does not accurately describe dendritic growth. The level

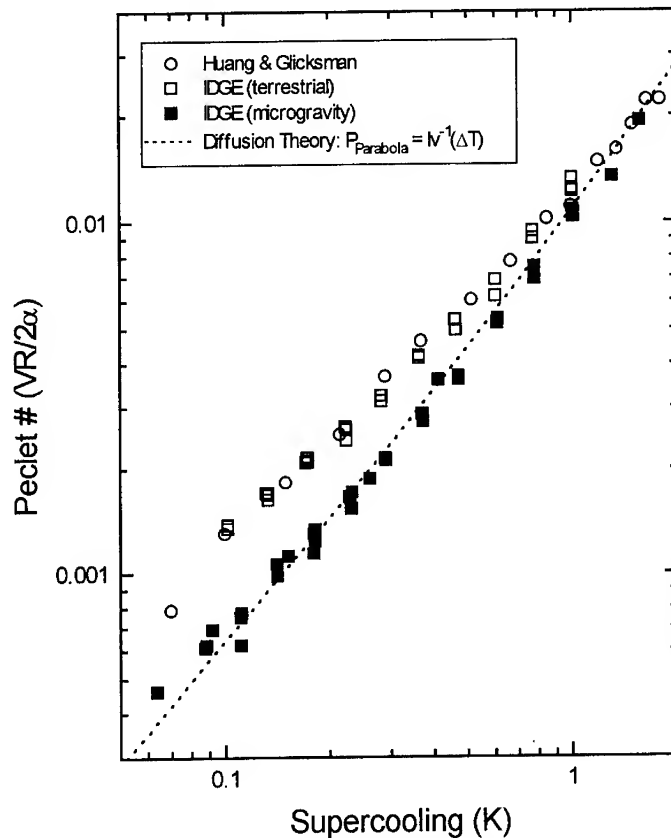


Figure 3. Dendrite tip Péclet number versus supercooling in both terrestrial and microgravity conditions.

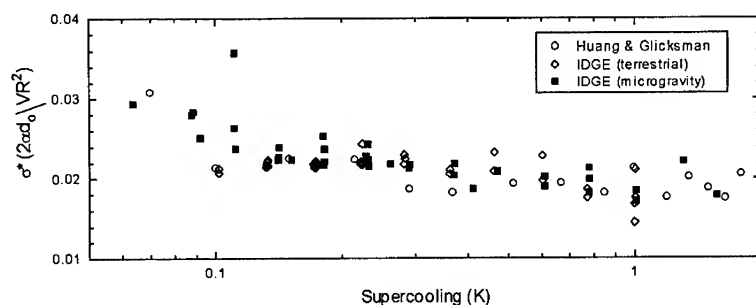


Figure 4. Dendrite tip scaling constant,  $\sigma^*$ , versus supercooling in both terrestrial and microgravity conditions.

of agreement between the theory and the data indicates that dendritic growth is properly governed by the diffusion of latent heat from the crystal-melt interface, but that the Ivantsov formulation is in need of some modification.

We offer here two possible explanations for this apparent deficiency in the Ivantsov solution. The first is that the diffusion field described by eqn. 1 is based on the dendrite tip which is a paraboloid of revolution, which is only true only near the tip itself. In addition, it has also been assumed that all the applied supercooling is associated with the diffusive field. If a portion of this temperature drop must be related to the "creation" of interfacial energy as the dendrite grows, the value of the supercooling used to plot the data in fig. 3 is high, and the data would need to be shifted to the left. Although neither of these explanations have yet to be examined quantitatively, both are consistent with the current microgravity data.

Although the Ivantsov component to dendritic growth theory is in need of modification, it is still instructive to examine the scaling law data. Fig. 4 shows three sets of  $\sigma^*$  data; the two terrestrial data sets, and the one microgravity data set. The scatter, both within and among the three data sets, make definitive conclusions very difficult at this time. However, it is striking that all the data, both in terrestrial and microgravity conditions, agree over almost the entire supercooling range. There also appears to be a trend where  $\sigma^*$  increases inversely with supercooling. In the diffusion-limited regime only, the microgravity  $\sigma^*$  data is ambiguous. The difficulty is that if  $\sigma^*$  does have a dependence on supercooling in this regime, that dependence is rather weak. Thus, assuming  $\sigma^*$  is constant over this limited supercooling range would only introduce a slight error in any quantity that depends on  $\sigma^*$ . Furthermore, this error would be hard to detect in a data set with uncertainties on the order of 10%. The familiar task of separating the signal from the noise is not a trivial one, either experimentally or analytically, and is an ongoing endeavor at this time.

## SUMMARY AND CONCLUSIONS

We measured the dendritic tip growth velocities and radii of curvature of succinonitrile in microgravity using the IDGE instrument mounted on the USMP-2 platform in the payload bay of the space shuttle Columbia (STS-62), March 4 - 14, 1994. The on-orbit data when compared to terrestrial dendritic growth data, demonstrate that: 1) Convective effects under terrestrial conditions

are dramatic at the lower supercoolings, and remain significant even up to 1.7K supercooling. 2) In the supercooling range from 0.47 K to 1.7 K, the data are convective free and can be used as a benchmark for examining diffusion-limited dendritic growth theories. 3) A diffusion solution to the dendrite problem, combined with the measured scaling constant,  $\sigma^*$ , does not yields growth velocity and radius predictions consistent with the observed dendritic growth velocities and radii as a function of supercooling. 4) The failure of this formulation is chiefly attributed to the failure of the Ivantsov diffusion solution which describes the overall dependence of Pe on supercooling, but predicts a higher value than the data in the diffusion-limited regime. The further analysis of IDGE data sets, particular the microgravity Pe and  $\sigma^*$  data sets, are continuing.

## ACKNOWLEDGEMENTS

Special thanks are due for the continuing interest, and financial support provided by the NASA, Life and Microgravity Sciences and Application Division, (Code U), Washington, DC, under Contract NAS3-25368, with liaison provided through the Space Experiments Division at NASA Lewis Research Center, Cleveland, OH.

## REFERENCES

1. M.E. Glicksman and S.P. Marsh, "The Dendrite", in Handbook of Crystal Growth, , ed. D.J.T. Hurle, (Elsevier Science Publishers B.V., Amsterdam, 1993), Vol 1b, p.1077.
2. M.E. Glicksman, R.J. Schaefer, and J.D. Ayers, Met. Trans. A, 7A, 1747, (1976).
3. S.C. Huang and M.E. Glicksman, Acta Metall., 29, 701, (1981).
4. M.E. Glicksman and S.C. Huang, Convective Transport and Instability Phenomena, ed. Zierp and Ortel, Karlsruhe, (1982), 557.
5. R. Ananth and W.N. Gill, Chem. Eng. Comm., 68, 1, (1988).
6. R. Ananth and W.N. Gill, J. Crystal Growth, 91, 587, (1988).
7. R. Ananth and W.N. Gill, J. Crystal Growth, 108, 173, (1991).
8. J. Robert Schrieffer, review of *Microgravity Science and Applications Flight Programs* (University Space Research Association, Washington, DC 1987).
9. M.E. Glicksman, et al., Met. Trans. A, 19A, 1945, (1988).
10. M.E. Glicksman, et al., Advances in Space Research, 11, 53, (1991).
11. M.E. Glicksman, M.B. Koss, and E.A. Winsa, Phys. Rev. Lett., 73, 573, (1994).
12. G.P. Ivantsov, Dokl. Akad. Nauk, USSR, 58, 56, (1947).
13. J.S. Langer and H. Muller-Krumbhaar, Acta Metall., 26, 1681, 1689, and 1697, (1978).
14. D. Kessler, J. Koplik, and H. Levine, Phys. Rev. A, 34, 4980 (1986).
15. Y. Miyata, M.E. Glicksman, and T.H. Tirmizi, J. Crystal Growth, 112, 683, (1991)
16. E.A. Brener and V.I. Mel'nikov, Adv. Phys. 40, 53, (1991).
17. E.R. Rubinstein, S.H. Tirmizi, and M.E. Glicksman, J. Crystal Growth, 106, 89, (1990).
18. M.E. Glicksman, et al., J. Crystal Growth, 137, 1, (1994).
19. J.C. LaCombe, M.B. Koss, and M.E. Glicksman, (article in preparation for submittal to Phys. Rev. E).

## DIFFUSION-LIMITED AGGREGATION AS BRANCHED GROWTH

THOMAS C. HALSEY\*

\* Exxon Research and Engineering, Route 22 East, Annandale, NJ 08801

### ABSTRACT

I present a first-principles theory of diffusion-limited aggregation in two dimensions. A renormalized mean-field approximation gives the form of the unstable manifold for branch competition, following the method of Halsey and Leibig [Phys. Rev. A **46**, 7793 (1992)]. This leads to a result for the cluster dimensionality,  $D \approx 1.66$ , which is close to numerically obtained values. Quenched and annealed multifractal dimensions can also be computed in this theory; the multifractal dimension  $\tau(3) = D$ , in agreement with a proposed "electrostatic" scaling law.

### INTRODUCTION

Diffusion-limited aggregation (DLA) is a model of pattern formation in which clusters grow by the accretion of successive random walkers.<sup>1</sup> Each random walker arrives from infinity, and sticks to the growing cluster at whichever surface point it first contacts. Only after the accretion of a walker does the next walker commence its approach to the cluster. The clusters thereby obtained are fractal in all dimensionalities  $d > 1$ , and are qualitatively and/or quantitatively similar to patterns observed in such diverse phenomena as colloidal aggregation, electrodeposition, viscous fingering, and dielectric breakdown.<sup>2</sup>

At the heart of the problem of diffusion-limited aggregation is the following question: what is the relationship between the scale-invariance of the diffusive growth process and the hierarchical structure of the clusters generated by this process?<sup>3</sup> We have proposed that the quantitative process by which one branch screens, i.e., takes growth probability from, a neighboring branch, has a specific form, independent of the length scale on which this process takes place.<sup>4</sup> This assumption allows the development of a qualitatively correct theory, which yields multifractal scaling of growth probability, as well as agreement with a phenomenological scaling law, the "Turkevich-Scher" law, relating the scaling of the maximum growth probability over all sites on the cluster to the dimension of the cluster as a whole.<sup>5</sup> In addition, a renormalization group (RG) computation of the branch competition dynamics, to be reviewed below, allows *quantitative* computation of the fractal properties of DLA clusters in two dimensions.

This RG approach is based upon a mean-field approximation which is implemented on all length scales. Thus, it is perhaps better to regard this theory as an *ansatz* solution in which certain types of fluctuations on all length scales are neglected, while others are included. The result obtained for the dimensionality of the cluster in spatial dimensionality  $d = 2$ ,  $D = 1.66$ , is within 3% of the oft-quoted value  $D = 1.71$  obtained from the scaling of the cluster radius-of-gyration in numerical studies. An additional scaling law (the "electrostatic scaling law"), relating the multifractal exponent  $\tau(3)$  of the growth measure to the dimensionality  $D$  by  $D = \tau(3)$ , is exact within this theory.<sup>6</sup>

## DYNAMICS OF BRANCH COMPETITION

In the growth process, each particle attaches itself to a unique “parent” particle in the pre-existing cluster. Furthermore, the cluster is observed to be a branched structure, with no loops and with each particle having asymptotically zero, one or two “children”, i.e. particles to whom it stands as a parent.<sup>7</sup> Very rarely particles have more than two children; primarily for reasons of convenience I neglect this possibility.

Consider a particle with two children. Each of the two children separately, with all particles descended from each, I term a “branch”. Thus these two-child particles are parents of two branches, which occupy neighboring regions of space. The total number of particles in one branch I term  $n_1$ , and the total in the other  $n_2$ . The total number of descendants of the parent particle is thus  $n_b \equiv n_1 + n_2$ . Now consider the next particle to accrete to the cluster. I say that this particle has a probability  $p_1$  to stick anywhere on the first branch, and a probability  $p_2$  to stick anywhere on the second branch, yielding a total probability  $p_b \equiv p_1 + p_2$  to strike either of these two branches.

Let us now consider the normalized quantities  $x = p_1/p_b$  and  $y = n_1/n_b$ . Clearly  $dn_1/dn = p_1$ , where  $n$  is the total number of particles in the cluster, and we are neglecting fluctuations of  $O(1/\sqrt{n_b})$ . Thus  $y$  obeys the following equation of motion:

$$\frac{dy}{d \ln n_b} = x - y. \quad (1)$$

The right-hand side of this equation is a function only of  $x$  and  $y$ . Now  $x$  will obey an equation of the form

$$\frac{dx}{d \ln n_b} = G(x, y; n_b; \{\phi_i\}), \quad (2)$$

where  $\{\phi_i\}$  is some parameterization of all of the other variables describing the structure of the cluster. Suppose that by averaging the right-hand side of this equation over these parameters  $\{\phi_i\}$ , one obtains  $dx/d \ln n_b = g(x, y)$ , where the right-hand side is now only a function of  $x$  and  $y$ . Given this function  $g(x, y)$ , one then has a closed system of equations describing the evolution of  $x$  and  $y$  as functions of  $\ln n_b$ . Note that it is crucial that this averaging process should leave no residual dependence upon  $n_b$ , or else  $g(x, y)$  will vary as the branches grow.

By symmetry,  $g(x, y) = -g(1 - x, 1 - y)$ , so  $(x, y) = (1/2, 1/2)$  must be a fixed point of this process of competition between the two branches. On general grounds, it is possible to argue that this fixed point is hyperbolic, with the unstable manifold emerging from the fixed point terminating in two stable fixed points at  $(x, y) = (0, 0)$  or  $(x, y) = (1, 1)$ , these latter representing the situation in which one branch has been completely screened by the other.<sup>4</sup> This assumption will be explicitly verified in the calculation below.

If the central fixed point at  $(x, y) = (1/2, 1/2)$  is hyperbolic, then branch pairs which commence their existence (with  $n_b \sim 1$ ) near the unstable fixed point will be quickly drawn onto the unstable manifold (Figure 1). Linearizing the system of equations for



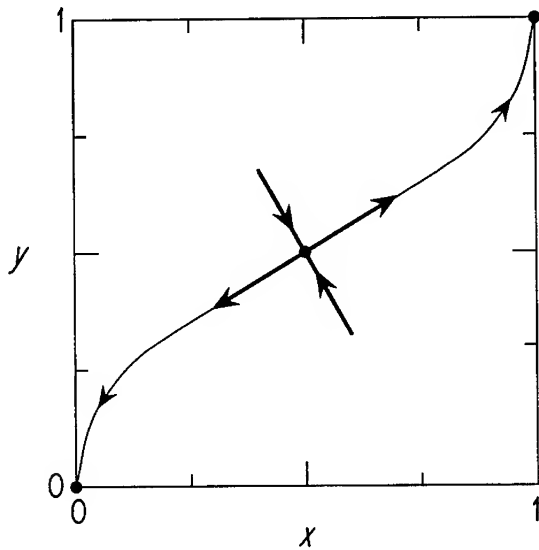


Figure 1. This diagram shows our model for the competition dynamics of two neighboring branches. The  $x$ -axis measures the relative growth probabilities of the two branches,  $x = p_1/(p_1 + p_2)$ , and the  $y$ -axis measures the relative masses of the two branches,  $y = n_1/(n_1 + n_2)$ . The development of these two quantities as functions of  $n_b = n_1 + n_2$  can be represented in this diagram. The fixed point at the center represents equal branches, the two fixed points at the corners represent branch pairs in which one branch completely dominates the other. At the central fixed point, we expect one stable and one unstable eigenvector.

$d(x, y)/d \ln n_b$  about the central fixed point, the hyperbolic assumption implies that there will be a stable and an unstable direction; the eigenvalue corresponding to the latter direction we define to be  $\nu$ .

#### Stochastic Nature of Tip-Splitting

When a pair of branches is first created by a tip-splitting event, its initial growth up to the stage at which  $n_b \gg 1$  is determined by complicated microscopic dynamics, which do not recognize the existence of the unstable fixed point. Thus we expect the probability that a newly created branch pair will be a distance  $\epsilon^\nu$  (projected along the unstable manifold) from the unstable fixed point will be  $\rho(\epsilon \ll 1)d\epsilon \propto \epsilon^{\nu-1}d\epsilon$ ; we are assuming a constant probability density of branch creation near the unstable fixed point. This assumption has been specifically verified by numerical study.<sup>4</sup> The choice of  $\epsilon^\nu$  for this initial distance

insures that position along the unstable manifold in the  $x - y$  plane can be parameterized by the product variable  $\epsilon n$ , due to the form of the evolution equations for  $x$  and  $y$ .

#### Branch Competition and Fractal Dimensionality

It is possible to relate the eigenvalue  $\nu$  to the cluster dimensionality  $D$  by the following argument. Consider the strongest branch in the cluster, that obtained by always following the stronger child (with the larger values of  $x, y$ ) at each branching. The total number of side-branches (or branch points) from such a branch is  $\sim r$ , where  $r$  is the cluster radius. In order that the cluster have a dimension  $D > 1$ , a number  $\sim 1$  of these side branches must have a total number of particles  $\sim n$ , the total number in the cluster. A side branch obeying this criterion must have  $\epsilon n \sim 1$ , so that at that branching, both descendant branches are roughly equal in size. The probability of this happening at any particular branching is  $\int \epsilon^{-1} d\epsilon \rho(\epsilon) \propto n^\nu$ , and there are  $\sim r$  different sidebranchings at which this might occur. Thus  $rn^\nu \sim 1$ , or  $D = 1/\nu$ .

#### **RG FOR BRANCH COMPETITION**

In order to determine  $g(x, y)$ , we turn to an explicit description of the growth process.<sup>6</sup> Suppose that we parameterize the accessible surface of the cluster by arc-length  $s$ . If a particle attaches at the surface point  $s'$ , it thereby reduces the growth probability at all points  $s$  for which  $|s - s'| > a$ , where  $a$  is the particle size. This is because a certain number of the random walks that would have reached  $s$  previously are now obstructed by the new particle at  $s'$ . If the probability that a particle lands at  $s'$  is  $p(s')$ , and the probability that a random walker goes from  $s'$  to  $s$  without contacting the surface is  $H(s, s')$ , this implies that

$$\frac{dp(s)}{dn} = - \int ds' (H(s, s') - h(s)\delta(s - s')) p^2(s'), \quad (3)$$

where we have modelled effects on the scale  $|s - s'| < a$  by the  $\delta$ -function, the coefficient of which,  $h(s)$ , is set by the conservation of the total growth probability,  $\int ds p(s) = 1$ . Note that in Eq. (3), two factors of  $p(s')$  appear—one corresponds to the original probability that a particle lands at  $p(s')$ , the other to the potential trajectories arriving at  $s$  that are blocked by such a particle.

For  $a \ll |s - s'| \ll an$ , conformal transformation shows that the function  $H(s, s')$  is given in two dimensions by the simple form<sup>9</sup>

$$H(s, s') = \frac{p(s)p(s')}{\left[ \int_s^{s'} ds'' p(s'') \right]^2}, \quad (4)$$

where the integral in the denominator is the total growth probability between the points  $s$  and  $s'$ . It is convenient to parameterize the interface by this quantity, the “growth probability” distance between points  $z(s)$ , defined by  $z(s') - z(s) = \int_s^{s'} ds'' p(s'')$ . Then our fundamental equation becomes

$$\frac{dp(z)}{dn} = p(z) \int dz' \left[ \frac{1}{(z-z')^2} - \tilde{h}(z)\delta(z-z') \right] p^2(z'), \quad (5)$$

where  $a$  serves as an ultra-violet cutoff to prevent divergence of the integral, and  $\tilde{h}(z)$  is related to  $h(s)$  and to the function  $z(s)$ ; its precise form is of no interest to us.

#### Determination of $g(x,y)$

I wish to use this equation to determine the function  $dx/d \ln n_b = g(x,y)$ . Repeated application of the chain rule yields

$$\frac{dx}{d \ln n_b} = \frac{n_b}{p_b^2} \left\{ (1-x) \frac{dp_1}{dn} - x \frac{dp_2}{dn} \right\}. \quad (6)$$

Consider a branch with probability  $p'$  and a number of particles  $n'$ . We suppose that this branch extends from  $z = 0$  to  $z = p'$ . Eqs. (5) and (6) imply that if we can write  $p^2(z)$  on this branch (and by extension, all other branches) as

$$p^2(z) = \frac{(p')^2}{n'} f(z/p'), \quad (7)$$

where  $f(z)$  is a universal function that depends neither upon  $p'$  nor upon  $n'$ , then we will be able to write  $dx/d \ln n_b = g(x,y)$ , with the right-hand side a function of  $x$  and  $y$  alone. Equation (7) is motivated by the fact that  $p^2(z)$  must be proportional to  $(p')^2$ ; the dependence on  $n'$  is specifically chosen to lead to an  $n'$ -independent  $g(x,y)$ . Only if we can find a method of computing an  $n'$ -independent  $f(z)$  will this *ansatz* be justified.

#### Computation of Branch Envelope Function $f(z)$

Thus the crux of the problem is this “branch envelope” function  $f(z)$ , which represents, with the appropriate normalization, the distribution of growth probability in different regions of a branch. Now in our picture, each branch can be divided into two distinct sub-branches, which compete according to the dynamics established by  $g(x,y)$ . Our central mean-field assumption is that we can compute  $f(z)$  by averaging the envelope functions  $f(z)$  of these sub-branches over the stochastic parameter  $\epsilon$  appropriate to the competition of these two sub-branches. In this way we obtain the following equation:

$$f(z) = \int_{-\infty}^{\infty} d\epsilon \rho(\epsilon) \left\{ \frac{x^2(\epsilon n_b)}{y(\epsilon n_b)} f\left(\frac{z}{x(\epsilon n_b)}\right) + \frac{(1-x(\epsilon n_b))^2}{(1-y(\epsilon n_b))} f\left(\frac{1-z}{1-x(\epsilon n_b)}\right) \right\}, \quad (8)$$

where  $x(\epsilon n_b)$  and  $y(\epsilon n_b)$  give the values of  $x$  and  $y$  along the unstable manifold as functions of  $n_b$  and the stochastic parameter  $\epsilon$ . For convenience, we are defining  $\rho(\epsilon)$  for negative values of  $\epsilon$  as  $\rho(-\epsilon) = \rho(\epsilon)$ , with  $x(-\eta) = 1 - x(\eta)$ ,  $y(-\eta) = 1 - y(\eta)$ . This leads to the relatively compact expression of Eq. (8). For large  $n_b$ , this equation has a solution independent of  $n_b$ , which is determined by

$$\int_{-\infty}^{\infty} d\eta |\eta|^{\nu-1} \left\{ \frac{x^2(\eta)}{y(\eta)} f\left(\frac{z}{x(\eta)}\right) + \frac{(1-x(\eta))^2}{(1-y(\eta))} f\left(\frac{1-z}{1-x(\eta)}\right) - f(z) \right\} = 0. \quad (9)$$

Since the integrand goes to zero as  $\eta \rightarrow \infty$ , we are justified in taking the small  $\epsilon$  form for  $\rho(\epsilon)$ .

Of course, in order to perform this integral, we must have the form of the unstable manifold, and thus we must already know  $g(x, y)$ . We can determine  $g(x, y)$  from  $f(z)$  by simply integrating Eq. (5) over the appropriate intervals. We do not integrate over regions exterior to the two competing branches, but only investigate the influence of the two branches on one another. (This assumption can be justified by convenience, or by an explicit demonstration that the influence of exterior branches on quantities such as  $f(z)$  leads to corrections of higher order in  $1/n^\nu$ .) It is then straightforward but tedious to write  $g(x, y)$  as a function of  $f(z)$ ; the somewhat cumbersome formulae are to be found elsewhere.<sup>4</sup>

The reader should note that we have a self-consistent procedure, because  $g(x, y)$  can be written as a function of  $f(z)$ , while  $f(z)$  is determined as a function of  $g(x, y)$ , and in particular by the unstable manifold in the  $x-y$  plane as determined by  $g(x, y)$ , by Eq. (9). Thus in practice we are looking for a solution of Eq. (9) where the functions  $x(\eta)$  and  $y(\eta)$  are implicitly determined by  $f(z)$ .

#### Solution of RG Equations

I have numerically obtained the unique solution to Eq. (9) under these conditions, which is displayed in the inset to Figure 2.<sup>10</sup> This validates our assumption regarding the scaling with  $n'$  in Eq. (7). The function  $g(x, y)$  determined from this function has all of the necessary qualitative features; in particular, the fixed point at  $(x, y) = (1/2, 1/2)$  is unstable and hyperbolic, and the unstable manifold leads from this point to stable fixed points at  $(x, y) = (0, 0)$  and  $(1, 1)$ , as illustrated in Figure 2. Figure 2 also shows numerical results for branch competition. The value of the unstable eigenvalue  $\nu$  is  $\nu \approx .6020$ , implying that  $D = 1/\nu \approx 1.661$ , which is within 3% of the standard numerical result  $D \approx 1.71$ .

#### **MULTIFRACTAL DIMENSIONS FOR DLA**

Multifractal dimensions  $\sigma(q)$  for the growth measure of a DLA cluster can be conveniently defined using a partition function  $\mathcal{Z}$ , which is defined by

$$\mathcal{Z}(q, \sigma, n) = n^\sigma \sum_{i=0}^n p_i^q, \quad (10)$$

where  $q$  and  $\sigma$  are parameters, and  $p_i$  is the probability that the next particle to attach itself to the cluster will do so to the  $i$ 'th current particle. The exponent function  $\sigma(q)$  is defined by requiring that  $\mathcal{Z}(q, \sigma(q), n) = 1$ . If this equation possesses a stable non-trivial

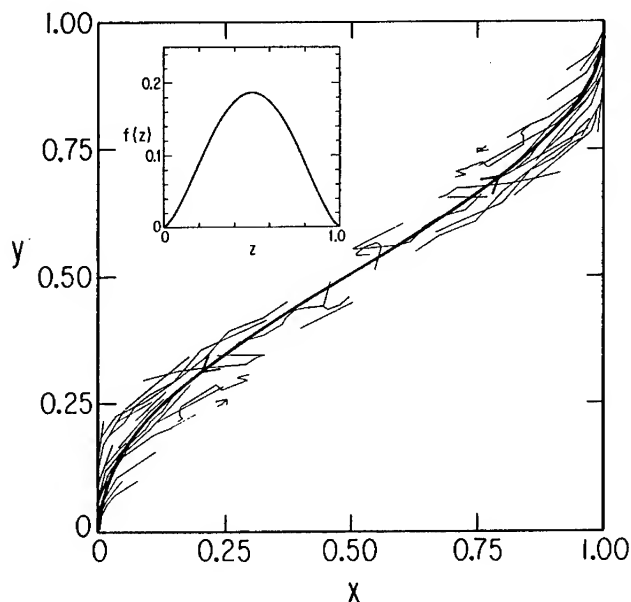


Figure 2. Trajectories of branch competition in the  $x - y$  plane. The light solid trajectories are numerical results for specific branch pairs in growing DLA clusters. The heavy solid line represents the unstable manifold predicted by the branch competition RG, which is quite close to the “average” numerical trajectory. The inset shows the computed branch envelope function  $f(z)$ .

asymptotic solution as  $n \rightarrow \infty$ , then the growth probability distribution  $\{p_i\}$  is said to be multifractal.

Normally, multifractal dimensions  $\tau(q)$  are defined according to the scaling of the growth probability distribution with respect to the radius of gyration of the cluster, and not its total number of particles. We thus expect that  $\tau(q) = D\sigma(q)$ .

Of course, there exists a large stochastic ensemble of DLA clusters for any given number of particles  $n > 2$ . Thus we must define  $\sigma(q)$  be some sort of ensemble averaging, in order to obtain well-defined, unique results. By analogy with the statistical mechanics of random systems, we expect that the most interesting quantities are the *annealed* average  $\sigma_a(q)$ , and the *quenched* average  $\sigma_q(q)$ , defined respectively by

$$\langle Z(q, \sigma_a(q), n) \rangle = 1, \quad (11a)$$

$$\langle \log \langle Z(q, \sigma_q(q), n) \rangle \rangle = 0, \quad (11b)$$

where the brackets  $\langle \rangle$  indicate the average over the appropriately weighted ensemble of DLA clusters with  $n$  particles. Because the annealed average will contain a larger contribution from rare, atypical members of the ensemble, we expect that  $\sigma_q(q)$  will be more relevant for typical ensemble members.

### Annealed Multifractal Dimensions

The annealed dimensions  $\sigma_a(q)$  are relatively simple to compute for the branched growth model. We start by writing a general relation for the partition function as an integral equation, which follows from the branched structure.

$$\langle \mathcal{Z}(q, \sigma, n) \rangle = \int_0^\infty d\epsilon \rho(\epsilon) \left[ \frac{x^q(\epsilon n)}{y^\sigma(\epsilon n)} \langle \mathcal{Z}(q, \sigma, y(\epsilon n)n) \rangle + \frac{(1-x(\epsilon n))^q}{(1-y(\epsilon n))^\sigma} \langle \mathcal{Z}(q, \sigma, (1-y(\epsilon n))n) \rangle \right]. \quad (12)$$

Note that the averages  $\langle \rangle$  on the right-hand side do not include the average over  $\epsilon$ , which is written explicitly. If we define  $x(-\epsilon n) = 1 - x(\epsilon n)$ ,  $y(-\epsilon n) = 1 - y(\epsilon n)$ , and  $\rho(-\epsilon) = \rho(\epsilon)$ , then Eq. (12) can be written more compactly as

$$\mathcal{Z}(q, \sigma, n) = \int_{-\infty}^\infty d\epsilon \rho(\epsilon) \frac{(1-x(\epsilon n))^q}{(1-y(\epsilon n))^\sigma} \mathcal{Z}(q, \sigma, (1-y(\epsilon n))n). \quad (13)$$

If we assume that the integral is dominated by values of  $(1-y(\epsilon n))n \sim n$ , then we can expand the integrand.

$$\begin{aligned} \mathcal{Z}(q, \sigma, n) &= \int_{-\infty}^\infty d\epsilon \rho(\epsilon) \frac{(1-x(\epsilon n))^q}{(1-y(\epsilon n))^\sigma} \mathcal{Z}(q, \sigma, n) \\ &+ \int_{-\infty}^\infty d\epsilon \rho(\epsilon) \log(1-y(\epsilon n)) \frac{(1-x(\epsilon n))^q}{(1-y(\epsilon n))^\sigma} \frac{d\mathcal{Z}(q, \sigma, n)}{d \log n} + O\left(\frac{d^2 \mathcal{Z}}{d(\log n)^2}\right). \end{aligned} \quad (14)$$

Let us write

$$\int_{-\infty}^\infty d\epsilon \rho(\epsilon) \frac{(1-x(\epsilon n))^q}{(1-y(\epsilon n))^\sigma} = 1 + \frac{g_0}{n^\nu} + \dots, \quad (15)$$

where the higher order terms vanish more quickly with  $n$  than  $n^{-\nu}$ . We also write

$$\int_{-\infty}^\infty d\epsilon \rho(\epsilon) \log(1-y(\epsilon n)) \frac{(1-x(\epsilon n))^q}{(1-y(\epsilon n))^\sigma} = -\frac{h_0}{n^\nu} + \dots, \quad (16)$$

since  $\lim_{\epsilon \rightarrow \infty} y(\epsilon n) = 0$ . Again, the higher order terms vanish more quickly with  $n$  than  $n^{-\nu}$ . Thus we obtain

$$\frac{d \log \mathcal{Z}}{d \log n} = \frac{g_0}{h_0} + \dots, \quad (17)$$

where the corrections vanish as  $n \rightarrow \infty$ . Thus we must have  $g_0 = 0$  in order that the partition function not diverge, or go to zero, as  $n \rightarrow \infty$ . Our final result is that  $\sigma_a(q)$  is determined by

$$\int_0^\infty d\eta \eta^{\nu-1} \left\{ \frac{x^q(\eta)}{y^{\sigma_a(q)}(\eta)} + \frac{(1-x(\eta))^q}{(1-y(\eta))^{\sigma_a(q)}} - 1 \right\} = 0. \quad (18)$$

Integrating Eq. (9) from  $z = 0$  to  $z = 1$ , one obtains precisely this criterion, with  $q = 3$  and  $\sigma_a(q) = 1$ . This result is identical to the “electrostatic” scaling law, derived previously in an entirely different way, which states that<sup>9</sup>

$$\left\langle \int ds p(s)^3 \right\rangle \propto n^{-1}, \quad (19)$$

where the integral is over the entire cluster surface. Equation (19) is equivalent to the more usual statement that  $\tau(3) = D$ .

#### Quenched Multifractal Dimensions

Quenched multifractal dimensions within the branched growth model are more difficult to compute; I have recently studied this problem in collaboration with B. Duplantier and K. Honda.<sup>10</sup> We found that it is possible to expand  $\langle \log \mathcal{Z} \rangle$  perturbatively, and then resum the most divergent terms at every order, thus obtaining a systematic result for  $\sigma_q(q)$ . A very curious feature of this result is that its value depends upon the order in which certain limits are performed. Normally, we would eliminate any residual  $n$  dependence in  $\mathcal{Z}$  by defining  $\sigma_q(q)$  in the limit  $n \rightarrow \infty$ , i.e.

$$\lim_{n \rightarrow \infty} \langle \log \mathcal{Z}(q, \sigma_q(q), n) \rangle = 0. \quad (20)$$

In fact, this definition leads to the conclusion that  $\sigma_q(q) = \sigma_a(q)$  *exactly*, so that there is no distinction between quenched and annealed averaging for this problem.

However, one only studies DLA clusters with a finite number of particles. It turns out that Eq. (20) reaches its asymptotic limit only for  $n \gg n_c(q)$ , where

$$n_c(q) \propto e^{\bar{a}e^{\bar{b}q}}. \quad (21)$$

The coefficients  $\bar{a}$  and  $\bar{b}$  are both positive numbers calculable from the branched growth model. Thus, even for quite moderate values of  $q$ , the “true” multifractal spectrum  $\sigma_a(q)$  will not be seen for typical clusters unless  $n$  is enormous. For values of  $n \ll n_c$ , an ersatz spectrum of the form  $\sigma(q) = \bar{\alpha}q$  will be observed, with  $\bar{\alpha}$  a calculable constant. We believe that this represents a breakdown of multifractality for typical DLA clusters.

#### ACKNOWLEDGEMENTS

This work was supported by the National Science Foundation through a Presidential Young Investigator award, Grant DMR-9057156. I am grateful to A. Coniglio for the

hospitality of the Dipartimento di Fisica, Università di Napoli, which made possible the work on quenched multifractal dimensions.

## NOTES

1. T.A. Witten, Jr. and L.M. Sander, Phys. Rev. Lett. **47**, 1400 (1981); P. Meakin, Phys. Rev. A **27**, 1495 (1983).
2. R. Brady and R.C. Ball, Nature (London) **309**, 225 (1984); L. Niemeyer, L. Pietronero, and H.J. Wiesmann, Phys. Rev. Lett. **52**, 1033 (1984); J. Nittmann, G. Daccord, and H.E. Stanley, Nature (London) **314**, 141 (1985).
3. This question is also the focus of real-space studies such as L. Pietronero, A. Erzan, and C. Evertsz, Phys. Rev. Lett. **61**, 861 (1988); Physica A **151**, 207 (1988), and X.R. Wang, Y. Shapir and M. Rubenstein, Phys. Rev. A **39**, 5974 (1989); J. Phys. A **22**, L507 (1989).
4. T.C. Halsey and M. Leibig, Phys. Rev. A **46**, 7793 (1992); T.C. Halsey, Phys. Rev. Lett. **72**, 1228 (1994).
5. L. Turkevich and H. Scher, Phys. Rev. Lett. **55**, 1026 (1985); Phys. Rev. A **33**, 786 (1986); see also R. Ball, R. Brady, G. Rossi, and B.R. Thompson, Phys. Rev. Lett. **55**, 1406 (1985), and T.C. Halsey, P. Meakin, and I. Procaccia, Phys. Rev. Lett. **56**, 854 (1986).
6. T.C. Halsey, Phys. Rev. Lett. **59**, 2067 (1987); Phys. Rev. A **38**, 4749 (1988).
7. The fact that there are no loops follows from the fact that every particle has a unique parent, which is true in off-lattice versions of DLA.
9. T.C. Halsey, Phys. Rev. A **35**, 3512 (1987).
10. T.C. Halsey, K. Honda, and B. Duplantier, unpublished.



## SINGULAR INTERFACIAL HYDRODYNAMICS AND THE DIELECTRIC BREAKDOWN MODEL

H.G.E. HENTSCHEL

Emory University, Department of Physics, Rollins Research Center, Atlanta, GA 30322

### ABSTRACT

The equations of motion for the interfacial dynamics in the dielectric breakdown model are derived. They form a set of coupled hydrodynamic equations for the interfacial curvature and growth probability in which the conserved densities are transported by a nonlocal velocity. From these equations the dynamical manner in which singularities in these conserved densities evolve can be studied both analytically and numerically. Shock-like behaviour associated with velocity attractor and repeller points on the evolving interface lead to bifurcations in the velocity field and finally to fractal structures in the curvature and growth probability in the absence of surface tension. In the presence of surface tension spatiotemporal chaos is observed.

### INTRODUCTION

Diffusion-limited aggregation originally introduced by Witten and Sander<sup>1</sup> as a model for aggregation has over the last decade become one of the most important models describing nonequilibrium growth phenomena. The recognition by Niemeyer et al.<sup>2</sup> that the equations for such growth are isomorphic to Laplacian growth provided the impetus for application of this model to dielectric breakdown and related phenomena: In such growth the local normal velocity of the interface  $v = -\nabla\phi$  is proportional to the gradient of a potential which is a solution of Laplace's equation  $\nabla^2\phi = 0$  with moving boundary conditions  $\phi(s) = 0$  on any point  $x(s)$  of the evolving interface (here we parametrize the two-dimensional interface by its distance  $s$  along the surface and for the moment we neglect surface tension) and  $\phi(\text{outer boundary}) = \phi_0$ . These equations have also been shown to describe such apparently diverse phenomena as electrochemical deposition<sup>3,4</sup> two-fluid flow<sup>5</sup> and even aspects of biological growth such as retinal vasculature<sup>6</sup> and neuronal arborization<sup>7</sup>. Only the nature of the field obeying Laplace's equation changes (for example, the concentration field in the case of aggregation, the electrical potential in the case of dielectric breakdown, or the pressure field in the case of two-fluid flow).

The growth process remains one of deep mystery. How are such equations related to the dendritic growth with its convoluted curvature  $\kappa(s)$  observed in experiments and computer simulations? How does the fractal<sup>8,9</sup> and multifractal<sup>10,11</sup> properties known to describe fully fledged DLA arise. How does the multifractal growth probability  $P(s)$  evolve<sup>12</sup>? The underlying cause of the singular behaviour in the absence of surface tension is the diffusive Mullins-Sekerka instability<sup>13</sup>, but the influence of surface tension is also known to be crucial in controlling the dynamical behaviour of the system.

It turns out that surface tension acts as a singular perturbation<sup>14,15</sup> on the basic instability underlying Laplacian growth. Thus in the Saffman-Taylor instability<sup>16,17</sup> in which a less viscous fluid is forced in with a velocity  $U$  and used to displace a more viscous one in a Hele-Shaw cell, and the initially flat interface becomes unstable with one finger becoming dominant at the expense of the rest at long times, a great deal of theoretical effort has gone into trying to understand the shape and stability of this asymptotic finger. Recent theoretical work<sup>18,19</sup> would suggest that the asymptotic finger remains stable even at high velocities to infinitesimal perturbations, though unstable to finite

perturbations. The size of the finite perturbations that can destroy the finger become, however, asymptotically small  $\sim \exp[-c (\gamma/U)^{-1/2}]$  as  $U \rightarrow \infty$  in the presence of surface tension  $\gamma$ . Such behaviour is also confirmed experimentally<sup>20,21</sup> as the finger is stable at low flow rates  $U$ , though for high flow rates  $U$  the asymptotic finger appears to become unstable with time-dependent chaotic fluctuations as well as finger bifurcations which distort the shape.

To understand further how such complex dynamics may arise, conformal mapping approaches have been employed because of the two dimensional nature of the flow. Thus Shraiman and Bensimon<sup>22</sup> studied partial differential equations for the conformal mapping  $z = f(w, t)$  between the physical plane  $z = x + iy$  in which the closed contour  $z(\sigma, t)$  lies (see Fig.1) and the region  $w$  outside the unit disk  $w = e^{i\sigma}$  (thus  $z(\sigma, t) = f(e^{i\sigma}, t)$ )

$$\frac{dz(\sigma, t)}{dt} = -i \frac{\partial z(\sigma, t)}{\partial \sigma} \frac{\partial \sigma}{\partial t} \quad (1)$$

Such partial differential equations had first been derived in the context of Laplacian growth with surface tension free boundary conditions in the first half of this century<sup>23,24</sup>, but what Shraiman and Bensimon managed to do by considering mappings whose derivatives had polynomial singularities which could be represented in terms of its zeros  $Z_n$  and poles  $P_n$

$$\frac{\partial f(z, t)}{\partial z} = A(t) \prod_n (z - Z_n(t)) / (z - P_n(t)) \quad (2)$$

was to transform Eq.(1) into a set of coupled but highly nonlinear ordinary differential equations for the zeros and poles which behave as quasiparticles, effectively transforming the dynamics to a many body form. The critical points must all lie inside the unit disk because the mapping is analytic outside, but as the critical points reach the unit circle (which they do in a finite time in the absence of surface tension) cusp singularities appear in the contour.

Recently this method has been extended by the observation of Blumenfeld<sup>25</sup> that the equations of motion for the quasiparticles have an integrable Hamiltonian formulation in terms of new action angle variables  $H(\{J\}, \{\theta\})$  that depend on the zeros  $\{Z\}$  and poles  $\{P\}$  of the original mapping perhaps accounting for known integrals of the motion<sup>26,27</sup>. Thus there exists the exciting possibility that the whole apparatus of many body theory may one day be applied to DLA and used to derive its geometric, fractal and multifractal properties. Despite the inherent possibilities in this approach, there is also the weakness that though the existence of a Hamiltonian formalism has been demonstrated, an explicit Hamiltonian has not so far been derived.

We therefore propose here to focus on conserved variables during Laplacian growth -- the two most obvious being the curvature of the evolving surface  $\kappa(s)$  and the growth probability  $P(s) = |\nabla \phi(s)| / \int |\nabla \phi(s')| ds'$ . During growth we know that  $\int \kappa(s) ds = 2\pi$ ; while from its definition  $\int P(s) ds = 1$ . These variables turn out to behave like hydrodynamic conserved densities with associated currents which we derive below using conformal methods coupled with the geometrical approach of Brower, Kessler, Koplik, and Levine<sup>28</sup>. In addition, it turns out that the method used can be generalized to the dielectric breakdown model<sup>2,8</sup> where the normal velocity is proportional to a power  $\eta$  of the local field  $\mathbf{v} \cdot \mathbf{n} = |\nabla \phi|^\eta$  so we derive the equations of motion for the general model. The coupling of this geometric and hydrodynamic approach result in equations of motion which are very transparent to analysis and suggest how singular structure is built up during Laplacian and more general growth models. It is this approach we describe here focusing on the early time behaviour and the singular nature of the surface tension in controlling the observed dynamics.

## THEORY

We wish to derive equation of motion for the curvature  $\kappa(s)$  and the growth probability or normalized electric field  $P(s) = |\nabla\phi(s)| / \int |\nabla\phi(s')| ds'$  in the continuum dielectric breakdown model. For this model the velocity of the interface is

$$dx(s)/dt = \lambda |\nabla\phi(s)|^{(\eta-1)} \nabla\phi(s) + \gamma \partial^2 \kappa / \partial s^2 \mathbf{n}(s) . \quad (3)$$

where the potential  $\phi$  obeys Laplace's equation  $\nabla^2\phi = 0$  with moving boundary conditions  $\phi(s) = 0$  on any point  $x(s)$  of the evolving interface (here we parametrize the two-dimensional interface by its distance  $s$  along the surface and  $\mathbf{n}(s)$  is the normal unit vector at any such point on the interface) and  $\phi(R_0) = \phi_0$  a distance  $R_0$  away. The exponent  $\eta = 1$  for pure Laplacian growth, and we have added to the right hand side of the equation a surface diffusion term due to the surface tension  $\gamma$  which will be needed to control the Mullins-Sekerka instability by introducing a short scale cutoff. This is not the unique effect of surface tension. For two-fluid flow for example we should use the boundary condition  $\phi(s) = -\gamma\kappa(s)$ , and indeed such a term can be treated using the Poisson integral formula, but at the cost of a great loss of simplicity in the resulting equations. More general non-conservative effects of surface tension such as evaporation at regions of high curvature can be incorporated into the equations of motion by replacing  $\gamma \partial^2 \kappa / \partial s^2$  by  $(\gamma \partial^2 \kappa / \partial s^2 - \sigma \kappa)$ .

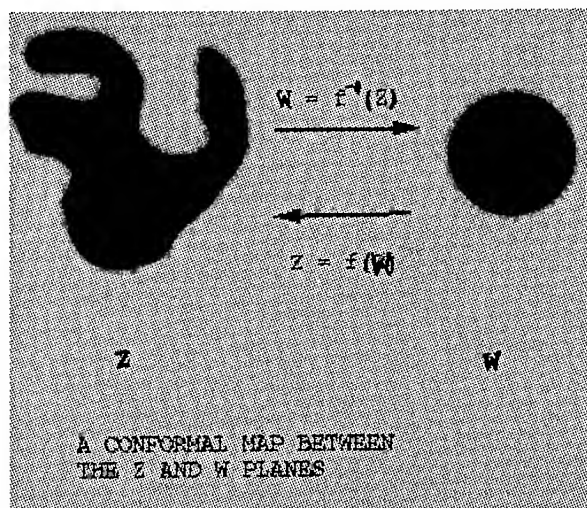


Fig.1 A conformal map between the Z and W planes

We now use conformal mapping techniques to derive the partial differential equation for the interface evolution directly. Treat the interface as a simple closed contour lying in the 'physical' complex plane  $z = x + iy$ , and define a conformal map  $z = f(w)$  between the outside of the contour and the outside of a unit disk lying in the complex  $w$  plane. Specifically if we parametrize the disk using the angle  $\sigma$  where  $0 < \sigma < 2\pi$ , then the contour of the evolving interface  $z(\sigma, t) = f(e^{i\sigma}, t)$ . To

find an equation of motion for the interface we define the complex analytic potential  $V(z) = \phi(x,y) + i\psi(x,y)$  in terms of which Eq.(3) can be transformed into

$$dz/dt = \lambda |dV/dz|^{(\eta-1)} (dV/dz)^* + \gamma \partial^2 \kappa / \partial s^2 \mathbf{n} . \quad (4)$$

where  $\mathbf{n} = -ie^{i\theta(s)}$  is the normal unit vector in the complex plane, defined in terms of  $\theta(s)$  the angle between the interfacial tangent at  $s$  and the  $x$  axis.

Because the conformal mapping is to the unit disk, the complex potential obeying the relevant boundary conditions in the  $w$  plane is  $V(w) = \phi_0 \ln w / \ln R_0$ , and consequently we may take  $V(z) = \phi_0 \ln f^{-1}(z) / \ln R_0$  to be the complex potential in the  $z$  plane. Using this potential and Eq.(4) we find

$$dz/dt = -i \Lambda \partial z / \partial \sigma \partial z^* / \partial \sigma^{-(1+\eta)} + \gamma \partial^2 \kappa / \partial s^2 \mathbf{n} . \quad (5)$$

where  $\Lambda = \lambda (\phi_0 / \ln R_0)^\eta$ , which is the generalization of Eq.(1) to the dielectric breakdown model supplemented by a surface diffusion term induced by surface tension.

Using Eq.(5), we are now in a position to extract the equations for the tangent angle  $\theta(s)$  and the metric  $g = \partial z / \partial \sigma \partial z^* / \partial \sigma$  by noting that  $\partial z / \partial \sigma = (\partial z / \partial s) (\partial s / \partial \sigma) = e^{i\theta(s)} g^{1/2}$ . We find

$$\begin{aligned} dg/dt &= 2\kappa g [\Lambda g^{-\eta/2} + \gamma \partial^2 \kappa / \partial s^2] \\ d\theta/dt &= [(\Lambda \eta / 2) g^{-(1+\eta/2)} \partial g / \partial s - \gamma \partial^2 \kappa / \partial s^2] \end{aligned} \quad (6)$$

The tangent angle  $\theta(s)$  and curvature are related by  $\kappa(s) = \partial \theta / \partial s$ ; while the metric  $g(s)$  is related to the growth probability  $P(s)$  by observing that the conformal map between the original interface and the conformally mapped disc implies that  $P(s)ds = P(\sigma)d\sigma = d\sigma/2\pi$ , and therefore  $g(s) = (2\pi P(s))^{-2}$ . These two identities combined with Eq.(6) can now be used in turn to derive equations of motion for  $\kappa(s)$  and  $P(s)$ .

$$dP/dt = -\kappa P [DP^\eta + \gamma \partial^2 \kappa / \partial s^2] \quad (7a)$$

$$d\kappa/dt = -(\kappa^2 + \partial^2 / \partial s^2) [DP^\eta + \gamma \partial^2 \kappa / \partial s^2] \quad (7b)$$

where  $D = (2\pi)^\eta \Lambda$ . In deriving Eq.(7b) we used the operator identity  $\partial / \partial s (d/dt) = d/dt (\partial / \partial s) + (\partial / \partial s) \kappa (DP^\eta + \gamma \partial^2 \kappa / \partial s^2)$  for the dielectric breakdown model. Finally as for any variable  $\zeta$  we know  $d\zeta/dt = \partial \zeta / \partial t|_s + \partial \zeta / \partial s \int_0^s \kappa (DP^\eta + \gamma \partial^2 \kappa / \partial s^2) ds$  we can find the hydrodynamic-like equations for the curvature and growth probability

$$\partial P / \partial t = -\partial / \partial s [Pv] \quad (8a)$$

$$\partial \kappa / \partial t = -\partial / \partial s [\kappa v + \partial / \partial s (DP^\eta + \gamma \partial^2 \kappa / \partial s^2)] \quad (8b)$$

which behave like conserved densities which are transported with a velocity given by the nonlocal expression

$$v(s) = \int_0^s \kappa(DP^\eta + \gamma \partial^2 \kappa / \partial s^2) ds \quad (9)$$

There exists one further important point which needs to be emphasised: the curvature and growth probability are not independent variables. In principle we can now solve any initial value problem given  $\kappa(s, t=0)$  and  $P(s, t=0)$ . For real growth processes, however, it must always be remembered that given the initial curvature we have also been supplied with our initial conditions for the growth probability as the two are related nonlocally.

## SINGULAR HYDRODYNAMICS

Let us now analyze Eqs.(8) and (9). Despite their nonlinearity and nonlocality, it proves possible to make quite a bit of headway in analysing these equations because of their transparent physical meaning, and our good intuition with hydrodynamics. As the total length of the interface is growing at a rate  $dl/dt = v(l)$ , let us discuss the build up of structure in terms of the transformed velocity  $u(s) = v(s) - (s/l)v(l)$  which removes the trivial flow due to average global interfacial stretching or contraction, the velocity  $u(s)$  remaining then does not simply induce a simple dilation in the variables, but will transport the curvature and growth probability around the interface in a nontrivial manner. It is this velocity which we argue lies at the root of the build up of multifractal structure.

The growth probability obeys a pure transport equation and therefore flows in the direction set by the nonlocal velocity  $v(s)$ . Thus the build up of structure can be described in terms of the singular points where the transformed velocity  $u(s)$  is zero. These stagnation points  $s^*$  can be classified as attractors or repellers of  $P(s)$  and  $\kappa(s)$  depending on their gradients  $\partial u / \partial s = \kappa(DP^\eta + \gamma \partial^2 \kappa / \partial s^2) - \langle \kappa(DP^\eta + \gamma \partial^2 \kappa / \partial s^2) \rangle$  where  $\langle \rangle$  means a global average over the evolving interface. If  $\partial u / \partial s > 0$  at the stagnation point  $s^*$ , then the point is a repeller -- for  $u(s) > 0$  at  $s > s^*$  while  $u(s) < 0$  for  $s < s^*$ , carrying conserved densities away from  $s^*$ . On the other hand if  $\partial u / \partial s < 0$  at the stagnation point  $s^*$ , then the point is an attractor -- for  $u(s) < 0$  at  $s > s^*$  while  $u(s) > 0$  for  $s < s^*$ , carrying conserved densities towards  $s^*$ . Thus these repellers and attractors will tend to reallocate both curvature and probability in a nonuniform way, and in the absence of surface tension shocks will form as the conserved densities build up or are depleted at the stagnation points. Linearizing Eq.(8,9) locally near stagnation points suggests that build-up or depletion occurs exponentially fast  $\sim \exp(-(\partial u / \partial s^*)t)$  resulting in the observed cusps which build up in finite times in simulations.

Where are we likely to observe repellers and attractors. First, note that as the actual position of stagnation points is given by the set of nonlocal quantities  $u(s^*(t)) = 0$ , their positions are only weakly dependent on the local geometry and growth probability. Whether, they are attractors or repellers is, however, much more strongly influenced by local geometry. Neglecting for the moment the contribution of surface tension, the dielectric model would suggest  $\partial u / \partial s \approx D(\kappa P^\eta - \langle \kappa P^\eta \rangle)$ . Thus attractors may be expected at regions of less than average curvature and low growth probability or negative curvature and large growth probability. Such points occurring typically in fjords, may be expected to accumulate growth probability resulting in time in local maxima  $\partial^2 P / \partial s^2 < 0$  in the growth probabilities. On the other hand at hot tips of large positive curvature one would expect repellers to appear and the growth probability will be transported away from the tip to the sides of the dendrite. If the transport is large enough, local maxima in  $P$  will be transformed into local minima  $\partial^2 P / \partial s^2 > 0$  of the growth probability. This transport dynamics of growth probability can be seen in Fig.2 which shows the spatiotemporal evolution of curvature, growth probability, and velocity  $u$  for one specific set of initial conditions (the  $y$  axis represents time, while the  $x$  axis

represents the variable  $0 < s/l(t) < 1$ ). Initially the growth probability is large at regions of large positive curvature (positive curvature is light colored in Fig. 2 (a) and negative at darker colors; while growth probability is lighter coloured when larger in Fig. 2(b) and darker at lower values) and repellers exist at these points (see Fig. 2 (c): the velocity  $u(s) > 0$  is plotted is dark, and  $u(s) < 0$  is light; thus attractors exist at dark-light transitions, while repellers occur at light-dark transitions), while attractors exist at the regions of negative curvature. The growth probability is transported away from the repellers toward the attractors initially as can be seen in Fig. 2b.

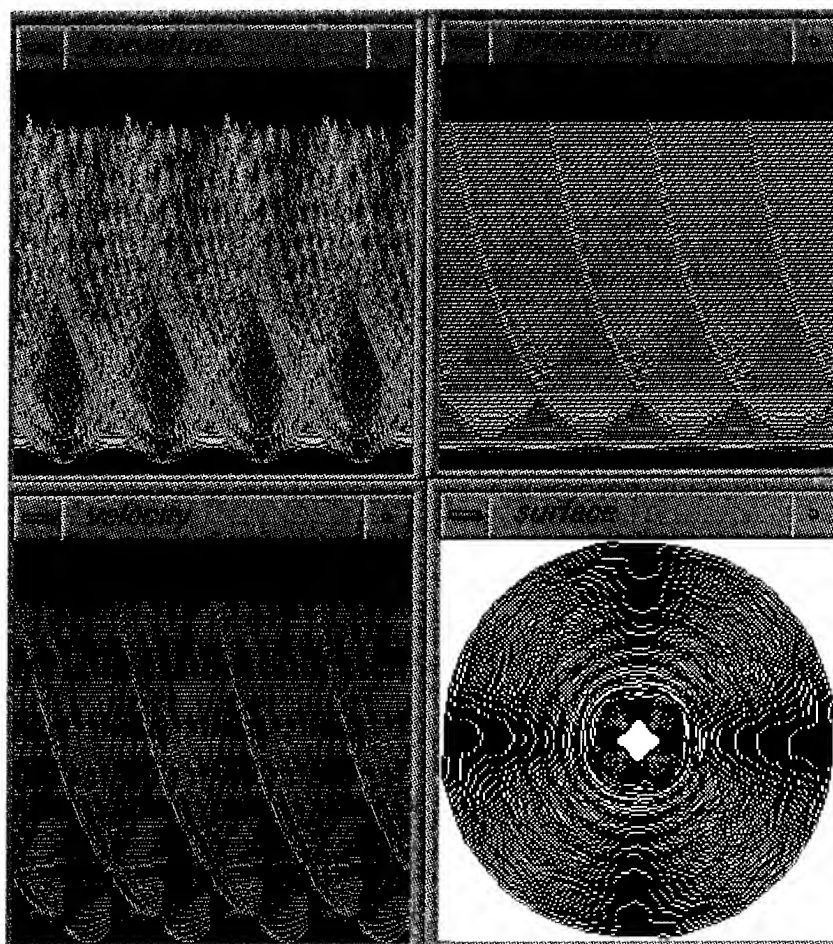


**Fig.2 The development of fractal structure through a series of bifurcations in the absence of surface tension. (a) Curvature; (b) Probability; (c) Velocity; (d) Surface evolution.**

In this manner the curvature influences the growth probability. How does this evolving growth probability influence the curvature? While the probability flux is of a pure transport form  $j_p = Pv$ , the curvature flux  $j_\kappa = \kappa v + \partial/\partial s(DP\eta + \gamma\partial^2\kappa/\partial s^2)$  contains contributions from the growth probability. Specifically if  $\partial^2 P/\partial s^2 < 0$  as can occur in invaginations the growth probability will tend to increase the curvature, while if  $\partial^2 P/\partial s^2 > 0$  can occur at hot tips the growth probability will tend to decrease curvature. This suggests that in regions of negative curvature there is a competition between transport of negative curvature to attractor points and the influence of  $P(s)$  tending to increase the curvature. While at regions of positive curvature tip splitting may occur from the combined influence of curvature transport away from repellor stagnation points and the influence the growth probability. The combined influence of these transport processes is to create cusp-like singularities in the curvature (see Fig. 2a).

Another major result of this competition is the appearance of bifurcations in the velocity field as function of time (see Fig. 2c) in the numerical maps which are created when we discretise Eqs. (8) and (9) (in the real continuum equations in the absence of surface tension at this point cusps would appear in the curvature and growth probability and the partial differential could not be integrated further forward in time). The discretisation procedure, which may also be associated with the essential discreteness of the DLA algorithm itself, allows one to follow the time evolution beyond the singularities in the partial differential equation. Depending on the initial conditions both forward and backward (in time) period-doubling and tangent bifurcations have been observed in both the attractors A and repellors R. By a forward period-doubling bifurcations we mean a bifurcation  $A \rightarrow ARA$  where the old attractor becomes a repellor and two new attractors are created in the velocity field; or  $R \rightarrow RAR$  creating two new repellors (see Fig. 3a). By tangent bifurcations we mean the sudden creation of AR pairs from the 'vacuum' as the velocity field  $u(s)$  traverses the  $u = 0$  line (see Fig. 3b). Note in all bifurcations the attractors and repellors are created in pairs and therefore despite the fact that their total number is not conserved, if the attractors and repellors can be treated as the particle-antiparticle pairs annihilating on contact.

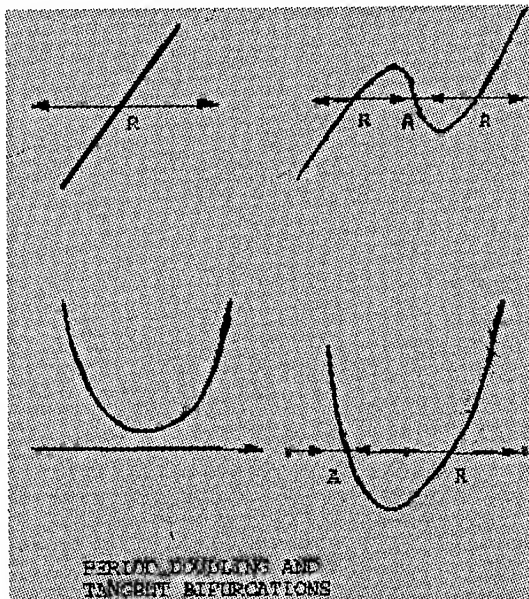
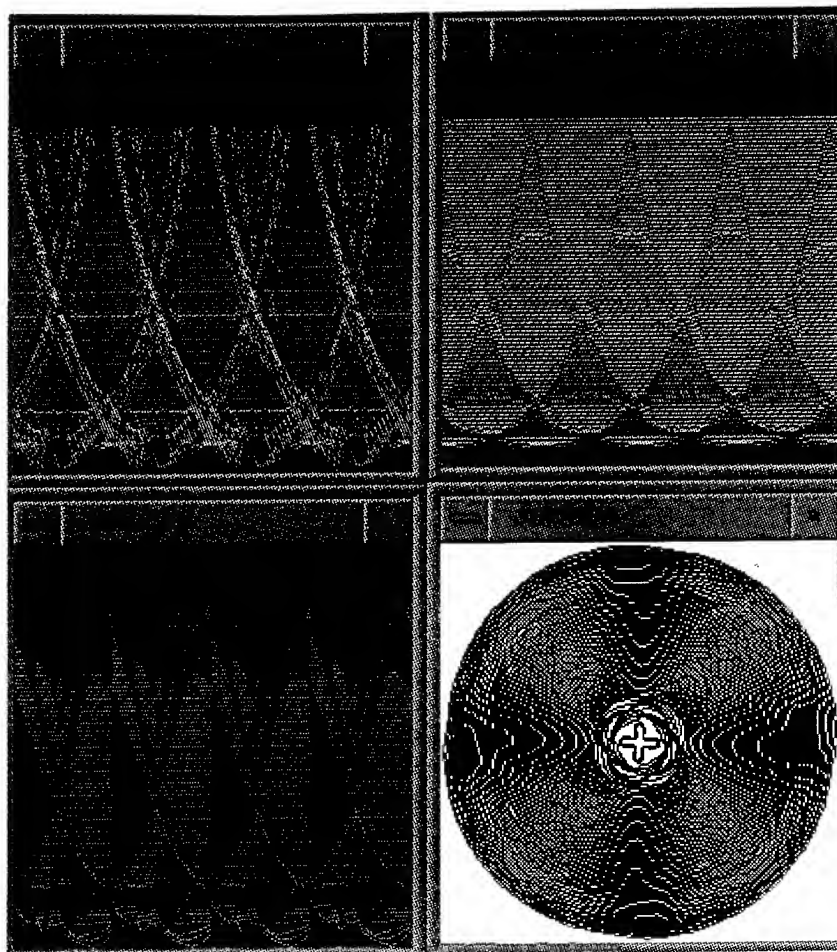


Fig.3 Bifurcations in the velocity field. (a) A repellor period-doubling bifurcation; (b) A tangent bifurcation.

In the absence of surface tension there is numerical evidence that such bifurcations occur deterministically in time for example  $RA \rightarrow RARA \rightarrow RARARA$  etc. leading to tree-like structures in the velocity field, and resulting in self-similar geometric structures in the curvature and probability with position on the interface (see Fig.2) which we argue are the short time signal of fractal and multifractal behaviour at long times.

What is the influence of surface tension on this dynamics? We have numerically integrated the equations in the presence of surface tension and the behaviour is dramatically different for even the smallest surface tension, confirming the singular nature of the perturbation applied. Qualitatively at very short times the velocity transport will build up cusp singularities in a manner described above similar to shock formation in hydrodynamics. Then, when the derivatives in the curvature become large enough the surface tension makes its presence felt, resulting in almost discontinuous changes in the dynamics (see Fig.4).



**Fig.4 Spatiotemporal chaos in the presence of surface tension**



The future dynamics then becomes extremely sensitive to the exact shape of these gradients in curvature when surface tension becomes important and the long-time dynamics appears to show spatiotemporal chaos. This spatiotemporal chaos can be understood qualitatively as being due to the sensitive influence of surface tension on the bifurcation sequences observed in the absence of surface tension. Thus both period-doubling and tangent bifurcations still make an appearance, but random rather than deterministic sequences occur eg RA  $\rightarrow$  RARA  $\rightarrow$  RAARRA  $\rightarrow$  RAARARRARA as surface tension suddenly reorients the local direction of the velocity field.

## DISCUSSION

The process we are observing appears to be recursive creating structure at smaller and smaller scales with time as the velocity transports curvature and growth probability away from repellors and towards attractors and in the process creating new attractors and repellors at smaller scales which start the transport process again. If this is correct a dynamically recursive mechanism will have been associated with the equations for Laplacian growth, and more generally with the dielectric breakdown model, which despite creating beautiful self-similar structures have obstinately kept secret the manner in which the process was occurring.

Clearly intensive large-scale numerical investigations need to be performed to extract more fully the mechanisms hinted at by these small-scale short-time simulations. Topics needing investigation include the nature of the discretization process itself in transforming the partial differential equations into spatiotemporal maps for the curvature and growth probability; the influence of the growth exponent  $\eta$  on pattern formation especially in the large  $\eta$  limit, as well as the nature of the transition between these equations as  $\eta \rightarrow 0$  and those for  $\eta = 0$  self-affine surfaces such as the KPZ equation<sup>29</sup>; the influence of external noise on interfacial structure obtained by adding delta-correlated noise terms to the right hand side of Eq.(8b) for the curvature; and the influence of anisotropy.

## Acknowledgements

I should like to thank Dr. F. Family for useful conversations, and the Cherry Emerson Center for Scientific Computation, Emory University for computational facilities.

1. T.A. Witten Jr. and L.M. Sander, Phys. Rev. Lett. **47**, 1400 (1981).
2. L. Niemeyer, L. Pietronero, H.J. Wiesmann, Phys. Rev. Lett. **52**, 1033(1984).
3. R.M. Brady and R.C. Ball, Nature **309**, 225 (1984).
4. M. Matsushita, M. Sano, Y. Hayakawa, H. Honjo, Y. Sawada, Phys. Rev. Lett. **53**, 286 (1984).
5. L. Paterson, Phys. Rev. Lett. **52**, 1621 (1984).
6. F. Family, B.R. Masters, and D.E. Platt, Physica **D38**, 98 (1989).
7. F. Caserta, H.E. Stanley, W.D. Eldred, G. Daccord, R.E. Hausman and J. Nittman, Phys. Rev. Lett. **64**, 95 (1990).
8. T. Vicsek, Fractal Growth Phenomena (World Scientific, Singapore, 1989).

9. See P. Meakin, in Phase Transitions and Critical Phenomena, edited by C. Domb and J. L. Lebowitz (Academic Press, Orlando, 1988).
10. H.G.E. Hentschel and I. Procaccia, *Physica* **8D**, 435 (1983).
11. T.C. Halsey, M.H. Jensen, L.P. Kadanoff, I. Procaccia, B.I. Shraiman, *Phys. Rev.* **A33**, 1141 (1986).
12. T.C. Halsey, P. Meakin, and I. Procaccia, *Phys. Rev. Lett.* **56**, 854 (1986).
13. W.W. Mullins and R.F. Sekerka, *J. App. Phys.* **52**, 1 (1963).
14. See for example Dynamics of Curved Fronts edited by Pierre Pelce (Perspectives in Physics, Academic Press 1990).
15. D. Bensimon, L.P. Kadanoff, S. Liang, B.I. Schraiman, C. Tang, *Rev. Mod. Phys.* **58**, 977 (1986); in Directions in Condensed Matter Physics edited by G. Grinstein and G. Mazenko (World Scientific, Singapore 1986).
16. P.G. Saffman and G.I. Taylor, *Proc. Roy. Soc. Lond.* **A245**, 312 (1958).
17. G.I. Taylor, *Proc. Roy. Soc. Lond.* **A201**, 192 G.I. (1950).
18. A.J. DeGregoria, and L.W. Schwartz *J. Fluid Mech.*, **164**, 383 (1986) .
19. D. Bensimon, *Phys. Rev.* **A33**, 1302 (1986).
20. J. Maher, *Phys. Rev. Lett.* **54**, 1498 (1985) .
21. P. Tabeling and A. Libchaber, *Phys. Rev.* **A33**, 794 (1986); P. Tabeling, G. Zocchi , A. Libchaber, *J. Fluid Mech.* **177**, 67 (1987).
22. B. Shraiman and D. Bensimon, *Phys. Rev.* **A30**, 2840 (1984); in *Kinetics of Aggregation and Gelation*, edited by F. Family and D.P. Landau (Elsevier, North-Holland 1984) pp. 29-32.
23. L.A. Galin, *Dokl. Akad. Nauk. SSSR* **47**, 246 (1945).
24. P. Ya Polubarinova-Kochina, *Dokl. Akad. Nauk. SSSR* **47**, 254 (1945).
25. R. Blumenfeld, *Phys. Rev.* **E50**, 2952 (1994).
26. S. Richardson, *J. Fluid. Mech.* **56**, 609 (1972).
27. M. B. Mineev, *Physica* **D43**, 288 (1990).
28. R.C. Brower, D.A. Kessler, J. Koplik, H. Levine, *Phys. Rev.* **A29**, 1335 (1984); *Phys. Rev.* **A30**, 3161 (1984); *Phys. Rev.Lett.* **51**, 1111 (1983).
29. M. Kardar, G. Parisi, and Y. Zhang, *Phys. Rev. Lett.* **56**, 889 (1986).

## WAVELET BASED STRUCTURAL ANALYSIS OF ELECTROLESS DEPOSITS IN THE DIFFUSION LIMITED REGIME

A. ARNEODO, F. ARGOUL, A. KUHN AND J.F. MUZY  
Centre de Recherche Paul Pascal, Avenue Schweitzer, 33600 Pessac, France

### ABSTRACT

We discuss the actual relevance of thin gap geometry electrodeposition to generate fractal patterns that mimic the morphology of Witten and Sander's diffusion-limited aggregates (DLA). Eliminating migration and convection, as well as electrochemical side reactions, we show that electroless deposition is a good candidate to meet the requirements for diffusion to be the rate limiting step of the growth process. We use the wavelet transform microscope to achieve a comparative structural characterization of both experimental electroless deposits and numerical DLA clusters. The fact that five-fold symmetry and Fibonacci hierarchical ordering are found as common predominant statistical features is, to our knowledge, the first demonstration, relying on an appropriate structural fractal analysis, of the existence of DLA morphologies in an experimental context.

### INTRODUCTION

Since the early eighties, many experimental works<sup>1-7</sup> have been carried out in physics, chemistry and biology with the intention of testing the relevance of the DLA model introduced by Witten and Sander<sup>8</sup> in 1981, to fractal growth processes. In particular, much effort has been devoted to characterize the scaling properties of experimental clusters and numerical aggregates computed with the DLA model using the concepts of fractal and multifractal<sup>5,9-13</sup>. This has been done in the spirit of gathering these diffusion-controlled growth processes into a universal geometrical class<sup>2-9</sup>. Among the various experimental illustrations of fractal pattern forming phenomena, electrodeposition has been emphasized as the paradigm for theoretical studies of diffusion-limited aggregation<sup>10,14-17</sup>. Actually, electrodeposition experiments have attracted a lot of interest<sup>10,14-24</sup> because they provide a way to explore a rich variety of morphologies at little cost by simply varying some control parameter, e.g., the concentration of metal ions or the voltage. When investigating the electrodeposition of various metals like zinc, copper and silver from aqueous solutions without supporting electrolyte, some resemblance with DLA morphologies was found for specific domains of the current (or voltage)-concentration parameter space. Fractal dimensions were measured in remarkable agreement with those of DLA clusters<sup>10,24</sup>. However, several attempts to classify the morphologies observed in electrodeposition have led to different phase diagrams<sup>16,17,22,23</sup>, which is, a posteriori, a strong indication that electrodeposition is a more complex system than a simple random walker aggregation process. Moreover, since fractal dimension measurement only provides statistical information about the scaling properties of fractal aggregates<sup>24</sup>, there has been for years the need of a new technique for structural analysis, powerful enough to unambiguously recognize DLA geometry.

In this communication, we report on the results of a recent structural analysis of electroless deposits using the wavelet transform<sup>25</sup>. We first define an experimental protocol to bring the electrodeposition system close to the conditions where the growth is limited by diffusion. Then we use the wavelet transform microscope<sup>24</sup> to explore the intricate arborescent geometry of the so-obtained electroless deposits with the specific goal to establish some quantitative morphological correspondances between these experimental fractal aggregates and large mass off-lattice DLA clusters.

## EXPERIMENTAL PROTOCOL

During the past few years, there has been several attempts to analyze the different mechanisms that come into play in thin layer electrodeposition<sup>26-32</sup>. There are mainly of two types : (i) on the one hand, the chemical reactions that take place in the diffusive layer as well as in the bulk of the cell<sup>23,31-33</sup> ; (ii) on the other hand, the transport processes such as surface diffusion, bulk diffusion, migration and convection<sup>30,33,34</sup>. Both of them have a major impact on the dynamic and the morphology (fractal, dense, dendritic) of the growth<sup>23,28,30-34</sup>.

In order to ensure the bulk diffusion to be the rate limiting step in the aggregation process, we thus need to cancel, or at least to minimize, migration and convection but also to avoid any parasitic reaction on the interface besides the metal reduction itself. Working in open circuit (electroless deposition<sup>20,21</sup>) removes the effects of a global electric field and consequently suppresses any electrohydrodynamic instability of the fluid around the tips of the branches<sup>29</sup>. To get rid of parasitic phenomena induced by the presence of a global electric field, we have chosen electroless deposition rather than working with highly concentrated supporting electrolytes, because the addition of salt modifies the adsorbed layer on the metallic interface and progressively favours the reduction of other species such as protons<sup>31,32</sup>. To damp down natural convection driven by buoyancy forces<sup>30,33,34</sup>, it is necessary to work with very small gap cells ( $\sim 50 \mu\text{m}$  or less). Then, only diffusion remains for the feeding of the neighborhood of the interface which is progressively depleted in reducing species. The chemistry of metal ion reduction is, in this quasi 2D geometry, a tedious question since impurities such as oxygen or alkali cations which are found naturally in the electrolytes, have been shown recently to have a great influence on the morphology of both copper and zinc deposits<sup>31,32</sup>. In particular, if one prepares a solution of zinc salt which is free of oxygen and alkali cations, one recovers a phase diagram which is simpler than the ones previously published<sup>16,17,22,23</sup>, disordered branched patterns becoming more unlikely under these conditions. Let us point out also that the reduction of protons (which is active in pure aqueous electrolytes) can lead, in supported electrolytes, to the formation of hydrogen bubbles which are a real nuisance for the growth process, since they shake the solution and destroy any fine structure of the deposit.

Therefore, the three fundamental requirements to get DLA morphologies in electrodeposition are no external electric field, ultra pure solutions and very thin gap geometry<sup>25</sup>. To make fractal analysis tractable, it is fundamental to grow clusters as large as possible. In that perspective, it is absolutely necessary to get rid of morphological transition (e.g. Hecker effect<sup>26,27,30-32,35</sup>) which could arise in closed electrochemical cells. To avoid such finite size effects, we run our experiments in a reservoir-fed layer as illustrated in Fig. 1. A thin foil of copper (99.99 % purity) is inserted between two circular glass plates that are sealed at a fixed distance ( $50 \mu\text{m}$ ), prior to filling by a  $0.05 \text{ mol.L}^{-1}$  silver nitrate solution (Prolabo normapur). The cell is in contact by its outer circumference with a 2cm deep reservoir which contains the same solution. This experimental set-up has been devised in order to impose quasi-infinite boundary conditions like in DLA simulations.

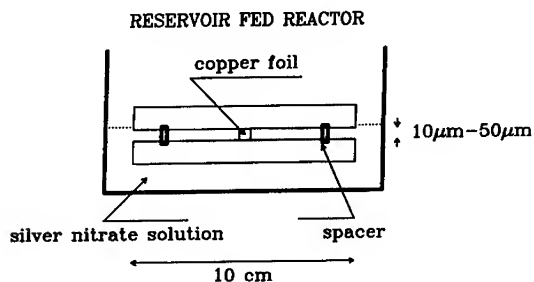


Fig. 1 Reservoir fed reactor for quasi two-dimensional electroless deposition

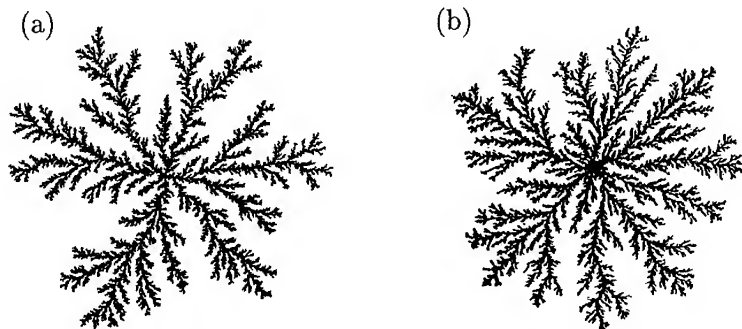


Fig. 2 (a)  $10^6$  particle off-lattice DLA cluster. (b) Silver electroless aggregate.

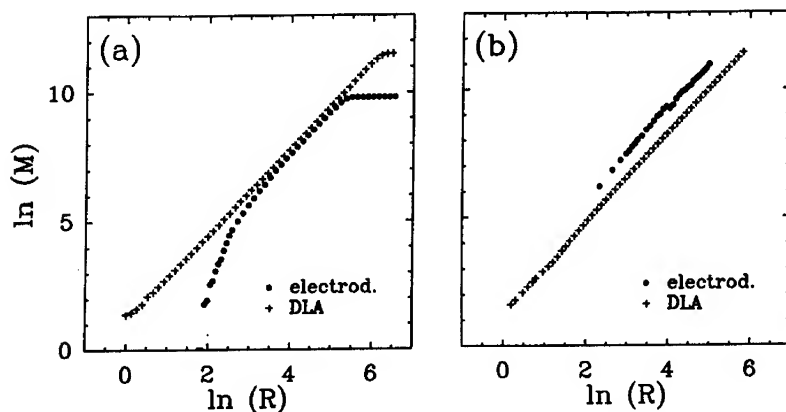


Fig. 3 Fractal dimension analysis of DLA and electroless clusters. (a) Fractal dimension : log-log plot of the mass of the final cluster contained in a disk versus the radius  $R$ . (b) Dynamical dimension : log-log plot of the mass of a growing cluster versus its giration radius during the growth process.

#### DIMENSION MEASUREMENT

Provided all the experimental requirements we just described be fulfilled, we get the type of electroless deposit morphology shown in Fig. 2b. In Fig. 2a is illustrated for comparison a large mass DLA cluster ( $M = 10^6$ ) computed with an off-lattice algorithm<sup>36</sup>. To quantify the qualitative resemblance revealed from simple visual inspection, we report in Fig. 3 the results of a fractal dimension analysis of both the numerical and the experimental aggregates<sup>33</sup>. In Fig. 3(a) the fractal dimension is estimated as the pointwise dimension which characterizes how the mass around the central seed scales as the function of the length ; as seen on this figure, there exists a finite range of scales where the DLA and the electroless clusters scale with the same exponent :  $D_F^{DLA} = 1.65 \pm 0.03$  and  $D_F^{elec} = 1.66 \pm 0.05$ . This similarity is confirmed by the results of box-counting and fixed-mass fractal dimension measurement<sup>24</sup> ; the generalized fractal dimensions of the electroless deposit are found to be equal to the fractal dimension  $D_q = D_F^{elec} = 1.65 \pm 0.05$ ,  $\forall q$  in rather good agreement with the estimates obtained for large-mass off-

lattice DLA cluster<sup>37-39</sup>  $D_q = D_F^{DLA} = 1.63 \pm 0.05$ . This observation strongly suggests that in the experiment as well as in the simulations, we grow clusters that are likely to be homogeneous fractals. In Fig. 3(b) are reported the results of the measurement of the dynamical dimension describing the dependence of the mass of a cluster on its average radius of gyration during the growth process ; again the comparison is quite satisfactory<sup>33</sup> :  $D_d^{DLA} = 1.71 \pm 0.03$  and  $D_d^{elec} = 1.70 \pm 0.05$  (let us note that the fact that the dynamical dimension is found significantly larger than the fractal dimension still remains an unsolved problem). But since fractal dimensions provide only degenerate statistical informations<sup>24,40,41</sup>, the remarkable consistency reported in this section is not sufficient to conclude that electroless and DLA clusters have the same morphology.

## 2D WAVELET ANALYSIS

In a recent work<sup>37-39</sup>, we have used the wavelet transform to explore the ramified structure of large mass ( $M = 10^6$ ) off-lattice DLA clusters. This study has revealed two previously unnoticed structural features that are statistically predominant : (i) the existence of a preferential screening angle consistent with five-fold symmetry<sup>38</sup> ; (ii) the presence of a Fibonacci hierarchical ordering<sup>37-39</sup>. Here we will reproduce this wavelet-based analysis on a statistical sample of 20 electroless deposits grown in the same experimental conditions as the one shown in Fig. 2(b), using the structural characteristics (i) and (ii) as morphological tests<sup>25</sup>.

The wavelet transform (WT) of a 2D distribution of mass  $\mu$  with respect to a radially symmetric real analyzing wavelet  $\psi$  is defined as<sup>24</sup> :

$$T_\psi[\mu](b, a) = \int \psi\left(\frac{x-b}{a}\right) d\mu(x), \quad (1)$$

where  $\psi$  is generally supposed to be of zero mean for the transform to be invertible. As previously tested to investigate the well organized fractal architecture of snowflake patterns<sup>24</sup>, the WT can be regarded as a mathematical microscope<sup>24,39</sup> whose position and magnification are  $b$  and  $1/a$  ( $> 0$ ) and whose optics are given by the choice of the analyzing wavelet  $\psi$ . When examining an electroless deposit with the WT microscope, by increasing the magnification parameter, one reveals progressively and quite naturally the successive generations of branching.

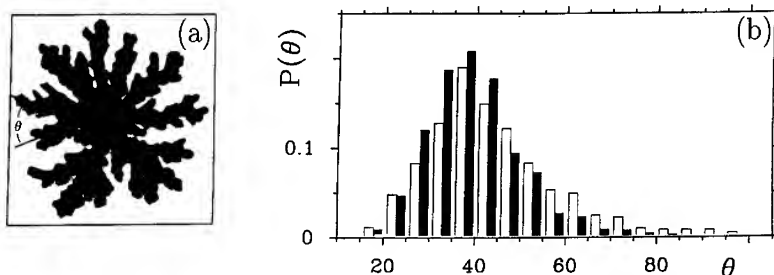


Fig. 4 (a) 2D WT of an electroless deposit at a coarse scale ; the analyzing wavelet is the mexican hat  $\psi(x) = (2 - |x|^2) e^{-|x|^2/2}$ . (b) Histogram of screening angle values between branches of successive generations as computed from the WT analysis of 20 electroless deposits (black bars) and 20 off-lattice DLA clusters of mass  $M = 10^6$  (white bars), at a comparable magnification.

A first qualitative confirmation of the statistical homogeneity of these experimental aggregates is the fact that these branchings occur rather uniformly in space without any preferential location and this at all scales. Moreover, at each generation of branching, the WT provides an efficient way to measure the screening angles between bifurcating branches<sup>24,25</sup> as illustrated in Fig. 4(a). Let us point out<sup>38,39</sup> that these screening angles differ from the angles between the stems of the branches which do not take into account the hierarchy of sub-branches originating from these stems<sup>42</sup>. In Fig. 4(b) are reported the results of a systematic investigation<sup>25</sup> of the screening angles of 20 electroless and DLA clusters. In both experiment and simulation, we have adjusted the WT magnification in order to resolve similar generations of branching. The two histograms so-obtained are in remarkable agreement ; they both display a unique maximum around the value  $\theta^* = 37^\circ \pm 2.5^\circ \sim \pi/5$ . Moreover, we have checked (for 3 generations of branching in the DLA clusters and 2 generations in the electroless deposits) that these histograms are scale invariant.

## 1D WAVELET ANALYSIS

This observation of a predominant structural five-fold symmetry, is a very promising first clue to the existence of a hierarchical ordering in the electroless deposits. Whether these aggregates display a Fibonacci fractal organization similar to the one discovered in the DLA morphology<sup>38</sup> is the next challenge we want to address. For that purpose we could simply try to identify Fibonacci sequences in the ramification process that results from screening effects in the deposition growth process. But in order to make our demonstration quantitative, we will rather focus our WT analysis on the so-called azimuthal Cantor sets<sup>37</sup> obtained by intersecting the experimental clusters with a circle of radius  $R = 2 R_g/3$  (where  $R_g$  is the gyration radius) centered at the origin. More precisely, we use the wavelet-based tree matching algorithm, recently implemented for solving the inverse fractal problem in one-dimension<sup>43</sup>, to process these azimuthal cuts<sup>44</sup>. A typical representation in the  $(\theta, a)$  half-plane of the 1D WT of an experimental azimuthal Cantor set is shown in Fig. 5(a). As explained in [37,44], this figure does not illustrate the whole WT but simply its skeleton defined by the position of the maxima of its modulus. From the tree organization of this skeleton, one can extract structural properties. In particular, by computing the ratio  $r = a_n/a_{n-1}$  ( $< 1$ ) between the scales where two successive bifurcations occur in the WT skeleton, one can identify some characteristic scale ratios. A systematic investigation of 50 experimental WT skeletons similar to the one in Fig. 5(a), actually yields an overall scale ratio histogram which again is in remarkable agreement with the corresponding histogram obtained for DLA clusters<sup>25</sup>. Moreover, this analysis reveals a preferential scale ratio  $r^* = 0.43 \pm 0.05$ , which means that the generations of branching in the WT skeletons are expected to occur preferentially at scales  $a_n = a_0 r^{*n}$ , where  $a_0$  is a macroscopic scale that is determined by the size of the cluster branch under study. The horizontal lines in the  $(\theta, a)$  half-plane in Fig. 5(a) are drawn as guide marks for those successive generations. As seen on this particular example, the number of WT maxima lines at each generation follows closely the Fibonacci series defined by the iteration :  $F_n = F_{n-1} + F_{n-2}$  with  $F_0 = F_1 = 1$ . Furthermore, one can encode the whole WT skeleton according to the Fibonacci recursive law :

$$A \rightarrow AB, B \rightarrow A \quad (2)$$

The branching ratio in the WT skeleton is therefore likely to converge to the golden mean  $\phi = \lim_{n \rightarrow +\infty} F_{n+1}/F_n = (1 + \sqrt{5})/2 = 1.618\dots$

As far as the statistical pertinence of this Fibonacci structural ordering is concerned, we report in Fig. 6, the results of a comparative analysis of 50 (resp. 240) WT skeletons of electroless deposit (resp. DLA cluster) azimuthal Cantor sets<sup>25</sup>. The different histograms correspond to the statistical distribution of the number of WT maxima lines that exist at scales  $a_n = a_0 (0.43)^n$  for successive generations from  $n = 1$  to 6. Each of these histograms displays a well defined maximum at the value  $F_n$  given by the Fibonacci series. Therefore, when zooming

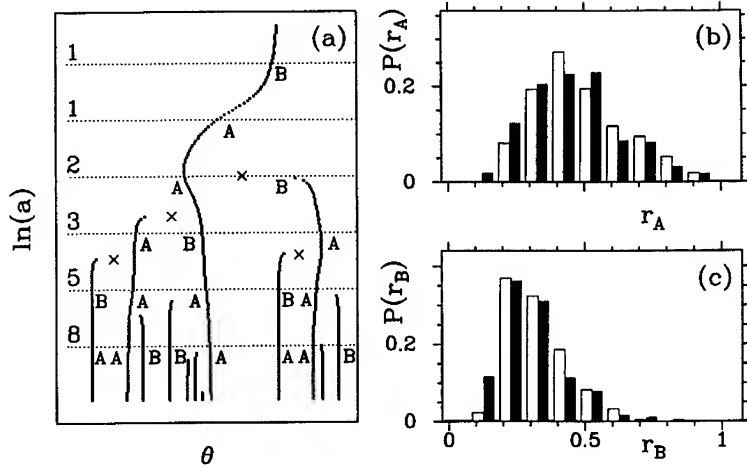


Fig. 5 (a) WT skeleton of a part of the azimuthal Cantor set corresponding to one main branch of an electroless deposit ; large scales are at the top. The analyzing wavelet is  $\psi(x) = \exp(-x^2)$ . The bifurcation points ( $\times$ ) are located at a scale where a WT modulus maxima line appears, at equal distance between this line and the closest longer line. The horizontal dashed lines mark the scales  $a_n = a_0 (0.43)^n$ , where the successive generations of branching are statistically expected to occur ; the WT skeleton is coded with symbols A and B according to the Fibonacci recursive process (2). (b) Histogram of scale ratios  $r_A = a_n/a_{n-1}$  between two successive bifurcation points of the WT skeleton when following a A branch. (c) Histogram of scale ratios  $r_B$  when following a B branch. The black (resp. white) histogram corresponds to the statistical analysis of 50 (resp. 240) main branches of 10 electroless deposits (resp. 50 large mass off-lattice DLA clusters).

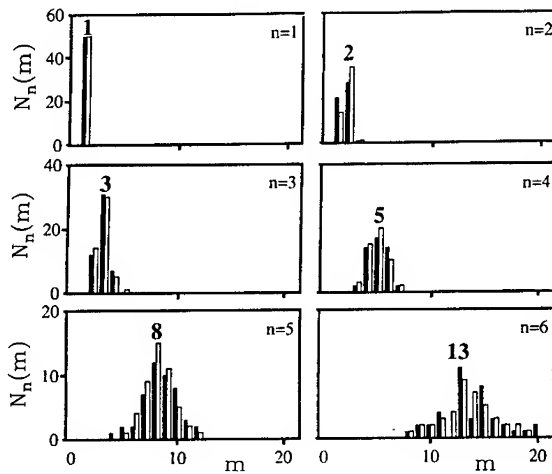


Fig. 6 Statistical distributions of the number of maxima lines that exist at scales  $a_n = a_0 (0.43)^n$ , for successive generations  $n = 1$  to 6 in the WT skeletons of the azimuthal Cantor sets of electroless deposits (black histograms) and off-lattice DLA clusters (white histograms) ; same statistics as in Fig. 5.



the WT microscope on the azimuthal Cantor sets extracted from electroless deposits, the way new details appear at higher levels of refinement is statistically governed by the Fibonacci recursive process (2). But according to this process, one expects to observe another privileged scale ratio, namely  $r^{*2}$ , originating from the delay required by B to become A before bifurcating again. The two histograms  $P(r_A)$  and  $P(r_B)$  obtained by computing the scale ratios between two successive bifurcations in the WT skeleton when following either the outcoming A branch or its pendant B branch are shown in Figs. 5(b) and 5(c) respectively. The corresponding experimental (electroless deposits) and numerical (DLA clusters) histograms are almost indistinguishable and display a maximum for respectively  $r_A^* = 0.43 \pm 0.05$  and  $r_B^* = 0.22 \pm 0.05$ , in good agreement with the expected relationship  $r_B^* = r_A^{*2}$ .

To complete our demonstration, let us apply to our experimental sample of azimuthal Cantor sets, the wavelet-based tree matching algorithm described in [44]. This algorithm consists in matching branches of the WT skeleton with the whole WT skeleton tree ; in particular it associates the bifurcation point  $(x_n, a_n)$  of an order  $n$  branch to its hierarchical homologous  $(x_{n-1}, a_{n-1})$  of an order  $n-1$  branch. The results obtained for 20 (resp. 240) azimuthal Cantor set WT skeletons of electroless deposits (resp. DLA clusters) are shown in Fig. 7 (resp. Fig. 8). By plotting  $x_{n-1}$  versus  $x_n$ , one gets similar noisy 1D maps for the experimental<sup>25</sup> and numerical<sup>44</sup> azimuthal Cantor sets ; the data points statistically fall on two distinct branches. The solid lines in Figs. 7(a) and 8(a) correspond to the piece-wise linear 1D map :

$$T(x) = \begin{cases} T_A(x) = \lambda_A^* x & \text{for } x \in [0, \lambda_A^{*-1}] \\ T_B(x) = \lambda_B^* (x - 1) + 1 & \text{for } x \in [1 - \lambda_B^{*-1}, 1] \end{cases} \quad (3)$$

that provides a rather natural understanding of the origin of the Fibonacci structural hierarchy<sup>44</sup>. This 1D map is made of two linear branches whose slopes  $\lambda_A^* = 2.2 \sim r_A^{*-1}$  and  $\lambda_B^* = 4.8 \sim r_B^{*-1}$  correspond respectively to the inverse of the preferential scale ratios found in the histograms  $P(r_A)$  and  $P(r_B)$  in Figs 5(b) and 5(c). A straightforward computation shows that if one assumes the equality  $\lambda_B^* = \lambda_A^{*2}$ , then the number of intervals of a given size  $r_A^{*n}$ , generated by iterating  $T^{-1}$ , is exactly the Fibonacci number  $F_n$ . The accumulation of data points around the two lines  $T_A$  and  $T_B$  in Fig. 7(a) is thus the clue to a statistically predominant Fibonacci multiplicative

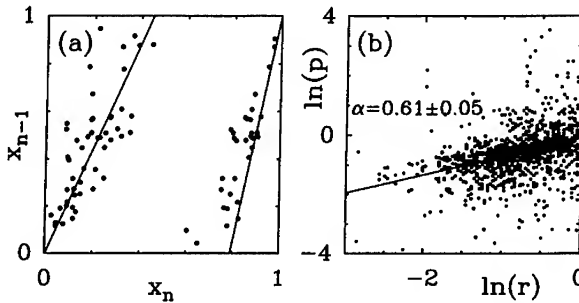


Fig. 7 (a) 1D map extracted from 20 WT skeletons of the azimuthal Cantor sets of electroless deposits. The solid lines correspond to the two branches of the linear cookie-cutter (3) with the respective slopes  $\lambda_A^* = 2.2$  and  $\lambda_B^* = 4.8$ . (b)  $\ln(p)$  vs  $\ln(r)$ , where  $r = a_n/a_{n-1}$  ( $p = |T_\Psi[\mu](\theta_n, a_n)| / |T_\Psi[\mu](\theta_{n-1}, a_{n-1})|$ ) is the ratio between the scales (amplitudes) of two bifurcation points associated by our tree matching algorithm. A linear regression fit of the data provides the slope  $\alpha = 0.61 \pm 0.05$ .

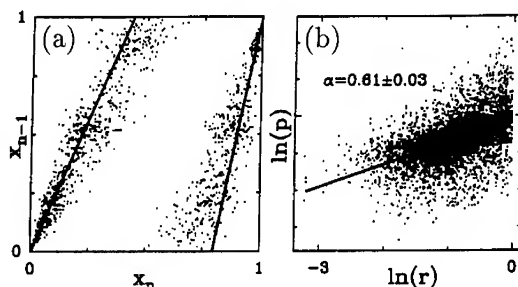


Fig. 8 Same as Fig. 7 but for a statistical sample of 240 WT skeletons of DLA azimuthal Cantor sets.

process, whereas the fluctuations around these lines can be seen as the signature of the presence of structural defects. These fluctuations are not specific to the experimental situation ; they are clearly evidenced in Fig. 8(a) when investigating a richer statistical sample of DLA clusters and they prove to be intrinsic<sup>44</sup>. Moreover, let us note that there exists another source of randomness hidden in the Fibonacci multiplicative process itself since, for both the experimental and numerical azimuthal Cantor sets, at each bifurcation  $A \rightarrow AB$  in the WT skeleton, the relative position of A with respect to B (to the left or to the right) is found to be governed by a fair tossing coin<sup>44</sup>.

From our tree matching algorithm, one can also extract the amplitude ratios  $p = |T_\Psi[\mu](\theta_n, a_n)|/|T_\Psi[\mu](\theta_{n-1}, a_{n-1})|$  of the WT modulus evaluated at two associated bifurcation points. This amplitude ratio is found to fluctuate with a rather broad distribution, but as shown in Fig. 7(b), the random variables  $\ln(p)$  and  $\ln(r)$  turn out to be strongly correlated according to the law  $p \sim r^{0.61}$ . These experimental results<sup>25</sup> mimic remarkably what is observed in Fig. 8(b) for DLA clusters<sup>44</sup>. Moreover, this estimate of the local scaling exponent  $\alpha = 0.61 \pm 0.05$  of the azimuthal Cantor set is in good agreement with the value obtained for the fractal dimension of both the electroless deposits and DLA clusters :  $D_F^{\text{elec}} \simeq D_F^{\text{DLA}} \simeq 1 + \alpha = 1.61 \pm 0.05$ .

## CONCLUSION

To summarize, we have taken advantage of the WT microscope abilities to show that electroless deposits grown under diffusion-limited conditions, display the same morphological characteristics, e.g. five-fold symmetry and Fibonacci structural ordering, than the numerical aggregates generated with an off-lattice DLA algorithm. This correspondence also extends to the statistics of the fluctuations (structural defects) around these predominant features. To our knowledge, this is the first demonstration of the existence of fractal DLA morphologies in an experimental context, that relies on an appropriate structural fractal analysis. Further comparative applications of the WT microscope to various experimental morphologies and their numerical modelling look very promising.

## Acknowledgements

We are very grateful to E. Bacry and J. Elezgaray for valuable discussions. This work was supported by the CNES under contract 93/0409, NATO under grant RG900685 and the DRET under contract 92/097. One of us (A.K.) is deeply indebted to the Penguin Foundation for financial support.

## References

1. H.E. Stanley and N. Ostrowsky, eds., *On Growth and Form : Fractal and Nonfractal Patterns in Physics* (Martinus Nijhof, Dordrecht, 1986) ; *Random Fluctuations and Pattern Growth* (Kluwer, Dordrecht, 1988).
2. L. Pietronero and E. Tosatti, eds., *Fractals in Physics* (North Holland, Amsterdam, 1986).
3. W. Guttinger and D. Dangelmayr, eds., *The Physics of Structure Formation* (Springer-Verlag, Berlin, 1987).
4. J. Feder, *Fractals* (Pergamon, New York, 1988).
5. T. Vicsek, *Fractal Growth Phenomena* (World Scientific, Singapore, 1989).
6. A. Bunde and S. Havlin, *Fractals and Disordered Systems* (Springer-Verlag, Berlin, 1991).
7. J.M. Garcia-Ruiz, E. Louis, P. Meakin and L.M. Sander, eds., *Growth Patterns in Physical Sciences and Biology* (Plenum, New York, 1993).
8. T. Witten and L.M. Sander, Phys. Rev. Lett. **47**, 1400 (1981) ; Phys. Rev. B **27**, 5686 (1983).
9. P. Meakin, in *Phase Transitions and Critical Phenomena*, edited by C. Domb and J.L. Lebowitz, Vol. 12 (Academic Press, New York, 1988) p. 355.
10. F. Argoul, A. Arneodo, G. Grasseau and H.L. Swinney, Phys. Rev. Lett. **61**, 2558 (1988) ; **63**, 1323 (1989).
11. G. Li, L.M. Sander and P. Meakin, Phys. Rev. Lett. **63**, 1322 (1989).
12. T. Vicsek, F. Family and P. Meakin, Europhys. Lett. **12**, 217 (1990).
13. H.E. Stanley, A. Bunde, S. Havlin, J. Lee, E. Roman and S. Schwarzer, Physica A **168**, 23 (1990).
14. R.M. Brady and R.C. Ball, Nature **309**, 225 (1984).
15. M. Matsushita, M. Sano, Y. Hayakawa, H. Honjo and Y. Sawada, Phys. Rev. Lett. **53**, 286 (1984).
16. D.G. Grier, E. Ben Jacob, R. Clarke and L.M. Sander, Phys. Rev. Lett. **56**, 1264 (1986).
17. Y. Sawada, A. Dougherty and J.P. Gollub, Phys. Rev. Lett. **56**, 1260 (1986).
18. G.L.M.K.S. Kahanda and M. Tomkiewicz, Phys. Rev. B **38**, 957 (1988).
19. D.B. Hibbert and J.R. Melrose, Phys. Rev. A **38**, 1036 (1988).
20. A.S. Paranjpe, S. Bhakay-Tamhane and M.B. Vasan, Phys. Lett. A **140**, 193 (1989).
21. I. Mogi, S. Okubo and Y. Nakagawa, J. Phys. Soc. Jap. **60**, 3200 (1991).
22. P.P. Trigueros, J. Claret, F. Mas and F. Sagues, J. Electroanal. Chem. **328**, 165 (1992).
23. A. Kuhn and F. Argoul, J. Electroanal. Chem. **371**, 93 (1994).
24. F. Argoul, A. Arneodo, J. Elezgaray, G. Grasseau and R. Murenzi, Phys. Lett. A **135**, 327 (1989) ; Phys. Rev. A **41**, 5537 (1990).
25. A. Kuhn, F. Argoul, J.F. Muzy and A. Arneodo, Phys. Rev. Lett. **73** (1994) to appear.
26. J.R. Melrose, D.B. Hibbert and R.C. Ball, Phys. Rev. Lett. **65**, 3009 (1990).
27. J.R. Melrose, Chemometrics and Intelligent Laboratory Systems **15**, 231 (1992).
28. V. Fleury, J.N. Chazalviel, M. Rosso and B. Sapoval, J. Electroanal. Chem. **290**, 249 (1990).
29. V. Fleury, J.N. Chazalviel and M. Rosso, Phys. Rev. Lett. **68**, 2492 (1992) ; Phys. Rev. E **48**, 1279 (1993).
30. M. Rosso, J.N. Chazalviel, V. Fleury and E. Chassaing, Electrochimica Acta **39**, 507 (1994).
31. A. Kuhn and F. Argoul, Fractals **1**, 451 (1993) ; Phys. Rev. E **49**, 4298 (1994).
32. F. Argoul and A. Kuhn, J. Electroanal. Chem. **359**, 81 (1993).
33. F. Argoul and A. Kuhn, Physica A **213** (1994) to appear.
34. J. Huth, W.B. Mc Cormick, H.L. Swinney, F. Argoul and A. Kuhn, Phys. Rev. E (1994) submitted.
35. N. Hecker, D.G. Grier and L.M. Sander, in *Fractals Aspects of Materials*, edited by R.B. Laibowitz, B.B. Mandelbrot and D.E. Passoja (Mat. Res. Soc. Proc., University Park, PA, 1985).
36. M. Tabard, Thesis, University of Bordeaux (1993).
37. A. Arneodo, F. Argoul, E. Bacry, J.F. Muzy and M. Tabard, Phys. Rev. Lett. **68**, 3456 (1992) ; in [7], p. 191.
38. A. Arneodo, F. Argoul, J.F. Muzy and M. Tabard, Phys. Lett. A **171**, 31 (1992) ; Physica A **188**, 217 (1992).

- 
39. A. Arneodo, F. Argoul, E. Bacry, J. Elezgaray, J.F. Muzy and M. Tabard, in *Progress in Wavelet Analysis and Applications*, edited by Y. Meyer and S. Roques (Editions Frontières, Gif sur Yvette, 1993) p. 21.
  40. J.F. Muzy, E. Bacry and A. Arneodo, *Int. J. of Bifurcation and Chaos* **4**, 245 (1994).
  41. A. Arneodo, E. Bacry and J.F. Muzy, *Physica A* **213** (1994) to appear.
  42. P. Ossadnik, *Phys. Rev. A* **45**, 1058 (1992).
  43. A. Arneodo, E. Bacry and J.F. Muzy, *Europhys. Lett.* **25**, 479 (1994).
  44. A. Arneodo, F. Argoul, J.F. Muzy, M. Tabard and E. Bacry, *Fractals* **1**, 629 (1993) ; *J. Diff. Eq. and Appl.* (1994) to appear.

## **A theory for growing interfaces in Laplacian fields:**

### **A many-body formulation and statistical analysis**

**Raphael Blumenfeld**

Center for Nonlinear studies and Theoretical Division, MS B25

Los Alamos National Laboratory, Los Alamos, NM 87545, USA

#### **Abstract**

I formulate a theory for the growth of an interface in a Laplacian field. The problem is mapped to a many-body system and the process is shown to be Hamiltonian. The corresponding set of dynamical equations is analysed and surface effects are introduced as a term in the Hamiltonian that gives rise to a repulsion between the quasi-particles and the interface. The theory accommodates anisotropic surface effects. The underlying Hamiltonian allows a statistical-mechanical analysis of the limit distribution of the quasi-particles. Noise can be naturally incorporated in this formalism. Finally the distribution of the particles is translated into the statistics of the interface, which leads to predictions on the morphology. The main thrust of this approach is in finding a statistical mechanical approach to this nonequilibrium process.

#### **Introduction**

Despite the abundance of diffusion controlled growth processes, the morphologies that these interfaces result in are not well understood theoretically. Few examples are solidification of supercooled liquids, diffusion-limited aggregation, electrodeposition and growth of bacterial colonies. Existing approaches mostly use scaling and two methods recently lead to quite accurate predictions of the fractal dimension.<sup>(1)</sup> Yet, there is currently no theory that starts from the local equations of motion (EOM) and predicts the statistics of such patterns or whether they become fractal at all. Here I propose such a first-principles theory.

The first step is to write down a p.d.e. for the evolution of the interface. Consider

an interface in two dimensions,  $\gamma(s)$ , that is parametrized by  $s$ , and which encloses a (say, solidifying) region, outside which there exists a Laplacian field  $\nabla^2\Phi = 0$ . The interface is fixed at a given value of  $\Phi$  (say, the concentration) and a higher value of  $\Phi$  is assigned to a circular boundary much larger than the growth's size. The interface advances at a rate proportional to the local gradient of the field,  $v_n = -\nabla\Phi$ . This rate is assumed sufficiently slow to allow a quasi-static treatment. By conformally mapping the interface onto the unit circle at each time step, solving for the field in the new plane, deriving  $\nabla\Phi$  in terms of the map and then equating to the local growth rate,  $\gamma_t$  one finds<sup>(2)(3)</sup>

$$\partial_t\gamma(s, t) = -i\partial_s\gamma(s, t) [|\partial_s\gamma(s, t)|^{-2} + ig(s)] . \quad (1)$$

In fact, it is only the first term within the square brackets that is derived in this way and it represents local growth normal to the interface. The second term is introduced by hand (although it is uniquely determined for analyticity) and represents a tangential velocity. Rewriting (1) in terms of the conformal map  $F(z, t)$  (where  $\gamma(s, t) = \lim_{z \rightarrow e^{is}} F(z, t)$ ) one finds

$$\frac{d}{dt} \ln F' = \frac{1}{F'} \frac{d}{dz} (z F' G) , \quad (2)$$

where  $G(z, t)$  is an analytic function that tends to the term in the square brackets of (1) as  $z$  tends to the unit circle. Generally, the map can be written in the form

$$F' = A(t) \prod_{n=1}^N \frac{z - Z_n(t)}{z - P_n(t)} , \quad (3)$$

where the time dependence appears in the scaling factor,  $A$ , and the locations of the zeros and poles (the particles of the many-body system). The map is

$$\zeta = F(z, t) = A(t) \left[ 1 + \sum_{n=1}^N R_n \ln(z - P_n) \right] . \quad (4)$$

The quantities  $R_n$  are the residues of the product (without  $A$ ) in (3) at  $P_n$ . Contour-

integrating around the location of the poles and zeros in (2), one finds their EOM:

$$\begin{aligned} -A^2(t)\dot{Z}_n &= f_n^{(Z)}(\{Z\}; \{P\}) \\ -A^2(t)\dot{P}_n &= f_n^{(P)}(\{Z\}; \{P\}) \\ \dot{A}(t) &= A(t)f^{(A)}(\{Z\}; \{P\}) . \end{aligned} \tag{5}$$

The quantities  $A(t)R_n(t)$  can be shown to be *independent constants of the motion* determined only by initial conditions.<sup>(4)(5)</sup>

### The Hamiltonian structure

The fact that the process is Hamiltonian is hinted upon by Eq. (1), when we consider the normal rate alone,

$$\partial_t \gamma(s, t) = -i \frac{\delta s}{\delta \gamma^*} . \tag{6}$$

Expression (6) is equivalent to Hamilton's equations, suggesting that the (rescaled) length of the actual growth,  $s$ , plays the role of a Hamiltonian, while  $\gamma$  is a complex field. It can be shown that this appealing observation can be extended for the map,  $F$ ,<sup>(6)</sup>

$$\dot{F} = -i \frac{\partial}{\partial F^*} \text{Im}\{\Phi\} , \tag{7}$$

where  $\Phi$  is *the complex potential* in the physical plane and  $\text{Im}\{\Phi\} = \text{Const.}$  represent the stream lines. Thus not only is the process Hamiltonian, it is also related to the real (electrostatic) potential energy. There are a couple of alternative Hamiltonian structures that will not be elaborated on here.<sup>(7)(8)</sup>

Following Hamiltonian dynamics means that the p.d.e. that describes the curve's enjoys a conserved energy-like quantity. Since the many-body formulation is an equivalent description of the interface's dynamics it follows that the system of the particles, the poles and zeros, must also conserve that quantity and hence it must also support a Hamiltonian structure. Finding the explicit Hamiltonian for the two-dimensional many-body system proves very difficult and this problem is currently unsolved. But the very realisation that such a Hamiltonian exists allows access to a bag of powerful tools.

### Surface effects

It is known that without surface effects, or capillary forces, cusps form along the interface, corresponding Saffman-Taylor instability.<sup>(9)</sup> Real interfaces, however, avoid cusps because the energy cost increases with curvature. Since a locally high curvature corresponds to a zero approaching the unit circle then smoothening surface effects must correspond to an *effective repulsive potential* between the particles and the interface. I should emphasize that only the existence of a Hamiltonian makes it possible to use the term 'repulsive potential' with a proper physical meaning.

As traditional in physics, the potential should be based on knowledge about the specifics of the system under study and the nature and form of the potential term determines to a large extent the asymptotic morphology. Several models are possible: 1) Simply introducing a surface potential term in the many-body Hamiltonian. Although the explicit form of this Hamiltonian is unknown yet one can insert such a term in the Hamiltonian of the p.d.e.,  $H = H_0 + \sigma(z)V$ , and analyze the particles' trajectories. The stronger the repulsion, the smoother the resulting interfaces. Anisotropy can be introduced via the  $z$ -dependence of  $\sigma$ . 2) The field that the boundary induces can effect *creation and annihilation* of zeros and poles (in pairs, due to constraints on the map). This corresponds to tip-splitting and side-branching in the real system and therefore constitutes a better description of the real system than when the number of particles is constant in time.<sup>(5)</sup> In fact, it was argued that the form of the map is naturally suited for such creation and annihilation.<sup>(6)</sup>

### Statistical analysis

The foregoing discussion focused on a deterministic evolution. Yet, these dynamics are known to be chaotic, i.e., very close initial conditions lead to rapidly diverging structures.<sup>(10)</sup> The Hamiltonian allows to use statistical mechanics and in particular, one



can construct the partition function

$$\mathcal{Z} = \int e^{-\beta H_{\text{many-body}}} \mathcal{DR} ,$$

where  $\mathcal{DR} \equiv \prod_{n=1}^N d^2 Z_n d^2 P_n$  is an infinitesimal volume in phase space. The parameter  $\beta$  reflects the ‘noise’ in the system. Averages of the moments of the curvature and the growth probability distributions can be found from this partition function. Since, at present, the form of  $H_{\text{many-body}}$  is unknown, this approach is not yet easy to implement.

Alternatively, one can construct the master equation for the evolution of the spatial distribution of the particles,  $\mathcal{N}(\{Z\}, \{P\})$ , using Liouville’s theorem

$$\frac{\partial \mathcal{N}}{\partial t} + \sum_{n=1}^N f_n^{(Z)} \frac{\partial \mathcal{N}}{\partial Z_n} + f_n^{(P)} \frac{\partial \mathcal{N}}{\partial P_n} = 0 . \quad (8)$$

Anticipating a steady state after rescaling  $A(t)$  to unity, one can discard the explicit time derivative in the new coordinates (which probably correspond to a similarity solution). I will not attempt to solve this equation in any limit, but rather assume that a solution has been found. Then this distribution can be directly converted into *complete knowledge* of the asymptotic morphology. For example, the distribution of the curvature,  $\mathcal{P}_K$ , is directly derivable from  $\mathcal{N}$  by

$$\mathcal{P}_K = \int \mathcal{N}(\{Z\}, \{P\}) \delta \left\{ K - \left[ 1 + \text{Re} \sum_{n=1}^N \left( \frac{1}{1 - Z_n e^{-is}} - \frac{1}{1 - P_n e^{-is}} \right) \right] \right\} \mathcal{DR} , \quad (9)$$

where  $K$  is the measurable curvature along the interface. Similarly, any morphology-related quantity that can be written in terms of the locations of the particles is attainable in this fashion. For example, of great interest are the moments of the growth probability distribution along the interface. These yield the so-called multifractal spectrum, that has been measured extensively for diffusion-limited-aggregation and similar phenomena. The growth probability at a point  $s$  along the interface is

$$p(s) = C_0 |\nabla \Phi(s)| = \lim_{z \rightarrow e^{is}} C_0 |F'(z)| \quad ; \quad C_0 = 1 / \oint_{\text{along the interface}} |\nabla \Phi(l)| dl .$$

Therefore, (after algebra) we find that the integer moments of this distribution are exactly<sup>(5)</sup>

$$M_{2\nu+1>1} = A(t)^{-2\nu} \left\{ \left( \prod_{n=1}^N \frac{P_n}{Z_n} \right)^\nu + \frac{1}{\nu!} \sum_{n=1}^N \frac{d^{\nu-1}}{dz^{\nu-1}} \left[ \frac{(z-P_n)^\nu}{z J^\nu(z)} \prod_{k \neq n} \left( \frac{z-P_k}{z-Z_k} \right)^\nu \right]_{z=Z_n} \right\}, \quad (10)$$

where  $J(z)$  is a known function of  $z$ ,  $\{Z\}$  and  $\{P\}$ . In particular, the third moment can be found explicitly, which immediately yields the fractal dimension<sup>(11),(12)</sup> through  $D_f = \ln M_3 / \ln R$ , where  $R$  is the growth size (say, the radius of gyration). Similary one can find the moments with  $2\tilde{\nu} + 1 < 1$

$$M_{q<1} = A(t)^{2\tilde{\nu}} \left\{ \left( \prod_{n=1}^N \frac{Z_n}{P_n} \right)^{\tilde{\nu}} + \frac{1}{\tilde{\nu}!} \sum_{n=1}^N \frac{d^{\tilde{\nu}-1}}{dz^{\tilde{\nu}-1}} \left[ \frac{(z-Z_n)^{\tilde{\nu}} J(z)^{\tilde{\nu}}}{z} \prod_{k \neq n} \left( \frac{z-Z_k}{z-P_k} \right)^{\tilde{\nu}} \right]_{z=P_n} \right\}. \quad (11)$$

It is possible to simplify these expressions using a dilute gas approximation, where only particles that are sufficiently close to the unit circle are taken into account.<sup>(6)(8)</sup> This approximation corresponds to probing only the distribution of the exposed parts of the growth and also allows to calculate the distribution of the curvature,  $\mathcal{P}_K$ , in terms of the distribution of the distances of these zeros from the unit circle,  $\mathcal{P}_n(\rho)$ . This approximation yields an interesting result, namely,

$$\mathcal{P}_K = \text{Const. } K^{-3/2} \mathcal{P}_n \left( \rho = (C/K)^{1/2} \right). \quad (12)$$

$\mathcal{P}_n$  is unknown at the moment, but regardless of its exact form we can see that the distribution of  $K$  develops an *algebraic tail*. Such tail usually leads to fractal behavior and therefore this feature immediately points to onset of fractality. If  $\mathcal{P}_n$  decays rapidly, the above calculation would imply that the moments of the curvature distribution are

$$\mu_q \equiv \int_0^{K_{max}} K^q \mathcal{P}_K dK \sim K_{max}^{(2q-1)/2} \sim a^{(1-2q)/2}, \quad (13)$$

where  $a$  is a small cutoff lengthscale. But since the entire aggregate grows this cutoff also renormalizes with time by a factor of  $1/A^2(t)$  and therefore

$$\mu_q \sim A^{(2q-1)}(t). \quad (14)$$

If  $\mathcal{P}_n$  also entertains an algebraic tail then the behaviour of  $M_q$  is directly affected and a multifractal behaviour of  $\mu_q$  should emerge.

### Summary

To conclude I showed that the p.d.e. that governs the growth of an interface in a Laplacian field is Hamiltonian and pointed out the relation between this Hamiltonian and the two-dimensional complex field. I discussed the implications of the Hamiltonian on converting the problem into an equivalent many-body system, whose dynamics are equivalent to the curve's evolution. Surface energy was proposed to give rise to a repulsive potential term (possibly anisotropic) in the Hamiltonian, which naturally prevents cusp singularities along the interface and regularizes the growth. This regularization method avoids the pitfall of traditional singular perturbation approaches, namely, the extreme sensitivity of the asymptotic morphology to initial conditions. The distribution of the particles was discussed. The construction of the partition function and the solution of the pertinent master equation are difficult, but this is no different than in usual statistical mechanical treatments, where some physically valid approximations are needed to obtain exact solutions. The curvature's distribution along the interface (viz., the morphology) was related to the distribution of the particles in the plane. The moments of the growth probability distribution along the interface were calculated exactly, which allows to calculate the fractal dimension and the multifractal spectrum. A dilute gas approximation showed that the distribution of the curvature in the exposed regions of the growth develops an *algebraic tail*, and it has been conjectured that this tail indicates the onset of fractality in such processes. This observation should hopefully shed light on the mysterious origin of fractality in stochastic growth processes in general. The miraculous availability of an equilibrium formalism to describe the highly nonlinear nonequilibrium Laplacian growth makes this first-principles approach a promising candidate for a full theory for the morphology of these and other diffusion-controlled processes.

## REFERENCES

1. L. Piteronero, A. Erzan and C. Evertsz, *Phys. Rev. Lett.* **61** (1988) 861, *Physica A* **151** (1988) 207; T. C. Halsey, *Phys. Rev. Lett.* **72** (1994) 1228.
2. L. A. Galin, *Dokl. Akad. Nauk USSR* **47** (1945) 246; P. Ya. Polubarinova-Kochina, *Dokl. Akad. Nauk USSR* **47** (1945) 254; *Prikl. Math. Mech.* **9** (1945) 79.
3. B. Shraiman and D. Bensimon, *Phys. Rev. A* **30** (1984) 2840.
4. S. Richardson, *J. Fluid Mech.* **56** (1972) 609; M. B. Mineev, *Physica D* **43** (1990) 288.
5. R. Blumenfeld and R. C. Ball, *Phys. Rev. E*, submitted.
6. R. Blumenfeld, in *Nonlinear Evolution Equations and Dynamical Systems*, ed. V.G. Makhankov (World Scientific, 1995).
7. R. Blumenfeld, in *Fluctuations and Order: The New Synthesis*, ed. M.M. Milonas (Springer-Verlag, 1994).
8. R. Blumenfeld, *Phys. Rev. E*, To be published.
9. W. W. Mullins and R. F. Sekerka, *J. Appl. Phys.* **34** (1963) 323.
10. S. D. Howison, *J. Fluid Mech.* **167** (1986) 439.
11. T. C. Halsey, *Phys. Rev. Lett.* **59** (1987) 2067.
12. R. C. Ball and R. Blumenfeld, *Phys. Rev. A* **44** (1991) R828.

## FROM FACETS TO FRACTALS - GROWTH MORPHOLOGIES IN MOLECULAR CRYSTALS OF CARBON TETRABROMIDE (CBr<sub>4</sub>) AND FULLERENE C<sub>60</sub>

RONG-FU XIAO

Department of Physics, the Hong Kong University of Science & Technology, Clear Water Bay, Kowloon, Hong Kong

### ABSTRACT

We have experimentally studied the growth morphologies of carbon tetrabromide CBr<sub>4</sub> and fullerene C<sub>60</sub> crystals in their orientationally disordered solid phases. Very rich growth morphologies have been observed from these crystals, ranging from facets to dendrites and to fractals. In the vapor growth of CBr<sub>4</sub> crystals, we found that the growth morphologies depend not only on temperature and supersaturation, but also sensitively on the total pressure of the inert gas in the growth chamber. With increasing total pressure, under otherwise the same growth conditions, crystals with initially smooth surfaces evolve into dendritic structures. For fullerene C<sub>60</sub>, the growth morphologies from solution are mainly fractals with strong anisotropy in the individual crystals. The growth morphologies from vapor are normally faceted and the growth proceeds via a layer-by-layer mode.

### INTRODUCTION

Study of pattern formation in crystal growth is technologically as well as theoretically important. A good surface morphology is necessary for the growth of high quality single crystals that are needed in device applications. A crystal with poor morphology can induce composition inhomogeneities, grain boundaries and lattice imperfections, which would greatly degrade the performance of a device. The study of pattern formation is theoretically important because it is so ubiquitous. Pattern formation occurs not only in crystal growth, but also in many other different growth systems, for instance, electro-deposition [1], colloid aggregation [2], viscous fingers [3], bacteria growth [4] and bio-convection [5], to name a few. Though these phenomena are typically dealt with in different research areas, the physics of their formation is the same, i.e., the growth is governed by diffusion-limited transport. If we understand pattern formation in crystal growth, we may readily solve other pattern formation problems.

When a substance grows by diffusion-limited transport its surface morphology may lose the stability of a smooth or faceted form and evolve into a dendrite, or even a fractal. Morphological instabilities occur most commonly in melt and solution growth (see ref.[6]). They also appear in vapor growth [7] and sometimes in thin film epitaxial growth [8]. Recently, we have found that morphological instabilities may even occur during solid-solid phase transitions [9]. Among various crystals, growth of molecular crystals is particularly interesting. Owing to weak intermolecular interaction, molecular crystals are usually orientationally disordered in their high temperature solid phase. That is, the molecules in the crystal can readily rotate about their translationally fixed positions [10]. As a result, molecular crystals can quickly relax to their equilibrium state during growth. This special property of molecular crystals facilitates the *in-situ* observation of morphological transitions within a short experimental time.

In this work we report our study of the growth of CBr<sub>4</sub> and C<sub>60</sub> crystals. Both are molecular crystals with orientational disorders in their high temperature solid phase. The reasons for choosing these two molecular crystals for the study of crystal growth pattern formation are as follows. As for CBr<sub>4</sub>, its relatively high vapor pressure near room temperature is convenient for experimental control [11]. As for C<sub>60</sub>, large size of its molecules provides us with an opportunity to examine the effect of molecular size on material transport during growth. Besides, C<sub>60</sub> is a newly discovered material [12] and many of its physical and chemical properties are still unknown. The search for the optimal conditions for growing large C<sub>60</sub> single crystals is deemed to be of great practical significance.

### EXPERIMENTAL PROCEDURES

The growth of CBr<sub>4</sub> crystals was conducted in a vapor growth cell which was specially designed for *in-situ* observation of the crystal morphology under well-defined conditions of temperature, supersaturation and total pressure (for details, see ref. [11]). The source

temperature  $T_s$  and the crystal temperature  $T_c$ , and thus the supersaturation  $\sigma \sim \Delta T = T_s - T_c$ , were controlled within a resolution of  $\pm 0.01^\circ\text{C}$ . After introduction of the source material, the growth cell was evacuated and back-filled to a desired inert gas pressure. Since the vapor pressure of  $\text{CBr}_4$  at the current experiment temperature range was much less than that of the inert gas pressure, the total pressure was actually the pressure of the inert gas. Nucleation on the glass substrate was initiated via a sudden decrease of the  $T_c$  (increase in supersaturation). The growing crystals were monitored *in-situ* with an optical microscope. The images were either directly recorded with an automatic camera or stored in high resolution video and digital recorders with  $1024 \times 1024$  pixels/screen and 256 gray levels. Stored images were selectively processed and quantified with a lateral resolution of 0.3 micrometers. The final images were photographed directly from the screen of a high resolution monitor.

For  $\text{C}_{60}$  crystals, two different experiments, solution growth and vapor phase deposition, were conducted. For the solution growth, toluene was used as a solvent. First,  $\text{C}_{60}$  powder of high purity (99.5%) was dissolved in the solvent. Then, saturated  $\text{C}_{60}$  solution was poured onto a glass slide which was kept at room temperature. The slide was covered by a glass lid with a small opening to allow toluene to evaporate. By adjusting the size of the opening, the supersaturation of the  $\text{C}_{60}$  solution could be controlled. An optical microscope was used to monitor the whole growth process. For the vapor growth of  $\text{C}_{60}$  crystals, elevated temperatures ( $500^\circ\text{C} - 600^\circ\text{C}$ ) were used to achieve an appreciable vapor pressure. The growth was conducted in a quartz vacuum tube (with a base pressure of  $\times 10^{-6}$  torr) in a gold mirror transparent furnace with three temperature zones (for details, see ref. [13]). Due to the high growth temperature, in this case, we were unable to carry out a close-up *in-situ* observation. The observation of crystal growth morphology was done right after the crystal was removed from the vacuum chamber after the experiment was completed.

## RESULTS AND DISCUSSION

### A. GROWTH MORPHOLOGIES OF $\text{CBr}_4$ CRYSTALS

There is a polymorphic phase transition at around  $47^\circ\text{C}$  in  $\text{CBr}_4$  [11]. The low temperature phase is monoclinic and the high temperature phase is face-centered cubic (fcc). In the fcc phase the  $\text{CBr}_4$  crystal is orientationally disordered. We observed a very different morphology of  $\text{CBr}_4$  at its two solid phases. In the low temperature phase  $\text{CBr}_4$  crystals were all faceted, but in the high temperature fcc phase crystals were not faceted at all, and in many situations dendritic crystals occurred (Fig. 1(b)). The reason for such a big change in growth morphology is due to a large reduction of anisotropic surface kinetics as the crystal undergoes a surface roughening transition near the polymorphic transition point [11].

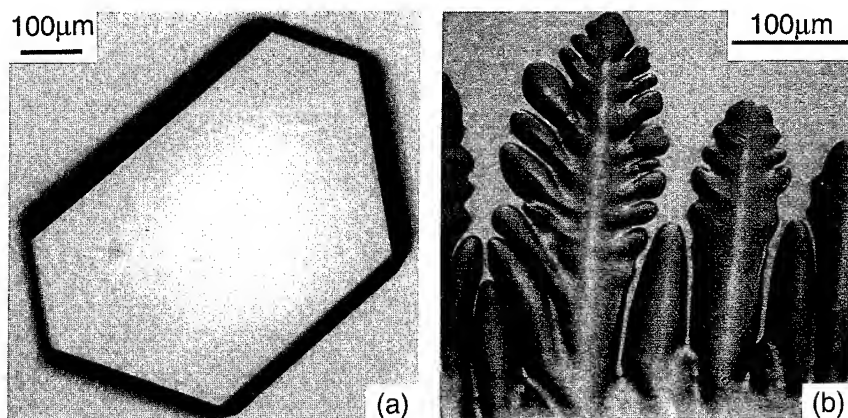


Fig. 1. Typical growth morphologies of  $\text{CBr}_4$  crystals. (a) in the monoclinic phase, at  $P = 12$  torr,  $T_c = 41.46^\circ\text{C}$  and  $\Delta T = 0.06^\circ\text{C}$ ; (b) in the fcc phase,  $P = 12$  torr,  $T_c = 49^\circ\text{C}$ ,  $\Delta T = 0.2^\circ\text{C}$ .

It is known that when a crystal surface is atomically rough it easily becomes unstable in against a perturbation, and even a very small supersaturation can induce crystal morphological instability. Results in Figs. 2(a) and (b) clearly show a morphological break-down as supersaturation was increased. At zero supersaturation, a crystal shows a smooth surface morphology [Fig. 2(a)]. By introducing a very small supersaturation ( $\Delta T = 0.05^\circ\text{C}$ ), cellular patterns appeared [Fig. 2(b)]. In addition to supersaturation, the total pressure in the chamber can also greatly affect crystal growth morphology. The result in Fig. 2(c) was obtained under the same growth conditions as that shown in Fig. 2(b) except that the total pressure was increased from 50 torr to 200 torr. As one can see, at a total pressure of  $P = 50$  torr, cellular structures with large widths occurred [Fig. 2(b)]. However, as the total pressure increased to  $P = 200$  torr [Fig. 2(c)] a much finer cellular pattern developed.

The evolution of crystal morphologies from smooth to cellular structures (as shown in Fig. 2) with increasing total pressure is due to a decrease in diffusivity of  $\text{CBr}_4$  molecules in the vapor phase. From the theory of gas kinetics, we know that the mass diffusivity is inversely proportional to the total pressure. With increasing total pressure,  $\text{CBr}_4$  molecules undergo more collisions with vapor particles (mainly inert gas), and diffusion limited conditions become more pronounced, and hence, the crystal becomes more unstable. Such changes of crystal morphology with increasing total pressure is in good agreement with our earlier results of computer simulation [14]. By employing a modified diffusion limited Monte Carlo model, we have found that crystal surfaces change from completely flat to center-depressed and finally become dendritic with increasing mean free path (or decreasing total pressure) in the vapor phase.

In the diffusion limited growth regime, the means of material transport is a key factor in the control of growth morphology. Due to an insufficient supply of material, growing crystals always compete for material from the nutrient. This is clearly shown from Fig. 3, in which two dendrites were found to grow toward each other. When they were far away, the two tips grew independently at a constant rate ( $\sim 1.2 \mu\text{m}/\text{sec}$ ) [Fig. 3(a)]. However, as they grew closer to within a critical distance of about 15 micrometers their growth rates started to slow down, and in the mean time their tip-radii became larger (fatter). We found that the closer the tips were the slower they grew and the fatter they became. It seemed as though these two dendritic tips were avoiding contact [Fig. 3(b)]. Only after approximately 20 minutes did the two tips finally meet. We explain this phenomenon as follows. The vapor source materials first impinged onto the substrate surface, and then diffused toward the growth front by means of surface diffusion. When these two dendritic tips grew to within certain distance, their diffusion fields overlapped and the material supply became depleted due to growth species competition, and hence, their growth rates decreased. The closer the dendritic tips became, the more severe was the depletion of the material supply and the more difficult it was for the tips to grow. From the distance at which the growth of two dendritic tips began to slow down, we could estimate the width of the surface diffusion boundary layer, which was about 15 micrometers in this case.

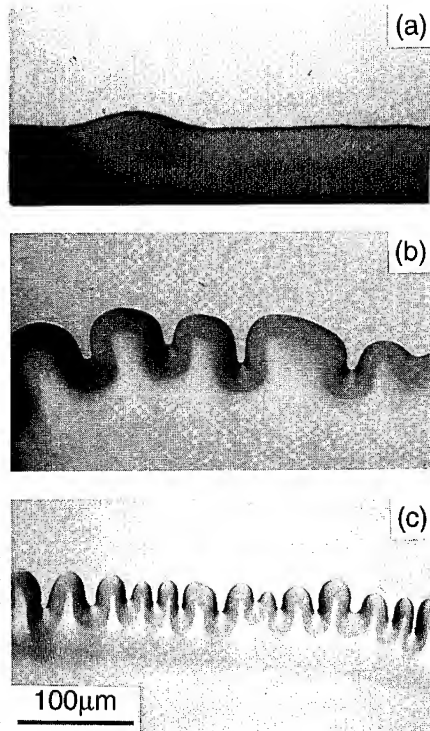


Fig. 2. Effect of supersaturation and total pressure on the growth morphologies. (a)  $P = 50$  torr,  $T_c = 49^\circ\text{C}$ ,  $\Delta T = 0.0$ ; (b)  $P = 50$  torr,  $T_c = 49^\circ\text{C}$ ,  $\Delta T = 0.08^\circ\text{C}$ ; (c)  $P = 200$  torr,  $T_c = 49^\circ\text{C}$ ,  $\Delta T = 0.08^\circ\text{C}$ .

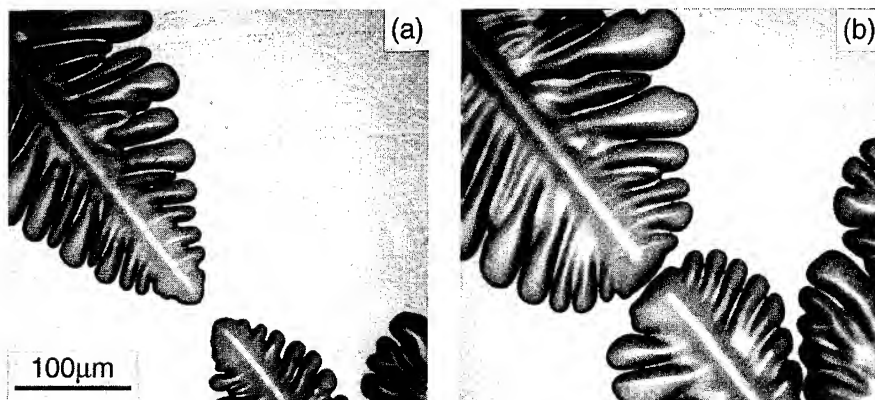
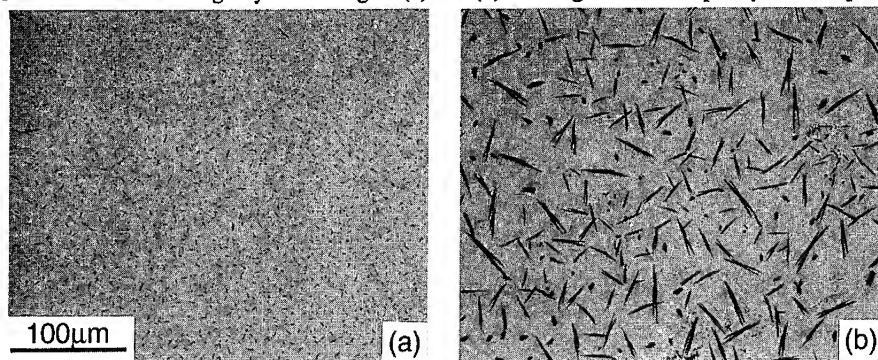


Fig. 3. Growth competition and depletion of material supply at the growth front. (a) fast growing tips when they were far away (no material depletion); (b) very slow tip growth (10 min later) due to material depletion.

#### B. GROWTH MORPHOLOGIES OF $C_{60}$ CRYSTALS

One of the polymorphic phase transitions in  $C_{60}$  occurs at about 260 K [15]. The low temperature phase is simple cubic and the high temperature phase is fcc. Only the high temperature fcc phase is orientationally disordered. In comparison to  $CBr_4$  molecules, the diameter of the  $C_{60}$  molecules is quite large (about 7.1 Å). For such a large-size molecule the material transport during growth is expected to be very difficult. As a result, the diffusion limited transport condition should be more apparent, especially during solution growth. This can be clearly seen from the result shown in Fig. 4, in which  $C_{60}$  crystals were grown from a toluene solution with different supersaturations established by adjusting the opening of the cover-glass. The supersaturation was successively reduced from Figs. 4(a) to 4(d). The result shown in Fig. 4(a) was obtained with the cover-glass fully open, which resulted in, as one can see, many tiny crystals. As the glass opening became smaller, the size of crystals became bigger and longer [Figs. 4(b) - 4(d)]. We measured the fractal dimension ( $N \sim r^D$ ) of the growth pattern shown in Figs. 4 (a) and (b), which was approximately 1.55 in both cases. The fractal dimension of the patterns shown in Figs. 4(c) and (d) could not be measured due to limited sampling size.

It is interesting to note that, although the overall growth patterns are all fractal-like, the individual crystals in Fig. 4 were all grown with large anisotropy (all crystals are elongated with a very large aspect ration) no matter how different the supersaturations were. Intuitively, crystals with weak intermolecular bonding, should show an more isotropic morphology. The results in Fig. 4 are clearly contrary to our expectation. It is amazing that small crystals could not form between the big crystals in Figs. 4(c) and (d) although there was plenty of free space.





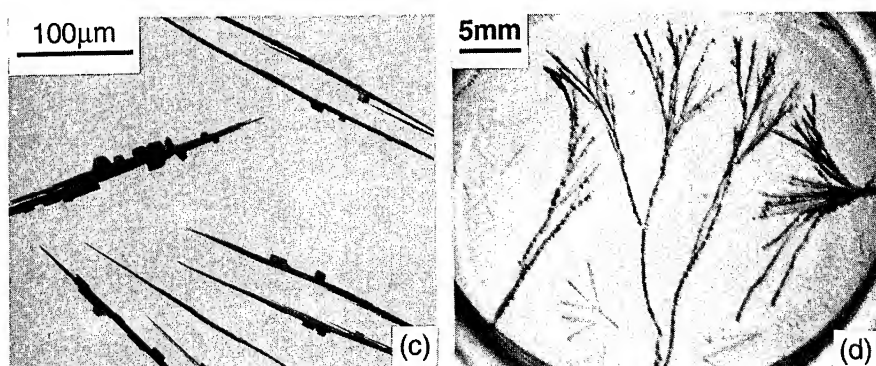


Fig. 4. Morphologies of solution-grown  $C_{60}$  crystals at room temperature. (a) at the highest supersaturation (cover-glass fully open); (b) at an intermediate supersaturation (cover glass half open); (c) at a small supersaturation (cover-glass slightly open); (d) near the equilibrium (cover-glass nearly closed, slow growth for 24 hours).

The material was depleted near the growing crystals, a similar phenomenon as that shown in Fig. 3. Of course, the depletion in solution growth was more severe, which can be further seen in Fig. 5. Here, big crystals grew at the expense of small crystals, and they were surrounded by wide depletion zones. In some cases, grass-like patterns [Fig. 5(b)] would be formed readily.

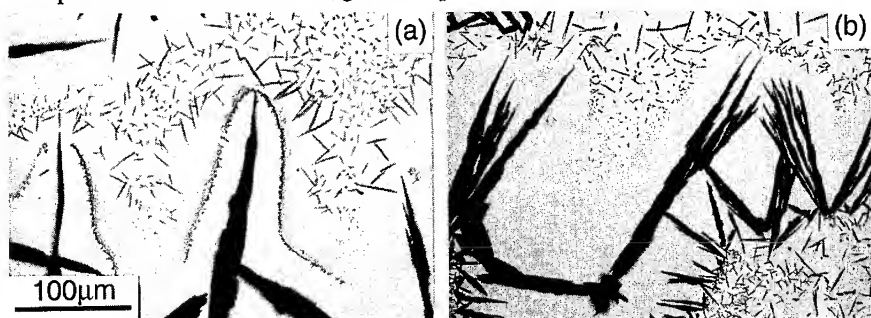


Fig. 5. Depletion of nutrient material near the growing  $C_{60}$  crystals. (a) Depletion zone around big crystals; (b) grass-like growth pattern with wide depletion zones.

In comparison to the solution growth, the surface morphologies of vapor-phase deposited  $C_{60}$  crystals are quite different. We have found that  $C_{60}$  crystals grown from vapor are usually faceted [Fig. 6(a)]. Close-up observation by a high resolution (Nomarski) microscope reveals that the faceted  $C_{60}$  crystal grew in a layer-by-layer mode [Fig. 6(b)]. This is because at 500 °C - 600 °C the vapor pressure of  $C_{60}$  was quite high and, hence, the supply of material was not limited. Also, the spherical shape of  $C_{60}$  molecules may have aided surface diffusion. Due to a large molecular size of  $C_{60}$ , we were able to see monolayer steps under a high resolution (Nomarski) microscope in conjunction with a double-beam interferometer.

In conclusion, we have studied the growth morphologies of carbon tetrabromide  $CBR_4$  and fullerene  $C_{60}$  crystals in their orientationally disordered solid phases. Very rich growth morphologies have been observed from these crystals, ranging from facets to dendrites and even fractals. In the vapor growth of  $CBR_4$  crystals, we found that the growth morphologies depend not only on temperature and supersaturation, but also on the total pressure of the inert gas in the

growth chamber. With increasing total pressure, under otherwise the same growth conditions, crystals with initially smooth surfaces evolve into dendritic structures. For fullerene  $C_{60}$ , the crystal morphologies grown from solution are mainly fractals with strong anisotropy in the individual crystals. The crystal morphologies grown from vapor are normally faceted and the growth proceeds in a layer-by-layer mode.

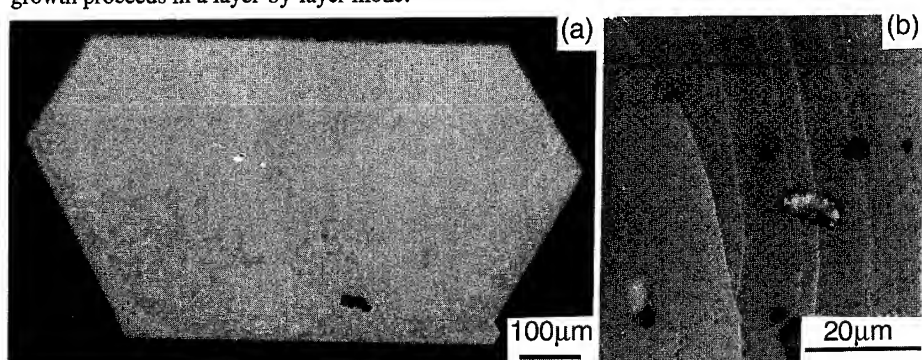


Fig. 6. Morphologies of vapor-phase grown  $C_{60}$  crystal (with a base pressure of  $P = 15 \times 10^{-3}$  torr),  $T_c = 520^\circ\text{C}$ ,  $\Delta T = 30^\circ\text{C}$ . (a) faceted  $C_{60}$  crystal; (b) locally enlarged view of the crystal in (a), showing crystal growth in a layer-by-layer mode. Note that the large particles in picture (b) were dust which stuck onto the crystal after exposing it to air.

#### ACKNOWLEDGMENT

Part of the experiment was done when the author was with the Center for Microgravity and Materials Research at the University of Alabama in Huntsville (USA).

#### REFERENCES

- [1] M. Matsushita, M. Sano, Y. Hayakawa, H. Honjo, and Y. Sawada, *Phys. Rev. Lett.* 53 (1984) 286; Y. Sawada, A. Dougherty, and J.P. Gollub, *Phys. Rev. Lett.* 56 (1986) 1260.
- [2] D.A. Weitz, and M. Oliveria, *Phys. Rev. Lett.* 52 (1984) 1433.
- [3] J. Nittmann, G. Daccord, and H.E. Stanley, *Nature* 314 (1985) 141.
- [4] H. Fujikawa and M. Matsushita, *J. Phys. Soc. Jpn.* 58 (1989) 3875.
- [5] D.A. Noever, *Phys. Rev. Lett.* 65 (1990) 1953.
- [6] M.E. Glicksman, in *Proc. Indo-United States Workshop on Solidification Principles and Metastable Microstructures*, Hyderabad, Jan. 1988; S.-C. Huang, and M.E. Glicksman, *Acta Metall.* 29 (1981) 707 and 717; J.P. Gollub, in Nonlinear Phenomena Related to Growth and Form, edited by M. Ben Amar, P. Pelce, and P. Tabeling (Plenum, 1991).
- [7] U. Nakaya, *Snow Crystals* (Harvard Univ., Cambridge, MA, 1954); T. Kobayashi, and T. Kuroda, in *Morphology of Crystals*, edited by I. Sunagawa (Terra Sci., Tokyo, 1987), Part B, p. 645, and references therein.
- [8] R.T. Tung, and F. Schrey, *Phys. Rev. Lett.* 63 (1989) 1277; K. Kato, Y. Hasumi, A. Kozen, and J. Temmyo, *J. Appl. Phys.* 65 (1989) 1947.
- [9] R.-F. Xiao, and F. Rosenberger, *J. Crystal Growth* 114, 549 (1991).
- [10] J. Timmermans, *J. Phys. Chem. Solids* 18, 1 (1961); R.M. Hooper, and J.N. Sherwood, in: *Surface and Defect Properties of Solids*, Vol. 6 (Chemical Soc., London, 1977) p. 308.
- [11] R.-F. Xiao and F. Rosenber, *J. Crystal Growth* 114, 536 (1991); R.-F. Xiao, *Phys. Rev. E* 47, 3463 (1993).
- [12] H.W. Kroto, J.R. Heath, S.C. O'Brien, R.F. Curl, R.E. Smalley, *Nature* 318, 162 (1985); W. Kratschmer, L.D. Lamb, K. Fostiropoulos, D.R. Huffman, *Nature* 347, 354 (1990).
- [13] R.-F. Xiao, W.C. Ho, L.Y. Chow, K.K. Fung and J.Q. Zheng, *Appl. Phys. Lett.*, accepted.
- [14] R.-F. Xiao, J.I.D. Alexander, and F. Rosenber, *J. Crystal Growth* 109, 43 (1991).
- [15] W.I.F. David, R.M. Ibberson, T.J.S. Dennis, J.P. Hare, and K. Prassides, *EuroPhys Lett.* 18, 219 (1992).

## REAL SPACE RENORMALIZATION GROUP FOR SELF ORGANIZED CRITICALITY IN SANDPILE MODELS

S. ZAPPERI<sup>†</sup>, A. VESPIGNANI<sup>‡</sup> AND L. PIETRONERO\*

<sup>†</sup> Center for Polymer Studies and Department of Physics, Boston University, Boston, MA 02215, USA

<sup>‡</sup> Department of Mathematics, Yale University, New Haven, CT-06520-8283 USA

\* Dipartimento di Fisica, Università di Roma "La Sapienza", P.le A. Moro 2, 00185 Roma, Italy

### ABSTRACT

We have introduced a new renormalization group approach that allows us to describe the critical stationary state of sandpile models (Phys. Rev. Lett. **72**, 1690 (1994)). We define a characterization of the phase space in order to study the evolution of the dynamics under a change of scale. We obtain a non trivial attractive fixed point for the parameters of the model that clarifies the self organized critical nature of these models. We are able to compute the values of the critical exponents and the results are in good agreement with computer simulations. The method can be naturally extended to several other problems with non equilibrium stationary state.

### INTRODUCTION

The words Self Organized Criticality (SOC) define a vast class of dynamical systems which evolve spontaneously toward a critical point without the need to fine tune any critical parameter. To illustrate these ideas Bak and co-workers [1] introduced a cellular automaton inspired by the flow of avalanches in a pile of sand. These models have been investigated extensively by computer simulations [2-8] and some exact results have been derived by Dhar and co-workers [9]. In this paper we develop a Real Space Renormalization Group scheme for the dynamics of these models [10]. We are able to identify the scale invariant dynamics and to compute from that the critical exponents. This procedure is similar to the Fixed Scale Transformation [11] for fractal growth models where the fractal dimension is computed from the knowledge of the parameters at the critical point. This is in contrast with the case of ordinary critical phenomena where the presence of a relevant critical parameter allows one to evaluate the critical exponents linearizing the RG transformation. In SOC systems this procedure is conceptually impossible because by definition no relevant critical parameter can be identified.

### THE MODEL

Sandpile models are cellular automata defined on a lattice. In the following discussion we will refer to the two dimensional Critical Height Models [6]. A variable that we call energy, is assigned to every lattice site. Energy is added randomly on the system until the energy at some site reaches a given threshold ( $E_c$ ). When this happens the site becomes unstable and the energy is released to the neighbours according to the specific rules of the model. In particular, in the BTW model [1] energy takes discrete values and when the energy reaches the threshold ( $E_c = 4$ ) four grains are equally distributed between the four neighbours. In this way subsequent relaxation events will generate avalanches. The system has open boundary conditions that allow the dissipation of energy outside. After some time the system reaches a stationary critical state characterized by power law distributions for avalanche amplitudes.

Various modifications of the original model have been proposed. The values energy can be chosen as continuous [7] or dichotomic [5], the flux can be directed [3] or a certain degree of dissipation [8] can be introduced in the dynamical rules. It is possible to describe all these different variations in term of universality classes. For example the introduction of non conservation changes dramatically the critical properties of the model. Our renormalization scheme provides a natural framework to understand many of these differences.

### THE RENORMALIZATION TRANSFORMATION

In order to construct a Renormalization Group transformation for the dynamics of sandpile models we have first to identify a suitable parameter space. In full generality we can define three classes of sites:

- i) *Stable sites* are those whose energy is far from the threshold value. This implies that the addition of a "quantum" of energy will not induce relaxation.
- ii) *Critical sites* are those whose energy is critical in the sense that the addition of a "quantum" of energy will induce relaxation.
- iii) *Unstable sites* are those that will relax at next time step according to the specific rules assigned.

These definitions can be easily generalized if we want to describe the system at a coarse grained scale. A relaxation event happens at scale  $b$  if an avalanche cluster spans the cell and transfers some energy to the neighbouring cells. We define  $\rho(b)$  as the density of critical cells at scale  $b$ . The way in which the relaxation event takes place in the coarse grained system is described by the dynamical rules at scale  $b$ . In general energy can be transferred to one, two, three or four neighbors with a probability distribution defined by the vector

$$\vec{P} = (p_1, p_2, p_3, p_4), \quad \sum_{i=1}^4 p_i = 1 \quad (1)$$

The actual values of this vector will depend on the model we chose and on the scale under consideration. For example the BTW dynamics at the minimal scale is described by  $P^{(0)} = (0, 0, 0, 1)$ . The vector  $\vec{P}$  is the natural candidate on which to act with the RG transformation. In order to find the actual form of this transformation we consider a cell at scale  $b = 2^{k+1}b_0$  composed by critical and stable subcells at scale  $b/2$ . We assume that one of the critical subcells relaxes and we study how the energy is distributed to the neighboring cells at scale  $b$  (figure 1). For every starting configuration  $(\alpha)$  we obtain in this way a contribution to the value of the renormalized  $\{p_i^{(k+1)}\}$  in terms of the values of the probabilities  $\{p_i^{(k)}\}$  defined at a smaller scale. We average over all the possible starting configurations and we obtain a renormalization equation for the component of the vector  $\vec{P}$ :

$$p_n^{(k+1)} = \sum_{\alpha=2}^4 W_\alpha(\rho^{(k)}) p_n^{(k+1)}(\alpha) \quad (2)$$

where  $W_\alpha$  is the weight of the configuration  $\alpha$  expressed in terms of  $\rho^{(k)}$ . The density of critical cells at scale  $k+1$  can be computed considering a stationarity condition for the flow of energy in and out of the cell. Namely the energy that goes into the cell in average is equal to the energy that goes out. This can be expressed as

$$\delta E(b) = \rho^{(k+1)}(\delta E(b)p_1^{(k+1)} + 2\delta E(b)p_2^{(k+1)} + 3\delta E(b)p_3^{(k+1)} + 4\delta E(b)p_4^{(k+1)}). \quad (3)$$

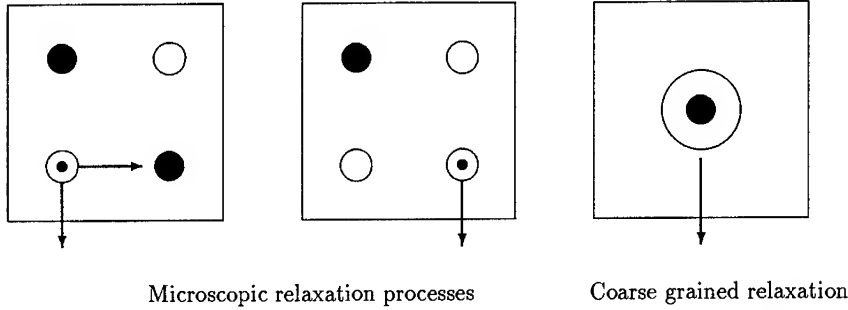


Figure 1: Example of the renormalization scheme for the relaxation dynamics. The process shown in the figure contributes to the value of  $p_1^{(k+1)}$ .

where  $\delta E(b)$  represent the energy “quantum” at scale  $b$ . These equation reflect a conservation law present in the dynamics and provides a feedback mechanism between statics and dynamics that is an essential element for the process of self organization. Equations 2 and 3 can be iterated in order to study the nature of the phase space. We found that no matter how it is the value of the small scale parameters  $(\rho^{(0)}, \vec{P}^{(0)})$  the system flows into the same non trivial fixed point  $(\rho^*, \vec{P}^*)$ . This fact defines the universality class of the model. In particular different microscopic rules give all rise to the same asymptotic dynamics.

### CRITICAL EXPONENTS

The attractiveness of the fixed point reflects the self organized nature of the problem and corresponds to a lack of relevant control parameter. Therefore the critical exponents can not be found in the usual way by linearizing the RG equations. The exponents have to be computed from the values of the fixed point parameters that describe the asymptotic dynamical rules for the model. As an example we show here how to compute the dynamical critical exponent  $z$  relating the linear size of an avalanche with its duration. This can be expressed using the discretized lenght of our scheme

$$t_k \sim (b^{(k)})^z. \quad (4)$$

using the fact that  $b^{(k)} = 2^k b_0$  we obtain

$$\frac{t_{k+1}}{t_k} = (2)^z \quad (5)$$

The time scale  $t_{k+1}$  can be obtained as a function of the time scale  $t_k$  from the RG equations. In fact, the renormalized dynamical process is given by the weighted average of the series of sub-processes at scale  $b^{(k)}$ , whose time scale is  $t_k$ . Therefore we have

$$t_{k+1} = \langle t \rangle t_k \quad (6)$$

where  $\langle t \rangle$  is the average number of steps at scale  $b^{(k)}$  needed to have a relaxation process at scale  $b^{(k+1)}$ . For example the process shown in figure 1 is composed by two steps. In general  $\langle t \rangle$  can be computed in terms of the fixed point parameters. Using equation (5) we obtain

$$z = \frac{\log \langle t \rangle}{\log 2} = 1.168. \quad (7)$$

|                 | Critical exponents |          |           |       |
|-----------------|--------------------|----------|-----------|-------|
|                 | $\tau$             | $\alpha$ | $\lambda$ | $z$   |
| RG scheme       | 1.253              | 1.432    | 1.506     | 1.168 |
| BTW simulations | 1.22               | 1.38     | 1.44      | 1.21  |

Table I: In this table are summarized the value of the critical exponents calculated with our RG scheme. For comparison we also list the values obtained from large scale simulations on the BTW model ( $d = 2$ ) [6]. We define  $\tau$ ,  $\lambda$  and  $\alpha$  respectively as the exponents of the distribution of avalanche sizes, linear sizes and durations. For the definition of  $z$  see text.

This value can be readily compared to existing estimates of  $z$  and our analytical prediction is in very good agreement with the numerical results that give  $z \simeq 1.20$  [1, 4, 6]. The avalanche distribution exponent  $\tau$  can be computed using similar methods, the details of the calculation are reported in [10]. In table I we report the value of the various critical exponents of the model obtained with our method compared with the best numerical estimates.

## CONCLUSIONS

In this paper we have presented a new renormalization approach suited to study the SOC state of sandpile models. Using this method we were able to understand the nature of the critical state and to compute the critical exponents. According to our scheme all the Critical Height Models with isotropic conservative dynamics belong to the same universality class. The method has been extended to non conservative cases as well [12]. It has been shown that the introduction of a dissipation parameter turns the attractive fixed point into a repulsive one. Therefore a dissipation in the dynamical rules destroys the critical properties of the model. This result has been confirmed by computer simulations [8]. Recently this formalism has been applied to directed sandpile models [13] and to the Forest Fire model [14]. The results are in good agreement with computer simulations and with exact results [9].

## References

- [1] P.Bak, C.Tang and K. Wiesenfeld, Phys. Rev. Lett. **59**, 381 (1987); Phys. Rev. A **38**, 364 (1988).
- [2] P.Grassberger and S.S.Manna, J.Phys.France **51**, 1077 (1990).
- [3] L.P.Kadanoff, S.R.Nagel, L.Wu and S.Zhu, Phys.Rev. **A39**,6524 (1989)
- [4] K.Christensen, H.C.Fogedby and H.J.Jensen, J. Stat. Phys. **61**, 653 (1991).
- [5] S.S.Manna, J.Phys. A **24**, L363 (1991).
- [6] S.S.Manna, J. Stat.Phys. **59**,509 (1990); Physica A **179**,249 (1991)
- [7] Y.C.Zhang, Phys. Rev. Lett., **63**, 470 (1989).
- [8] S.S.Manna, L.B. Kiss and J. Kertesz, J.Stat.Phys.**61**, 923 (1990).
- [9] D.Dhar and R. Ramaswamy, Phys. Rev. Lett. **63**, 1659 (1989); D.Dhar, Phys. Rev. Lett. **64**,1613 (1991); S. N.Majumdar and D. Dhar, Physica A **185**, 129 (1992) Phys. Rev. A **38**, 364 (1988).

- 
- [10] L.Pietronero, A.Vespignani and S.Zapperi, Phys. Rev. Lett. 72, 1690 (1994).
  - [11] L.Pietronero, A. Erzan and C. Evertsz, Phys.Rev.Lett. 61, 861 (1988); A.Erzan, L. Pietronero and A. Vespignani, *The Fixed Scale Transformation Approach to Fractal Growth*, submitted to Rev. Mod. Phys 1994.
  - [12] A. Vespignani, S. Zapperi and L. Pietronero, to be published on Phys. Rev. E .
  - [13] R. Hallgass and V. Loreto , (unpublished)
  - [14] V.Loreto, L. Pietronero, A.Vespignani and S.Zapperi, (to be published)

## THE GEOMETRY OF DLA: DIFFERENT ASPECTS OF THE DEPARTURE FROM SELF-SIMILARITY

B.B.MANDELBROT, A.VESPIGNANI AND H.KAUFMAN  
Department of Mathematics, Yale University, New Haven, CT-06520-8283, USA

### ABSTRACT

In order to understand better the morphology and the asymptotic behavior in Diffusion Limited Aggregation (DLA), we studied a large numbers of very large off-lattice circular clusters. We inspected both dynamical and geometric asymptotic properties, namely the moments of the particle's sticking distances and the scaling behavior of the transverse growth crosscuts, i.e., the one dimensional cuts by circles. The emerging picture for radial DLA departs from simple self-similarity for any finite size. It corresponds qualitatively to the scenario of infinite drift starting from the familiar five armed shape for small sizes and proceeding to an increasingly tight multi-armed shape. We show quantitatively how the lacunarity of circular clusters becomes increasingly "compact" with size. Finally, we find agreement among transverse cuts dimensions for clusters grown in different geometries, suggesting that the question of universality is best addressed on the crosscut.

### INTRODUCTION

The first model of irreversible growth that generates fractal structures was Diffusion Limited Aggregation (DLA) [1], followed few years later by the Dielectric Breakdown Model [2]. These models account for origin of fractal structure in a great variety of process: dendritic growth, viscous fingers in fluids, dielectric breakdown, electrochemical deposition etc. [3,4]. DLA's most characteristic feature is that it is intrinsically critical and gives rise spontaneously to a fractal structure. However, as soon as one tries to make this statement precise and quantitative, diverse problems appear, many of which are still open. We tackle the question of asymptotic self-similarity, which has not to this day been resolved adequately. In fact, several clues suggests that asymptotic self-similarity is not the only possible scenario: conflicting values of the fractal dimension, slow cross-over to the asymptotic regime, weak universality with respect to the growth geometry and deviations from simple self-similarity such as lacunarity etc. [1,5,6,7]. To gain a deeper understanding of these problems we have undertaken a systematic study of the properties of large numbers of very large clusters of off-lattice circular DLA.

The construction of DLA clusters is very simple. It begins with a particle at a random location on a "birth" circle at some distance to the existing cluster. The new particle undergoes Brownian motion until it comes in contact to the cluster, at which point it becomes permanently stuck. A new particle is then added at random along the birth circle, and the process continues. Our study is based on 50 clusters of 1M particles and 20 clusters of 10M particles, grown under meticulous control to avoid large scale instabilities due to approximations in the algorithm [8]. We investigate the geometric structure of circular DLA from two points of view. A) Growth of various relative moments and of the maximum cluster radius. B) Structure of the transverse growth crosscuts, i.e., the one-dimensional cuts by circles. On these cuts we study the fractal dimension, the gap distribution, the behavior of the maximum gap and other morphological properties.

We find that the moments of the distribution of the particle's sticking distance fail to cross over to the behavior characteristic of self-similarity, even for very large clusters. The measurement of the fractal dimension on the transverse cuts reveal a correction term that can be accounted for by postulating a power law behavior in the prefactor that measures the mass lacunarity. This "misbehavior" may help understand previous disagreements between estimates of the fractal dimension and suggests, moreover, that the question of universality is best addressed on the transverse-cuts. The analysis of gap also is fully compatible with this picture,



and the maximum gap behavior is compatible with a lacunarity effect revealing that the cluster drift to an increasingly tight multi-armed shape.

The conclusion is that, for radial geometry, the present results support Mandelbrot's scenario [6] in which, as samples grow, some properties of DLA drift without non trivial limit and with diverse departures from the simple self-similarity for any finite size cluster. This paper is a survey of various forms of analysis and the corresponding results. For the sake of clarity and concision, we avoid most of the technical details that will be reported elsewhere [9,10,11].

### "MOMENTS" ANALYSIS USING NORMALIZED SCALE FACTORS

First we investigated the distributions we call radial density profiles [9]. Given a cluster of  $N$  particles let  $F(R,N)$  be the number of particles at a distance  $\leq R$  from the seed. The particles that become part of the cluster when cluster size ranged between  $N - \Delta N$  and  $N$  are said to form a cluster shell. The radial cluster shell profile is therefore

$$\Delta F(R,N) = F(R,N) - F(R,N - \Delta N) \quad (1)$$

For  $\Delta N = N$ , the cluster shell is of course the entire cluster. The function  $F(R,N)$  is a cumulative distribution relative to distances  $\ll R$ , and is often usefully replaced by a density-like function. For that, one divides  $\log R$  into uniform bins and plots the number of atoms in each bin. Letting  $R_k$  be the distance from the seed to the  $k$ -th particle (in order of absorption into the cluster), the moment-based scale factors of the cluster shell are defined as

$$\sigma_q(N, \Delta N) = \left[ \frac{1}{\Delta N} \sum_{k=N-\Delta N+1}^N \left| R_k - \frac{1}{\Delta N} \sum_{n=N-\Delta N+1}^N R_n \right|^q \right]^{1/q} \quad (2)$$

In all cases, the  $q \leq 0$  values of  $\sigma_q$  are without interest, being dominated by the inner cutoff due to the atoms' positive size. It is obvious indeed, that  $\sigma_0 = 1$  and it is easy to show that  $q < 0$  yields  $\sigma_q \propto N^{1/q}$ . To the contrary, when  $q > 0$  and  $N \gg 1$ , the atom's size no longer matters. As  $q \rightarrow \infty$ ,  $\sigma_q$  converges to  $R_{\max}(N)$ , the largest distance from the seed to a particle in a cluster. It is important to notice that our shell analysis focuses particularly on the active region of the DLA cluster, where new particles become part of the aggregate. If, beyond atom size, the cluster had been statistically self-similar, it would have been characterized by a single well-defined  $D$ , and all the quantities  $\sigma_q(N, \Delta N)$  would have been proportional (for large  $N$ ) to  $N^{1/D}$  and to each other.

The first inference from our data is a very familiar one. For  $q = 1$  we find, as previous authors observed again and again, that  $\sigma_1(N) = 1/N \sum_{k=1}^N R_k \propto N^{1/D}$ , where  $D = 1.71$ . The study of the cluster shell moment continues more easily by normalizing and writing

$$\sigma_q(N) = \sigma_1(N) \cdot \lambda_q(N); \text{ and } R_{\max} = \lim_{q \rightarrow \infty} \sigma_q(N) \cdot \lambda_q(N). \quad (3)$$

For given  $N$ , the factors  $\lambda_q(N)$  necessarily increase with  $q$ . A necessary but not sufficient condition for the clusters' being self-similar is that each  $\lambda_q(N)$  tends to a limit as  $N \rightarrow \infty$ . To test this inference, we evaluated these quantities for logarithmically spaced values of  $N$ , and plotted them in doubly logarithmic coordinates (see fig.1). Our most striking observation is that

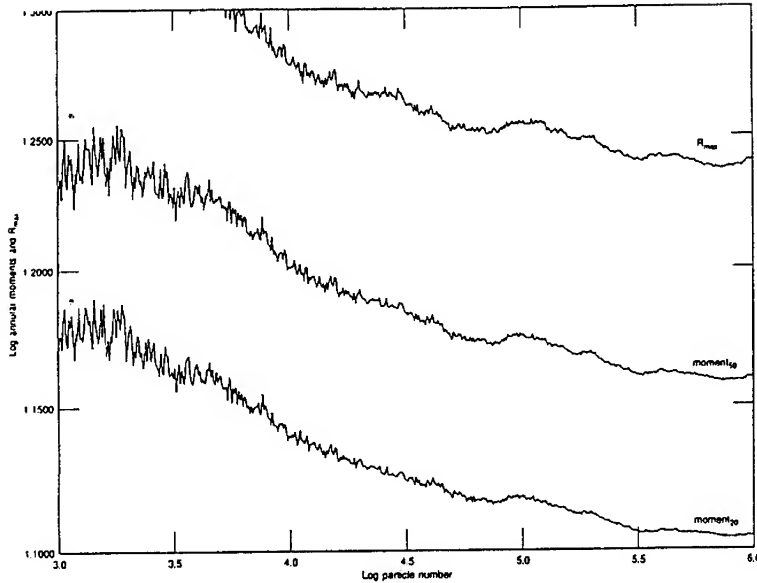


Fig.1) Analysis of DLA circular clusters based on the annular moments behavior. The various moments are normalized with respect to the first one and averaged over 50 one million particle clusters.

$\lambda_q(N)$  continually decrease for every value of  $q > 2$ , including  $q \rightarrow \infty$ . In fig.1, it is easy to note the curvature of the  $\lambda_q(N)$  up to the limit sample size. In order to visualize this behavior, we perform a local slope analysis of  $\lambda_q(N)$  (fig.2). The local slope is definitely different from zero even for  $N \approx 10^6$ , and approaches zero only for very large size clusters. The cross-over from fast to slow decrease depends on  $q$ . For large  $q$ ,  $\lambda_q(N)$  continues to decrease rapidly, even in the range where, in absence of other information, it might have been argued that  $\lambda_2(N)$  has finally settled down. Thus,  $\lambda_q(N)$  continues to decrease non trivially up to the size of our simulations. Moreover, accurate analysis shows that a logarithmic behavior of the  $\lambda_q(N)$  curves seems consistent up to  $N \approx 10^4$  but not for larger clusters. Therefore, these results support the scenario of an "infinite drift" with persistent deviations from self-similarity for arbitrary large finite size samples and an unusual approach to the thermodynamic limit.

#### ANALYSIS OF THE TRANSVERSE GROWTH CROSSCUTS

The moments-based analysis in the preceding section is two dimensional, but can also be performed geometric and quantitative analysis on various one-dimensional sub sets of the cluster. In this spirit, we analyzed DLA via transverse growth crosscuts, namely one-dimensional cuts by circles of different radius  $R$ . Each is roughly transverse to the growth direction of the aggregate. "Generically" a one-dimensional cross-section (slice) of a fractal of dimension  $D$  is a fractal dust of dimension  $D-1$ . For DLA the widely accepted value  $D=1.71$

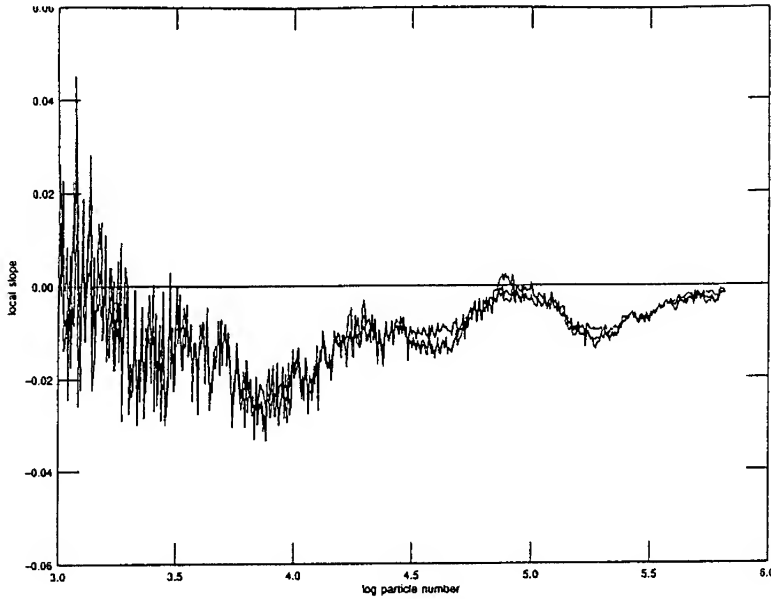


Fig.2) Local slope analysis of the moments behavior. Excluding the initial region (small sizes effect), the local slope is appreciably and definitely lower than zero.

obtained from the mass-radius relation yielded the heuristic expectation that the fractal dimension of the crosscuts is  $D_c = 0.71$ .

We measured the fractal dimension of the crosscuts of 20 10M particles clusters and intersecting circles with a radius ranging from  $R = 200$  to  $R = 5000$  particle diameters. The radius did not exceed  $3/4$  of the radius of gyration of the clusters to ensure that our study concerns the frozen part of the aggregates that is extraordinarily unlikely to change in the further growth.

Our first method to obtain the fractal dimension on the crosscut set is box-counting. We rescale each crosscut in the unit circle and then we coarse grain with boxes of different lengths. Our second method uses the mass-radius relation in one dimension. It measures the total number of particles within an increasing distance from an occupied point of the crosscut. The scaling behavior corresponding to the values of the fractal dimension is obtained from the log-log plots of the number of occupied boxes or cluster's points versus the scaling size. To eliminate noise, we always average the data over several clusters of the same size. Both methods are clearly affected by finite size effects corresponding to very small sizes (particle radius) and very large sizes (the entire crosscut), therefore, as the radius of intersection for the crosscut increases the fractal dimension is measured more precisely. In our experience a reliable result is possible only with very large samples that ensure enough statistics on the crosscuts.

Strikingly, the fractal dimension obtained in this way is lower than the expected value 0.71. In fact, both methods thus agree the fractal dimension is practically constant from  $R = 1500$ , its average value being

$$D_c = 0.65 \pm 0.01 \quad (4)$$

This result differs strongly from the expected one and can be related to a mass-lacunarity effect in the measurement of the fractal dimension. In fact, as already done in [6], we can write

the exact scaling relation on a crosscut as

$$N_c\left(\frac{R}{\ell}\right) = \lambda(R) \cdot \left(\frac{R}{\ell}\right)^{D_c} \quad (5)$$

where  $N$  is the number of particles and  $\ell$  is the scaling length. For each crosscut  $R$  is a constant, namely the radius of the intersection, and  $\lambda(R)$  is therefore a constant prefactor. The fractal dimension of the crosscut is obtained from the scaling with respect to the size  $\ell$  and with our method we have the result of eq.(4).

For the whole cluster, we can relate the mass-radius fractal dimension, i.e., scaling behavior in the two-dimensional embedding space, to the scaling on the crosscuts by using the following formula

$$N_t(R) = \int_0^R \lambda(R) \cdot \left(\frac{R}{\ell}\right)^{D_c} dR \quad (6)$$

where  $N_t$  is the total number of particles in a cluster of radius  $R$  and  $\ell$  is fixed and corresponds to the resolution scale. We know that

$$N_t(R) \propto R^D \quad (7)$$

with  $D=1.71$  with a scaling behavior confirmed on several decades. If  $\lambda(R)$  changes gradually, there is only one way for  $\log(N_t)$  to be represented by a straight line; one must have  $\lambda(R) \propto R^{\delta D}$  from which we have

$$N_t(R) \propto \int_0^R R^{\delta D} \cdot \left(\frac{R}{\ell}\right)^{D_c} dR \propto R^{1+D_c+\delta D} \quad (8)$$

By comparing this relation with eq.(7) we have

$$\delta D = D - 1 - D_c \quad (9)$$

and substituting the numerical values obtained for the crosscuts fractal dimension we can estimate the bias due to the lacunarity prefactor as :

$$\delta D \approx 0.05 \quad (10)$$

It is easy to recognize that the prefactor  $\lambda(R)$  is a characteristic of the clusters. It is a numerical rate that contributes to measuring lacunarity. Therefore, our results indicate that the lacunarity decreases as the DLA cluster grows and becomes increasingly compact. This lacunarity effect is specific to DLA grown in circular geometry and could explain the discrepancies among various measurements of the fractal dimension. The discrepancies among DLA clusters growing with different boundary conditions indicate a sort of "weak" universality of this phenomenon. However, it is worth observing that the value of the fractal dimension we measure for circular crosscuts is the same as that obtained for crosscuts of cluster grown in cylindrical geometry. This seems to suggest that the question of the universality of DLA is best addressed on the crosscuts. In fact, this is the only set that possesses an important geometric characteristic that is independent of the growth boundary conditions: it is always transverse to the growth direction. Therefore it is possible that measurements on this set take into account only the intrinsic growth dynamics of the phenomenon leaving apart the effects induced by the geometry of the boundary conditions.

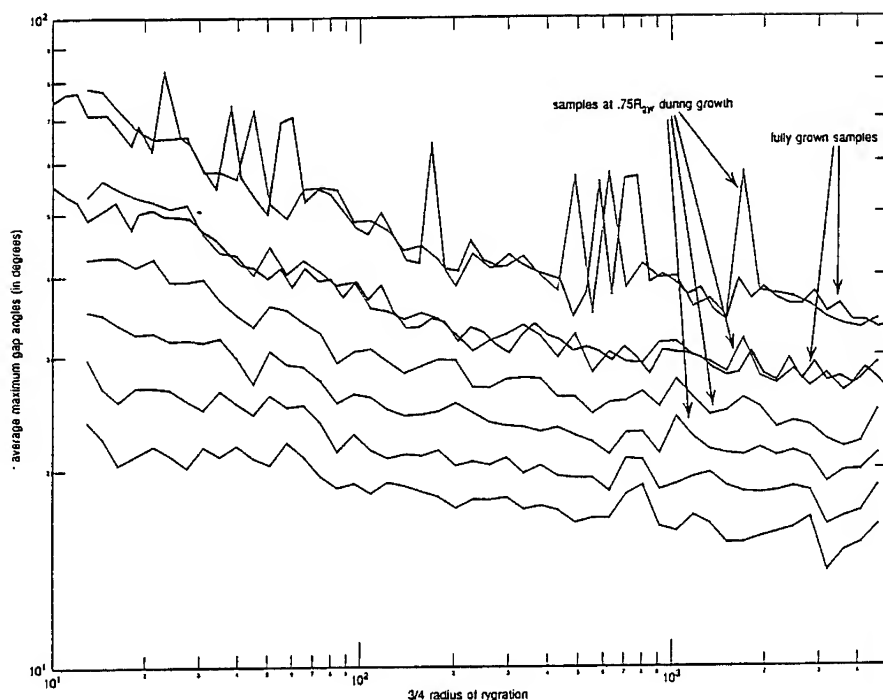


Fig.3) Average angles of the six largest gaps on the crosscuts with respect to the radius of intersection. The fact that the gaps become smaller corresponds to a decreasing lacunarity on the crosscuts.

In support of the previous numerical result we performed a detailed analysis of the gap lengths on the crosscuts. This kind of analysis was introduced in Ref [6]. A gap is defined as an interval whose end points belong to the fractal set but whose interior points do not. Denote by  $\gamma$  a possible value of the gap on the crosscut. To compare the gap length distribution for different crosscuts of different radius we rescale each intersection by the radius  $R$ , so that gaps are measured in angles. In fig. 3 we plot on a doubly logarithmic scale the average angles of the six largest gaps with respect to the radius of intersection of the crosscut. In the usual picture of DLA the structure evolves rapidly towards a five fold symmetry (five main branches), suggesting that largest gaps fluctuate around the constant value  $\gamma = 2\pi/5$ . In sharp contrast, our data show that the largest gaps continuously decrease as  $R$  increases and the value of  $\gamma_{\max}$  is definitely  $< 2\pi/5$ . The fact that the few largest gaps become smaller as the cluster grows indicates that the structure drifts to a tighter multi-armed shape. It is simple to recognize that this corresponds to a decreasing lacunarity on the crosscuts. In fact, the narrowing of the larger fjords implies the presence of an increasing number of main branches, and therefore a less lacunar structure even if the scaling properties on the crosscut remain the same.

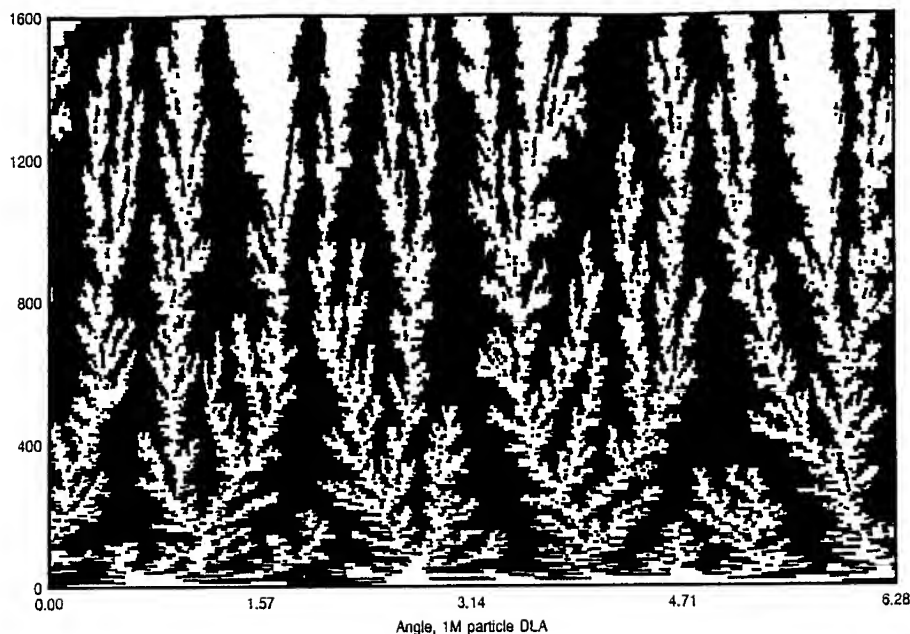


Fig4) Plot of a 1M particle DLA circular cluster in polar coordinates. The coordinates of each particle represent the radial distance from the seed and the angle on the circumference.

In order to visualize this effect we introduced a novel graphical way to seek on the structure of DLA clusters, namely polar coordinates. Fig.4 shows a circular DLA cluster in which each point is identified by the radial distance from the seed and the corresponding angle on the circumference. This figure is the pictorial counterpart of the quantitative analysis shown so far. The fjords' geometric behavior is particularly well represented and, confirming the previous analysis, we observe that the fjord widths tend, on the average, to decrease. Evidently fjord widths correspond to angular gaps on the crosscuts and the perception that they "shrink" is indeed the pictorial confirmation of the lacunarity effect on the structure morphology.

## DISCUSSION AND CONCLUSION

Our analysis of very large DLA clusters suggests a new picture of this phenomenon, and likely of other irreversible growth phenomena. In fact, DLA is mainly a non-equilibrium phenomenon in which the dynamical aspects play a major role. We can identify two different cluster regions. The first is a fully grown core that will not be further modified by growth. The second region is the active zone where the growth process continues. This situation differs strongly from the usual equilibrium problems, such as percolation and the Ising clusters, where there is no distinction between cluster regions. Moreover, in these problems the deviations from the asymptotic behavior is solely due to finite size effects. Growth phenomena, specifically DLA, also raise the problem of the internal boundary conditions, i.e., the growing structure itself and the irreversible nature of the process. This means that the "old" part of the cluster had been "young" and preserves a memory of the dynamical process by which it has been generated.

This effect is emphasized in the circular DLA, in which it is the growing structure itself that defines the boundary conditions size. That dynamical aspects are present in this geometry from the early stages of the growth process up to the very large size we have analyzed and suggest the infinite drift scenario supplied previously [6]. This scenario allows persistent deviations from self-similarity for arbitrary large finite size samples and therefore calls for other quantitative characterization of the clusters such as lacunarity.

The present picture it is also compatible with a "weak" universality of DLA. In fact, the dynamical process generates different transient effects depending upon the growth geometries. For example there are numerical indications that large DLA clusters grown in cylindrical geometry do not present deviations from self-similarity. This is probably due to the fact that the cylinder size is defined externally and it does not depend upon the growth process. In this sense we believe that keeping in mind the dynamical nature and the "weak" universality of the DLA phenomenon helps discriminate among the quantities and features that are really universal and thus which can be considered as clues or elements for a theory of fractal growth [12,13].

#### Acknowledgments

The programs to generate large DLAs develop earlier programs contributed by L. Woog. The assistance of Lewis N. Siegel at IBM is gratefully acknowledged. The investigations carried out at Yale University were supported by the Office of Naval Research under grant N00014-90-J-1026, and were performed on two IBM RS/6000 RISC computers, made available at Yale by IBM's Technical Computing Systems Group (Mathematical Sciences Area).

#### REFERENCES

- [1] T.A.Witten and L.M.Sander, Phys.Rev.Lett. **47**, 1400 (1981).
- [2] L.Niemeyer, L.Pietronero and H.J. Wiesmann, Phys.Rev.Lett. **52**, 1038 (1984).
- [3] T.Vicsek, Fractal Growth Phenomena, World Scientific, Singapore (1992).
- [4] For a recent review see T.Vicsek, M.Schlesinger and M.Matsushita, proceedings of Fractals in Natural Science: International Conference on the Complex Geometry of Nature, World Scientific, Singapore (1994).
- [5] P.Meakin, in "Phase Transition and Critical Phenomena" Vol. 12, edited by C.Domb and J.Lebowitz, Academic Press, N.Y. (1988).
- [6] B.B.Mandelbrot Physica A **191**, 95 (1992).
- [7] P. Ossadnik, Physica A **195**, 319, (1993).
- [8] R.Voss, Fractals, **1**, 141 (1993).
- [9] B.B.Mandelbrot, H. Kaufman, A.Vespignani, I. Yekutieli and C.H.Lam, to be published (1994).
- [10] H.Kaufman, B.B.Mandelbrot and A.Vespignani, in preparation (1994).
- [11] Y. Yekutieli, B.B. Mandelbrot and H. Kaufman, J. Phys. A **27**, 275 (1994).
- [12] L.Pietronero, A.Erzan and C.Evertsz, Phys.Rev.Lett. **61**, 861 (1988). For a recent review see: A.Erzan, L.Pietronero and A.Vespignani: The Fixed Scale Transformation Approach to Fractal Growth, Review of Modern Physics, submitted (1994).
- [13] T.C. Halsey and M.Leibig, Phys. Rev.A **46**, 7793 (1992).

---

## PART II

---

### **Fracture and Breakdown of Materials**



## FRactal Properties of Fracture Surfaces: Roughness Indices and Relevant Lengthscales

ELISABETH BOUCHAUD

Direction Matériaux, O.N.E.R.A., 29 Av. de la Division Leclerc  
B.P. 72, 92322 Châtillon Cedex, FRANCE

### ABSTRACT

Experiments aiming at the measurement of the roughness index  $\zeta$  of "rapid" fracture surfaces are briefly reviewed. For rapid crack propagation, measured values of  $\zeta$  are close to 0.8, which seems to be a *universal* exponent. However, it is argued, by re-writing the Griffith criterion for a self-affine crack, that the self-affine correlation length  $\xi$  might depend upon the microstructure, and hence on the fracture toughness. More recent experiments are also described, which reveal at smaller lengthscales the existence of a quasi-static fracture regime separated from the previously studied rapid fracture regime by a crossover length which decreases with increasing crack velocity.

### INTRODUCTION

It is now clearly established that fracture surfaces can be considered as self-affine fractal objects [1, 2, 3, 4, 5]. After the pioneering work of B. Mandelbrot and coworkers [7], many experiments using various experimental techniques (profilometry [8, 9], microscopy and image analysis [10, 11, 12, 13, 14, 15, 16], electrochemistry [17]...) on materials as different as steels [7, 11, 17], aluminium alloys [13], rocks [9], intermetallic compounds [14, 15], ceramics [10], visco-elastic pastes [16], have shown that fracture surfaces exhibit scaling properties on two [8, 14, 15] or three decades [13] of lengthscales. At "large enough" lengthscales (the micron scale for metallic materials), for rapid crack propagation modes (uncontrolled fracture), all reported values of the roughness index (or Hurst exponent)  $\zeta$  [1], [2], [3], [6] are close to 0.8. It was suggested [13] that this value might be "universal", i.e. independent of the fracture mode and of the material. Very recent one million particles molecular dynamics simulations [21] strongly support this assumption, which, however, remains controversial. In order to explain that the fracture toughness should increase with the fractal dimension, A. Mosolov [34] proposed a re-writing of the Griffith criterion [33] in the case of self-affine cracks. Although we do not agree with his conclusions, we have investigated this idea with J.P. Bouchaud [35], and shown that the revisited criterion leads in fact to a correlation of the fracture toughness  $K_{Ic}$  with the "spikiness"  $z_{max}/\xi$  of the fracture surface, where  $\xi$  is the self-affine correlation length and  $z_{max}$  is the typical height on the fracture surface outside the fractal regime.

On the other hand, significantly smaller values of the roughness index are measured either at very small lengthscales (nanometers), or in the case of slow crack propagation. As a matter of fact, STM experiments [18] report values of the roughness exponent close to 0.6 in the case of fractured tungstene (regular stepped region), and close to 0.5 for graphite [19]. On the micrometer scale, low cycle fatigue tests on a steel sample have led to a value of  $\zeta$  close to 0.6 [20]. These results are particularly attractive since they report roughness indices close to the roughness of a *minimum energy surface* in a random environment [23], [24], [25]. It was suggested by A. Chudnowsky and B. Kunin [26], M. Kardar [27], and by S. Roux and D. François on the basis of a fracture model for porous ductile materials [28], that the path chosen by a crack in a random environment should be such that the overall fracture energy is minimised. It seems that this quasi-static assumption is not fulfilled for rapid crack propagation, but might be valid at small enough lengthscales or for low enough velocities. As a matter of fact, we have shown on a Ti<sub>3</sub>Al-based alloy that this assumption is valid indeed up to a distance  $\xi_{QS}$  which decreases with increasing crack velocity. At larger lengthscales, the previously reported roughness index close to 0.8 is recovered. Let us note finally that these two regimes do not seem to exist in two dimensions: experiments on wood (which can be considered as two-dimensional in the plane perpendicular to the fibers) [29], and on paper sheets [30] have reported a roughness index close to 2/3, which is expected for a directed random walk in a random environment [31]. This result is also predicted by a model due to A. Hansen and S. Roux [32].

In the following, however, attention is paid only to the three-dimensional case. A non-exhaustive review of the main experimental results is proposed (section A). In section B of this paper, the Griffith criterion [33] is revisited for self-affine cracks, and new conclusions are drawn concerning a close relation between  $K_{Ic}$  and the spikiness parameter  $z_{max}/\xi$  of the fracture surface [35]. Finally, section C is devoted to a very recent experiment performed in collaboration with S. Navéos [36], which shows the existence of a quasi-static fracture regime at low lengthscales, and some conclusions and perspectives are given in section D.

## A- EXPERIMENTAL DETERMINATIONS OF THE ROUGHNESS OF FRACTURE SURFACES: PRINCIPLES AND RESULTS

Experimental apparatus usually requires to perform cuts of the sample, either within a plane perpendicular to the anisotropy axis  $z$  or in a plane containing it. Thus the first following sections are concerned with the analysis you can make on the two kinds of cuts. The last paragraph is devoted to the very few techniques which provide a three-dimensional information.

### *Cuts perpendicular to the anisotropy axis $z$*

The first experiment in this field is due to B. Mandelbrot, D. Passoja and A. Paullay [7]. It concerns six samples of steel to which different heat treatments had conferred different fracture energies measured through Charpy tests. The experimental procedure consists in plating the fracture surfaces with vacuum deposited nickel. Subsequently, cuts by a  $z = \text{constant}$  plane are obtained by polishing the plated specimen. Images of the "islands" of steel emerging from an "ocean" of nickel are analysed, and both the area  $\mathcal{A}$  and the perimeter  $\mathcal{P}$  of the islands are measured. The islands themselves are dense bidimensional objects, but their contours being the intersection of the fracture surface with a  $z = \text{constant}$  plane, they have a dimension  $d_F - 1$  if the surface itself is self-affine of "box" dimension [2, 6]  $d_F$ . Thus:

$$\mathcal{A} \propto \mathcal{P}^{\frac{2}{d_F-1}} \quad (1)$$

Plotting  $\mathcal{A}$  versus  $\mathcal{P}$  on a log-log plot should then show two linear increasing regimes. At lengthscales smaller than the correlation length  $\xi$ , one should measure a slope  $2 - \zeta$ , and at higher lengthscales, one should get back the usual slope 2. Note that with this method of measurement, a slight overestimation of  $\xi$  leads to an underestimation of the exponent, i.e. to an overestimation of  $\zeta$ . This remark will be exploited in section B. Measured values of  $\zeta$  lie between 0.70 and 0.85. The apparent increase of  $\zeta$  with decreasing fracture energy, which means that rougher fracture surfaces correspond to lower energies, will however be re-interpreted in the following.

With G. Lapasset and J. Planès [13], we have redone the same kind of measurements on a commercial aluminium alloy, the 7475, with a different experimental procedure, however. Four samples are studied, to which different solution heat treatments and quenches confer different fracture toughnesses.  $K_{Ic}$  is measured on CT (compact tension) specimens first precracked in fatigue. The fracture surfaces are electrochemically nickel-plated – a route which is far less directional than vacuum evaporation –, and polished surfaces corresponding to cuts by a  $z = \text{constant}$  plane are observed at various magnifications with a scanning electron microscope, using backscattered electrons which give a very good contrast between aluminium and nickel. Attention is paid to focus on the plane-strain unstable fracture zone. Images are binarised, and the self-correlation function  $\mathcal{C}(r)$  of the cut is computed for each micrograph. Since the fractal dimension of the set of contours is equal to  $d_F - 1$ , then  $\mathcal{C}(r)$  is expected to behave as  $\mathcal{C}(r) \propto r^{-\zeta}$  within the self-affine region.  $\mathcal{C}(r)$  exhibits a power-law decrease extending up to a size  $\Lambda$  comparable to the size of the micrograph itself.

The curves relative to the same sample are put on the same diagram by plotting  $\mathcal{C}(r)$  versus  $r/\Lambda$ . In these reduced units, the scaling domain extends over two decades, but it corresponds to three decades in real scale:  $0.5\mu\text{m} < r < 0.5\text{mm}$ . Exponents are measured in each case, and no systematic variation of  $\zeta$  with  $K_{Ic}$  is found. We thus conclude to no correlation between the roughness exponent and the fracture toughness, and propose that this exponent might be *universal*, i.e. independant of the fracture mode, fracture toughness and material. As we will see in the following, this idea is still very controversial, but we

do think that, except for very slow crack propagation modes, or at very small lengthscales, 3-dimensional fracture surfaces should exhibit the same roughness, but relevant lengthscales, among which the self-affine correlation length, do depend upon the microstructure and fracture toughness of the material. Our experimental results read:

$$\zeta = 0.80 \pm 0.05 \quad (2)$$

Finally, let us quote an experiment on steel, due to P. Mc Anulty and collaborators [20]. These authors study two samples: one is broken during a Charpy test, and the other one is fractured in fatigue. The slit island method is used in both cases. In the first case, a value of  $\zeta$  rather close to 0.8 is reported, but in the latter one, a significantly smaller value, close to 0.6, is measured. As already discussed, this value is close to the one expected for a *minimum energy surface*. It is shown in section C that this result is probably of kinetic origin, i.e., in this case, the crack propagates slowly enough to justify a quasi-static assumption. The fact that the reported value is nevertheless higher than the expected  $\zeta \sim 0.5$  is probably due to the fact that the observed regime is partly in a crossover between the quasi-static and the rapid fracture regimes.

#### Cuts containing the anisotropy axis $z$

Malloy and coworkers [8] have studied six very different brittle materials (plaster, bakelite, porcelain, graphite, steel and Al-Si) by recording the fracture profiles with an opto-mechanical profilometer. In each case, they compute both the first return probability  $P_1(r)$  (the probability that the height goes back to its initial value after a distance  $z$  within the horizontal plane), which scales as  $r^{-2+\zeta}$  and the power spectrum, which is supposed to scale with an exponent  $-1 - 2\zeta$ . They find consistent values of  $\zeta$  which do not vary much from one material to the other, and they conclude that  $\zeta$  seems indeed to be *universal*, with an average value:

$$\zeta = 0.87 \pm 0.07 \quad (3)$$

One could object that this value of  $\zeta$  — although compatible with ours in regard of error bars —, is closer to 0.9 than to 0.8. It will be seen in section C that the limit of the self-affine domain  $\xi$  may be very sensitive to the material properties, and slight differences in the measured values of the roughness index might be explained by the pollution of the scaling regime by the crossovers.

An other very different material is studied by E. Lemaire and collaborators [16]. A visco-elastic paste made of sand and resin is put between two plates which are driven away from each other at a given velocity until the paste "breaks". Five velocities ranging from 1 to 10 mm.s<sup>-1</sup> are studied. After fracture, the hardened paste is sliced parallel to the tensile direction, and the fractal dimension of the profiles is determined by two methods: directly on one hand, with a box counting procedure, and on the other hand from the computation of the power spectrum. It is found that  $\zeta$  is independant of the velocity and:

$$\zeta = 0.88 \pm 0.05 \quad (4)$$

This value is remarkably close to the one determined by Malloy and coworkers [8].

With G. Lapasset, J. Planès and S. Navéas, we also investigate mode II cracks in polycrystalline Ni<sub>3</sub>Al [14]. In fact, the morphology of these cracks is more complex than for previously reported experiments, because, although the fracture mode is simply brittle intergranular, the fracture surface is "branched" with secondary cracks developping during crack propagation.

Two samples are plated with either opaque resin or electrochemically deposited NiPd, and polished within a plane perpendicular to the direction of propagation of the main crack. Three series of observations are made on these samples, using one optical micrograph and two scanning electron microscopes with rather different resolutions. Computing the return probability  $P_0$  (the probability that the height goes back any time to its initial values), which scales as  $P_0(r) \propto r^{-\zeta}$  for an ordinary (univalued  $z$ ) self-affine profile, one finds:

$$\zeta \simeq 0.83 \pm 0.04 \quad (5)$$

This value concerning the whole structure (i.e. including secondary branches) is similar to the one obtained only by considering only the backbones. Compatible results are obtained by computing  $z_{max}$  defined in the following way:

$$z_{max}(r) = \langle \text{Max}\{z(r')\}_{x < r' < x+r} - \text{Min}\{z(r')\}_{x < r' < x+r} \rangle_x \propto r^\zeta \quad (6)$$

Once again, although the morphology of the fracture surface is very different, one finds back an exponent close to the value 0.8.

Let us finally quote two methods which are able to perform a global analysis of the three dimensional object.

### Global methods

The electrochemical method, extensively studied for other purposes [44] is successfully used for fracture surfaces for the first time by A. Imre [17] and coworkers. The diffusion controlled current  $I(t)$  is plotted against time  $t$ . It can be shown that, at time  $t$ , one has to determine the area using tiles of size  $\sqrt{Dt}$ , which leads to:

$$I(t) \propto t^{-\frac{(2-\zeta)}{2}} \quad (7)$$

The Imre experiment is performed on a polished steel surface, for which the expected  $\zeta = 1.00 \pm 0.02$  is recovered, and on a fracture surface of the same material, for which it is found:

$$\zeta \simeq 0.81 \pm 0.02 \quad (8)$$

Other techniques which provide a three-dimensional information in the nanometer range [18], [19], are the STM and the AFM (Atomic Force Microscope). New experiments are currently being performed with an AFM both on glass and on metallic alloys [22], but, to our knowledge, there is no yet available result. Note also that, in principle, stereoscopy performed with a scanning electron microscope should be able to provide the same information on the micrometer scale [38]. Values of the roughness exponent seem to vary strongly in space at the very small lengthscales explored with an STM. Furthermore, reported values are significantly smaller than 0.8, lying, according to the material, either around 0.4, or around 0.6. On the basis of these experiments, V. Milman and coworkers contradicted the idea of *universality*. We will come back to these results in the section after next one, when kinetic effects will be discussed. It will be shown that the *minimum energy surface* roughness fits with experiments at any velocity, but for small enough lengthscales.

However, next section is more devoted to the upper limit of the self-affine regime.

## **B- REVISITED GRIFFITH CRITERION FOR SELF-AFFINE CRACKS: RELEVANT LENGTHSCALES AND APPARENT ROUGHNESS**

The recently proposed idea to write the Griffith-Irwin criterion [33,34] for a self-affine crack is followed, and new computations are made in collaboration with J.-P. Bouchaud [35].

### The "classical" Griffith criterion

Let us first briefly recall the content of the classical Griffith criterion [33] for a crack propagating in mode I in a sample of width  $b$  submitted to a uniaxial tension (see Fig. 1).

The critical value of the stress at which propagation actually takes place is determined by equating the elastic energy  $\Delta U_{el}$  due to crack propagation to the energy  $\Delta U_s$  required to create two free surfaces in the material. Furthermore, it is assumed that the stress field is singular in the vicinity of the crack tip:

$$\sigma(r) \simeq K r^{-\alpha} \quad (9)$$

at a distance  $r$  ahead of the crack front.  $K$  is the stress intensity factor.

When the fracture path is regular, the surface energy is proportional to:

$$\Delta U_s = 2\gamma bR \quad (10)$$

where  $\gamma$  is the surface tension and  $R$  is the crack length increment.

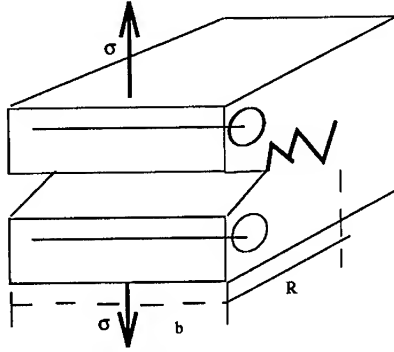


Figure 1: Mode I crack propagation through a notched specimen of width  $b$ .

On the other hand, the released elastic energy can be estimated by noting that the stress field is essentially relaxed on scales  $r < R$  and unperturbed on larger scales:

$$\Delta U_{el.} \simeq \frac{K^2}{2E} \int_a^R r^{-2\alpha} b r dr \simeq \frac{K^2}{2(-2\alpha + 2)E} b R^{(-2\alpha + 2)} \quad (11)$$

where  $a$  is a microscopic cut-off below which the stress field saturates, and  $E$  is Young's modulus of. At the onset of fracture, the two energies should be of the same order of magnitude. This implies first that:  $\alpha = \frac{1}{2}$ , which is the classical result in elasticity theory [33].

Second, one obtains the critical value  $K_{Ic}$  of the stress intensity factor below which the crack is unable to progress because the elastic energy is not high enough to compensate for the creation of two free surfaces. One finds a material dependent fracture toughness, given by:  $K_{Ic} \propto \sqrt{\gamma E}$ .

#### Griffith criterion for a self-affine crack

Let us now describe very simply the self-affine fracture surface:

$$h(r) = \eta(r) z_{max} \left( \frac{r}{\xi} \right)^\zeta \quad (r \ll \xi) \quad (12-a)$$

$$h(r) = \eta(r) z_{max} \quad (r \gg \xi) \quad (12-b)$$

where  $\eta(r)$  is a random variable of order 1 which varies on the scale of  $r$  itself.

The surface energy corresponding to the opening of the crack along a distance  $R \ll \xi$  can be expressed in the following way:

$$\Delta U_s \simeq 2\gamma b \int_a^R \sqrt{1 + \left( \frac{dh(r)}{dr} \right)^2} dr \quad (13)$$

with:  $dh(r)/dr \simeq h(r)/r$  ( $r \ll \xi$ ) since  $d\eta(r)/dr$  is also of order  $h(r)/r$ .

From equation (13), one can see that a new lengthscale  $r^*$  appears.  $r^*$  is the distance where the local slope of the self-affine relief is of order one:  $\frac{dh}{dr}(r = r^*) \simeq 1$ , while for  $r \ll r^*$ ,  $dh/dr \gg 1$ .

It can be shown that:

$$\frac{r^*}{\xi} \simeq \left( \frac{z_{max}}{\xi} \right)^{\frac{1}{1-\zeta}} \quad (14)$$

Since  $\zeta$  is an exponent lying between 0 and 1, two cases may occur:

\*"Shallow" regime :  $z_{max} \ll \xi$  or  $r^* \ll \xi$

In this case, the surface is fractal but rather "shallow", and  $r^*$  is smaller than  $\xi$ . An estimation of the surface energy then provides:

$$\Delta U_s \propto 2\gamma b \xi \left( \frac{z_{max}}{\xi} \right) \left( \frac{R}{\xi} \right)^\zeta \quad (15)$$

as long as  $R < r^*$ . Note that this result is different from Mosolov's expression [34].

On the other hand:  $\Delta U_s \simeq 2\gamma b R$  as soon as  $R > r^*$  (even if  $R < \xi$ ). In this case, even at lengthscales smaller than the correlation length  $\xi$ , provided that these lengthscales are larger than  $r^*$ , the surface energy is similar to the one necessary to create a flat surface, although the surface is actually rough up to distances of the order of  $\xi$ , which may even be infinite! One consequence of this is that the stress field singularity is the usual  $-1/2$  one at lengthscales greater than  $r^*$ . On the contrary, equation (15) implies the existence of a non-trivial singularity closer to the crack tip, i.e. at distances from it smaller than  $r^*$ :  $\sigma \simeq K' r^{-\alpha}$  ( $r < r^*$ ) which gives rise to an elastic energy term  $\Delta U_{el}$ , the expression of which is given in equation (11). Equating  $\Delta U_{el}$  and  $\Delta U_s$  leads to the relation:  $-2\alpha + 2 = \zeta$ , which is valid in two as well as in three dimensions. When the surface is flat, i.e. when  $\zeta$  is equal to unity, the value  $\alpha = 1/2$  is recovered. As expected intuitively, "rougher" cracks (smaller  $\zeta$ ) are associated to more singular stress fields.

The crossover between this regime and the " $-1/2$ " singularity regime takes place at  $r = r^*$ , yielding:  $K' r^{*\frac{(\zeta-2)}{2}} = K r^{*-1/2}$ . On the other hand, the equality  $\Delta U_s = \Delta U_{el}$  applied in the regime  $R > r^*$  leads to a critical value of  $K$ , corresponding to the measured fracture toughness  $K_{Ic}$ , which is independent of the characteristic lengthscales of the problem in the "shallow" regime:  $K_{Ic} \simeq \sqrt{\gamma E}$ . It is now shown that this conclusion is not valid when "spiky" surfaces are considered.

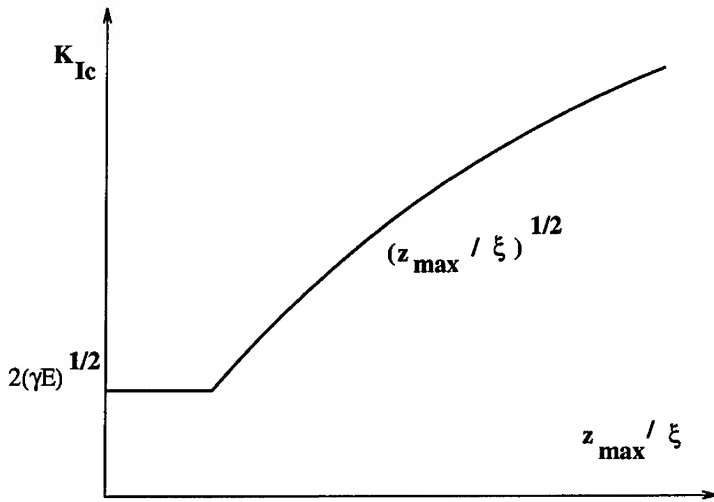


Figure 2: Evolution of the fracture toughness  $K_{Ic}$  as a function of the spikiness  $z_{max}/\xi$ .

\*"Spiky" regime :  $z_{max} \gg \xi$  or  $\xi \ll r^*$

From the definition of  $r^*$ , one realizes that this case corresponds to  $\xi < r^*$ . This means that, in the whole fractal domain, the local slope of the surface is much larger than one. This also implies that, close to the crack tip ( $r < \xi$ ), the stress field singularity is characterized by an exponent  $\alpha = \frac{2-\zeta}{2}$ . The crossover between the  $-\frac{2-\zeta}{2}$  and the  $-1/2$  singularities now takes place for  $r = \xi$ :  $r^*$  is no longer a relevant length of the problem. Thus, one can write:  $K' \xi^{\frac{(\zeta-2)}{2}} = K \xi^{-1/2}$  (stress field continuity, which allows to find  $K'$ ) and, for  $R > \xi$ ,  $\Delta U_s \simeq 2\gamma b \left(\frac{z_{max}}{\xi}\right) R$  which leads to an interesting expression for the fracture toughness:

$$K_{Ic} \simeq 2\sqrt{\gamma E} \left(\frac{z_{max}}{\xi}\right)^{\frac{1}{2}} \quad (16)$$

The evolution of  $K_{Ic}$  as a function of the "spikiness"  $z_{max}/\xi$  of the surface is shown in Fig. 2.

Note that the results pertaining to the case of a penny shaped crack are similar to those reported above since in that case, the sample width  $b$  is replaced by the crack radius  $R$ . Indeed, in the short lengthscales regime ( $r < r^*$  in the shallow case and  $r < \xi$  in the spiky case), the surface energy scales as  $\Delta U_s \simeq R^{1+\zeta}$  while the elastic energy is proportional to:  $\Delta U_{el} \simeq R^{(-2\alpha+3)}$ .

Thus, although the roughness index of fracture surfaces is universal, morphology of the fracture surface and fracture toughness are closely related. For "shallow" fracture surfaces, for which the maximum height

$z_{max}$  is smaller than the self-affine correlation length  $\xi$ , the relevant length is the distance  $r^*$  smaller than  $\xi$  for which the local slope becomes of the order of unity. In this case,  $K_{Ic}$  does not depend on the various lengthscales, and the energy spending is the same that for fracturing through a regular flat surface.

On the contrary, in the "spiky" case for which the ratio  $z_{max}/\xi$  is greater than unity,  $\xi$  is the only relevant lengthscale in the "horizontal" plane, and  $K_{Ic}$  is proportional to the square root of this ratio.

This could well be an explanation for the difference in  $K_{Ic}$  measured for crack propagations in two orthogonal directions on anisotropic materials.

It might also explain the apparent correlation between  $K_{Ic}$  and the fractal dimension  $d_F$  of the fracture surface, observed by B. Mandelbrot et al. [7] (see previous section). If tougher samples correspond to smaller correlation lengths  $\xi$ , assuming  $z_{max}$  is fixed and the regime is "spiky", the apparent exponent measured in a fixed lengthscale window is larger than the actual one, which leads to an apparent fractal dimension smaller than the real one. This could also be the reason why from one experiment to the other, reported values of  $\zeta$  may slightly differ. However, in the case of our experiments on the 7475 aluminium alloy [13],  $\xi$  cannot be measured because it is larger than the limit length imposed by the microscope. Hence these measurements should not be sensitive to the variation of  $\xi$  and the measured exponent might be closer to its actual value.

We now turn back to the lower lengthscale limit of the regime which was just described.

### C- FROM QUASI-STATIC TO RAPID FRACTURE

Let us now analyse a recent experiment performed with S. Navéas [36], where kinetic effects were considered. A notched CT sample (dimensions 12.5mmx30mmx31mm, see Fig. 3) of the Supera<sub>2</sub> alloy [39] – Ti<sub>3</sub>Al based – is first precracked in fatigue at 30 Hz, with a fixed R ratio of 0.1; the ratio  $a/W$  is of order 0.6. Fracture is achieved through uniaxial tension in mode I. The broken sample is electrochemically nickel or NiPd-plated, and four profiles are obtained by subsequently cutting and polishing the sample perpendicularly to the direction of propagation of the crack.

These profiles are observed with a scanning electron microscope at various magnifications – from x50 to x2000 approximately –, with a backscattered electron contrast. See an example in Fig. 4.  $z_{max}(r)$  (Eq. (6)) is computed on each micrograph, for profiles 1 to 4. In the four cases, all the curves relative to the various micrographs are put on the same spectrum. The behaviour of the spectrum relative to profile 1 (fracture in fatigue) at smaller distances is first studied, revealing a rather noisy power law increase with an exponent lying between 0.4 and 0.5, i.e. close to the theoretical roughness index  $\zeta_{QS}$  of a *minimum energy surface*. Then  $z_{max}/r^{\zeta_{QS}}$ , with  $\zeta_{QS} = 0.4, 0.45$  and  $0.5$  is plotted against  $r$ , and the three plots are fitted with a non linear curve fit using the expression:

$$\frac{z_{max}}{r^{\zeta_{QS}}} = A + B r^{\zeta - \zeta_{QS}} \quad (17)$$

Expression (17) is the simplest to account for the asymptotic power law behaviours corresponding, at short distances, to a quasi-static fracture mode – power law with a roughness index  $\zeta_{QS}$  – and at larger distances, to a rapid fracture mode – power law with a roughness index  $\zeta$  yet to be determined –. The real crossover function is certainly more complex, but, as it will be seen in the following, this assumption is not too far from reality, especially for profiles 1 (fatigue) and 4 ("instantaneous fracture"), which are closer to the asymptotic cases. Furthermore, this allows to define the crossover length  $\xi_{QS,i}$  for profile  $i$  between the quasi-static fracture zone and the rapid fracture one as the length at which the two asymptotic terms are equal, i.e.:

$$\xi_{QS,i} := \exp \left( \frac{1}{(\zeta - \zeta_{QS})} \ln \left( \frac{A}{B} \right) \right) \quad (18)$$

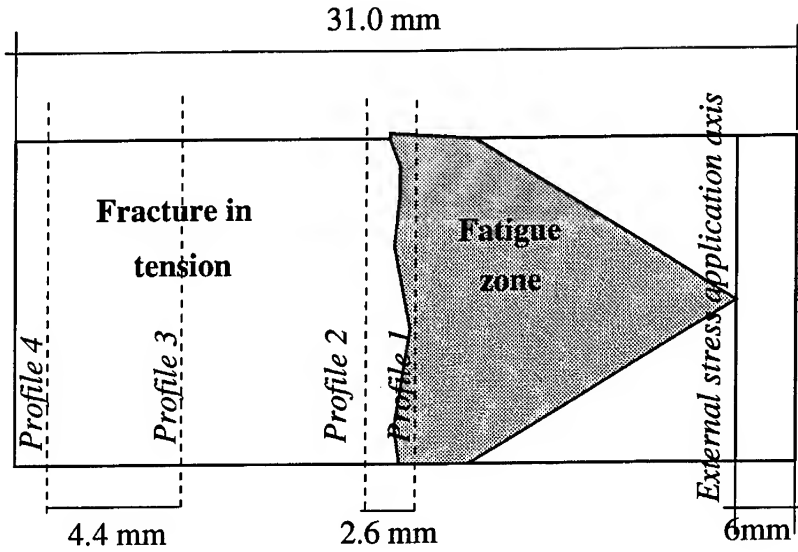


Figure 3: Sketch of the broken sample where profiles 1 to 4 are defined. Profile 1 stands in the fatigue crack zone, while profiles 3 and 4 lie within the unstable fracture regime.

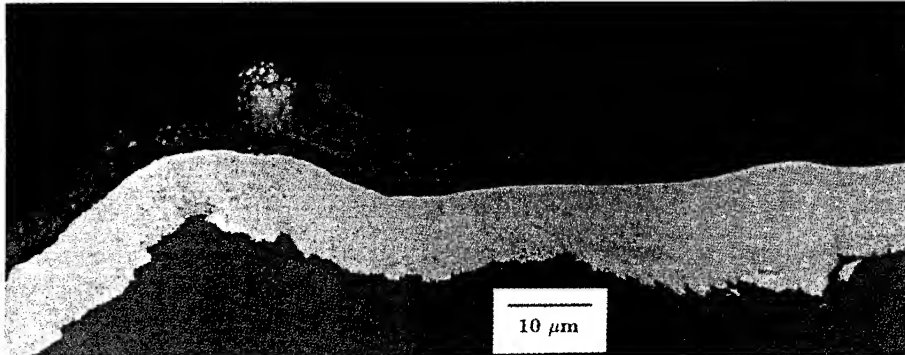


Figure 4: 256 grey levels 1024 pixels long image obtained from the scanning electron microscope with a backscattered electron contrast. The plating (NiPd in this case) appears in very light grey, while the alloy is darker. This good contrast allows for a straightforward binarization and edge detection in image analysis, and hence a precise determination of the fracture profile.

The fit obtained for  $\zeta_{QS} = 0.45$  (profile 1) is shown in Fig. 5.

Results concerning the three following sets of results obtained are summarised in Table 1.

Consistency with previously measured values of  $\zeta$  for high velocity cracks [1-15], as well as the short distance power law behaviour (see insert of Fig. 5) favours a value of  $\zeta_{QS}$  close to 0.45;  $\zeta_{QS} = 0.5$  leads to a particularly high value of  $\zeta$ . Subsequently, the spectra relative to profiles 2 to 4 are fitted also according to Eq. (28), but  $\zeta$  is kept equal to its previously determined value, while  $A$  and  $B$  are the results of the fitting procedure. Values of the  $\xi_{QS,i}$  ( $i = 2, 3, 4$ ) are again determined through Eq. (29). For  $\zeta_{QS}=0.45$ , one finds:  $\xi_{QS} = 5, 2, 1$  and  $0.3\mu\text{m}$  for profiles 1 to 4 respectively. In fact, the actual values of the  $\xi_{QS,i}$  are very sensitive to the value of  $\zeta_{QS}$  (for profile 1,  $\xi_{QS,1}$  is found to be equal to  $3\mu\text{m}$  for  $\zeta_{QS}=0.4$  and  $10\mu\text{m}$  for  $\zeta_{QS}=0.5$ ), for which the precision is not so good because of the too few experimental points



at short distances, even in the case of profile 1. Further investigations with an AFM are currently being performed [22]. On the other hand, it is clear that  $\xi_{QS,i}$  decreases when the local stress intensity factor  $K$  – or, correlatively, the crack velocity – increases. Lying in the micrometer region for fracture in fatigue, it could decrease below 1 micron at the end of the fracture process, in the unstable crack propagation regime, for which the crack velocity is much higher.

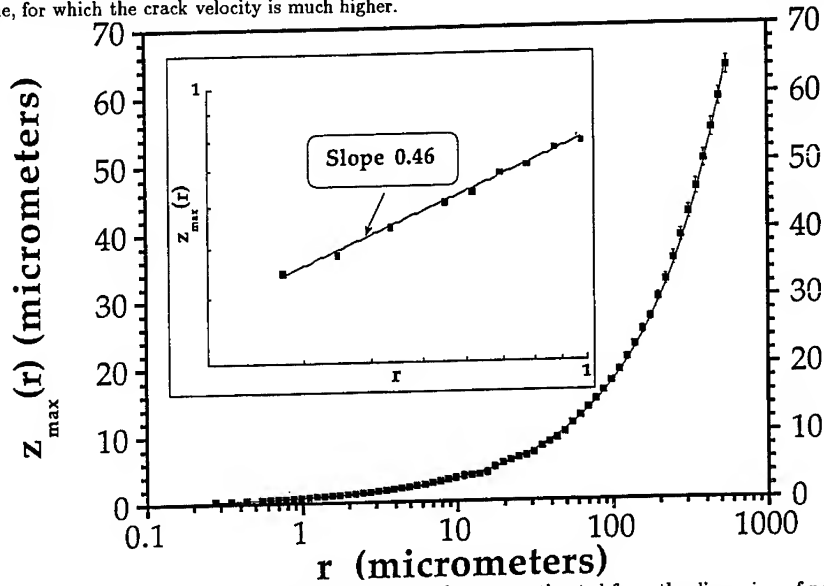


Figure 5:  $z_{max}(r)$  is plotted as a function of  $r$ ; error bars are estimated from the dispersion of points measured on various micrographs. The fit is given by Eq. (28) with  $\zeta_{QS} = 0.45$ :  $A = 0.56 \pm 0.02$ ;  $B = 0.28 \pm 0.01$ ;  $\zeta = 0.838 \pm 0.07$ . The confidence ratio is equal to:  $r \simeq 0.987$ . Insert: small lengthscales power-law fit of the data, giving a roughness index of 0.46.

| $\zeta_{QS}$ | $\zeta$ | $\xi_{QS,1}$ | $\xi_{QS,2}$ | $\xi_{QS,3}$ | $\xi_{QS,4}$ |
|--------------|---------|--------------|--------------|--------------|--------------|
| 0.40         | 0.815   | 3            | 2            | 0.6          | 0.05         |
| 0.45         | 0.838   | 5            | 2            | 1            | 0.3          |
| 0.50         | 0.875   | 10           | 6            | 3            | 1            |

Table I:  $\zeta$  is the long distance/high velocity regime roughness index and is poorly sensitive to the value of  $\zeta_{QS}$ , contrarily to the crossover lengths  $\xi_{QS,i}$  ( $i=1$  to 4 for profiles 1 to 4, expressed in micrometers).

Fracture can be seen in the following way – borrowed from polymer physics –: within a "quasi-static blob", i.e. over distances smaller than  $\xi_{QS}$ , the crack is able to optimize its own path in order to minimise its energy spending. An alternative description might be the following: it was recently suggested that the fracture surfaces could be modelled as the *trace* of a line propagating at a non-zero velocity  $V$  in a random environment [42]. From this picture and using the results of Ertas and Kardar [45] for the motion of vortex lines in dirty superconductors, one finds that the high velocity fracture surface should be anisotropic, with a roughness index perpendicular to the direction of crack propagation  $\zeta^\perp \simeq 0.75$  in a certain regime, which is rather close to the experimental values reported here (indeed measured perpendicularly to propagation). Interestingly, however, there is also a low velocity regime for this problem, where the line is close to the 'depinning' transition, below which the crack would not propagate at all. Ertas and Kardar recently investigated this regime [46], with the result that  $\zeta_{QS}^\perp$  is slightly smaller than 1/2. Furthermore, this low velocity behaviour is predicted to hold below a velocity dependent crossover length decreasing as  $\xi \sim V^{-\phi}$ , with  $\phi = 3$ , in qualitative agreement with our observations. For a given velocity,  $\xi_{QS}$  has to be related with the range of the stress field; even if in the case of a purely brittle material – this is not the case of the Super $\alpha_2$  which exhibits some plasticity – shielding might provide a finite cut-off in the actual stress field felt by the crack, because of the complexity of the environment. Further experiments in fatigue, for which crack velocities can be measured electrically, should provide a precise determination of the relationship between  $\xi_{QS}$  and the crack velocity, and between  $\xi_{QS}$  and  $K$ . The roughness of fracture surfaces strongly depends on the kinetics of crack propagation. One can emphasize also the importance of disorder in that respect: for homogeneous materials, one often observes very flat fracture surfaces at low crack velocities, referred to as "mirror" [37]. Higher crack velocities lead to rougher fracture surfaces, but it seems now that this roughening is due to an instability [40] which has never been observed on metallic alloys, to our knowledge. In the latter case, further crack morphology transformations only concerns secondary crack branching [14], [37], [41], [42], which increases with the crack velocity. An influence of the size of the defects is shown in a study of a microstructure of the Super $\alpha_2$  which is similar but three times coarser than the one described here [36].

#### D. CONCLUSION

In conclusion, there are clearly two distinct fracture regimes. The "high speed/ large lengthscales" one was extensively studied experimentally, for various materials, using different experimental techniques. Reported values of the roughness index nevertheless remain rather close to the value 0.8 in these cases, in agreement with the recent simulation due to Nakano and coworkers [21]. This value might well be *universal*, whereas relevant lengthscales, as, for example, the self-affine correlation length, might depend on the microstructure, and hence be related to mechanical properties.

As a matter of fact, it was shown by re-writing the Griffith criterion for a self-affine crack that the ratio  $z_{max}/\xi$  increases with the fracture toughness, whenever the surface is "spiky".

Note that there is, up to now, no model available to understand this regime (for an attempt see for example [42]).

At very small lengthscales, or for lower crack velocities, fracture can be regarded as "quasi-static", since the experimental measurements report values of the roughness index significantly closer to the value 0.45, which is supposed to describe *minimum energy surfaces*. The crossover length which separates the two regimes was shown to decrease with increasing crack velocity. Further experiments should enable to make more quantitative observations. This crossover seems to be specific of three dimensional systems, since no smoothing of cracks at high velocities has been observed yet for bidimensional samples. This might be due to various reasons, in particular to stronger topological constraints in two dimensions.

Finally, at even higher fracture speeds, one observes crack branching in disordered materials. In more "homogeneous" materials, crack flow instabilities are observed, which might be shielded in the case of heterogeneous microstructures. One can wish that in future, more experiments are carried on model materials for which microstructural disorder can be controlled, exploring various ranges of lengthscales thanks to the use of many different techniques.

**Acknowledgements:** These results could not have been obtained without the collaboration of J.-P. Bouchaud, P. Daguerre, G. Lapasset, J. Planès and S. Navéas. I am also indebted to S. Roux for many interesting discussions and suggestions.

## References

- [1] B.B. Mandelbrot, J.W. Van Ness, SIAM Rev. **10**, 422 (1968).
- [2] B.B. Mandelbrot, Phys. Scr. **32**, 257 (1985).
- [3] M.B. Isichenko, Review of Modern Physics **64**, 961 (1992).
- [4] E. Bouchaud, in *Dislocations 93*, edit. Y. Bréchet, L. P. Kubin, J. Rabier, Sol. Stat. Phenomena **35-36**, Scitec Publications, 353 (1993).
- [5] F. Family, in *Fractals in the Natural and Applied Sciences*, edit. M. M. Novak, Elsevier Science B.V. (North-Holland), 1 (1994).
- [6] J. Feder, *Fractals*, Plenum Press (New-York), (1988).
- [7] B.B. Mandelbrot, D.E. Passoja, A.J. Paullay, Nature (London) **308**, 721 (1984).
- [8] K.J. Maloy, A. Hansen, E. L. Hinrichsen, S. Roux, Phys. Rev. Lett. **68**, 213 (1992).
- [9] J. Schmittbuhl, S. Gentier, S. Roux, Geophys. Lett. , **20**, 639, (1993).
- [10] J.J. Mecholsky, D.E. Passoja, K.S. Feinberg-Ringel, J. Am. Ceram. Soc. **72**, 60 (1989).
- [11] Z.Q. Mu, C.W. Lung, J. Phys. D : Applied Physics **21**, 848 (1988).
- [12] R.H. Dauskardt, F. Haubensak, R.O. Ritchie, Acta Metall. Mater. **38**, 143 (1990).
- [13] E. Bouchaud, G. Lapasset, J. Planès, Europhys. Lett. **13**, 73 (1990).
- [14] E. Bouchaud, G. Lapasset, J. Planès, S. Navéos, Phys. Rev. B, **48**, 2917 (1993).
- [15] J. Planès, E. Bouchaud, G. Lapasset, Fractals, **1**, 1059 (1993).
- [16] E. Lemaire, Y. Ould Mohamed Abdelhay, J. Larue, R. Benoit, P. Levitz, H. Van Damme, Fractals **1**, 968 (1993).
- [17] A. Imre, T. Pajkossy, L. Nyikos, Acta Metall. Mater. **40**, 1819 (1992).
- [18] V. Y. Milman, R. Blumenfeld, N. A. Stelmashenko, R. C. Ball, Phys. Rev. Lett. **71**, 204, (1993).
- [19] V. Y. Milman, N. A. Stelmashenko, R. Blumenfeld, preprint (1994).
- [20] P. McNulty, L.V. Meisel, P.J. Cote, Phys. Rev. A **46**, 3523 (1992).
- [21] A. Nakano, R. K. Kalia, P. Vashishta, Phys. Rev. Lett. **73**, 2336 (1994).
- [22] S. Hénaux, P. Daguer, E. Gailloteau, F. Creuzet, E. Bouchaud, in preparation.
- [23] M. Kardar, Nul. Phys. **B290**, [FS20], 582 (1987).
- [24] M. Mézard, G. Parisi, J. Phys. France I **1**, 809 (1991).
- [25] T. Halpin-Healy, Phys. Rev. A **42**, 711 (1990).
- [26] A. Chudnovsky, B. Kunin, J. Appl. Phys. **62**, 4124 (1987).
- [27] M. Kardar, in *Disorder and Fracture*, edited by J.C. Charmet, S. Roux, E. Guyon, (Plenum, New York (1990).
- [28] S. Roux, D. François, Scripta Metall. **25**, 1092 (1991).
- [29] T. Engoy, K. J. Maloy, A. Hansen, S. Roux, Phys. Rev. Lett., **73**, 834 (1994).
- [30] J. Kertész, V. Horváth, F. Weber, Fractals **1**, 67 (1993).
- [31] M. Kardar, Y.-C. Zhang, Europhys. Lett. **8**, 233 (1989).

- [32] A. Hansen, E.L. Hinrichsen, S. Roux, Phys. Rev. Lett., **66**, 2476 (1991).
- [33] A.A. Griffith, Phil. Trans. Roy. Soc. Lond. **A221**, 163 (1920).
- [34] A.B. Mosolov, Europhys. Lett. **24**, 673 (1993).
- [35] E. Bouchaud, J.-P. Bouchaud, accepted for publication in Phys. Rev. B, Rapid Communication (1994).
- [36] E. Bouchaud, S. Navéas, submitted to Physical Review Letters (1994).
- [37] B.R. Lawn, *Fracture of brittle solids*, Cambridge University Press (Cambridge), 2<sup>nd</sup> edition, (1993).
- [38] G. Le Besnerais, S. Menet, E. Bouchaud, D. Boivin, G. Lapasset, in preparation.
- [39] M.J. Blackburn, M.P. Smith, US Patent n° 4,716,020, (1987).
- [40] J. Fineberg, S.P. Gross, M. Marder, H.L. Swinney, Phys. Rev. Lett. **67**, 141 (1984).
- [41] see for example J.E. Field, Contemp. Phys. **12**, 1 (1971); E.H. Yoffe, Phil. Mag. **42**, 673 (1961); K. Ravi-Chandar, W.G. Knauss, Int. J. Fract. **26**, 65 (1984); ibid 141 (1984)
- [42] J.-P. Bouchaud, E. Bouchaud, G. Lapasset, J. Planès, Phys. Rev. Lett. **71**, 2240, (1993); E. Bouchaud, J.-P. Bouchaud, J. Planès, G. Lapasset, Fractals **1**, 1051 (1993). **294**, 835 (1982).
- [43] B. Sapoval, J.-N. Chazalviel, J. Peyrière, Phys. Rev. A **38**, 5867 (1988).
- [44] D. Ertas, M. Kardar, Phys. Rev. Lett. **69**, 889, (1992).
- [45] D. Ertas, M. Kardar, preprint (1994).

## SPATIAL AND TEMPORAL PROBES OF DEFORMATION AND FRACTURE AT INTERFACES

J. T. DICKINSON, S. C. LANGFORD, AND LOUIS SCUDIERO

Physics Department, Washington State University, Pullman, WA 99164-2814

### ABSTRACT

During the peel of a ductile material from a rigid substrate, a number of instabilities can arise in the shape and motion of the peel front. For instance, void formation, viscous fingering, and fibril formation and bifurcation can modulate the local rate of detachment between the two materials. These fluctuations affect the rate of energy dissipation and depend directly on the micromechanics of the detachment zone. Exploiting the consequences of contact charging between dissimilar materials, we have developed sensitive methods for detecting fluctuations during interfacial failure. We have also developed a sensitive probe of ductile deformation in reactive metals and use these measurements to probe energy dissipation during interfacial failure. We present examples of chaotic behavior and discuss the relation between these results with our current understanding of energy dissipation during interfacial crack growth.

### INTRODUCTION

The chemical forces responsible for adhesion between dissimilar materials are electronic in nature (e.g., ionic, covalent, metallic or Van der Waals bonding), and thus interfacial failure often produces strong electrical effects. These may include intense emissions of light and charged particles,<sup>1</sup> as well as transient electrical signals in conducting phases.<sup>2</sup> Since the processes responsible for these signals are inherently atomic in nature, they can often be exploited to yield time-resolved information about the process of failure.

We have recently employed sensitive current measurements to study the peel of a pressure sensitive adhesive from a copper substrate. The extremely nonlinear, viscous behavior of pressure sensitive adhesives results in considerable energy dissipation during peeling over a wide range of peel speeds and substrates. In particular, the formation and elongation of adhesive fibrils during adhesive detachment is generally the dominant dissipative process during peeling,<sup>3</sup> provided that these fibrils do not fail prematurely (cohesively or adhesively). The interplay between fibril release and the viscoelastic properties of the adhesive is of fundamental importance in the design and application of pressure sensitive adhesives. The current fluctuations during peel change dramatically with peel speed and can be analyzed to extract information on the dynamics of the peel process. Numerical analysis of these signals is strongly suggestive of deterministic chaos.

In metal-ceramic composites, the plastic deformation associated with void formation in the metallic phase is often the dominant dissipative process during interfacial failure. This deformation is a strong function of the tortuosity or roughness of the interface,<sup>4,5</sup> the thickness of the metallic phase,<sup>6,7</sup> and the presence of interphase materials.<sup>8</sup> When competing mechanisms of energy dissipation operate simultaneously, the contribution of deformation to the measured toughness must be estimated by careful fractographic examination and numerical modeling. More direct methods are desirable, and can be especially useful when ductile deformation of the metallic phase and brittle fracture at or near the interface occur simultaneously.<sup>9</sup> In this work, we exploit the phenomenon of chemisorptive emission (CSE—electron emission accompanying the adsorption of reactive gases with clean metal surfaces) to provide such a probe. This procedure depends on the ability of CSE to detect small patches of fresh metal produced by the growth of ductile voids during failure.

## ELECTRICAL TRANSIENTS GENERATED DURING PEEL<sup>10</sup>

In related work,<sup>11</sup> we have shown that measurable electrical transients are induced in a copper substrate when a pressure sensitive adhesive is peeled from its surface. These currents show significant fluctuations associated with micromechanical events during peeling. However, the interpretation of these fluctuations at low peel speeds is complicated by current spikes accompanying strong electrical breakdown events. In this work we analyze the current signals obtained at somewhat higher peel speeds in the 180° peel geometry, where strong electrical breakdown events are seldom observed. Additional modifications in the experimental geometry further enhance the sensitivity of the current signals to micromechanical events along the peel front (the line of adhesive detachment from the substrate). We show that these fluctuations are neither random nor strictly deterministic. This suggests that the current fluctuations and the underlying process of adhesive detachment are chaotic.

A diagram of the experimental geometry is shown in Fig. 1. Figure 2 shows typical current measurements in air at three peel speeds. At these peel speeds (2-6 mm/s), a large number of small negative current spikes are observed. Sensitive measurements of photon and long-wavelength, radio-frequency emissions confirm that these current spikes accompany small gaseous discharge events. The magnitude of the average current (between negative spikes) increases with peel speed. Under these conditions a strong correlation between load and low-frequency current fluctuations are observed, where the highest currents are observed during periods of falling load. This is consistent with the expectation that the current is proportional to the rate of detachment. When the tape is drawn at a constant speed, transient increases in the rate of detachment decrease the applied load and increase the current.

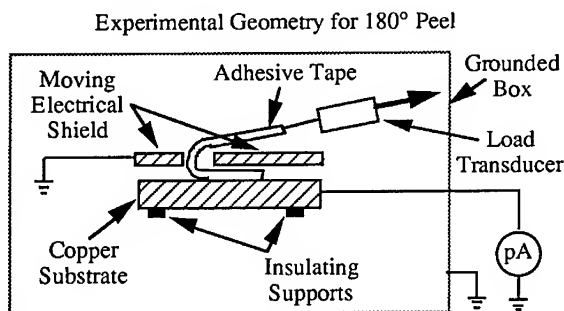


Fig. 1. Diagram of typical 180° peel experiment.

The current fluctuations are readily analyzed by a variety of numerical techniques. For instance, the power spectra of the current signals at three different peel speeds are shown in Fig. 3. These spectra were computed by two distinct methods, once from the Fourier transform of the current signals and once by a maximum entropy technique.<sup>12</sup> Maximum entropy methods typically render broad band features in a smoother fashion, but are also capable of representing isolated, sharp features.

At the two lower peel speeds, the power spectra show a relatively constant level of "power" at the low frequencies, a broad peak in the 50-60 Hz region, and a rapid drop in power as a function of frequency at the higher frequencies. (The contribution of 60 Hz electrical noise to the observed signals is evident in the sharp 60 Hz peak in the Fourier transform power spectra of Fig. 3(a). This peak is well below the "signal" in the other two power spectra.) The total power, as measured by the area under the power spectra, is about five times greater at 4.5 mm/s than at 2.2 mm/s. Since the "power" associated with a fluctuation varies as the square of its amplitude, this is consistent with the doubling of the amplitude of the current fluctuations observed as the peel speed is raised from 2.2 mm/s to 4.5 mm/s [Figs. 2(a) and 2(b)].

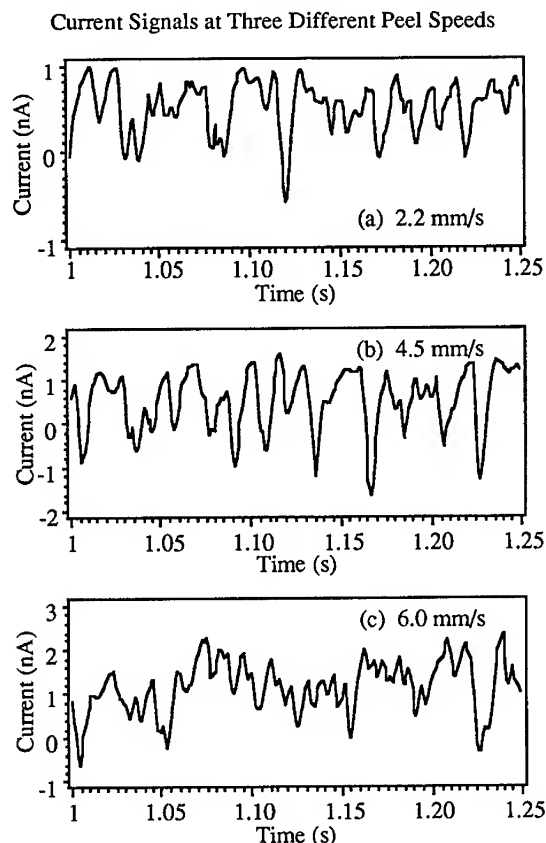


Fig. 2. Current observed at peel speeds of (a) 2.2 mm/s, (b) 4.5 mm/s, and (c) 6 mm/s.

The maximum entropy "spectral estimates" follow the average behavior of the power spectra computed from the Fourier transforms quite well. At the lower two peel speeds, the general shape of the spectral estimates are similar to the spectra of an underdamped harmonic oscillator with a resonant frequency of 50-60 Hz. As noted below, this comparison can be made quantitative. It is important to note that the features in the 50-60 Hz range are at frequencies too low to be attributed to individual discharge events (which produce the negative current spikes) and are too broad to be attributed to electrical noise (which produces distinctive, but much smaller features). Thus they appear to reflect a mechanical resonance along the peel front.

As the peel speed is increased to 6.0 mm/s, the power spectra of the current fluctuations change dramatically. A broad peak centered at zero frequency appears, suggesting a highly overdamped mechanical response, although a shoulder at about 75 Hz suggests a weak underdamped response remains. The power spectrum at 6 mm/s is well described by two harmonic oscillators in parallel, one overdamped and one underdamped. This behavior may reflect an inhomogeneity in the mechanical response. For instance, void formation and interfacial failure *ahead* of the nominal peel front could yield current fluctuations with an entirely different (highly damped) character than interfacial failure along the peel front itself. Alternatively, the peel front as a whole may be oscillating between two different mechanical behaviors (intermittency).

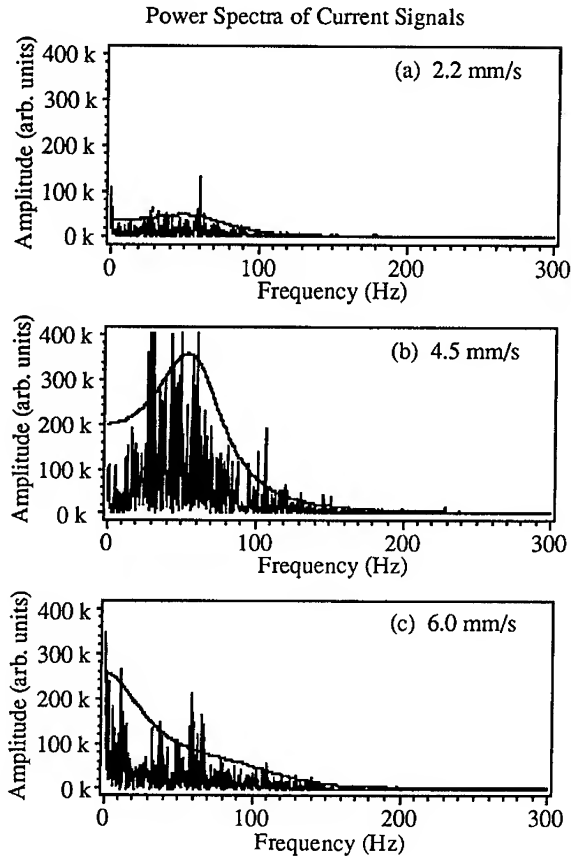


Fig. 3. Power spectra of the current signals of Fig. 2 accompanying peel at (a) 2.2 mm/s, (b) 4.5 mm/s, and (c) 6 mm/s. The vertical bars show the power spectra computed from the Fourier transforms of the current signals, while the smooth curves show power spectra estimates computed by the maximum entropy method.

The maximum entropy spectra of Fig. 3 can be quantitatively modeled in terms of underdamped (at the lower peel speeds) and overdamped (at the higher peel speeds) harmonic oscillators. The power spectrum,  $S$ , of a perturbed harmonic oscillator has the form<sup>13,14</sup>

$$S(f) = \frac{N}{(f^2 + \delta)^2 + \epsilon}, \quad (1a)$$

where  $N$  is the (constant) spectral amplitude of the random perturbations,  $f$  is the frequency,

$$\delta = \frac{\gamma^2}{2m^2} - k/m, \quad \text{and} \quad \epsilon = \frac{\gamma^2 k}{m^3} - \frac{\gamma^4}{4m^4}. \quad (1b)$$



In a simple mass-spring-dashpot system,  $\gamma$  is the damping constant,  $k$  is the spring constant, and  $m$  is the effective mass. Underdamping prevails when  $\delta < 0$  and overdamping when  $\delta > 0$ . The least square fit of the maximum entropy spectral estimates to Eq. (1) are displayed in Fig. 4. As suggested above, the power spectrum at 6.0 mm/s is modeled by two mass-spring-dashpot elements (arranged in parallel), one overdamped and one underdamped. Given the simplicity of these models, the fits to the experimental power spectra are excellent.

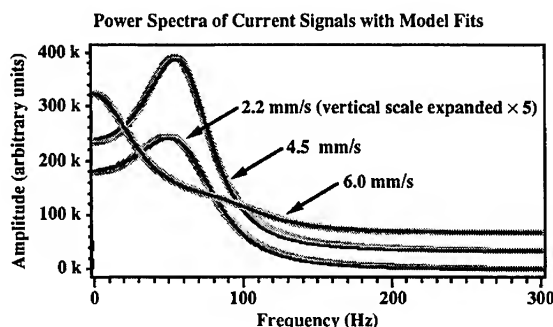


Fig. 4. The maximum entropy power spectra of Fig. 3 (dark lines) and the least squares fit to the power spectra from Eq. 1 (light lines).

Peeling at lower relative humidities increases the amplitude of the fluctuations at all peel speeds, and raises the peel speed for the transition from underdamped to overdamped behavior. We attribute the greater fluctuations in large part to the improved adhesive-substrate adhesion at lower humidities. This produces greater strains in the adhesive along the peel front, and thus more rapid and extensive fibril movements. Assuming a rubber-like response in the adhesive, these greater strains are also associated with higher stiffness [higher  $k$  in Eq. (1b)]. Overdamping is more difficult with "stiff" springs [smaller  $\delta$  in Eq. (1a)], which would account for the higher velocities required for the transition.

The origin of the onset of overdamped behavior between 4 and 6 mm/s is not entirely clear. Overdamped behavior is typical of highly dissipative systems—and is thus desired in adhesive systems. Since the performance of a pressure sensitive adhesive depends on dissipation in a large area adjacent to the region of actual detachment, this transition may not be evident in more broad measures of peel behavior, such as the peel force. (The power spectra of fluctuations in the peel force become increasingly broad in this region of peel speeds, but is otherwise not remarkable.) Nevertheless, the highest strains in the adhesive system occur along the peel front, which is thus the "weak link" in the peel system. Thus any change in the behavior of the peel front is of considerable importance.

The broad, low frequency peaks in the power spectra of the current fluctuations can be described in terms of a simple mechanical response to a perturbation. However, the perturbation appears to be quite complex. For instance, attempts to model the current signals with random, autoregressive processes (constructed from analysis of the maximum entropy spectra) yield signals which are incompatible with the data. Chaotic systems typically display broad band noise similar to that observed here.<sup>15</sup> The definitive test for chaos is an extreme sensitivity to initial conditions, which can be quantified in terms of Lyapunov exponents. Chaotic systems have at least one positive Lyapunov exponent. Unfortunately, the available algorithms do not yield reliable Lyapunov exponent estimates in many experimental systems,<sup>16</sup> including this one. An important alternative analysis involves testing for fractal behavior (the search for a "strange attractor").<sup>17</sup> Although fractal character does not mathematically require chaos, few fractal, nonchaotic systems have been identified.<sup>18</sup> This analysis confirms that the current signals are indeed fractal ( $5.5 < D < 5.6$ ),<sup>10</sup> consistent with a chaotic origin. These dimension measurements also exclude the possibility that the corresponding current fluctuations (reflecting

mechanical and/or electrical perturbations along the peel front) are random. Random signals are inherently infinite dimensional,<sup>19</sup> so that dimension estimates on random signals fail to converge altogether.

#### CHEMICAL STIMULATED EMISSION AS A PROBE OF PLASTIC DEFORMATION<sup>20</sup>

In previous work,<sup>21</sup> we showed that CSE is a sensitive measure of plasticity during tensile deformation of a number of metals. In principle, the method is similar to the use of photoelectron emission as a probe of tensile deformation<sup>22</sup> and fatigue damage<sup>23</sup> in metals such as Al and Mg. Steps produced by the intersection of dislocations with the surface increase the surface area of the low work function metallic phase and thus increase the photoelectron emission intensities. The chief advantage of CSE is its uniform sensitivity to deformation in a variety of sample geometries. Gas molecules tend to be adsorbed uniformly on complex surfaces, whereas in photoelectron measurements, portions of the surface are often shadowed from the uv source. Further, the background CSE signals from undeformed material are often quite low due to the presence of a thin oxide layer. CSE requires adsorption on fresh metal, whereas uv photons and photoelectrons can penetrate sub- $\mu\text{m}$  oxides to produce intense signals even in the absence of deformation. Thus, CSE is often a superior probe of the increase in surface area accompanying plastic deformation.

The experiments here were conducted in two vacuum systems with base pressures less than  $1 \times 10^{-5}$  and  $1 \times 10^{-7}$  Pa, respectively. A schematic of the experimental arrangement is shown in Fig. 5(a). Oxygen was used as the reactive gas and was leaked into the system through a clean manifold and leak valve, raising the pressure in the vacuum system to  $4 \times 10^{-4}$  Pa. Electron emission was detected with a Channeltron electron multiplier (CEM). The front cone of the CEM was biased at +1000 V for efficient electron detection. Within about 2 s after the completion of peel, the two sides of the sample were drawn apart, allowing for efficient detection of electrons emitted from the Mg surface.

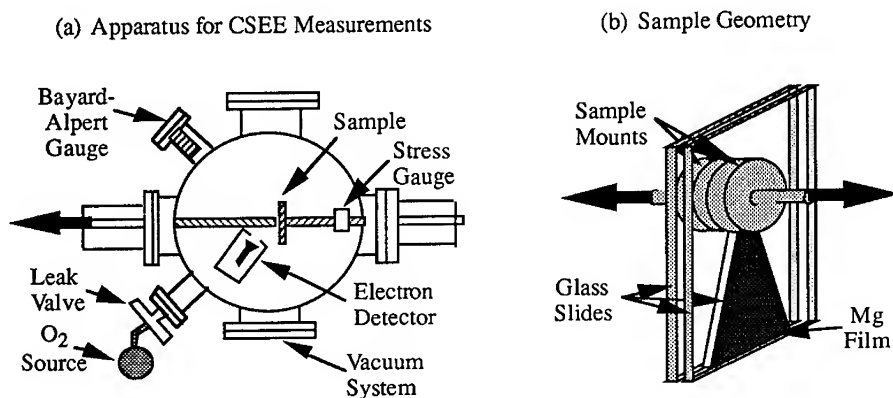


Fig. 5. Diagram of the (a) apparatus employed in the CSE measurements and (b) geometry of the peel sample.

Measurements of CSE intensity as a function of Mg surface area (by exposing a freshly evaporated Mg film to oxygen) yielded  $3 \times 10^8$  electrons/cm<sup>2</sup>, which corresponds to a yield of  $1 \times 10^{-7}$  electrons/Mg surface site. AFM scans of the Mg film surface confirmed that its surface roughness was negligible. All AFM images were acquired with a Digital Instruments Nanoscope III in the contact mode using commercial Si<sub>3</sub>N<sub>4</sub> tips with nominal radii of curvature of 40 nm.

The Mg/glass interfaces were formed by evaporation in vacuum. After cleaning, the slides were mounted in an ion-pumped deposition system with a base pressure of  $< 1 \times 10^{-5}$  Pa. The film thickness was monitored by a quartz microbalance positioned near the glass slide. Small angle x-ray scattering measurements on a typical 1- $\mu\text{m}$  film indicated a high degree of orientation in the polycrystalline film, with the c-axis of the grains aligned normal to the surface. A similar preferential orientation has been observed in Mg films deposited by "cluster-beam" techniques onto room temperature glass substrates.<sup>24</sup>

The sample geometry employed is shown in Fig. 5(b). A triangular piece of Mg-coated glass was epoxied between two other glass slides to which the load was applied. Sandwiching the metal film between brittle substrates minimized the effect of residual stresses on crack growth.<sup>9</sup> Failure initiated at the tip of the triangle and proceeded along the Mg/glass interface, the Mg remaining on the epoxy. After initial "pop-in" of a small starter crack, steady crack growth followed at roughly constant load. Microscope observations indicated that the starter crack represented only a small fraction ( $< 1\%$ ) of the total surface area.

The total energy expended during crack growth (here designated the peel energy) was determined from the total area of the constant load portion of the load vs displacement curve. We note that the energy so derived is not simply related to the critical strain energy release rate at the onset of crack growth (except possibly in very brittle materials), but represents an average energy for surface formation during *continuous* crack growth. As the great majority of the surface is formed during continuous crack growth, the peel energy is a more appropriate measure of deformation for comparison with emission measurements.

Figure 6 shows the CSE emission intensities (log) vs time from a high peel energy surface (a 1- $\mu\text{m}$  film with a peel energy of about 16 J/m<sup>2</sup>) and a low peel energy surface (a 0.5- $\mu\text{m}$  film with a peel energy of 3.2 J/m<sup>2</sup>). Both samples yielded intense emissions during the peel

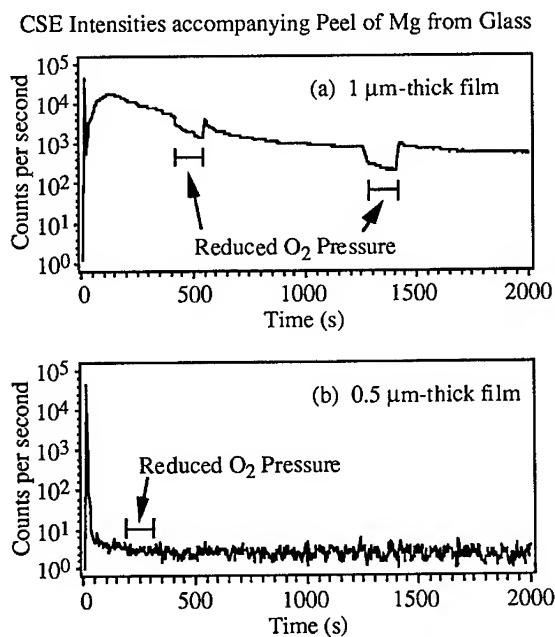


Fig. 6. Typical CSE signals following the peel of Mg films from soda-lime glass: (a) a 1- $\mu\text{m}$  film and (b) a 0.5- $\mu\text{m}$  film. The partial pressure of  $\text{O}_2$  was lowered from  $4 \times 10^{-4}$  Pa to about  $7 \times 10^{-6}$  Pa twice in (a) and once in (b).

event itself, saturating the electron counting electronics. The emission from the 0.5- $\mu\text{m}$  film drops rapidly after peel and continues to drop for the duration of data acquisition. Although the emission from the 1- $\mu\text{m}$  film drops two orders of magnitude after peel, it subsequently returns to high levels before beginning a long, slow decay. Furthermore, the emission from the 1- $\mu\text{m}$  film depends strongly on the partial pressure of  $\text{O}_2$ , falling sharply when the  $\text{O}_2$  pressure is reduced and rising when the  $\text{O}_2$  pressure is restored. A strong pressure dependence is characteristic of CSE. In contrast, the emissions from the 0.5  $\mu\text{m}$ -film are not significantly affected by changing the  $\text{O}_2$  partial pressure, implying very small CSE intensities. Thus peeling the 0.5- $\mu\text{m}$  film has exposed very little metallic Mg, consistent with failure through a brittle interphase. In contrast, the emissions from the 1- $\mu\text{m}$  film correspond to a metallic Mg surface coverage of about 16% of the nominal surface area. This is still a relatively small fraction of the nominal surface area, consistent with localized patches of deformed material in conjunction with failure through a brittle interphase. This apparently small amount of deformation has a dramatic effect on the peel energy.

Electron emission during and immediately after crack growth has been investigated previously,<sup>25,26</sup> and occurs with or without  $\text{O}_2$ ; the fracture-induced emission alone is weakly correlated with peel energy. For instance, both samples in Fig. 6 show intense emissions during peel. To reduce the influence of these prompt emissions on sample-to-sample comparisons, the emissions during the first fifty seconds after peel were not included in the analysis. Good results were obtained when the electron counts were integrated from 50 s to 1200 s after the onset of peeling. The resulting CSE intensities are plotted in Fig. 7 as a function of peel energy. The peel energies of the 1- $\mu\text{m}$  films (determined from the load curves) range from about 8 to about 16  $\text{J}/\text{cm}^2$  and are strongly correlated with the CSE intensities. The low peel energy point corresponding to the 0.5- $\mu\text{m}$  film of Fig. 6(b) is also included in Fig. 7, along with a least squares fit to the data corresponding to the 1- $\mu\text{m}$  films (omitting the 0.5- $\mu\text{m}$  film point). The least squares fit to the 1- $\mu\text{m}$  film data crosses the x-axis near the point corresponding to the 0.5- $\mu\text{m}$  film, which yielded extremely weak emissions. Thus the peel energy of the 0.5- $\mu\text{m}$  film appears to represent the "zero plastic deformation" limit of failure in this system.

The peel energy of the 0.5- $\mu\text{m}$  film, about 3  $\text{J}/\text{m}^2$ , is well below metallic fracture energies, and is significantly lower than the fracture energy of the soda lime glass substrate (about 9  $\text{J}/\text{m}^2$ ). Magnesium oxides [e.g.,  $\text{MgO}(100)$ <sup>27</sup>] have fracture energies similar to that of the 0.5- $\mu\text{m}$  film and would readily form in the early stages of deposition at the pressures employed in this work. The presence of a brittle interphase can have dramatic effects on the fracture of metal-ceramic composites.<sup>6</sup> We attribute the rather large sample-to-sample variation in peel energies of the 1- $\mu\text{m}$  films to variations in the metal microstructure and interphase composition. Both phases are strongly affected by the deposition rate, which varied somewhat

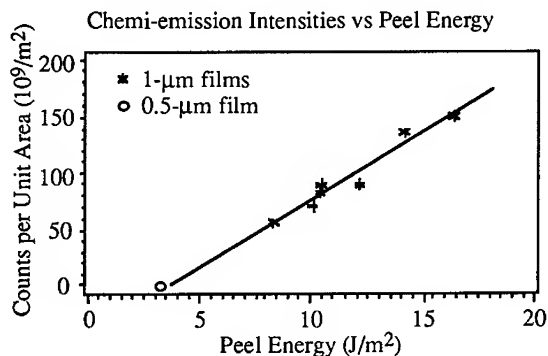


Fig. 7. A plot of CSE intensities vs peel energy, where the CSE intensities include the total number of electrons detected beginning 50 s after the peel event and ending 1200 s later. The line represents the least squares fit to the data from the 1- $\mu\text{m}$  films only.

from sample to sample. The good correlation between peel energy and CSE intensities suggest that the sample-to-sample variations in peel energy are due to real differences in material behavior, rather than measurement uncertainties.

Figure 8 shows typical AFM images of the Mg surfaces which yielded the emissions of Fig. 6. All of the high peel energy, high emission surfaces showed large numbers of submicron-sized voids along the surface, similar to those in Fig. 8(a), confirming the presence of ductile deformation. No similar voids were observed on the low peel energy surface, as shown in Fig. 8(b). The voids in the high peel energy samples were typically about 10 nm deep, with relatively flat bottoms and angular sides. The angular sides contrast markedly with the smooth ellipsoidal profiles of ductile voids in FCC metals. The formation of smooth ellipsoidal features in Mg (HCP structure) is hindered (relative to the FCC metals) by the absence of the five equivalent slip planes required to accommodate arbitrary deformations.<sup>28</sup>

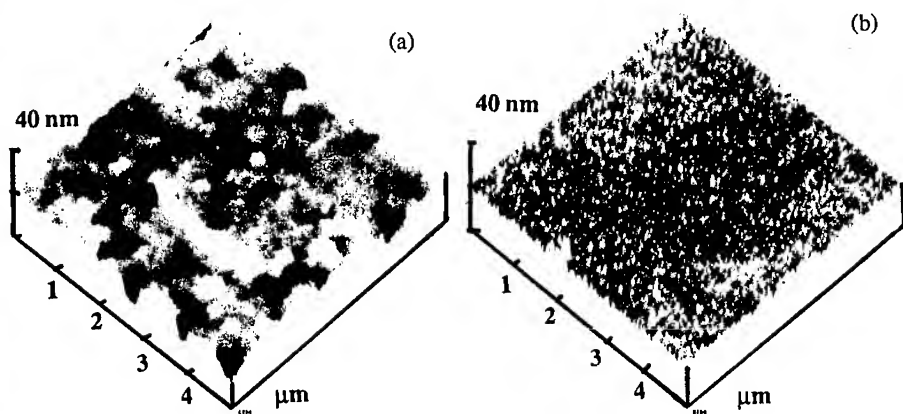


Fig. 8. AFM images of peeled Mg surfaces: (a) the 1- $\mu\text{m}$  film yielding the intense CSE shown in Fig. 6(a), and (b) the 0.5- $\mu\text{m}$  film yielding the very weak CSE shown in Fig. 6(b).

AFM images of the mating glass surfaces show no evidence for voids or protrusions comparable to the voids on the high peel energy Mg surfaces. Therefore we attribute void formation in the Mg to nucleation and ductile growth, similar to the formation of ductile dimples in thicker metallic films.<sup>29</sup>

Chemisorptive electron emission is believed to occur immediately prior to the collision of an electronegative atom or molecule (e.g., O, O<sub>2</sub>, X, X<sub>2</sub>—where X = halogen) with an appropriate metal surface.<sup>30-32</sup> As the gas atom approaches the surface, the energy of its lowest unfilled electron state (whose energy defines the electron affinity of the molecule,  $E_A$ ) drops. If  $E_A$  falls below the Fermi level of the metal,  $E_F$ , an electron can tunnel from the metal to the atom to produce a negative ion. In the rare event that the difference between  $E_A$  and  $E_F$  is greater than the metal work function  $\phi$ , tunneling leaves behind a hole in the valance band deep enough to stimulate electron emission. Although the emission probability per incident molecule is small (typically  $\leq 10^{-6}$ ), the number of surface sites is very large (typically  $10^{15} \text{ cm}^{-2}$ ). With our nearly single-electron sensitivity, CSE is readily observable for reactive metals such as Mg, Ti, Zr, Al, and alkali metals exposed to gases such as oxygen and the halogens.

The CSE signals from Mg are extremely high due to its high affinity for oxygen. Newly formed oxide is incorporated into islands,<sup>33,34</sup> leaving small patches of low work function material in between. These patches yield intense emissions long after the surface would otherwise be completely covered with oxide. In the early stages of absorption, the work function of the surface actually decreases.<sup>33,35</sup> Since the CSE efficiency depends exponentially on the

work function, the emission intensities may peak long after the onset of O<sub>2</sub> exposure, as in Fig. 6(a). By integrating the CSE intensities over several hundred seconds after the peel event, uncertainties due to variations in emission rate as a function of time can be minimized. CSE intensities do depend somewhat on the crystallographic orientation of the emitting surfaces. In this work, this effect introduces little uncertainty because deformation is generally dominated by slip on a set of equivalent planes. Thus the increase in CSE intensities due to deformation should be very nearly proportional to the new surface area created by slip.

Assuming a simple geometry for the deformation process, the relation between the creation of surface area and the work of deformation can be made more quantitative. An edge dislocation of length  $l$  oriented parallel to the surface and moving into the material will produce a step of length  $l$  and height  $b$ , where  $b$  is the magnitude of the Burgers vector. The corresponding change in surface area is  $\Delta A = b \cdot l$ , and the work of performed as this dislocation moves a distance  $d$  into the material is on the order of  $\sigma_y \cdot b \cdot d \cdot l$ , where  $\sigma_y$  is the stress required to move the dislocation. The work done per unit surface area,  $W_{\text{plastic}}/A$ , can then be expressed as

$$\frac{W_{\text{plastic}}}{A} \approx \sigma_y \cdot d \cdot \frac{\Delta A}{A}, \quad (2)$$

where  $\Delta A/A$  is the ratio between the surface area produced by deformation and the nominal area of the peeled surface. This line of reasoning equates  $\Delta A/A$  with the effective strain at failure,  $\epsilon_0$ , where one expects  $W_{\text{plastic}}/A \sim \sigma_y \cdot d \cdot \epsilon_0$ .

Quantitative CSE measurements can be used to infer  $\Delta A/A$ ; thus the only two unknowns in Eq. 2 are  $\sigma_y$  and  $d$ . When the distance between ductile voids is much greater than one tenth the film thickness (as in this work), it is generally adequate to assume that the film is uniformly deformed throughout its thickness.<sup>6</sup> However, the effective yield stress is somewhat uncertain. Cold rolled Mg sheet yields substantially at a stress of 100 MPa. With  $\sigma_y \approx 100$  MPa and  $d \approx 1$   $\mu\text{m}$ , the maximum observed value of  $\Delta A/A \approx 0.16$  corresponds to a predicted work of deformation  $W_{\text{plastic}}/A \approx \sigma_y \cdot d \cdot \Delta A/A \approx 16$  J/m<sup>2</sup>. The corresponding experimental peel energy was about 16 J/m<sup>2</sup>, which corresponds to a work of plastic deformation  $W_{\text{plastic}}/A \approx 13$  J/m<sup>2</sup>. In view of the uncertainties, better agreement is not expected. The surface areas inferred from CSE measurements are clearly of the correct order of magnitude to account for the observed enhancements in peel energy due to plastic deformation.

CSE signals are sensitive to small amounts of deformation. The work of deformation corresponding to a CSE signal ten times the "zero deformation" limit (from the 0.5- $\mu\text{m}$  film point in Fig. 7) is less than 0.1 J/m<sup>2</sup>. In smaller samples, with correspondingly small background count rates, a fresh Mg surface of area  $\Delta A = 10^{-2}$  mm<sup>2</sup> would yield a readily detectable 10<sup>3</sup>-10<sup>4</sup> counts.

Roughness measurements based on AFM observations were also made for potential correlation with peel energy measurements. These measurements displayed significant "magnification effects,"<sup>36</sup> in that the measured roughness was a strong function of the scan size. Quantitatively, the measured roughness was poorly correlated with peel energy at the smallest scan sizes attempted (500  $\times$  500 nm<sup>2</sup>) and only moderately correlated with peel energy at larger scan sizes (up to 50  $\times$  50  $\mu\text{m}^2$ ). The poor correlation with peel energy is apparently due to the wide range of length scales required for proper characterization—from atomic steps (associated with the Burgers vectors of individual dislocations) to the dimensions of the ductile voids (some hundreds of nm in diameter). Atomic resolution has not yet been demonstrated by either AFM or STM of surfaces as rough as the Mg surfaces in this work. Novel acquisition methods, such as large-area scans with extremely high digitization densities, may help solve this problem. Due to its high lateral resolution, scanning tunneling microscopy (STM) can also be a valuable tool. For instance, Warner and Bonnell<sup>37</sup> have used STM to examine the metal side of a fractured ceramic-metal interface and noted correlations between the observed topography and fracture energy. Nevertheless, the resolution of STM can be limited by surface roughness and the presence of insulating interphases and oxides formed after failure.

Applying these techniques to interfaces involving other non-ferrous metals would be interesting. For instance, FCC metals like Al deform more homogeneously (due to local strain hardening) and yield smoother (although often larger) surface features. In contrast, the HCP metals, such as Mg, Ti, and Zr, tend to deform more inhomogeneously (due to local strain softening) and produce rougher surfaces. CSE measurements on these materials would yield reproducible surface area values despite the contrasting morphologies.

## CONCLUSIONS

Current signals accompanying interfacial failure between conducting and nonconducting phases can provide time-resolved information on the course of failure. In the case of pressure sensitive adhesives, visual observations of adhesive detachment reveal a highly branched structure of adhesive "fingers" in a constant state of flux—branching, merging, extending, and retracting. However, these visual observations are very difficult to quantify in a time resolved fashion. Current measurements provide a time-resolved picture of the collective behavior of this very complex dynamical system. Numerical analysis of the current signal yields direct information on the mechanical response of the peel front, and indicates that the peel front is perturbed in a nonrandom, probably chaotic manner. Our present efforts are focused on improving the sensitivity and frequency range of the electrical measurements, as well as improving observational techniques for characterizing the events occurring in the peel zone.

In ceramic metal composites involving reactive metals, CSE measurements have considerable potential as a probe of deformation in material and process evaluation. The ductility of thin metal films may be a key to understanding deformation 10-100 nm ahead of the crack tip, where the local stresses are not well understood.<sup>6</sup> The sensitivity of CSE measurement to deformation in the metallic phase is particularly valuable in systems where the contribution of competing fracture processes (e.g., fracture through a brittle interphase or fracture of brittle reinforcements) is variable or not known. We expect that this technique can be readily extended to thicker metallic structures (possibly commercial metal-ceramic composites) and to other reactive metals, including Ti, Zr, and Al, to provide quantitative measures of the integrated work of plastic deformation over entire fracture surfaces.

Current and particle emission processes ultimately depend on atomic-level events, which allows for potentially very high spatial and temporal resolution. Departures from *adiabatic* separation of atomic planes or molecular bonds are reflected in the topographical, electrical, and chemical states of the resulting fracture surface. Thus these signals typically reflect energy-consuming processes of great interest for their potential to limit the rate of crack growth. The details provided by these and similar studies complement recent developments in fracture mechanics, where atomic scale models of fracture are being extended to still larger length scales. Microscopic, dynamic descriptions of crack growth and related processes may require new syntheses of mathematical formalisms, where fractal geometry and chaos play key roles.

## ACKNOWLEDGMENTS

We wish to thank Sumio Nakahara for performing CSE and AFM measurements, Wenbiao Jiang for performing x-ray measurements, and John Hirth for helpful discussions. This work was supported by the Air Force Office of Scientific Research under contract AFOSR-F49620-91-C-0093, the National Science Foundation under grants DMR-8912179 and DMR-9201767, the Dow Chemical Company, the 3 M Company, the Murdock Charitable Trust, the Washington Technology Center, and the Japan Private School Promotion Foundation.

## REFERENCES

1. J. T. Dickinson, in *Non-Destructive Testing of Fibre-Reinforced Plastics Composites*, edited by John Summerscales (Elsevier Applied Science, London, 1990), pp. 429-482.

2. K. A. Zimmerman, S. C. Langford, and J. T. Dickinson, *J. Appl. Phys.* **70**, 4808 (1991).
3. R. J. Good and R. K. Gupta, *J. Adhesion* **26**, 13 (1988).
4. A. G. Evans and J. W. Hutchinson, *Acta Metall.* **37**, 909 (1989).
5. Z. Chen and J. J. Mecholsky, Jr., *J. Mater. Res.* **8**, 2362 (1993).
6. A. G. Evans and B. J. Dalgleish, *Mater. Sci. Engin.* **A162**, 1 (1993).
7. J. Kim, K. S. Kim, and Y. H. Kim, *J. Adhesion Sci. Technol.* **3**, 174 (1989).
8. A. G. Evans, B. J. Dalgleish, M. He, and J. W. Hutchinson, *Acta Metall.* **37**, 3249 (1989).
9. I. E. Reimanis, B. J. Dalgleish, and A. G. Evans, *Acta Metall. Mater.* **39**, 3133 (1991).
10. Louis Scudiero, J. T. Dickinson, L. C. Jensen, and S. C. Langford, to appear in *J. Adhesion Sci. Technol.*
11. Sunkyo Lee, L. C. Jensen, S. C. Langford, and J. T. Dickinson, to appear in *J. Adhesion Sci. Technol.*
12. W. H. Press, B. P. Flannery, S. A. Teukolsky, and W. T. Vetterling, *Numerical Recipes in Pascal: The Art of Scientific Computing* (Cambridge University, Cambridge, 1981), pp. 473-479.
13. Keith R. Symon, *Mechanics*, 3rd Ed. (Addison Wesley, Reading, MA, 1971), pp. 50ff.
14. Aldert Van der Ziel, *Noise: Sources, Characterization, Measurement*, (Prentice-Hall, Englewood Cliffs, NJ, 1970), pp. 16-18.
15. Heinz Georg Schuster, *Deterministic Chaos: An Introduction*, 2nd Ed. (VCH, Weinheim, Germany, 1988), pp. 1-16.
16. Francis C. Moon, *Chaotic and Fractal Dynamics*, (John Wiley, New York, 1992), pp. 78-82, 307-310.
17. P. Grassberger and I. Procaccia, *Physica* **9D**, 189 (1983).
18. The only exceptions (non-chaotic systems with non-integral dimensions) of which we are aware are dissipative systems driven simultaneously at two incommensurate frequencies: W. L. Ditto, M. L. Spano, H. T. Savage, S. N. Rauseo, J. Heagy, and E. Ott, *Phys. Rev. Lett.* **65**(5), 533 (1990). The peeling process (which can be viewed as dissipative process driven at zero frequency) is not likely to constitute another exception.
19. Avraham Ben-Mizrachi and Itamar Procaccia, *Phys. Rev. A* **29**, 975 (1984).
20. Sumio Nakahara, S. C. Langford, and J. T. Dickinson, submitted to *J. Mater. Res.*
21. J. T. Dickinson, L. C. Jensen, S. C. Langford, and R. G. Hoagland, *J. Mater. Res.* **9**, 1156 (1994).
22. B. Sujak and A. Gieroszyński, *Acta Phys. Polon.* **28**, 249 (1968).
23. W. J. Baxter, *Fatigue Engin. Mater. Struc.* **1**, 343 (1979).
24. O. F. Hagena, G. Knop, R. Fromknecht, and G. Linker, *J. Vac. Sci. Technol. A* **12**, 282 (1994).
25. L. A. K'Singam, J. T. Dickinson, and L. C. Jensen, *J. Am. Ceramics Soc.* **68**, 510 (1985).
26. D. L. Doering, S. C. Langford, J. T. Dickinson, and P. Xiong-Skiba, *J. Vac. Sci. Technol. A* **8**, 2401 (1990).
27. J. J. Mecholsky, Jr., S. W. Freimam, and R. W. Rice, *J. Mater. Sci.* **11**, 1310 (1976).
28. Richard W. Hertzberg, *Deformation and Fracture Mechanics of Engineering Materials*, 3rd Ed. (John Wiley, New York, 1989), pp. 81-83.
29. A. G. Evans and B. J. Dalgleish, *Acta Metall. Mater.* **40**, S295 (1992).
30. B. M. McCarroll, *J. Chem. Phys.* **50**, 4758 (1969).
31. B. Kasemo, E. Törnqvist, and L. Walldén, *Mater. Sci. Engin.* **42**, 23 (1980).
32. R. H. Prince and R. Persaud, *Surf. Sci.* **207**, 207 (1988).
33. H. Namba, J. Darville, and J. M. Gilles, *Surf. Sci.* **108**, 446 (1981).
34. G. C. Allen, P. M. Tucker, B. E. Hayden, and D. F. Klemperer, *Surf. Sci.* **102**, 207 (1981).
35. T. F. Gessell and E. T. Arakawa, *Surf. Sci.* **33**, 419 (1972).
36. E. E. Underwood and K. Banerji, *Mater. Sci. Engin.* **80**, 1 (1986).
37. C. P. Warner and D. A. Bonnell, in *Interface Dynamics and Growth*, edited by K. S. Liang, M. P. Anderson, R. F. Bruinsma, and G. Scoles, (Materials Research Society, Pittsburgh, PA, 1992), 393. [*Mater. Res. Soc. Symp. Proc.* **237**]



## NATURE OF ENVIRONMENTALLY ASSISTED FRACTURES IN POLYCRYSTALS

LEONARDO GOLUBOVIĆ and ANATOLI PEREDERA  
Physics Department, West Virginia University, Morgantown, WV 26506

### ABSTRACT

Environmentally assisted fracture is in practice one of the most important fracture modes. It is especially dramatic in polycrystalline super-alloys, which are believed to be embrittled by oxygen diffusing along their grain boundaries. We used a large scale atomistic Monte-Carlo simulation to study phenomena of the environmentally assisted fracture nucleation in solids with grain boundaries exposed to an oxygen atmosphere. We find nucleation of inter-granular microcavities in a region which is well in front of the oxidized zone of the sample, apparently due to inhomogeneous stresses induced by the presence of oxide particles. This effect *increases* with *decreasing* oxidation rate since then the oxidation front becomes fuzzier and inhomogeneous stresses stronger. These findings compare well with the experimental data on super-alloys which indicate that the environmental embrittlement effects are strong for slower oxidation rates, whereas at higher oxidation rates the embrittlement may be suppressed.

### INTRODUCTION

Fundamental aspects of the fracture physics, such as the very nature of the state of a stressed solid and the role of thermal fluctuations has been addressed in a number of recent studies.[1]-[6] A common belief is that a stressed solid can be treated as a metastable state of matter analogous to, say, supercooled liquids. In this picture, the failure threshold corresponds to a metastability limit, at which the external stress  $\sigma$  as a function of strain reaches its maximum  $\sigma_{max}$ .

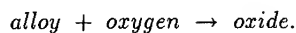
If the external tensile stress is smaller than  $\sigma_{max}$ , the stressed solid will still break, however, with time-delayed fracture. The sample lifetime depends on the temperature and the applied stress.[7] This phenomenon is believed to be directly related to the processes of microcavity nucleation and growth.[6] Recent theoretical studies of time-delayed fracture have discussed this phenomenon in monocrystals and in the absence of an environment surrounding the stressed solid.[4][5] However, most of the technologically interesting materials are polycrystals and the intergranular fracture is in practice one of the most interesting fracture modes.[8] Moreover, the environment plays an important role in assisting fracture nucleation and growth in polycrystals.[8] An example is the oxygen embrittlement observed in polycrystalline nickel based super-alloys.[9][10]

In this work we present results of the first atomistic Monte-Carlo simulation of the fracture nucleation ( time-delayed fractures) in polycrystals in the presence of an environment chemically reacting with the stressed solid.

### MONTE-CARLO SIMULATION

Atomistic Monte-Carlo simulations are at present unique modeling method capable of treating extremely slow fracture nucleation phenomena characterizing time-delayed fractures.[4][6] To date, Monte-Carlo dynamics has been used to study fracture nucleation in mono-, [4][6] and polycrystals,[6] in vacuum. Here we incorporate an atmosphere chemically reacting with a solid polycrystalline sample ( say, an alloy) under an external tensile stress. In our simulation we have three molecular species, namely three species of united atoms representing the alloy, oxygen, and oxide molecules. We model their interactions by pairwise Lennard-Jones potentials. In addition to atomistic Monte-Carlo

dynamics, we include a chemical reaction, irreversible oxidation fusing alloy and oxygen molecules into oxide molecules, i.e.



In our simulations we used solid samples with a single grain boundary. The sample is under a vertical tensile stress perpendicular to the grain boundary.

In Figure 1 we present time evolutions of the stressed sample in three characteristic cases: in vacuum; in case of "rigid" oxide with cohesion energy greater than that of the alloy; and in case of "soft" oxide with cohesion energy smaller than that of the alloy molecules. From this figure, we see that the situation with *rigid* oxide at time=8000 is like that in vacuum at a *longer* time=12000. It thus appears that the presence of the rigid oxide enhances the rate of intergranular fracture nucleation and growth. We find, however, that this embrittlement occurs only at *small* oxidation rates. With higher oxidation rates we find that a protective oxide layer is formed and the fracture is slowed down.

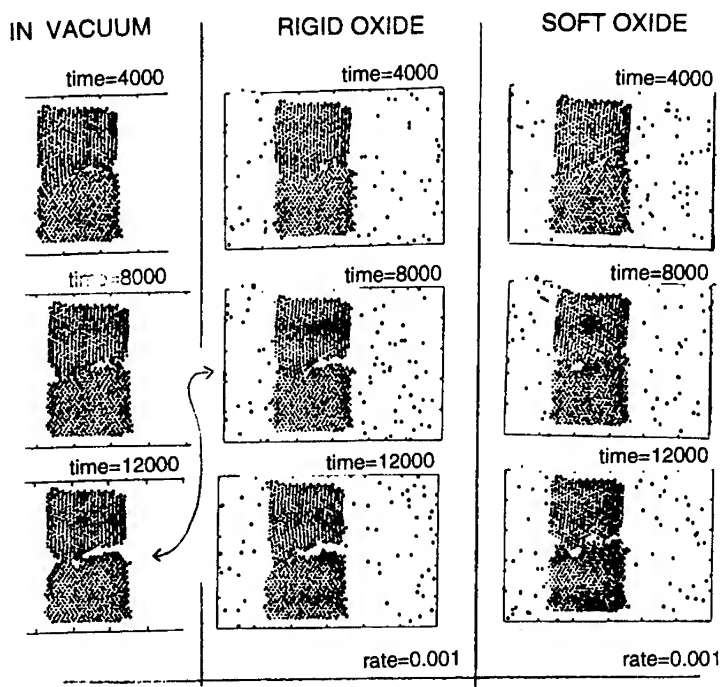


FIG. 1: Evolution of a stressed sample with a grain boundary in vacuum; with rigid; and with a soft oxide. Rigid oxide assists the intergranular fracture nucleation.

To illustrate this, in Figure 2 we give samples obtained at fixed time=7000 using different oxidation rates. Note that the sample obtained in vacuum and that obtained with a very high oxidation rate look surprisingly similar. However, a much faster intergranular fracture growth is observed for a small oxidation rate. Note also, that for high oxidation rates a continuous, apparently "protective" oxide layer is formed on the surface of the sample. On the other hand, for smaller rates the oxide is formed in *patches* rather than as a continuous layer.

Similar trends have been observed in nickel-based super-alloys.[9]-[11] For example, in  $Ni_3Al_2$  in air, at temperatures around  $700^\circ C$  one has a slow formation of the oxide and significant embrittlement effects. On the other side, at temperatures around  $1000^\circ C$  there is a fast formation of the oxide in the form of a protective layer and no embrittlement has been observed.

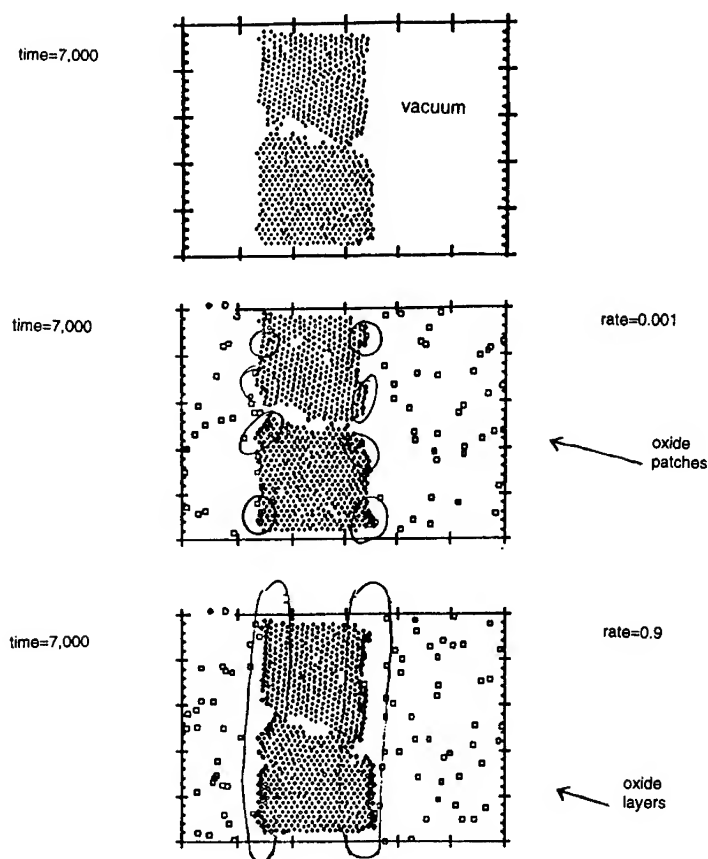


FIG. 2: Samples obtained at time=7000 in vacuum; with a small oxidation rate yielding patches of the oxide; and with a high oxidation rate yielding a continuous oxide layer.

## PHYSICAL ORIGIN OF THE EMBRITTLEMENT PHENOMENA

We saw that two conditions favor these fracture nucleation phenomena: (i) a low oxidation rate ensuring that the oxide forms in patches, *not* as a continuous layer, and (ii) oxide has to be more rigid than the alloy. These two conditions conspire to enhance fracture nucleation in the way indicated in the Figure 3: Since the oxide is more rigid than the alloy (i.e., has bigger elastic moduli than the alloy), the oxide patches are causing local stretching stresses in the regions between the patches. These stresses assist in the opening of the grain boundary via enhancing the *intergranular microcavity nucleation*. This is documented in Fig. 4 from our simulations, which illustrates a nucleation of an intergranular microcavity in the presence of the oxide, and the absence of such nucleation for a sample in vacuum. [ Here we applied a weaker stress than in Figs. 1 and 2 in order to obtain longer sample lifetimes.]

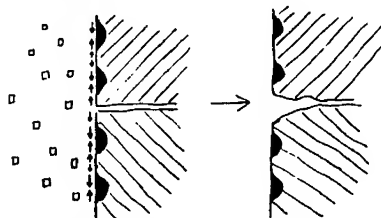


FIG. 3: Rigid oxide patches are causing local stretching stresses which assist in the opening of a grain boundary going between the patches.

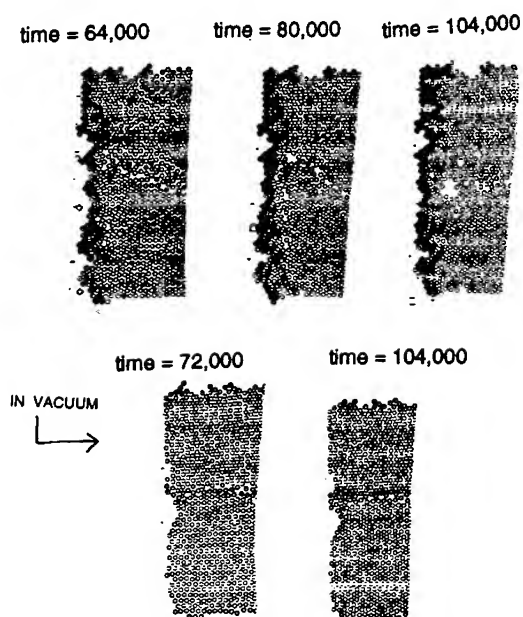


FIG. 4: Oxide patches assist nucleation of an intergranular microcavity. For comparison, we also give the situation for the same sample in vacuum.

## ENVIRONMENTALLY ASSISTED INTERGRANULAR CRACK GROWTH

Based on these observation, we propose a model for environmentally assisted intergranular crack growth in polycrystals such as super-alloys in air, see Fig. 5: First, as discussed above, the grain boundary opening is assisted by the internal stresses induced by the oxide patches. Then the oxygen can go further and produce new patches on the walls of intergranular microcavities. These new patches then assist in opening the grain boundary portions between intergranular microcavities. As this process continues, the crack grows.

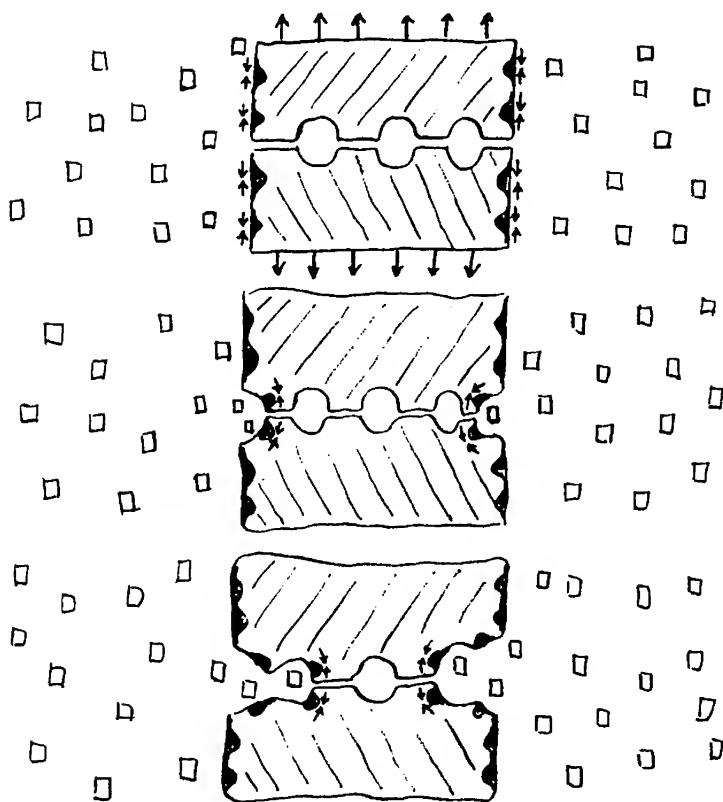


FIG. 5: Physical picture of the environmentally assisted intergranular crack growth.

## ACKNOWLEDGMENTS

We thank Bruce Kang for discussions. This work is supported by the NSF/WV EPSCoR program.

## REFERENCES

1. K. Nishioka and J. K. Lee, *Philos. Mag.* **A44**, 779 (1981).
2. R.L.B. Selinger, Z.-G. Wang, W.M. Gelbart, and A. Ben-Shaul, *Phys. Rev.* **A43**, 4396 (1991).
3. Z.-G. Wang, U. Landman, R.L.B. Selinger, and W.M. Gelbart, *Phys. Rev.* **B44**, 378 (1991).
4. R.L.B. Selinger, Z.-G. Wang, and W.M. Gelbart, *J. Chem. Phys.* **95**, 9128 (1991).
5. L. Golubović and S. Feng, *Phys. Rev.* **A43**, 5223 (1991).
6. L. Golubović and A. Peredera, preprint ( October 1994).
7. S.S. Brenner, in Fiber Composite Materials ( American Society for Metals, Metals Park, OH, 1965), p. 11.
8. S.F. Pugh, An Introduction to Grain Boundary Fracture in Metals ( The Institute for Metals, London, 1991).
9. C.A. Hipsley and J.H. DeVan, *Acta Metall.* **37**, 1485 (1989).
10. P. Valerio, M. Gao, and R.P. Wei, *Scripta Metallurgica et Materialia* **30**, 1269 (1994).
11. Bruce Kang ( private communication).

## DISCRIMINATION OF SURFACE TEXTURES USING FRACTAL METHODS

JILL P. CARD\*, J. M. HYDE\*, AND T. GIVERSEN\*

\*Digital Equipment Corp., 77 Reed Rd., Hudson, MA 01749-2810

### ABSTRACT

This paper investigates the use of fractal metrics for discrimination of copper surface textures. Measurements of copper surfaces, using contacting profilometry, provided the raw data for the fractal analysis. The samples tested included copper foil samples and a copper lead frame, typical of those in use in plastic electronic packages. The fractal Hausdorff dimension and upper/lower ranges of fractal scale are analyzed by the coastline method and compared using Bonferroni multiple confidence limits. Metrics show significant differences between sample couplets, indicating significant precision in the fractal approach to adequately quantify surface texture qualities.

### INTRODUCTION

Many techniques are used to measure surface roughness and to obtain a quantitative value descriptive of the properties of the surface. Contacting stylus profilometers output metrics such as average roughness, average peak height, and maximum peak to valley height difference. These quantities, though useful for some measurements, may not adequately differentiate among complex surface textures for which the distributions of peak heights and valleys differ, although the ranges and/or means do not. A more powerful metric, containing a more detailed description of the surface, is required.

A precise characterization of surface features is required for adhesion studies. Adhesion involves both mechanical and chemical contributions, which are interdependent. A rough surface does not necessarily imply poorer adhesion than a smooth surface although the latter has better wetting characteristics. In some cases, notably that of the adhesion of epoxy resin to copper, rougher surfaces can improve the adhesion strength<sup>1</sup>. That example is of particular interest due to the similarity to adhesion between epoxy-type molding compounds and copper lead frames in plastic electronic packaging.

Adhesion is a crucial factor in plastic packaging where delamination, or loss of adhesion, can lead to corrosion problems and device failures. It is important to optimize the adhesion between the lead frame and the molding compound. This paper looks at various copper foils, as prepared by suppliers for printed wiring boards, and at a copper alloy lead frame, representative of those used in plastic electronic packages.

The textures of various metal surface finishes have been recently successfully distinguished utilizing 2D or 3D fractal analytic techniques<sup>2-7</sup>. Fractal-based metrics capture texture properties, such as the ranges and frequency of self-similar surface peaks, not previously possible using traditional measures (e.g., average roughness and peak-to-valley metrics). This enables the use of metrics as predictors of physical texture-dependent phenomena such as fracture toughness<sup>7</sup>, cleanability of metal surfaces<sup>2</sup>, and silicon wafer surface quality<sup>8</sup>. The motivation for this study is to define a set of fractal-based metrics which are sufficiently accurate to capture the concept of surface texture in characterizing

metal lead frame to plastic package adhesion.

The coastline method<sup>9</sup> of fractal dimension computation is used for all analyses presented here. Other profile and surface area based methods for determining the fractal dimension are well documented<sup>10-13</sup> and will be investigated for future comparison of fractal dimension estimation accuracy and precision.

The fractal descriptors of surface texture represent a parameter subset involved in the prediction of mechanical and/or chemical adhesion. Future work will incorporate the fractal metrics as well as other process parameters (e.g., temperature, pressure, viscosity) as inputs to an adhesion prediction neural network. A similar approach, using fractal characterization for feature extraction as an input into a neural network was proposed by Stubbendieck and Oldham<sup>8</sup> for the detection of flaws in silicon wafers via neural network using a surface area fractal dimensioning technique for feature extraction.

## EXPERIMENTAL PROCEDURE

The samples tested were four copper foils and a copper lead frame. The foil samples were: Sample 1, 1 ounce double treated; Sample 2, 9 micron foil with aluminum backing; Sample 3, 1/2 ounce JTCAM; Sample 4, 1 ounce JTCAM; and Sample 5, lead frame. The 1 ounce double treated foil was from Gould Electronics and was representative of the current standard foil preparation technology, also referred to as JTC. The 9 micron foil was from Foil Technology and was expected to have a smoother surface than JTC. The JTCAM foils were from Gould and represented a new process intended to produce foils with finer surface texture and higher surface area than the standard JTC treatment. The lead frame sample was representative of those used in plastic packaging.

The surfaces were measured using a Tencor P-1 profilometer with a 0.26 micron radius diamond stylus. Each scan was 0.5mm long and was comprised of 2561 height measurements. Five scans were made at five different locations on each sample. SEM images of the surfaces are shown in Figure 1. An example of the profilometer output is shown in Figure 2.

## ANALYTIC METHOD

Fractal models have been successfully applied to describe a wide variety of natural surfaces and processes such as cloud formations, wave harmonics, coastline lengths, etc. Mandelbrot<sup>9</sup> proposed that the relationship between the measured length  $\mathcal{L}$  and the ruler size  $\mathcal{N}$  observed by Richardson<sup>14</sup>:

$$\mathcal{L}(\mathcal{N}) = L_0 \mathcal{N}^{(1-D)} \quad (1)$$

represents a fractal curve of Hausdorff dimension  $D$ , for  $1 \leq D \leq 2$ . The  $\log \mathcal{L}(\mathcal{N})$  vs.  $\log \mathcal{N}$  plot, with measured slope  $(1-D)$ , provides a means for estimating the fractal dimension of surfaces. Underwood and Banerji<sup>15</sup> proposed a modification of (1):

$$\log R_L(\mathcal{N}) = \log C - (D-1)\log \mathcal{N} \quad (2)$$



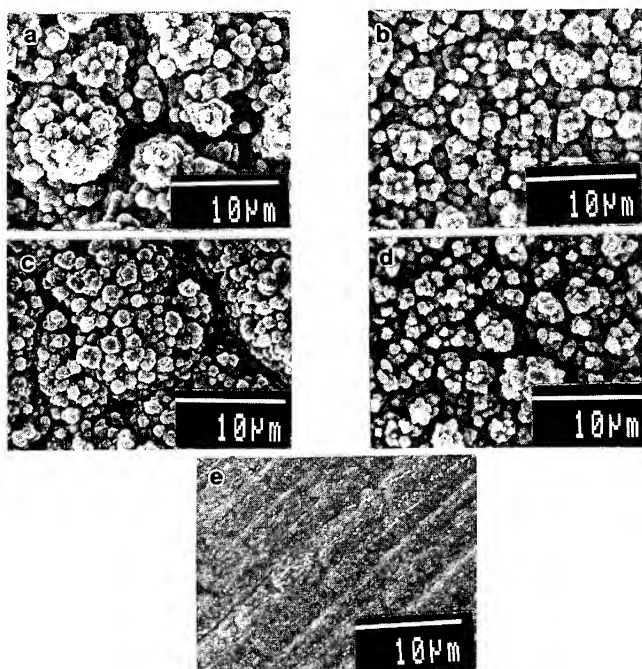


**Figure 1.** SEM micrographs of (a) Sample 1, (b) Sample 2, (c) Sample 3, (d) Sample 4 and (e) Sample 5, all at 2000X.

### 1 ounce JTCAM

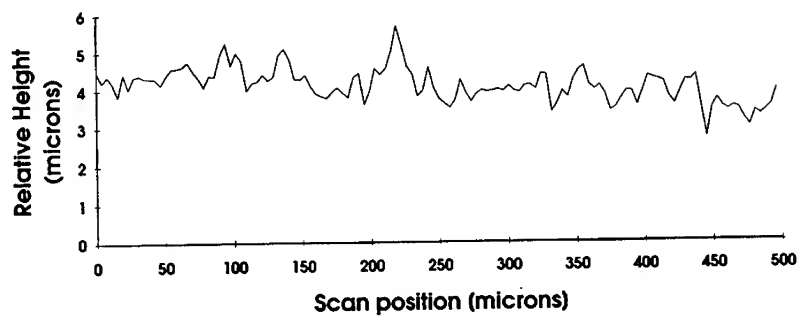


**Figure 2.** Example of a profilometer scan.

where  $C$  is a constant and  $R_L$ , the profile roughness parameter, is defined as the apparent profile length divided by its projected length.

The COASTFRAX<sup>16</sup> software used for this study employs the above "coastline" method of fractal dimension computation. The estimation of the fractal dimension  $\mathcal{D}$  is determined by obtaining the most negative slope parameter fit ( $\min\{-(1-\mathcal{D})\}$ ) via regression analyses, the domain of each spanning a decade of ruler lengths and the collective domain of analyses spanning the total range of ruler lengths<sup>6</sup>.

In addition to the slope parameter  $-(\mathcal{D}-1)$ , lower and upper log ruler length crossover points were identified. These points represent the minimum and maximum ruler scale range over which the measured surface is fractal in nature. Below and above the minimum and maximum values, respectively, the slope of the log-log plot approaches zero. In instances where the minimum crossover point coincides with the size of the stylus diameter, the stylus is the limiting factor, rather than a change in the fractal nature of the surface. In this study, the stylus was .26 micron radius and was well below the anticipated lower crossover point. The COASTFRAX program computes the minimum (maximum) scale range crossover for a sample profile as the ruler scale value at which the profile roughness,  $R_L$ , first decreases by 10% (90%).

## RESULTS

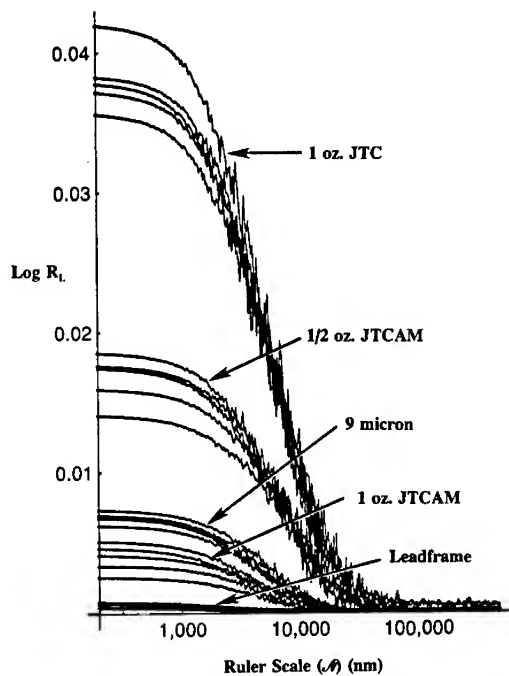
All of the profile scans for the samples were analyzed using the coastline method described for obtaining the slope and the minimum and maximum crossover points bounding the scale region of fractal features. Figure 3 shows all 25  $\log R_L$  vs.  $\log \mathcal{N}$  plots. The sample slopes decrease with increasing sample surface roughness, as seen in Figure 1.

Table I lists the Bonferroni Confidence interval groupings for the five sample types for the three variables computed (slope, minimum crossover, and maximum crossover) for Type 1 error ( $\alpha$ ) = .05. The slope values for all 5 samples are significantly different from one another when compared by all possible pairs, with the exception of the Samples 2 and 4. The difference between these two means is .0019 and falls short of the .0029 delta required for significance at  $\alpha$  = .05. However, investigation of these two samples' dispersion in Fig. 1 suggests that a larger sample size would enable a more precise estimation of the fractal dimension and would result in discrimination between samples in the correct roughness order.

The Bonferroni simultaneous confidence intervals for all 2-sample comparisons for the minimum and maximum crossover metrics indicate that three distinct groups evolve, wherein the first group contains Samples 1 and 3, the second group contains Samples 2 and 4, and the third group contains Sample 5. As expected, the minimum and maximum fractal feature scale values for the coarser surfaces (Samples 1 and 3) show a significant shift toward a larger scale values than those of the very smooth lead frame.

## CONCLUSION

Results of this preliminary investigation of texture discrimination of Cu surface foils via computation of fractal dimension and feature range from profilometric data proved to be promising. Of the 5 foil types investigated, all fractal dimension estimates significantly



**Figure 3.** Plot of log (relative length) vs. log (ruler length) for all samples.

**Table I:** Bonferroni tests for multiple 2-sample mean comparisons. For dependent variables (slope, maximum scale crossover, and minimum scale crossover) a series of ten 2-sample mean difference comparisons are made, controlling overall Type I error = 0.05. Means with the same Bonferroni Group number are not significantly different.

| Sample                   | Slope<br>-( $\mathcal{D}$ -1) | Group | Min. Scale<br>Crossover | Group | Max. Scale<br>Crossover | Group |
|--------------------------|-------------------------------|-------|-------------------------|-------|-------------------------|-------|
| 1                        | -.0312                        | A     | 1408.0                  | A     | 21400                   | A     |
| 3                        | -.0138                        | B     | 1496.0                  | A     | 21180                   | A     |
| 2                        | -.0054                        | C     | 1106.0                  | B     | 15140                   | B     |
| 4                        | -.0036                        | C     | 1036.0                  | B     | 12820                   | B     |
| 5                        | -.0005                        | D     | 521.6                   | C     | 6516                    | C     |
| Min. Sign.<br>Difference | .0029                         |       | 156.77                  |       | 4802.6                  |       |

discriminate between all samples, taken two at a time, with the exception of the 1 ounce JTCAM and 9 micron samples. For the latter two samples, the mean fractal dimensions were ordered rough vs. smooth, consistent with a visual assessment. The lack of statistical significance here is principally attributed to the small sample size used for the comparisons. Alternatively, another method of surface data collection, such as stereo scanning electron microscopy, may yield more precise measurements, thereby reducing the variance, and may be able to detect smaller mean differences than those obtained with the Tencor profilometer. In addition, a more precise algorithm for fractal dimension estimation, for either profiles or surfaces (e.g. box-counting, power spectrum, and the variation method) could also improve the discrimination among sample textures.

Use of the fractal dimension is anticipated to more thoroughly characterize textures and profiles than traditional surface measures such as peak-to-valley range and average roughness, due to the built-in mathematical aspects of fractal analysis reflecting the quantity, height, and slope of the peaks. Given the intention to use fractal metrics as input features to a neural network designed to predict the adhesion quality of metal lead frame materials to plastic packaging, it is important that the metric can discriminate at, or better than, the precision level of surface differences impacting adhesion. To this end, work will continue to investigate other fractal-based analyses of both profiles and surfaces (e.g. boxcounting, power spectrum and the variation method for fractal dimension estimation) as well as other means of surface data collection.

## REFERENCES

1. D.E.Packham, in Adhesion Aspects of Polymeric Coatings, edited by K.Mittal (Plenum, NY, 1983). pp. 19 - 41.
2. S. Chesters, H. Wang, G. Kasper, Solid State Technology, Jan. 1991, 73.
3. J.W. Martin and D.P. Bentz, J. Coatings Tech., **59** (745), 35-41 (1987).
4. A. Majumdar and C.L. Tien, Wear, **136**, 313 (1990).
5. C.A. Brown, P.D. Charles, W.A. Johnsen, S. Chesters, Wear, **161**, 61 (1993).
6. C.A. Brown and G. Savary, Wear, **141**, 211 (1991).
7. Y. Fahmy, J.C. Russ, C.C. Koch, J. Mater. Res., **6** (9), 1856-1861 (1991).
8. G.T. Stubbendieck and W.B. Oldham, IEEE Int. Joint Conf. on Neural Networks, **3**, 717-23 (1992).
9. B.B. Mandelbrot, The Fractal Geometry of Nature, (W.H. Freeman and Co., New York, 1983), p. 25-57.
10. B. Dubuc, S.W. Zucker, C. Tricot, J.F. Quiniou, D. Wehbi, Proc. R. Soc. Lond. A, **425**, 113 (1989).
11. S. Peleg, J. Naor, R. Hartley, D. Avnir, IEEE Trans. Pattern Anal. and Mach. Intell., **PAMI-6** (4), 518-523, (1984).
12. H. Fischer and J. Nittmann, CEC-Vienna Report No. 94-05, 1994.
13. B Dubuc, J.F. Quiniou, C. Roques-Carmes, C. Tricot, S.W. Zucker, Physical Rev. A, **39** (3), 1500-1512 (1989).
14. L.F. Richardson, General Systems Yearbook, **6**, 139 (1961).
15. E.E. Underwood and K. Banerji, Mater. Sci. and Eng., **80**, 1 (1986).
16. C.A. Brown, Coastfrax U.S. Patent pending, 1993.

## COMPUTER SIMULATION OF BENDING PLASTIC DEFORMATION AND CREATION OF DISLOCATIONS IN COPPER THIN FILMS

H.TSUKAHARA, Y.NIWA, T.TAKAYAMA AND MASAO DOYAMA  
The Nishi-Tokyo University, Uenohara, Yamanashi 409-01 Japan

### ABSTRACT

A small single crystal of copper with a notch has been bent by use of the molecular dynamics method. The bend axis was [110]. Dislocations were created near the tip of the notch and moved on (111) slip plane. Pulling a copper single crystal, half dislocations were created in such a way that the bending was compensated.

### INTRODUCTION

It is well known that creation, motion and interaction of dislocations play an important role in the plastic deformation of crystalline solids. It is important to know how the dislocations are automatically created and moved in metals. In this paper creation and motion of dislocations were simulated by use of molecular dynamics in case of bending. Copper was selected as an example, because it is one of the most common metals with a face centered cubic lattice.

### INTERATOMIC POTENTIALS

In metals, the conduction electrons travel from one atom to another atom and the interaction cannot be represented by a pairwise potential but by many body potentials. The interaction between the  $i$ -th atom and the  $j$ -th atom depends not only on the distance between them but also other factors. By the embedded function, surface problems can be treated. The  $n$ -body embedded function proposed by Oh and Johnson [1,2] was used in this paper. The total energy is given by

$$E_{\text{total}} = \sum E_i \quad (1)$$

$$r_{ij} = |r_i - r_j| \quad (2)$$

$$E_i = F(\rho_i) + (1/2) \sum \Phi(r_{ij}) \quad (3)$$

$$F(\rho) = a(\rho/\rho_e)^n + b(\rho/\rho_e) \quad (4)$$

$$\rho_i = \sum f(r_{ij}) \quad (5)$$

Here  $E_{\text{total}}$  is the total internal energy.  $E_i$  is the internal energy associated with atom  $i$ .  $\rho_i$  is the electron density at atom  $i$  due to all other atoms.  $F(\rho_i)$  is the embedding energy of atom into electron density  $\rho_i$ .  $\Phi(r_{ij})$  is the two body central potential between atoms  $i$  and  $j$  separated by  $r_{ij}$ .  $f(r_{ij})$  is the contribution to the electron density at atom  $i$  due to atom  $j$  at the distance  $r_{ij}$  from atom  $i$ .

$$f(r) = f_{\text{old}}(r) - f_c(r) \quad (6)$$

$$f_{\text{old}} = f_e \exp\{-\beta(r/r_e) - 1\} \quad (7)$$

$$f_e(r) = f_{\text{old}}(r_c) + g(r)f'_{\text{old}}(r_c)/g'(r) \quad (8)$$

$$\Phi(r) = \Phi_{\text{old}}(r) - \Phi_c(r) \quad (9)$$

$$\Phi_{\text{old}}(r) = \Phi_e \exp\{-\gamma(r/r_e - 1)\} \quad (10)$$

$$\Phi_c(r) = \Phi_{\text{old}}(r_c) + g(r) \Phi'_{\text{old}}(r_c) / g'(r_c) \quad (11)$$

$$g(r) = 1 - \exp\{\delta(r/r_e - r_c/r_e)\} \quad (12)$$

For copper Oh and Johnson [1] give  $\beta=5$ ,  $\gamma = 8.5$ ,  $\delta=20$ ,  $r_c = 1.9 r_e$ ,  $\phi_e=0.36952$  eV,  $a = -4.0956$ ,  $b = -1.6979$ ,  $n = 0.44217$ , and  $\rho_e = 12.793$ .

## SPECIMENS

Specimen A is a rectangular parallelepiped having the faces of (001), (00 $\bar{1}$ ), ( $\bar{1}10$ ), ( $1\bar{1}0$ ), (110) and ( $\bar{1}\bar{1}0$ ). A notch was introduced near the center of (001) (see Fig. 1(a)). The x-axis was taken to be [110], y [ $\bar{1}10$ ], and z [001]. Specimen A contains 2296 atoms. Specimen B is also a rectangular parallelepiped but having the faces of (110), ( $\bar{1}\bar{1}0$ ), (001), (00 $\bar{1}$ ), ( $\bar{1}10$ ) and ( $1\bar{1}0$ ). x, y and z directions were taken to be in the directions of [110], [001] and [ $\bar{1}10$ ], respectively. The size of Specimen B is 12dx8ax20d, where d is the nearest neighbor distance and a is the lattice parameter (see Fig. 1(b)). The number of atoms in Specimen B is 4896. The surfaces are free and periodic boundary conditions were not used.

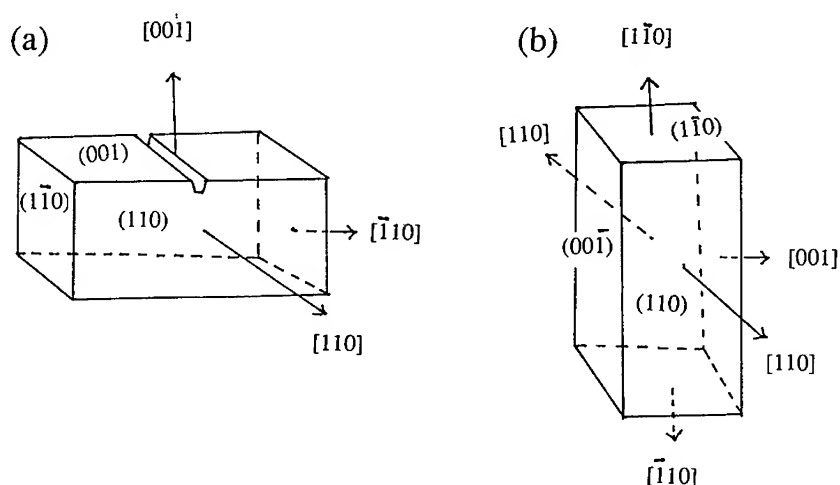


Fig. 1. Copper Specimens. (a) Specimen A is a rectangular parallelepiped having the faces of (001), (00 $\bar{1}$ ), ( $\bar{1}10$ ), ( $1\bar{1}0$ ), (110) and ( $\bar{1}\bar{1}0$ ). A notch was introduced near the center of (001). Specimen B is also a rectangular parallelepiped but having the faces of (110), ( $\bar{1}\bar{1}0$ ), (001), (00 $\bar{1}$ ), ( $\bar{1}10$ ) and ( $1\bar{1}0$ ). x, y and z directions were taken to be in the directions of [110], [001] and [ $\bar{1}10$ ], respectively.

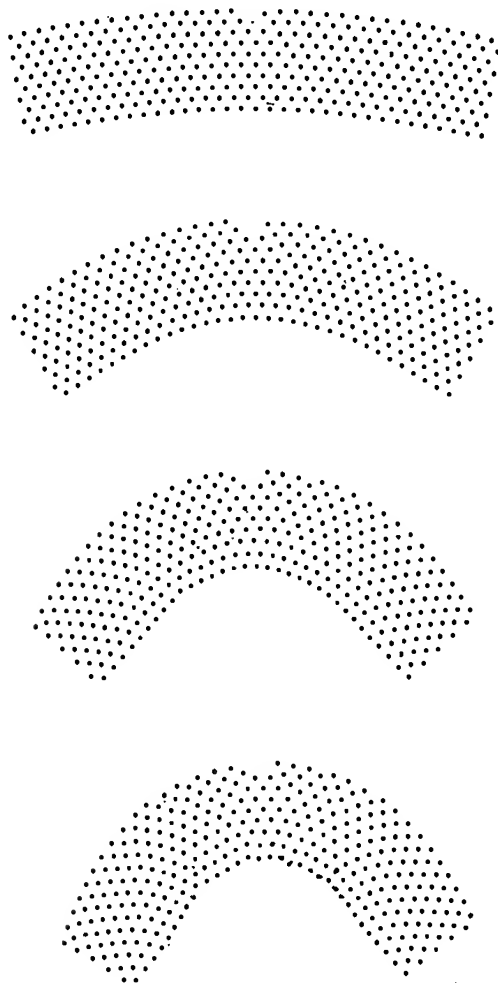


Fig.2. The projections of atom positions of Specimen A on (110). A dislocation was created near the tip of the notch (b) and moved on (111) (c).

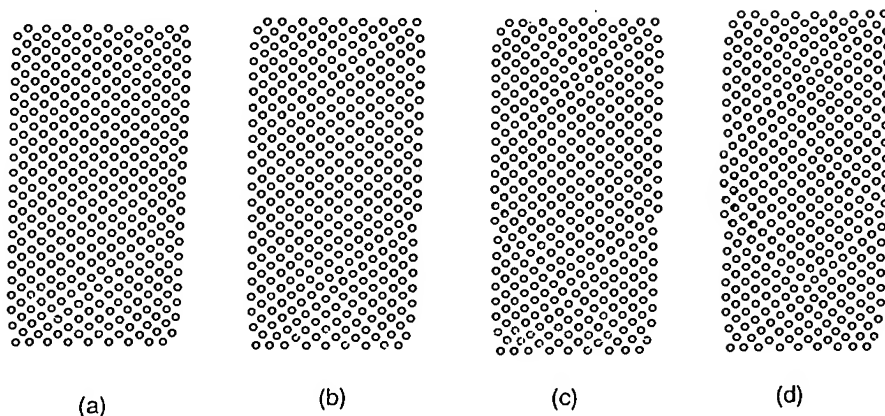


Fig.3. The projection of atom positions of Specimen B. (a) 9% elongation, (b) 12% elongation, (c) 13.5% elongation and (d) 15% elongation.

## DEFORMATION

Specimen A was uniformly bent around the x-axis[110] and relaxed all the atoms. Every 25 cycles uniform small amount of bent was given. After giving a uniform bent all atoms in the specimens were relaxed 25 cycles and then bend again. This process is repeated. Specimen B was uniformly pulled in the direction of z-axis[110] and relaxed all the atoms. Every 25 cycles uniform small amount of elongation was given. After giving a uniform elongation all atoms in the specimens were relaxed 25 cycles and then pulled again. The time step of the molecular dynamics was  $5 \times 10^{-15}$  sec.

## RESULTS AND DISCUSSION

The projections of atom positions of Specimen A on (110) are given in Fig. 2. A dislocation was created near the tip of the notch (Figs. 2(b)) and moved on (111) (Figs 2(c)). Uniform bending without notch could not initiate dislocations but at certain stage the specimen became polycrystal.

In Fig. 3 the atomic positions of Specimen B are projected on (110). Fig3(a) at 9% elongation, a half dislocation was created at the left lower corner. In fig.3(b) at 12% elongation the half dislocation was ejected from (001) and another (the second) half dislocation was created at the right lower corner of the specimen in such a way that the deformation compensate the bending of the specimen. In Fig3(c) at 13.5% elongation the second half dislocation was ejected and another half dislocation was created at the right upper corner of the specimen.



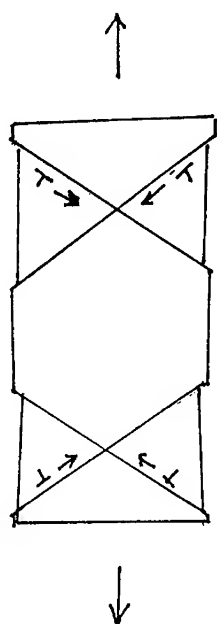


Fig. 4. Schematic figure of the creation of edge dislocations in the tensile deformation of a copper single crystal.

This is schematically shown in Fig. 4.

#### ACKNOWLEDGEMENT

This research is supported by the Grant-in-aid by the Ministry of Education, Science and Culture under Priority Area "Crystal Growth Mechanism in Atomic Scale".

#### REFERENCES

1. D.J. Oh and R.A. Johnson, *J. Materials Research*, **3**, 471 (1986).
2. D.J. Oh and R.A. Johnson, in *Atomic Simulation of Materials*, edited by V. Vitek and D.J. Srolovitz, (Plenum Press, New York, 1989) p.233-238.

## MICROSTRUCTURAL FRACTAL DIMENSION OF AISI 316L STEEL.

M. Hinojosa, R. Rodríguez and U. Ortiz.

DIMAT, Facultad de Ingeniería Mecánica y Eléctrica, Universidad Autónoma de Nuevo León, A.P. 076 suc F, 66450. San Nicolás de los Garza, N.L. México.

### ABSTRACT

Fractal dimension of the microstructure of AISI 316L steel (17 Cr, 12.7 Ni, 2.1 Mo, 1.5 Mn, 0.01 C) with different degrees of strain were obtained from Richardson plots of grain boundary perimeter against magnification. Grain boundaries were revealed using conventional metallographic techniques and measurements were taken with the aid of an automatic image analyzer (Quantimet 520) attached to an optical microscope. The magnifications used were 50, 100, 200, 400, and 1000X. The samples were obtained from a 4" diameter tubing, machined according to ASTM A370 standard test method and deformed to 5, 10, 15, and 20 % tensile strain. The results show that the fractal dimension of the grain boundaries changes as deformation is imparted to the material.

These results suggest that fractal dimension may be used to describe microstructural evolution of metals during deformation processes.

### INTRODUCTION

Fractal Geometry offers an alternative tool for the description of the real world<sup>1</sup>. Essential features of a fractal object are self-similarity and fractal dimension (Hausdorff-Besicovitch dimension). This fractal dimension is a measure of the complexity of the figure or the efficiency of a set to fill the metric space in which it lies<sup>2,3</sup>. Recently, efforts had been made to apply these concepts to the analysis of microstructures<sup>4,5</sup>. The fractal nature of microstructural features (grain boundaries, dislocations, dendrites, fracture surfaces, among others), had been established by a number of authors<sup>2,6-9</sup>. Attempts had been made to elucidate the possible relationship between fractal dimension of microstructure and the mechanical properties<sup>10-11</sup>, for example, there seems to be a relationship between fractal dimension of fracture surfaces of metals and the energy absorbed by the material. It can be said that fractal analysis of microstructures assumes that some microstructural features are well described as "natural fractals" which had a fractal dimension that can be measured by different experimental methods. The aim of this work is to report the fractal dimension of the grain boundaries of AISI 316L stainless steel with different degrees of strain.

## MATERIALS

The material analyzed was an AISI 316L stainless steel of the following composition (% wt): 17 Cr, 12.7 Ni, 2.1 Mo, 1.5 Mn, 0.01 C. Samples were obtained from a 4" diameter tubing. For comparison, we also analyzed a hot rolled low carbon steel with composition (%wt): 0.04 C, 0.21 Mn, 0.012 P, 0.031 S, 0.09 Cu, 0.04 Ni, 0.053 Cr. Fig. 1 illustrates the mechanical properties of the AISI 316L as measured in tension test.

### AISI 316 L STAINLESS STEEL

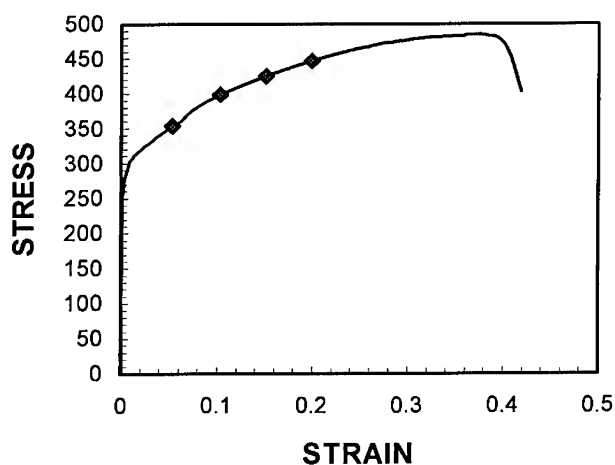


Fig. 1.- Stress-strain curve in tension for the AISI 316L stainless steel. Markers show the strain applied to the different samples analyzed.

## EXPERIMENTAL

Samples were machined according to ASTM A370 standard test method and deformed to 5, 10, 15 and 20 % tensile strain on a Sintech universal testing machine. The microstructures were revealed using conventional metallographic techniques and observed on a Nikon epiphot optical microscope. Observations were made on planes perpendicular to the longitudinal axis of the specimens. Images were digitized to 640 \* 480 pixels with the aid of an automatic image analyzer.

(Leica Quantimet 520) carefully calibrated. . Magnifications used were 50, 100, 200, 400 and 1000X and calibration factors were 1.904, 0.952, 0.479, 0.236, and 0.094 microns per pixel respectively. Measures of perimeter of grain boundaries at the different magnifications were taken over representative grains of the microstructures for each one of the samples. Fractal dimension of the microstructures was estimated using Richardson plots of grain boundary perimeter against the reciprocal of the yardstick ( calibration factor) . In the case of the low carbon steel only the non deformed (as rolled) condition was analyzed .

## RESULTS

Figs. 2a to 2c shows the microstructures of the AISI 316L stainless steel at 0, 5, 20% strain. For the purpose of this work, attention was focused exclusively on grain boundaries so the presence of twin boundaries was ignored. Fig. 3 shows Richardson plots utilized in the estimation of fractal dimension of the grain boundaries for the different samples. Fractal dimensions were estimated as 1.106, 1.104, 1.103, 1.09 and 1.08 for the 0, 5, 10, 15 and 20% strain conditions respectively. Fig. 2d shows the microstructure of the low carbon steel, its estimated fractal dimension was 1.04.

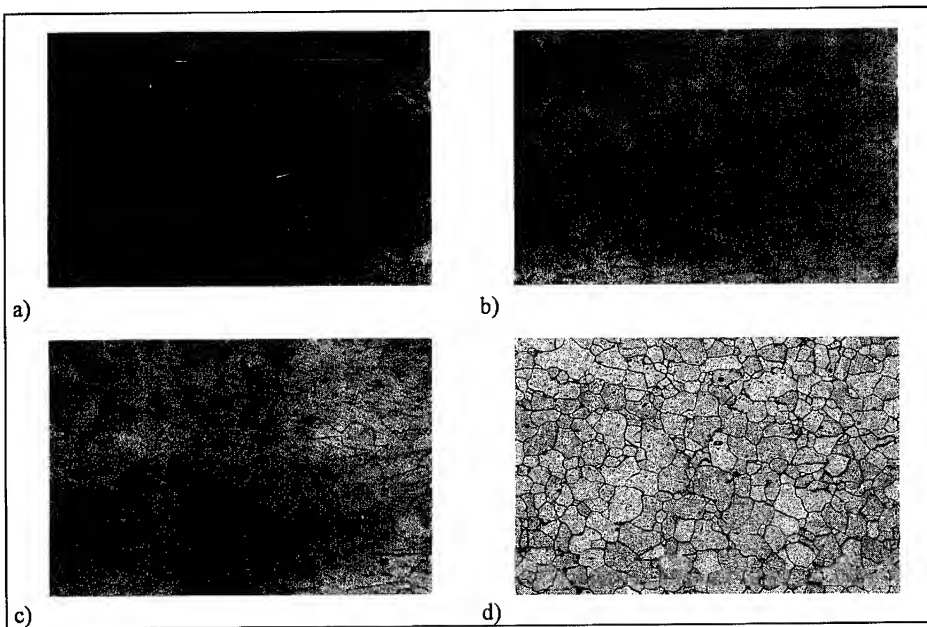


*Fig 2.- Microstructures of AISI 316L stainless steel at: a) 0% strain, b) 5% strain, c) 20 % strain and d) Low carbon steel in the as rolled condition.*

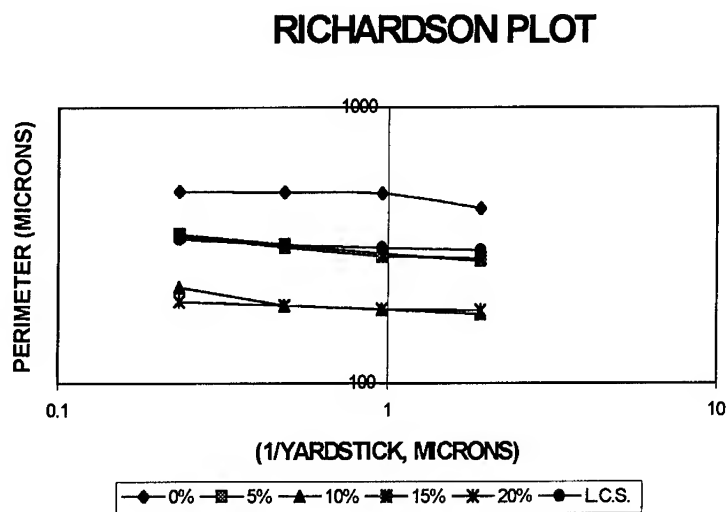


Fig 3-. Richardson plots illustrating the fractal character of the microstructures analyzed.

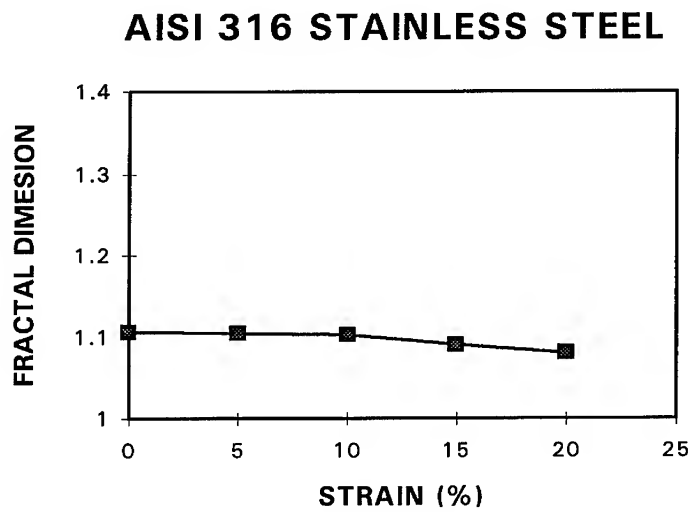


Fig 4.- Effect of tensile strain on fractal dimension for the AISI 316L stainless steel.

## DISCUSSION

Although the microstructures of the samples show grain boundaries that look quite straight, the perimeter of the grains (length of grain boundary) increases as it is measured at progressively higher magnifications, this is reflected on the respective Richardson plots, thus revealing their fractal character. Our results confirm that these grain boundaries have a measurable fractal dimension. Values estimated are similar to those reported on literature for a variety of natural curves, for example, fractal dimension of the coast of Great Britain<sup>12</sup> (a highly irregular curve) is 1.25. Results obtained show a decrease on fractal dimension as deformation is increased, this may reflect a higher degree of order of the microstructure as it is deformed in tension.

## CONCLUSIONS

Grain boundaries of AISI 316L stainless steel can be treated as natural fractals with a measurable fractal dimension. This fractal dimension changes as deformation is imparted to the material. This facts suggest the possibility to apply fractal dimension to the description and modeling of microstructural evolution during deformation processes.

## ACKNOWLEDGEMENTS.

Authors wish to express their gratitude to CONACYT (National Science and Technology Council) for financial support.

## REFERENCES

- 1.- Mandelbrot, B.B.. *The Fractal Geometry of Nature*. Freeman, New York, 1982.
- 2.- Falconer, K.J. *Fractal Geometry*, John Wiley and sons, 1990.
- 3.- Barnsley, *Fractals Everywhere*. Academic Press, 1988.
- 4.- Hornbogen.E. International Materials Review 1989, **34**,277.
- 5.- Hornbogen. E. Trans. ASM, 1961,**53**, 569.
- 6.- Underwood. E. and Banerji. K., Mater. Sci. Eng. **80** (1986) 1.
- 7.- Mitchell M. and Bonell D. . J. Mater. Res., **5**, No 10, Oct 1990. 2244.
- 8.- Richards and Dempsey. Scripta Metallurgica **22**, 1988, p. 687.
- 9.- Gao. H.J. et al. J. Mater. Res., **9**, No. 9, sep 1994, 2216
- 10.- Mandelbrot, B.B., D.E. Passoja and Paullay A. J. Nature 1984, **308**, 721.
- 11.- Tsuda et al. J.of the Society of Materials Science, Japan/Zayro, **40**, No. 455 Aug 1991 p. 1066.
- 12.- Mandelbrot, B.B. , Science 1967, **156**, 636.

## RUPTURE OF RANDOM FUSE NETWORKS: DUCTILE TO BRITTLE CROSSOVER

Rafael F. Angulo and Ernesto Medina

Intevep S.A., Apartado 76343, Caracas 1070A, Venezuela.

### ABSTRACT

We study the rupture process of Random Fuse Networks (RFN's) with quenched disorder in the microscopic threshold voltages. If lattices are driven to breakdown in *one blow* by an externally applied voltage the RFN's are shown to be equivalent to the toughest percolation backbone. Critical path analysis holds exactly in this case for *all* disorder distributions. For *gradual* rupture, it is shown that the existence of a lower cutoff in the disorder distributions entails a crossover from ductile to brittle behavior. The crossover length is a function of microscopic disorder and diverges in the limit of infinite disorder.

### INTRODUCTION

Scalar models of rupture are amongst the simplest caricatures of material failure. The rupture properties of Random Fuse Network (RFN) models have attracted considerable interests in recent years, not only because of their relation to important technological problems such as fracture and corrosion[1], but also because –beyond their apparent simplicity– they exhibit extraordinarily complex behavior.

A RFN is a discrete lattice whose bonds are fuses, each one characterized by a value of conductance and threshold voltage,  $v_c$ . Fuses behave as ordinary resistors if the voltage drop  $v$  across them is smaller than  $v_c$ , but turn irreversibly into insulators if  $v > v_c$ . Quenched disorder may be introduced in several ways[2]: via random conductances[3], random thresholds[4,6] or both; or it may be introduced as bond dilution[5]. Here we study disorder in the threshold voltages. The conductances are set all to one and it is assumed that the samples are driven to rupture by an external source of voltage, as opposed to current control[6].

Two types of mechanical tests are often conducted experimentally[1]: 1) toughness tests for which a large drive is applied to a sample, trying to break it in *one blow*, and 2) yield tests, whereby the external drive is increased *gradually*, until the sample breaks. The corresponding two cases for scalar electric models have been studied before. Rupture in one blow can be analyzed rather simply if Hierarchical Lattices (HL's) are used as geometrical support (see Fig. 1). The recursive eqns. for the probability to survive a microscopic voltage drop  $v_c$  can be obtained by simple means, and it allows to explore the macroscopic limit probabilities[7]. The analogy of this type of rupture mechanism with the case of infinite disorder (i.e. threshold voltage distributions  $\sim v_c^{-1}$ ) has also been noted[8]. Here we show that the analogy between rupture in one blow and extreme disorder is a formal equivalence, indeed.

As to gradual rupture, it has been noted that the existence of a lower cutoff in the Probability Distribution Function (PDF) of threshold voltages induces a crossover from ductile to brittle behavior[4]. Here we also simulate the process of gradual rupture numerically for large two dimensional (2D) lattices. The crossover is clearly observable from our simulations, and the crossover length dependence on microscopic disorder is estimated numerically.

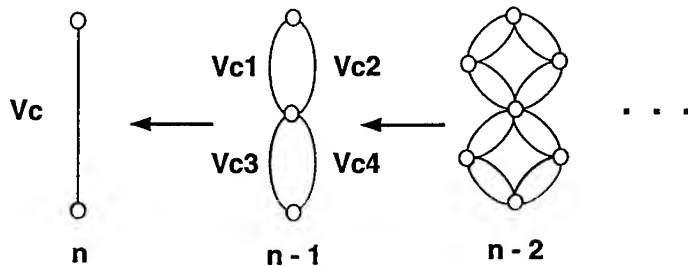


Figure 1. First three generations of the construction of a 2D, *eight-shaped* HL. Generations are numbered from microscopic (zeroth) order on the rightmost position to macroscopic ( $n^{\text{th}}$ ) order on the left of the figure.

## RUPTURE IN ONE BLOW

This type of process can be understood in terms of Critical Path Analysis (CPA). This theory arose from an observation by Ambegaokar, Halperin and Langer[9], that the equivalent conductance of a random resistor network with *extreme* distribution of conductances is *identical* to the conductance of the most conducting percolation backbone. Given a realization of disorder, such a backbone is produced by removing all resistors—keeping record of their locations—and bringing them back in decreasing order of conductance, until the lattice percolates for the first time. The numerical value of the last conductance laid down equals the conductance of the full lattice. For lattices above the percolation threshold this recipe holds exactly for extreme disorder *only*[10]. If disorder is *close* to extreme, however, there is a one-to-one correspondence between statistical disorder in the conductances and percolation *above* the threshold [11]. Next, it is shown that for one blow rupture the toughness of RFN's is equivalent to that of the strongest percolation backbone, for *all* distributions of disorder in the threshold voltages. For the HL of Fig. 1, we show that the recurrence formulae to extract the toughest backbone is identical to the recurrence eqn. relating the breakdown voltages  $v_c(n+1)$  and  $v_c(n)$  at two consecutive hierarchical orders.

In order to produce the toughest backbone of the HL of Fig. 1 one needs to find the *largest* voltage  $v_c(n)$ , satisfying the condition that, if all microscopic fuses with threshold voltage  $v_c(0)$  smaller than  $v_c(n)$  are removed, the lattice still conducts. Consider a cell of microscopic bonds with threshold voltages  $v_{ci}(n=0)$  ( $i=1, \dots, 4$  for the HL of Fig. 1). The first order *representative* cutoff value  $v_c(n=1)$  that



satisfies these conditions is given by

$$v_c(n+1) = \min[\max(v_{c1}(n), v_{c2}(n)), \max(v_{c3}(n), v_{c4}(n))], \quad (1)$$

with  $n = 0$ . The process is repeated recursively  $n$  times, until only one representative value  $v_c(n)$  remains. The toughest backbone is obtained by removing all microscopic bonds with  $v_c(0) < v_c(n)$ .

Now we show that eqn. (1) also gives the voltage drop required to break the lattice in one blow. From Fig. 1 it is clear that in order to break the basic cell one must break either the upper or the lower *blob* or both. To break a blob (i.e. two fuses in parallel) one must apply a voltage drop –across each microscopic bond– equal or larger than the maximal threshold voltage of the two fuses. As the two blobs are in series, the voltage needed to break the cell is the minimal of the two maximal values, as given by (1), indeed. The analysis is independent of the PDF and can be extended to HL's of any dimension.

The advantage of this approach, compared to following the renormalization flow[7], is that the microscopic breakdown voltage  $v_c(n)$  is obtained directly from the percolation condition[9]

$$\int_{v_c}^b P(x)dx = p_c, \quad (2)$$

where  $p_c$  is the percolation threshold and  $b$  is the upper limit of  $P(x)$ . From eqn. 2 it follows that  $v_c$  is *independent* of lattice length  $L = 2^n$ . In order to put this result to test we performed numerical simulations on 2D HL's of various lengths, assigning threshold voltages from power law PDF's. Eq. (1) was used recursively to calculate  $v_c(n)$ . In Fig. 2 we show numerical results obtained from a family of power law distributions with strong tails towards large values of  $v_c$ , namely

$$P(v_c) = |\mu|v_c^{-(\mu+1)}. \quad (3)$$

Several values of  $\mu$  are plotted in the range from 0.3 to 1.0. From (1) and (3) one obtains  $v_c = p_c^{-1/\mu}$ , where  $p_c = (3 - \sqrt{5})/2 = 0.381966\dots$ . Fig. 2 also shows a plot of  $\log_{10}(v_c)$  (for large  $L$ ) versus  $-(1/\mu)\log_{10}(p_c)$ . The agreement of theory and simulations is excellent. Similar agreement is obtained for other values of  $\mu$  (positive and negative) and for other PDF's (Weibull and Log-Normal)[12].

## GRADUAL RUPTURE

In order to explore the scaling properties of gradual rupture we selected again the PDF (3). Our simulation's settings are the same as carried out by several authors[2,4,7,8], except for the geometrical support, which in our case is a 2D HL. Numerical simulations in HL's can be carried out much faster than in regular lattices. As an illustration, two hours of CPU time are required for an IBM 3090

mainframe to bring one 2D regular lattice of length  $L = 80$  with mild disorder (i.e.  $\mu = -1$ ) to breakdown[6]. A comparable simulation for a HL of length  $L = 128$  takes 40 seconds in a Sun4 workstation.

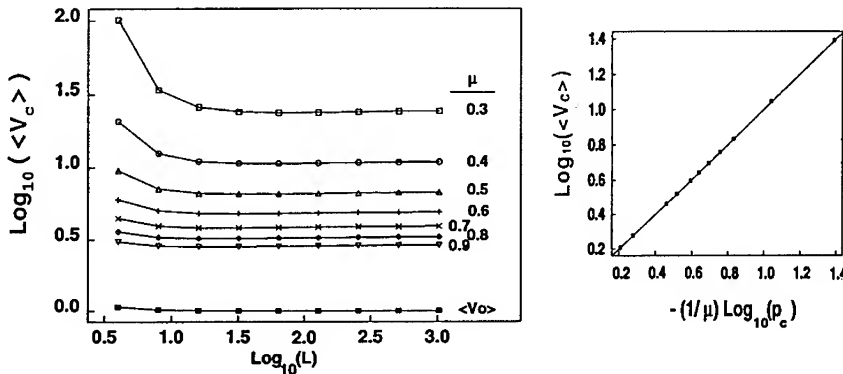


Figure 2. The breakdown voltage (per unit of lattice length)  $v_c$  for rupture in one blow is constant, independent of  $L$ . Departure from a constant for small  $L$  indicates that the renormalized PDF's have very strong tails, so average values increase with statistical sample size. For larger  $L$  the renormalized PDF's are self-averaging. The inset shows the dependence of  $v_c$  as a function of  $\mu$ . The line corresponds to eqn. (2).

In our simulations, the external voltage is increased the right amount to break only the weakest bond. Voltages and currents redistribute according to Kirchhoff's laws and the process is repeated until the lattice yields. Two values of driving voltage (per unit of lattice length) are recorded: the voltage  $v_o$  required to break the weakest fuse and the yield voltage  $v_b$ . Many realizations of disorder are simulated, renormalized distributions are estimated and averages are calculated from them. Fig. 3 shows numerical data for PDF's (3) for  $\mu > 0$  with a cutoff at  $v_c = 1$ . The variations of  $\langle v_c \rangle$ ,  $\langle v_b \rangle$  and  $\langle v_o \rangle$  with  $L$  are shown. The horizontal axis is the logarithm of lattice length measured in units of crossover length  $\xi$ . This quantity is determined from the condition that all the data set, corresponding to several values of  $\mu$ , cross over to a flat line at the same point. The best collapse of the crossover point is obtained for  $\xi = 0.3\mu^{-2.63}$ . The vertical axis is the logarithm of the voltage measured in units of  $-\mu/\log_{10}(p_c)$ , in accord to CPA.  $\langle v_c \rangle$  is an upper bound for  $\langle v_b \rangle$  for  $10L/\xi \ll 1$ .  $\langle v_b \rangle$  scales as  $L^{-\theta}$  with non-universal exponent  $\theta \sim \mu$ . It is clear that  $\langle v_b \rangle$  progressively approaches the voltage of the first breaking fuse. For larger lattices the two voltages coincide.  $10L = \xi$  signals the onset of brittle behavior.

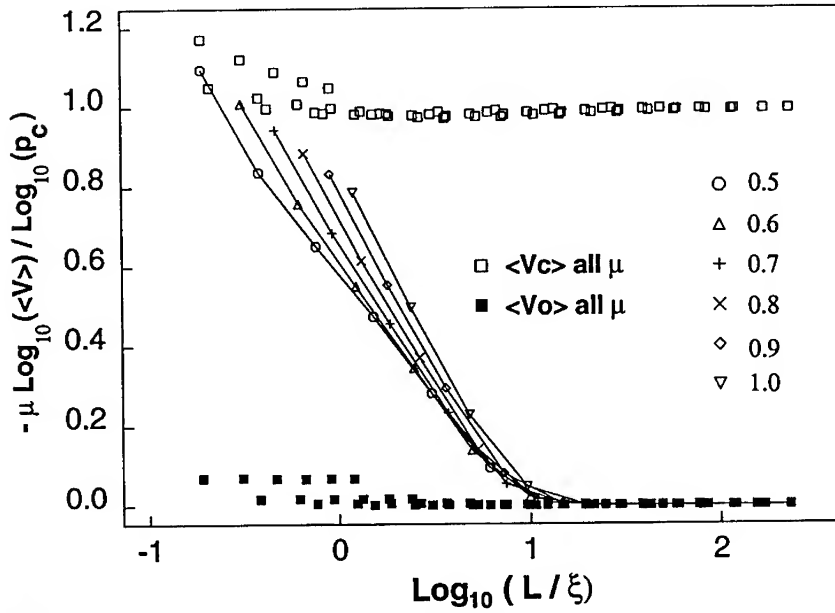


Figure 3. Scaling of  $\langle v_c \rangle$  (empty boxes),  $\langle v_b \rangle$  (symbols in the legend for different  $\mu$ ) and  $\langle v_o \rangle$  (filled boxes). 65000 realizations of disorder are sampled for  $L < 128$  and 1000 for larger lattices.

## SUMMARY AND CONCLUSIONS

We have shown that the toughness of fully occupied HL's of random fuses, with disorder in the threshold voltages is equivalent to that of the toughest backbone, for all distributions of disorder. The same conclusion should hold if a fraction  $p > p_c$  of fuses are removed, for the lattice renormalizes into a full lattice at some point. This applies to toughness test, whereby the lattice is driven to breakdown in one blow. Numerical simulations are in excellent agreement.

For gradual rupture, our numerical simulations confirm the observation of Ref. [4], in the sense that the existence of a lower cutoff in the PDF of threshold voltages induces a crossover from ductile to brittle behavior. Furthermore, our simulations for large lattices and several values of disorder strength (controlled by  $\mu$ ) enable to estimate the dependence of the crossover length on  $\mu$  as  $\xi \sim \mu^{-z}$ , where  $z = 2.63 \pm 0.05$ . The rupture voltage  $\langle v_b \rangle$  shows power law scaling  $\langle v_b \rangle \sim L^{-\theta(\mu)}$ , with non-universal exponent (probably varying linearly with  $\mu$ ). The scaling of  $\langle v_b \rangle$  does not seem to be affected by the lower cutoff.

Simulations for other PDF, such as Weibull, Log-Normal and double exponential

are being carried out[12]. preliminary results indicate that the incidence of the lower cutoff to the crossover is also present, but  $\langle v_b \rangle$  no longer scales as a power of  $L$ . The crossover length also scales as a power of  $|\mu|$  but the absolute value of the exponent is somehow smaller.

#### ACKNOWLEDGEMENTS

The authors thank M. Araujo, R. Callarotti and J. Vera for helpfull discussions and INTEVEP S.A. for permission to publish this paper.

#### REFERENCES

- [1] *Fracture*, edited by H. Liebowitz (Academic, New York,1884), Vols. I-VIII; *Statistical Models for the Fracture of Disordered Media*, edited by H. J. Herrmann and S. Roux (Elvesier, Amsterdam, 1990).
- [2] S. Roux, A. Hansen, H. J. Herrmann and E Guyon, J. Stat. Phys. **52**, 237 (1988).
- [3] H. Takayasu, Phys. Rev Lett. **54**, 1099 (1985); M. Sahimi and J. D. Goddard, Phys. Rev. B **33**, 7848 (1986);
- [4] B. Kahng, G. G. Batrouni, S. Redner, L. de Arcangelis and H. J. Herrmann, Phys. Rev. B **37**, 7625 (1988).
- [5] L. de Arcangelis, S. Redner and H. J. Herrmann, J. Phys. (Paris) **46**, 585 (1885); P. M. Duxbury, P. D. Beale and P. L. Leath, Phys. Rev. Lett. **57**, 1052 (1986); P. M. Duxbury and P. L. Leath, J. Phys A **20**, L411 (1987); Y. S. Li and P. M. Duxbury, Phys. Rev. B **36**, 5411 (1987); S. Roux, A. Hansen, E. L. Hinrichsen and D. Sornette, J. Phys A **24**, 1625 (1991); B. Kahng, G. G. Batrouni and S. Redner, J. Phys A **20**, L827 (1987);
- [6] P. M. Duxbury and P. L. Leath, Phys. Rev. Lett. **72**, 2805 (1994);
- [7] D. Sornette, J. Phys (Paris) **50**, 745 (1989).
- [8] A. Hansen, E. L. Hinrichsen and S. Roux, Phys. Rev. B **43**, 665 (1991).
- [9] V. Ambegaokar, B. I. Halperin and J. S. Langer, Phys. Rev. B **4**, 2612 (1971).
- [10] P. Le Doussal, Phys. Rev. B **39**, 881 (1989).
- [11] R. F. Angulo and E. Medina, Physica A **191**, 410 (1992); J. Stat. Phys. **75**, 135 (1994).
- [12] R. F. Angulo and E. Medina, to be published.

## FRACTURE CHARACTERISTICS OF IRON-COPPER SINTERED COMPACTS

KAMRAN TABESHFAR

Bournemouth University, Talbot Campus, Fern Barrow, Poole, BH12 5BB, UK.

### ABSTRACT

A study of fatigue cracking in iron-copper compacts was carried out to compare and analyse the performance of four different types of commercially used iron powders. The compacts were all sintered at above the iron copper peritectic temperature to facilitate liquid phase sintering. Results showed that the powder with a high specific surface had inferior fatigue properties, especially at high stress levels. The other powders, however, had very similar fatigue properties, except that at low stresses the grade with the large average particle diameter resulted in significantly longer fatigue lives. The differences in performance were discussed in terms of the microstructure of the compacts and the powder characteristics.

### INTRODUCTION

PM parts are used in many automotive applications, and of their more important mechanical properties are fracture toughness and fatigue strength especially where moving components are involved. Among these, iron copper compacts are widely used. In the last decade, there were some important developments in the understanding of the microstructure and its formation during sintering of iron copper compacts (refs 1 and 2). A model was proposed (ref 2) which explained the dimensional changes observed during sintering of these compacts, predicting the extent of the volume change for different types of powders. The explanation was in terms of liquid copper flow during sintering, and of the final site of the copper phase in the microstructure. It is inevitable that these microstructural features also have a controlling influence on the processes of fracture in the compacts. This paper presents the results of a study of fatigue cracking in iron copper sintered compacts with different types of microstructure. The various microstructures were produced by using different types of commercially used iron powders.

### EXPERIMENTAL

#### Powders

Four types of commercially used iron powder with different specific surfaces and compressibilities and an electrolytically produced copper powder were chosen. The details of the four powders are as follows:

- i) Normal compressibility sponge iron (NC 100.24), specific surface =  $50 \text{ m}^2/\text{kg}$ , 100 mesh.
- ii) Reduced mill scale pyron iron (PYRON D63), specific surface =  $150 \text{ m}^2/\text{kg}$ , 63 mesh.

- iii) Atomised super compressibility iron (ASC 100.29), specific surface  $\approx 25 \text{ m}^2/\text{kg}$ , 100 mesh.
- iv) Reduced mill scale pyron iron (PYRON - P100), specific surface  $= 150 \text{ m}^2/\text{kg}$ , 100 mesh.
- v) 90.2% pure electrolytic irregular Cu, 100 mesh

#### Compaction and sintering

Each of the four types of iron powder was mixed with 10wt% copper powder before compacting into green compacts. The die dimensions were  $55 \times 12.5 \times 12 \text{ mm}$ . At least five compacts were made from each of the four types of powder mixture, each at a compacting pressure of approximately  $700 \text{ MNm}^{-2}$ . The volume and density of each compact were measured accurately using a micrometer and a microbalance.

Liquid phase sintering of the compacts was carried out at a temperature of  $1135^\circ\text{C}$  in an atmosphere of 90% N + 10%  $\text{H}_2$  to avoid oxidation. All the samples were kept at this temperature for a period of 60 minutes and then cooled in the furnace.

The volume and density of the sintered compacts were then measured to compare with the data from the green compacts.

#### Fatigue tests

Specimens for fatigue tests were machined from the sintered compacts without any intermediate treatment. Machining was carried out by roughing the test-piece and then machining and grinding to the final finish size.

The fatigue tests were carried out in a reversed bending machine with a cycle frequency of  $\sim 50 \text{ Hz}$ . Each test-piece was mounted in the machine in a manner so that stresses at the gauge length, other than those imposed by the applied load, were avoided.

### **RESULTS**

The results of the fatigue tests are shown in Figure 1. These show that at high stress levels, there is little difference between the different powders, except that the compacts with the Pyron 100 have a significantly lower life cycles. At low stress levels, however, it is evident that the compacts with the Pyron D63 have measurably longer fatigue lives than those with the other powders. At intermediate stress levels the Pyron D63 generally gives the longest lives, while the compacts with the Pyron 100 seem to have the shortest fatigue lives in comparison with the other compacts.

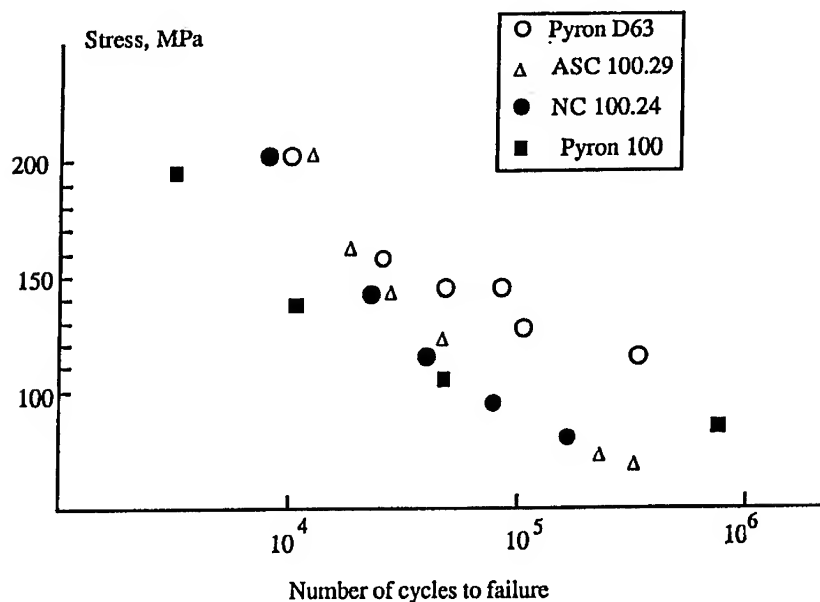


Figure 1 Influence of iron powder characteristics on the fatigue strength of Fe-Cu sintered compacts, with

## DISCUSSION

The fatigue results in figure 1 indicate that the compacts with NC 100 and ASC 100 powders have similar endurance at all stress levels. The similarity of performance between these two types of compacts is interesting, but perhaps not surprising when considered in the light of previous data (ref 2) for their microstructure. These two types of powders, although substantially different in loose form, produce essentially very similar microstructures when compacted at high compacting pressures, as was the case in this work. The result was confirmed by microstructural observations supporting the proposition that the microstructure in these compacts has a determining influence on their fatigue properties.

When the fatigue data for the Pyron 100 and Pyron D63 powders, however, are compared to the data for the others, significant differences are apparent, especially at the two extreme stress levels. Thus at the highest stress level, compacts with the Pyron 100 have significantly shorter lives, whereas at lower stress levels, the compacts with Pyron D63 have longer lives.

An explanation of the different performances of these powders at different stress levels may be given in terms of their behaviour at the crack initiation and growth stages. Thus at the high stress levels, where normally the crack initiation time is relatively short and life is determined by the crack growth stage, compacts with the Pyron 100 powders with a higher microporosity had shorter total lives because fatigue cracks found easy paths by bridging between the existing micropores. In the other powders, crack growth seems to be mainly intergranular, but along paths which generally avoid the copper filled boundaries. It is interesting to note that at the low stress levels, the relatively large pores (see ref 2) do not seem to influence the crack path. At the lower stress levels, however, where life is mostly dominated by the crack initiation stage, the effect of micropores on the life seems to be less significant than at high stress levels. The better performance of the Pyron D63 at low stresses must be due to its higher resistance to crack initiation as its crack growth features seem to be essentially the same as that in the ASC 100 and NC 100 powders.

It should be noted that the above observations and arguments are based on a limited amount of data and a more comprehensive experimental programme is required for more reliable deductions.

## CONCLUSIONS

- i) At long stress levels the Pyron 100 powder with high microporosity has the lowest endurance among the four different powders. The other three powders had very similar endurances at these stresses.
- ii) At low stress levels, Pyron 100, NC 100 and ASC 100 powders had very similar fatigue lives, while the Pyron D63 was clearly stronger.
- iii) The microstructure had a determining influence on the crack growth characteristics of the compacts and could explain the different performances of the four different powders.

## REFERENCES

1. D. Berner, H.E. Exner and G. Petzow, Modern Developments in Powder Metallurgy, 237 (1974).
2. K. Tabeshfar and G.A. Chadwick, Powder Metallurgy, 27, (1), 19 (1984)



# THE INFLUENCE OF CRYSTALLOGRAPHIC ORIENTATION OF THE CRACK PLANE AND CRACK FRONT ON THE FRACTURE OF TUNGSTEN SINGLE CRYSTALS

V.GLEBOVSKY\*, H.FISHMEISTER\*\*, J.RIEDLE\*\*, V.SEMENOV\* and P.GUMBSCH\*\*

\*Institute of Solid State Physics, Chernogolovka, Russia

\*\*Max-Planck-Institute fuer Metallforschung, Stuttgart, Germany

## ABSTRACT

For fracture studies on oriented W monocrystalline specimens it is necessary to produce very sharp, stopped precracks, which presents difficulties in the case of W. The experimental procedure and technique to produce precracks is described. The fracture experiments gave strong indications for a preference of the {100} plane as cleavage plane. It was found that the {110} planes successfully resist crack propagation, although they are the planes with the lowest surface energy. The appearance of the {121} plane as a cleavage plane in our experiments makes further studies with oriented W monocrystalline samples necessary.

## INTRODUCTION

The mechanical behaviour of *bcc* metals, e.g. Mo and W, is characterized by a ductile-to-brittle transition, based on a strong temperature dependence of the flow stress. In experiments, the brittle behaviour can be observed as cleavage mostly on low index planes like {100} or {110}. The explanation of preferred planes is usually given in physical continuum terms, which do not consider plasticity, invoking the low surface energy of these planes [1]. In this model, the crack resistance is determined only by the surface energy  $\gamma_{hkl}$  besides the elastic constants. The sequence of the surface energies for the low index planes in W begins with the {110} plane (lowest  $\gamma_{hkl}$ ), followed by the {100}, {211}, {311}, {233} and {111} planes [2]. From this one would expect {110} to be the primary cleavage plane in W single crystals, but this is not confirmed experimentally [3]. This caused us to perform fracture mechanical experiments with oriented single crystals of high-purity W, with exactly defined crack planes and crack propagation directions, aiming for measurements of the dependence of crack resistance on the crystallographic orientation of the crack system. By the term "crack system" we describe the combination of a crack plane and the direction of crack front.

## EXPERIMENTAL

**Tungsten single crystals** of 18 mm dia. and 250 mm length with growth axes [011] and [111] were grown by the electron-beam floating zone melting technique using an apparatus equipped with a specially designed circular electron-beam gun [4,5]. The circular electron beam emitted from the heated circular tungsten wire cathode was accelerated and focused on the vertically positioned specimen bar by a set of focusing water-cooled copper electrodes. The specimen to be melted served simultaneously as the anode of the electron gun. Because of the electron gun design, the radial temperature distribution on the solidification front is completely

defined, so that by using monocrystalline seeds, single crystals can be grown with predetermined orientations. The crystallographic parameters of the seeds and of the grown single crystals were determined by means of X-ray Laue back reflection patterns with an accuracy of  $1-2^\circ$ . The single crystals were grown with three liquid zone passes: two refining passes at a rate of 4-6 mm/min and one growing pass at a rate of 2 mm/min.

The W crystals were analysed by fast-neutron activation, deuteron activation, spark mass-spectrometry and atomic absorption with sensitivity limits of  $10^{-5}$  at.% for oxygen and carbon and  $10^{-6}-10^{-7}$  at.% for all other impurities [6,7]. The chemical composition of the high-purity W single crystals was as follows ( $\times 10^{-4}$  at.%): O 0.5; C 1; N 0.6; Si 0.3; Al 0.1; K 0.1; Ca 0.1; Na 0.3; P 0.3; S 0.3; Mn 0.3; Nb 0.1; Ta 0.1; Re 0.1; V 0.3; Fe 0.1; Ni 0.06; Co 0.3; Cr 0.05; Cu 0.05; Pb 0.1. Furthermore, the residual resistivity, which is an indicator of the integral chemical purity of the metal, was determined by means of both a four-point technique and a contactless rotating induction field technique. For the W single crystals examined, the residual resistivity (the ratio of the resistivities at room temperature and liquid helium) was higher than  $3 \times 10^4$  [4]. The dislocation density was estimated in the scanning electron microscope by averaging of 20 fields of view of  $0.4 \times 0.4 \text{ mm}^2$ . A subgrain structure was observed. The mean dislocation density in the subgrains was about  $5 \times 10^5 \text{ cm}^{-2}$ .

We used round compact **tension specimens** (RCT specimens) [8]. In order to select a desired crystallographically oriented crack system, the single crystals were oriented by the X-ray Laue back reflection technique and then the single crystals were spark machined into flat disks. These disks, with a thickness of 4.1 mm, were additionally spark machined in order to produce the cylindrical contour and the holes for the loading bolts.

**Experimental device.** Because we are interested in the brittle fracture mode, the mobility of the dislocations was reduced by cooling the specimens to low temperatures. Furthermore, we want to compare our experimental results with an atomistic calculation of the fracture behaviour, which simulates low temperature conditions [9]. Therefore, the fracture experiments were performed in a liquid nitrogen bath (77K). For these purposes, an immersible testing device was developed and placed in a cryostat (Fig. 1). The specimens were fixed in a cardanic suspension to

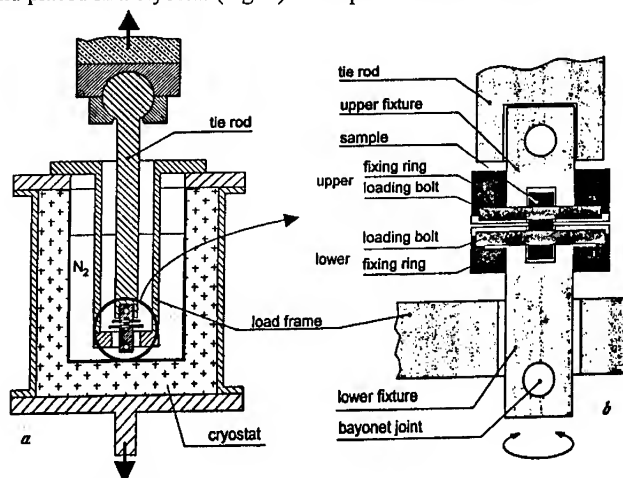


Fig. 1. The experimental device (a) and depiction of the sample fixture (b).

avoid mode II and mode III loading conditions. For the quantitative study of crack resistance, a correct measurement of the loading point displacement is necessary. Because of the low temperatures and small sizes of the specimens, such measurements are rather problematic. Therefore, a direct strain gauge technique was developed, which is described elsewhere [10].

**Precracking.** For the fracture toughness measurements, the generation of geometrically well defined, (atomically) sharp precracks is of great importance. The fracture mechanical validity of the experimental data is assured only when the precracks are sharp. In the present case the preparation of such precracks turned out to be very delicate because monocrystalline specimens are exceedingly brittle. It is very difficult to get a crack started in the crystal, but once having started it will propagate easily through the whole specimen, driven by the stored elastic energy. Therefore, the specimens were often destroyed during precracking.

A chevron notch was used to facilitate the start by concentrating stresses at the tip of the chevron, and inducing a rapid stress drop immediately afterwards. To minimize the stored elastic energy, a very stiff bending beam was used to load the specimen. However, the chevron geometry was not sufficient to stop the crack. Therefore, we tried to superimpose an additional stress field, supplying a crack closing force. Cracking was initiated by a shock wave produced by defined impacts on a wedge positioned in the notch.

The lateral compression technique, which has been successfully applied to high-speed steels [11,12], produces a through-thickness compression stress field directly at the end of the notch. However, the W single crystals do not show the same fracture behaviour as the steels: The crack surmounts counter stresses of any level up to the point when the crystal is fractured by the compression force. The technique depicted in Fig.2 produces the most favourable stress distribution: propagation into the ligament is counteracted by a continuous increase of the compression stress field. This technique produced usable specimens, but it still destroyed more than 50%. Again the counterstress is limited by fracture initiating from the loading points.

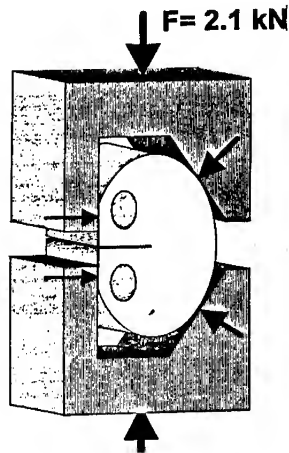


Fig. 2. Pressure fixture for superimposing the crack closing stress field.

The compression stress field can be seen in an elastic finite-element (FE) calculation of the specimen fixing. Fig. 3 shows the stress distribution in  $y$ -direction in the RCT specimen. There is a stress gradient in the specimen ligament, increasing towards the end. In view of the symmetry, the FE model comprises only a quarter of the RCT specimen, therefore only the half-contour of the chevron notch can be seen in the ligament. These calculations are performed using quaternary elements with linear displacement functions and considering the non-linear Green's strain tensor (geometrical non-linearity) within the commercial FE code 'LARSTRAN' [13].

## EXPERIMENTAL RESULTS AND DISCUSSION

In this section we present results of fracture experiments at low temperatures. Photographs of fracture surfaces of broken specimens with different crystallographic orientations are shown and discussed. Since up to now we have not been able to perform enough experiments to guarantee statistical reliability of our data, we will not give values for fracture toughnesses.

**Crack system (110)[001].** Fig.3 shows a side view of a fractured specimen notched and loaded so as to produce a [001] crack front on a (110) crack plane. However, the crack deflected onto a macroscopic plane of (100) orientation. The SEM micrograph shows a somewhat oblique view of the fracture surface close to the point of crack initiation. The spark machined notch flank can be seen. At the tip of the notch, the crack starts, but it does so on the (100) plane, instead of (110). Propagation occurs on (100) facets in a zig-zag path until the crack deflects onto a smoother path close to (110), before finding the final (100) plane. Towards the end of the specimen, the fracture surface becomes corrugated, which is due to increasing mode-mixity leading to instability of the crack path. The crack front remained [001] throughout.

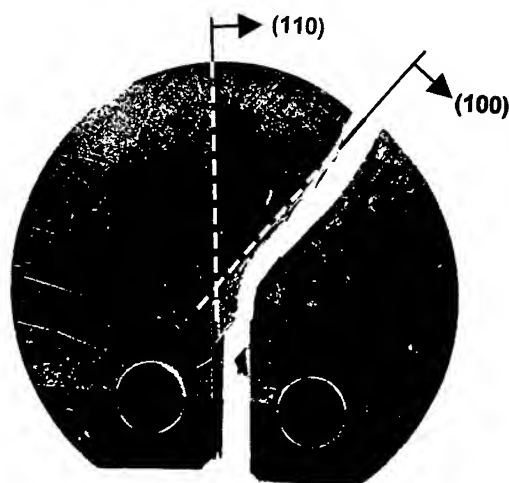


Fig. 3. Side view of the broken specimen with crack system (110)[001].

**Crack system (110)[111].** The orientation of the crack front in the  $[111]$  direction distinguishes this case from the preceding one. This specimen was notched on the  $(110)$  plane for an intended crack front orientation of  $[111]$ . In contrast to the earlier specimen, crack propagation now shifted to a  $(121)$  plane, see Fig. 4. The crack seems to refuse to advance on the

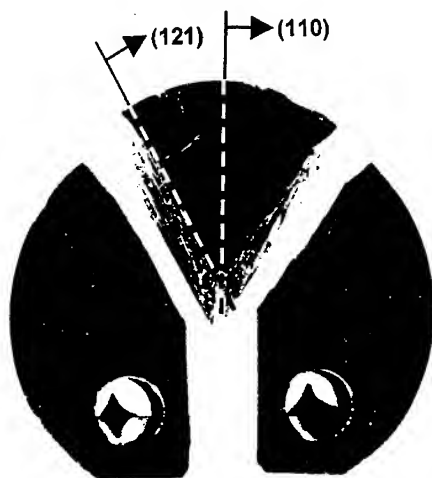


Fig. 4. Side view of the broken specimen with crack system  $(110)[111]$ .

mode I loaded  $(110)$  plane. The crack started from the chevron notch. The macroscopic orientation of the fracture surface is  $(121)$ , but the surface shows many terraces. Many of them are oriented in the  $(100)$  direction. However, a great part of the surface consists of  $(121)$  cleavage planes. The orientation of the terraces and facets was checked by X-ray Laue back reflection.

**Crack system  $(100)[011]$  and  $(100)[001]$ .** When the notch and the loading were oriented so as to activate a crack system with the crack plane in the  $(100)$  orientation and the crack front in the  $[011]$  or  $[001]$  direction, the crack started on this imposed plane, and in all cases continued straight through. An almost flat cleavage surface is seen, with fine terrace lines indicating the propagation direction. The lines lie near the  $[100]$  direction. The micrograph shows the fracture surface of a specimen with an imposed crack front orientation along  $[001]$ . A flat cleavage plane is observed. The crack propagation direction is again indicated by terrace edges. Regions of different brightness reflect the substructure of the single crystal which is due to slight growth faults. No influence of the subgrain boundaries on the crack propagation could be observed.

## CONCLUSIONS

A reliable experimental technique for preparation of fracture specimens with sharp, stopped precracks in oriented W single crystals, as well as a low temperature device for fracture

experiments are described. The (110) planes successfully resist crack propagation, although they are the planes with the lowest surface energy. In contrast to this, a preference for (100) planes as cleavage planes is obvious in the monocrystalline specimens. Crack propagation on both the (110) plane and (100) plane is strongly influenced by the crack front orientation, as predicted by an atomistic calculation [8]. The appearance of (121) as the cleavage plane in our experiments is not understood at this point. It encourages further research on oriented monocrystalline specimens.

## ACKNOWLEDGEMENTS

The studies were partially supported by the Netherlands' Organization for the Advancement of Scientific Research (NWO), the Netherlands, and the VW Foundation, Germany.

## REFERENCES

1. A.A. Griffith, Phil. Trans. R. Soc. A, **221**, 163 (1921).
2. G.J. Acklund and M.W. Finnis, Phil. Mag. A, **54**, 301 (1986).
3. D. Hull, P. Beardmore and A.P. Valentine, Phil. Mag. A, **12**, 1021 (1965).
4. V.G. Glebovsky, V.N. Semenov and V.V. Lomeyko, J. Crystal Growth **87**, 142 (1988).
5. V.G. Glebovsky, V.N. Semenov and V.V. Lomeyko, J. Less-Common Metals **117**, 385 (1986).
6. V.G. Glebovsky, B.M. Shipilevsky, I.V. Kapchenko and V.V. Kireyko, J. Alloys & Compounds **184** 297 (1992).
7. V.G. Glebovsky, I.V. Kapchenko and B.M. Shipilevsky, J. Alloys & Compounds **184**, 305 (1992).
8. G. Feddern and E. Macherauch, Zeitschr. f. Metallkde. **64**, 882 (1973).
9. S. Kohlhoff, P. Gumbsch and H.F. Fischmeister, Phil. Mag. A, **64**, 851 (1991).
10. J. Riedle, J. Wulff and S. Schmauder, Engng. Fract. Mech., (1994) submitted.
11. K. Eriksson, Scand. J. Metallurgy **4**, 182 (1975).
12. V.T.T. Miihkinen and J. Pietikäinen, Mat. Sci. Engng. **78**, 45 (1986).
13. R. Diez, U. Hindenlang and A. Kurz, "LARSTRAN 80 Documentation", Lasso Engineering Association, Stuttgart (1988).

---

### PART III

---

## **Surfaces and Interfaces**

## CRITICAL CLUSTER SIZE: ISLAND MORPHOLOGY AND SIZE DISTRIBUTION IN SUBMONOLAYER EPITAXIAL GROWTH

JACQUES G. AMAR AND FERREYDOON FAMILY

Department of Physics, Emory University, Atlanta GA 30322

### ABSTRACT

The island-size distribution scaling function  $f_i(u)$  corresponding to submonolayer epitaxial growth with critical island size  $i$  is studied via kinetic Monte Carlo simulations for  $i = 0, 1, 2$ , and 3. An analytic form for  $f_i(u)$  based on a conjecture for the small- $u$  behavior is also presented. For  $i = 1$ , the scaled island-size distribution is found to depend on island morphology. In particular, for fractal islands with  $i = 1$  there is excellent agreement with our analytical form as well as with experiments on low temperature Fe/Fe(100) deposition. However, for compact islands with  $i = 1$ , the scaled distribution is found to deviate slightly at small  $u$ . We also find excellent agreement between our analytical form, simulations, and experiment for  $i = 2$  and  $i = 3$ . Good agreement between our simulation results for  $i = 0$  and recent experiments on Fe/Cu(100) deposition is also found. Results for the scaling of the island-density as well as crossover scaling forms for the transition from  $i = 1$  to  $i = 2$  and from  $i = 1$  to  $i = 3$  are also presented and used to determine the one-bond activation energy and critical island size transition temperature for Fe/Fe(100). The morphology of fractal islands for  $i = 2$  is also studied and compared with experiments on Au/Ru(0001).

### INTRODUCTION

Recently considerable theoretical and experimental efforts have been made to understand the kinetic processes which control the nucleation and subsequent growth of islands in submonolayer epitaxial growth. A concept which is crucial for understanding these processes is that of a critical island size  $i$  corresponding to the number of atoms in the largest unstable island. For example (see Fig. 1), depending on the bond energies, temperature, and deposition rate, one may have a situation in which monomers diffuse but dimers are stable ( $i = 1$ ), or in which a trimer is the smallest stable island ( $i = 2$ ), or in which the smallest stable island size corresponds to a tetramer ( $i = 3$ ). Standard rate equation theory [1],[2] predicts that for a given critical island size  $i$ , the island density  $N$  in the pre-coalescence regime scales as  $N \sim R^{-\chi_i}$  where  $R = D/F$  is the ratio of the (monomer) diffusion rate  $D$  to the deposition flux  $F$  and where  $\chi_i = i/(i + 2)$ . The exponent  $\chi_i$  has been measured in a variety of experiments and used to determine the critical island size as well as the activation energy  $E_a$  for diffusion.

Here we present kinetic Monte Carlo simulation results for both compact and fractal islands as well as an approximate analytic expression for the asymptotic scaled island-size distribution  $f_i(u)$  as a function of  $i$  for  $i = 0, 1, 2$ , and 3. Our analytical form is based on a conjecture for the small- $u$  behavior of  $f_i(u)$ . We find good agreement between our simulations and experimental measurements of the island-size distribution for Fe/Fe(100) at low temperature ( $i = 1$ ) and at high temperature ( $i = 3$ ) as well as with our conjectured analytical form. The dependence of the scaled island-size distribution on morphology for  $i = 1$  is also studied. We also find good agreement between our simulation results for  $i = 0$  and experimental results for Fe/Cu(100) deposition. We also present results for the scaling of the island-density as a function of critical island size as well



as crossover scaling forms for the transition from  $i = 1$  to  $i = 2$  and from  $i = 1$  to  $i = 3$  as a function of deposition rate and temperature. These crossover scaling results may be used to predict the crossover temperature for transitions, and in conjunction with experimental results for the island density, to predict bond-energies for detachment as in Fe/Fe(100). The morphology of fractal islands for the case  $i = 2$  is also studied and compared with experiments on Au/Ru(0001).

### SCALING THEORY

The fundamental quantity in the kinetic description of island growth is the island size distribution function  $N_s(\theta)$ , which gives the density of islands of size  $s$  (where  $s$  is the number of atoms or particles in the island) at coverage  $\theta = Ft$ . According to the dynamic scaling assumption there exists only one characteristic size in the problem which is the mean island size  $S(\theta)$ . This implies that one may write the general scaling form [3-5]

$$N_s(\theta) = \theta S^{-2} f_i(s/S) \quad (1)$$

where the scaling function  $f_i(u)$  satisfies the sum-rules,  $\int_0^\infty f_i(u) u du = \int_0^\infty f_i(u) du = 1$  corresponding to mass-conservation and the scaling relation  $N \simeq \theta/S$ .

### RATE EQUATION APPROACH: POINT-ISLAND MODEL

The traditional method for studying the kinetics of cluster growth processes is based on the theoretical approach developed by Smoluchowski [6] who wrote down an equation for the evolution of the cluster size distribution using a mean-field argument which neglects fluctuations and geometry. For the point-island model, the islands have zero lateral extent and the capture probability  $K_s$  is independent of island size  $s$ . Assuming a critical stable island size  $i$  such that there is no dissociation for  $s > i$  as well as the quasi-equilibrium Walton relation [7] that  $N_i \sim A_i N_1^i$  where  $A_i = e^{E_i/k_B T}$  is a temperature-dependent prefactor and  $E_i$  is the binding energy of the critical cluster of size  $i$  one obtains,

$$\frac{dN_1}{d\theta} = 1 - RN_1^2 - RN_1N + \frac{1}{F} \sum_{2 \leq s \leq i} \gamma_s N_s \quad (2a)$$

$$\frac{dN_x}{d\theta} = RN_1^{i+1} A_i \quad (2b)$$

where  $N_x = \sum_{s>i} N_s$  is the stable island density and  $\gamma_s$  corresponds to the monomer detachment rate from islands of size  $s$ . In the late-time (asymptotic) limit, we assume that for  $s \leq i$ ,  $N_s \ll N \simeq N_x$  and  $\frac{dN_x}{d\theta} \simeq 0 \simeq 1 - RN_1N$  to obtain the point-island rate-equation predictions,  $N_1 = (1/B_i) R^{-2/(i+2)} \theta^{-1/(i+2)}$  and  $N = B_i R^{-i/(i+2)} \theta^{1/(i+2)}$  where  $B_i = [(i+2)A_i]^{-\frac{1}{i+2}}$ . Substituting for  $A_i$  and  $B_i$  yields the temperature dependence of the island density at fixed coverage,  $N \sim e^{[E_i/(i+2) + \chi_i E_a]/k_B T}$  with  $\chi_i = i/(i+2)$  and where  $E_i$  is the critical cluster binding energy and  $E_a$  is the activation energy for monomer diffusion. Substituting the scaling form for the island-size distribution (1) into the full rate-equation leads to the point-island rate-equation solution for the asymptotic scaled island-size distribution function [8],[9],

$$f_i(u) = \frac{1}{i+2} \left(1 - \frac{i+1}{i+2} u\right)^{-\frac{i}{i+1}} ; \quad 0 \leq u \leq \frac{i+2}{i+1} \quad (3a)$$

$$f_i(u) = 0 \quad ; \quad u > \frac{i+2}{i+1} \quad (3b)$$

The divergence of  $f_i(u)$  for finite  $u$  as well as the linear behavior at  $u = 0$  is a particularly unphysical feature of this result. This is due to the neglect of the effects of island-size as well as correlations in the point-island model.

#### ANALYTIC FORM FOR THE SCALING FUNCTION $f_i(u)$

We have derived an analytical expression [10] for  $f_i(u)$  which appears to agree quite well with our asymptotic simulation results and with experimental data in the pre-coalescence regime. Our analytical expression for  $f_i(u)$  is based in part on the observation [5] that for the case of fractal islands for  $i = 1$ , the island-size distribution scaling function  $f_1(u)$  has approximately linear behavior for small  $u$ , with  $f_1(0)$  approaching zero with increasing  $D/F$ . For  $i > 1$  we expect smaller islands to have a lower density and  $f_i(u)$  to go to zero faster than the first power. We have therefore conjectured [10] that for general  $i$ , the island-size distribution behaves as  $u^i$  for small  $u$ . We also expect  $f_i(u)$  to have a peak at  $u = 1$  corresponding to the average island size and to decrease rapidly for large  $u$  with an exponential cutoff. These assumptions lead to the following approximate general scaling form for  $i \geq 1$ ,

$$f_i(u) = C_i u^i e^{-ia_i u^{1/a_i}} \quad \text{with} \quad C_i = \frac{(ia_i)^{(i+1)a_i}}{a_i \Gamma[(i+1)a_i]} \quad ; \quad \frac{\Gamma[(i+2)a_i]}{\Gamma[(i+1)a_i]} = (ia_i)^{a_i} \quad (4)$$

where the relations for  $a_i$  and  $c_i$  are determined by the sum-rules for  $f_i(u)$ . We note that this form is quite different from the point-island rate equation result (3) which predicts a divergence at a finite  $u > 1$  and a finite value for  $f_i(0)$ .

#### SIMULATION RESULTS

In order to investigate the scaling behavior of the submonolayer island density and size-distribution as a function of critical island size  $i$ , we have studied a simplified model in which atoms are randomly deposited at a rate  $F$  per site per unit time onto a regular lattice while monomers, including those deposited on top of existing islands, are assumed to diffuse at the rate  $D = D_0 e^{-E_a/k_B T}$  in units of nearest-neighbor hops per unit time. In our model [10] a monomer becomes stable when it has at least  $z$  nearest-neighbors, so that the critical island size  $i$  depends on both the underlying lattice and  $z$  (see Fig. 1). For atoms which have  $0 < n < z$  nearest-neighbor surface atoms, we assume that the activation energy for diffusion is given by  $E_n$  so that the relative diffusion rate is given by  $r_n = D_n/D = e^{-\Delta E_n/k_B T}$  where  $\Delta E_n = E_n - E_a$ . In order to study the effects of edge-diffusion on island morphology we have also included an additional parameter  $r_e = e^{-\Delta E_e/k_B T}$  corresponding to diffusion of atoms with one-nearest neighbor (i.e. "one-bond diffusion") along the edge of an island. By varying  $r_n$ ,  $r_e$ , and  $z$  and studying various lattices, we have studied the island-size distribution, density, and morphology for  $i = 0, 1, 2$  and  $3$ .

##### Island-Size Distribution for $i = 0$

The case of a critical island size of zero corresponds to deposition in the presence of impurities or surfactants which lead to heterogeneous nucleation. This case has also recently been studied

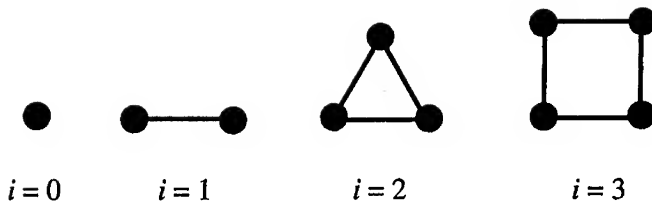


**Fig. 1:** Diagram showing stable island configurations for different critical island sizes  $i = 0$  to 3. The case  $z = 1$  corresponds to  $i = 1$  on any lattice, while  $z = 2$  corresponds to  $i = 2$  and 3 on triangular and square lattices respectively. Also shown is the case  $i = 0$  which corresponds to freezing of monomers.

experimentally by Chambliss and Johnson [11] in Fe/Cu(100) deposition. In this experiment, isolated Fe atoms which have been deposited on a Cu(100) surface spontaneously embed into the surface and form stable islands. To simulate this case, we have studied a model in which monomers spontaneously ‘freeze’ and form stable islands at a rate given by  $R_s = r_s D$ , where  $r_s = e^{-\Delta E_s/k_B T}$  corresponds to the extra activation energy beyond that for normal diffusion. In addition, any monomers which become nearest-neighbors of an embedded island are immediately added irreversibly to the embedded island. Fig. 2 shows our simulation results for the island size distribution scaling function for  $r_s = 10^{-3} - 10^{-5}$  and  $\theta = 0.06 - 0.3$  as well as various values of  $D/F$ . The island-size distribution scaling function  $f_0$  is essentially independent of the embedding probability ratio  $r_s$  as well as  $D/F$  over all coverage. As expected from our conjecture for the small  $u$  behavior of  $f_i(u)$ , the island-size distribution scaling function in this case is non-zero at  $u = 0$ . In addition, the scaling function looks quite similar to that obtained in the experiment. As observed in experiment, we also find very weak or essentially no dependence of the peak island density on  $D/F$  corresponding to  $\chi_0 = 0$ . We also find that  $N$  scales as  $N \sim r_s^{\phi_s}$  with  $\phi_s \simeq 1/2$ , in agreement with the predictions of the point-island rate equations [11] for  $i = 0$  although the coverage dependence of  $N$  is quite different from the point-island model prediction. Thus, a measurement of the temperature-dependence of the island density, may allow the determination of the activation energy difference  $\Delta E_s$  between that for monomer embedding and for diffusion in this case.

#### Island-Size Distribution for $i = 1$

Our results for the asymptotic (large  $D/F$ ) scaled island-size distribution for the case of fractal islands with  $i = 1$  are shown in Fig. 3(a) along with experimental results [12] for Fe/Fe(100) at low temperature and our analytical form (4). As can be seen there is very good agreement between our simulation results and our analytical form as well as with the Fe/Fe(100) experimental results. Similar results have also been obtained from simulations on a triangular lattice with  $i = 1$  [10]. Our results [5],[10] indicate that the linear behavior of the island-size distribution scaling function at small  $u = s/S$  extends to lower and lower  $u$  with increasing  $D/F$ , even at relatively low coverage. Thus, in the asymptotic limit of large  $D/F$ , we find linear behavior for  $f_1(u)$  as predicted by our conjecture and good agreement with our analytical form.

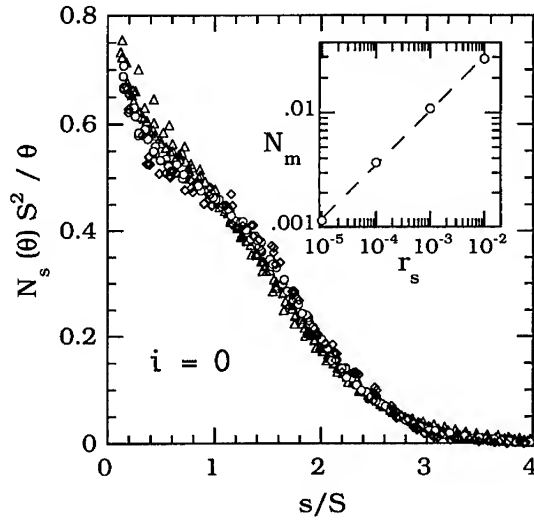


**Fig. 2:** Island size distribution scaling function  $f_0(u)$  from simulations on a square lattice for  $i = 0$  with  $r_s = 10^{-3}$  (triangles),  $10^{-4}$  (circles) and  $10^{-5}$  (diamonds) with  $R \geq 10^9$ . Inset shows log-log plot of maximum island density  $N_m$  versus relative embedding probability  $r_s$ . Dashed line fit has slope equal to 0.48.

We have also studied the island-size distribution for compact islands on a square-lattice with  $i = 1$  by including a significant amount of one-bond edge-diffusion in our simulations. Fig. 3(b) shows the scaled-island size distribution for large  $D/F$  in this case for three different values of  $\theta$  in the aggregation (constant island density) regime, along with our analytical form (4). As can be seen, while there is good agreement with our analytical form beyond the peak of the distribution, for small  $u$  the agreement is not so good, and in particular one has  $f_1(0) \neq 0$  in contrast to the fractal island case. Similar behavior has previously been observed by Bartelt and Evans [13] in simulations in which the islands were forced to grow in a square (spiral) fashion in order to mimic the very fast edge-diffusion limit. Thus, the asymptotic scaled island-size distribution for the compact case with  $i = 1$  appears to be somewhat different (and more complicated) than for the fractal case, although with increasing coverage, the compact distribution appears to approach the fractal distribution and our analytic form. Interestingly, the experimental distribution for Fe/Fe(100) appears to show better agreement with the fractal scaled distribution than with the compact one for  $u < 1$ , even though in the experiment the islands are compact (square). This is most likely due to the enhanced diffusion of small clusters with increasing temperature (due in part to edge-diffusion) which leads to a depletion in the number of small islands. It is interesting to compare the value of  $f_1(0)$  from our simulations with that obtained from the point-island model. From our simulations, one finds in the asymptotic limit for  $\theta = 0.12 - 0.3$ ,  $f_1(0) \simeq 0.25 - 0.16$ , which may be compared with the point-island model prediction  $f_1(0) = 1/(i + 2) = 1/3$ .

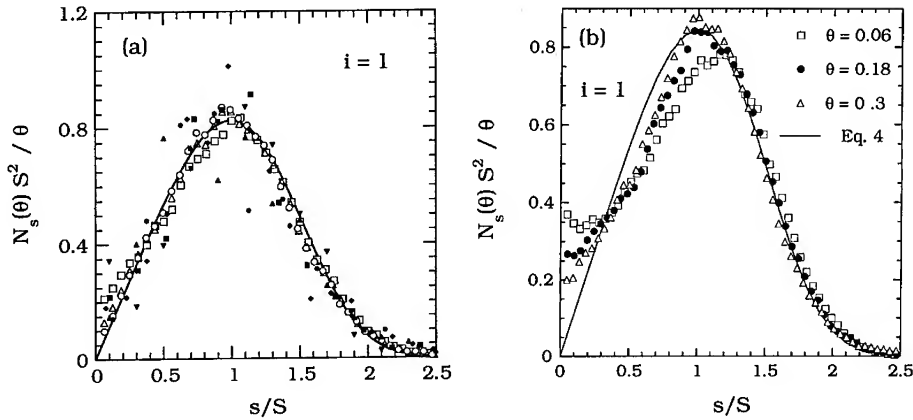


**Fig. 3:** Island-size distribution scaling function  $f_i(u)$  for  $i = 1$ . (a) Fractal Case. Open symbols correspond to simulation results on square-lattice with  $R = 10^{10}$ ,  $r_1 = r_e = 0$  and  $\theta = 0.1$  (squares),  $0.2$  (triangles), and  $0.3$  (circles). Completely filled symbols correspond to experimental results [12] at  $T = 20$  C (circles),  $108$  C (squares),  $132$  C (diamonds),  $163$  C (triangles), and  $207$  C (inverted triangles). Solid line is Eq. 4 for  $i = 1$ . (b) Compact Case.  $R = 10^{10}$  and  $r_e = 0.0001$ .

#### Island-Size Distribution for $i = 2$

The case  $i = 2$  was studied using a simple model [10] on a triangular lattice in which any atom with two or more nearest-neighbors is irreversibly 'frozen' (i.e.  $z = 2$ ) so that the minimal stable island is a trimer, while the additional activation energy  $\Delta E_1$  for an atom which has only one bond was taken to be finite. Fig. 4(a) shows our simulation results for the island-size distribution scaling function for  $i = 2$  with  $D/F = 10^7 - 10^8$ ,  $\theta = 0.1 - 0.4$  for  $r_1 = 0.003 - 1$ . As can be seen there is very good agreement with our analytic result (4) for the scaled island-size distribution, and in contrast to the point-island prediction for  $i = 2$ , the scaled island-size distribution clearly goes to 0 at  $u = 0$ . A fit to the small- $u$  behavior (not shown) [14] gives  $f_2(u) \sim u^{2.05}$  in agreement with our conjecture that  $f_i(u) \sim u^i$ .

#### Island Morphology for $i = 2$

From a comparison of simulations without edge-diffusion [10], we find that deposition with  $i = 2$  on a triangular lattice corresponds to fractal islands which have significantly fatter arms than for  $i = 1$ . Thus, the existence of one-bond detachment may provide a partial explanation [9],[10],[15] of the fat fractal islands observed in room temperature Au/Ru(0001) deposition [16]. A careful study of the island morphology in room temperature Au/Ru(0001) deposition indicates that edge-diffusion is also significant. To mimic this, we have added a significant amount of one-bond edge-diffusion as well as a small amount of two-bond detachment in our simulations [9]. Fig. 4(b) shows the results of our simulations at an island density slightly higher than in the

experiment and a coverage  $\theta = 0.37$ . As can be seen, the island morphology and arm thickness are now quite similar to what is observed experimentally. Although we have included a small amount of two-bond detachment, the critical island size is still  $i = 2$  so that the island density still scales as  $N \sim (D/F)^{-0.5}$ . We note however, that the flux dependence of the island density for Au/Ru(0001) indicates that the critical island size is actually larger than 2, possibly due to enhanced two-bond detachment from small islands. Therefore, further work will be needed to fully understand this case.

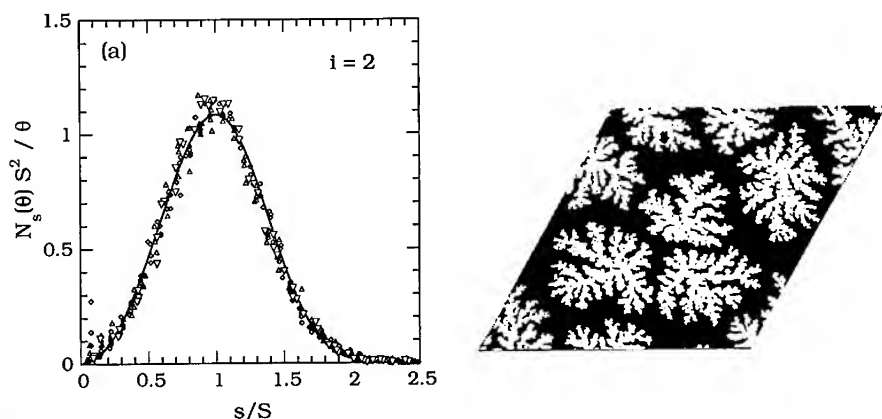


**Fig. 4:** (a) Island-Size distribution for  $i = 2$ . Simulation results (open symbols) are for  $R = 10^7 - 10^8$ ,  $r_e = 0$  and  $r_1 = 0.003 - 1$  on a triangular lattice with  $\theta = 0.1 - 0.4$ . Solid line is Eq. 4 for  $i = 2$ . (b) Morphology of islands formed on triangular lattice with  $R = 10^{11}$ ,  $r_1 = 10^{-4}$ ,  $r_2 = 10^{-8}$ , and  $r_e = 10^{-2}$  (system size  $L = 600$ ) at  $\theta = 0.37$ .

#### Island-Size Distribution for $i = 3$

The case  $i = 3$  has been suggested as the critical cluster size for Fe/Fe(100) deposition at elevated temperatures [12]. In this case the minimal stable configuration is a tetramer and in order to determine the island-size distribution we have studied a model with  $r_1 \neq 0$  and  $z = 2$  on a square lattice. We note that in this case the islands tend to be compact, even without significant edge-diffusion, since the requirement that only atoms with two bonds do not detach leads to compact islands on a square lattice [17]. Figure 5(a) shows our results for the island-size distribution scaling function for a range of values of  $R = D/F$  and  $r_1$  both with and without edge-diffusion. The simulation results cover a wide range of coverages including  $\theta \simeq 0.07$  for which the island-size distribution was measured for Fe/Fe(100). Also shown are experimental results for the scaled island-size distribution for Fe/Fe(100) deposition at  $T = 301$  C and  $T = 356$  C as well as our analytical expression (4) for  $f_3(u)$  with  $C_3 = 3.239$  and  $a_3 = 0.3086$ . As can be seen, there is very good agreement between our simulation results and the analytical form (4) as well as with the experiments. This confirms that  $i = 3$  is the critical island size at elevated temperatures for Fe/Fe(100) deposition.

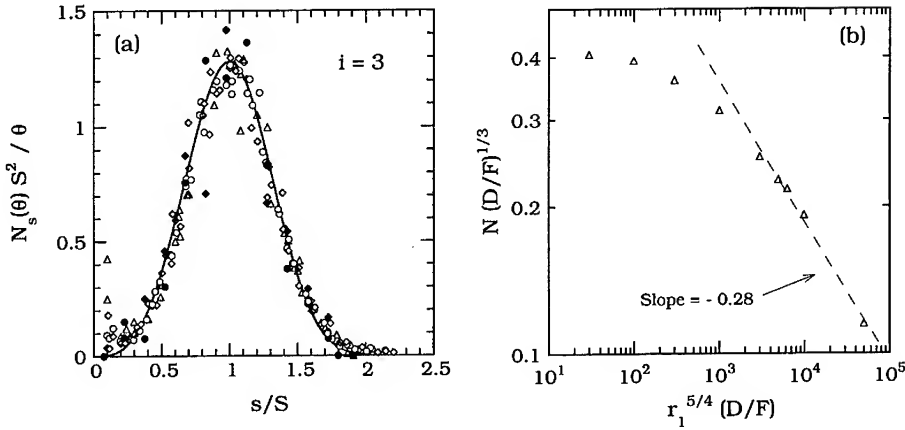


**Fig. 5:** Results for  $i = 3$ . (a) Island-Size distribution. Simulation results on a square lattice (open symbols) for  $\theta = 0.06 - 0.3$  with  $R = 5 \times 10^9 - 10^{11}$ ,  $r_1 = 10^{-6} - 10^{-4}$ , with and without edge diffusion. Filled symbols are experimental results for Fe/Fe(100) [15] at  $T = 301$  C (diamonds) and  $T = 356$  C (circles). Solid line is Eq. 4 for  $i = 3$ . (b) Plot of crossover scaling function  $f_{13}$ .

#### Crossover Scaling as a Function of Temperature and Deposition Rate

We have also studied the scaling of the island density  $N$  with  $D/F$  for  $i = 2$  and 3 and find reasonable agreement with the rate equation prediction  $\chi_i = i/(i+2)$ . For example, for simulations on a square-lattice with large  $D/F$  and finite  $r_1$  and island densities in the range of those observed for Fe/Fe(001) at high temperature, we find  $N \sim (D/F)^{-0.58} r_1^{-\phi_{13}}$  with  $\phi_{13} \simeq 0.33$  [10]. However, for smaller  $D/F$  or very small  $r_1$ , we find a crossover to  $\chi_1 = 1/3$  corresponding to  $i = 1$ . This implies the crossover scaling form,

$$N \sim R^{-1/3} f_{13}(r_1^{5/4} R) \quad (5)$$

where  $f_{13}(u) \sim \text{constant}$  for  $u \ll 1$  and  $f_{13}(u) \sim u^{-4/15}$  for  $u \gg 1$ . A scaling plot of this form for  $D/F = 2 \times 10^9 - 2 \times 10^{11}$  and  $r_1 = 10^{-6} - 10^{-4}$  is shown in Fig. 5(b). We note that the result  $\phi_{13} = 1/3$  disagrees with the prediction  $\phi_{13}^W = 2/5$  based on the Walton relation coupled with the point-island rate equations [9]. A similar scaling form for the crossover from  $i = 1$  to  $i = 2$  has also been found with  $\phi_{12} = 1/4$  [10],[14].

Our results for the island density may be used (along with experimental values of the island-density and  $D/F$  at  $T = 356$  C obtained in Ref. [17]) to estimate the activation energy  $\Delta E_1$  for "one-bond" detachment in Fe/Fe(100). We find  $\Delta E_1 \simeq 0.6$  eV. These results also yield a prediction of the ratio  $m = (\chi_3 E_a + \phi_{13} \Delta E_1) / \chi_1 E_a$  of the slope in the high-temperature ( $i = 3$ ) region to the slope in the low-temperature ( $i = 1$ ) region in the semilog plot of  $\log(N)$  versus  $1/T$  for Fe/Fe(100) which is in good agreement with that obtained in Ref. [12]. Using the value of  $E_a = 0.45$  eV determined in Ref. [17] and our values for  $\phi_{13}$  and  $\Delta E_1$  we obtain  $m = 3.14$

in good agreement with the experimental value 3.27. The crossover scaling function  $f_{13}$  can also be used along with our estimate for  $\Delta E_1$  and the previously estimated values of  $D_0$  and  $E_a$  [17], to estimate the transition temperature  $T_x$  from  $i = 1$  to  $i = 3$  behavior. Using the experimental value  $F = 0.0115$  ML/sec, and taking  $r_1^{5/4}(D/F) = 200$  as the criterion for the onset of deviations from  $i = 1$  behavior and  $r_1^{5/4}(D/F) = 5000$  as the criterion for full-blown  $i = 3$  behavior, we obtain  $T_x = 260 - 300$  C. This is in excellent agreement with the experimental observation [12] of deviations in the island-size distribution from  $i = 1$  behavior at  $T = 250$  C and of good agreement with our  $i = 3$  simulations and analytical form for the island-size distribution at  $T = 301$  C.

#### Acknowledgements

This work was supported by National Science Foundation grant DMR-9214308 and by the Office of Naval Research. Part of this work was carried out using the computational facilities of the Cherry L. Emerson Center for Scientific Computation at Emory University.

#### REFERENCES

1. J.A. Venables, *Philos. Mag.* **27**, 697 (1973). J. A. Venables, G.D. Spiller, and M. Hanbucken, *Rep. Prog. Phys.* **47**, 399 (1984).
2. S. Stoyanov and D. Kashchiev, in *Current Topics in Materials Science*, edited by E. Kaldis (North-Holland, Amsterdam, 1981), Vol. 7, pp. 69-141.
3. F. Family and P. Meakin, *Phys. Rev. Lett.* **61**, 428 (1988); *Phys. Rev. A* **40**, 3836 (1989).
4. M.C. Bartelt and J.W. Evans, *Phys. Rev. B* **46**, 12675 (1992).
5. J.G. Amar, F. Family, and P.-M. Lam, in *Mechanisms of Thin Film Evolution*, MRS Symposia Proceedings No. 317 (Materials Research Society, Pittsburgh, 1994), p. 167; *Phys. Rev. B* **50**, 8781 (1994).
6. M. von Smoluchowski, *Z. Phys. Chem.* **17**, 557 (1916); *ibid*, **92**, 129 (1917).
7. D. Walton, T.N. Rhodin, and R.W. Rollins, *J. Chem. Phys.* **38**, 2698 (1961).
8. J.W. Evans and M.C. Bartelt, *J. Vac. Sci. Technol. A* **12**, 1800 (1994).
9. F. Family and J.G. Amar, *Mat. Sci. and Eng. B (Solid State Mat.)*, (to be published, 1994).
10. J.G. Amar and F. Family, submitted to *Physical Review Letters*.
11. D.D. Chambliss and K.E. Johnson, *Phys. Rev. B* **50**, 5012 (1994).
12. J.A. Strosio and D.T. Pierce, *Phys. Rev. B* **49**, 8522 (1994).
13. M.C. Bartelt and J.W. Evans, *Surf. Sci.* **298**, 421 (1993).
14. J.G. Amar and F. Family, submitted to *Physical Review B*.
15. Z. Zhang, X. Chen, and M.G. Lagally, *Phys. Rev. Lett.* **73**, 1829 (1994).
16. R.Q. Hwang, J. Schroder, C. Gunther, and R.J. Behm, *Phys. Rev. Lett.* **67**, 3279 (1991); R.Q. Hwang and R.J. Behm, *J. Vac. Sci. Technol. B* **10**, 256 (1992).
17. C. Ratsch, A. Zangwill, P. Smilauer, and D.D. Vvedensky, *Phys. Rev. Lett.* **72**, 3194 (1994).
18. J.A. Strosio, D.T. Pierce, and R.A. Dragoset, *Phys. Rev. Lett.* **70**, 3615 (1993).



## DYNAMIC SCALING IN ELECTROCHEMICAL DEPOSITION

Hiroshi IWASAKI, Atsushi IWAMOTO, Koichi SUDOH  
AND Tatsuo YOSHINOBU  
The Institute of Scientific and Industrial Research,  
Osaka University, 8-1 Mihogaoka, Ibaraki, Osaka 567, Japan

### ABSTRACT

Static and dynamic scaling behavior in copper electrochemical deposition in the stable growth condition (non-bulk fractal growth) was studied by atomic force microscopy and numerical simulation. We found two distinct scaling regimes with roughness exponent  $\alpha$  of 0.6 and  $0.87 \pm 0.05$  corresponding to the concentrations of the "brightener" organic additive higher and lower than 1 mL/l, respectively. The rms surface width of the whole measured area of the surfaces in the former regime was smaller than that in the latter regime. For the latter rougher surface, we observed dynamic scaling behavior for longer length scales as well as the stationary scaling behavior for shorter length scales: surface width did not further increase with linear size of the area for longer length scales than a characteristic correlation length and increased as a power of deposition time with the dynamic exponent  $\beta$  of 0.45. The sum of  $\alpha + (\alpha/\beta)$  was larger than the value expected for KPZ local growth, 2. This was understood that in electrochemical deposition there is enhancement of growth at protrusions owing to non-local Laplacian field effect. The smoother ( $\alpha = 0.6$ ) and the rougher (0.87) surfaces were reproduced by numerical solutions of KPZ + (the growth term proportional to height) for the shorter and the longer growth times, respectively. Bifurcation of the surface morphology is understood as a result of decrease of weight of the additional term owing to increase of the additive.

### INTRODUCTION

A growth generates rough surfaces in many cases [1-3]. According to Family and Vicsek [1] and others [2], roughness of compact growing films on flat substrates often exhibits scale invariance. Then, the rms surface width  $W$  increases as a power of linear size  $L$  with the roughness exponent  $\alpha$  for the shorter length scales and saturate at the correlation length  $L_c$ . The scaling is stationary but the saturated value increases as a power of growth time with the exponent  $\beta$ . That is

$$W(L, t) \propto L^\alpha \quad \text{for } L \ll L_c, \quad (1a)$$

$$W(L, t) = \Delta(t) \propto t^\beta \quad \text{for } L \gg L_c, \quad (1b)$$

where  $L_c = t^{1/2}$  and  $Z = \alpha / \beta$ . This is caused by random processes such as particle deposition which inevitably take part in the growth. It is interesting why and how random addition of very small particles to the growing surface in a particular manner results in universally scaled roughness.

To study kinetic roughening, it is important to investigate the time dependent scaling of the surface. There have been, however, very few experimental studies of dynamic scaling [4,5]. In this paper we study dynamic scaling in electrochemical copper deposition in stable growth mode by experiment and simulation. Electrochemical deposition is suited for kinetic roughening study because the growth conditions are well controllable.

Roughening in electrochemical deposition is widely studied both from academic and technological points of view [4-13]. Study of fractal growth in the diffusion limited growth regime described below is intensively studied but roughening in stable mode which is of technological importance has scarcely been studied.

## KINETIC ROUGHENING IN ELECTROCHEMICAL DEPOSITION

In electrochemical deposition, reacting cations (metal ions) get electrons and stick to the cathode electrode and their concentration is reduced from the bulk concentration to form the boundary layer. The cations distribute according to convection and diffusion outside and inside of the boundary layer, respectively. Electromigration can be neglected for usual conductive solutions with supporting electrolyte. Air bubbling enhances convection and makes the boundary layer thinner.

Stability of flat surface growth in electrochemical deposition has been studied [9,12,13]. With increasing current density, concentration of cations becomes eventually zero everywhere at the surface and the current is limited by diffusion of the cations. Thus, at higher currents near the limiting current, the growth is governed by diffusion-limited non-local mechanism to produce rough patterns such as dense-branching morphology and dendrites [7-10,14].

At lower current densities in the so called Tafel regime, where we performed the present electrodeposition, the growth instability is weak for length scales shorter than  $\lambda_c = D$  and the growth rate is given in the steady state as follows [9,15],

$$\frac{\partial h(r)}{\partial t} \approx \frac{2v}{\lambda_c - D} (h(r) - \langle h(r) \rangle_A), \quad (2a)$$

$$\text{where } \lambda_c = \frac{C_0 D}{C_0 - C_s} \quad , \quad (2b)$$

$D$ ,  $C_0$  and  $C_s$  are boundary layer thickness, concentrations of the cations outside of the boundary layer and at the surface, respectively, and  $h(r)$  is height of the interface measured from the plane averaged over the whole measured area moving at constant growth velocity  $V$  and  $\langle h(r) \rangle_A$  is average over the local area of length scale  $A$  which is of the order of smaller one of  $D$  and  $\lambda_c - D$ . Because of this averaging over the area, the growth term given by eq. (2) is non-local.

The stability analyses of growth do not take into account random processes such as particle deposition and nucleation. To take the random process into account, one uses Langevin equation such as KPZ equation [16]. In this model, the interface growth is described as

$$\frac{\partial h(r)}{\partial t} = \gamma \nabla^2 h(r) + \frac{V}{2} (\nabla h(r))^2 + \eta(r, t) \quad , \quad (3)$$

where the first term on the right-hand side describes relaxation of the interface by a surface tension  $\gamma$ . The second term is included to describe lateral growth, i.e. equal growth velocity  $V$  normal to local surface. The noise  $\eta(r, t)$  has a Gaussian distribution. To simulate electrochemical deposition, we start from the limiting local KPZ equation and add the non-local growth term that appeared in the continuum growth eq. (2).

Nucleation and anisotropic crystal growth, if they exist, would affect surface topology and apparent scaling behavior [12]. On larger length scale than nuclei size, we can consider them as elemental particles. Because faceting is not observed in the present Cu deposit films (see Fig. 1 below), we neglect the effect of anisotropic crystal growth on the present kinetic surface roughening.

In ballistic deposition model which is believed to belong to the KPZ universality class, extended surface migration of sticking particles and relaxation after addition do not take place and thus it is called non-volume conservative growth while MBE growth is called conservative growth [17,18]. Copper electrodeposition is also non-volume conservative: copper electrodeposit films are usually annealed in boiling water to stabilize their mechanical and electrical properties.

## EXPERIMENTAL AND SIMULATION

In this paper, we investigate dynamic scaling behavior of copper growth in a  $\text{CuSO}_4$  solution at slow rates under stable growth conditions similar to those of standard electroplating [12,13]. Copper was electrodeposited on copper plates in an acid copper sulfate solution (  $0.30\text{M CuSO}_4 \cdot 5\text{H}_2\text{O}$  /  $1.2\text{M H}_2\text{SO}_4$  ). The copper plating bath was stirred with air bubbles during electrodeposition. Electrodeposition was carried out for various deposition time (1-60min) at room temperature at several current densities ( $1.2 - 4.8 \times 10^{-2}\text{A/cm}^2$ ). The current density of  $2.4 \times 10^{-2}\text{A/cm}^2$  corresponds to deposition rate of  $0.5\mu\text{m/min}$ . Some samples were grown in solutions containing  $0.5 - 10 \text{ ml/l}$  of organic additive "Copper Gleam PCM" as the brightener (a sulfonium-alkane-sulfonate-type additive [11], LeaRonald, NY). The standard concentration is  $5 - 10 \text{ ml/l}$ .

Atomic force microscopy (AFM) was employed to measure the roughness of the copper surface. AFM is capable of measurement of surface topograph not only with high-resolution but also for wide areas, and thus, is suitable for scaling analysis: the dynamic range of length scale is  $1\text{nm} \sim 100\mu\text{m}$ . The AFM measurements were carried out in air with constant-force of  $5.0 \times 10^{-9}\text{N}$ . We performed measurements on a variety of area sizes, i.e.,  $5 \times 5$ ,  $20 \times 20$ , and  $50 \times 50 \mu\text{m}^2$ . In each measurement, the height data were acquired at a resolution of  $256 \times 256$  or  $512 \times 512$  pixels. The interface width is calculated by

$$W(L) = \left[ \frac{1}{N(L)} \sum_{ij}^{N(L)} (h_{ij} - h_{av}(L))^2 \right]^{1/2}, \quad (4)$$

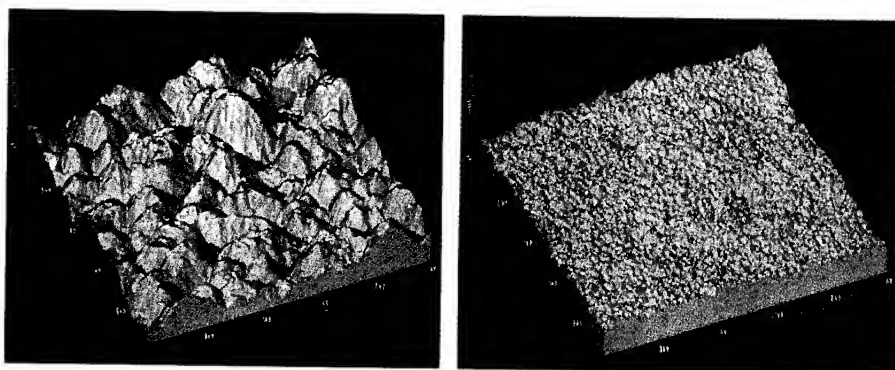
where  $N(L)$  is the total number of surface sites of a surface of size  $L$ ,  $h_{ij}$  is the distance of the  $i, j$  surface site from the substrate and  $h_{av}(L)$  is average over the surface of size  $L$ . For each measurement, we canceled the sample mounting error by putting the average over the whole measured area of  $h_{ij}$ , along the every  $i(j)$ -th line is equal [19]. A series of  $W(\text{measured size}/2^n)$  ( $n$ : integer) are calculated for the  $4^n$  divided surfaces of the whole surface for each measurement except for those for  $n=1-3$  which may be underestimated by the error canceling procedure.

Deposits are also grown by computer using the numerical solution method [20]: the KPZ terms and those with the additional term (eq.(2)) were solved numerically for  $256 \times 256$  lattice points [21].

## RESULTS AND DISCUSSIONS

Figure 1 (a) and (b) show  $50 \times 50 \mu\text{m}^2$  AFM topographs of the copper electrodeposits for the samples grown for 1 hour without and

with 10 ml/l organic additive, respectively. It is clear that the surface roughness depends strongly on the concentration of the organic additive; note that the vertical scale of Fig. 1 (b) is expanded by about 20 times than that of (a). In Fig. 1(a), humps of various heights and sizes are present.



(a)

(b)

Fig. 1 AFM topographs of the copper electrodeposits grown for 1 hour at  $2.4 \times 10^{-2} \text{ A/cm}^2$  : (a) without and (b) with 10 ml/l organic additive. The vertical scale is greatly expanded in (b).

Figure 2 shows the dependence of the surface width  $W$  on the size of the surface  $L$  calculated for several measured topographs of different sizes for the samples grown for 1 hour at  $2.4 \times 10^{-2} \text{ A/cm}^2$  with various additive concentrations.

It is clear from Fig. 2 that the copper electrodeposits exhibit two distinct scaling regimes depending on the concentrations of the organic additive; the roughness exponents have the smaller ( $0.6 \pm 0.05$ ) and the larger ( $0.87 \pm 0.05$ ) values for concentrations of the organic additive higher and lower than 1 ml/l, respectively. The scaling is universal in each regime for some range of additive concentrations.

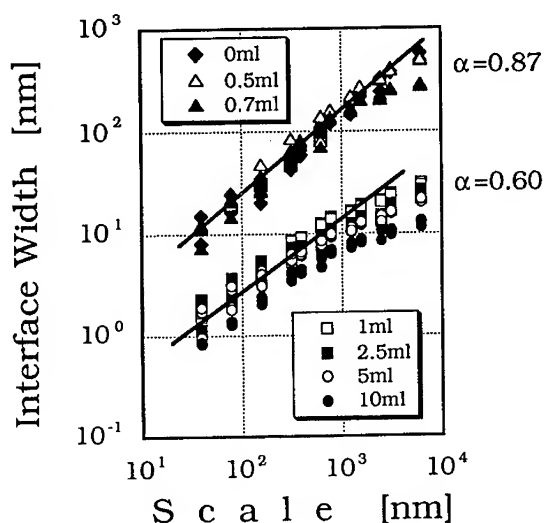


Fig. 2 Interface width  $W$  vs. surface size  $L$  for the samples grown for 1 hour at  $2.4 \times 10^{-2} \text{ A/cm}^2$  with various additive concentrations. Solid lines of slopes 0.6 and 0.87 are drawn as guides to the eye.

Figure 3 shows the interface width  $W(L, t)$  of electrodeposited copper for 1-60min at  $2.4 \times 10^{-2} \text{ A/cm}^2$  with no organic additive. The thickness varies from 0.5 to  $30 \mu\text{m}$  corresponding to electrodeposition time ranging from 1 to 60min. For each deposition time, the curve consists of two regimes separated by the correlation length  $L_c$ , i.e., the scale-dependent region and the saturated region. For  $L < L_c$ ,  $W$  increases as a power of  $L$ , and the roughness exponent  $\alpha$  is almost constant at  $0.87 \pm 0.05$  for all the surfaces measured. Furthermore, Fig. 3 clearly shows that the scaling in the shorter length regime is indeed stationary after an initial growth of about 1min. The interface width of the initial copper substrate was smaller than that of the deposits by several orders of magnitudes on the measured length scales.

The saturated value of the interface width,  $\Delta(t)$  ( $=W(L)$  for  $L \gg L_c$ ) increases as the deposit grows thicker:  $\Delta(t)$  depends on the deposition time  $t$  as  $t^\beta$  with the growth exponent  $\beta$  of  $0.45 \pm 0.05$  [6]. Thus,  $Z$  is found to be 1.93, which is much larger than 1.6 expected for KPZ model. The correlation length  $L_c$  increases in accordance with  $t^{1/2}$  although determination of  $L_c$  is somewhat ambiguous. For the present case,  $Z$  is smaller than but close to 2 and

thus the temporal spread of surface fluctuations  $L_c(t)$  is almost diffusive.

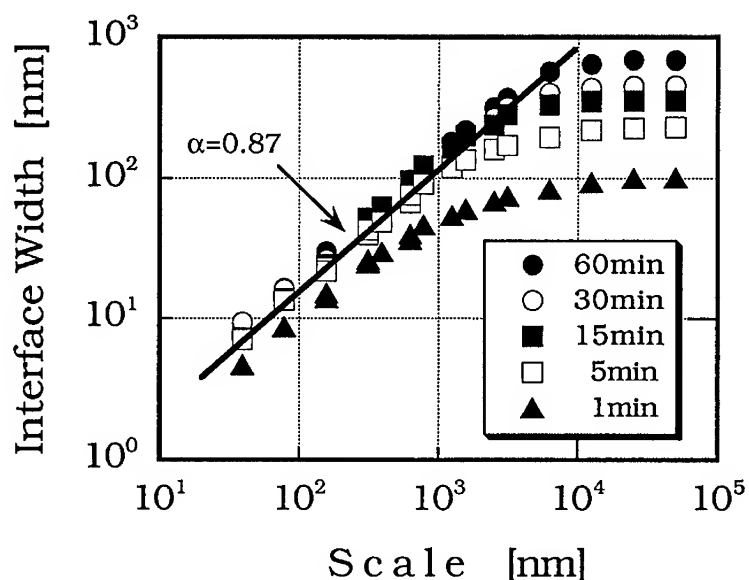


Fig. 3 The interface width of the copper electro-deposits  $W(L,t)$  versus length scale  $L$  for electrodeposits grown at  $2.4 \times 10^{-2} \text{ A/cm}^2$  with no organic additive for 1, 5, 15, 30, and 60min.

Figure 3 and the above result show clearly the two independent spatial and temporal scalings, shown by eq. (1) which was predicted by theory and simulation but until now lacked detailed experimental verification. Constant values of  $\alpha$  and  $\beta$  also imply that the growth process is governed by a single process for length scales from  $\sim 50 \text{ nm}$  to  $\sim 50 \mu\text{m}$  and deposition times from 5 to 60min. Perspective view images of the electrodeposited copper surfaces for 5, 30, and 60min with anisotropically rescaled vertical and horizontal dimensions ( $14 \times 14$ ,  $28 \times 28$ , and  $49 \times 49 \mu\text{m}^2$ , respectively) in accordance with the spatial and the temporal scaling exponents derived above do indeed look like similar as expected [6].

The scaling behavior with  $\alpha = 0.87$  was also observed for electrodeposition with conditions similar to those used for Fig. 3 but with a current density of  $1.2 \times 10^{-2} \text{ A/cm}^2$ . Growth in the solution with no organic additive became unstable at the current density of  $4.8 \times 10^{-2} \text{ A/cm}^2$ : bulk-fractal-like microstructures were formed for thicker films.

Now, let us compare the observed scaling behavior with computer

simulation [21]. Figure 4 (a) and (b) show topographs of KPZ (eq. (3)) computer grown deposits and that grown by KPZ + the term proportional to  $h(r)$  (eq. (2)), respectively. For simplicity,  $A$  is taken to be the whole a size. Figure 5 shows  $W(L,t)$  versus length scale  $L$  for the computer grown deposits shown in Fig. 4.

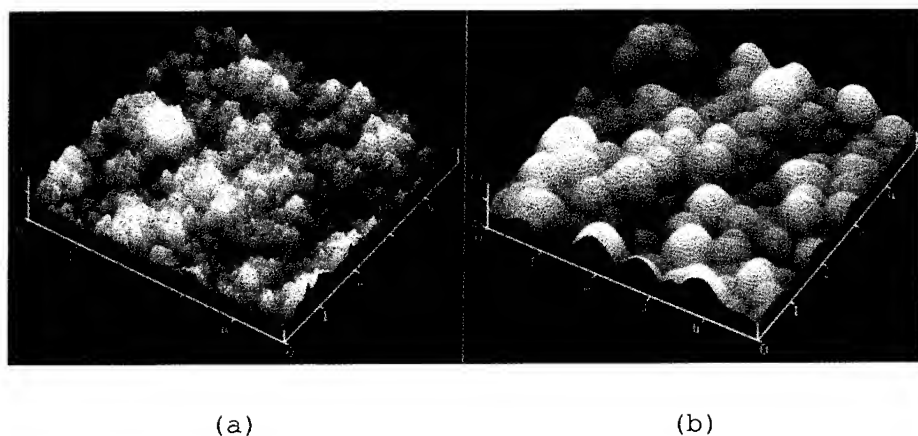


Fig. 4 Computer grown topographs by (a) KPZ and (b) by KPZ + (the growth term proportional to height).

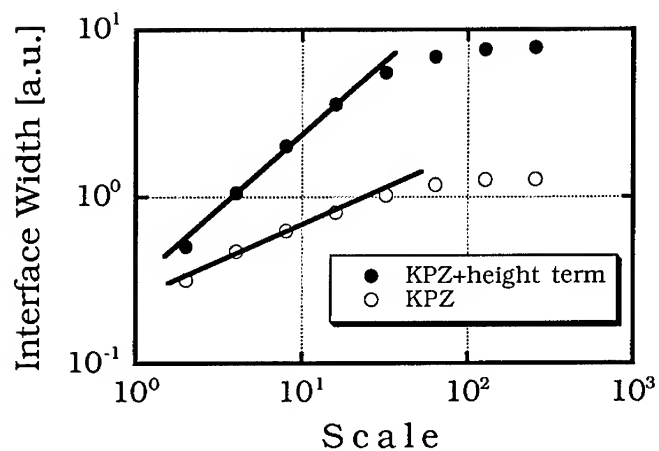


Fig. 5 The interface width  $W(L,t)$  of the computer grown deposits shown in Fig. 4 vs. length scale  $L$ . Solid lines of slopes 0.4 and 0.87 are drawn as guides to the eye.



In the case of KPZ growth, the value of the exponent  $\alpha$  is close to 0.4 [20] and is quite insensitive to the parameters such as surface energy and the exponent of the second term of the right hand side of eq. (3). In the case of KPZ + (the growth term proportional to height) growth, the surface morphology is KPZ like and the exponent  $\alpha$  is around 0.6 for a certain initial period and then humps emerge and the exponent jumps to about 0.85 and after that it increases slightly. It needs more detailed computations to see how the structures change after much longer times and depend on averaging area size. The rounded humps observed on copper electrochemical deposits with less organic additive look similar to the computer grown morphology.

The term proportional to height enhances vertical growth like auto-catalytic reaction: higher growth fronts makes those heights higher. Enhanced vertical growth of protrusions and successive lateral growth and surface energy induced rounding are considered to lead to the characteristic rounded humps of the rougher surfaces. Bifurcation of the surface morphology is understood as a result of decrease of weight of the additional term owing to increase of the additive. The critical condition of the bifurcation may be where height growth is smoothed out by surface energy and random noise before the auto-catalytic enhancement takes place.

#### SUMMARY

We investigated kinetic roughening of copper surfaces during stable electrochemical deposition. There were two distinct scaling regimes, the overall smoother surface with roughness exponent  $\alpha$  of 0.6 and the rougher one with  $0.87 \pm 0.05$  for the concentrations of the organic additive higher and lower than 1 ml/l, respectively. The exponent and surface topograph of the former surface were similar to those expected for KPZ model. For the rougher surface, the surface width scaled with length scale  $L$  as  $W \sim L^{0.87}$  for shorter length scales, and then saturated at the value which scaled with time as  $t^\beta$  ( $\beta = 0.45 \pm 0.05$ ). Formation of the smoother and the rougher surfaces were reproduced by numerical solutions of KPZ + (the growth term proportional to height) for the shorter and the longer growth times, respectively. The latter growth was characterized by survival of bigger particles as a result of non-local growth effects in addition to the local KPZ growth.

#### ACKNOWLEDGMENT

The authors acknowledge helpful discussions with E. D. Williams, N. Bartelt and N. Akutsu and J. Sato, H. Matsuda, and A. Ikeda at Asahi Chemical Industry Co. Ltd. This work was supported by a Grant-in-Aid for Scientific Research (contract No. 04452092) from the Ministry of Education, Science and Culture. One of the

authors (H. I.) received financial support from Yamada Science Foundation.

### References

1. F. Family and T. Vicsek, eds., Dynamics of Fractals Surfaces (World Scientific, Singapore, 1991).
2. J. Krug and H. Spohn, in Solids Far From Equilibrium: Growth, Morphology, and Defects, ed. C. Godreche (Cambridge University Press, Cambridge, 1990) pp. 479-582.
3. H. Iwasaki and T. Yoshinobu, Phase Transitions, to be published.
4. H. Iwasaki and T. Yoshinobu, Phys. Rev. B **48**, 8282 (1993).
5. G. L. M. K. S. Kahanda, X. Zou, R. Farrell, and P. Wong, Phys. Rev. Lett. **68**, 3741 (1992).
6. A. Iwamoto, T. Yoshinobu and Hiroshi Iwasaki, Phys. Rev. Lett. **72**, 4025 (1994).
7. R. M. Brady and R. C. Ball, Nature **309**, 225, (1984).
8. Y. Sawada, A. Dougherty, and J. P. Gollub, Phys. Rev. Lett. **56**, 1260, (1986).
9. T. C. Halsey, Phys. Rev. **A36**, 3512 (1987).
10. P. Garic, D. Barkey, E. B. Jacob, E. Bochner, N. Broxholm, B. Miller, B. Orr, and R. Zamir, Phys. Rev. Lett. **62**, 2703, (1989).
11. R. Haak, C. Ogden and D. Tench, Plat. and Surf. Finishing **69**, 62 (1982).
12. D. P. Barkey, R. H. Muller, and C. W. Tobias, J. Electrochem. Soc. **136**, 2199, (1989) and *ibid.*, **136**, 2207, (1989).
13. M. D. Pritzker and T. Z. Fahidy, Electrochim. Acta, **37**, 103, (1992).
14. W. W. Mullins and R. F. Sekerka, J. Appl. Phys. **34**, 323 (1963); **35**, 444 (1964).
15. In ref. [9], Halsey analyzed electrodeposition without convective transport and supporting electrolyte. Here we use Halsey's result with only replacing the separation distance of the electrodes by the boundary layer thickness.
16. M. Kardar, G. Parisi, and Y. C. Zhang, Phys. Rev. Lett. **56**, 889 (1986).
17. J. Villain, J. Phys. **11**, 19 (1991).
18. Y. L. He, H. N. Yang, T. M. Lu, and G. C. Wang, Phys. Rev. Lett. **69**, 3770 (1992).
19. T. Yoshinobu, A. Iwamoto and H. Iwasaki, Jpn. J. Appl. Phys. **33**, L67 (1994).
20. Jacques G. Amar and Fereydoon Family, Physical Review A, **41**, 6 (1990).
21. A. Iwamoto, K. Sudoh, T. Yoshinobu, and H. Iwasaki, unpublished.

## 2-D AND 3-D ELECTROCONVECTION, EXPERIMENTS AND MODELS.

V.FLEURY AND J.-N. CHAZALVIEL.

Laboratoire de Physique de la Matière Condensée,  
CNRS, Ecole Polytechnique, 91128 Palaiseau, France.

### INTRODUCTION.

In recent years, a lot of work has been devoted to electrochemical growth without supporting electrolyte<sup>1</sup>. A model, proposed by one of us<sup>2</sup>, predicts the existence of a positive space charge and of a large electric field in the active zones of the deposit. This leads to the existence of a coulombic force on the liquid. We show that this coulombic force triggers convective vortices in Hele-Shaw cells<sup>3,4</sup>, while it triggers vortex rings in three-dimensional cells<sup>5</sup>. We then couple the electrochemical process to the convective flow and show that, while the border between the depleted and concentrated zones has the shape of an arch in Hele-Shaw cells, it has a toroidal shape in 3-D. When many vortex rings are present, the border between the depleted and the concentrated solution is in the form of domes. We give experimental evidence of the vortex rings. (The original presentation was accompanied by a video movie which can be obtained upon request).

### I. THE HYDRODYNAMIC MODEL.

#### I.a Modeling the force.

In Chazalviel's model<sup>2</sup> (which does not include convection) a space charge forms in the vicinity of the active zones of the deposit. Whenever the deposit morphology is of filaments, the space charge is located around the tips, and it is translated with them during growth. For all practical purposes, the size of the space charge is very small, smaller than a few microns. Moreover, it has been shown that the effect of an incoming fluid flow is to reduce the size of the space charge<sup>4</sup>. Since the filaments thickness is generally larger than 100 microns, we may consider the space charge as point-like. Therefore, the force will appear in the Navier-Stokes equation as a delta-force. It can be shown that the total force is proportional to the local current at the tip, for a given size of the space charge.

#### I.b.Simplifying the fluid flow.

Starting from the Navier-Stokes equation

$$\frac{\partial \mathbf{v}}{\partial t} + \mathbf{v} \cdot \nabla \mathbf{v} = \nu \Delta \mathbf{v} + \frac{\mathbf{f}}{\rho} + \frac{1}{\rho} \text{grad} P \quad (1)$$

We consider the steady state only, and restrict ourselves to "creeping flows", so we simplify the N-S equation and consider only the Stokes equation<sup>7,8</sup>, with a delta force located in  $\mathbf{r}$  at an active tip, as explained earlier:

$$\nu \Delta \mathbf{v} = -\frac{f}{\rho \nu} \delta(\mathbf{r}) \mathbf{k} + \frac{1}{\rho} \mathbf{g} \text{grad} P \quad (2)$$

The geometry of the cell arises in the boundary conditions. We shall give solutions for filaments in Hele-Shaw cells, infinite media, and in a spherical cell.

## II. SOLUTIONS IN A HELE-SHAW CELL.

In a Hele-Shaw cell one can invoke the classical Poiseuille flow<sup>7,8</sup> and replace the 3-D speed by an average in the direction perpendicular to the cell, which becomes a 2-D vector  $\langle \mathbf{v} \rangle$  :

$$\mathbf{v}(x,y,z) = g(z) \langle \mathbf{v} \rangle(x,y) \quad \text{with} \quad g(z) = \frac{6}{s^2} z(s-z) \quad (3)$$

( $s$  is the spacing of the cell and  $\langle \mathbf{v} \rangle$  the average speed). Next, Laplacian of  $\langle \mathbf{v} \rangle$  decomposes into two terms:

$$\Delta \mathbf{v}(x,y,z) = g(z) \Delta \langle \mathbf{v} \rangle + \langle \mathbf{v} \rangle \frac{\partial^2 g(z)}{\partial z^2} \quad (4)$$

At this stage, one can neglect the laplacian in the plane, because, in the previous equation, it is clear that the variation of the fluid speed is much larger across the cell (it is zero on the plates and maximum midway) than in the plane of the cell.

### II.a Neglecting the laplacian in the plane.

From now on we note  $\mathbf{v}$  the 2-D vector  $\langle \mathbf{v} \rangle$ . If we neglect the Laplacian of  $\mathbf{v}$  in the plane, we have

$$\nu \text{curl} \mathbf{v}(x,y) = -\frac{s^2}{12\rho} \text{curl} f \quad (5)$$

This is basically the equation of an *irrotational* flow or, of a *potential* flow<sup>7,8</sup>. We can introduce the streamvector  $\underline{\Psi}$ , such that  $\underline{\Psi} = (0,0,\Psi(x,y))$ , and  $\mathbf{v} = \text{curl} \underline{\Psi}$ , and obtain the following equation for  $\Psi$  (here  $x$  is parallel to the electrode, and  $y$  to the filaments) :

$$\Delta \Psi = \frac{s^2}{12\rho \nu} f \frac{\partial \delta(r)}{\partial x} \quad (6)$$

The solution of this equation gives the stream function :

$$\Psi = \frac{1}{2\pi} \frac{s^2}{12\rho \nu} f \frac{x}{r^2} \quad (7)$$

The streamlines (constant-  $\Psi$  lines) corresponding to this flow are :

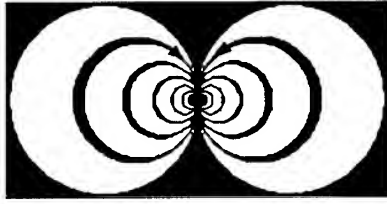


Figure 1. Streamlines near a tip carrying a point-like hydrodynamical force.

They correspond to a classical *vortex dipole*<sup>7,8</sup>. Different solutions can then be obtained, for different growth speeds or distributions of tips by linearly superimposing terms analogous to [7]

#### II.b Taking into account the laplacian in the plane.

Let us suppose that we do not neglect the Laplacian in the plane, *i.e.* that we wish to solve :

$$\Delta\omega - \frac{12}{s^2}\omega = -\frac{f}{\rho v} \partial_x \delta(\mathbf{r}) \quad (8)$$

where  $\omega$  is the vorticity. As we see, the main difference with the previous case is that the vorticity will no longer vanish everywhere, because of the laplacian term  $\Delta\omega$ . A simple integration gives :

$$\omega(\mathbf{r}) = \frac{f}{4\pi\rho v} x e^{-\sqrt{12}r/s} \left( \frac{1}{r^3} + \frac{\sqrt{12}}{sr^2} \right) \quad (9)$$

It corresponds to a fluid flow whose vorticity is not point-like, but spreads over a core of very small size, namely  $s/\sqrt{12}$ . This shows that the presence of glass plates, in the Hele-Shaw cell is responsible, *via* the parabolic distribution of the fluid speed, for the irrotational nature of the fluid flow, and for the corresponding vortices. If a more precise treatment (Eqs [8-9]) is given, one obtains a vorticity which is merely confined to a very small core. However, in 3-D, there are no glass plates, therefore, one should expect a quite different fluid flow.

### III. SOLUTIONS IN THREE DIMENSIONS.

We now wish to solve Eq. [2] inside a 3-D cell. In an infinite cell, a general transient solution is given by Phillips<sup>9</sup>, and also by Saffman<sup>10</sup>; it is of a *vortex ring* whose size increases like  $(vt)^{1/2}$ . This means that when one starts imparting a point-like force on a viscous liquid, one creates a vortex ring whose size increases (vorticity diffuses). Vortex rings are a classical and difficult topic in hydrodynamics<sup>9-19</sup>, especially considering viscous vortex rings. We shall not go into the intricacies and subtleties of this subject and give simply the steady-state fluid flow in

a spherical shell<sup>5</sup> :

$$\mathbf{v} = \frac{f}{4\pi\nu\rho} \left( xz \left[ \frac{1}{2R^3} - \frac{1}{2r^3} \right], yz \left[ \frac{1}{2R^3} - \frac{1}{2r^3} \right], -\frac{z^2}{4R^3} - \frac{z^2}{2r^3} - \frac{1}{2r} \right) \quad (10)$$

and the corresponding streamfunction is given by

$$\Psi \approx \frac{\gamma^2}{2(\gamma^2+z^2)^{1/2}} + \frac{z^2 \gamma^2}{4R^3} - \frac{3\gamma^2}{4R} + \frac{\gamma^4}{4R^3} \quad (11)$$

[with  $\gamma = (x^2+y^2)^{1/2}$ ,  $r = (x^2+y^2+z^2)^{1/2}$ ,  $R$ =radius of the sphere, and  $\rho$ =fluid density]

A picture of the streamlines is :

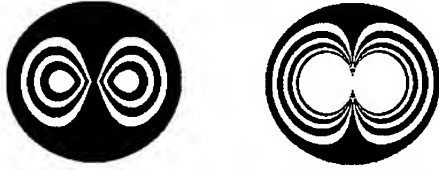


**Figure 2.** The streamlines generated by a point-like force in a spherical cell (left) and, for comparison, in a circular Hele-Shaw cell (right).

There is a remarkable difference between the 2-D and the 3-D case : the vortices do not merge at the tip in the 3-D case (Fig.2). The tip is point-like, but the streamlines do not go through the tip. Instead, there is a vortex ring with a *wide* hole. In principle, in an infinite medium, the hole size increases like  $(\nu t)^{1/2}$ . In a spherical or a cylindrical cell we expect that the hole of the vortex ring will be a fraction of the diameter of the cell, as it appears in Fig. 2.

If we considered a growing needle with growth speed  $V$ , in an infinite medium, the fluid speed, in a transient regime would be<sup>10</sup>

$$\mathbf{v} = \text{curl}(\psi) + \mathbf{V}, \quad \text{with } \psi = \left( \frac{\pi}{4\nu t} \right)^{3/2} e^{-r^2/4\nu t} \quad (12)$$

#### IV. COUPLING TO THE ECD PROCESS.

##### IV.a A Remark on the global motion of the vortices.

Let us first remark that in order to couple the fluid flow to the ECD process, one must invoke a set of tips growing at a constant speed, the recession speed of the anions<sup>2</sup>. Since the flow is oriented inwards at the tip, and since the tips move forward, we see that the vortex dipoles, in 2-D, and the vortex rings, in 3-D, move ahead, as a whole, with a translational speed which is oriented in the direction opposite to the flow direction at the tip. This is the opposite direction of the *natural* hydrodynamical direction<sup>8,10,16</sup>.

#### IV.b The concentration maps and the ionic motion.

Coupling the migration of the ions to the convective flow leads to the following picture<sup>3</sup> : anions are frozen, in the moving frame of the tips. Cations follow streamlines with a speed equal to  $(\mu_a + \mu_c)E$  where  $E$  is the local field. The border between the depleted and concentrated zone is a field line, in 2-D, and a stream surface, in 3-D. The depleted zone is found inside the vortices, and the concentrated zone is found ahead of the vortices, in the zone facing the bulk. The ions, therefore, do not penetrate inside the vortices.

Next, coupling *diffusion* to migration and advection shows that this border is "blurred". Therefore, the model predicts that, in 2-D, the border between the depleted and the concentrated zone should have the shape of a "blurred" arch, spanning vortices and linking active zones. This arch moves in the solution at a speed equal to the recession speed of the anions. It is already known that this picture is perfectly consistent with the observations<sup>3</sup>. In three dimensions, one must compose a set of vortex rings with a translational speed. The border between the depleted and the concentrated solution will have the shape of a torus, if there is only one branch, and the shape of a lattice of domes, if many vortex rings are present. These domes will be the stream surfaces spanning the circulatory zone, and linking the active zones. However, while the nip between vortices is infinitely small in 2-D (in principle), it is wide in 3-D and it would tend to increase with time (in an infinite medium).

#### **V. EXPERIMENTAL OBSERVATIONS.**

We have already amply reported observations of vortex pairs and arches in ECD<sup>3</sup>. These have been confirmed by several authors<sup>20,21,22</sup>. We report here on the first observation of vortex rings. These were obtained in capillary tubes (1mm in diameter), with a solution of copper sulphate 0.02 molar. An emulsion of oil droplets was used to see the stream. The growth was performed downwards, in order to reduce the effect of gravito-convection. The growth speeds were about 10microns per second. In these experiments, we repeatedly observed a well defined vortex ring moving downwards, as a whole. The convective motion was triggered by the electrochemical process at the tip of one single filament which was growing in the hole of the vortex ring (Fig. 3). However, the centre of the tube did not seem a perfectly stable growth zone. Hence, symmetrical and asymmetrical vortex rings were observed (Fig. 4). For higher growth speeds, several branches were observed in the tube (up to four or five), and generation of new vortex rings was observed, concomitantly with the formation of new branches. For very fast growth, the fluid flow seems turbulent, but the general trend is still that the fluid flow is inwards at tips.



**Figure 3.** Sequence of snapshots showing a roughly symmetrical vortex ring in a capillary tube. The interval between frames is 1second.

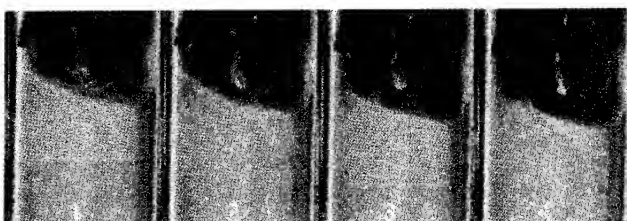


**Figure 4.** Sequence of snapshots showing a very asymmetrical vortex ring.

## CONCLUSION.

Electroconvection is a major process in electrochemical growth without supporting electrolyte, for concentrations below  $0.05\text{Mol.l}^{-1}$ . It couples to the migration and diffusion in a simple way when the fluid speed is slow, and it generates sharp borders between depleted and concentrated solution. It has been recognized that the vortex dipoles play a very important role in the pattern formation, in 2-D<sup>4-8</sup>. In 3-D, we have shown that vortex rings, predicted by theory, do exist. One should expect concentration boundaries (analogous to the arches), in the form of domes separating concentrated and depleted solution. The morphological consequences remain to be studied. It is a pleasure to thank M. Rosso for his support and interest in this work.

## REFERENCES.

- <sup>1</sup>V. Fleury, M. Rosso and J.-N. Chazalviel, these proceedings.
- <sup>2</sup>J.-N. Chazalviel, Phys. Rev. A **42**, 7355 (1990).
- <sup>3</sup>V. Fleury, M. Rosso and J.-N. Chazalviel, Phys. Rev. E **48**, 1279 (1993).
- <sup>4</sup>V. Fleury, J. H. Kaufman and D. B. Hibbert, Phys. Rev. E **48**, 3831 (1993).
- <sup>5</sup>V. Fleury, M. Rosso and J.-N. Chazalviel, submitted.
- <sup>6</sup>V. Fleury, J. H. Kaufman and D. B. Hibbert, Nature **367**, 435 (1994).
- <sup>7</sup>Arnold Sommerfeld, Mechanics of Deformable Bodies, Chapter IV.
- <sup>8</sup>Etienne Guyon, Jean-Pierre Hulin and Luc Petit, Hydrodynamique Physique, InterEditions/CNRS, 1991, (Paris).



- <sup>9</sup>O. M. Phillips, Proc. Camb. Phil. Soc. **52**, 135 (1954).
- <sup>10</sup>P. G. Saffman, Studies in Applied Mathematics **XLIX**, 371 (1970).
- <sup>11</sup>K. Shariff and A. Leonard, Vortex Rings, Ann. Rev. Fluid. Mech. **24**, 235 (1992), and references therein.
- <sup>12</sup>T. Maxworthy, J. Fluid. Mech., **51**, part I, 15 (1972).
- <sup>13</sup>Mahrung K., Proc. Ninth International Congress Appl. Mech. Brüssels, **1**, 173 (1957).
- <sup>14</sup>J. Norbury, J. Fluid. Mech. **57**, part 3, 417 (1973).
- <sup>15</sup>L.E. Fraenkel, J. Fluid. Mech. **51**, part I, 119 (1972).
- <sup>16</sup>A. Fetter, Phys. Rev. A **10**, 724 (1974).
- <sup>17</sup>T. Kambe, Journal of the Physical Society of Japan, **53**, 13 (1984). T. Kambe and U. Mya Oo, Journal of the Physical Society of Japan **53**, 2263 (1984).
- <sup>18</sup>T. Kambe and Y. Oshima, Journal of the Physical Society of Japan **38**, 271 (1975).
- <sup>19</sup>Cantwell and Rott, Phys. Fluids **31** (11) (1988).
- <sup>20</sup>D. Barkey, D. Watt, Z. Liu and S. Raber, J. Electrochem. Soc. **141**, 1206 (1994).
- <sup>21</sup>Mu Wang, Willem J.P. van Enkevort, Nai-ben Ming and Piet Bennema, Nature **367**, 438 (1994).
- <sup>22</sup>Z. Liu, PhD. dissertation, University of New Hampshire (1994).
- <sup>23</sup>A. Kuhn, PhD Dissertation, University of Bordeaux I (1994).

## PULSED ELECTRODEPOSITION OF TREE-LIKE COPPER AGGREGATES

Y. HUTTEL\*, E. CHASSAING\*\*, M. ROSSO\* AND B. SAPOVAL\*

\* Laboratoire de Physique de la Matière Condensée,  
CNRS-Ecole Polytechnique, 91128 Palaiseau, France

\*\* Centre d'Etudes de Chimie Métallurgique-CNRS,  
94407 VITRY-SUR-SEINE Cedex, France

### ABSTRACT

Using pulsating current technique, we have been able to grow self-sustained, tree-like copper aggregates with a length of a few mm. The size of these aggregates allowed us to perform impedance and scanning electron microscope analysis. The morphology of the aggregates is found to be more compact than for deposits obtained in fixed-current dc conditions. However, their structure is still very irregular, and depends on the parameters characterizing the pulse sequence.

### INTRODUCTION

Electrodeposition is well known to produce metal deposits with a large variety of morphologies. In the last decade, much attention has been paid to dendritic and filamentary growth in electrodeposition, in relation to the wide interest on diffusion limited aggregation (DLA)<sup>1</sup> and fractal structures.<sup>2</sup> Since the pioneer work<sup>3</sup> of Matsushita et al., and Brady and Ball, many authors have studied morphological and electrochemical aspects of what can be called fractal electrodeposition.<sup>4</sup> However, most of the obtained deposits had a very fragile structure, and evolved rapidly in time, both during and after deposition : as a consequence they could hardly be withdrawn from the electrolysis cell for further study, or for practical use. For example, when studying electrodeposited silver aggregates,<sup>5</sup> Kahanda and Tomkiewicz had to change the electrolyte before measuring the impedance of the deposits, and subsequently destroyed part of the aggregate.

Several methods have been proposed to grow stronger deposits: Hibbert and Melrose<sup>6,7</sup> have obtained copper deposits embedded in filter paper. Imre et al<sup>8</sup> have shown that it is possible to obtain a remarkably solid, although tree-like cobalt deposit, from a vigorously stirred electrolyte. Fleury<sup>9</sup> has obtained ultra-flat copper deposits, sticking to the surface of the glass plates.

Here we present an alternative method which takes advantage of the recent understanding of the steady-state electrodeposition process itself.<sup>4</sup> From these studies we know that the branches can only grow at their foremost part, because the electrolyte is depleted from ions in the region between the branches. However this is a dynamical effect : after the applied voltage is suppressed ions refill the depleted region by diffusion. Using this phenomenon we have been able to grow consolidated deposits with pulsed electrodeposition. The strength of the samples allowed ex-situ analysis.

### EXPERIMENTAL PROCEDURE

The experimental setup has been described elsewhere<sup>10</sup> : as in our previous experiments copper electrodeposits were obtained from copper sulfate aqueous solutions. In the present case we used solutions with concentration ranging from 0.1 to 0.5 M. The thin electrolyte layer is

sandwiched between two transparent plates. The electrodes were two parallel copper foils (0.1 to 0.5 mm thick, 80 mm long), 10 mm apart. A copper wire (of diameter 0.2 mm) located at a distance of 3-4 mm from the cathode was used as a reference electrode.

It is important to keep the cell in constant conditions during the electrodeposition process, which may last several hours. In particular evaporation of the electrolyte must be avoided. For this purpose, the cell was kept in a closed box, with an excess of electrolyte around it.

During the growth, we measured optical absorption of the electrolyte<sup>11</sup>; this gave access to the concentration maps around the deposits. Time evolution of the cell potential was used to monitor the deposition process.<sup>11</sup> In-situ impedance measurements were performed before electrodeposition, and at different stages of the deposition,<sup>10</sup> giving information on the transfer impedance at the interface of the deposit, and the serial resistance due to the electrolyte. These measurements allowed us to monitor the solution relaxation to homogeneity.

After removing the deposits from the cell, we could observe their structures, using standard optical and electronic microscopy. We also report on preliminary measurements of the crystallographic structure, and impedance spectroscopy of the different aggregates.

## EXPERIMENTAL RESULTS

Several authors have reported that, in standard experimental conditions, tree-like, fractal deposits partly dissolve after the growth has been stopped.<sup>12,13</sup> This dissolution might be due to the large electrochemical potential difference between the filaments and the solution (caused by the ions depletion around the deposit) just after the growth has been interrupted. A similar behavior has been found in our experiments<sup>10,14</sup>; it is illustrated in Fig. 1a-c. This may also partly explain the evolution of the in-situ impedance diagram after deposition. Mainly two different behaviors have been observed. For pure copper-sulfate solution, the impedance diagram eventually returns to its initial state (i.e. before electrodeposition): the impedance measurement does not "see" the deposit. The addition of dilute hydrochloric acid ( $5 \cdot 10^{-3}$  M), which was shown to impede copper oxidation, partly reduces this effect.

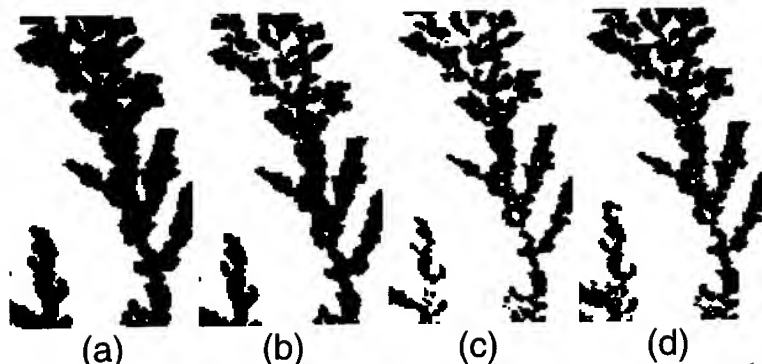


Fig. 1 Four pictures of a copper deposit, taken a) just after the deposit has been grown, b) 40 mn later, c) one day later, d) just after a second deposition. All pictures are approximately 4 mm long.

In fact, the above results show that the electrode formed by the deposit changes in time, and possibly disappears, due to dissolution and/or reorganization of the aggregate. This has been confirmed by a "second deposition" experiment: after a first electrodeposition is obtained, the cell is maintained either at zero voltage or zero current, for a time allowing complete homogenization

of the solution (from several minutes to a few hours, depending on the length of the deposit, electrolyte concentration, cell thickness...). The electrodeposition process is then restarted, under the same conditions as before. Surprisingly enough, the deposition does not start from the tips of the previous deposit, but from the cathode, growing along the old aggregate (Fig.1d). This results in a thickening and strengthening of the deposit.

Concentration profiles have been measured during this second deposition process (Fig.2a), showing that depletion seems uniform along the cathode, independently of the shape of the old deposit. This is very different from what is expected from an irregular electrode, where, due to enhancement of the electric field at the tips, one should observe maximum depletion around the largest protuberances.

We have repeated the above deposition sequence several times, and observed i) further thickening of the deposit and ii) a change in the concentration profiles (Fig.2b) to a situation closer to the expectation for an irregular electrode, i.e. a maximum depletion at the tip of the deposit.

Based on this effect we now propose a method for producing highly irregular, although solid metal deposits.

We have used a method consisting in growing the deposit very gradually, using the typical sequence of pulses shown in Table I. The time between two successive polarizations of the cell (noted relaxation time in Table I) is of the order of the minimum time required for homogenization. It is monitored by impedance and optical absorption measurements.

The sequence parameters were chosen to consolidate the already grown deposit and to simultaneously extend the aggregate length. Typically we deposited an amount of copper corresponding to several thousands of Coulombs per  $\text{cm}^2$  with a given current intensity and then increased the current intensity for the next polarisations. When needed we used some sequences with a lower current intensity to only consolidate the aggregates (see for example line 2 in Table I). We always limited the deposition time in order not to overpass the voltage corresponding to the onset of fast irregular deposition.<sup>11</sup>

Scanning electron microscopy, using secondary electron emission has been used to examine the deposits. A tree-like structure is observed at low magnification, showing crystalline faces at higher magnification (see Fig.3). Schematically we observed two different morphologies, related to the growth velocity conditions. For lower growth velocities (corresponding to high current densities), the deposits appear more compact, whereas for lower growth velocities, they appear more tenuous, with a powder-like structure.

Energy dispersive X-ray analysis shows that the deposits are pure copper. Some contamination by chlorine has been observed on some samples at the outer ends of the deposit (remember that the electrolyte contains dilute hydrochloric acid ( $5 \cdot 10^{-3}$  M)). X-ray diffraction has

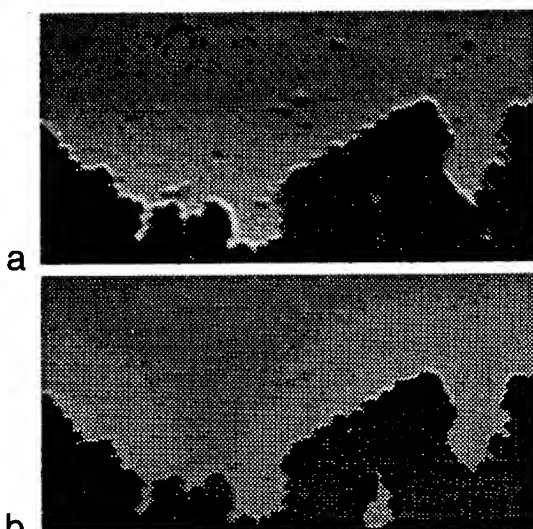


Fig.2 : Concentration maps around a deposit: a) during the second deposition, b) during the fourth deposition. The deposit is visible at the bottom of the pictures.

| Number of<br>Polarisations | Current<br>intensity (mA) | Total Polarisation<br>time (s) | Relaxation<br>time (s) |
|----------------------------|---------------------------|--------------------------------|------------------------|
| 1 (initial growth)         | 8.3                       | 100                            | 1100                   |
| 10                         | 6                         | 3000                           | 2100                   |
| 1                          | 7                         | 220                            | 2180                   |
| 1                          | 8                         | 150                            | 2250                   |
| 14                         | 10                        | 1600                           | 2300                   |
| 5                          | 11                        | 850                            | 1110                   |
| 25                         | 13                        | 3750                           | 2250                   |
| 21                         | 12                        | 3500                           | 2250                   |
| 11                         | 13                        | 1650                           | 2250                   |
| 1                          | 12                        | 150                            | 2250                   |
| 1                          | 13                        | 150                            | 2250                   |
| 21                         | 12                        | 4470                           | 2200                   |
| 3                          | 12.5                      | 1200                           | 2000                   |

Table I : A typical sequence of pulses used to grow a solid copper deposit. Copper sulfate concentration is 0.1 M. Cell thickness is 0.5 mm. The maximum voltage increase allowed during a polarisation was 0.7 V.

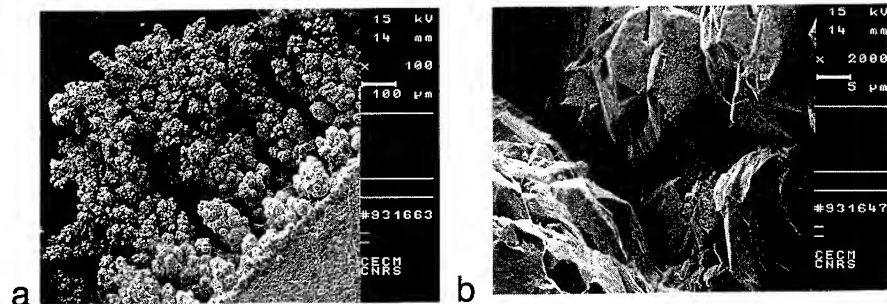


Fig. 3 : Electron micrographs of two copper deposits, at a) low and b) high magnification. Two different morphologies are clearly visible on the low magnification picture.

been carried out on parts of the deposit removed from the electrode. The diagrams exhibit the characteristic lines of the copper f.c.c. structure. We have observed no preferential orientation. The lattice parameter is equal to 0.3615 nm, i.e. that for standard copper, which indicates the absence of internal stress. The line broadening is low, indicating a particle size larger than 100 nm.

Impedance measurements have been recorded for different samples, both in-situ, and in a  $\text{Na}_2\text{SO}_4$  solution with concentration 0.2 M. In the latter case, impedance spectra were recorded in quasi-blocking conditions. Typical diagrams are shown in Fig.4, for the initial electrode, and for two different deposits samples 1 and 2. Both samples were grown with a total charge close to  $3 \times 10^6 \text{ C/cm}^2$ . The polarization sequence of sample 1 is given in table I; for sample 2 we used a similar sequence but with lower current density in order to increase the strength of the deposit. The diagrams of Fig.4 may be interpreted as follows<sup>15,16</sup> : At low enough frequencies, the total surface of the deposit participates in the impedance, and we find impedance ratios between the deposited and the naked electrode ranging from 100 (for sample 2) to 1000 (for sample 1).

Assuming that the impedance is simply proportionnal to the area of the electrode, these ratios reflect an increase of the electrodes areas up to a factor of 1000! At high frequency, the impedance

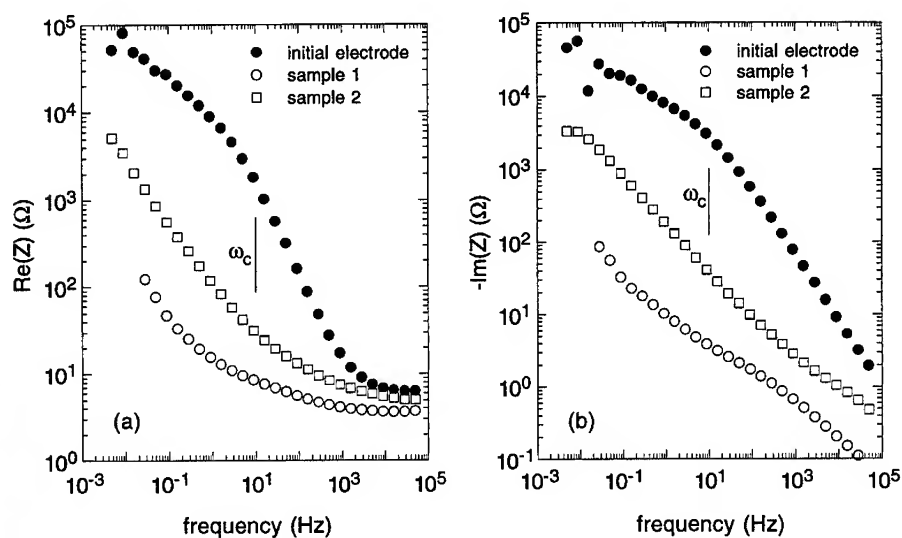


Fig. 4 : Real (a) and imaginary (b) parts of the impedance of the initial electrode (●), and of two samples, obtained for overall integrated currents of  $2.8 \times 10^6$  C/cm<sup>2</sup> (○) and  $3.1 \times 10^6$  C/cm<sup>2</sup> (□). At high frequencies the real part of the impedance reduces to the series impedance of the electrolyte.

is dominated by an active region of the deposit, which is only a part of the total surface, but still larger than its foremost part. Both the imaginary and the real parts of the deposit impedance are closer to the corresponding quantities obtained for the naked electrode. Assuming that the deposit is fractal, with fractal dimension  $D$ , the crossover frequency  $\omega_c$ , under which the overall surface of the deposit participates in the impedance may be evaluated from<sup>15,16</sup> :

$$\frac{1}{\rho\gamma\omega_c} = \ell \left( \frac{L}{\ell} \right)^{D-1} \quad (1)$$

where  $\rho$  is the resistivity of the solution,  $\gamma$  is the specific capacitance of the interface,  $\ell$  is the size of the individual grains,  $L$  is the size of the branches of the deposit. In the same fractal picture one can estimate the ratio of the deposit area  $S$  to the area  $s$  of the naked electrode from :

$$\frac{S}{s} = \left( \frac{L}{\ell} \right)^{D-2} \quad (2)$$

From (1) and (2) one simply obtains :

$$\frac{1}{\rho\gamma\omega_c} = L \frac{S}{s} \quad (3)$$

Relation (3) does not involve directly the fractal dimension. It corresponds to the fact that the admittance  $S\gamma\omega_c$  of the total surface at the crossover frequency  $\omega_c$  is equal to the admittance  $s/L\rho$ , measuring the access to this surface. This result is general and should apply even if the surface is

not a perfect fractal.<sup>17</sup> Taking  $L = 1\text{ mm}$ ,  $\rho = 40\ \Omega\text{cm}$ ,  $\gamma = 10^{-4}\text{F/cm}^2$  we find a value of the order of 10 Hz for the cross-over frequency (see Fig.4) : this is the order of magnitude of the frequency under which we observe that the impedance ratio between the naked and the deposited electrode is almost constant. This indicates that general arguments about the geometrical dependance of the impedance of irregular electrodes might apply to our objects.

## CONCLUSION

We have proposed a new method to grow self-sustained tree-like metal electrodeposits. This method should be applicable to various metals. The overall size of the deposit (a few mm in the present study) is only limited by the deposition time : fully three-dimensional aggregates with larger sizes might be obtained. The resulting deposits can be withdrawn from the cell where they are produced and further analysed. We have observed different morphologies, which appear to depend on the current density used for electrodeposition. Finally we have evidenced the very large surface area of these deposits, up to 1000 times larger than that of the initially flat electrode.

## ACKNOWLEDGEMENTS

We wish to thank J.-N. Chazalviel and V. Fleury for stimulating discussions.

## References

- 1 T.A. Witten and L.M. Sander, Phys. Rev. Lett. **47**, 1400 (1981).
- 2 B.B. Mandelbrot, The Fractal Geometry of Nature, (Freeman, San Francisco, 1982).
- 3 M. Matsushita, M. Sano, Y. Hayakawa, H. Honjo and Y. Sawada, Phys. Rev. Lett. **53**, 286 (1984) ; R.M. Brady and R.C. Ball, Nature, **309**, 225 (1984).
- 4 J.-N. Chazalviel, V. Fleury and M. Rosso, in Trends in Electrochemistry, p.231 (ed. by the Council of Research Integration, Research Trends, India, 1992), and references therein.
- 5 G.L.M.K.S. Kahanda and M. Tomkiewicz, J. Electrochem. Soc. **137**, 3423 (1990).
- 6 D.B. Hibbert and J.R. Melrose, Phys. Rev. **A38**, 1036 (1988).
- 7 J.R. Melrose and D.B. Hibbert, Phys. Rev. **A40**, 1727 (1989).
- 8 A. Imre, Z. Vértessy, T. Pajkossy and L. Nyikos, Fractals **1**, 59 (1993).
- 9 V. Fleury, J. Mater. Res. **6**, 1169 (1991).
- 10 E. Chassaing, M. Rosso, B. Sapoval, and J.-N. Chazalviel, Electrochimica Acta **38**, 1941 (1993).
- 11 M. Rosso, J.-N. Chazalviel, V. Fleury and E. Chassaing, Electrochimica Acta **39**, 507 (1994).
- 12 J.R. Melrose and D.B. Hibbert, in Fractal aspects of materials, ed. by J.H. Kaufman, J.E. Martin and P.W. Schmidt, Mat. Res. Soc. Extended Abstracts, p.257 (1989).
- 13 Y. Deng and M. Pritzker, J. Electroanal. Chem. **336**, 25 (1992).
- 14 M. Rosso, V. Fleury, J.-N. Chazalviel, B. Sapoval and E. Chassaing, in Fractal structure and dynamics, ed. by J.P. Stokes and M.O. Robins, Mat. Res. Soc. Extended Abstracts, p.245 (1990).
- 15 B. Sapoval, R. Gutfraind, P. Meakin, M. Keddad and H. Takenouti, Phys. Rev. **E48**, 3333 (1993).
- 16 E. Chassaing and B. Sapoval, J. Electrochem. Soc. **141**, 2711 (1994).
- 17 B. Sapoval, Phys. Rev. Lett., in print.

## RECENT PROGRESS IN ELECTROCHEMICAL DEPOSITION WITHOUT SUPPORTING ELECTROLYTE

V. FLEURY, M. ROSSO and J.-N. CHAZALVIEL  
Laboratoire de Physique de la Matière Condensée,  
CNRS, Ecole Polytechnique, Palaiseau, France.

### I. INTRODUCTION.

Electrochemical deposition (ECD) of metals is a very old subject[1], which has considerable applications in the context of electroshaping or electroplating. Electrochemists and chemical engineers have long known the different growth conditions of these metal aggregates and the different parameters which drive morphological changes, at least empirically[2-4]. However, in the recent years, after the introduction of the concept of fractal aggregation[5,6], in the field of non-linear pattern formation[7,8], a lot of work has been devoted to the specific problem of growth of electrodeposits from binary electrolytes [9-51] (*i.e.* without supporting electrolyte). These studies aimed at understanding the morphology, on the large scale ( $\sim 1\text{cm}$ ) of the deposits and, more specifically, the transitions between morphologies. It is the aim of this paper to review the progress which has been achieved in the past five years on this question.

In section II, we recall the motivation for the study, from a fundamental point of view, of the electrochemical growth of deposits, and the questions raised by the first studies aiming at observing the fractal structure of these deposits.

In Section III, we explain the electrochemical features which come into play, and explain briefly the model proposed by one of us to describe the ionic motion and the electric field in the vicinity of a growing deposit. We review the experimental evidence which corroborates a number of predictions of this model. However, the inability of the model to describe correctly the concentration maps leads to the introduction of convection through electroconvection and natural convection. These are discussed theoretically and experimentally in Section IV.

We turn to morphological issues in section V, and distinguish between macroscopic and microscopic phenomena. The macroscopic phenomena refer to morphological changes on a scale larger than the thickness of the cell (generally about  $50\text{-}200\mu\text{m}$ ). We explain how the transport mechanisms, electroconvection, natural convection, interaction between branches or other phenomena, can explain the existence of different morphologies, and, to some extent, observed transitions. The microscopic phenomena refer to modifications of the grain morphology on the  $1\text{-}1000\text{nm}$  scale, generally due to contaminants or pH modifications, or both.

### II. PATTERN FORMATION BACKGROUND.

Growth of complicated structures, rough, porous or branched is very common in nature, and has been extensively studied since the introduction of the concept of fractal by Benoît Mandelbrot[52]. Especially, the branched structures have received a lot of attention after the work of Witten and Sander[53]. The latter authors have shown that a simple aggregation of random walkers leads to branched fractals with a fractal dimension 1.7 in 2-D. Very rapidly, it has been recognized that different systems exhibit, in the limit where growth is driven by a laplacian potential, a fractal branched structure which can be related to the DLA model. These systems can be grouped into the "DLA universality class". It has been proposed by Matsushita et al[9] that ECD could serve as one example of laplacian growth. In ECD, a metal cluster grows on a cathode of an electrochemical cell (filled with a solution of a salt of a metal) by aggregation of metal ions which are reduced when they arrive on the surface of the cathode, or of the deposit. It was believed that, at least in some limit, the growth was driven by the electrochemical potential in the bulk, which itself was considered



as laplacian, in a first and quite crude approximation. Early work[9-12] showed that, indeed, complex branched structures could be obtained by this simple experiment. However, many different morphologies were observed, apart from seemingly fractal patterns. This is not surprising since a laplacian limit exists only very far in the slow growth regime. In principle, the growth is diffusion limited for potential differences between electrodes smaller than 25mV. Above that, the electrochemical problem is rather involved, and one cannot argue that the electric potential is laplacian, nor that the concentrations are constant. For high growth speeds (up to  $\sim 100 \mu\text{m.s}^{-1}$ ), one would typically find[10-12] dendritic patterns, dense branched, "comb-like" patterns, filaments etc.... Some "morphological diagrams" were proposed[11,12,26,42], which reveal themselves as idiosyncratic since the same systems studied by different groups give different or even contradictory results. Clearly, the experiments are hardly reproducible, though general trends can be identified : more branched structures at low growth speeds, regular "combs" at higher growth speeds, macroscopic crystalline dendrites for some metals, no such dendrites for copper, and a clear effect of the cell thickness : more compact patterns for larger gaps. Lots of empirical observations were made which can hardly be reviewed here. Let us mention, however, that sharp morphological changes during single runs, taking place at some fraction of the distance between electrodes, were repeatedly observed[7] by independent groups.

In the last decade, a flurry[9-51] of work has been devoted to ECD. Progressively, the view on ECD has considerably changed, and one understands more clearly now what are the actual phenomena involved : migration and diffusion of the ions, electroconvection, and natural convection around a growing interface. Moreover, it has been recognized that microscopic effects linked to the presence of contaminants, or to genuine changes in electrochemical parameters (such as current density or concentration) play an important role. In particular, the sharp changes of morphology observed in single runs were shown to be provoked by contaminants[20,25], and also, by convective changes during growth[41,51]. It is clear now that ECD without supporting electrolyte is very far from a DLA growth system. However, in the limit of very slow growth, it is reasonable to expect fractal DLA-like structures, and these have indeed been observed[9].

### III. ECD WITHOUT CONVECTION.

After the discovery of different morphologies in ECD, it was realized that this kind of growth (referred to as "dendritic" or as "runaway growth" in standard electrochemistry) had received so far only modest attention. Chazalviel has proposed a model of growth[16] which takes into account the transport of both ion species in the solution by migration and diffusion. The transport equations are :

$$\partial C_c / \partial t = D_c \Delta C_c - \mu_c E \cdot \text{grad} C_c - \mu_c C_c \text{div} E \quad (1)$$

$$\partial C_a / \partial t = D_a \Delta C_a + \mu_a E \cdot \text{grad} C_a + \mu_a C_a \text{div} E \quad (2)$$

[Where D's are diffusion constants, C's concentrations and  $\mu$ 's mobilities, the subscript a stands for anion and the subscript c stands for cation.  $z_c$  and  $z_a$  are the charge numbers of the cations and of the anions respectively. E is the electric field, -e the charge of the electron and  $\epsilon$  the dielectric constant of the solvent].

They are coupled to the Poisson equation :

$$\text{div} E = e(z_c C_c - z_a C_a) / \epsilon \epsilon_0 \quad (3)$$

and they must be solved around a moving boundary. One immediately observes that the problem is much more complicated than a DLA process, because there are three coupled fields : cation and anion concentration, in addition to the electric potential. In this model convection and surface effects are neglected. This model has been solved on different geometries and it leads to the conclusion that unusually large space charges are formed in the active zones of the deposit[16]. If the deposit is in the form of filaments, then the tips of the

filaments carry an excess of positive charge which is translated while the tip grows (Fig. 1).

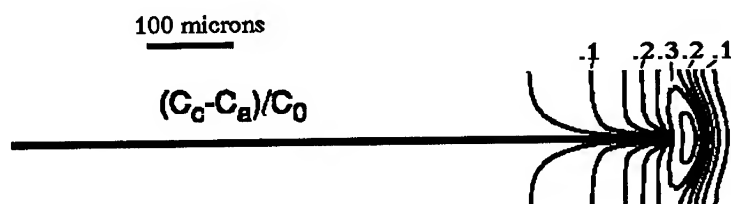


**Figure 1.** The excess of positive charges in the vicinity of a comb-like deposit. The cathode is far to the right, and the bulk electrolyte far to the left. The deposit is represented by a straight bar. There is a space charge surrounding the active zone. (from ref. 16).

The model predicts that the growth speed of the deposit is the migration speed of the *anions*. The growth speed, in fact, adjusts itself so that the space charge in the active zone does not increase arbitrarily. Another prediction of the model is that the mass in the deposit is simply proportional to the mass of metal in an equivalent volume of bulk electrolyte with a factor  $(1 + \mu_c/\mu_a)$ . This mass does not depend on how fast the deposit is actually grown. The model contains only one adjustable parameter: the potential across the active zone, which is related to the microscopic instabilities of the interface. Melrose and Hibbert[25], arrive independently, by conservation arguments, to the same conclusion concerning the growth speed. The predictions of this model have been extensively tested. Potential measurements in the vicinity of the tips showed that a local and very sharp potential does indeed take place in the vicinity of the tips[19,49]. By varying the electric field, the cell geometry and the salt formula, the growth speed was shown to be quite accurately given by the recession speed of the anions[17,19,25,33,42,48]. It was even proposed that this kind of experiment could serve to measure ion mobilities[19,39]. The mass of the deposit was shown to be related by  $(1 + \mu_c/\mu_a)$  to the concentration in the bulk of the electrolyte[17-19,49].

Measurements of the concentration in the vicinity of the electrode before the onset of branch growth (when convection is negligible) compared quite accurately to the predictions[29,30] (Fig. 2).

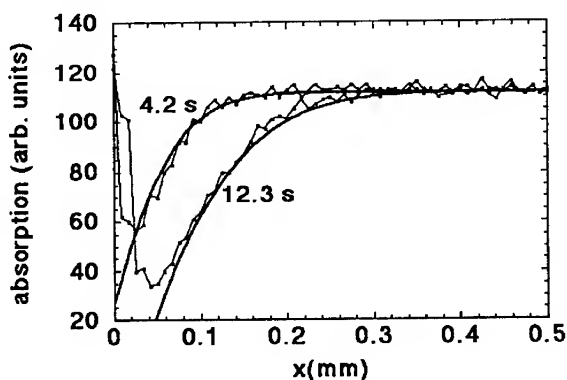


**Figure 2.** Concentration near the cathode (experiment and theory), before the onset of branched growth, in a gelled electrolyte (from ref.29). The agreement between the model and the observations is excellent.

However, measurements around actual branches were very different from what predicted by

the model[18,29,34]. For example, Barkey[34] had observed sharp concentration borders emanating from the deposits or from the anode, whose shape and sharpness could hardly be understood quantitatively. In a different experiment, Fleury et al. had observed that the border between the depleted and the concentrated zones has the shape of arches linking the active parts of the deposits[18,29], which disagrees with the model even qualitatively. It proved necessary to introduce convection in the model. This is explained in the next section.

#### IV. CONVECTIVE EFFECTS.

##### IV.a Electroconvection.

When a charged fluid is submitted to an electric field, a coulombic force is imparted on the fluid which can trigger a convective motion. It turns out that the concomitant existence of a positive charge near the deposit (Fig.1) and of a large electric field creates such a coulombic force on the fluid. As a result, an electroconvective motion of the fluid may start. In the case of growth of rather thin and sharp filaments, the coulombic force is located in a very narrow region around the tip, and the force density acting on the fluid is almost singular. The shape of the convective motion, near a filament, can be obtained rather simply[27,28]. The fluid flow consists of contra-rotating vortices which flow inwards at tips. In a Hele-Shaw cell, the vortices are irrotational[45,54,55], and models predict the existence of pairs of vortices (vortex dipoles) hooked to the active tips. A given tip grows in the nip between the two vortices which are found at its apex. In three dimensions, models predict the formation of vortex rings[44,45,56,57], and the tips grow in the holes of the vortex rings.

When several branches are present, the model predicts the existence of arrays of vortex dipoles, in 2-D (Fig. 3).

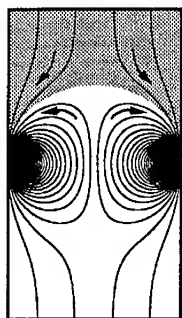


**Figure 3.** The vortices between two filaments in the moving frame of the growing deposit. Because of the assumption of Poiseuille flow, the flow is irrotational (the vorticity vanishes everywhere except at tips). As a consequence, the vortices are classical potential vortices, and classical vortex dipoles are hooked at each active tip.

The vortices define a zone where the liquid circulates. Ahead of it lies a zone where the liquid is almost translated. The borderline between the two zones is a streamline which has the shape of an arch. When the ECD process Eqs.(1-3) is coupled to the convective pattern, one infers that, in the steady state, the ions cannot penetrate inside the vortices. In the moving frame, the ions are frozen, and the cations are transported towards the tips through the "funnels" which are formed by the nips between the vortices. Since the anions are frozen, and since the cations migrate in an opposite direction, one can show that the actual speed of the cations is equal to  $(\mu_a + \mu_c)E(r)$ , itself equal to  $v(r).(1 + \mu_c/\mu_a)$ , where  $E(r)$  and  $v(r)$  are the local electric field and fluid speed. The model then predicts formation of a border between the concentrated and the depleted solution which follows the shape of the arch spanning pairs of vortices. The vortices are depleted, and the electrolyte ahead of the tips is concentrated. This picture is entirely consistent with the observations (Figs. 4 and 5).

**Figure 4:** Image of the gradient of the concentration map showing the border between the concentrated and the depleted solution. As predicted by the model, this border has the shape of an arch.

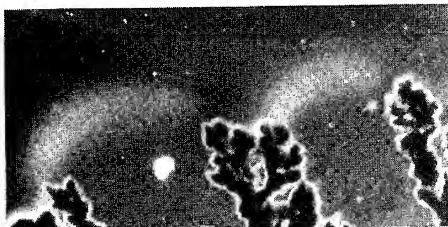
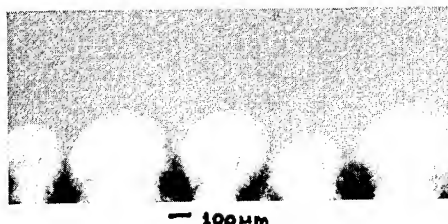


**Figure 5.** Image of the vortices, obtained with an emulsion of oil. The vortices appear lighter in color. The streamline which spans the vortices is clearly visible.



Quantitative analyses have shown that the concentration map compares very well to the prediction[28,29]. The fluid speed is also fairly well described by a slightly more refined model in which the branch is not infinitely thin[51]. The model is easily extended to three dimensions, where it predicts vortex rings. These have been experimentally observed in capillary tubes[44,45]. In this instance, the border between the depleted and the concentrated solution should have the shape of a "doughnut".

#### IV.b Natural convection.

It turns out that, for concentrations above  $0.05 \text{ mole.l}^{-1}$  and cell thickness  $0.1 \text{ mm}$ , approximately, natural convection becomes stronger than electroconvection. The buoyant flow is entirely different from the electroconvective flow. While the electrochemical process generates a charge near the active zones, it also depletes the electrolyte (near the cathode, or as shown in Fig.1, around a filament)). As a consequence, density gradients are formed. The concentration difference between the depleted and the concentrated solution is at most, near the cathode, of  $C(\text{bulk})$ . This induces a density contrast of a few percent, which is sufficient to trigger a motion of the electrolyte. (Mind that in Rayleigh-Bénard convection, the density contrast between the top-cold and the bottom-hot plates is at most of a few percent). Depending on the orientation of the cell, plumes or gravity currents[29,35,41,45,50,51,58,59] can be observed. Actually, the concentration gradients form on both ends of the cell (cathodic and anodic), density contrasts are similar, so natural convection is equally present at the anodic and cathodic ends. It turns out that the fluid motion can be modeled analytically around a flat electrode, or around a filamentary deposit.

##### IV.b.1 Gravity current along a flat electrode.

In this instance, one can refer to existing hydrodynamical models which relate the shape and speed of gravity currents to the relevant parameters : fluid viscosity, density contrast between the depleted and the concentrated liquid and cell geometry. The hydrodynamical situation is schematically as follows : the electrochemical process depletes the electrolyte at a constant rate which is proportional to the current flowing through the cell. The depleted electrolyte, close to the electrode, is lighter than the bulk electrolyte, so it starts flowing over the bulk electrolyte while bulk electrolyte flows below the lighter electrolyte and towards the electrode where deposition of metal occurs (Fig. 6).

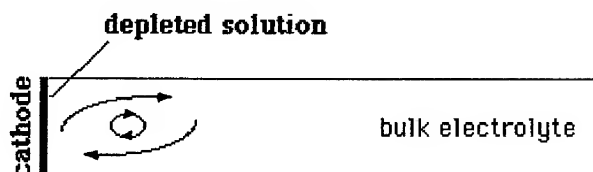


**Figure 6.** Scheme of the natural convection near the cathode, when the cell is horizontal. The depleted solution flows over the concentrated solution.

A convective roll called a gravity current forms[58,59], which progressively invades the cell. The position of the gravity current as a function of time, when diffusion is neglected is given by Huppert[59] :  $L(t) = 1.13[(g\Delta\rho/\rho\eta)(v_a d)^3]^{1/5} t^{4/5}$  where  $\eta$  is the viscosity,  $d$  the cell thickness,  $v_a$  the speed of the anions,  $g$  the acceleration due to gravity and  $\Delta\rho/\rho$  the relative density contrast between the bulk electrolyte and the depleted solution.

Comparison with experiments show that the speed of the gravity current compares well with experiments for very fast growth and short times only. The hydrodynamical model, which is already involved, neglects interdiffusion of the depleted and concentrated electrolyte. Since the cell thickness is only about 100 microns and since the diffusion constants are about  $10^{-5} \text{ cm}^2 \cdot \text{s}^{-1}$  it is clear that diffusion will play a role after a few tens of seconds. If one takes into account diffusion, one finds[60] a different convective regime, slower than the previous one :  $L(t) = 0.2x [(g\Delta\rho/\rho\eta)(v_a)(d^4/\sqrt{D})]^{1/3} t^{1/2}$ . (where  $D$  is the ambipolar diffusion constant).

So far, the known evidence is compatible with these results though no comprehensive study of the gravity current has been published yet[29,35,41,48,50,51].

#### IV.b.2 Gravity currents around filaments.

The gravity current is rather easy to study along the anode, or along the cathode. However, after a short induction time, the deposit starts growing, and the convective pattern will interact with the growth. Since the distance grown by the deposit is proportional to  $t$ , while the distance of the gravity current is proportional to  $t^{4/5}$  at first, and to  $t^{1/2}$  later on, the deposit generally catches up the gravity current. After overcoming the gravity current, a deposit in the form of a filament (or of a dendrite) generates a novel convective pattern which is of two rolls of varying size on each side of the deposit. In steady state the size of the roll is zero at the tip, then it is proportional to  $L^{4/5}$  at a small distance  $L$  from the tip, and it is proportional to  $L^{1/2}$  far in the back. The overall shape of the "boundary layer" which is created in this way by natural convection is entirely consistent with the shapes first reported by Barkey[34] (Fig. 7): the straight filaments are surrounded by some sort of a well defined envelope. Envelopes emanating from different dendrites or filaments collapse on each other leaving a sharp line in between branches which correspond to merging gravity currents.

**Figure 7.** Observation of gravity currents around sharp dendrites (courtesy of D. Barkey). The lighter liquid flows away from the active zone. The gravity current embodies the dendrite in a seemingly parabolic "boundary layer".



Let us remark that natural convection can also be observed in 3-D experiments[46,44,45]. In that instance, a deposit can be found to grow facing an incoming flow driven by the depleted electrolyte which flows upwards. Let us also mention that the shape of the natural convection clearly depends on the orientation of the cell. When performing the growth vertically from top to bottom, electroconvection can be recovered in instances where natural convection is otherwise observed[29,34].

## V. MORPHOLOGICAL ASPECTS.

Morphology is what mostly interested early researches in this field. However, very little could be extrapolated from DLA models to actual ECD, because DLA was one limit only of ECD. Now that the transport and the growth mechanisms are better understood, morphological issues can, to some extent, be addressed.

### V.a Morphology in the simplest electrochemical model.

Chazalviel's model[16], which incorporates diffusion and migration only, already addresses the morphological aspects. It is clear from this model that a potential barrier is generated by space charges against the penetration of the ions between existing branches. As a consequence, the DLA model is recovered in the limit of very slow growth only. When the growth speed is increased, branching in the back of the active tip is less possible, and a more compact deposit is formed, which has a comb-like structure. The distance between teeth is given by

$$b \sim (\pi/5)(\delta V/E)[1 + (e\delta V/5kT) \cdot (1 + \mu_c/\mu_a) \cdot z_c z_a / (z_c + z_a)]^{-1/2} \quad (4)$$

Where  $\delta V$  is the potential drop across the space charge region, and  $E$  the field in the bulk. This model may apply in instances where convection is suppressed. However, as shown before, convection is present in most experimental conditions, and new morphological consequences arise.

### V.b Effect of electroconvection.

A couple of morphological consequences of electroconvection are rather simple to understand. First of all, the very shape of the vortex dipoles (Fig. 3) enhances forward growth, because the inner part of the vortices, and hence the sides of the branches, are depleted. It is not surprising that filamentary structures are observed, and that branching never occurs by side-branching but, in the presence of vortices, by tip-splitting only. Tip-splitting itself can occur only via the concomitant formation of a new pair of vortices in the active zone. It has been shown[32] that this is only possible at moderate growth speeds. Indeed, the early steps of the tip-splitting proceed through a "pitchfork" opening of the active zone. The electrochemical process and the fluid flow imparts a torque on this "pitchfork". If the growth speed is too fast, there is a symmetry breaking of the tip-splitting and, instead of generating two symmetrical vortices, the electrochemical process forces one of the tips to grasp the existing vortex dipole while the other tip is pushed aside in the depleted zone where it stops growing. Therefore, one expects a transition from ramified to bare filaments when the growth speed is increased. This transition is observed[32].

Next, when both tip-splitting and side-branching are almost impossible, one observes growth of regular "comb-like" deposits, which can be found in the literature as "dense parallel morphology", or "cellular growth" or "channel growth". The question remains of how the distance  $b$  between the "teeth" is determined. We tentatively propose the following argument. If one assumes that above a certain Reynolds number  $R$ , of order 1, the turbulence in the active zone is responsible for the morphological transitions, then one can infer the distance between branches by writing that the fluid speed  $v$  in the active zone is approximately  $v \sim \mu_a E \cdot (b/d)$  where  $d$  is the spacing of the cell, and that  $v \cdot b/v \sim 1$  which implies  $b \sim (d \cdot v / \mu_a E)^{1/2}$ . This expression for the distance between branches gives a good order of

magnitude and it does show the correct trends : the distance between branches decreases with increasing growth speed and decreasing cell thickness. Though a systematic study of this question has not been performed yet, it is admitted by many authors[28,32,35,36] that hydrodynamics is what drives the morphology, in this régime.

#### V.c. Natural convection.

Natural convection has a clear effect on morphology, since experiments performed in different orientations may lead to different morphologies [35]. Experimental results show that natural convection overcomes electroconvection for concentrations above  $0.05\text{mol.l}^{-1}$  (when horizontal cells are used). One then enters in a new mode of growth, whose effect on the overall morphology of the deposit is not well known yet. It has been proposed by several authors [31,36,51] that an inward flow of concentrated electrolyte reduces the growth speed through different mechanisms : a change in actual fluxes, and a change in the size of the space charge which drives the instabilities in the active zone. It has indeed been observed that the deposit grows more slowly in an incoming fluid flow, especially of gravitational origin. The morphological consequences are twofold. The local effect of a natural convection is to slow down the most active tips, since the fluid flow is faster there. Also, the global effect of natural convection is to homogenize the solution, so to bring concentrated electrolyte from the concentrated to the depleted zones, where growth may continue. As a consequence, in instances where natural convection is strong, one may expect more compact deposits. Though the actual mechanisms are not clear and though other causes may contribute to the same effect, it is an overall trend of the ECD process that more compact deposits are observed for more concentrated solutions and thicker cell. Sagues et al[2], Pochy et al[23] and Kuhn and Argoul[51] show very clear evidence that increasing the cell thickness induces more compact growth.

#### V.d Physical displacements.

While morphological changes may occur through changes of the growth speed along the active zone, one should keep in mind that physical displacements of the deposit can provoke morphological changes too. It has already been shown that physical displacements in the active zone are responsible for the symmetry breaking of the tip, and hence, for the hindrance of tip-splitting. But there also exist macroscopic translations of branches in the solution via two mechanisms : fluid advection and electrostatic interaction. It is a well known fact in hydrodynamics[45,54,57], that distributions of vortices induce on a given vortex a global speed equal to the speed imparted by all the other vortices. As a consequence, an irregular distribution of vortices provokes physical displacements of a given vortex or of a given vortex dipole, which is oriented from the more active zones towards the less active ones. This is a stabilizing effect. Also, the active tips carry electrostatic dipoles, which are formed by the excess of positive charges on the liquid side and the excess of electrons on the metal side. Therefore there exists a dipole-dipole interaction between tips, which, again, is oriented from the active zones towards the less active zones. This too, is a stabilizing effect. If one starts a growth from a "saw tooth electrode" one observes that the holes in the electrode are healed by macroscopic displacements of the branches. A branch which finds itself on the edge of such a hole feels a maximum force, since there is no branch on one side to compensate the force imparted by the branches located on the other side. One clearly observes, in such instances, rotations of the branches which can reach  $90^\circ$ . This kind of non-linear healing of large gaps is also observed when a deposit grows around a hydrogen bubble, for example (though capillary phenomena may contribute to the same effect).

#### V.e Microscopic phenomena

Standard electrochemical deposition is well known to provide a realm of morphologies which depend on physical-chemical properties of the deposits and of the electrolyte. As a matter of fact, study of the morphology of deposits is the most active part of electrodeposition. Also, the role of contaminants is very actively studied in chemical

engineering, where it plays an essential role in different technical instances. As pointed out by Dini[3] : "the results [on growth] obtained with additives seem to be out of proportion to their concentration in the solution" and, quoting Lashmore : "electrodeposition is the science of poisoning; one needs to do something to inhibit the growth of dendrites". While the transport mechanisms, in electrochemical deposition without supporting electrolyte, are entirely different from the ones in standard electrochemistry, the surface phenomena are essentially the same. Therefore, it is not surprising that contaminants play an important role in the morphology of the deposits which are discussed here.

As a matter of fact, some sudden morphological changes during deposition had been observed by many authors[7,61], in even the simplest experimental conditions. It seemed that the deposit was first of one morphological kind and that, after crossing some invisible line in the solution, it started to be of a different sort. The change in morphology could be really considerable (for example, from rough to crystalline). It has been shown by Melrose and Hibbert[25], and also by Fleury et al[20], that the morphological changes are merely due to migration of protons and of contaminants from the anode towards the cathode. Three different things may happen : (i) the solution can become contaminated by the dissolution of the anode. A front of cationic impurities may arrive on the deposit which will thereafter grow in a "dirty" solution, or conversely (ii) contaminants can be removed from the solution by the electric field, so that the deposit will first grow in a "dirty" solution and next in a purer solution. Also (iii), a sharp change in pH may migrate into the solution under the influence of the electric field. In all instances, one expects sudden morphological changes after crossing the border between the two solutions. Extensive analytical and experimental evidence have shown that this is the correct explanation of the changes in morphology observed during growth (known as Hecker-effect). Since then, different authors have evidenced different morphological changes[41,42,51], by considering different impurities, or salts. Especially, Kuhn and Argoul have shown that oxygen is one of the impurities which plays a role in zinc deposition[51], a fact which is also known in the case of copper, in standard electrodeposition[4].

Let us mention also that since growth kinetics is linked to convective flows, the morphology of the deposit may change when the convective flow changes. Especially, the morphology of the deposit may change[41,51] after meeting a gravity current emanating from the anode.

It must be said that, though the effect of impurities has been recognized, there is so far no clear and well established mechanism able to explain their actual consequences, and it is very daring to relate morphological changes due to impurities to known models of pattern formation. It is clear, for example, that impurities are able to change considerably the properties of different crystal facets (especially exchange currents) therefore modifying the anisotropy of the surface kinetics. Since surface anisotropy is one of the most important issues in pattern formation of well defined dendrites[8,7,62], it does not come as a surprise that additives can drive the system from one morphology to another. Still, this question remains largely unsolved. One must keep in mind that growth generally starts on a subset of a few favorable sites where adsorption energies are lowered. However, the very same mechanisms which allow growth on these sites allow adsorption of impurities there too. Therefore, additives will play a considerable role, even in low concentrations.

## VII. CONCLUSION.

In recent years, considerable progress has been achieved in electrochemical deposition without supporting electrolyte. By focusing on the transport of ions in the bulk, it has proved possible to sort out all the possible transport mechanisms, and to largely quantify the different effects. The coupling to the morphology remains a complex problem, especially in view of the tremendous role played by contaminants. The surface kinetics is certainly one of the most important issues in pattern formation of electrochemical deposits. It can be forecasted that additives play a role in surface anisotropy, that this role will be understood in the near future, and probably related to existing models of dendritic growth. However, additives may provoke astounding morphological changes for which a theoretical framework remains to be found. Now that the transport mechanisms in the bulk are well understood, it is probable that the surface kinetics will receive much more attention in the near future, both



experimentally and theoretically.

## REFERENCES

- <sup>1</sup>S. Sheldon and G. M. Downing, *Phys. Rev.* **1** (1) 51 (1893). This reference shows that morphological aspects were addressed in very early work on electrochemical deposition.
- <sup>2</sup>J. O.'M. Bockris and K. N. Reddy, *Modern Electrochemistry* Plenum/Rosetta New York(1977) .
- <sup>3</sup>Jack W. Dini, *Electrodeposition*, Noyes Publications (New Jersey, USA) (1992).
- <sup>4</sup>P. Ramasany, in *Handbook of crystal growth* **1a**, C. J. Hurler editor, North Holland, (1993).
- <sup>5</sup>NATO ASI Series **100** (1986): *On Growth and Form*, and **157** (1989): *Random Fluctuations and Pattern Growth*, Edited by Gene Stanley and Nicole Ostrowsky. Martinus Nijhoff Publishers, Kluwer Academic Publishers Group (Boston).
- <sup>6</sup>Tamas Vicsek , *Fractal Growth Phenomena*, World Scientific (Singapore), Second Edition (1992) and references therein.
- <sup>7</sup>Eshel Ben-Jacob and Peter Garik, *Nature* **343**, 523 (1990).
- <sup>8</sup>P. Pelcé, *Dynamics of curved fronts*, Academic Press (London, 1991), and references therein.
- <sup>9</sup>M. Matsushita, M. Sano, Y. Hayakawa, H. Honjo and Y. Sawada, *Phys. Rev. Lett.* **53**, 286 (1984).
- <sup>10</sup>Y. Sawada, A. Dougherty, and J. P. Gollub, *Phys. Rev. Lett.* **56**, 1260 (1986).
- <sup>11</sup>D. Grier, E. Ben-Jacob, R. Clarke and L. M. Sander, *Phys. Rev. Lett.* **56**, 2315 (1986).
- <sup>12</sup>D. G. Grier, E. Ben-Jacob, R. Clarke and L. M. Sander, *Phys. Rev. Lett.* **56**, 1264 (1986) and David G. Grier and Daniel Mueh, *Phys. Rev. E* **48**, 3841 (1993).
- <sup>13</sup>F. Argoul, A. Arneodo, G. Grasseau and H. L. Swinney, *Phys. Rev. Lett.* **61**, 2558 (1988).
- <sup>14</sup>D. B. Hibbert and J. R. Melrose, *Phys. Rev. A* **38**, 1036-1048, (1988).
- <sup>15</sup>J. R. Melrose and D. B. Hibbert, *Proc. R. Soc. Lond. A* **423**, 149, (1989).
- <sup>16</sup>J.-N. Chazalviel, *Phys. Rev. A* **42**, 7355 (1990).
- <sup>17</sup>V. Fleury, J.-N. Chazalviel, M. Rosso and B. Sapoval, *J. Electroanal. Chem.* **290**, 249 (1990).
- <sup>18</sup>V. Fleury, J.-N. Chazalviel, M. Rosso, and B. Sapoval, *Ann. Chim. Fr.* **16**, 143 (1991).
- <sup>19</sup>V. Fleury, M. Rosso, J.-N. Chazalviel, and B. Sapoval, *Phys. Rev. A* **44**, 6693 (1991).
- <sup>20</sup>V. Fleury, M. Rosso and J.-N. Chazalviel, *Phys. Rev. A* **43**, 6908 (1991).
- <sup>21</sup>G.L.M.K.S. Kahanda and M. Tomkiewicz, *J. Electrochem. Soc.* **136**, (1989).
- <sup>22</sup>L. Lam, R. D. Pochy and V. M. Castillo, in *Non-linear Structures in Physical Systems*, eds. L. Lam and H. C. Morris (Springer, New York, 1990).
- <sup>23</sup>R. D. Pochy, A. Garcia, R. D. Freimuth, V. M. Castillo and L. Lam, *Physica D* **51** 539, (1991).
- <sup>24</sup>M. Matsushita, Experimental Observation of Aggregations, *The Fractal Approach to Heterogeneous Chemistry*, Edited by D. Avnir, John Wiley & Sons Ltd, 1989.
- <sup>25</sup>J. R. Melrose, D.B. Hibbert and R. C. Ball, *Phys. Rev. Lett.* **65**, 3009 (1990).
- <sup>26</sup>P. P. Trigueros, J. Claret, F. M. Mas and F. Sagués, *J. Electroanal. Chem.* **328**, 165 (1992) and *J. Electroanal. Chem.* **312**, 219 (1991).
- <sup>27</sup>V. Fleury, M. Rosso and J.-N. Chazalviel, *Phys. Rev. Lett.* **68**, 2492, (1992).
- <sup>28</sup>V. Fleury, M. Rosso and J.-N. Chazalviel, *Phys. Rev. E* **48**, 1279 (1993).
- <sup>29</sup>M. Rosso, J.-N. Chazalviel, V. Fleury, and E. Chassaing, *Electrochimica Acta* **39**, 507-515 (1994).
- <sup>30</sup>R.H. Cork, D.C. Pritchard and W.Y. Tam, *Phys. Rev. A* **44**, 6940 (1991).
- <sup>31</sup>V. Fleury, J. H. Kaufman and D. B. Hibbert, *Phys. Rev. E* **48**, 3831, (1993).
- <sup>32</sup>V. Fleury, J. H. Kaufman and D. B. Hibbert, *Nature* **367**, 435 (1994).
- <sup>33</sup>D. Barkey, P. Garik, E. Ben-Jacob, B. Miller and B. Orr, *J. Electrochem. Soc.* **139**, (1992).
- <sup>34</sup>D. Barkey, *J. Electrochem. Soc.* **138**, 2912 (1991).
- <sup>35</sup>D. Barkey, D. Watt, Z. Liu and S. Raber, *J. Electrochem. Soc.* **141**, 1206(1994).

- 36 Mu Wang, Willem J.P. van Enkevort, Nai-ben Ming and Piet Bennema, *Nature*, **367** 438-441 (1994).
- 37 S.Okubo, I. Mogi and Y. Nakagawa, *Sci. Rep. Ritu, A* **38** 383-390 (1993) and I. Mogi, S.Okubo and Y.Nakagawa, *Journal of Crystal Growth* **128** 258-261 North Holland Elsevier (1993).
- 38 P. Garik, J. Hetrick, B. Orr, D. Barkey and E. Ben-Jacob, *Phys. Rev. Lett.* **66**, 1606 (1991).
- 39 A. Kuhn and F. Argoul, *Phys. Rev. E* **49**, 4298 (1994).
- 40 A. Kuhn and F. Argoul, *Fractals* **1**, 451 (1993),
- 41 Argoul, Kuhn and Arneodo, to appear in *J. Electrochem Soc.* and to appear in *Physica A*.
- 42 P. Trigueros, F. Sagues and J. Claret, *Phys. Rev. E* **49**, 4328 (1994).
- 43 G. P. Luo, Z. M. Ai, Z. H. Lu and Y. Wei, *Phys. Rev. E* **50**, 409 (1994).
- 44 V. Fleury, M. Rosso and J.-N. Chazalviel, in preparation.
- 45 V. Fleury, M. Rosso and J.-N. Chazalviel, proceedings of the 1994 Materials Week of the Metals, Minerals and Metals Society (Rosemont), Harish Merchant Editor.
- 46 P. Carro, S. L. Marchiano, A. Hernandez Creus, S. Gonzalez, R. C. Salvarezza and A. J. Arvia, *Phys. Rev. E* **48**, R2374 (1993).
- 47 R. Bruinsma and S. Alexander, *J. chem. Phys.* **92**, 3074 (1990).
- 48 K. Linehan and J. de Bruyn, to appear in *Canadian Journal of Physics* (1994).
- 49 V. Fleury, PhD dissertation, Ecole Polytechnique, (1991).
- 50 Z. Liu, PhD dissertation, University of New Hampshire, (1994).
- 51 A. Kuhn, PhD dissertation, University of Bordeaux I, (1994).
- 52 Benoit Mandelbrot, *Fractals: Form, Chance and dimension*, Freeman (San Francisco, 1977).
- 53 T.A. Witten and L.M.Sander, *Phys. Rev. Lett* **47**, 440 (1981).
- 54 Arnold Sommerfeld, *Mechanics of Deformable Bodies*, Chapter IV.
- 55 E. Guyon, J.-P. Hulin and L. Petit, *Hydrodynamique Physique*, InterEditions/CNRS, 1991, (Paris).
- 56 O. M. Phillips, *Proc. Camb. Phil. Soc.* **52**, 135 (1954).
- 57 P. G. Saffman, *Studies in Applied Mathematics XLIX*, 371 (1970).
- 58 John E. Simpson, *Gravity Currents*, Ellis Howood (1987).
- 59 H. E. Huppert, *J. Fluid. Mech.* **121**, 43 (1982).
- 60 J.-N. Chazalviel, in preparation.
- 61 The so-called "Hecker effect" seems to have been observed independently by several authors, including Lui Lam and the eponymous Nancy Hecker. As a matter of fact, images of inhomogeneous deposits exhibiting transitions lines can be found in the literature, and the effect of impurities is so ordinary in electrochemistry that it had not received a specific name.
- 62 *Handbook of crystal growth* **1**. C. J. Hurler Editor, North Holland (1993).

## FORMATION OF SELF-AFFINE SURFACE DURING THE GROWTH OF NICKEL THIN FILMS

M.V.H. RAO, V. SRINIVAS, B.K. MATHUR and K.L. CHOPRA  
Department of Physics and Meteorology, Indian Institute of Technology,  
Kharagpur 721 302.

### ABSTRACT

Thin films of nickel deposited on various substrates have been investigated by using an STM. Topographic data recorded at different stages of the film growth reveal that the surface structure at one location of the film resemble that at another location of the same film. The repetitive structures are made up of a few coalescing clusters and forming exactly similar looking islands. As the film thickness increases, the shape and size of these repetitive patterns changes but the self-affinity of the surface structure is maintained.

### INTRODUCTION

The general physical structure of a thin film has been classified [1] into three distinct structure zones (SZ) as a function of reduced temperature  $T/T_m$  where  $T$  is the substrate temperature and  $T_m$  is the melting point of the material in question. The first zone creates a structure of tapered columns with domed tops and is in a region of low adatom mobility. In the second zone, the film structure is of straight columnar nature and has a smooth surface morphology while in zone three the physical structure resembles small crystallites. This classification has been further improved upon by taking into account two new parameters viz., the sputtering gas pressure [2] and the film thickness [3]. The evolutionary SZ model [3] considers the growth evolution of physical structure under low adatom mobility conditions ( $T/T_m < 0.5$ ). These SZ models are found to be applicable to a wide range of materials [4-8] and also appears to be independent of the deposition process. This indicates that the surface structure at one location of the film should resemble that at another location of the same film. This kind of self-similarity in the structural evolution, and universality in the physical structure points toward a common origin of thin film growth. All the previous observations of thin film structure are done with either SEM or TEM and the structure patterns are of columnar type. STM is an ideal tool to observe the thin film physical structures and also to verify these SZ models.

Existence of self-similarity in the surface structure suggests that in the initial stages of growth we should expect certain repetitive patterns in the surface morphology. The nature, size and shape of the repetitive structure are dependent on the growth parameters and the substrate material. To verify these expectations, nickel, which has a high melting point, thereby low adatom mobility at room temperature, has been used in the present investigation.

## EXPERIMENTAL

Nickel films of 100, 200 and 500 Å nominal thicknesses are deposited on different substrates of silicon and mica. The films are deposited on substrates kept at room temperature by electron beam evaporation (LEYBOLD AG, UNIVEX 300) at a base pressure of  $2 \times 10^{-6}$  mbar. The deposition rate is monitored at 0.5 Å/sec by a thickness monitor. The silicon wafers are etched in hydrofluoric acid and then rinsed in water and ethanol. Mica substrates are prepared by freshly cleaving in air and immediately mounted in the evaporation unit.

The surface topographic data was recorded using STM (RHK Technology Inc.) in the atmospheric conditions. The STM images were taken with electrochemically etched tungsten tip [9] with a bias voltage of 400 mV and 0.5 nA tunneling current in the topographic mode. Exposure of the thin film surface to air during STM imaging, a few monolayers of adsorbed gasses may be present on the surface. However, with a proper sample bias tunneling can still occur through the adsorbed layers and the effect on tunneling current is expected to be uniform all over the film surface. For the metals used in the present study large topographic features are not expected to be influenced by surface contamination due to atmospheric exposure. In fact, in related papers on STM imaging by ionic conduction through condensed water films, Yuan et al. [10] concluded that the local forces and pressures developed within a condensed layer of fluid cannot give rise to sample deformation during imaging. Thus, the topographic data collected by operating STM in constant current mode represents the true surface profile.

## OBSERVATIONS & DISCUSSIONS

Nickel films deposited on silicon and mica are observed to have certain interesting topographic features. It is observed that nickel follows a specific type of growth pattern on each one of these substrates which is indicated by a specific growth structure that repeats itself at each one of the nucleation centers. It may be an indication of self-similarity exhibited by thin film physical structures, and may answer the question raised by Yehoda and Messier [11].

Fig.1 shows growth islands made up of 3-4 coalescing clusters but forming exactly similar looking islands in a 100 Å nickel film on silicon. Such islands are seen over a large area. As thickness increases these 2D islands develop into structures of similar size and shape. The repetitive growth structure persists with increasing film thickness and has taken a definite shape at around 500 Å as shown in fig.2. The images show a repetitive physical structure of exactly same size and shape - even down to finer details - formed at different locations.

In fig.3 repetitive physical structure observed on a much smaller scale on a 200 Å thin film on silicon is shown. Fig.3a shows several grains of similar shape and size that have formed at various locations. Fig.3b shows a single such grain with its fine structure. The structures look exactly similar even down to nanometric scale and are stacked one over the other. Thin films of nickel of thickness 100 Å on mica also showed similar repetitive structures (fig.4) of very small size (~5 nm).

In order to visualize the nature of the surface profile, we carried out fractal characterization of the surfaces in terms of the scaling exponent  $H$ . In the steady state, the surface is a scale-invariant self-affine fractal [12]. If one rescales the surface by a factor of  $b$  in the horizontal direction the surface must be rescaled by a factor of  $b^H$  in the direction perpendicular to the surface in order to observe the similarity between

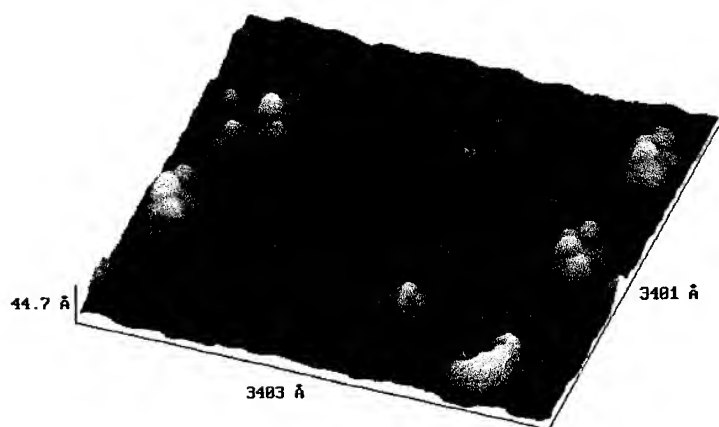


FIGURE 1. Development of 2D islands into thin film growth structures of similar size and shape on a 100 Å nickel film on silicon.

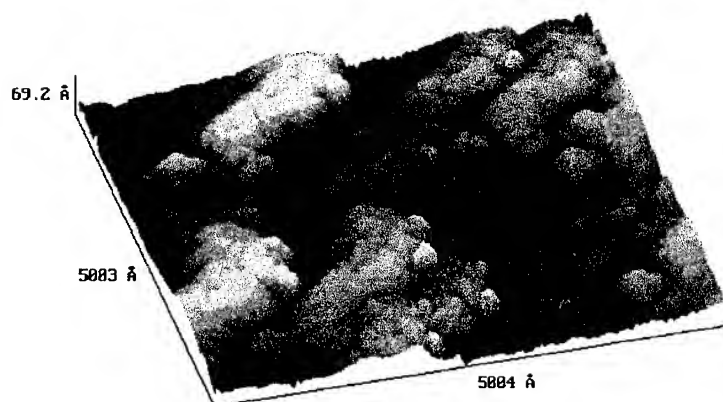
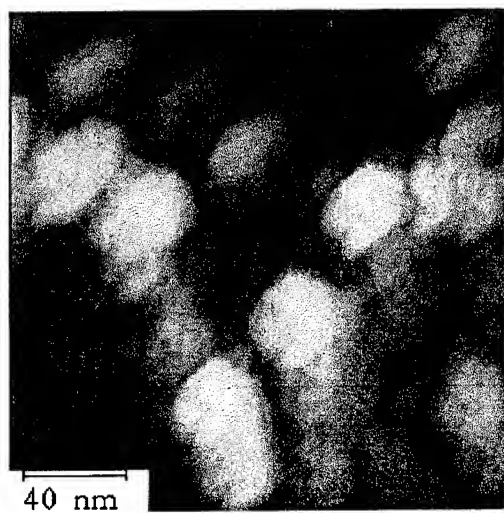


FIGURE 2. Surface Morphology of 500 Å thick nickel films on silicon substrates. The images show a repetitive physical structures of exactly same size and shape formed at different locations.

(a)



(b)

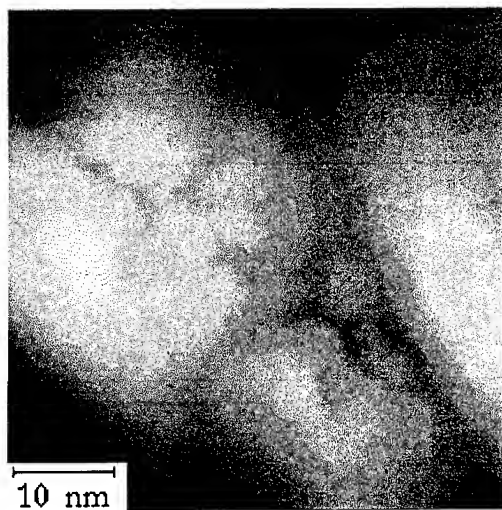


FIGURE 3 Repetitive physical structure observed on a much smaller scale on a 200 Å thin film on silicon. (a) shows a single grain shape and size has formed at several locations. (b) shows a single such grain with its fine structure.

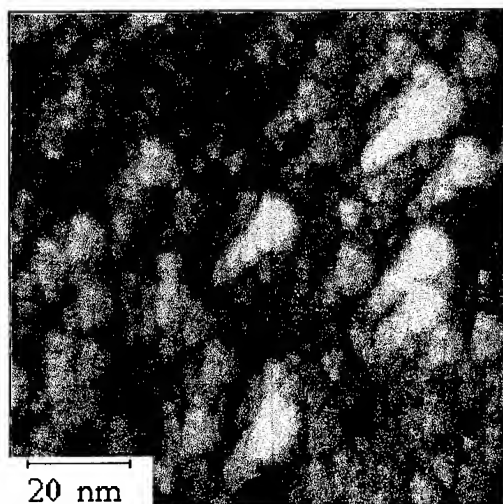


FIGURE 4. Repetitive patterns of very small size ( $\sim 5$  nm) observed on  $100 \text{ \AA}$  film on mica.

the original and the rescaled surfaces.

The mean-height-difference method of determination of scaling exponent [13] is reported to be the most accurate and a direct procedure. Using this method, films of different thicknesses have been analyzed and it is observed that the scaling exponent decreases from 0.8 to 0.6 as the film thickness increases from  $100 \text{ \AA}$  to  $500 \text{ \AA}$ , which is in direct correlation with the surface roughness.

A possible explanation for the formation of these structures is as follows. If the substrate surface has several nucleation centers having exactly similar physical, chemical and electronic structure and these are exposed to a deposit vapor under similar conditions, then one would expect the nucleation and growth of the vapor atoms at and around those nucleation centers to be exactly same. The significant part of this observation is that such repetitive structures are present up to a thickness range of  $200 \text{ \AA}$  indicating the influence of substrate nucleation centers on the growth of the deposit matter.

Repetitive physical structures of different sizes and shapes have been observed on nickel thin films on silicon and mica. The formation of such structures in film growth may be an indication of order in a seemingly random process.

## REFERENCES

1. B.A. Movchan and A.V. Demchishin. Phys. Metals Metallogr. **28**, 83 (1969).
2. J.A. Thornton, Ann. Rev. Mater. Sci. **7**, 239 (1977).
3. R. Messier, A.P. Giri, and R.A. Roy, J. Vac. Sci. Technol. A **2** (1984).
4. R. Messier, and R.C. Ross, J. Appl. Phys. **59**, 6220 (1982).
5. R.A. Roy, and R. Messier, J. Vac. Sci. Technol. A **2**, 312 (1984).
6. S. Nakahara, Thin Solid Films, **64**, 149 (1979).
7. Y. Murayama, J. Vacuum Sci. Technol. **12**, 818 (1975).
8. S.V. Krishnaswamy, R. Messier, Y.G. Ng, T.T. Tsong, and S.B. McLane, J. Non-Cryst. Solids **35/36**, 531 (1980).
9. M. V. H. Rao and B. K. Mathur, Ind. J. Pure & Appl. Phys. **31**, 574 (1993).
10. J.Y. Yuan, Z. Shao and C. Gao, Phys. Rev. Lett. **67**, 863 (1991); **68**, 2564 (1992)
11. Joseph. E. Yehoda, and Russell Messier, Appl. Surf. Sci. **22/23**, 590 (1985).
12. B. B. Mandelbrot, Fractal Geometry of Nature (Freeman, San Francisco, 1982).
13. M.V.H. Rao, B.K. Mathur and K.L. Chopra, Appl. Phys. Lett. **65**, 1 (1994).



---

## PART IV

---

### **Disordered Materials: Percolation and Porous Media**

## FRACTALS IN POROUS MEDIA: FROM PORE TO FIELD SCALE

MUHAMMAD SAHIMI, HOSSEIN RASSAMDANA, AND ALIREZA MEHRABI

Department of Chemical Engineering, University of Southern California, Los Angeles, CA 90089-1211

### ABSTRACT

Two applications of fractal concepts to problems involving porous media are discussed. One of them occurs at the pore level and involves the formation of large molecular aggregates as the result of injecting a fluid into an oil reservoir, or because of compositional changes in the oil. Formation of such aggregates and their precipitation on the pore surfaces cause severe problems for enhanced recovery of oil, and also many processes which use porous catalysts. We argue that these molecular structures are similar to diffusion-limited cluster-cluster aggregates, and small-angle neutron scattering data support our argument. The second application involves field-scale distributions of the porosity and permeability of oil reservoirs. We show that, contrary to the recent assertions that such distributions are described by fractional Brownian motion or fractional Gaussian noise with positive correlations (persistence), they are described by Lévy distributions with *negative* correlations (*anti-persistence*).

### INTRODUCTION

In recent years the complex behavior of wide variety of phenomena of interest to chemists, physicists, and engineers has been characterized quantitatively by using the ideas of fractal distributions that correspond in a unique way to the geometrical shape and dynamical properties of the system under study. The key to this remarkable progress has been the fact that many disordered systems possess scale symmetry and invariance. Isotropic systems with such scale symmetry and invariance are self-similar, and can be characterized by a fractal dimension  $D_f$ , a property that corresponds in a unique fashion to the geometrical shape of the system. Anisotropic systems with scale symmetry are *self-affine* which means that such systems preserve their scale invariance only if lengths in different directions are rescaled by direction-dependent scale factors. Such self-affine fractals no longer can be described by a single fractal dimension. Examples of self-affine fractals include the fractional Brownian motion (fBm) and fractional Gaussian noise (fGn) which are discussed in this paper. Several books and articles discuss various aspects of fractal phenomena and their applications to many branches of science and technology [1-6].

An area in which the application of fractal concepts has proven fruitful is characterization of, and flow and transport through, porous media [7,8]. In addition, fractal concepts have provided us with a much deeper understanding of reaction and precipitation in porous media [4,9-11] which result in the dynamical evolution and restructuring of porous media, and nucleation and propagation of fractures in natural rock [12,13], which are crucial to flow of oil in underground reservoirs, the development of groundwater resources, and the generation of heat and vapor from geothermal reservoirs for use in power plants. Such fractures provide high permeability paths for fluid flow in reservoirs that are otherwise of very low permeabilities and porosities, and would not be able to produce at economical rates. We

do not intend to discuss all the applications of fractal concepts to porous media, as they are well-documented [7-14]. Instead, we focus on just two of such applications. One of them, which occurs at the pore level, is new and has not been discussed before. This is a phenomenon in which large molecular aggregates are formed and precipitate on the surface of the pores of an oil reservoir, when a fluid is injected into the pore space to displace the oil and enhance its recovery. A similar phenomenon occurs in many processes involving porous catalysts. For example, during catalytic coal liquefaction and coal liquid upgrading, and also many refining processes that use porous catalysts, large molecular aggregates are formed whose precipitation on the surfaces of the catalyst's pores cause severe problems for efficient operation of such processes. In the chemical and petroleum industries such molecular aggregates are referred to as *asphalts*. These aggregates have many unusual properties, and have also been used [15] for manufacturing strong composites that have many industrial applications. The second application we discuss is characterization of field-scale distributions of the porosities and permeabilities of reservoir rock. Such an application was pioneered by Hewett [16,17], who showed that the porosities and permeabilities of many oil reservoirs obey fractal statistics. However, our recent work indicates that, although the original ideas of Hewett about the applicability of fractals to field-scale reservoirs are valid, many of his conclusions regarding the type of fractal distributions that the porosities and permeabilities follow need to be re-evaluated.

This paper is organized as follows. In the next section we discuss the application of fractals to the formation and precipitation of molecular aggregates in porous media. Next, we discuss fractal characterization of field-scale porous media. In the last section the paper is summarized, and possible future research directions are pointed out.

## FORMATION OF MOLECULAR AGGREGATES IN POROUS MEDIA

The asphalt aggregates usually are highly polar, and there is strong evidence [18] that they are colloidal particles, which means that they cannot be processed with the current refining technology. When they are formed in an oil reservoir, they precipitate on the surface of the pores and plug them and thus reduce the effective permeability of the reservoir. In order to disperse the asphalt aggregates in refining operations, or prevent their formation and precipitation in an oil reservoir or in a porous catalyst, it is of fundamental importance to understand their molecular structure and the mechanisms that give rise to their formation. However, despite many years of research, and particularly extensive experimental work [19], up until very recently a model of the asphalt aggregates whose properties are all consistent with the experimental data had not emerged.

There are several methods for measuring various properties of the asphalt aggregates that provide insight into their structure. One popular method has been measuring their effective diffusivity in a well-defined system such as a porous membrane with non-intersecting pores. Since the pores are non-intersecting, possible complications due to the tortuosity of the membrane do not arise. Because the size of the aggregates is comparable with that of the pores, diffusion of the asphalts is *hindered* or restricted, which means that their effective diffusivity in the pores is smaller than its corresponding value in an unbounded solution. The experimental data are then correlated using the hydrodynamic theories of hindered diffusion [20-23]. These theories provide reasonably accurate approximate description of the data, but as far as providing insight into the structure of the aggregates is concerned, they can be used only if we assume that the aggregates can be represented as spherical molecules with an effective hydrodynamic radius, or as ellipsoidal molecules with given major and

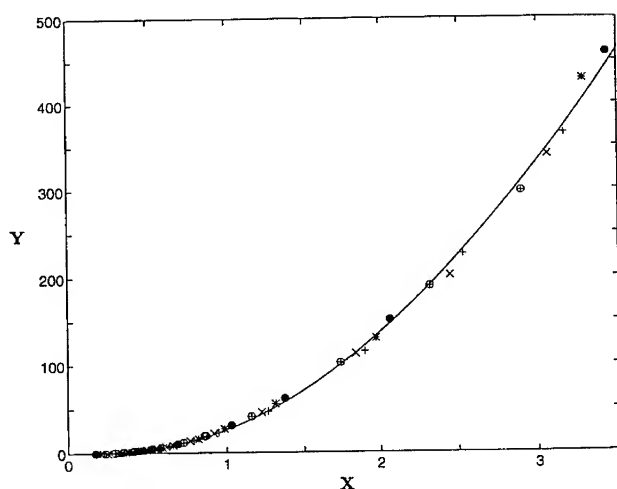


Figure 1: The rescaled experimental data (symbols) for precipitation of the asphalts with  $X = r/M^{1/4}$  and  $Y = Wr^2$ . The curve is the universal scaling function and represents the best fit of the data.

minor axial lengths. Despite this severe shortcoming, such correlations have been derived by several authors [24,25], mainly because an understanding of transport properties of asphalts is essential to the successful design of refining and coal liquefaction operations. Another approach was proposed by Klein and coworkers [26,27] by which an iterative stochastic model of the aggregates is constructed, beginning with some hypothesized structure and matching its properties with measured macroscopic properties such as the average molecular weight of the aggregates, their viscosity, density, etc. However, this approach is very tedious and requires a considerable amount of accurate experimental data, some of which are not even available yet.

As far as oil recovery and refining processes involving porous catalysts are concerned, it is of great importance to know the amount of precipitated aggregates on the surface of the pores [28]. However, despite their significance, accurate precipitation data are relatively rare, because their measurement is difficult. The structure of the aggregates and their precipitation on the pore surface are sensitive to the temperature and pressure of the system, the chemical composition of the fluid that is injected into the pore space, and a variety of other factors. We have recently carried out [29] a careful experimental study of asphalt formation in a pore using crude oils and a variety of alkanes, ranging from  $C_3$  to  $C_{10}$ , as the injection or solvent fluid. We have measured the amount of the precipitated asphalt that is formed when an alkane is injected into the pore that contains a crude oil. At a given temperature and pressure, the parameters of the measurements were the molecular weight  $M$  of the solvent, the solvent to crude ratio  $r$  (in  $\text{cm}^3/\text{gr}$ ), and the weight percent  $W$  of the precipitated asphalt. We have shown [29] that an scaling equation can be developed by combining the three variables into two variables  $X = r/M^z$  and  $Y = Wr^{z'}$ , thereby collapsing all the experimental data for various values of  $M$ ,  $W$ , and  $r$  onto a single curve. We have shown that  $z$  and  $z'$  are *universal*, i.e., they are independent of the temperature

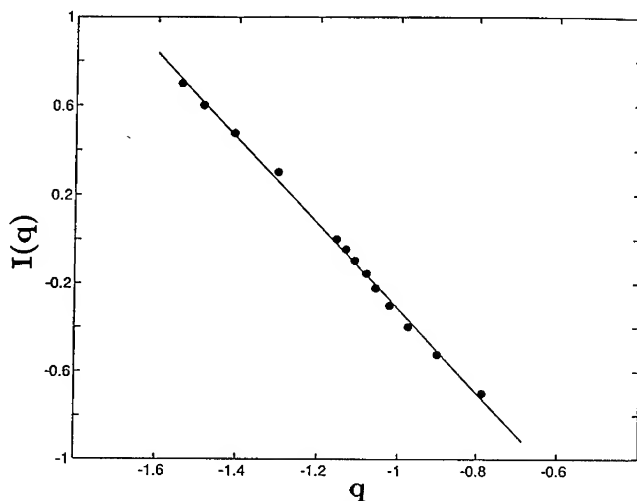


Figure 2: Logarithmic plot of the SANS intensity  $I(q)$  versus the magnitude of the scattering vector  $q$ , for a toluene solution that contains 5% asphalt, at  $T = 25^\circ$ .

and pressure of the system, or the composition of the crude oil, and that  $z = 1/4$  and  $z' = 2$ . Therefore, the scaling function provides a universal equation of state that may be used for predicting the amount of the precipitated asphalts under wide variety of conditions. Figure 1 shows the universal scaling equation together with the experimental data at  $T = 26^\circ\text{C}$ . We have shown [30] that our universal scaling equation can successfully predict the experimental data for a variety of crude oils.

The existence of such universal scaling variables and functions strongly suggests that the asphalt aggregates are fractal and self-similar. Thus, motivated by this observation, we have analyzed [31] small-angle neutron scattering (SANS) data on asphalt solutions in toluene at various temperatures [32,33]. Suppose that  $I(q)$  is the scattering intensity, where  $q$  is the magnitude of the scattering vector. If the aggregates have a fractal structure, then [34]

$$I(q) \sim q^{-D_f}, \quad (1)$$

where  $D_f$  is the fractal dimension of the aggregates. Figure 2 shows the log-log plot of  $I(q)$  versus  $q$  for a solution that contains 5% asphalt in toluene at  $T = 25^\circ\text{C}$ , very close to the temperature at which the data shown in Fig. 1 were measured. As can be seen, over about one order of magnitude variations in  $q$ , we have a straight line with an slope

$$D_f = 1.8 \pm 0.05. \quad (2)$$

What is the interpretation of this value of the fractal dimension? From our experimental observations the following picture of formation of the aggregates emerges. As the solvent is injected into the oil, very small solid particles are formed in the solution. These particles diffuse in the solution, and upon collision with each other they stick together. After some time, one has a number of small clusters of solid particles in the solution, whose sizes are not yet large enough to prevent their diffusion in the solution. Thus, the solid clusters also

diffuse in the solution until they collide and are attached to each other. After some time the aggregate becomes too large and heavy, and thus it precipitates onto the pore surface. This picture of formation of the aggregates is based on the experimental observations, but it is also the way diffusion-limited cluster-cluster (DLCC) aggregates are formed [35]. Such aggregates have a fractal dimension  $D_f \simeq 1.75 - 1.8$ , in very good agreement with our result. This confirms our assertion that the asphalt aggregates have a fractal structure, and the SANS data as well as and precipitation data indicate that these aggregates are in fact DLCC aggregates that have been studied extensively in the past several years.

The discovery that asphalts are colloidal aggregates with a fractal structure has important practical implications. The kinetics of the aggregation of asphalts can be described in terms of the mean-field Smoluchowsky equation

$$\frac{dn_k}{dt} = \frac{1}{2} \sum_{i+j=k} K(i,j)n_i n_j - \sum_{j=1}^{\infty} K(k,j)n_k \quad (3)$$

where  $n_i$  is the number of clusters of size  $i$ , and  $K(i,j)$  is a kernel. The first term of the right hand side represents the formation of clusters of size  $k$  from the two smaller clusters of sizes  $i$  and  $j = k - i$ , while the second term represents the loss of clusters of size  $k$  by reaction with other clusters to form larger clusters. For DLCC aggregates the appropriate kernel is given by [36]

$$K(i,j) = (i^\delta + j^\delta) (i^{1/D_f} + j^{1/D_f}) \quad (4)$$

where  $\delta$  is the exponent that relates the diffusion coefficient  $\mathcal{D}$  of the individual clusters to their mass  $M$ ,  $\mathcal{D} \sim M^\delta$ . This mean-field description is valid in three or higher dimensions, and thus should be highly accurate for the asphalt aggregation. Using this mean-field theory, one can calculate various quantities of interest, such as the molecular weight distribution of the asphalts. Identifying the asphalts as DLCC aggregates also enables us to impose an upper bound on the typical molecular weight  $M$  of the asphalt aggregates, an unsolved problem to date. Moreover, this upper bound tells us that  $M$  cannot exceed a few thousands, contrary to some assertions in the literature that  $M$  can be as large as  $10^5$ , since if  $M$  becomes too large thermal fluctuations in the solution disturb the mechanical stability of the aggregates and force them to rearrange themselves. Thus, the mean-field approach, together with our universal scaling equation for the amount of the precipitated asphalts, give us a relatively complete theory of aggregation and deposition of molecular aggregates in porous media.

## CHARACTERIZATION OF FIELD-SCALE POROUS MEDIA

Although characterization of laboratory-scale, or *macroscopic* porous media can be done in great detail, and reasonable understanding of such systems has been obtained, the same is not true about field-scale, or *megascopic* porous media. Experimental data for the morphology of such porous media is incomplete, their effective properties such as the porosity and the permeability vary greatly at different length scales, often by several orders of magnitude, and the relations between such properties and the volume or the linear size of the porous media which one wishes to study or exploit are often unknown. For this reason, modelling field-scale porous media usually involves *stochastic* techniques. Thus, although field-scale reservoirs are, in principle, intrinsically deterministic, because of the great uncertainties one often has to speak of the stochastic nature of such porous media, and describe their properties in terms of statistical quantities. As flow in field-scale porous media is greatly important

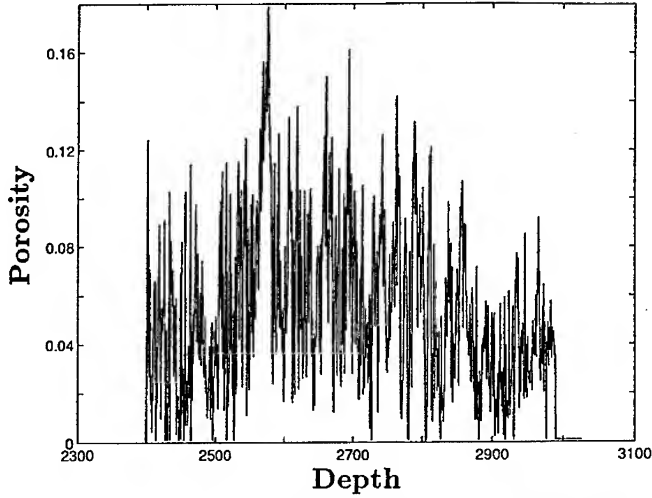


Figure 3: The porosity log of a 600m-deep well in the Middle East.

to oil and gas recovery from underground reservoirs, and to the development of groundwater resources in aquifers, it has captured the attention of scientist and *politicians*, since pollution of groundwater resources has become a “hot” political issue in the USA.

To give the reader some idea about the complexities that are involved in the characterization of a field-scale porous medium, we show in Fig. 3 a vertical porosity log that was obtained from an oil well in the Middle East. The well’s depth was about 600m and the porosity  $\phi$  was measured every 20cm, so that over 3,000 data points were collected. As can be seen, the pattern of the variations of  $\phi$  is very complex. How do we analyze such complex variations of  $\phi$  and uncover any mathematical structure that they may have? The analysis of such data is usually done by using the rescaled-range technique by which a quantity  $R(L)/S(L)$  is calculated, where  $R(L)$  is the range of the accumulated departure from the mean of the variable at length scale  $L$ , and  $S(L)$  is the standard deviation (see Feder [3] for more details). This method was first used by Hurst [37] for analyzing annual flows in rivers. In mathematical terms, if a variable  $v$  takes the value  $v(\ell)$  at position  $\ell$ ,  $R(L)$  is given by

$$R(L) = X_{max}(\ell, L) - X_{min}(\ell, L), \quad 1 \leq \ell \leq L, \quad (5)$$

$$X(\ell, L) = \sum_{u=1}^{\ell} [v(u) - \langle v \rangle_L], \quad (6)$$

$$\langle v \rangle_L = \frac{1}{L} \sum_{\ell=1}^L v(\ell), \quad (7)$$

and  $S(L)$  is given by

$$S(L) = \left\{ \frac{1}{L} \sum_{\ell=1}^L [v(\ell) - \langle v \rangle_L]^2 \right\}^{1/2}. \quad (8)$$

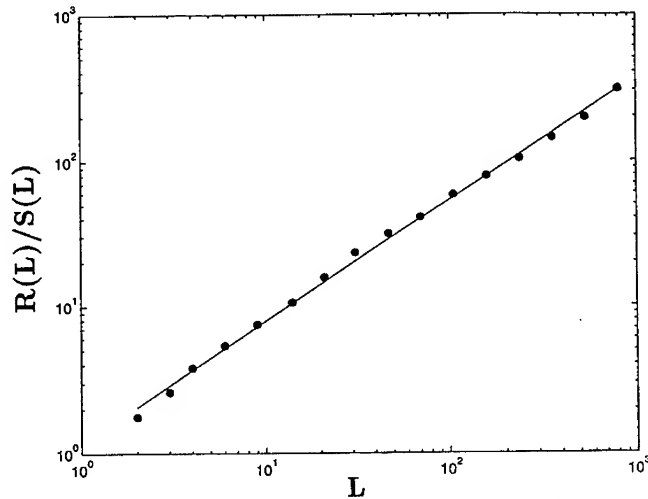


Figure 4: Rescaled-range analysis of the porosity log shown in Fig. 3. The slope of the straight line is  $H \simeq 0.83$ .

It can be shown that if the data follow an fBm, then [38]

$$\frac{R(L)}{S(L)} \sim L^H, \quad (9)$$

where  $H$  is called the Hurst exponent, and  $0 \leq H \leq 1$ .  $H > 0.5$  signifies positive correlations or persistence, i.e., a trend (a low or high value) at  $x$  is followed by a similar trend at  $x + \Delta x$ , whereas  $H < 0.5$  is indicative of negative correlations or anti-persistence. An fBm is a fractal distribution whose spectral density  $S(\omega)$ , the Fourier transform of its variance, in one dimension is given by

$$S(\omega) \sim \frac{1}{\omega^{2H+1}} \quad (10)$$

where  $\omega$  is the Fourier component. An fGn has a similar spectral density with the exponent  $2H + 1$  replaced by  $2H - 1$ . We carried out a rescaled-range analysis of the data shown in Fig. 3, the results of which are shown in Fig. 4. For nearly 3 orders of magnitude variations in  $L$  we obtain  $H \simeq 0.83$ . A similar value of  $H$  was obtained by Hewett [16] who carried out the first rescaled-range analysis of a porosity log. However,  $H \simeq 0.83$  is indicative of strong persistence and positive correlations in the data, whereas the porosity log shown in Fig. 3 indicates clearly the existence of anti-persistence or negative correlations, as a high value of  $\phi$  is followed by a low value, and vice versa. From a geological point of view, the existence of anti-persistence seems more plausible, since reservoir rock usually is stratified and layered, and the properties of the neighboring layers differ greatly.

To obtain a better understanding of the data, we first construct the experimental histogram of the increments  $\phi(x + \ell) - \phi(x)$ , where we fix the separation length  $\ell$  [39]. The results are shown in Fig. 5 for  $\ell = 20\text{cm}$ . Also shown is the fit of the data to a Lévy



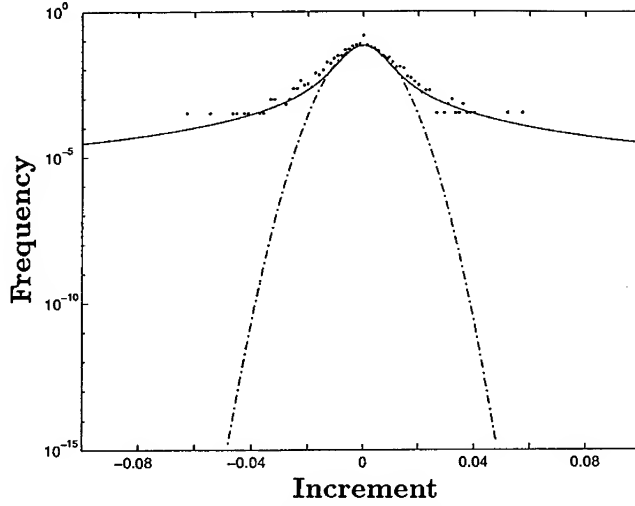


Figure 5: Frequency distribution of the increments in the data shown in Fig. 3 (symbols) and its fit by a Lévy distribution (solid curve). Also shown is the Gaussian distribution (dashed curve).

distribution, a fractal distribution given by [40]

$$P(y) = \frac{1}{\pi} \int_0^\infty \exp \left\{ -[C(\ell)\omega]^{D_w} \right\} \cos(\omega y) d\omega, \quad (11)$$

where  $D_w$  is the fractal dimension of the set of points that are visited by a random walker whose step sizes obey the Lévy distribution, and  $C(\ell)$  is a scale parameter. Of course,  $D_w = 2$  corresponds to a Gaussian distribution of the data, which has been used extensively in the petroleum engineering literature, but Fig. 5 shows clear deviations of the data from a Gaussian distribution. From Fig. 5 we obtain  $D_w \simeq 1.49$  and  $C \simeq 0.0043$ . Moreover, as is well-known, because of the long tails of the distribution the second and higher moments of a Lévy distribution are all divergent. Such tails decay very slowly, which make the moments of the distribution divergent. A similar analysis was carried out by Painter and Paterson [39] for acoustic transit time of some oil wells in northwest Australia. Note that up until now an fBm or fGn with  $H > 0.5$  has been used by many researchers to characterize the porosity or permeability distribution of rock.

The fact that the increments in the porosities obey a Lévy distribution also suggests another method for estimating the parameter  $H$ . If we vary the separation length  $\ell$ , the same value of  $D_w$  is obtained. This is indicative of self-similarity of the data, and suggests that if we plot  $C(\ell)$  as a function of the separation distance  $\ell$ , we should obtain

$$C(\ell) \sim \ell^H. \quad (12)$$

If the increments are not correlated, then  $H = D_w^{-1}$ . For positive (negative) correlations and persistence (anti-persistence) we should have  $H > D_w^{-1}$  ( $H < D_w^{-1}$ ). For short separation distances we obtain  $H \simeq 0.68 \simeq D_w^{-1} \simeq 0.67$ , indicating that at such length scales the

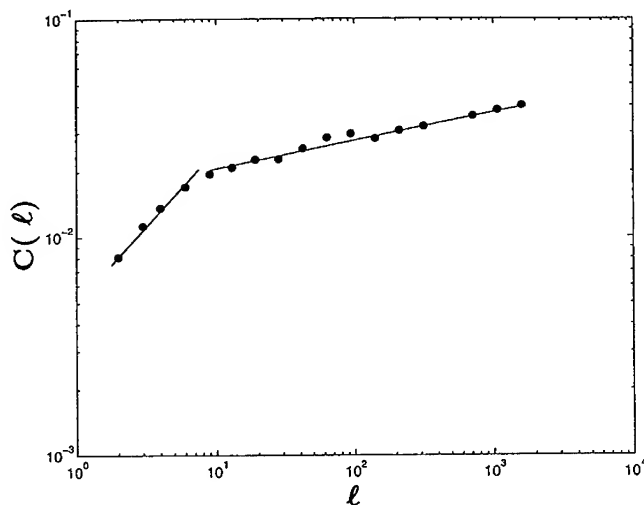


Figure 6: Logarithmic plot of the scale parameter  $C(\ell)$  versus the separation distance  $\ell$  for the data shown in Fig. 3. The slope of the straight line is  $H \simeq 0.13$ .

porosities are distributed essentially at random. This is presumably because at such short length scales one samples the rock properties within a stratum where the morphology is more or less random. However, at large separation distances that are of interest to us, which span many strata, the rock is highly heterogeneous, since the strata's properties greatly differ, and thus we expect negative correlations and anti-persistence, and indeed from Fig. 6 we obtain  $H \simeq 0.13 \ll D_w^{-1} \simeq 0.67$ , i.e., the data indicate negative correlations and anti-persistence, completely consistent with the porosity log shown in Fig. 3.

Another method for uncovering the fractal nature of the data is based on calculating the variance of the increments  $\gamma(\ell)$ , since for a fractal distribution one has

$$\gamma(\ell) \sim \ell^{2H}. \quad (13)$$

Figure 7 shows the results using this method. Note the similarity between this figure and Fig. 6. From Fig. 7 and for large separation distances we obtain  $H \simeq 0.17$ , consistent with the result obtained from Fig. 6, and confirming our assertion that, at least for the porosity log that we have analyzed, there are long-range negative correlations in the data.

To further check these results, we used an fBm to generate several one-dimensional sequences of numbers with various values  $0 < H < 1$ , and then analyzed the resulting synthetic data with the rescaled-range method. We found that, *regardless of the value of  $H$  used in the generation of the synthetic data by an fBm*, the rescaled-range analysis *always* predicts that  $H \simeq 0.9$ . This indicates that there is a fundamental bias in such an analysis, and therefore it may not be a reliable tool for analyzing geological as well as other types of data. We intend to carry out an extensive study of the previous data that have been analyzed by this method, in order to assess its reliability.

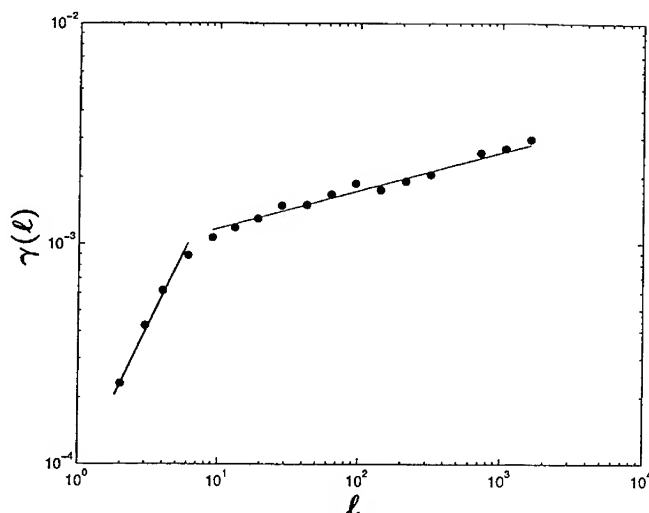


Figure 7: Logarithmic plot of the variogram of the data of Fig. 3.

## SUMMARY

We discussed application of fractal concepts to two problems involving porous media. One of them, the formation of large molecular aggregates and their precipitation on the surfaces of the pores, gives rise to diffusion-limited cluster-cluster aggregates that have been studied extensively over the past decade. In the second application, we considered characterization of the distribution of the porosity of a field-scale reservoir. We argued that previous studies that used a rescaled-range analysis of the data could not reveal the true nature of the statistical correlations in the data.

Work is currently in progress to analyze extensive porosity and permeability data of several oil fields, as well as other types of data. The results will be published elsewhere [41].

## ACKNOWLEDGMENTS

This work was supported in part by the Department of Energy. We would like to thank Scott Painter and Lincoln Paterson for many useful discussions, and for providing us with the copies of their papers prior to publication.

## REFERENCES

1. F. Family and T. Vicsek (eds.), *Dynamics of Fractal Surfaces* (World Scientific, Singapore, 1991).
2. B. B. Mandelbrot, *The Fractal Geometry of Nature* (Freeman, San Francisco, 1982).
3. J. Feder, *Fractals* (Plenum, New York, 1988).
4. D. Avnir (ed.), *The Fractal Approach to Heterogeneous Chemistry* (Wiley, New York, 1990).

5. A. Bunde and S. Havlin (eds.), *Fractals and Disordered Systems* (Springer, Berlin, 1991).
6. T. Vicsek, *Fractal Growth Phenomena*, 2nd ed. (World Scientific, Singapore, 1992).
7. M. Sahimi, *Flow and Transport in Porous Media and Fractured Rock* (VCH, Weinheim, Germany, 1995).
8. M. Sahimi, *Rev. Mod. Phys.* **65**, 1393 (1993).
9. M. Sahimi, G. R. Gavalas, and T. T. Tsotsis, *Chem. Eng. Sci.* **45**, 1343 (1990).
10. M. Sahimi, *Chemtech* **22**, 687 (1992).
11. M. Sahimi, T. T. Tsotsis, and G. R. Gavalas, *Statistical and Continuum Models of Fluid-Solid Reactions in Porous Media* (Oxford University Press, New York, in press).
12. M. Sahimi, *Physica A* **186**, 160 (1992).
13. M. Sahimi, M. C. Robertson, and C. G. Sammis, *Phys. Rev. Lett.* **70**, 2186 (1993).
14. M. Sahimi, *Applications of Percolation Theory* (Taylor and Francis, London, 1994).
15. K. Drake, J. Bauer, T. Serafini, and P. Cheng (eds.), *Moving Forward with 50 Years of Leadership in Advanced Materials*, Proceedings of the 39th International SAMPE Symposium and Exhibition (Society for the Advancement of Material and Process Engineering, Anaheim, California, 1994).
16. T. A. Hewett, Society of Petroleum Engineers paper 15386, New Orleans, LA (1986).
17. T. A. Hewett and R. A. Behrens, *SPE Form. Eval.* **5**, 217 (1990).
18. See, e.g., S. E. Moschopedis, J. F. Fryer, and J. G. Speight, *Fuel* **55**, 227 (1976).
19. J. G. Speight, *The Chemistry and Technology of Petroleum* (Marcel Dekker, New York, 1991).
20. J. L. Anderson and J. A. Quinn, *Biophys. J.* **14**, 130 (1974).
21. H. Brenner and L. J. Gaydos, *J. Colloid Interface Sci.* **58**, 312 (1977).
22. W. M. Deen, *AIChE J.* **33**, 1409 (1987).
23. M. Sahimi, *J. Chem. Phys.* **96**, 4718 (1992).
24. R. E. Baltus and J. L. Anderson, *Chem. Eng. Sci.* **38**, 1959 (1983).
25. V. S. Ravi-Kumar, T. T. Tsotsis, M. Sahimi, and I. A. Webster, *Chem. Eng. Sci.* **49** (December 1994).
26. P. E. Savage and M. T. Klein, *Chem. Eng. Sci.* **44**, 393 (1989).
27. D. M. Trauth, S. M. Stark, T. F. Petti, M. Neurock, and M. T. Klein, *Energy and Fuels* **8**, 576 (1994).

- 
28. A. Hirschberg, L. N. J. de Jong, B. A. Schipper, and J. G. Meijer, *SPE J.* **24**, 283 (1984).
  29. H. Rassamdana, B. Dabir, M. Nemati, M. Farhani, and M. Sahimi, *AIChE J.* (in press).
  30. H. Rassamdana and M. Sahimi, *Fuel* (to be published).
  31. M. Sahimi and H. Rassamdana, *Phys. Rev. Lett.* (submitted).
  32. B. Overfield, E. Y. Shue, K. S. Liang, and S. K. Sinha, *Fuel Sci. & Tech. Int.* **7**, 611 (1989).
  33. E. Y. Shue, K. S. Liang, S. K. Sinha, and R. E. Overfield, *J. Colloid Interface Sci.* **153**, 399 (1992).
  34. D. W. Schaefer, J. E. Martin, P. Wiltzuis, and D. S. Cannel, *Phys. Rev. Lett.* **52**, 2371 (1984).
  35. P. Meakin, in *Phase Transitions and Critical Phenomena*, vol. 12, edited by C. Domb and J. L. Lebowitz (Academic, London, 1988), p. 335.
  36. R. M. Ziff, E. D. McGrady, and P. Meakin, *J. Chem. Phys.* **82**, 5269 (1985).
  37. H. E. Hurst, *Trans. Amer. Soc. Civil Eng.* **116**, 770 (1951).
  38. B. B. Mandelbrot and J. W. Van Ness, *SIAM Rev.* **10**, 422 (1968).
  39. S. Painter and L. Paterson, *Geophys. Res. Lett.* (in press).
  40. M. F. Shlesinger, *Annu. Rev. Phys. Chem.* **39**, 269 (1987).
  41. A. Mehrabi, H. Rassamdana, and M. Sahimi (to be published).

# FRactal Structure of a Porous Cross-Linked Polymer Resin and Dynamical Behavior of Adsorbed Solvents

J.-P. KORB\* and C. CHACHATY\*\*

\*Laboratoire de Physique de la Matière Condensée, C.N.R.S., Ecole Polytechnique, 91128 Palaiseau, France.

\*\*C.E.N. de SACLAY, DSM/DRECAM/SCM, 91191 Gif sur Yvette, France.

## ABSTRACT

The fractal distribution of pore sizes in a poly-4-vinylpyridine resin cross-linked by diamagnetic ( $\text{Cd}^{2+}$ ) or paramagnetic ( $\text{VO}^{2+}$ ,  $\text{Cu}^{2+}$ ) divalent metallic ions has been characterized by small-angle-X-ray scattering, nuclear paramagnetic relaxation and proton-pulsed-field gradient. These complementary techniques show a continuity in the fractal distribution of pore sizes through the same surface fractal dimension,  $D_f = 2.6$ , over four orders of magnitude between 3 nm to 50  $\mu\text{m}$ . Electron spin resonance yields a direct estimate of the overall fraction of solvent into the adsorption shell of the cross-linked polymer network as well as the dynamics and local viscosity of the solvent in this disordered material.

## INTRODUCTION

The properties of functional groups as well as the microscopic structure of cross-linked polymer gels and resins are essential factors in their application as catalysts or in chemical separation processes. In presence of solvents, the reversible gels form a seemingly homogeneous phase, whereas the resins give rise to biphasic systems. The structure of gels has been the subject of a numerous works and is now quite well known. This is not the case for resins which are rigid systems in which porosity is the main property governing the diffusion of solvents.

These resins can be obtained with a polymer whose the functional groups are able to give stable complexes with divalent or tervalent ions to form three-dimensional cross-linked networks. This is the case of poly(4-vinylpyridine) (P4VP) whose copper II complexes have been subjected to several works dealing with its catalytic activity in redox reactions [1]. These systems have been also studied due to their applications for removal of organic impurities in water [2]. The cross-linking of P4VP has been performed in ethanol solution by addition of diamagnetic or paramagnetic metallic divalent ions such as cadmium, vanadyl and copper (Fig.1). At low metal concentration one obtains an homogeneous gel which can swell. Above a critical metal concentration, one observes a shrinkage of the gel network with expulsion of the

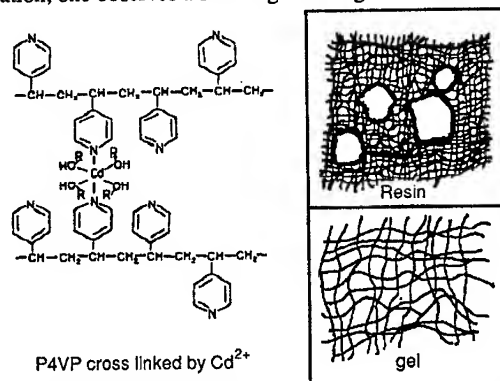


Fig. 1. The P4VP polymer cross linked by  $\text{Cd}^{2+}$  and schematic diagrams of the cross linked polymeric gel and resin

solvent resulting in a demixion of phases. This is the so-called phenomenon of syneresis [3]. After drying under vacuum, the resin is obtained as a brittle porous material of apparent density 0.4, which presents a large distribution of pore sizes and which is able to adsorb two molecules of solvent per monomer unit (Fig. 1) [4].

There are three main objectives in this work.

- (i) Obtain the pore size distribution over a large range of length-scale using different and complementary techniques.
- (ii) Make a direct measurement of the overall fraction of solvent at the pore interface.
- (iii) Obtain information on the dynamics of the solvent embedded in this highly disordered system.

To find the pore size distribution, three quite different methods concur to show that P4VP resin presents a fractal distribution of pore sizes over four orders of magnitude (4 nm - 50  $\mu$ m) [5]. The small angle X-ray scattering (SAXS) has provided a direct determination of the surface fractal dimension  $D_f \sim 2.6$  for the pores between 4 and 45 nm as well as the mass fractal dimension  $D_f \sim 2.75$  below 4 nm. Proton pulsed-field-gradient nuclear magnetic resonance (PFG-NMR) on adsorbed methanol have evidenced the same fractal distribution of pore radii but, in the 1-50  $\mu$ m range. Finally, the pores of radii between 3 nm and 1  $\mu$ m have been sampled by the nuclear relaxation of  $^2\text{H}$  and  $^{13}\text{C}$  of methanol in resins cross-linked by paramagnetic ions. The analysis of the data confirms the  $D_f$  obtained by the two other methods.

As the interpretation of nuclear relaxation data appears to be somewhat model-dependent, we propose a model-independent method to be used as a complement. The electron spin resonance (ESR) concentration measurement of polymer radicals, selectively formed by  $\gamma$ -irradiation at the polymer-solvent interface, gives a direct estimate of the overall fraction of solvent into the adsorption shell of the cross-linked polymer network.

Finally the molecular dynamics of a nitroxide radical (TEMPO) diluted in ethanol and saturating this resin has been studied by ESR at various temperatures. The temperature dependence of the reorientational correlation time of such spin label gives a direct information on such dynamics. The large distribution of pore sizes is responsible of the anomalous temperature behavior of the exchange rate between the bounded and free spin label concentration.

## DETERMINATION OF A FRACTAL DISTRIBUTION OF PORE SIZES

The preparation of the cross-linked resin samples as well as the details on the experimental methods used to probe the distribution of pore sizes have been described elsewhere [4, 5]. Here we just outline the description of these complementary methods and present an overview of the main results and discussions.

### Small-angle X-ray scattering (SAXS)

SAXS is now commonly used to characterize porous media [6-8]. Let us briefly summarize the main theoretical aspects of SAXS on porous media modelled as fractals [6-8]. In the Born approximation, the scattering intensity  $I(q)$  is simply proportional to the Fourier transform of the geometric correlation function of the electron density. For self-similar fractals, this leads to a non integer power-law behavior in the scattering at large value of  $qR$  ( $R$  being the average pore size) :  $I(q) = A q^{-\beta} + B$  where  $B$  represents the incoherent background. If the volume (or mass) of the scatterer is a fractal, one has  $\beta = D_f$  (mass fractal dimension). If only the surface is a fractal, then  $\beta = 6 - D_f$ . Since  $D_f \leq 3$  and  $6 - D_f \geq 3$ , surface and volume fractals can be in principle distinguished.

In fig. 2a, we present the scattered intensity  $I(q)$  of the non-cross-linked P4VP. The power law behavior observed,  $q^{-4}$ , at large  $q$  is characteristic of the Porod regime. It is typical of a sharp interface between two regions of different densities, which is what we expect for a non-cross-linked polymer. In fig. 2b, we present the scattered intensity of the resin P4VP cross-linked by  $\text{Cd}^{2+}$  in the absence and presence of ethanol. In the absence of solvent, one observes for  $q < 1/40 \text{ \AA}^{-1}$  ( $\log_{10} q = -1.6$ , corresponding to a distance  $\xi \sim 4 \text{ nm}$ ) a power-law behavior  $q^{-\beta}$  with  $\beta = 3.42$  which gives  $D_f = 2.58$  as surface fractal dimension. For  $q > 1/40 \text{ \AA}^{-1}$ , one observes, at least asymptotically, another power law with  $\beta = 2.75$ . This latter exponent is characteristic of

a mass fractal. These power laws and the crossover between the two regimes persist when the cross-linking is made with  $\text{Cu}^{2+}$  [5].

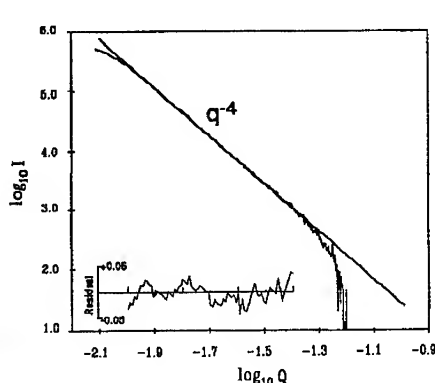


Fig.2a.

Logarithmic plots of the small angle X-ray scattering  $I$  vs the momentum transfer  $q$  ( $\text{\AA}^{-1}$ ) for a non cross-linked polymer P4VP (Fig 2a) and for a P4VP- $\text{Cd}^{2+}$  sample (Fig 2b). The sample with ethanol is materialized with S. The arrows indicate the crossover between the surface and volume fractal regimes. The residuals correspond to the difference between the experimental curve and linear plots.

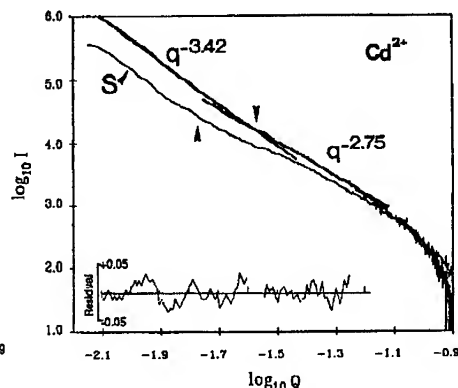


Fig.2b

We present also in figure 2b, the scattered intensity  $I(q)$  with ethanol. It is known that for a system of electronic density  $\rho$  embedded in a medium of density  $\rho_0$ ,  $I(q)$  is proportional to  $(\rho - \rho_0)^2$ . So filling the pores with ethanol will decrease significantly this difference, as it is observed in the fig. 2b. This proves that the scattering is due to some pores and not to non-cross-linked polymers for which  $(\rho - \rho_0)^2$  stays constant. The presence of such pores has also been evidenced by scanning electron microscopy before and after wetting with ethanol [5].

In the  $q$  range of surface fractal domain, one probes fluctuations on electronic densities over distances which are small compared to the size  $R$  of the pores, but large compared to the largest width of the dense polymer region  $\xi \sim 4$  nm (i.e. for pore sizes  $R_{\min} \sim \xi \leq R \leq R_{\max} \sim 45$  nm). The structure of the pore sizes may be modelled by a power-law distribution  $P(r)$  :

$$P(R) = \frac{dN}{dR} = \frac{1}{R_{\max}} \left( \frac{R}{R_{\max}} \right)^{-1-D_f}, \quad (1)$$

where  $dN$  represents the number of pores between  $R$  and  $R+dR$ ,  $D_f$  being the fractal dimension of surface. According to this distribution the total area of the pores diverges as  $(R_{\min}/R_{\max})^{2-D_f}$  when  $R_{\min}$  tends to zero, while the total volume stays finite. A transposition of the Porod's calculation of the average intensity scattered by a single pore to a continuous distribution of closed pores according to Eq. (1) leads also to  $I(q) \propto q^{-(6-D_f)}$ .

For  $q \xi > 1$ , one probes fluctuations over distances smaller than  $\xi$  inside the relatively dense polymer as suggested by the value,  $D_f=2.75$ , of the mass fractal dimension.

#### Pulsed-field-gradient nuclear magnetic resonance (PFG-NMR)

The pulsed-field-gradient (PFG-NMR) has proved to be one of the most suitable methods for studying molecular diffusion in heterogeneous systems [9, 10]. Basically this method corresponds to a proton magnetic resonance in presence of a sequence of pulsed field gradients. More specifically two field gradients pulses of intensity  $G$  and duration  $\delta$  are applied during a usual spin echo sequence of proton NMR. When diffusion occurs the transient magnetic field



experienced by the protons of moving molecules is not the same during the first and second gradient pulses separated by a time delay  $\Delta$  ( $\Delta \gg \delta$ ). The imbalance between the defocusing and refocusing processes results in an attenuation of the proton echo signal  $A(G)$  which is given by a weighted sum of spin dephasings between the two pulses. We have shown [5] that analyzing the variation of  $A(G)$  vs  $G^2$  for different values of the time delay  $\Delta$  can give information on both diffusion coefficient and distribution of pore sizes.

In the present work, this method has been applied to the self-diffusion of methanol in P4VP gel and resin, both cross-linked by diamagnetic  $\text{Cd}^{2+}$  ions. One shows in figure 3 the variation of the proton echo attenuation  $A(G)/A(0)$  vs  $G^2$  for a gel (Fig. 3a) and a resin (Fig. 3b). The mono-exponential attenuation observed for the gel is characteristic of a free diffusion of the solvent in an homogeneous system. The slope of the semi logarithmic plot of figure 3a yields precisely the diffusion coefficient  $D$  in that case. For the resin, the free-diffusion contribution dominates the signal at low gradient field intensity  $G^2$  (see the initial slope of Fig. 3b). The diffusion coefficient obtained,  $D = 5 \cdot 10^{-6} \text{ cm}^2/\text{s}$ , is smaller than the one of neat methanol ( $D = 3 \cdot 10^{-5} \text{ cm}^2/\text{s}$ ), suggesting that the translational motion of the solvent is affected by the pore roughness. On the contrary, at large gradient field intensity  $G^2$ , the non-exponential attenuation observed for the resin (Fig. 3b) is characteristic of a bounded-diffusion contribution of the solvent in an heterogeneous system which depends on the pore-size distribution. We have given in ref. [5] a theoretical expression of the average of  $A(G)$  over the power law  $P(R)$  of Eq. (1) which allows to extract,  $D_r = 2.6$ , from a fit of the experimental data.

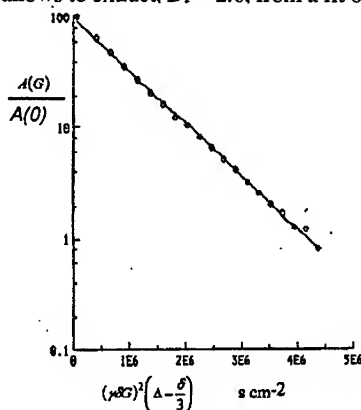


Fig. 3a

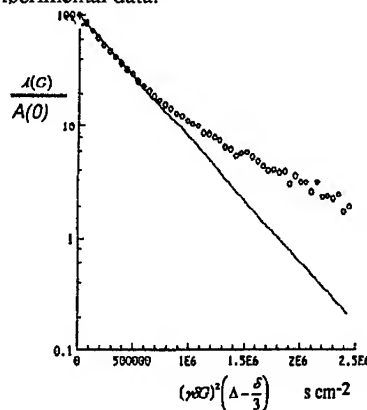


Fig. 3b

Semi logarithmic plots of the proton-echo attenuation  $A(G)/A(0)$  vs the square of the field gradient  $G^2$  in PFG-NMR experiments on methanol adsorbed on P4VP- $\text{Cd}^{2+}$  gel (a) and resin (b) (with  $[\text{Cd}^{2+}]/[\text{P4VP}] = 1/15$ ). The time delay  $\Delta$  between these two pulse-field-gradients and their duration  $\delta \ll \Delta$  are fixed in a given experiment.

In figure 4, we have reported the same experiment but on a resin presenting a higher degree of cross-linking ( $[\text{Cd}^{2+}]/[\text{P4VP}] = 1/5$ ). Now the length of diffusion,  $[6 D \Delta]^{1/2}$ , exceeds the largest pore size  $R_{\text{max}}$  and we have shown [5] that the theoretical expression of  $A(G)$  becomes simply :

$$\frac{A(G)}{A(0)} \propto \left( \frac{\gamma^2 \delta G^2}{5} \right)^{(D_r-3)/2}, \quad (2)$$

where  $\gamma$  is the gyromagnetic ratio of the proton. This form gives a slope of  $(D_r-3)/2$  on a logarithmic plot of  $A(G)/A(0)$  versus  $G^2$ . The least square adjustment of such a plot (Fig. 4) yields, -0.196, thus giving  $D_r \approx 2.6$ , and confirms our determination from the fits of Fig. (3b).

Anticipating the discussion on the relaxation-time distribution versus pore-sizes, it may be

said that under the most of our experimental conditions, pores smaller than 0.1  $\mu\text{m}$  have virtually no contribution to the signals recorded in PFG-NMR experiments.  $R_{\min}$  actually increases with the delay  $\Delta$  and is generally found in the 0.5-2  $\mu\text{m}$  range.  $R_{\max}$  is of several tens of micrometers ( $\sim 50 \mu\text{m}$ ) and,  $D_f \sim 2.6$ , as found by SAXS experiments on similar systems but on much smaller pore sizes.

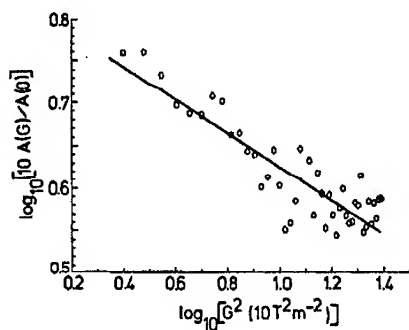


Fig.4. Logarithmic plot of the proton-echo attenuation  $A(G)/A(0)$  vs the square of the field gradient  $G^2$  in PFG-NMR experiments on methanol adsorbed on P4VP- $\text{Cd}^{2+}$  resin (with  $[\text{Cd}^{2+}]/[\text{P4VP}]=1/5$ ) for  $\Delta=0.105$  s.

#### Paramagnetic nuclear relaxation

In complement with SAXS and PFG-NMR experiments which provide evidence of a fractal distribution of pore sizes in the 4-45 nm and 0.5-50  $\mu\text{m}$  ranges, respectively, we have performed  $^2\text{H}$  and  $^{13}\text{C}$  nuclear relaxation measurements on methanol adsorbed on a resin cross-linked by paramagnetic divalent ions. In such systems, indeed, the solvent relaxation within a pore is strongly dependent on the surface-to-volume ratio. If the pores are weakly connected, it may be expected that the overall multi exponential relaxation behavior will allow a sampling of an intermediate range of pore sizes.

The results obtained with a P4VP sample cross-linked by vanadyl ions ( $[\text{VO}^{2+}]/[\text{P4VP}]=1/30$ ) are shown in Figs.(5 a-c). As previously pointed out [4, 5], a distribution of pore sizes results, at short times in paramagnetic systems, in a multi exponential decay of the transverse,  $R_{x,y}(t)$ , and longitudinal,  $R_z(t)$ , relaxation rates. This behavior has been ascribed to a fast exchange of the solvent between the core and surface of the pores. Within the pores the relaxation is exponential and its rate is weighted by the solvent fractions in the bulk and in an adsorption shell of effective thickness,  $\epsilon$ , surrounding the pores.  $\epsilon$  is related to the roughness of the pore surface and/or to the extent of penetration of the solvent in the polymer network. This method requires, for the fits of the experimental data, a theoretical expression for the magnetization decay due to the translational diffusion of solvent in a large distribution of pore sizes which is [5] :

$$R_i(t) \sim \exp\left(-\frac{t}{T_{ib}}\right) \left[ 1 - \Gamma(D_f 2) \left( \frac{3\epsilon}{R_{\max}} \frac{t}{\tau_{ia}} \right)^{3-D_f} \right] \quad \text{for } i = x, y \text{ or } z, \quad (3)$$

when  $t \ll (R_{\max}/3\epsilon)\tau_{ia}$ . Here  $1/T_{ib}$  is the bulk relaxation rate, independent of the pore size, which dominates at long times and  $1/\tau_{ia} = 1/T_{ia} - 1/T_{ib} \sim 1/T_{ia}$ , where  $1/T_{ia}$  is the solvent relaxation rate of the adsorption shell surrounding the pores (Fig. 1).

The best fit of the experimental data obtained with Eq. (3) yields  $D_f = 2.6$ ,  $\epsilon/R_{\max} \sim 1.7 \cdot 10^{-4}$ ,

and  $R_{\min}/R_{\max} \sim 10^{-4}$ . Although  $R_{\max}$  is not accessible by this method, it may be reasonably found to be of several tens of  $\mu\text{m}$  from PFG experiments on similar diamagnetic samples. It may therefore be estimated that  $\epsilon$  and  $R_{\min}$  are of the order of 2-5 nm. Calculations show that the paramagnetic relaxation of the solvent is governed by the adsorption shell contribution below  $R/R_{\max} < 10^{-3}$  and is still appreciable in the  $10^{-3}$ - $10^{-2}$  range, i.e. for  $R$  values up to  $1\mu\text{m}$ .

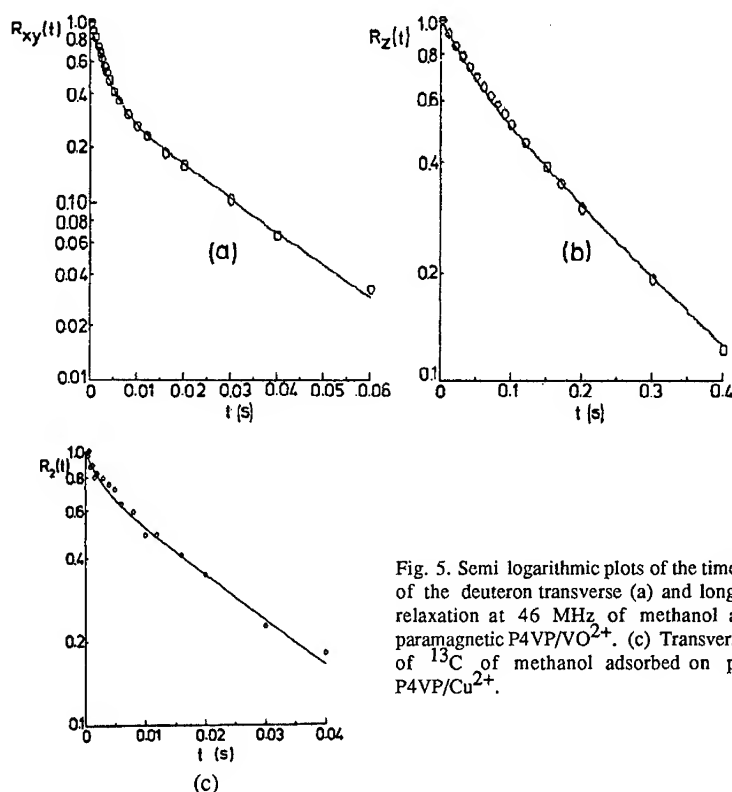


Fig. 5. Semi logarithmic plots of the time dependence of the deuteron transverse (a) and longitudinal (b) relaxation at 46 MHz of methanol adsorbed on paramagnetic P4VP/ $\text{VO}_2^+$ . (c) Transverse relaxation of  $^{13}\text{C}$  of methanol adsorbed on paramagnetic P4VP/ $\text{Cu}^{2+}$ .

In summary, we have evidenced, in the P4VP cross-linked resin, a continuity in the fractal distribution of pore sizes ( $D_f = 2.6$ ) over 4 orders of magnitude, typically between 3 nm to 50  $\mu\text{m}$  by using three complementary techniques : SAXS, paramagnetic relaxation and PFG-NMR.

#### A DIRECT DETERMINATION OF THE OVERALL FRACTION OF SOLVENT AT THE PORE INTERFACE

As the interpretation of nuclear relaxation data appears to be somewhat model-dependent, we propose a model-independent method to be used as a complement. This has been done by measuring the overall fraction  $F_a$  of ethanol in the adsorption shell surrounding the pores (Fig.1), from the relative concentration of free radicals selectively formed by  $\gamma$ -irradiation of frozen ethanol (77K) in a resin of the same composition as for nuclear paramagnetic experiment.

In first, we have verified that the concentration of radicals is absolutely negligible in absence of solvent. The radicals formed in the sample of Fig. 6 are therefore directly or indirectly derived from the ethanol radiolysis [11]. In alcohol glassy solutions, the pyridine behaves as electron scavengers forming anion radicals that are converted into pyridinyl radicals  $[PYRH]_r$  upon protonation of the nitrogen. These radicals are separately observable at 120 K (Fig.6). In the frozen gel, these radicals are uniformly distributed whereas, in the resin, there are only formed at the interface between the pores and the polymer network, i.e. in the solvent adsorption shell (fig.1). On the other hand, the  $[EtOH]_r$  radicals are formed both in these shells and in the bulk. The overall fraction of ethanol adsorbed at the interface  $F_a$  can therefore be deduced from the proportions of  $[PYRH]_r$  and  $[EtOH]_r$ . These proportions have been obtained from the second moments of ESR absorption at 77 K and 120 K where only the  $[PYRH]_r$  radicals remains (Fig.6). From the ratio of the pyridinyl to the total radicals concentration, we found  $F_a=0.20$  and  $F_a=1$  in the resin and in the homogeneous gel, respectively. For the resin such a value of  $F_a$  is in good agreement with the paramagnetic nuclear study.

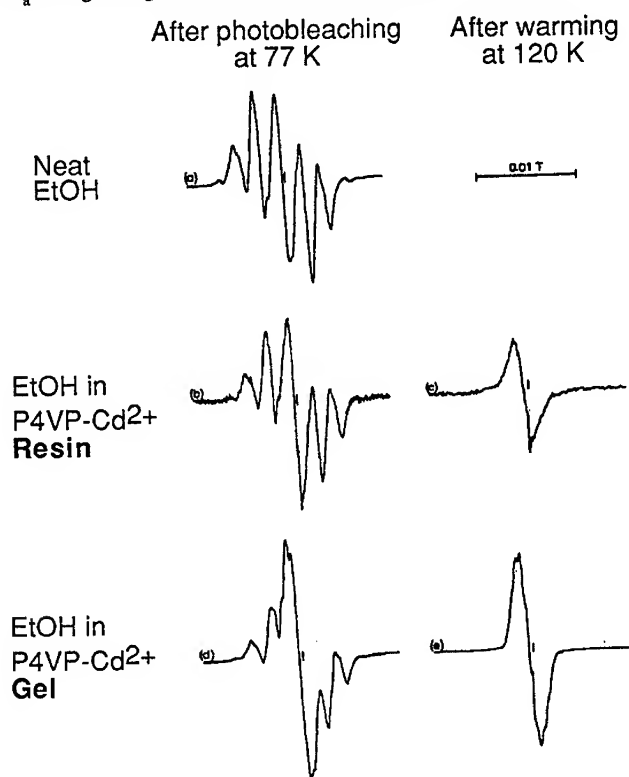


Fig. 6: ESR spectra of  $\gamma$ -irradiated neat ethanol (a), resin (b) and gel (d) at 77K (a, b, d) and 120K (c, e). The vertical bar corresponds to  $g=2.0023$ .

#### DYNAMICS OF SOLVENT IN THE POROUS RESIN

We have seen above that the diffusion coefficient of methanol,  $D=5 \cdot 10^{-6} \text{ cm}^2/\text{s}$ , obtained in the diamagnetic resin by the PFG-NMR method is smaller than the one of neat methanol ( $D=3 \cdot 10^{-5} \text{ cm}^2/\text{s}$ ). This has suggested that the translational motion of the solvent is affected by the

pore roughness. Similar dynamical information are also found indirectly by the paramagnetic nuclear relaxation method [4, 5]. Sometimes, nuclear relaxation can give direct dynamical information on liquids in porous media provided that the surface and geometrical confinement contributions on the nuclear relaxation rates of the liquids have been clearly identified via their different pore-size and frequency dependencies. This was the case in our previous work on *calibrated* porous silica glasses [12, 13]. However, in presence of a large distribution of pores, it is often difficult to separate these two contributions. We find an alternative way of studying the dynamics of a solvent in this porous resin: the ESR, at various temperatures, of a paramagnetic spin label dissolved in ethanol and adsorbed in P4VP- $\text{Cd}^{2+}$  resin (Fig. 7). The spin label used is the so-called nitroxide radical TEMPO (2-2-6-6-tetramethyl-piperidine-1-oxyl) which has been shown to be entirely surrounded by ethanol molecules. The net evolution of the ESR spectra, with the temperature, then allows a possible determination of the reorientational correlation time  $\tau$  of this spin label and then of the local viscosity as well as its exchange rate between unequivalent sites. The method used consists in the complete simulation of these spectra by considering the molecular reorientation of the spin label and its exchange rate between a rigid and free binding sites [14]. These two molecular motions result in a temperature-dependent reduction of the anisotropy of the hyperfine A and g tensorial couplings.

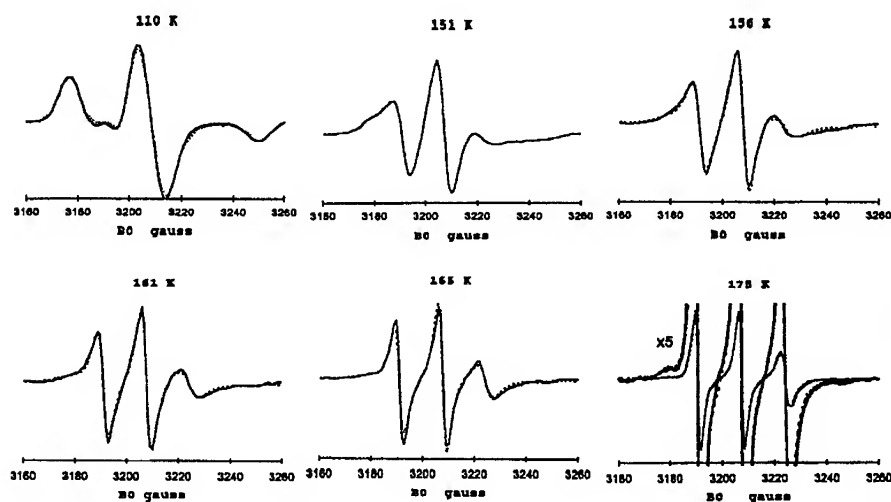


Fig. 7. ESR spectra of spin label TEMPO, dissolved in ethanol adsorbed in the P4VP resin, at various temperatures. The continuous lines correspond to the experimental data while the dashed lines are calculated. At high temperature, the slow component is still present due to the absence of measurable exchange with the fast component.

It occurs a progressive transformation of the ESR spectra from a large and asymmetric spectrum in the slow motional regime at low temperature up to a symmetric spectrum of three equally spaced lines in the "fast motion limit" at high temperature. The value of the reorientational correlation time  $\tau$  at the transition between these two limits is about 2 ns.

Finally the figure 8, presents the temperature dependencies of the reorientational correlation time  $\tau$  of the radical TEMPO in the cross-linked gel, resin and neat ethanol. One observes that these times are much higher for the gel than for the resin. The gel behaves as a highly

concentrated polymeric solution with a large viscosity. On the contrary, in the resin, there is a real phase separation between a shallow adsorption shell in the mass of the cross-linked polymer and the "free" solvent inside the pores of sizes  $R$  in the range (2 nm - 2  $\mu$ m).

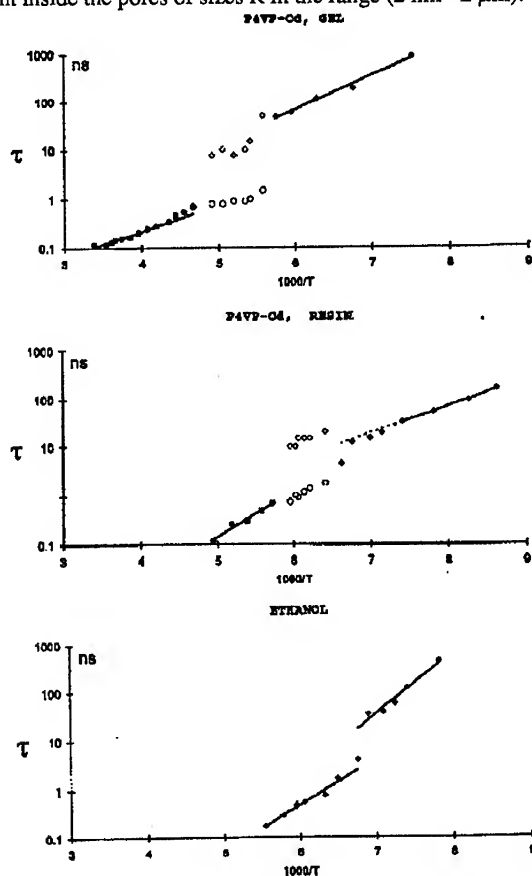


Fig. 8. Arrhenius plots of the temperature dependence of the reorientational correlation time  $\tau$  of the radical TEMPO in the gel, resin and neat ethanol. The isolated points  $\diamond$  and  $\circ$  correspond to the domain where the exchange rate between two inequivalent sites can be evaluated by a simulation of the ESR spectra. For the resin, the dashed line materializes the temperature range where it has not been possible to identify the frequency of exchange between two sites in the slow motion regime.

The temperature dependence of  $\tau$  in neat ethanol is classical and one clearly observes the glass transition of this solvent at 148 K. The apparition of a two-component ESR spectrum in the gel is significant of an heterogeneity of this system. This is not evidenced by nuclear relaxation, owing to fast exchange condition.

A two-component signal is also observed for the resin. In the temperature range where the exchange rate can be measured ( $5 \cdot 10^6 \leq \nu_{ex} \leq 5 \cdot 10^7 \text{ s}^{-1}$ ), one observes a decrease of  $\nu_{ex}$  when increasing the temperature. This seemingly paradoxical result is due to the large distribution of pore sizes in the resin. When the temperature increases, one observes the exchange of the spin label in more and more small pores where  $\nu_{ex}$  decreases.

## CONCLUSION

We have used three complementary techniques to characterize the fractal distribution of pore sizes in a poly-4-vinylpyridine resin cross-linked by diamagnetic ( $\text{Cd}^{2+}$ ) or paramagnetic ( $\text{VO}^{2+}$ ,  $\text{Cu}^{2+}$ ) divalent ions. Small-angle-X-ray scattering, nuclear paramagnetic relaxation and pulsed field gradient spin echo show a continuity in the fractal distribution of pore sizes by means of the same surface fractal dimension,  $D_f = 2.6$ , over four orders of magnitude, typically between 3 nm to 50  $\mu\text{m}$ .

The electron spin resonance (ESR) concentration measurement of polymer radicals, selectively formed by  $\gamma$ -irradiation at the polymer-solvent interface, has given a direct estimate of the overall fraction of solvent into the adsorption shell of the cross-linked polymer network.

Last, the molecular dynamics of a nitroxide radical (TEMPO) diluted in ethanol and saturating this resin has been studied by ESR at various temperatures. The temperature dependence of the reorientation correlation time of such spin label has informed about the solvent dynamics.

All these informations are of particular importance in the interpretation of physicochemical processes in catalysis and chemical separation on this organic disordered material.

## References

- [1] E. Tsuchida, H. Nishide and T. Nishiyana, *J. Polym. Sci.* **47C**, 35 (1974).
- [2] N. Kawabata, I. Higuchi and I. Yoshida, *Bull. Chem. Soc. Jpn.* **54**, 3523 (1981).
- [3] P. Spacek and M. Kubin, *J. Polym. Sci.* **C16**, 705 (1978) ; C.J. Brinker and G.W. Scherer, *Sol-gel Science* (Academic Press, New York, 1990), Ch. 6.
- [4] J.-P. Korb, B. Sapoval, C. Chachaty, and A. M. Tistchenko, *J. Phys. Chem.* **94**, 953 (1990).
- [5] C. Chachaty, J.-P. Korb, J.R.C. Van der Maarel, W. Bras and P. Quinn, *Phys. Rev.* **B44**, 4778 (1991).
- [6] H.D. Bale and P. W. Schmidt, *Phys. Rev. Lett.* **53**, 596 (1984).
- [7] P.Z. Wong and J. Howard, *Phys. Rev. Lett.* **57**, 637 (1986).
- [8] J. Teixeira, in *On growth and form*, edited by H.E. Stanley and N. Ostrowski (Nijhoff, Boston, 1985), p. 145.
- [9] P.T. Callaghan, *Aust. J. Phys.* **37**, 359 (1984).
- [10] J. Karger, H. Pfeifer and W. Heink, *Adv. Magn. Reson.* **12**, 1 (1989).
- [11] C. Chachaty, *C. J. Chim. Phys.* **64**, 608 (1967).
- [12] J.-P. Korb, S. Xu, and J. Jonas, *J. Chem. phys.* **98**, 2411 (1993).
- [13] J.-P. Korb, A. Delville, S. Xu, G. Demeulenaere, P. Costa and J. Jonas, *J. Chem. phys.* **101**, 7074 (1994).
- [14] C. Chachaty, *J. Chim. Phys.* **88**, 153 (1991).

## NON-LINEAR RESPONSE OF SELF-SIMILAR ELECTRODES AND ACTIVE MEMBRANES

B. SAPOVAL

Laboratoire de Physique de la Matière Condensée, C.N.R.S. Ecole Polytechnique, 91128 Palaiseau Cédex, France

### ABSTRACT

We describe a simple way to compute the response of an irregular resistive interface to a Laplacian field in  $d=2$ . It permits to find the linear response of electrodes with an arbitrary geometry from the image only of the electrode. It also allows to compute the non-linear response of self similar electrodes. This method applies in principle to arbitrary irregular geometry in  $d=2$  and it permits to predict generally that the slope of the Tafel plot is divided by the fractal dimension. These results may be transposed to the calculation of the steady state diffusion flux across an active self-similar membrane.

### INTRODUCTION

It has been shown recently that it is possible to obtain the response of electrodes of arbitrary geometry in the small voltage linear regime through a coarse-graining procedure.[1] The same type of analysis may be used to find the response of self-similar electrodes in the non-linear regime.[2] In order not to duplicate these papers I will recall here only the general idea on which these results were obtained and discuss their transposition to other domains where transport to an irregular interface is the consequence of the existence of a force deriving from a Laplacian potential. The particular case of the transport across an active irregular membrane will be discussed. The general problem is to find the response of an irregular "working" electrode in an electrochemical cell as represented in Fig.(1).

In principle one has to solve the Laplace equation  $\Delta V = 0$  which governs the electric field distribution in the bulk of the electrolyte but one must use the boundary condition that reflects the electrochemical processes at the surface electrode. In the simplest linear approximation, a small "flat" element of the surface behaves as a resistor  $r$  (the Faradaic resistor which measures the finite rate of the electro-chemical reaction) across a capacitance  $\gamma$  (which describes the charge accumulation at the interface). At frequency  $\omega$  the current density normal to the boundary is then, for small voltages

$$j_{\perp} = -V(r^{-1} + j\gamma\omega). \quad (1)$$

Because the surface presents a surface impedance, what is known about the properties of Laplacian fields on irregular surfaces which are totally absorbing (i.e. with  $V=0$ ) cannot be applied directly. This situation is unfortunate since the Laplacian problem with the Dirichlet boundary condition  $V=0$  (the situation of an irregular capacitor) has been thoroughly studied, at least in  $d=2$ , and a theorem of important significance, namely the Makarov theorem which describes the properties of the charge distribution on a irregular (possibly fractal) capacitor has been demonstrated.[3] This theorem states that the information dimension of the harmonic measure (the distribution of electrostatic charge for the capacitor case) on a singly connected object in  $d=2$  is exactly equal to 1. Here, the harmonic measure is the mathematical name of the distribution of the current density at the surface of the working electrode (in the unrealistic Dirichlet case where  $r=0$ ).



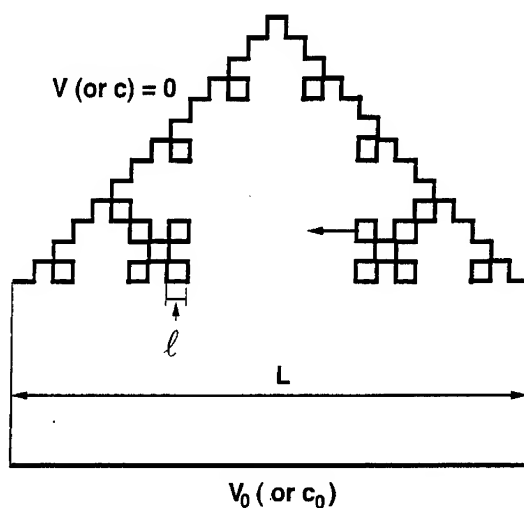


Fig. 1: Electrochemical cell with a self-similar electrode. The irregular electrode of interest ( the working electrode in electrochemistry ) has an inner cut-off  $\ell$  and a size or diameter  $L$ . The arrow indicates the orientation of the normal. This paper deals with the electrochemical problem in which the applied voltage is  $V_0$  on the planar counter electrode and 0 on the working electrode. There exists an exactly equivalent diffusion problem in which a planar source of diffusion is maintained at a constant concentration  $c_0$  and particle diffuse towards an irregular membrane with finite permeability  $W$ .

#### SCREENING EFFICIENCY OF THE GEOMETRY AND THE S NUMBER

The Makarov theorem can be imaged in the following manner: If one considers a cell with an irregular electrode, the size of the region where the current accumulates is proportional to the overall size (or diameter)  $L$  of the electrode under an homothety transformation. This result generalizes to arbitrary geometry facts which are known for a long time for simple geometries. It has in fact a very significant meaning to describe the efficiency of the screening. First we call  $S$  the ratio of the electrode perimeter  $L_p$  divided by its size  $L$ , [4]

$$S = L_p/L. \quad (2)$$

Now, if the active zone, that is the zone where the current accumulates, has a size  $L$  whatever the geometry, then trivially  $L = L_p(L/L_p) = L_p/S$  and consequently,  $1/S$  can be considered as the Dirichlet "screening efficiency" due to the irregularity of the geometry. Although trivially introduced the  $S$  number acquires now an important physical meaning.

#### COARSE-GRAINING THE REAL ELECTRODE TO A GEOMETRY OBEYING DIRICHLET CONDITION

The procedure that is used in [1] is to shift from the real geometry obeying the real boundary

condition to a coarse-grained geometry obeying the condition  $V = 0$  for which we know the effective screening from the above argument. To simplify we describe here the d.c. case ( $\omega=0$ ). Because of charge conservation, the current crossing the electrode surface must be equal to the current coming from the bulk by Ohm's law:  $j = -\nabla_{\perp} V/\rho$  with  $\rho$  being the electrolyte resistivity. As a consequence the d.c. boundary condition can be written as

$$\nabla_{\perp} V = \Lambda \quad \text{with} \quad \Lambda = r/\rho \quad (3)$$

The value of the length  $\Lambda$  determines the scale of the coarse graining in the following manner. We consider a part  $i$  of the surface with a perimeter length  $L_{p,i}$ . If the thickness of the cell is  $b$ , this surface possess an admittance  $Y_i = bL_{p,i}/r$  but the admittance to access the surface is of order  $Y_{acc} = b/\rho$  because in  $d=2$  the resistance of a square of electrolyte of thickness  $b$  is equal to  $b/\rho$  whatever its size. There exists then two situations:  $Y_i < Y_{acc}$  or  $Y_i > Y_{acc}$ , depending of the length  $L_{p,i}$ . If  $L_{p,i}$  is small, we have  $Y_i < Y_{acc}$ , and the current is limited by the surface admittance. On the contrary if  $L_{p,i}$  is large enough we have  $Y_i > Y_{acc}$ , and the current is limited by the resistance to access the surface. But in that latter situation we are, in first approximation, back in the case of a pure Laplacian field with the boundary condition  $V = 0$ . The idea is then to coarse-grain the real geometry to a scale  $L_i = L_{cg}$  such that the electrode perimeter  $L_{p,cg}$  in a region of size (diameter)  $L_{cg}$  is given by the condition  $Y_i = Y_{acc}$ , or

$$L_{p,cg} = \Lambda = r/\rho \quad (4)$$

Consequently, if we coarse-grain the original geometry to macrosites of perimeter  $\Lambda = r/\rho$ , in the new coarse-grained geometry we are dealing with a purely Laplacian field and we can then use the screening factor  $1/S_{cg}$  of this new geometrical object to find its effective active surface. The  $S$  number of the coarse-grained electrode is simply

$$S_{cg} = N_p/(L/L_{cg}) \quad (5)$$

where  $N_p$  is the number of yardsticks of length  $L_{cg}$  to measure the perimeter of the electrode whereas  $L/L_{cg}$  is the number of yardsticks to measure the size (or diameter) of the electrode. The quantity  $1/S_{cg}$  is the effective fraction of the surface which is active and the admittance of the electrode will simply be given by  $Y(r) = Y_p(r)/S_{cg}$  or its impedance by

$$Z(r) = Z_p(r) \cdot S_{cg} \quad (6)$$

where  $Z_p(r)$  would be the surface impedance of a "stretched" electrode with a length  $L_p$ . In this frame the number  $S_{cg}$  of the coarse-grained object determines directly how the impedance of the total surface is multiplied due to screening. If we consider a self-similar electrode with a inner cut-off  $\ell$  and fractal dimension  $D_f$  there exist a simple relation  $\Lambda = \ell (L_{cg}/\ell)^{D_f}$  between the size  $L_{cg}$  of the coarse graining and the length of the perimeter. (For a list of references on the response of fractal electrodes see [5,6]) Using this argument one obtains for the admittance of a self-similar electrode of macroscopic size  $L$  and thickness  $b$  the value  $Z = (Lb)^{-1}(\ell\rho)^{D_f-1}r^{1/D_f}$ . We substitute  $r$  by  $(r^{-1}+j\gamma\omega)^{-1}$  to obtain the general a.c. response and for blocking electrodes (for which  $r^{-1}=0$ ) we find

$$Z(\omega) = (Lb)^{-1}(\ell\rho)^{(D_f-1)/D_f} (j\gamma\omega)^{-1/D_f} \quad (7)$$

The d.c. form of this result has been verified by numerical simulation and the a.c. form which represents the so-called Constant Phase Angle (C.P.A.) response has been verified by experiments on model electrodes as described in detail in reference [7]. Generalization of the above procedure to arbitrary geometry is presented in [1]. It should be mentioned that slightly different values for the C.P.A. exponent have been proposed [8,9]. Up to now they are not distinguishable from  $1/D_f$  in simulations and experiments and they rely on complex theoretical formulation which cannot be extended simply to arbitrary geometry.

One should also mention that the same type of expression as that given by Eq. (7) allows to understand quantitatively the impedance diagram of blocking quasi-fractal 3-d electrodes [10].

## EXTENSION TO NON-LINEAR RESPONSE

The same method can be used to study the non-linear response (see [2]). The electrochemical response of a planar electrode is always non-linear when the applied voltage  $V$  exceeds a few millivolts. In general the d.c. current density across an electrode obeys the Butler-Volmer equation [11]

$$j = j_0 \{ \exp[(1-\beta_t)eV/kT] - \exp[-\beta_t eV/kT] \} \quad (8)$$

where  $e$  is the electron charge,  $k$  the Boltzmann constant,  $T$  the temperature and  $b_t$  a number smaller than one called the cathodic transfer coefficient. Note that for the linear regime ( $eV/kT \ll 1$ ) we have  $j = j_0 eV/kT$  and consequently the small voltage Faradaic surface resistance  $r$  is related to  $j_0$  by  $r = V/j = kT/ej_0$ . If we work with large positive voltage such that  $(eV/kT) \gg 1$  the Butler-Volmer equation simplifies to  $j = j_0 \exp[(1-\beta_t)eV/kT]$ . Then, there exist locally on the electrode a non-linear surface resistivity  $r(V)$  which is given by  $r(V) = (V/j_0) \exp[(\beta_t-1)eV/kT]$ . To this non-linear surface resistivity corresponds a non-linear length  $\Lambda(V) = r(V)/\rho = (V/\rho j_0) \exp[(\beta_t-1)eV/kT]$ . The coarse-graining size  $\ell (\Lambda(V)/\ell)^{1/D_f}$  is then given by

$$L_{cg}(V) = \ell \{ (V/\rho j_0) \exp[(\beta_t-1)eV/kT] \}^{1/D_f} \quad (9)$$

and the non-linear d.c. impedance response of the electrode is given by

$$Z = (bL)^{-1}(\rho\ell)^{(D_f-1)/D_f} (V/j_0)^{1/D_f} \exp[(\beta_t-1)eV/D_f kT] \quad (10)$$

The current across a self-similar electrode in the non-linear regime will then be given by an apparent Butler-Volmer response which for  $(eV/kT) \gg 1$  is

$$I = bL(\rho\ell)^{(1-D_f)/D_f} j_0^{1/D_f} V^{(D_f-1)/D_f} \exp[(1-\beta_t)eV/D_f kT]. \quad (11)$$

Hence, for fractal electrodes there exists a strong modification of the response due to the fractal geometry because the fractal dimension enters the argument of the exponential. One usually study in electrochemistry the so-called Tafel plots which are plots of  $\log(I)$  as a function of  $V$  [11]. For an ordinary case ( $D_f=1$ ) one finds a straight line and the slope of this line gives a

measure of the quantity  $(1-\beta_t)$ . Here, apart from the slight discrepancy due to the  $V^{(D_f-1)/D_f}$  factor, one will also find a straight line but now the slope will involve  $(1-\beta_t)/D_f$  instead of  $(1-\beta_t)$ . The effective Tafel slope is then divided by the fractal dimension. This fact has already been indicated by Nyikos and Pajkossy [12] for specific self-affine model electrodes for which specific computations can be made and discussed for self-similar electrodes by Mulder et al [13]. What we add here is a very simple geometrical interpretation which relates the size of the coarse-graining to the applied potential and permits to find directly the size of the active zone.

## ACTIVE TRANSFER ACROSS A SELF-SIMILAR MEMBRANE OR CATALYSTS

This method can be used to compute the active transfer across a self-similar membrane or the activity of a catalyst with the same geometry. The case of transfer across a self-similar passive membrane has been discussed in [14]. We consider the steady state diffusion transfer across an active self-similar membrane. The concentration  $c$  of the species of interest obeys Laplace equation  $\Delta c = 0$ . The flux in the bulk is given by Fick's law  $\Phi = -D \nabla c$  ( $D$  is the diffusion coefficient). The local flux across the membrane is proportional (in our example of active transfert) to the square of the local concentration  $\Phi = -w_a c^2$ . In that case there would exist a concentration dependent length

$$\Lambda(c) = D / w_a c \quad (12)$$

Along the same lines one can compute an admittance for diffusion

$$Y = bL \ell^{(1-D_f)/D_f} D^{(D_f-1)/D_f} (w_a c)^{1/D_f} \quad (13)$$

The total flux  $\Phi_T$  is equal to  $Y c_0$  if the concentration  $c_0$  is maintained near the entrance of the system, for instance by a horizontal flow in the case of Fig. 1. surface and

$$\Phi_T = bL \ell^{(1-D_f)/D_f} D^{(D_f-1)/D_f} w_a^{1/D_f} c_0^{(1+D_f)/D_f} \quad (14)$$

The flux is then found to obey a power law as a function of the concentration with an exponent  $(1+D_f)/D_f$

## DISCUSSION

The hypothesis which is used implicitly in this discussion of the non-linear responses is that the potential (electric potential for the case of the electrode or concentration or chemical potential in the case of the active membrane) is applied in the same manner everywhere on the active zone. The justification for that is to be found in the fact that this approximation was found to be a very good approximation to compute the linear response [7]. Of course this must not be considered as a proof. However, the approximation that there exist a totally passive region should be an even better approximation in the case of non-linear response because the local "activity" will vary as a power or an exponential function of the harmonic measure and consequently be very small in region which are only approximately passive in the linear regime.

Acknowledgments: It is a pleasure to acknowledge valuable discussions with P. Pfeifer. The

Laboratoire de Physique de la Matière Condensée is "Unité associée du C.N.R.S. n° 1254".

References:

- [1] B. Sapoval, Phys. Rev. Lett., in print (1994)
- [2] B. Sapoval, Solid State Ionics, in print (1994)
- [3] N. G. Makarov, Proc. London Math. Soc. 51,369 (1985)
- [4] R. P. Wool and J.M. Long, Macromolecules,26,5227 (1993) and R.P. Wool, Structure and strength of polymer interfaces (Hanser publ. New York, 1994). In these references the S number is used to describe fractal "diffusion fronts" relative irregularity.
- [5] T. Pajkossy, J. Electroanal. Chem.,300,1 (1991)
- [6] B.Sapoval, "Fractal electrodes, fractal membranes and fractal catalysts" in Fractals and disordered systems, (Ed. A. Bunde and S. Havlin, Springer-Verlag, Heidelberg,1995)
- [7] B. Sapoval, R. Gutfraind, P. Meakin, M. Keddam and H. Takenouti, Phys. Rev. E,48,3333 (1993)
- [8] T.C. Halsey and M. Liebig, Europhys. Lett.,14,815 (1991).and Phys. Rev.A 43,7087(1991).
- [9] R. Ball, in "Surface Disordering, Growth, Roughening and Phase Transitions" ed. by R. Julien, P. Meakin and D. Wolf (Nova Science Publisher,1993) p.277
- [10] E. Chassaing and B. Sapoval, J. Electrochem. Soc. **141**,2711 (1994)
- [11] J.O'M. Bockris and A.N. Reddy, Modern Electrochemistry (Plenum/Rosetta), New York (1977)
- [12] L. Nyikos and T. Pajkossy, Electrochim. Acta,35, 1567 (1990)
- [13] W. H. Mulder, J.H. Sluyters, T. Pajkossy and L. Nyikos, J. Electroanal. Chem.,285,103 (1990)
- [14] B.Sapoval, "Transfer to and across Irregular Membranes Modelled by Fractal Geometry" in *Fractals in Biology and Medecine*, (Ed. T.F. Nonnenmacher, G.A. Losa and E.R. Havlin, Birkhäuser, Basel ,1994) p.241.

## NEW SCALING FOR AC PROPERTIES OF PERCOLATING COMPOSITE MATERIALS

F. BROUERS AND A.K. SARYCHEV

Etude Physique des Matériaux, Institut de Physique, University of Liège, 4000 Liège, Belgium.

### ABSTRACT

In real conductor-insulator composites one observes a sharp change of the dc resistivity and a large increase of the low frequency dielectric constant at the percolation threshold  $p_c$ . However in many cases the a.c. data do not follow the scaling behaviour predicted by the percolation theory. To account for these discrepancies, we have proposed an alternative model which incorporates quantum tunnelling into the percolation theory. This model leads to a new "tunnelling" scaling law for the complex conductivity which gives rise for concentration below  $p_c$  to an exponential variation of the d.c. conductivity with concentration and a dispersion of the ac complex conductivity with non universal exponents. This new scaling law depends on two new exponents and reduces to the usual one for metal concentration well above  $p_c$ . We apply this more general scaling to discuss the relation between the film morphology and the low frequency dispersion in granular metallic composites.

### 1. A TUNNELLING SCALING LAW

The electrical, dielectric and optical properties of metal-insulator composites close to the percolation threshold can be very different from those of both constituents. The complex conductivity of metal-dielectric mixtures exhibit dispersion properties which have been discussed in the framework of the percolation theory [1]. For finite frequencies in a critical region near the percolation threshold  $p_c$  the complex conductivity is assumed to obey a scaling law of the form

$$\sigma_{\text{eff}}(p, \omega) = \sigma_{\text{eff}}(p, 0) \phi \left( \frac{-i \omega \epsilon_{\text{eff}}(p, 0)}{\sigma_{\text{eff}}(p, 0)} \right) \quad (1)$$

In this expression the static effective conductivity and the dielectric constant are given by

$\sigma_{\text{eff}}(p, 0) \propto \sigma_m \Delta p^t$  for  $p \geq p_c$  and  $\epsilon_{\text{eff}}(p, 0) \propto \epsilon_i |\Delta p|^s$  where  $\sigma_m$  and  $\epsilon_i$  are the bulk static metal conductivity and insulator dielectric constant,  $p$  the metal concentration,  $p_c$  the percolation threshold and  $\Delta p = p - p_c$ . For any type of lattice the critical exponents  $t$  and  $s$  depend only on the dimensionality  $d$  of the system (e.g.  $t \approx 2.0$ ,  $s \approx 0.7$  for  $d=3$  and  $t = s \approx 1.3$  for  $d = 2$ ). From this law it follows that when both  $|\Delta p|$  and the ratio  $\epsilon_i \omega / \sigma_m$  are small in the critical region around  $p_c$  defined by  $|\Delta p| < (\epsilon_i \omega / \sigma_m)^{t/(t+s)}$ , the a.c. conductivity and dielectric constant exhibit a dispersive behavior:  $\sigma_{\text{eff}}(\omega) \propto \omega^x$  and  $\epsilon_{\text{eff}}(\omega) \propto \omega^y$  with  $x = t/(t+s)$  and  $x+y = 1$ . As a typical good metal conductivity  $\sigma_m$  is of the order of  $10^{17} \text{ sec}^{-1}$  if the measurement frequency  $\omega < 10^8 \text{ Hz}$  the concentration range where the dispersion can be observed shrinks to  $|\Delta p| < 10^{-4}$ . In that region however dispersion of the conductivity and conductivity has been observed and reported for thin Au films of varying thickness or

concentration  $p$  near  $p_c$  from 100 Hz to 10 MHz [2]. It was found that  $x \approx 0.95$  and  $y \approx 0.13$ , which are different from the predictions for either  $d = 2$  ( $x=y=0.5$ ) or for  $d = 3$  ( $x=0.74$  et  $y=0.26$ ). Similar results have been reported for carbon-teflon mixtures, computer modelled aluminium percolation thin films and NbC-KCl composites.[3,6]. Recently to interpret these results, we have proposed a new percolation theory incorporating the effect of quantum tunnelling and introduced a new "tunnelling" scaling equation to describe the AC properties of such composites materials [7]

We refer to the original paper for a detailed discussion of this new theory. Here we will summarize the new results for two-dimensional systems and show how the new scaling function can account for the low frequency conductivity and dielectric dispersion of granular gold films reported in [1-6]. The new scaling function reads

$$\sigma_{\text{eff}}(p, \omega) = \sigma_{\text{eff}}(p, 0) \phi \left( \frac{\Sigma_{\omega}}{\Sigma_t} (\lambda(\Delta p))^a \right) \quad (2)$$

where  $\lambda$  is a renormalized tunnelling constant which will be defined later. The universal scaling function  $\phi$  depends on the ratio of the capacitive conductance  $\Sigma_{\omega}$  to the tunnelling conductance  $\Sigma_t$ , both being between the large metallic clusters in the system. It also depends on the renormalized tunnelling constant  $\lambda$  to some power  $a$ , where  $a$  is a new critical exponent. The analytical function  $\phi(x)$  must have the following asymptotic behavior  $\phi(x) \rightarrow \text{constant}$  when  $x \rightarrow 0$  and  $\phi(x) \propto x^r$  when  $x \rightarrow \infty$   $r$  is yet another critical exponent, which will not necessarily have the values expected from the classical percolation theory. To estimate values of  $\Sigma_{\omega}$  and  $\Sigma_t$ , when the concentration approaches  $p_c$ , one proceeds as follows. The typical size of a metallic cluster is of the order of the correlation length  $\xi \approx a_0 \Delta p^{-\nu}$  where  $a_0$  is the size of a metal grain and the critical exponent  $\nu = 4/3$  for  $d = 2$  and  $\nu \approx 0.9$  for  $d = 3$ . These clusters are extremely large just below  $p_c$  and have a very ramified shape. The typical inter-cluster capacitive conductance  $\Sigma_{\omega}$  between two adjacent conducting clusters, proportional to the number of points of close approach  $N(\Delta p)$  is

$$\Sigma_{\omega} \propto -i \omega a_0 \epsilon_i N(\Delta p) \propto -i \omega (\Delta p)^{-s} \quad (3)$$

$N(\Delta p)$  goes to infinity when  $p \rightarrow p_c$ , leading to a divergence of the static dielectric constant. To determine the typical tunnelling conductance one has to consider two large metal clusters connected through  $N(\Delta p)$  tunnelling junctions. The tunnelling conductance of a single junction is given by the well known exponential expression  $\Sigma_t \approx a_0 \sigma_m \exp(-\ell / \ell_t)$ . The intergranular separation is  $\ell$  with  $0 < \ell < a_0$  and the quantum tunnelling distance  $\ell_t$  is of the order of a few Å. The conductance of the  $i$ -th junction is then written as  $\Sigma_t^i \approx a_0 \sigma_m \exp(-\lambda_0 x_i)$  where  $\lambda_0 = a_0 / \ell_t$  and the dimensionless distances  $x_i = \ell_t / a_0$  are distributed in the interval  $0 < x_i < 1$ . The contact conductances are spread out over an exponentially large range and only the lowest of these makes a significant contribution to the tunnelling current. If one now considers all the adjacent cluster pairs (i.e. all  $jk$ ) it is possible to show [9] that the distribution of the intercluster conductances can be written as  $\Sigma_t^{jk} \approx a_0 \sigma_m \exp(-\lambda(\Delta p) y)$ ,  $0 < y < 1$  where the renormalized tunnelling constant  $\lambda$  is  $\lambda(\Delta p) = \lambda_0 / N(\Delta p)$  (4).

When  $p \rightarrow p_c$ , the number of junctions  $N(\Delta p)$  tends to infinity, making it easier and easier for electrons to tunnel from one cluster to another. To calculate the effective tunnelling conductivity below the percolation threshold, one has to compute the (self-averaging) macroscopic conductivity on a random network of bonds where the bond conductance  $\Sigma_t^{jk}$  are distributed according to (4). It has been shown [8-9] that in such systems the typical inter-granular conductance can be estimated to be

$$\Sigma_t^{\text{eff}} \approx a_0 \sigma_m \exp(-\lambda(\Delta p)p_c). \quad (5)$$

Hence the static conductivity  $\sigma_{\text{eff}}(p,0) \propto \Sigma_t^{\text{eff}}$  increases exponentially as  $p \rightarrow p_c - 0$ . Below the percolation threshold the critical conductance  $\Sigma_t^{\text{eff}}$  is the single natural scale for active conductance in the system. Using Eq.(3-5), the scaling equation (2) can be written [7] as

$$\sigma_{\text{eff}}(p,\omega) = \sigma_{\text{eff}}(p,0) \phi \left[ \frac{-i \omega \epsilon_i(\lambda(\Delta p))^{a-1}}{\sigma_m \exp(-p_c \lambda(\Delta p))} \right] \quad (6)$$

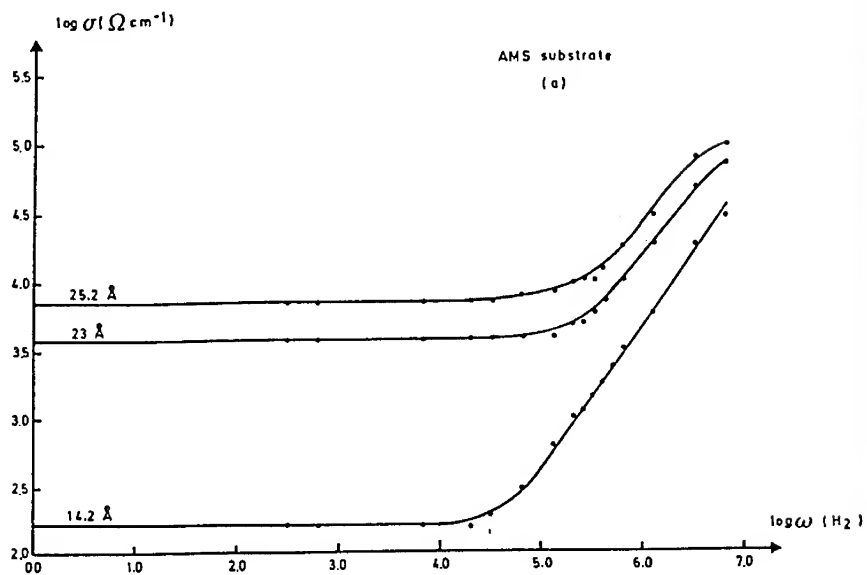
Eq. (6) quantitatively shows how the dispersion of the effective complex conductivity  $\sigma_{\text{eff}}(p,\omega)$  of such systems depends on the ratio of the static conductivity  $\sigma_{\text{eff}}(p,0) \propto \sigma_m \exp(-p_c \lambda(\Delta p))$  to  $\omega \epsilon_i(\lambda(\Delta p))^{a-1}$ . As  $\omega$  increases  $\sigma_{\text{eff}}(p,\omega)$  starts to become frequency dependent when  $\omega \epsilon_i(\lambda(\Delta p))^{a-1}$  approaches the effective static conductivity  $\sigma_{\text{eff}}(p,0)$ . Since this quantity is exponentially small somewhat below  $p_c$  the dispersive behavior  $\sigma_{\text{eff}} \propto \omega^r$  and  $\epsilon_{\text{eff}} \propto \omega^{r-1}$  should then be observable at very low frequencies.

Two dimensional simulation calculations [7] give for  $a$  and  $r$  the following values  $a \approx 1.4$  and  $r = 0.90 \pm 0.05$ .

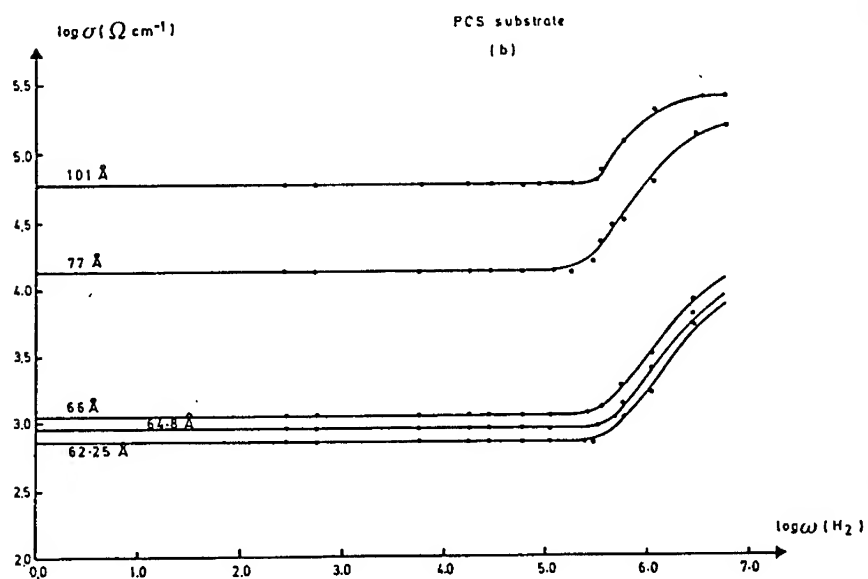
## 2. DISPERSION IN GRANULAR FILMS. INFLUENCE OF MORPHOLOGY

Such a dispersion is observed in granular gold films. Fig 1 and 2 show the frequency variation of the conductivity corresponding to gold thin films whose morphological analysis has been studied in great details [11]. We have applied the new scaling law to these data and the collapse of the curves corresponding the two sets of curves can be seen in Fig 3 and 4. We have used  $a = 1.4$  and  $\lambda(\Delta p) = \lambda_0 (\Delta p)^s$  with  $s = 1.3$ . The ratio of the tunnelling constants  $\lambda_0^{\text{am}} / \lambda_0^{\text{pc}} \approx 0.5$  we have used in our fitting calculations expresses the fact that the tunnelling probability is larger on the amorphous substrate. This can be understood easily if we refer to the results of the morphological analysis of these films [11]. On the amorphous substrate before the percolation threshold, one observes a transition from a granular morphology towards a worm-like morphology. This can explain why there is not a perfect collapse at higher frequencies in Fig2b. As one approaches  $p_c$  the probability of small inter-cluster distances increases. This probability is larger on the amorphous substrate and correspond to a larger probability of small effective tunnelling distances in the worm-like morphology of this films. This corresponds to a smaller tunnelling constant  $\lambda_0$  compared to the one of the films grown on a polycrystalline substrate where the granular morphology persists until concentrations close





**Figure 1:** Measurement of the frequency dependent conductivity of thin films for different Au concentrations on AMS (a) and PSC (b) substrates.



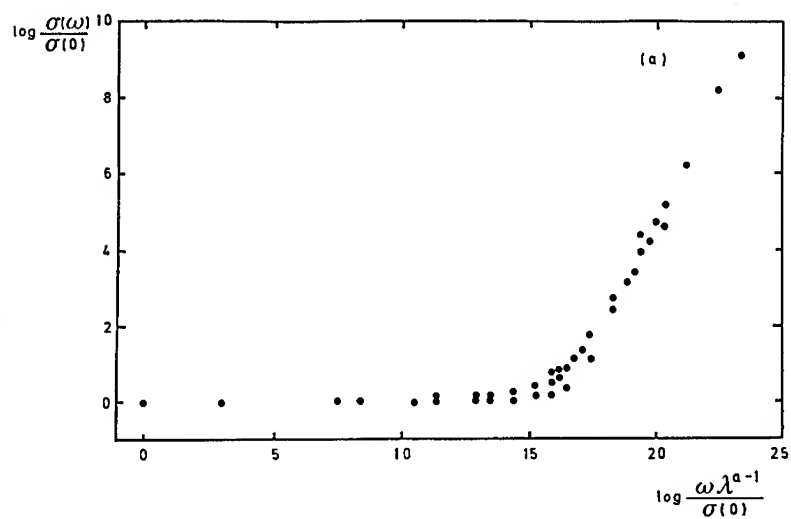
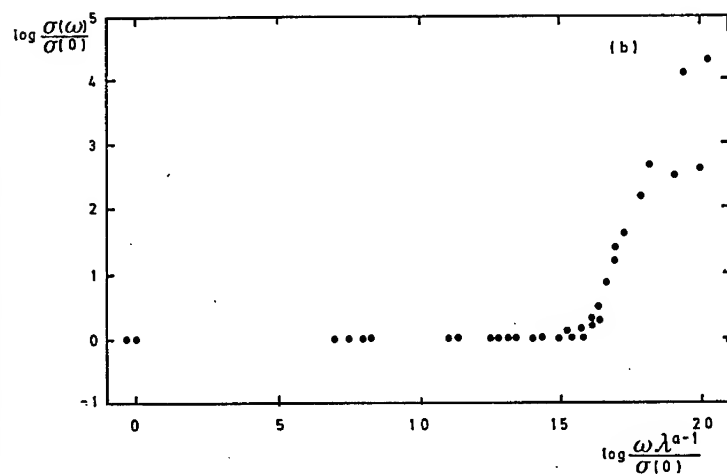


Figure 2 : Theoretical collapse curves of the frequency dependent conductivity obtained from the Sarychev-Brouers scaling law for Au thin films on AMS (a) and PSC (b) substrates .



to the percolation transition. A more detailed discussion of this relation between  $\lambda$  and the morphology can be found in Ref. [8].

### 3. CONCLUSIONS.

In this paper we have reported new recent results on granular thin films which show unambiguously that the low frequency dispersion of the electrical conductivity for concentrations lower or of the order of  $p_c$  can be related to tunnelling conductivity. The observed exponents are in agreement with the new scaling law and exponents and the tunnelling parameter  $\lambda_0$  has a direct relation to the morphology of the films.

Our paper illustrates the interest of conducting simultaneous studies of the morphology and of the low frequency dispersion of the conductivity and dielectric constant of conducting-dielectric composites.

### REFERENCES

1. J.P. Clerc, G. Giraud and J.M. Luck, Adv. Phys. **39**, 191 (1990).
2. R.B. Laibowitz and Y. Gefen, Phys. Rev. Lett. **53**, 380 (1984).
3. Y. Song, T.W. Noth, S. Lee and G.R. Gaines, Phys. Rev. B **33**, 904 (1986).
4. M.F. Hundley and A. Zettl, Phys. Rev. B **38**, 10290 (1988).
5. C.S. Yoon and S. Lee, Phys. Rev. B **42**, 4594(1990).
6. D.S. McLachlan, I.Oblacova, A.Pakhomov, Physica A **207**, 234 (1994).
7. A.Sarychev and F.Brouers, Phys.Rev.Lett.**73**,2895 (1994)
8. S.Blacher, F.Brouers, A.Sarychev, A.Ramsamugh Langmuir(1995) in the press.
9. Electronic properties of Doped Semiconductors by B.I. Shklovskii and A.L. Efros, Springer Ser. on Sol. St. Phys. 1984.
10. P. Le Doussal, Phys. Rev. B **39**, 881 (1989).
11. S. Blacher, F. Brouers, P. Gadenne and J.Lafait, J. Appl. Phys. **74**, 207(1993).

## SCALAR TRANSPORT BY DIFFUSION AND RANDOM ADVECTION

Mariela Araujo

Intevep S.A., Apartado 76343, Caracas 1070-A, Venezuela

### ABSTRACT

The transport of a scalar by jump-type random advection and diffusion is described by a mean field formulation in terms of a Langevin equation for the fluctuations of the scalar. It is shown how the distribution of the scalar fluctuations is sensitive to the relative strength of advection versus diffusion, and the details of the advection process.

### INTRODUCTION

The understanding of the mechanisms of transport of a scalar in the presence of randomness has become an important subject in science and engineering. In various turbulence experiments, the probability distribution of temperature, velocity gradients, concentration, etc., are observed to be non-Gaussian. In particular, exponential tails have been seen where Gaussian distributions were expected by naively invoking the central limit theorem [1-4]. Recently, models of such transport, based on mean field analyses of stochastic processes, have been used with some success, to explain the experimentally observed non-Gaussian behavior of the probability distribution [5-6].

Here, we study the distribution of a scalar  $\theta$ , released at some point in a turbulent flow with an externally imposed uniform gradient. The turbulent flow is modeled as a random superposition of eddies, that have a characteristic size  $\xi$  and last for a characteristic time  $\tau$ . This model is known as the Kerstein model for turbulence mixing [7]. The small scale motion is not considered, instead the description is given at a mesoscopic scale, the correlation length of the flow  $\xi$ . In this turbulent flow, the scalar is transported by diffusion except when it gets close to an eddy, and it is advected by the flow. It has been found that the distribution of the fluctuations of such scalar,  $c = \theta - \langle \theta \rangle$ , shows exponential tails. Pumir *et al.* [8], proposed a phenomenological model to explain such tails. Later on, Holzer and Pumir [5], studied the model by using a mean field analysis of stochastic processes that emulate the advection and diffusion of such scalar, and their approach was generalized by Kerstein and McMurtry [6] who stated clearly all the assumptions involved in the previous models, clarifying which were essential to reproduce the observed distributions.

The advection process is considered as discrete, with eddies simulated as a time sequence of statistically independent jump events that appear at different locations on a lattice. Their effect on the scalar is a partial rotation. For example, in  $d = 1$  an eddy will just flip the scalar field  $\theta$  around its center  $x_o$ , as illustrated schematically

in Figure 1. In higher dimensions the rotational effect is easier to visualize. Between flips or advection events, the scalar diffuses. The uniform, linear mean gradient, acts as a spatially homogeneous source of fluctuations  $\theta(\vec{r}, t) = c(\vec{r}, t) + \langle \theta(\vec{r}, t) \rangle$ , and is externally imposed through the boundary conditions by fixing the values of the scalar on the walls of the system. If the mean profile  $\langle \theta \rangle$  is linear in  $\vec{r}$ , it is conserved by the advective-diffusion equation

$$\frac{\partial \theta}{\partial t} + \vec{v} \cdot \nabla \theta = D \nabla^2 \theta, \quad (1)$$

where  $D$  is the molecular diffusivity, and  $\vec{v}$  the turbulent velocity field. In the absence of the linear gradient the scalar fluctuations will eventually relax to a delta function corresponding to a completely mixed state without fluctuations.

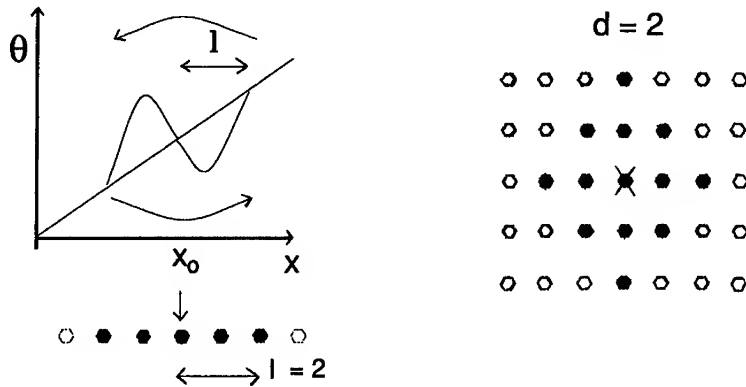


Figure 1. Schematic drawing of the action of an eddy at location  $x_0$  in  $d = 1$  and the points affected for a size  $l = 2$ . On the right are shown the sites involved in a typical eddy in  $d = 2$ .

## **LANGEVIN MEAN FIELD THEORY**

Previous mean field approaches to study this model [5-7] incorporated the effect of advection into a fine-grained description of the diffusion process starting with a discretized representation of the diffusion equation with an advection term, i.e.,

$$c_i(t + \Delta t) = (1 - \epsilon)c_i(t) + \epsilon[c_{i-1}(t) + c_{i+1}(t)] + \eta, \quad (2)$$

where  $\eta$  is a random forcing term that represents advection, and  $\epsilon = D\Delta t/a^2$ ,  $a$  being the lattice constant. The index  $i$  refers to a particular lattice site. The correlations between neighbor fluid elements (here lattice sites, at the mesoscopic scale)

were neglected by considering the random variables  $c_i, c_{i-1}$  and  $c_{i+1}$  as statistically independent, and independent of the random variable  $\eta$ .

An alternative mean field formulation is obtained when the term in brackets in eqn.(2) is set equal to zero, thus the quantities  $c_{i+1}$  and  $c_{i-1}$  are been replaced by their mean values. Now, eqn.(2) reduces to a linear Langevin equation

$$\frac{dc}{dt} = -\beta c + \eta'(t), \quad (3)$$

with  $\beta = 2D/a^2$  and  $\eta'(t) = d\eta/dt$ . Eqn.(3) can be solved for any realization of the random process  $\eta$ ,

$$c(t) = \int_{-\infty}^t \eta'(t') e^{-\int_{t'}^t \beta(t'') dt''} dt'. \quad (4)$$

Kerstein and McMurtry [6] studied the case of  $\beta$  constant in eqn.(4). They find that as function of a parameter  $K$  ( $K \propto \beta$ ) the probability distribution of  $c$  has exponential tails. In a more general case  $\beta$  depends on time, the scalar value  $c$ , and the details of the advection process, i.e., the statistics of  $\eta$ . If all these dependences are known, eqn.(4) gives the history in time of the scalar within a fluid element.

We consider here the situation where  $\beta$  depends on time and the statistics of  $\eta$ . For the jump advection process, events occur at times  $t_j < t$ , i.e.,  $\eta'(t) = \sum_{j=1}^{\infty} \eta_j \delta(t - t_j)$ , where the terms  $\eta_j$  are taken from a given distribution. The distribution of times between advection events are considered as having an exponential, Gaussian and Cauchy form. For all cases eqn.(4) is reduced to a sum of correlated terms

$$c(t) = \sum_{j=1}^{\infty} \eta_j e^{-\int_{t_j}^t \beta(t') dt'}, \quad (5)$$

and for constant  $\beta$ , it reduces to [6]  $c(t) = \sum_j \eta_j e^{-\sum_{k=1}^j \beta s_k}$ .

## NUMERICAL PROCEDURE

The advection-diffusion process is directly simulated by using a lattice with evenly spaced points on which a mean gradient is imposed by fixing the values of  $\theta$  on the walls (for example in 2D, the wall at  $y = -L/2$  is kept with  $\theta = 0$  while the other boundary at  $y = L/2$  with  $\theta = 1$ . Periodic boundary conditions are imposed along the  $x$  axis). At each set of randomly chosen times, an advection event occurs at a randomly chosen position. As mentioned above, the effect of such flip event is to partially rotate the scalar  $\theta$ , (see Fig.1), and between them, the scalar is transported by diffusion. The system is let evolve until a statistically stationary state is reached. Then,  $\theta$ 's values at different sites on the lattice are recorded, subtracted from their mean values, and accumulated in a histogram of  $c = \theta - \langle \theta \rangle$ ,  $P(c)$ . Several realizations

of the space-time distribution of advection events were considered to get an average distribution.

For the Langevin approach a large number of  $c$  samples ( $\sim 10^7 - 10^8$ ) are generated by a Monte Carlo-type sampling of  $\eta_j$ , and the spacings between advection events  $s_j = t_j - t_{j-1}$  by using eqn.(5). The  $\eta_j$ 's and  $s_j$  values are obtained from given distributions. About  $10^2 - 10^3$  terms were added to obtain a convergent  $c$  value. With those  $c$  samples, the histogram  $P(c)$  is constructed.

The histograms obtained with the two procedures described above are compared for different conditions in which the distributions of spacing between advection events, and their strength, and different forms of the  $\beta$  parameter in the Langevin equation (eqn.(4)) are used.

## RESULTS AND DISCUSSION

It is found that the distribution function of the deviation of the scalar from its mean value  $P(c)$ , is very sensitive to the statistics of the advection events. For a distribution of time spacings between advection events of exponential form,  $H(s) = 1/\langle s \rangle e^{-s/\langle s \rangle}$  it was found in Ref. [6] that for constant  $\beta$ ,  $P(c)$  is Gaussian and has exponential tails according to the values of a parameter  $K = \beta\langle s \rangle$ . For  $K \ll 1$  it has a Gaussian core, and exponential tails appear for  $K \geq 1$ . The Gaussian form is expected from the central limit theorem since for  $K \ll 1$ ,  $c$  is basically a sum of nearly identical random variables, thus its limit distribution has a Gaussian core.

We study the case of a time dependent  $\beta$  (but independent of  $c$  and  $\eta$ ) for the case where  $\beta$  decays as a power of time, i.e.,  $\beta = \beta_0/t^\alpha$  with  $\alpha > 0$ . It is found that  $P(c)$  has a Gaussian core for small values of the parameter  $K$ , and exponential tails appear for larger values of this parameter as is shown in Figure 2. If  $H(s)$  is Gaussian,  $P(c)$  is also Gaussian and for a Cauchy distribution of spacings, the tails are well fitted to the form  $1/(1+c^2)$ . These results suggest that for constant or time dependent  $\beta$ , the tails of the distribution have the form of the tails of  $H(s)$ .

The other case explored here, is the one where  $\beta$  is a function of the advection term. We study a Langevin equation of the form

$$\frac{dc}{dt} = -\beta c + \eta'_1 + \eta'_2 c, \quad (6)$$

where the  $\eta'_i$  are independent random variables with zero mean, such that

$$\langle \eta'_i(t) \eta'_j(t') \rangle = \eta_{oi} \delta_{ij} \delta(t - t').$$

This corresponds to  $\beta = \beta_0 + \eta'_2 = f(\eta')$ . The Langevin equation now has an additive noise term ( $\eta'_1$ ), and a multiplicative noise term ( $\eta'_2$ ). The distribution  $P(c)$  is non-Gaussian even though the distributions of  $\eta_j$ 's are Gaussian. Figure 3 shows how the distribution changes as we change the strength of the time correlations in the advection term, i.e the relative strength of the two noise terms.

It is clear that the mean field analysis of the advection-diffusion process studied here can explain the exponential tails observed in experiments and simulations of the process, however, it is sensitive to the details of the advection process, that selects the exponential statistics.

Recently Ching and Tu [9] reported results from simulations of eqn.(2) for an incompressible velocity field, whose stream function is a Gaussian random field with correlation length  $\xi$  and correlation time  $\tau$ . They found that the tails of  $P(c)$  are Gaussian, exponential, and stretched exponential in different regimes. They showed phase diagrams indicating the regions where these behaviors are expected as two parameters related to the relative strength of the diffusion and advection terms are varied. With the mean field approach used here, the transition from Gaussian, to exponential tails, and stretched exponential is also seen as the parameters of the model are varied.

We find that the qualitative features of  $P(c)$  do not depend on dimensionality. This result is in agreement with the basic assumption of this work of using a mean field approach to describe the transport process.

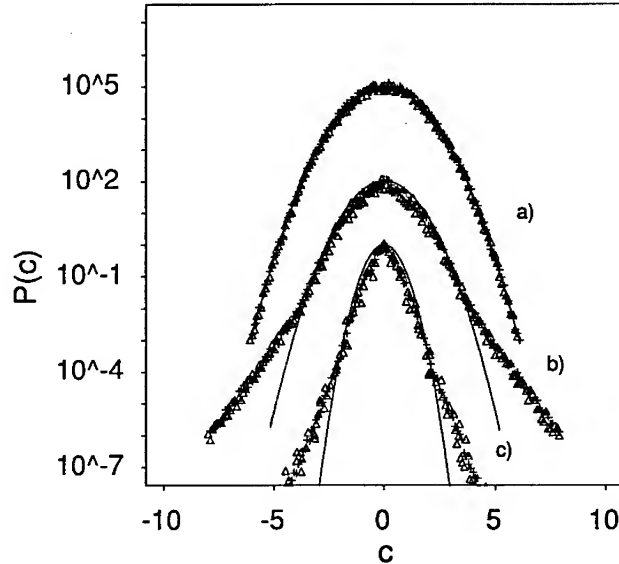


Figure 2. Plot of distributions of the scalar deviation,  $P(c)$ , with  $\beta = \beta_0/t^{1/2}$  and three different regimes of  $K$ : (a) for  $K = 0.1$ , (b)  $K = 1.5$ , and (c)  $K = 10$ . The solid line represents a Gaussian with the same variance.

In summary, a mean field approximation in terms of a Langevin equation is able to describe the transport of a scalar in a turbulent flow. It can predict the



exponential tails observed in experiments and simulations, and a variety of shapes such as stretched exponential, and Cauchy distributions can be seen for different values of the relevant parameters. The simplicity of the approach and the good agreement with the direct simulations of the advection-diffusion process encourages its application in the description of such transport processes.

The author thanks R.F Angulo for a critical reading of the manuscript and INTEVEP S.A. for permission to publish this paper.

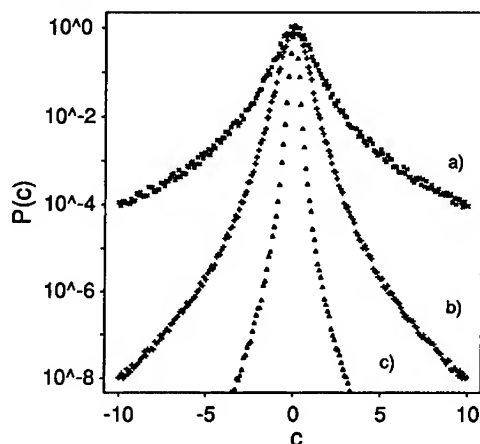


Figure 3. Distributions of scalar deviation  $P(c)$  from simulations of eqn.(6) in Langevin approach for various noise strengths: a)  $\eta_{01} = 0.0165, \eta_{02} = 10\eta_{01}$ , b)  $\eta_{01} = \eta_{02} = 0.165$ , and c)  $\eta_{01} = \eta_{02} = 0.5$ .

## References

- [1] B. Castaing *et al.*, J. Fluid Mech. **204**, 1 (1989); M. Sano, X. Wu, and A. Libchaber, Phys. Rev. A **40**, 6421 (1989).
- [2] Jayesh and Z. Warhaft, Phys. Rev. Lett. **67**, 3503 (1991); Phys. Fluids A **4**, 2292 (1992).
- [3] J.P. Gollub, J. Clarke, M. Gharib, B. Lane, and O. N. Mesquita, Phys. Rev. Lett. **67**, 3507 (1991).
- [4] C.W. Van Atta and W.Y. Chen, J. Fluid Mech. **44**, 145 (1970).
- [5] M. Holzer and A. Pumir, Phys. Rev. A **47**, 202 (1993).
- [6] A.R. Kerstein and P.A. McMurtry, Phys. Rev. E **49**, 474 (1994).
- [7] A. Pumir, B. Shraiman, and E.D. Siggia, Phys. Rev. Lett. **66**, 2985 (1991).
- [8] A. Kerstein, J. Fluid Mech. **231**, 361 (1991).
- [9] E.S.C. Ching and Y. Tu, Physical Review E, **49**, 1278 (1994).

## DAMPING AND SPATIAL DISTRIBUTION OF PERCOLATION FRACTONS

S. Russ and B. Sapoval,  
Laboratoire de Physique de la Matière Condensée,  
C.N.R.S. Ecole Polytechnique, 91128 Palaiseau Cédex, France

### ABSTRACT

The damping of the vibrations of very irregular discretized systems embedded in a viscous fluid is studied in the particular case of the vibrations of percolation clusters. We develop a formal description for the "regularity" of a vibrational mode. This permits us to measure numerically how the local fluctuations in the vibration amplitude contribute to the viscous damping. The fact that the regularity is found to be larger than that of a single localized state on a linear chain is indicative of the very structure of the percolation cluster made of blobs and red bonds.

### INTRODUCTION

It has been shown recently that the vibrations of fractal percolation clusters exhibit an enhanced damping due to the irregular distribution of the vibration amplitude [1]. In order to describe more precisely this effect we have developed a simple formalism which enables us to measure the spatial "regularity" of the vibrational amplitude [2]. In these papers we have obtained two main results. First the damping is dominated by a minority of pairs of second-nearest neighbors which are far in the "chemical space" but close in the real space. Second and surprisingly, the fracton amplitude distribution over first-nearest neighbor pairs is more regular than for an ordinary localized mode of a linear chain. This was qualitatively interpreted by describing fractons as "regular by pieces" and the present work is devoted to give a more precise numerical evidence of this fact. We recall first how the amplitude distribution regularity is connected to the viscous damping of a mode.

Classically the damping of a vibrational mode is measured by the so-called quality factor  $Q$ . This number is the dimensionless ratio of the reactive energy  $E$  to the losses  $P$  per cycle:

$$Q = 2\pi E/P. \quad (1)$$

We consider here the vibrations of a particular irregular object: a percolation cluster on a square lattice with spacing  $a$ . The vibrational elongation of an eigenmode of frequency  $\omega$  is  $z(i,j,t) = Ca\Psi_0(i,j) \cos(\omega t)$  where  $C$  is the amplitude and with a suitable normalization, the maximum kinetic energy  $E$  is equal to  $C^2 m\omega^2/2$  where  $m$  is the mass of the vibrating particles.

To compute the losses we suppose the vibrating system to be embedded in a viscous medium as presented in Ref.[1] and the dissipation due to the internal viscosity of the displaced medium. In first approximation we assume a laminar flow to ensure linear damping. In this picture the local damping forces are proportional to the vertical velocity difference between neighboring masses:

$$F(i,j) = -ab \sum_{i',j'} \mu |v(i,j) - v(i',j')| / r(i,j)(i',j') \quad (2)$$

where  $\mu$  is a shear viscosity,  $v(i,j) = dz(i,j)/dt = Ca\omega \sin(\omega t) \Psi_0(i,j)$  is the vertical velocity at site  $(i,j)$  and  $r(i,j)(i',j')$  is the distance between site  $(i,j)$  and site  $(i',j')$ . The length  $b$  represents the vertical size of the moving particles. The total viscous force at site  $(i,j)$  is a sum of the forces due to first-nearest neighbors, second-nearest neighbors and so on. If there are losses only between first nearest neighbors the quality factor can be written

$$Q_{\text{fnn}} = [m\omega/ab\mu] \Lambda_{\text{fnn}}(\omega) \quad \text{with} \quad (3)$$

$$\Lambda_{\text{fnn}}(\omega) = [a^2 \sum_{i,j} |\Psi_{\omega}(i,j)| \delta \Psi_{\text{fnn},\omega}(i,j)]^{-1} \quad \text{with} \quad (4)$$

$$\delta \Psi_{\text{fnn},\omega}(i,j) = (1/2a) \{ |\Psi_{i+1,j} - \Psi_{i,j}| + |\Psi_{i-1,j} - \Psi_{i,j}| + |\Psi_{i,j+1} - \Psi_{i,j}| + |\Psi_{i,j-1} - \Psi_{i,j}| \} \quad (5)$$

where we have used  $r(i,j)(i',j')=a$ , the first-nearest neighbor distance of the system.

The energy loss depends on the size, shape and "regularity" of  $\Psi_{\omega}(i,j)$  through the weighted sum of the local amplitude differences in (4,5). In general,  $\Lambda(\omega)$  will depend on the local "regularity" as well as on the localization of the vibrational amplitude. In [2] we have focused on a size-independent description of the "regularity" of an arbitrary mode in a resonator with arbitrary geometry. We have introduced a number  $R(\omega)$  which characterizes the "regularity" of the vibration distribution by relating  $\Lambda(\omega)$  to the size  $X(\omega)$  of the region where the system really vibrates:

$$R(\omega) = \Lambda(\omega)/X(\omega) \quad (6)$$

The size  $X(\omega)$  is, following Thouless [3], obtained from the quantity  $V(\omega)$ , which we call the localization "volume" (in a d-dimensional space) of a given normalized state  $\Psi_i(\omega)$ :

$$X(\omega) = [\sum_i a^d |\Psi_i(\omega)|^4]^{-1/d} \quad (7)$$

and the quality factor is now  $Q = [m\omega/ab\mu] X(\omega) R(\omega)$ .

We use the regularity  $R(\omega)$  to describe how an eigenfunction varies in space. For example, in the simplest classical case of a linear string of length  $L$ , we have  $\Psi(x) = (2/L)^{1/2} \sin(n\pi x/L)$  for the  $n$ th mode. For a discretized string (with  $L \gg a$ ) we find  $X = 2L/3$ , indicating that whatever the mode the localization volume is the same and  $R = 3/4n$ . This justifies the use of the word "regularity" to qualify the spatial behavior of a wave because a sine wave of long wavelength (small  $n$ ) is more regular than a sine wave of short wavelength, which exhibits more "mountains and valleys" along the same localization length  $X$ . An interesting case is the case of an infinite linear chain with one impurity for which there exists a single localized state of the form  $\Psi(x) = \lambda^{-1/2} \exp[-|x|/\lambda]$ . In this case  $X = 2\lambda$ ,  $\Lambda = \lambda$  and  $R = 1/2$ . The surprising result that we have for fractons is that we find regularities of the order of 1 for this most disordered system and this is discussed now.

## PERCOLATION FRACTONS REGULARITY

We consider the vibrations of a percolation cluster [4] (for a recent review of the topic we refer to [5]). We distinguish between two definitions of space. In the ordinary "r-space" the distance between two points is described by the ordinary Euclidean distance  $r$ , whereas in the " $\ell$ -space" this distance is described by the length  $\ell$  (the chemical distance) of the shortest conducting path between the two points [6] (see Fig.1).

Fractons are "regular" in  $\ell$ -space and "irregular" in  $r$ -space. It was recently shown [7,8], that in first approximation and for large distances  $\ell$ , fracton amplitudes decay exponentially along the shortest conducting path from the center of the fracton, chosen at site 0. Their envelope function  $\Psi_{\omega}(A)$  can be approximated in  $\ell$ -space by:  $|\Psi_{\omega}(A)| \propto \exp[-\ell_A/\lambda_{\ell}(\omega)]$  where  $\ell_A$  is the chemical distance of a point  $A$  from the center and  $\lambda_{\ell}(\omega)$  is the localization length measured along the chemical path.

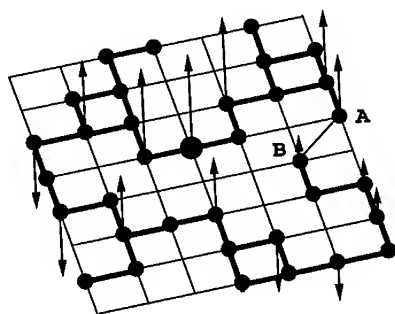


Fig.1. Schematic distribution of the fracton amplitude showing qualitatively why the viscous damping between second-nearest neighbors is enhanced by the irregular spatial distribution of the vibrational amplitudes. Note the different chemical paths, leading to the particles A and B.

In percolation clusters all nearest neighbors are connected and thus lie on the same chemical branch, resulting in small energy losses from nearest neighbor dissipation. But, if our percolation cluster is embedded in an Euclidean viscous medium, there will also exist a damping due to next-nearest neighbors. We know that there exists a substantial number of pairs of second-nearest neighbors A and B, pertaining to very *different* chemical distances  $\ell_A$  and  $\ell_B$ , i.e. with  $\Delta\ell > 2a$ . As indicated in Fig.1 these pairs exhibit in general very different values of  $\Psi_\omega(A)$  and  $\Psi_\omega(B)$  and can therefore create a large viscous damping. As a consequence, we expect for fractons a large viscous damping between second-nearest neighbors, especially between those with a chemical distance  $\Delta\ell > 2a$ . This damping can be characterized by the regularity  $R_{snn}$  which was described in [1].

For the numerical calculations discussed in [1,2] we have generated 10 percolation clusters at  $p_c = 0.592745$  [9] on a square lattice by the Leath method [10] with 300 shells. The fracton modes of frequency  $\omega = 0.1(k/m)^{1/2}$  ( $k$  is the strength of the spring constants) that we have studied are calculated numerically on each of the clusters by the Williams-Maris technique [11]. We have computed for these 10 different modes the first- and second-nearest neighbor regularities,  $R_{fnn}$  and  $R_{snn}$ .

## FRACTONS ARE REGULAR BY PIECES

The results are given in Tab.I. The first interesting comment to make is to remark that the first-nearest neighbor regularities are of order 1, an unexpected result in the sense that the vibration distribution is found more "regular" than that of a classical localized state on a regular system. This can be understood if one recalls first that the structure of the percolation cluster is made of blobs separated by red bonds [12]. Secondly there exists a very close link between vibration and diffusion over the same region. For us the fact that the regularity is large indicates that the vibration amplitude on a blob does not vary strongly. A vibration mode made as a collection of blobs vibrating in a rather homogeneous fashion and separated by red bonds would give rise to this effect. Fig.2 shows a qualitative picture of this type of amplitude distribution.

## FEM BASED SIMULATION OF PERCOLATION FEATURES OF DISORDERED HETEROGENEOUS MEDIA ELASTIC PROPERTIES

S.A. TIMAN AND V.G. OSHMIAN

Institute of Chemical Physics, RAS, Kosygin str. 4, Moscow,  
Russia

### ABSTRACT

The mechanical properties of the 2D elastic rigid-nonrigid disordered system in dependence on the concentrations of the rigid phase are studied. The system is constructed on the basis of the square lattice and finite element method (FEM) approximation. The elasticity threshold of the FE system and the critical exponents are determined by the phenomenological renormalization (PR) of the Monte Carlo data.

### Introduction

Experimental and theoretical investigations of the last ten years exposed the essential difference between elastic and conductive properties of disordered systems near the threshold.<sup>2-10</sup> The exact analogy takes place in the frameworks of the Born potential.<sup>1</sup> In this model equilibrium equations for every displacement component are of Kirchhoff type. Elasticity threshold and stiffness critical exponent are equal to the percolation threshold and conductivity exponent correspondingly. However, Born potential changes with the rotation of the system. This contradicts to the regularities of deformation.

Elastic properties of disordered lattices were studied in the frameworks of linearized central force potential.<sup>2,6-8</sup> Computer simulations and mean field approaches for 2D triangle and 3D fcc lattices revealed that elasticity thresholds noticeably exceed percolation ones. It was shown for the triangle lattice that this effect is determined by the formation of the specific "stiff" structures.

Bond-bending potential<sup>4,5,9</sup> based investigations established the congruence of elasticity and percolation thresholds. It is caused by the formation of the elastic unidimensional chains. Corresponding critical exponents differ both with the exponents determined by the central force potential and the conductivity.

The properties of the various lattice systems near the elasticity threshold are quite different. That conditions complexity and ambiguity of the simulation of the disordered continuum media mechanical behavior. Accordingly to the numerical methods for the solution of elastic boundary problems for homogeneous materials it is natural to replace the

homogeneous regions by finite elements (FE) with the proper mechanical stiffness parameters. The main advantage of the FE model is the possibility of the construction of the discrete analog of homogeneous continuum media with arbitrary Lamé coefficients. The approach described was suggested in<sup>10</sup>. However, imperfection of computational equipment and use of relaxation-type numerical methods considerably restricted the precision of the approximation of elasticity thresholds and modules.

#### Description of the model

The structure of 2D disordered media is simulated on the basis of square lattice with every cell randomly "filled" by the stiff or soft square FE with probabilities  $p=p_2$  and  $p_1=1-p$  correspondingly. Elastic energy of this discrete system is the sum of the energies of FEs. The last one depends upon displacements  $X_i$ ,  $Y_i$  of the sites:

$$W = \sum_{i,j} (a_{ij}X_iX_j + b_{ij}Y_iY_j + c_{ij}X_iY_j) \quad (1)$$

Coefficients  $a_{ij}$ ,  $b_{ij}$ ,  $c_{ij}$  are calculated through elastic modules  $C_{11}$  and  $C_{12}=\mu$  of corresponding phase.

Accordingly to FEM variational principle minimum value of (1) is attained on the solution of the equilibrium linear system:

$$\frac{\partial W}{\partial X_i} = 0, \quad \frac{\partial W}{\partial Y_i} = 0 \quad (2)$$

for the sites at the proper boundary conditions.

Effective elastic modules  $C_{11}$  and  $\mu$  were determined by the solution of the boundary problem for  $L \times L$  square domain with periodic conditions on vertical sides and fixed displacements on horizontal boundaries. Transfer-matrix method<sup>9</sup> was used for the exact solution of (2) and calculate the values of  $C_{11}$  and  $\mu$  of the discrete system.

## Results and discussion

Calculation of effective elastic modules  $\bar{C}_{11}$  and  $\bar{\mu}$  for the squares 10x10, 25x25 and 40x40 was performed at every volume contents  $p$ :

$$\begin{aligned}\bar{C}_{11} &= \langle \sigma_{11} \rangle / \langle \varepsilon_{11} \rangle & \text{at } \langle \varepsilon_{22} \rangle = \langle \varepsilon_{12} \rangle = 0, \\ \bar{\mu} &= 0.5 \langle \sigma_{12} \rangle / \langle \varepsilon_{12} \rangle & \text{at } \langle \varepsilon_{11} \rangle = \langle \varepsilon_{22} \rangle = 0.\end{aligned}$$

A large series of configurations ( $\approx 2000$  for arbitrary  $p$ ) were analyzed and the mean values of  $C_{11}$  and  $\mu$  were found:

$$C_{11}(p, L) = \langle \bar{C}_{11}(p, L) \rangle_{\text{conf}}, \quad \mu(p, L) = \langle \bar{\mu}(p, L) \rangle_{\text{conf}}.$$

This procedure may be interpreted as the method of calculation of the stiffness of the strip with infinite width and finite height  $L$  ( $L=10, 25, 40$ ) (Fig. 1).

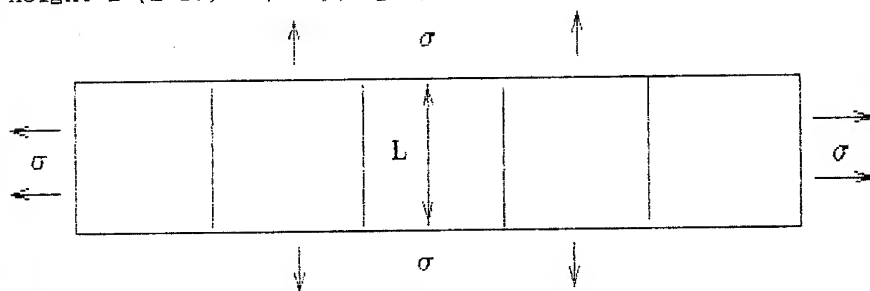


Fig. 1

Poisson ratios  $\Sigma(p, L)$  were found from the isotropic approximation:  $\Sigma(p, L) = 1 - 2\mu/C_{11}$ . Poisson ratios of both phases and shear module of the stiff component were fixed:  $\Sigma_1 = 0.37$ ,  $\Sigma_2 = 0.23$ ,  $\mu_2 = 1$ .

The system studied is geometrically identical to the site percolation problem on the square lattice with diagonal bonds. The last simulate mechanical interaction between FE via the tips. Percolation threshold for this lattice is equal to  $p_{c1} = 0.41$ . Infinite cluster by the ribs of the stiff FE's is formed at  $p_{c2} = 0.59$ . The elasticity threshold  $p_{ce}$  of such system is not known a priori. This situation is analogous to the central force potential model.<sup>2,5-7</sup> It is clear that  $p_{c1} \leq p_{ce}$ . Mean field estimation<sup>5</sup> gives:  $p_{ce} \leq 0.5$ .

The results of  $\mu$  concentration dependences, calculated for the systems of finite size  $L$  are represented on Fig. 2.

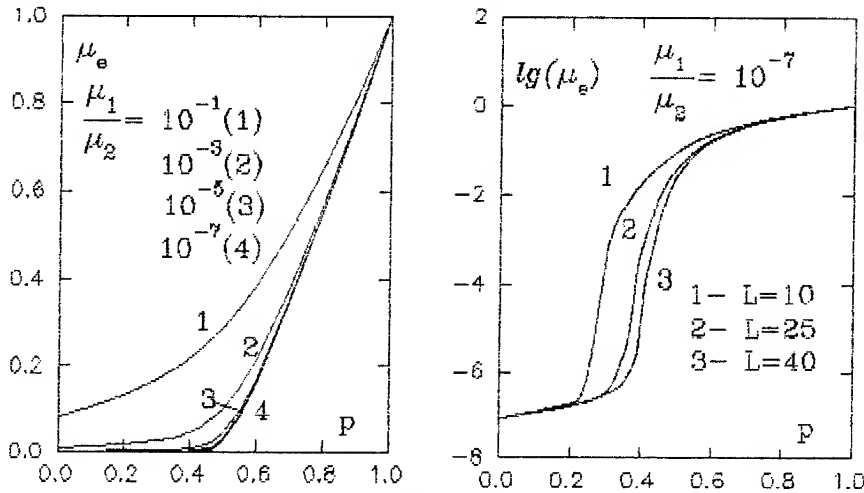


Fig. 2

The effect of the shift of the elastic threshold to the right with increase of  $L$  ( $p_{ce}(10) \approx 0.25$ ,  $p_{ce}(25) \approx 0.42$ ,  $p_{ce}(40) \approx 0.45$ ) may be seen from the Fig. 2 and is quite understandable. Probability of the existence of the stiff cluster at  $p < p_{ce}$  is not zero for the finite system. Certainly, it increases with  $p$ , but decreases with  $L$ . So up and down banks of the strip are connected by the finite stiff cluster at  $p < p_{ce}$ .  $p_{ce}(L)$  scaling dependence may be obtained by the assumption that percolation threshold of the finite strip occurs when the elastic coherence length  $\xi$  of the stiff cluster is equal to  $L$ :

$$p_{ce} - p_{ce}(L) = a L^{-1/\nu} \quad (3)$$

If we load the strip of finite height  $L$  in horizontal direction (analogous to simulation used in ) we could obtain decreasing dependences  $p_{ce}(L)$ . In this case the fact of the strip cross by the soft cluster is important.

In order to estimate elastic threshold  $p_{ce}$  for the infinite system we follow the idea of phenomenological renormalization (PR) of Monte Carlo data<sup>7</sup>. Taking (3) into account at  $p > p_{ce}(L)$  we have:

$$\mu = (p - p_{ce}(L))^T = L^{-T/\nu} \left[ (p - p_{ce}) L^{1/\nu + a} \right] \quad (4)$$



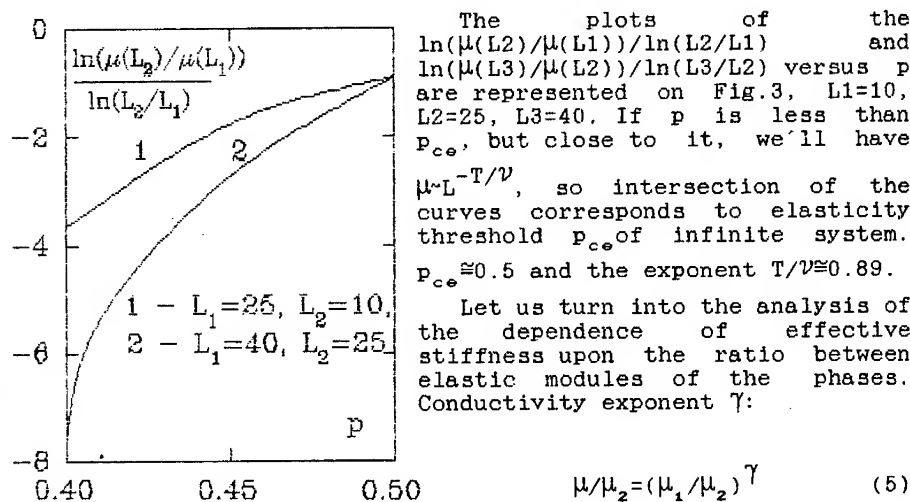


Fig. 3

of symmetrical disordered D2 mixture of two conductors  $\mu_1$  and  $\mu_2$  is of exact value 0.5. The construction of the scaling function  $\gamma$  corresponds to  $\gamma = s/(s+t)$ . In the D2 case we have  $s=t$  and  $\gamma=0.5$  that is in accordance with the mentioned exact result. The treatment of our calculations at  $L=40$  from this point of view is shown on Fig.4a. It is clear that for horizontal strips (Fig.1) the presence of stiff clusters between up and down banks leads to the saturation of the dependences  $\ln(\mu/\mu_2)$  upon  $\ln(\mu_1/\mu_2)$ .

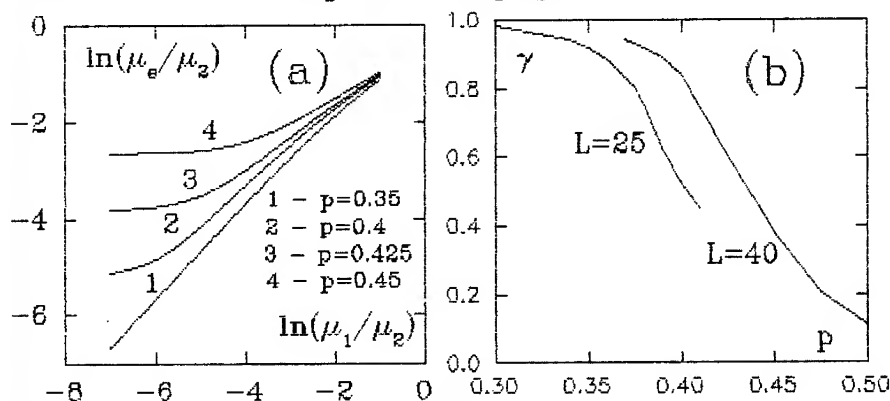


Fig. 4

This saturation takes place at larger  $\mu_1/\mu_2$  for smaller  $p$  because the stiff connections become more rare with the

decrease of  $p$ . So, in the case of finite system  $GAM = d\ln(\mu/\mu_2)/d\ln(\mu_1/\mu_2)$  is not constant and tends to zero with the decrease of  $\mu_1/\mu_2$ . An attempt of estimation of  $\gamma$  by the straitening at the media ( $\mu_1/\mu_2 = 10^{-3} - 10^{-5}$ ) parts of the dependences on Fig. 4a is represented on Fig. 4b. The value of  $\gamma$  drops with  $p$ . The increase of the strips height (Fig. 4b) leads to the shift of the curves to the right in accordance with the shift of the threshold. The of the concentration region were  $\gamma$  drops almost does not changes with the change of  $L$ . This

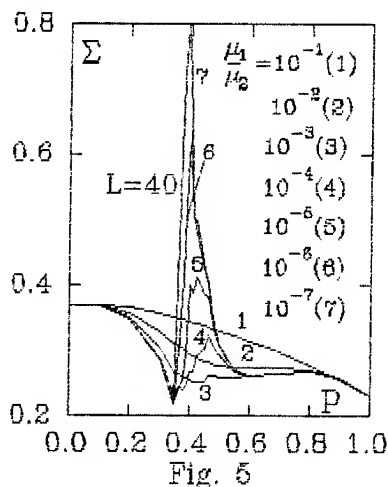


Fig. 5

fact likely points to the existence of not trivial continuous spectrum of  $\gamma$  at the certain concentration interval for the infinite system.

Concentration dependences of Poisson ratios  $\Sigma(p)$  at different  $\mu_1/\mu_2$  are represented on Fig. 5.

We have monotonous decrease of  $\Sigma$  at low  $\mu_1/\mu_2$ . The curves have minimum at media  $\mu_1/\mu_2$  values and exhibit

two minimums and maximum at height stiffness ratios. The results at low and media  $\mu_1/\mu_2$  are in

accordance with calculations of<sup>9</sup>. Bergman obtained negative Poisson ratio at infinite  $\mu_1/\mu_2$  in

the case of horizontal loading of the strip of disordered honeycomb lattice in percolation threshold.

## References

- <sup>1</sup> P.G. de Gennes, J.Phys(Paris)Lett. 37, L1 (1976)
- <sup>2</sup> L.Benguigui, Phys.Rev.B 34, 8176 (1986)
- <sup>3</sup> S.Feng and P.N.Sen, Phys.Rev.Lett. 52, 216 (1984)
- <sup>4</sup> S.Feng, P.N.Sen, B.I.Halperin, C.J.Lobb, Phys.Rev.B 30, 5386 (1984)
- <sup>5</sup> D.J.Bergman, Phys.Rev.B 31, 1696 (1985)
- <sup>6</sup> S.Feng, M.F.Thorpe, E.Garboczi, Phys.Rev.B 31, 276 (1985)
- <sup>7</sup> M.Sahimi and J.D.Goddard, Phys.Rev.B 32, 1869 (1985)
- <sup>8</sup> A.R.Day, R.R.Tremblay, A.-M.S.Tremblay, Phys.Rev.Lett. (1986)
- <sup>9</sup> E.Duering and D.J.Bergman, Phys.Rev.B 37, 9460 (1988)
- <sup>10</sup> L.I.Manevitch, M.I.Guy, R.A.Turusov, V.G.Oshmian et. al, J.Appl.Phys. 61, 5425 (1987)

## SCALING OF TRANSPORT PROPERTIES OF RESERVOIR MATERIAL AT LOW SATURATIONS OF A WETTING PHASE

Y. CAROLINA ARAUJO, PEDRO G. TOLEDO AND HADA Y. GONZALEZ

Intevep, S. A., Research and Technological Support Center of Petróleos de Venezuela, S. A.,  
P.O. Box 76343, Caracas, 1070-A, Venezuela

### ABSTRACT

Transport properties of natural porous media have been observed to obey scaling laws in the wetting phase saturation. Previous work relates power-law behavior at low wetting phase saturations, i.e., at high capillary pressures, to the thin-film physics of the wetting phase and the fractal character of the pore space of porous media. Here, we present recent combined porous-plate capillary pressure and electrical conductivity data of Berea sandstone at low saturations that lend support to the scaling laws. Power law is interpreted in terms of the exponent  $m$  in the relation of surface forces and film thickness and the fractal dimension  $D$  of the interface between pore space and solid matrix. Simple determination of  $D$  from capillary pressure and  $m$  from electrical conductivity data can be used to rapidly determine wetting phase relative permeability and capillary dispersion coefficient at low wetting phase saturations.

### INTRODUCTION

The distribution of a wetting phase, water, at low saturation is of interest to the petroleum engineer in connection with equity determinations and reservoir simulation. Also, it is of interest to the soil scientist in connection with agricultural crops, the balance of aquifers and the migration of agricultural, chemical and nuclear contaminants.

At high capillary pressure, i.e., at low water saturation, water in a water-wet porous medium exists as thin films which cover smooth pore walls, as pendular structures which fill nooks and crannies, i.e., asperities in pore walls on scales smaller than the mean radius of the pores, and as bulk liquid which fills the smallest pores. This we refer to as the low saturation regime. Recently, power-law behavior of transport properties at low wetting phase saturations has been related to the thin-film physics of the wetting phase and the fractal character of the pore space of natural porous media.<sup>1-7</sup> The power laws deduced are  $X = S_w^b$ , with  $X = P_c$ ,  $k_{rw}$ ,  $\sigma_w$ , and  $D_c$ , where for capillary pressure  $b_{P_c} = -1/(3 - D)$ , for wetting phase relative permeability  $b_{k_{rw}} = 3/[m(3 - D)]$ , for  $b_{\sigma_w} = 1/[m(3 - D)]$ , and for capillary dispersion coefficient  $b_{D_c} = [3 - m(4 - D)]/[m(3 - D)]$ , where  $m$  is the exponent in the relation of disjoining pressure and film thickness and  $D$  is the fractal dimension of the surface between the pore space and surface matrix.

Accurate measurements of transport properties at low saturations are challenges and reliable data are rare.<sup>8-15</sup> Here, we present recent combined capillary pressure and electrical conductivity data of Berea sandstone that exhibit scaling. Simple determination of  $D$  and  $m$  can then be used to predict  $b_{k_{rw}}$  and  $b_{D_c}$  at low wetting phase saturations.  $D$  reveals traits of the microscopic world of pore wall roughness<sup>1,3,15,16</sup>, and  $m$  of molecular-level forces which act between the wetting phase films and the solid matrix and largely determine surface wettability.<sup>18</sup>

## THEORY

We assume one of the fluids strongly wets the sample porous medium. At very high capillary pressure, bulk wetting phase does not span the sample. Instead, wetting phase is present as isolated pendular structures — that fill the asperities in pore walls, connected to one another through thin films of wetting phase. Thus, thin films furnish sample-spanning hydraulic connections through which wetting phase can be transported through the sample.<sup>1-7</sup>

Thus, the total saturation of wetting phase  $S_w$  is composed of water in pendular structures  $S_{ps}$  and water in films  $S_{tf}$ , i.e.,  $S_w = S_{ps} + S_{tf}$ . In the low saturation regime  $S_{tf}$  does not significantly contribute to  $S_w$ . Under these conditions the capillary pressure obeys the scaling law<sup>1,3,16</sup>  $P_c \propto S_w^{-1/(3-D)}$ , the wetting phase relative permeability obeys<sup>3,7</sup>  $k_{rw} \propto S_w^{3/[m(3-D)]}$ , the electrical conductivity obeys<sup>5,7</sup>  $\sigma_w \propto S_w^{1/[m(3-D)]}$ , and the capillary dispersion coefficient obeys<sup>6,7</sup>  $D_c \propto S_w^{[3-m(4-D)]/[m(3-D)]}$ .

Molecular-level forces act near and across the interfaces of the thin films, whose thickness and normal stress component are controlled by the chemical potential. The difference between the normal stress in the film and the pressure of bulk fluid in equilibrium with the thin film is called disjoining pressure  $\Pi$ . The dependence of  $\Pi$  on film thickness  $h$  has been theorized and measured for a variety of solid/liquid pairs; often these data are described well over a restricted range of film thickness by a simple monomial,  $\Pi \propto h^{-m}$ . The exponent  $m$  is a property of the solid/liquid pair;  $m$  does not depend on the configuration of the pore space containing the liquid. For example,  $m = 3$  applies to van der Waals interaction,  $m = 2$  applies to electrostatic interaction (dilute limit) and  $m = 1$  applies to short-ranged structural interaction.<sup>18</sup>

## SAMPLE PREPARATION

The core sample studied was a Berea sandstone. The sample, nominally 5.5 cm in diameter and 4.5 cm in length, was Soxhlet-cleaned with toluene and methanol for 16 hours and oven-dried at 100 °C. Gas permeability and porosity at confining pressure of 3000 psi were, respectively, 15 md and 6 %. The mineralogy of the sample as measured by X-ray diffraction revealed quartz only. The grain density was 2.6 g/cm<sup>3</sup>. Two matched disk-shaped samples of 5.5 cm in diameter and 0.5 cm in thickness were cored under fresh water from the whole core sample. The sample disks we referred to as M-6 and M-7. The disks were then prepared for the porous plate capillary pressure and electrical conductivity measurements.

Platinum contacts were made by sputtering directly onto the two opposite flat faces of the sample disks. The lateral surface of the disks was sealed with a shrinking rubber sleeve to prevent it from sputtering. The samples were again Soxhlet-cleaned with toluene and methanol for 16 hours and oven-dried at 100 °C. A detailed description of the experiment is given by Knight and Nur.<sup>19</sup>

## EXPERIMENTAL METHODS

Commercially available Soilmoisture 5, 15, and 100 bar pressure-plate extractors were used. Ceramic plates were used in the first two extractors. A cellulose membrane, also available from Soilmoisture, was used in the 100 bar extractor. The principle involved in the operation is well known. Saturated samples are placed directly on the porous plate and subjected to air pressure in the extractor. Diatomaceous earth is used to secure the capillary contact between the samples

and the porous plate. This precaution was not necessary in the case of the membranes. At any given air pressure in the extractor, water was observed to flow from the samples until capillary equilibrium was attained. No water production was a clear indication of that. Saturation at equilibrium was determined gravimetrically. Total run time for a single capillary pressure point was about 15 days. Temperature was about 21 °C.

The impedance of the capillary-equilibrated samples was measured with a two-contact cell and a Hewlett-Packard (4192A) impedance analyzer. Measurements were made in the frequency range of 5 Hz to 113 MHz. The oscillation amplitude was 1 V. To interpret the data we simply followed Knight and Nur.<sup>19</sup> The electrical response of the samples was modeled in terms of a Debye circuit which at low frequencies reduces to a series RC circuit and at high frequencies reduces to a parallel RC circuit. The crossover frequency  $\omega_c$  was determined here from a complex impedance plot of the data for the partially saturated Berea samples. In a complex impedance plot, the imaginary part of the impedance  $-X_s$  is plotted against the real part  $R_s$ . The impedance at  $\omega_c$  is almost entirely real, and thus  $R_s$  represents the best value for the d.c. resistance of the samples.

In principle, the d.c. conductivity of the samples at  $\omega_c$  can be calculated either from  $\sigma_w = h_d/A \times 1/R_s$  or from  $\sigma_w = h_d/A \times G_p$  where  $h_d$  and  $A$  are respectively the thickness and the area of the sample disks, and  $G_p$  is the conductance of the disks measured in the parallel mode. The d.c. conductivity of the partially saturated samples was determined from  $G_p$  measurements. We found, for the samples examined here, that a frequency of 60 kHz minimized the imaginary part of the samples' impedance at the various levels of saturations.

## RESULTS AND DISCUSSION

Figure 1 gives the capillary pressure of water (wetting phase) in the presence of air (nonwetting phase) for the matched samples M-6 and M-7, using the porous plate method. The saturation range studied,  $S_w = 2\%$  to  $6\%$ , is well below the percolation threshold of sample-spanning paths of water-filled pores. Thus water is present only as thin films and as pendular structures that are hydraulically connected to one another through thin films.

If the pore-wall roughness of samples M-6 and M-7 is nonfractal and consists of conical pits ( $P_c \propto S_w^{-3}$ ), hemispherical pits ( $P_c \propto S_w^{-3}$ ), and the spaces between fused grains ( $P_c \propto S_w^{-2}$ ), it is expected that the relation  $S_w = AP_c^{-2} + BP_c^{-3}$  would describe the data well. A least-squares fit of samples M-6 and M-7 data to this formula yields poor fit, namely  $S_w = 45.1935P_c^{-2} - 15.3932P_c^{-3}$  with a correlation coefficient of 0.96. At high capillary pressure ( $P_c \geq 20$  bar) the water saturation does not scale as either  $P_c^{-2}$  or  $P_c^{-3}$ . Adding a term proportional to  $P_c^{-1}$  to account for the inventory of thin films deteriorates the fit appreciably. A least-squares fit yields  $S_w = 25.34856P_c^{-1} - 12.91572P_c^{-2} - 1656.33097P_c^{-3}$  with a correlation coefficient of 0.63.

If the pore-wall roughness is fractal,  $P_c \propto S_w^{-1/(3-D)}$ , describes the relation of  $P_c(S_w)$ . A least-squares fit of samples M-6 and M-7 data to this equation yields  $P_c \propto S_w^{-3.37}$  with a correlation coefficient of 0.992. Figure 1 shows the quality of the fit. Interpreting the exponent  $b_{P_c}$  as  $1/(3-D)$  for samples M-6 and M-7 the fractal dimension is  $D = 2.7$  which is valid at length scales between  $2.9 \mu\text{m}$  and  $0.29 \mu\text{m}$  — the range of diameters of equivalent cylindrical pore segments emptied by the capillary pressures we imposed. This

fractal dimension is compatible with the range 2.57 to 2.87 found by Katz and Thompson from scanning micrographs.<sup>20</sup>

Combined capillary pressure and electrical conductivity data at low wetting phase saturations are rare. Here, for each of the capillary equilibrium points in Figure 1, we measured the electrical conductivity of the water in the presence of air (insulating) for samples M-6 and M-7.

At low frequencies  $\sim 60$  kHz and in the saturation range  $S_w \leq 5\%$ , we find a strong dependence of  $\sigma_w$  on the level of water saturation. Figure 2 shows the experimental data for samples M-6 and M-7. Conventionally, one often works instead of with the so-called resistivity index  $I$ , a normalized resistance defined via  $\sigma_{wo} = \sigma_w I$ , where  $\sigma_{wo}$  is the conductivity of a rock that is completely saturated with a brine of conductivity  $\sigma_o$ . Thus  $I \propto S_w^{-1/[m(3-D)]}$ . On the basis of experimental data, Archie proposed a power law of the form  $I \propto S_w^{-b_{\sigma_w}}$  where  $b_{\sigma_w}$  is a constant called saturation exponent of the rock.<sup>21</sup> Archie suggested a value of 2 for  $b_{\sigma_w}$  for both sandstones and unconsolidated sands. The value of  $b_{\sigma_w}$  is known to vary over a considerable range. Plainly,  $b_{\sigma_w}$  can be interpreted as  $1/[m(3-D)]$  at low saturations of wetting phase. A least-squares fit of the data at high capillary pressure yields  $b_{\sigma_w} = 1.796$ . Thus,  $m = -b_{\sigma_w}/b_{P_c} = 1/[(3-D)1.796]$ . With  $D = 2.7$  we find that  $m \sim 2$ , appropriate for thin films on silica surfaces of the kind present in samples M-6 and M-7. The value  $m \sim 2$  reveals a predominance of weak electrostatic interactions on the disjoining pressure. This is an expected result considering that some amount of salt from the sandstone dissolves into the pore fluid.

Recently, Melrose<sup>13</sup> estimated that the fraction of mineral surface available for adsorption of wetting thin films in the low saturation regime varies from 65 to 72% of the total available surface. From this and from film thickness estimates he concluded that thin films form a significant fraction of the total wetting phase saturation. Clearly, this is at variance with our hypothesis that thin films, over the  $P_c$  range shown in Figure 1, furnish hydraulic connections for the pendular structures but do not significantly contribute to the total wetting phase saturation. Melrose's estimates are based on model calculations for packings of spherical particles that completely miss the fractal character of sandstone roughness, i.e., that asperities are distributed over more than a few length scales as Figure 1 suggests. Figure 3 gives a drainage sequence of a partially saturated fractal object called Sierpinski carpet. Statistically, rocks resemble fractal objects but they do so only between upper and lower cutoffs of scale. Figure 3 clearly shows that at any given capillary pressure in the low saturation regime, the area available for adsorption of thin films is negligible if compared to the area occupied by pendular structures. Only when capillary pressure increases to ultrahigh values and pore structures are free of pendular water, a condition not studied here, the adsorbed wetting films comprise most of the wetting phase saturation.

Finally, according to the theory, the wetting phase relative permeability and capillary dispersion coefficient of samples M-6 and M-7 scale as  $k_{rw} \propto S_w^{5.35}$  and  $D_c \propto S_w^{1.02}$  respectively.

## CONCLUSIONS

The observed power-law behavior of  $P_c$  and  $\sigma_w$  of Berea sandstone at low wetting phase saturation  $S_w$ , is explained by theories of fractal geometry and thin-film physics. Asperities in pore walls are characterized over a limited range of length scales by a fractal dimension  $D$  determined from capillary pressure data. Liquid/solid interactions are characterized by the exponent  $m$  in the power-law dependence of disjoining pressure on film thickness. For the Berea

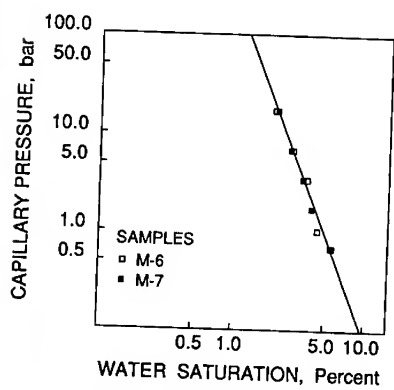


Figure 1. Drainage air/water  $P_c$ .

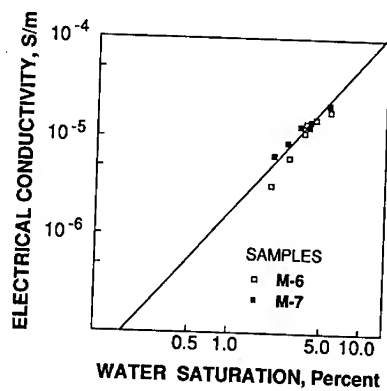


Figure 2. Electrical conductivity at 60 kHz.

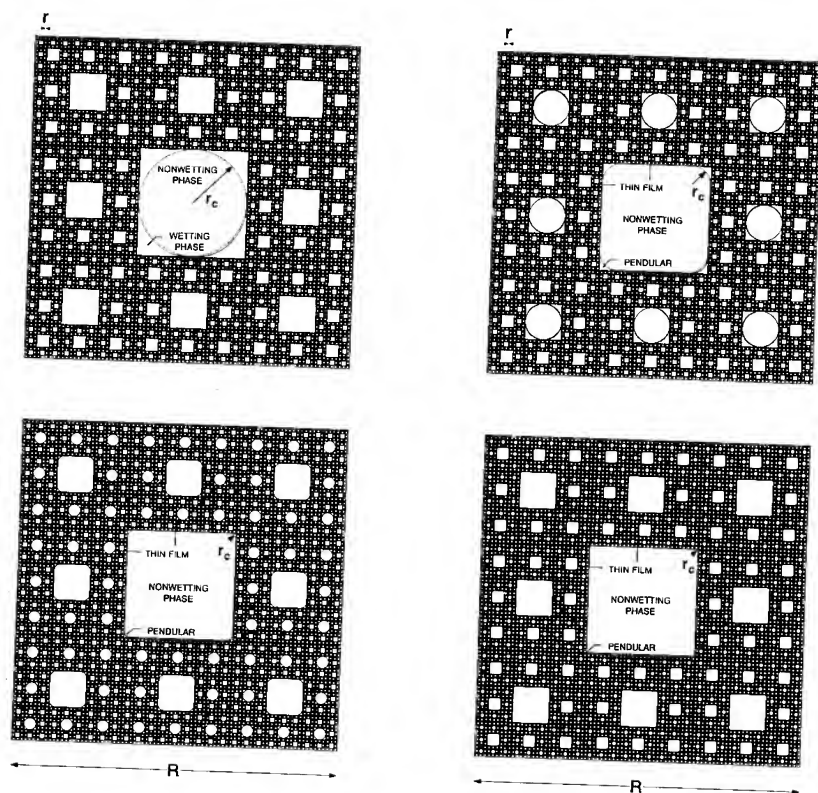


Figure 3. Drainage sequence of a partially saturated Sierpinski carpet.

sandstone studied here  $m \sim 2$  revealing a disjoining pressure dominated by weak electrostatic interactions. Simple determination of  $D$  and  $m$  from least-squares fit of  $P_c$  and  $\sigma_w$  respectively, can be used to rapidly determine the scaling of  $k_{rw}$  and  $D_c$  at low wetting phase saturations.

#### ACKNOWLEDGMENT

We thank Petróleos de Venezuela (PDVSA) and its subsidiary Intevep, S.A. for permission to publish this paper. We also thank R. A. Novy of Mobil E&P Technical Center for helping in the preparation of Figure 3 and for many useful discussions and A. A. Aponte of Intevep for his contribution at the beginning of this project.

#### REFERENCES

1. H. T. Davis, *Europhys. Lett.* **9**, 629 (1989).
2. R. A. Novy, P. G. Toledo, H. T. Davis, L. E. Scriven, *Chem. Eng. Sci.* **44**, 1785 (1989).
3. P. G. Toledo, R. A. Novy, H. T. Davis, L. E. Scriven, *Soil Sci. Soc. Am. J.* **54**, 673 (1990).
4. H. T. Davis, R. A. Novy, L. E. Scriven, P. G. Toledo, *J. Phys.: Condensed Matter* **2**, SA457 (1990).
5. P. G. Toledo, H. T. Davis, L. E. Scriven, *Physica A* **185**, 228 (1992).
6. P. G. Toledo, H. T. Davis, L. E. Scriven, *Transport in Porous Media* **10**, 57 (1993).
7. P. G. Toledo, R. A. Novy, H. T. Davis, L. E. Scriven, *SPE Advanced Technology Series* **1**, 136 (1994).
8. J. R. Nimmo, J. Rubin, K. C. Akstin, *Water Resour. Res.* **23**, 124 (1987).
9. J. R. Nimmo and K. C. Akstin, *Soil Sci. Soc. Am. J.* **52**, 303 (1988).
10. J. S. Ward and N. R. Morrow, *SPEFE* **2**, 345 (1987).
11. R. Knight and A. Endres, *SPWLA 30th Annual Symposium*, Denver, June 11–14, 1989.
12. J. C. Melrose, *SPERE* **2**, 913 (1987).
13. J. C. Melrose, *Langmuir* **3**, 661 (1987).
14. J. C. Melrose, *SPERE* **5**, 95 (1990).
15. R. Knight and A. Endres, *SPWLA 32nd Annual Symposium*, Houston, June 16–19, 1991.
16. P. G. de Gennes, in *Physics of Disordered Materials*, edited by Adler *et al.* (Plenum Press, New York, 1985) pp. 227–241.
17. P.-z. Wong, in *Physics and Chemistry of Porous Media II. AIP Conference Proceedings* **154**, edited by J. R. Banavar (AIP, New York, 1987) pp. 304–318.
18. K. K. Mohanty, H. T. Davis, L. E. Scriven, *SPERE* **2**, 113 (1987).
19. R. Knight and A. Nur, *Geophysics* **52**, 644 (1987).
20. A. J. Katz and A. H. Thompson, *Phys. Rev. Lett.* **54**, 1325 (1985).
21. G. E. Archie, *Trans. A.I.M.E.* **146**, 54 (1942).



---

---

## PART V

---

### **Kinetic Roughening**

## STEP-EDGE BARRIERS, RE-ENTRANT OSCILLATIONS, AND UNSTABLE EPITAXIAL GROWTH

DIMITRI D. VVEDENSKY<sup>†</sup> AND PAVEL ŠMILAUER<sup>†,‡</sup>

<sup>†</sup> The Blackett Laboratory, Imperial College, London, SW7 2BZ, United Kingdom

<sup>‡</sup> Interdisciplinary Research Centre for Semiconductor Materials, Imperial College, London, SW7 2BZ, United Kingdom

### ABSTRACT

The influence of step-edge barriers that inhibit the interlayer transport of atoms is discussed in the context of several material systems by using simulations of a solid-on-solid model. We show how the combined effect of this step-edge barrier and a non-thermal short-range incorporation process of freshly-deposited atoms can be used to explain several epitaxial phenomena on metal and semiconductor surfaces: (i) re-entrant oscillations seen with He-atom scattering and high-resolution low-energy electron diffraction during Pt(111) homoepitaxy, (ii) instabilities during growth on GaAs(001) and several metal (001) and (111) surfaces in the form of multilayer features that dynamically coarsen, while maintaining their shape, and (iii) re-entrant oscillations during etching of GaAs(001). In (iii), the incorporation is replaced by a short-range search for the atom to be removed.

### INTRODUCTION

The evolution of surface morphology during epitaxial growth is the result of a delicate interplay between the rate of deposition of atoms onto the surface and the subsequent relaxation of the surface profile through surface diffusion. The shot noise associated with the deposition promotes the kinetic roughening of the surface which is opposed by the tendency of the surface to flatten locally through the redistribution of atoms. The extent to which the surface atoms are able to explore different local configurations under the driving force of the deposition current then determines how the surface morphology develops.

Herring [1] first derived scaling laws for the various relaxation mechanisms as a function of the feature size, which Mullins [2] later cast in the form of differential equations for the growth front profile. More recently, generalizations of Mullins' equations of motion [3–6] have been proposed with the intent of describing the kinetic roughening of the surface in terms of a dynamic scaling hypothesis [7] for the variance  $W(L, t)$  of the surface height  $h(x, t)$ :

$$W(L, t) = \left[ \langle h^2 \rangle - \langle h \rangle^2 \right]^{1/2} \sim L^\alpha f(t/L^{\alpha/\beta}) \quad (1)$$

where  $L$  is the lateral viewing scale and  $f$  is a scaling function with the properties that  $f(x) \sim x^\beta$  for  $x \ll 1$  and  $f(x) \rightarrow \text{constant}$  for  $x \gg 1$ . The exponents  $\alpha$  and  $\beta$  are universal in the sense that they depend only on factors such as the dimensionality of the surface rather than the microscopic details of the interactions. For situations where this hypothesis is satisfied, the growth front profile evolves into a self-organized critical state [8].

The evident appeal of the scale-invariant structure implied by (1) has spawned a huge literature [9–11]. Recently, however, several experimental [12–17] and theoretical [5, 14–18] studies have revealed that the growth front profile may evolve into an altogether different morphology composed of fairly regular three-dimensional structures that maintain their shape but which dynamically coarsen as growth proceeds. The origin of this instability was predicted by Villain [5] to be a barrier at the edges of two-dimensional islands that inhibits the interlayer transport of atoms. In fact, such barriers were previously invoked [19] to explain the

phenomenon of re-entrant layer-by-layer growth, and there is a variety of other consequences of these barriers as well [20–22].

In this paper, we will examine the effect of step-edge barriers on several epitaxial phenomena from the standpoint of a solid-on-solid model of epitaxial growth. We will begin with a discussion of why this barrier must be included to explain surface electron diffraction experiments from GaAs(001) surfaces during epitaxial growth. We then review briefly the simulations of the experiments of Kunkel et al. [19], before turning our attention to the roughening of surfaces in the presence of step-edge barriers. We conclude with a discussion of re-entrant layer-by-layer oscillations observed with surface electron diffraction measurements when AsBr<sub>3</sub> is used to chemically etch GaAs(001).

### THE SOLID-ON-SOLID MODEL

In the solid-on-solid model of epitaxial growth [23–27], the crystal is assumed to have a simple cubic structure with neither bulk vacancies nor overhangs. The basic processes included in this model are the deposition of atoms onto the surface and the subsequent diffusion of surface adatoms. Growth is initiated by atoms being deposited onto the surface at a rate determined by the experimental deposition rate. A surface site is first selected randomly, and then a search is carried out within a square of a fixed linear size  $R$ , centered upon the selected site for the site with the maximum number of lateral nearest neighbors. The incident atom is then deposited on this site. The effect of this incorporation mechanism is to smoothen the growth front and lead to quasi layer-by-layer growth at temperatures low enough that thermally activated adatom hopping is negligible [28–31].

The migration of surface atoms is modeled as a nearest-neighbor hopping process at the rate

$$k(E, T) = k_0 \exp(-E/k_B T) \quad (2)$$

where  $E$  is the hopping barrier,  $T$  is the substrate temperature, and  $k_B$  is Boltzmann's constant. The pre-factor  $k_0$  is the attempt frequency for this hopping and is assigned the value  $k_0 = 2k_B T/h$ , where  $h$  is Planck's constant. The hopping barrier is the sum of a substrate term,  $E_S$ , an in-plane contribution,  $E_{NN}$ , and the step-edge barrier term  $E_{BB}$ . The in-plane term is taken to depend linearly on the number of nearest neighbors:  $E_{NN} = nE_N$ , where  $n=0, 1, 2, 3, 4$ . The vicinity of a step is detected by counting the number of next-nearest neighbors in the planes beneath and above the hopping atom before ( $m_i$ ) and after ( $m_f$ ) a hop. The additional (step-edge) barrier to hopping has a nonzero value only if  $m_i > m_f$  and equals  $(m_i - m_f)E_B$  where  $E_B$  is a model parameter. Thus, the total energy barrier  $E$  is given by

$$E = E_S + nE_N + (m_i - m_f)\theta(m_i - m_f)E_B \quad (3)$$

where  $\theta(x)=1$  if  $x>0$  and  $\theta(x)=0$  if  $x\leq 0$ . The parameters of this model are  $R$ ,  $E_S$ ,  $E_N$ , and  $E_B$ , which must be adjusted for any particular material system to obtain quantitative agreement with observed behavior. For vicinal GaAs(001) homoepitaxy, simulations with the values  $R=7$ ,  $E_S=1.54$  eV,  $E_N=0.23$  eV, and  $E_B=0.175$  [32] produce the agreement shown in Fig. 1 between the simulated step density and the measured [33] reflection high-energy electron-diffraction (RHEED) specular intensity. Both the incorporation and the step-edge barrier are required to achieve this level of agreement during both growth and post-growth equilibration of the surface. The effect of the incorporation is most directly evident at the onset of growth in the enhancement of the delay in the first maximum of the RHEED oscillations [34,35]. The step-edge barriers slow the equilibration of the surface by inhibiting the interlayer transport of atoms, which is seen most clearly in recovery profiles obtained from simulations performed with [32] and without [33] this barrier.

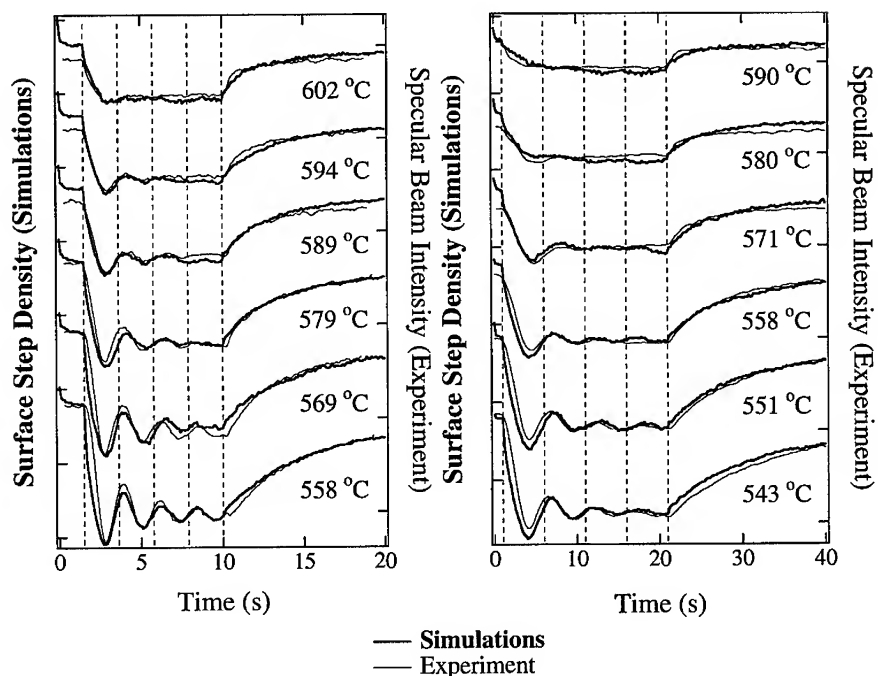


**Figure 1.** Direct comparison between measured RHEED intensity [33] and the step density of simulated surfaces [32] for a GaAs(001) vicinal surface misoriented by  $2^\circ$  toward the [010] direction at a growth rate of 0.47 ML/s (left panel) and 0.20 ML/s (right panel). The step density increases downward and data at different temperatures has been scaled by the same factor (for a given flux) to facilitate the comparisons with the RHEED intensity.

#### RE-ENTRANT OSCILLATIONS FOR Pt(111) HOMOEPITAXY

Among the first experiments that showed the influence of step-edge barriers during growth were the He-atom scattering measurements of Kunkel et al. [19] carried out during Pt(111) homoepitaxy. These measurements revealed a transition from an oscillatory intensity at high temperatures to a decaying intensity with no oscillations at lower temperatures, with intensity oscillations reappearing at still lower temperatures. Kunkel et al. [19] based their explanation of these observations on the existence of step-edge barriers. At high temperatures, atoms acquire large amounts of thermal energy from the substrate and thus can overcome the barrier near step edges. This promotes layer-by-layer growth. As the temperature is decreased, the thermal energy of the atoms decreases accordingly, and the barrier starts to be more effective in inhibiting atom hopping between layers. The adatom density on the terraces thus increases, which increases the likelihood of island formation. As this process is repeated, the surface morphology develops three-dimensional features. At still lower temperatures, the islands are either small or irregularly shaped [36,37], so the effect of the barrier is suppressed [38], and layer-by-layer growth is recovered.

We have modeled these observations using the model described in the preceding section with the parameters  $R=3$ ,  $E_S=0.75$  eV,  $E_N=0.18$  eV, and  $E_B=0.15$  eV [39]. A comment is

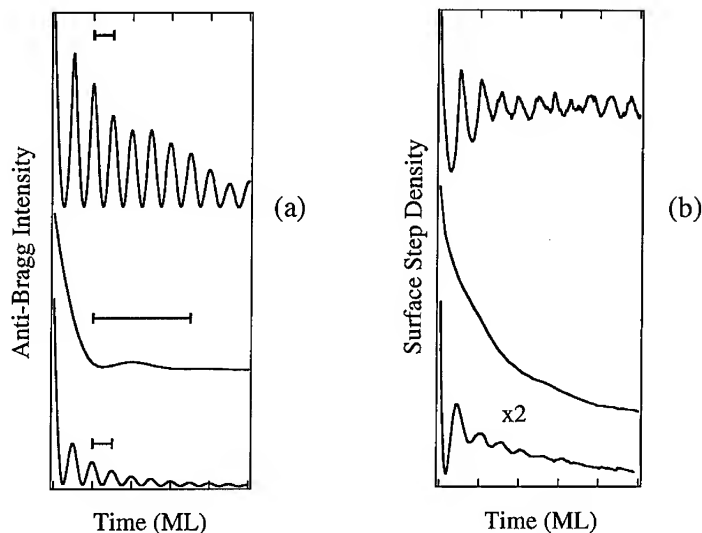


**Figure 2.** Specular beam intensity for He-atom diffraction in the kinematic approximation for a near-Bragg angle of incidence (a) and the step density (b) during the deposition at three different temperatures (from the top:  $T=480$  K,  $T=400$  K,  $T=280$  K) at a deposition rate of 0.025 ML/s. The time needed to deposit a monolayer at each temperature is indicated by a horizontal line in (a). A different vertical scale has been used for the intermediate temperature data.

in order regarding the choice of parameters in comparison with those estimated directly from experimental measurements [40]:  $E_S=0.23$  eV and  $E_N=0.35$  eV. Our intent in performing the simulations is simply to capture the essential physics behind the re-entrant behavior, rather than to quantitatively reproduce all of the experimental measurements. Additionally, simulations of our model with the “experimental” parameters would be impractical, even with the most powerful modern computers because of the size of the lattice required to avoid finite-size effects and the level of surface activity at the temperatures at which the measurements were taken. We must content ourselves, therefore, with an essentially qualitative approach to this phenomenon.

Our comparisons between simulations and experimental work are based on calculating (i) the intensity of the specular beam calculated near the anti-Bragg angle of incidence, (ii) the density of surface steps, which is a good, albeit approximate, analogue of the intensity of the Bragg peak in He-atom diffraction, and (iii) “snapshots” of the surface morphology. The first two of these are shown in Fig. 2. The re-entrant behavior is seen clearly in both sets of calculations. It is important to note that we obtained the oscillations in the low-temperature regime only by including the incorporation mechanism discussed above. This is because in this temperature range, the islands are very ramified (Fig. 3). Thus, upon deposition most of the atoms are incorporated directly at the step edges of these islands because these sites are locally the energetically most favorable in terms of the number of nearest neighbors. The incorporation mechanism thus, in effect, bypasses the step edge barrier. Without the incorporation mechanism, we observe only weak and strongly damped oscillations.

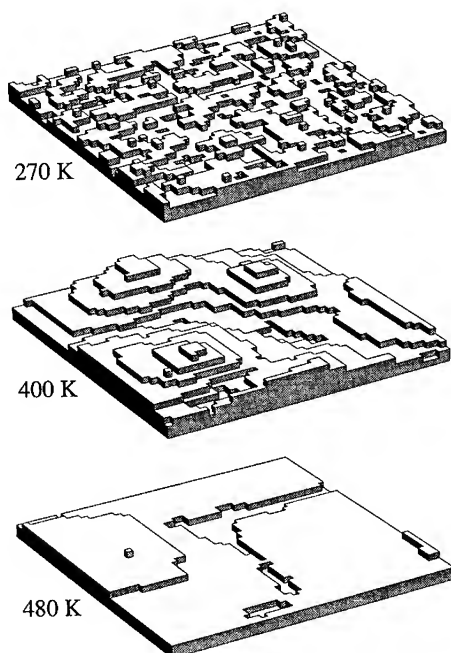


**Figure 3.** Surface morphologies after the growth of 2.4 ML at a deposition rate of 0.0033 ML/s for three substrate temperatures:  $T=270$  K,  $T=400$  K,  $T=480$  K. Shown are  $50 \times 50$  subsections of the lattice used, which was  $200 \times 200$ , except at the lowest temperature, where  $400 \times 400$  lattice were used.

The surface morphologies for the three temperature regimes are shown in Fig. 3. A comparison with the corresponding images taken with scanning tunneling microscopy in Ref. [12] reveals clear qualitative similarities. Of particular note is the appearance of the three dimensional structures for the three-dimensional growth regime. The morphology of this intermediate-temperature regime is strikingly different from that in the two temperature regimes where layer-by-layer growth is observed, showing "pyramidal" structures with several incomplete layers. There will be more discussion on the formation and evolution of these structures in the next section. The morphologies in the two-dimensional growth regimes differ from one another primarily in the island sizes. At low temperatures there are many small, ramified islands, while in the high-temperature regime there are fewer larger islands which are compact.

#### UNSTABLE EPITAXIAL GROWTH

Step-edge barriers give rise to instabilities in the surface morphology of a film growing on a singular surface, as first pointed out by Villain [5]. These instabilities take the form of pyramid-like features whose slope remains approximately constant [13-15] and whose separation increases with time according to a power law. Evidence of these features is seen

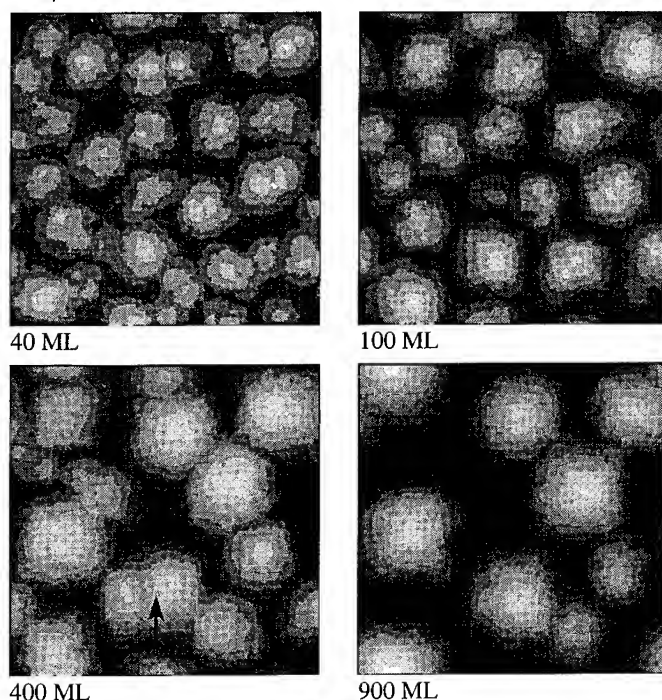


**Figure 4.** Simulated surface morphologies of GaAs(001) homoepitaxy on  $300 \times 300$  lattice at the substrate temperature  $T=555^\circ\text{C}$  and at the deposition rate of  $1/6$  ML/s. The arrow indicates a position where a mound has split into two mounds which rejoined later.

in the morphology in Fig. 3 for the intermediate temperature range. In our simulations of GaAs(001) homoepitaxy, we observe the development of mounds on the growing singular surfaces after the initial oscillations of the step density have died out. The mounds grow and merge (but occasionally also split, see the mound marked by the arrow in the lower left panel of Fig. 4, which split into two mounds that again merged after an additional several tens of monolayers were grown). Finally, the surface arrives at a state in which the number of mounds and their sizes change very slowly during deposition of several hundred monolayers, although the coarsening process still goes on and the shape of the mounds becomes more regular. Throughout the simulation, the mounds keep a constant average angle of inclination, in qualitative agreement with the experiment. In both the experiments and in our simulations the size of the terraces on the hillsides of the mounds and the average inter-island distance at submonolayer coverages are roughly the same. We also simulated equilibration of the mounds after the growth was stopped and observed a very slow approach to a flat surface, with residual mounds distinguishable even after 1000 s annealing, again in very good agreement with experimental observations [17].

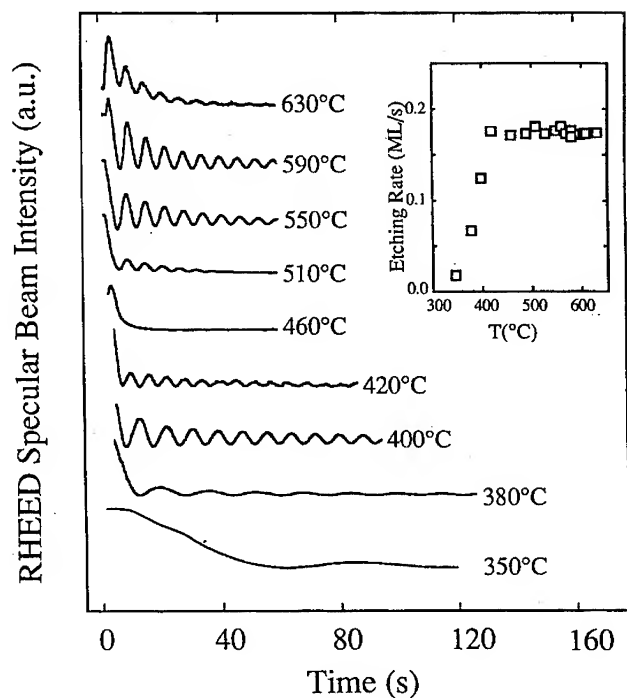


**Figure 5.** RHEED specular-beam intensity evolution during etching of GaAs(001) at a  $\text{AsBr}_3$  flux of 0.36 sccm and different substrate temperatures. The inset shows the etching rate vs. the substrate temperature.

#### RE-ENTRANT ETCHING OSCILLATIONS ON GaAs(001)

Most fundamental studies of relevance to heterostructure formation have focussed on the growth process. However, the removal of atoms during processes such as sputtering and etching also provide a way of manipulating surface properties and morphology. Several recent studies have used electron and helium-atom diffraction and scanning tunnelling microscopy to investigate the atomistic kinetics that occur during the removal of atoms from a surface, usually by sputtering [42–45]. These experimental studies, as well as computer simulations [46–48] have revealed several qualitative similarities with the processes that occur during epitaxial growth, with monovacancies and vacancy islands playing the roles of adatoms and adatom islands, respectively.

In this section, we describe a model for the chemical etching of GaAs(001) by  $\text{AsBr}_3$  that were motivated by recent RHEED measurements shown in Fig. 5, which show re-entrant behavior analogous to that discussed above. Other features to note are as follows. In the temperature range from 420°C to 630°C, the oscillations have the same period, while below 420°C, the period shows a significant increase. In the inset to Fig. 5 is shown the growth over this range, which is approximately constant rate above 420°C, but diminishes rapidly below this temperature. We conclude that the removal above 420°C is supply-rate limited, but below 420°C the removal is reaction limited. In particular, the re-entrant behavior is not



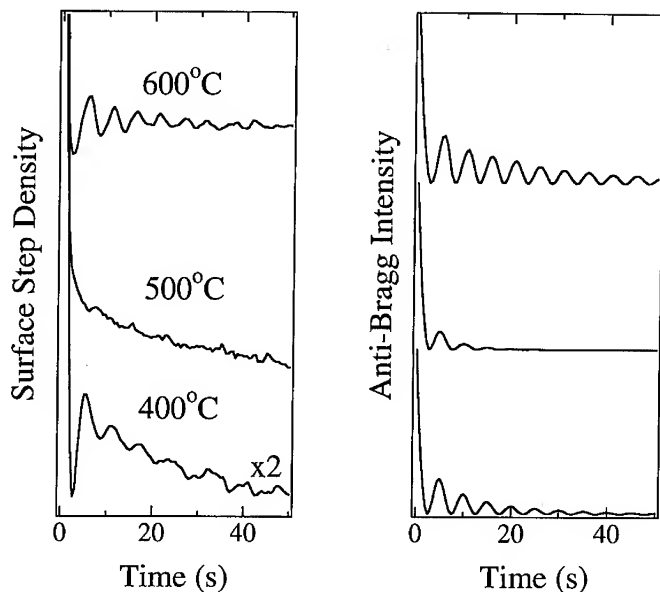


**Figure 6.** The surface step density and the intensity of the specular beam calculated in the kinematic approximation for an anti-Bragg angle of incidence during growth at three different substrate temperatures. The step density increases downwards. The upper two curves in both plots are given additional offsets to make comparisons easier.

due to any pathology in the  $\text{AsBr}_3$  decomposition rate over the temperature range of interest, but can be traced to factors involving surface kinetics.

To model these observations, we modify a model we have used previously to describe sputtering [47,48] by including a site selectivity for the removal of surface atoms. Atoms are removed from the substrate at a rate given by the experimentally observed rate of etching. A surface site is first selected randomly, and then a search is carried out within a square of a fixed linear size  $R$ , centered upon the originally selected site for the atom with the *minimum* number of lateral nearest neighbors. The atom on this site is then removed. Surface migration is modeled as we have summarized in equations (2) and (3) with one important exception. The nearest-neighbor contribution  $E_{NN}$  is given by  $E_{NN} = \frac{1}{2}n_i E_N + E'_N$ , where  $E'_N = (n_i - n_f)\theta(n_i - n_f)E_N$  is nonzero only if the number of in-plane nearest neighbors before a hop,  $n_i$ , is greater than that after the hop,  $n_f$ . This definition leads to faster diffusion along island edges and high vacancy mobility (consistent with experimental observations [42-45]) but preserves the difference in mobility of edge atoms with different coordination and the activation barriers to detachment of atoms from step edges ( $E_{NN} = n_i E_N$  for  $n_f = 0$ ). The model parameters used in this study were  $E_S = 1.58$  eV,  $E_N = 0.24$  eV,  $E_B = 0.175$  eV, and  $R = 3$ .

The results of the simulation are shown in Fig. 6. The re-entrant nature of the RHEED oscillations is seen to be reproduced by the step density. In the kinematic intensity, the oscillations do not disappear in the intermediate temperature, but they are much better defined for both lower and higher temperatures. Notice that the range of temperatures in the simulation

corresponds well to those in Fig. 5. Although not shown, the range of temperature over which the oscillations disappear is narrow ( $\approx 10$ – $20^\circ\text{C}$ ) in both the simulations and the experiments.

Based on the experimentally observed behavior and our simulations, the explanation of the re-entrant layer-by-layer etching is as follows. At low temperatures, the mobility of surface vacancies is relatively low and they form only small islands. Thus there is a high density of atoms with low coordination in the uppermost layer which are preferentially removed. This leads to the layer-by-layer removal of atoms from the surface. At higher temperatures, the vacancies become more mobile and large vacancy islands are formed on the surface. However, the adatoms and vacancies are prevented from moving between layers by the step-edge barrier. This results in multi-layer removal and the disappearance of RHEED oscillations. At still higher temperatures, the effect of the barrier is diminished and layer-by-layer removal is again observed. The transition from the low-temperature multilayer removal regime to the layer-by-layer removal regime at high temperatures has been observed in the ion-beam sputtering of Pt(111) [42–44], but to obtain the reappearance of the oscillations at lower temperatures requires a site-selective step such as the one we have proposed.

#### ACKNOWLEDGEMENTS

We thank Bruce Joyce, Tadaaki Kaneko, Takaaki Kawamura, Brad Orr, and Andy Zangwill for many helpful conversations. The support of Imperial College and the Research Development Corporation of Japan is gratefully acknowledged.

#### REFERENCES

1. C. Herring, J. Appl. Phys. **21**, 301 (1950).
2. W.W. Mullins, J. Appl. Phys. **30**, 77 (1959).
3. M. Kardar, G. Parisi, and Y.-C. Zhang, Phys. Rev. Lett. **56**, 889 (1986).
4. Z.-W. Lai and S. Das Sarma, Phys. Rev. Lett. **66**, 2348 (1991).
5. J. Villain, J. Phys. I **1**, 19 (1991).
6. D.D. Vvedensky, A. Zangwill, C.N. Luse, and M.R. Wilby, Phys. Rev. E **48**, 852 (1993).
7. F. Family, Physica A **168**, 561 (1990).
8. S. Das Sarma, J. Vac. Sci. Technol. B **10**, 1695 (1992).
9. J. Krug and H. Spohn, in *Solids Far From Equilibrium*, edited by C. Godr che (Cambridge University Press, Cambridge, 1992), pp. 479–582.
10. H.-N. Yang, G.-C. Wang, and T.-M. Lu, *Diffraction from Rough Surfaces and Dynamic Growth Fronts* (World Scientific, Singapore, 1993).
11. W.M. Tong and R.S. Williams, Ann. Rev. Phys. Chem. **45**, 401 (1994).
12. M. Bott, T. Michely, and G. Comsa, Surf. Sci. **272**, 161 (1992).
13. H.-J. Ernst, F. Fabre, R. Folkerts, and J. Lapujoulade, Phys. Rev. Lett. **72**, 112 (1994).
14. M.D. Johnson, C. Orme, A.W. Hunt, D. Graff, J.L. Sudijono, L.M. Sander, and B.G. Orr, Phys. Rev. Lett. **72**, 116 (1994).
15. J.A. Strosio, D.T. Pierce, M. Stiles, and A. Zangwill (unpublished).
16. A.W. Hunt, C. Orme, D.R.M. Williams, B.G. Orr, and L.M. Sander, Europhys. Lett. **27**, 611 (1994).
17. C. Orme, M.D. Johnson, J.L. Sudijono, K.T. Leung, and B.G. Orr, Appl. Phys. Lett. **64**, 860 (1994).
18. M. Siegert and M. Plischke, Phys. Rev. Lett. **73**, 1517 (1994).
19. R. Kunkel, B. Poelsema, L.K. Verheij, and G. Comsa, Phys. Rev. Lett. **65**, 733 (1990).

20. R.L. Schwoebel and E.J. Shipsey, *J. Appl. Phys.* **37**, 3682 (1966).
21. Y. Tokura, H. Saito, and T. Fukui, *J. Crystal Growth* **94**, 46 (1989).
22. G.S. Bales and A. Zangwill, *Phys. Rev. B* **41**, 5500 (1990).
23. J.D. Weeks and G.H. Gilmer, *Adv. Chem. Phys.* **40**, 157 (1979).
24. A. Madhukar and S.V. Ghaisas, *CRC Crit. Rev. Solid State Mater. Sci.* **14**, 1 (1988).
25. D.D. Vvedensky, S. Clarke, K.J. Hugill, A.K. Myers-Beaghton, and M.R. Wilby, in *Kinetics of Ordering and Growth at Surfaces*, edited by M.G. Lagally (Plenum, New York, 1990), pp. 297-311.
26. S. Das Sarma, *J. Vac. Sci. Technol. A* **8**, 2714 (1990).
27. H. Metiu, Y.-T. Lu, and Z. Zhang, *Science* **255**, 1088 (1992).
28. W.F. Egelhoff, Jr. and I. Jacob, *Phys. Rev. Lett.* **62**, 921 (1989).
29. J.W. Evans, D.E. Sanders, P.A. Thiel, and A.E. DePristo, *Phys. Rev. B* **41**, 5410 (1990).
30. J.W. Evans, *Phys. Rev. B* **43**, 3897 (1991).
31. P. Stoltze and J.K. Nørskov, *Phys. Rev. B* **48**, 5607 (1993).
32. P. Šmilauer and D.D. Vvedensky, *Phys. Rev. B* **48**, 17603 (1993).
33. T. Shitara, D.D. Vvedensky, M.R. Wilby, J. Zhang, J.H. Neave, and B.A. Joyce, *Phys. Rev. B* **46**, 6815 (1992).
34. H.T.W. Zandvliet, H.B. Elswijk, D. Dijkamp, E.J. van Loenen, and J. Dieleman, *J. Appl. Phys.* **70**, 2614 (1991).
35. T. Shitara, J. Zhang, J.H. Neave, and B.A. Joyce, *J. Appl. Phys.* **71**, 4299 (1992).
36. M. Bott, T. Michely, and G. Comsa, *Surf. Sci.* **272**, 161 (1992).
37. R.Q. Hwang and R.J. Behm, *J. Vac. Sci. Technol. B* **10**, 256 (1992).
38. B. Poelsema, R. Kunkel, N. Nagel, A.F. Becker, G. Rosenfeld, L.K. Verheij, and G. Comsa, *Appl. Phys. A* **53**, 369 (1991).
39. P. Šmilauer, M.R. Wilby, and D.D. Vvedensky, *Phys. Rev. B* **47**, 4119 (1993).
40. G. Rosenfeld, A.F. Becker, B. Poelsema, L.K. Verheij, and G. Comsa, *Phys. Rev. Lett.* **69**, 917 (1992).
41. B. Poelsema, A.F. Becker, G. Rosenfeld, R. Kunkel, N. Nagel, L.K. Verheij, and G. Comsa, *Surf. Sci.* **272**, 269, (1992).
42. B. Poelsema, L.K. Verheij, and G. Comsa, *Phys. Rev. Lett.* **53**, 2500 (1984); B. Poelsema, R. Kunkel, L.K. Verheij, and G. Comsa, *Phys. Rev. B* **41**, 11609 (1990).
43. T. Michely and G. Comsa, *Surf. Sci.* **256**, 217 (1991); T. Michely and G. Comsa, *Phys. Rev. B* **44**, 8411 (1991).
44. T. Michely, T. Land, U. Littmark, and G. Comsa, *Surf. Sci.* **272**, 204 (1992).
45. P. Bedrossian, J.E. Houston, J.Y. Tsao, E. Chason, and S.T. Picraux, *Phys. Rev. Lett.* **67**, 124 (1991); P. Bedrossian and T. Klitsner, *Phys. Rev. B* **44**, 13783 (1991); P. Bedrossian and T. Klitsner, *Phys. Rev. Lett.* **68**, 646 (1992); P. Bedrossian, *Surf. Sci.* **301**, 223 (1994).
46. E. Chason, P. Bedrossian, J.E. Houston, J.Y. Tsao, B.W. Dodson, and S.T. Picraux, *Appl. Phys. Lett.* **59**, 3533 (1991).
47. P. Šmilauer, M.R. Wilby, and D.D. Vvedensky, *Surf. Sci. Lett.* **291**, L733 (1993).
48. P. Šmilauer, M.R. Wilby, and D.D. Vvedensky, *Phys. Rev. B* **48**, 4968 (1993).

**FILM GROWTH:  
CONTROL OF SURFACE MORPHOLOGY FROM MONODISPERSE  
NANOPARTICLES THROUGH FRACTALS TO FLAT EPITAXIAL  
HETEROOSTRUCTURES**

R. STANLEY WILLIAMS, WILLIAM M. TONG AND TUE T. NGO  
Department of Chemistry and Biochemistry, University of California Los Angeles  
607 Circle Drive South, Los Angeles, CA 90024-1569

**ABSTRACT**

The study of the morphology of surfaces produced by vapor deposition began over 125 years ago with Lord Kelvin. Since then, many researchers have addressed this topic from very different theoretical viewpoints, including thermodynamics, kinetics, fractal geometry, and numerical simulations. Only recently, however, have scanning probe microscopes become available to measure the three dimensional topography of a deposited film, which provided the quantitative experimental data necessary to test the different models of film growth. The concept of scaling provides a good first description of the morphology of vapor deposited films of all types, but for heteroepitaxial films, scaling is only approximately valid. The competition between the surface roughening caused by island nucleation and growth versus the smoothening actions of surface diffusion and desorption can lead to the formation of correlated structures on a surface with a dominant spatial frequency. By rational control of the film growth conditions, one can produce a surface covered by a low density of nearly monodisperse nanoparticles, an essentially fractal surface, or a planar film surface.

**INTRODUCTION**

Recent advances in both scanning probe microscopes and x-ray scattering techniques now allow surface roughening during film growth to be studied in great detail. One mathematical method to characterize the kinetic roughening of a growing film is to measure the surface root-mean-square height, or interface width, as a function of measurement length and growth time to derive static ( $\alpha$ ) and dynamic ( $\beta$ ) scaling exponents, respectively, which can then be compared with theoretical predictions for the evolution of self-affine surfaces.<sup>1-3</sup> A complementary method is to determine the power density spectrum (PDS) of the surface, which is the Fourier transform (FT) of the autocorrelation function.<sup>4,5</sup> This approach is not only more sensitive to the scaling nature of a surface, but also more generally applicable to surfaces that are not self-affine.<sup>6,7</sup>

We have recently used the latter approach to examine the Atomic Force Microscope (AFM) topographs collected from epitaxial films of CuCl grown on  $\text{CaF}_2(111)$ ,<sup>8</sup> which displayed 3D-islanding (i.e. the Volmer-Weber or Stranski-Krastanov growth mode<sup>9</sup>). All the spectral densities of the films contained a peak at  $|\mathbf{q}| > 0$ , which demonstrated the existence of a dominant spatial frequency for each surface (see Fig. 1 for examples). Thus, none of these surfaces was truly

self-affine, even though log-log plots of the interface width versus length scale were essentially linear over a reasonably large length range.<sup>2</sup> The maximum intensity of each PDS was about an order of magnitude higher than the intensity at  $q=0$ . Inspection of the topographs revealed that the dominant spatial frequencies coincided with the characteristic island sizes and inter-island distances for the given sample.

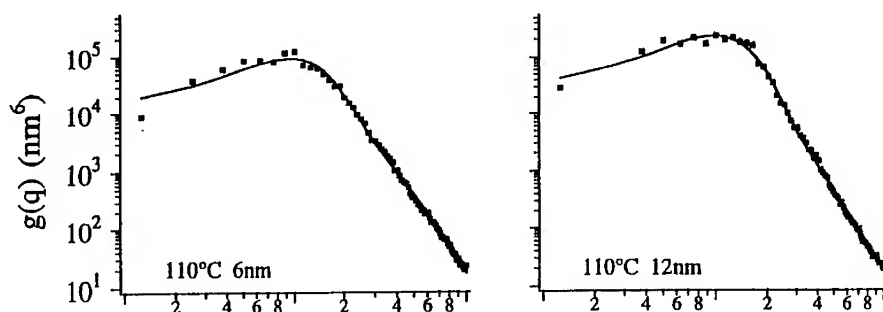


Fig.1 The PDS of two CuCl films grown on  $\text{CaF}_2$ , shown by the filled squares,<sup>8</sup> and the least squares fitting results to Eq. (2), shown by the solid line, are plotted on a log-log scale. The substrate temperature and the average film thickness are indicated for each sample.

We have proposed a new Langevin equation of motion (or mass continuity equation) to describe the three dimensional evolution of a surface of one material grown on another by a vapor deposition process:<sup>10</sup>

$$\frac{\partial h(q,t)}{\partial t} = [c_1|q| - c_2|q|^2 + c_3|q|^3 - c_4|q|^4]h(q,t) + \eta(q,t). \quad (1)$$

Here,  $h$  is the Fourier transform of the surface height (defined with respect to the average height of the surface in real space),  $q$  is the radially averaged spatial frequency, the  $c_n$ 's are physically meaningful parameters, as described below, and  $\eta(q,t)$  is the stochastic noise term with the property  $\langle \eta(q',t')\eta(q'',t'') \rangle = \delta(q'-q'')\delta(t'-t'')$ , which models the roughening of a surface by the random arrival of depositing particles.<sup>11</sup> This equation can be solved analytically by evaluation of the expectation value of  $h(q,t)$  to yield an expression for the PDS of a growing film:<sup>11</sup>

$$g(q,t) = \langle |h(q,t)|^2 \rangle = \Omega \frac{\exp[2t(c_1|q| - c_2|q|^2 + c_3|q|^3 - c_4|q|^4)] - 1}{c_1|q| - c_2|q|^2 + c_3|q|^3 - c_4|q|^4}. \quad (2)$$

The fits of Eq. (2) to the experimentally determined PDS for CuCl on  $\text{CaF}_2$  are also shown in Fig. 1. In the next section, we will provide the physical justification for Eqs. 1 and 2, and in the section following that we will illustrate the use of these equations for the rational design of desired surface structures.

## MECHANISTIC DESCRIPTION OF VAPOR HETERODEPOSITION

The goal is to understand how the fundamental mechanisms of film growth can produce a dominant spatial frequency such as those represented by the peaks in the PDS curves in Fig. 1, which violate the usual assumption of self-affinity for the morphology of vapor-deposited films.<sup>1</sup> The starting point for the analysis is a model for *nonislanding growth*. The scaling of surface features in nonislanding growth is a result of the interplay between stochastic roughening caused by white noise in the flux of the deposited species and smoothening by various surface transport mechanisms. Growth in which the randomly arriving particles stick where they land (the solid-on-solid model) would produce a surface height as a function of lateral position  $H(x,y)$  that is a Poisson distribution; the radially averaged PDS of such a stochastic surface would be represented by straight horizontal lines in Fig. 1, since totally random surfaces would contain features at all spatial frequencies with equal probabilities.

Stochastic roughening is opposed by various surface transport mechanisms that drive the system toward its thermodynamic energy minimum: a (locally) flat surface. Conyers Herring<sup>12</sup> was the first to derive scaling laws that quantify the smoothening effects as functions of feature size and mechanism. He showed with simple thermodynamic arguments that the sintering rate of any surface feature is inversely proportional to (feature size)<sup>n</sup>, where  $n=1$  for viscous flow of amorphous material,  $n=2$  for evaporation-recondensation,  $n=3$  for bulk diffusion, and  $n=4$  for surface self-diffusion. These scaling laws were later cast in the form of differential equations by Mullins,<sup>13</sup> and they would all appear in Eq. 1 with negative coefficients, since they act to make the root mean square surface height smaller. The smoothening of surface features is thus not independent of length scale; each of the four possible smoothening mechanisms will leave a unique fingerprint in the PDS of the growing surface. The essential features of an equation like Eq. (2) are that when the PDS is plotted against  $q$  on a log-log scale, it maintains a saturation value at small  $q$  and decreases with a slope of  $-n$  at large  $q$ , which identifies the dominant surface smoothening mechanism. Indeed, the limiting slope at large  $q$  for the PDS of the CuCl films in Fig. 1 is  $-4$ ,<sup>8</sup> which means that surface diffusion dominates the surface morphology at short length scales.

Equations similar to Eq. (1) containing only the  $n=2$  and/or  $n=4$  smoothening terms have been proposed previously by those concerned with the scaling behavior of vapor deposited surfaces.<sup>14-17</sup> Although variations of Eq. (2) have been successful in predicting the scaling behavior of vapor deposited films and ion-bombarded surfaces in the absence of island formation,<sup>4</sup> additional terms must be added to Eq. (1) to incorporate the nonstochastic roughening mechanisms of 3D island formation before it can reproduce a PDS with a peak at  $q>0$ . The origin of nonstochastic roughening in Volmer-Weber or Stranski-Krastanov systems<sup>9</sup> lies in the preferential enhancement of certain spatial frequencies during the formation and growth of *islands*.

We have derived scaling laws from mechanistic arguments that correspond to the  $n=1$  and  $n=3$  roughening terms, i.e. those with positive coefficients in Eq. (1), by following the procedures established by Herring.<sup>12</sup> The key to these derivations is to establish a scaling relationship between the sizes of features and the times needed to produce a geometrically similar change in them.<sup>10</sup> By Wulff's theorem,

3D islands grow in a self similar manner.<sup>18</sup> A general expression that governs the rate  $\rho$  for 3D islands to change in a geometrically similar fashion is

$$\rho \propto V^{-1} \cdot dV/dt, \quad (3)$$

where  $V$  is the volume of an island, which scales as  $(\text{size})^3$ , and  $dV/dt$  is the growth rate. There are two primary mechanisms of material supply to the growing island: the first involves the incident flux arriving directly on an island from the gas phase, and the second involves material arriving at the perimeter of the island by surface diffusion. These correspond to the  $n=1$  and  $n=3$  roughening mechanisms, respectively, seen in our PDS fits to Eq. (2).

In the first mechanism of roughening by direct incident flux,  $dV/dt$  is the product of the projected area of the island on the substrate and the incident flux. If the latter is assumed to be constant,  $dV/dt$  scales as  $(\text{size})^2$ . The rate of producing a self-similar change in a collection of islands is thus

$$\rho \propto (\text{size})^2/(\text{size})^3 \propto q, \quad (4)$$

which means the roughening rate is linearly proportional to the spatial frequency, or  $n=1$ . Such roughening by the incident flux was expected for our CuCl on CaF<sub>2</sub> samples, since the islands covered most of the substrate for the films examined.<sup>8</sup>

The second mechanism of material arrival at an island is via surface diffusion on the substrate, which may be different from the deposited material, to the perimeter of the growing island. Although the importance of this mechanism of roughening diminishes during the course of deposition because the substrate is eventually covered, it is the most significant process in the initial stages of film growth involving island nucleation. The rate of material arrival for this mechanism can be expressed as

$$dV/dt \propto (\text{perimeter of the island}) \times (\text{surface diffusion flux}). \quad (5)$$

The perimeter of the island scales linearly with  $(\text{size})$ , whereas the surface diffusion flux is proportional to the gradient of the concentration of diffusing species at the island boundary. The island size dependence of the surface concentration of diffusing species in the presence of multiple islands is a moving boundary problem for which no analytical solution exists. Numerous theoretical approaches have been attempted by researchers to obtain an estimate of the monomer concentration distribution. In one model, as derived by Steyer *et al.*<sup>19</sup> to explain the formation of breath figures (liquid droplets), diffusing species arrive by random walk from an infinitely far distance to the edge of the droplet and become incorporated. Two boundary conditions are imposed to make this problem soluble. First, the concentration of the diffusing species at the edge of a hemispherical island,  $\xi(r=R)$ , is required to be zero, where  $r$  is the distance from the center of the island and  $R$  is the radius of the island; this arises from the assumption that the monomer acquisition probability at the island edge is unity. Second,  $r \nabla \xi$  is set to zero at  $r=\infty$  to satisfy the requirement that  $\xi(r)$  is constant at

$r=\infty$ . With these two boundary conditions,  $\xi(r)$  has a logarithmic dependence on the distance from the island,

$$\xi(r;R) \propto \ln(r/R). \quad (6)$$

From Eq. (6),  $\nabla \xi(r)$  at  $r=R$  is proportional to  $R^{-1}$ , and thus  $dV/dt$  in Eq. (5) is a constant. The resultant roughening rate is proportional to the third power of the spatial frequency

$$\rho \propto (\text{size})^{-3} \propto q^3, \quad (7)$$

and thus  $n=3$  for this mechanism.

Although Eq. (6) yields the most common experimentally observed scaling behavior, it has been criticized as being unrealistic because  $\xi(r)$  diverges at  $r=\infty$ . A physically motivated model for the concentration distribution is to assume that  $\xi(r;R)$  increases monotonically from  $r=R$  to reach a saturation value at  $r=\infty$ .<sup>20</sup> This can be described by an equation of the following form

$$\xi(r;R) = \xi_{\infty} [1 - \sum_{m=1}^{\infty} a_m (R/r)^m], \quad (8)$$

where the boundary condition  $\sum_{m=1}^{\infty} a_m = 1$  is imposed to assure that  $\xi(r)$  at the island edge is zero. Regardless of the values of the  $a_m$ 's, the gradient of Eq. (8) at  $r=R$  will yield a diffusion flux that is also proportional to  $R^{-1}$  and thus it produces the same scaling law as Eq. (6).

To summarize this section, Eq. (1) provides a description for the PDS of a surface growing by vapor deposition. This equation is based on mechanistic principles and provides excellent agreement with the observed PDS for CuCl films grown on CaF<sub>2</sub>. There are three types of terms in the equation. The first is the noise in the arriving flux, which will make the surface roughen stochastically. The second are the smoothening terms (those with negative coefficients) that correspond to the  $n=2$  and  $n=4$  moments of  $q$ , which represent the mechanisms of desorption from the surface and diffusion on the surface, respectively. From our fits of experimental data to Eq. (2), these appear to be the most important smoothening mechanisms. Finally, there are the terms that represent the formation and growth of islands for Volmer-Weber and Stranski-Krastanov growth modes. In this case, we find that the terms with positive coefficients in Eq. 1 should have  $n=1$  and  $n=3$  moments of  $q$ , which represent the growth of islands by direct deposition and diffusion to the island perimeter, respectively.

## APPLICATIONS OF THE EQUATION OF MOTION FOR VAPOR DEPOSITION

Equation 1 also provides a model for tailoring the growth of a surface to obtain a desired morphology. Depending on the growth conditions, one can obtain a smooth and flat surface (desired for MBE), a fractal surface, or a surface covered by islands, just by controlling the deposition conditions.

According to Eq. 1, flat surfaces can only be obtained when the growth is dominated by the desorption term. Previous studies of similar linear growth



equations (such as the Edwards-Wilkinson equation<sup>14,15</sup>) show that only the  $n=2$  term can produce a surface that does not roughen more than logarithmically with time in the presence of noise. This may not at first appear reasonable, since most MBE growth is performed below the sublimation temperature of the films being deposited to achieve net growth. However, Herring<sup>12</sup> derived the  $q$ -dependence of desorption from the Kelvin equation,<sup>21</sup>

$$P(R) = P(R=\infty)\exp[2V_M\sigma/RN_AkT], \quad (9)$$

where  $P$  is the partial pressure of the material of interest,  $R$  is the radius of a particle of the material,  $V_M$  is the molar volume of the material,  $\sigma$  is the surface tension of the material,  $N_A$  is Avogadro's number,  $k$  is the Boltzmann constant, and  $T$  is the temperature of the system. This equation shows that at temperatures for which a flat surface ( $R=\infty$ ) is stable, an island can have a significantly higher vapor pressure because of its small radius of curvature. Thus, flat surfaces can be produced when growth occurs slowly to discourage the formation of islands and at a sufficiently high substrate temperature to cause the islands that do form to sublime at rates much (even several orders of magnitude) higher than flat regions on the surface.

Contrary to usual expectations, surface diffusion by itself does not produce a flat surface during vapor deposition. Instead, studies by Wolf and Villain<sup>16</sup> and by Lai and Das Sarma<sup>17</sup> have shown that the  $n=4$  term in Eq. 1, which represents the mechanism of surface diffusion,<sup>12</sup> produces a *self-similar* surface in the presence of deposition noise, or if nonlinear terms are present in the equation of motion, then the surface will be *self-affine*. Thus, if one desires to grow a surface with a fractal morphology, one should deposit the material with the highest flux possible to encourage surface roughening and with a substrate temperature low enough that features with small radii of curvature will not sublime. Surface diffusion introduces enough correlation to a growing film to turn a Poisson distribution into a fractal, but it cannot produce a globally flat surface during growth because it acts over too short a length scale.

Finally, we can examine Fig. 1 and wonder how narrow the distribution can be made. A narrow peak in the PDS represents a sinusoidally varying surface. However, if the growth of a Stranski-Krastanov system is halted before the islands coalesce, then the surface is covered by islands that may be called quantum dots if the island sizes are on the order of 1 nm or so. Is it possible to grow a surface covered with a monodisperse distribution of quantum dots? Actually, Reiss<sup>20</sup> demonstrated over 40 years ago that uniform distributions of three dimensional polymer spheres can be grown from solution by the proper control of the growth kinetics. We will demonstrate here that the growth of three dimensional islands on a two dimensional medium can in theory produce an even narrower size distribution. This model, which should be applicable to the initial growth stages of a wide range of island-forming systems, predicts that it is possible to grow nearly monodisperse nanoparticles on surfaces by the proper control of island nucleation and growth kinetics.

In order to understand the size distribution of a group of islands, one can first model the growth of an individual particle in real space by Eq. (10),

$$R^n - R_0^n = K(t - t_0), \quad (10)$$

where  $r$  is the radius of the island,  $r_0$  is the radius of the critical nucleus at which the growth law becomes valid,  $K$  is a rate constant, and  $t_0$  is the germination time for the formation of the critical nucleus. The value of  $n$  is dictated by the underlying mechanism that transports atoms to the island, and has been the subject of considerable research. We saw above that  $n=3$  (it is the same in reciprocal or real space), and this growth law has also been experimentally observed by several other investigators and attributed to a radially dependent concentration gradient centered on the island.<sup>19</sup>

We also require a nucleation model for the rate at which new particles germinate. Such models have been introduced to describe solid state phase transformations, as in the problem of recrystallization from an amorphous state.<sup>22,23</sup> For films growing on surfaces, nucleation often starts preferentially at defect sites on the substrate. If the defect density (number per unit area) is finite and constant, then the rate at which nuclei ( $N$ ) are generated is proportional to the number of the remaining unoccupied sites:

$$\frac{dN}{dt} = a(N_\infty - N) = aN_\infty \exp(-at), \quad (11)$$

where  $N_\infty$  is the total number of potential nucleation sites and  $a$  is the nucleation probability (per unit time). Since the rate at which new nuclei germinate decays as an exponential function of time, this model is termed the declining nucleation model.<sup>23</sup>

If  $a$  is very large, the declining nucleation model approximates site saturation, for which all particles start to grow simultaneously. This nucleation scheme obviously is the ideal scenario to grow monodisperse nanoparticles. However, for most systems, all the particles are not likely to germinate and begin growth simultaneously. According to Eq. (10) with  $n=3$ , particles with larger radii will grow at a *much slower* rate than those with smaller radii. Thus, particles born later in time will grow faster and can eventually attain nearly the size of the particles born earlier. As long as the nucleation density and growth times are not large enough to allow particles to overlap, nearly uniform size distributions of particles can be achieved.

The size distribution of particles can be found by combining Eq. (10) with  $n=3$  and Eq. (11) to yield:

$$\frac{\partial N}{\partial R} = 3bN_\infty R^2 \exp[b(R^3 - R_{\max}^3)], \quad (12)$$

where  $b = a/K$  is the ratio of the particle nucleation rate to the single island growth rate and  $R_{\max}^3 = Kt_{\max}$ , where  $t_{\max}$  is the amount of time the islands are allowed to nucleate and grow. This function is very strongly peaked with respect to the island size, and the width of the distribution decreases with increasing  $b$ . An alternate form for the size distribution function is

$$\frac{\partial N}{\partial V} = b'N_\infty \exp[b'(V - V_{\max})], \quad (13)$$

where  $V = \theta R^3$ ,  $\theta$  is a geometrical factor equal to  $\frac{2}{3}\pi$  if the islands are hemispherical, and  $b' = b/\theta$ . The island appearance frequency at the small-size tail of the distribution (at  $R=0$ ) is suppressed by the  $-R_{\max}^3$  term in the exponent, and the maximum in the distribution is cut off at  $R = R_{\max}$ . The distributions in Eqs. (12) and (13) do not include the effects of thermal fluctuations in the island growth (the growth rate is assumed to be constant here), which will introduce an additional broadening to the distributions. However, statistical broadening for most systems is small compared to the broadening introduced in Eq. (11).

With the size distribution function in hand, it is now possible to compute the average size of the particles in the distribution and their standard deviation, which can be done analytically using Eq. 13 (but not Eq. 12). The relative standard deviation is given by:

$$\frac{\sigma}{\langle V \rangle} = \left\{ \frac{[1 - \exp(-b'V_{\max})] [(b'V_{\max}-1)^2 + 1 - 2\exp(-b'V_{\max})]}{[b'V_{\max}-1 + \exp(-b'V_{\max})]^2} - 1 \right\}^{1/2}, \quad (14)$$

where  $\langle V \rangle$  is the average and  $\sigma$  the standard deviation of the volume distribution. In the limit that  $b'V_{\max} \gg 1$ , the relative standard deviation will reduce to  $(b'V_{\max})^{-1}$ . Thus, the particles will have a narrower size distribution as they grow larger, as long as they do not interfere with each other, since site exclusion broadens the distribution significantly. Plots of Eq. (14) for various values of  $b'$  are shown in Fig. (2).

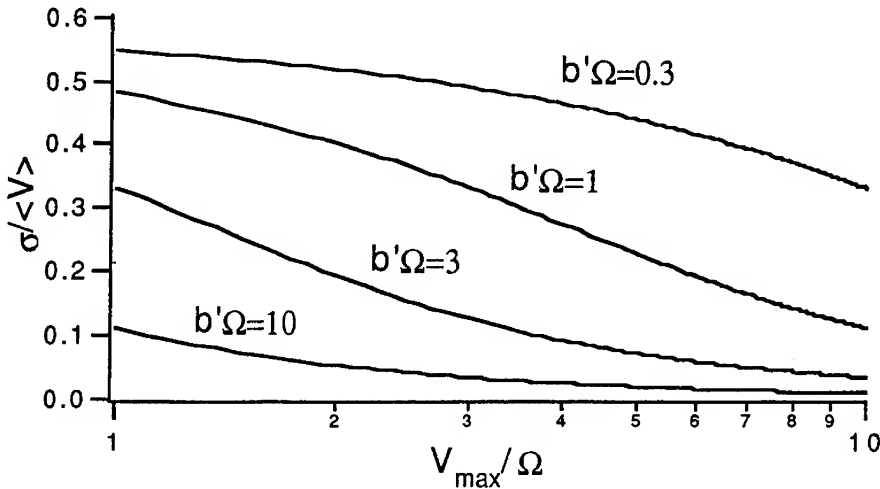


Fig. 2 Relative standard deviation of the volume distribution  $\sigma/\langle V \rangle$  of islands growing on a surface plotted as a function of the normalized maximum volume ( $V_{\max}/\Omega$ , where  $\Omega$  is a constant with units of volume) that an island can contain according to Eq. (14).

With the single island growth rule of Eq. (10) and the declining nucleation model of Eq. (11), we have shown that the particle size distribution can be expressed as in Eqs. (13) and (14). If the condition  $V_{\max} \gg (b')^{-1}$  is satisfied, the average particle size is essentially  $V_{\max}$ . In the absence of thermal fluctuations and particle interactions, Eq. (14) predicts that the relative standard deviation of the particle volume is inversely proportional to the particle volume. For a real system, Fig. 2 provides guidance in obtaining the narrowest possible size distribution of islands via a kinetic route. First, one should choose a system for which the islands are nucleated by a fixed number of immobile pinning centers. The rate of nucleation should be large, i.e. the incident flux of species on the surface should be as high as possible. However, the rate of island growth should be small, so the substrate temperature should be as low as possible to slow down the surface diffusion but not to stop it altogether. At the same time, the island separation must be kept large with respect to the island size, since the interaction of particles will cause a broadening in the size distribution. The requirements for growing monodisperse islands by kinetic control are stringent, but they should be broadly applicable.

Thus, the prescription for growing monodisperse islands is to grow with the highest possible flux to saturate the possible growth sites as quickly as possible on a substrate held at the lowest temperature that will still allow the deposited species to diffuse to the growing islands. If the deposition is halted before the islands start to coalesce, the size distribution will be narrow. If the deposition is allowed to proceed past the time when the islands coalesce, the resulting surface will be fractal.

## ACKNOWLEDGEMENTS

This research was supported by the Office of Naval Research. The authors thank the following for their assistance and insight: M. S. Anderson, R. Bruinsma, E. Chason, E. A. Eklund, F. Family, H. D. Kaesz, R. P. U. Karunisari, S. H. Liu, T. Mayer, J. Rudnick, E. J. Snyder, K. Stovall, and A. Zangwill.

## REFERENCES

1. F. Family and T. Vicsek, *J. Phys. A*, **18**, 75 (1985).
2. W.M. Tong *et al.*, *Phys. Rev. Lett.* **72**, 3374 (1994).
3. H. You *et al.*, *Phys. Rev. Lett.* **70**, 2900 (1993).
4. E. A. Eklund *et al.*, *Phys. Rev. Lett.* **67**, 1759 (1991).
5. E.A. Eklund *et al.*, *Surf. Sci.* **285**, 157 (1993).
6. J. Rudnick and R. Bruinsma, in *Low Energy Ion-Surface Interactions*, edited by J.W. Rabalais (Wiley, West Sussex, 1994) p.534.

7. W. M. Tong and R. S. Williams, *Ann. Rev. Phys. Chem.* **45**, 401 (1994).
8. W.M. Tong *et al.*, *Surf. Sci. Lett.*, **277**, L63 (1992).  
Color versions of the AFM images are posted on the World Wide Web -  
<http://www.chem.ucla.edu/dept/gifs/RSW/AUWT4.GIF>.
9. E. Bauer, *Z. Krist.* **110**, 372 (1958).
10. W. M. Tong, PhD thesis, UCLA, 1994.
11. R. Bruinsma *et al.*, in *Kinetics of Ordering and Growth at Surfaces*, edited by M.G. Lagally (Plenum, New York, 1990) pp. 395-402.
12. C. Herring, *J. Appl. Phys.* **21**, 301 (1950).
13. W.W. Mullins, *J. Appl. Phys.* **30**, 77 (1959).
14. S. F. Edwards and D. R. Wilkinson, *Proc. R. Soc. London Ser. A* **381**, 17 (1982).
15. M. Kardar, G. Parisi, and Y.-C. Zhang, *Phys. Rev. Lett.* **56**, 889 (1986).
16. D. E. Wolf and J. Villain, *Europhys. Lett.* **13**, 727 (1990).
17. Z.-W. Lai and S. Das Sarma, *Phys. Rev. Lett.* **66**, 2348 (1991).
18. R. Kern *et al.*, in *Current Topics in Materials Science*, edited by E. Kaldis (North Holland, Amsterdam, 1980).
19. A. Steyer *et al.*, *Phys. Rev. A* **44**, 8271 (1991).
20. H. Reiss, *J. Chem. Phys.* **19**, 482 (1951).
21. W. Thomson, *Phil. Mag.* **42**, 448 (1871).
22. H. V. Atkinson, *Acta metall.* **36**, 469 (1988).
23. H. J. Frost and C. V. Thompson, *Acta metall.* **35**, 529 (1987).

## WHEN INTERFACE GETS ROUGH....

TOH-MING LU\*, HONG-NING YANG\*\*, AND GWO-CHING WANG\*\*

\*Dept. of Physics, Applied Physics, and Astronomy and Center for Integrated Electronics

\*\*Dept. of Physics, Applied Physics, and Astronomy

Rensselaer Polytechnic Institute, Troy, NY 12180-3590, USA

### ABSTRACT

Interface roughness is one of the central features in many important thin film technologies. Roughness is a result of far from equilibrium dynamic growth process and is difficult to describe using conventional statistical mechanics. Recently a dynamic scaling hypothesis has been proposed to describe such a system in which both time and space scaling are considered simultaneously. This approach has generated tremendous interest, both theoretical and experimental, for scientists working in thin film growth/etching as well as many diverse fields. In this paper we shall discuss the origin of the formation of interface roughness, the difference between near equilibrium and far from equilibrium growth problems, the relevant parameters that are necessary to describe a rough interface, and the application of the self-affine scaling concept in growth problems. The experimental approaches to study rough interfaces and growth fronts using diffraction will be summarized. It is shown that there exist two types of dynamic scaling during growth, one with a stationary local slope and another one with a nonstationary local slope. Future directions in this new area of research are highlighted.

### I. INTRODUCTION

The growth of thin films is not only a subject of great interest from practical point of view but also of fundamental scientific interest. It is probably not exaggerating to say that the technological foundations of most high-tech industries are based primarily on the development and utilization of various kinds of thin films. A particularly interesting subject in thin film growth is the morphology of the surface growth fronts which directly controls many physical and chemical properties of the film. Growth processes are inherently non-equilibrium processes. For many decades the description of thin film growth processes mostly have been focused on "near-equilibrium" growth conditions where energetics of surface imperfections such as atomic steps and kinks play very important roles. Examples are the well known two- and three-dimension surface nucleation theories [1 - 3]. Very often, a well defined contour or morphology of growth front can be obtained. Figure 1a shows such a growth front where step edge plays an important role. Many experimental studies were performed under near equilibrium conditions in an attempt to obtain high quality films. However, the window (temperature, pressure, and growth rate) under which near-equilibrium conditions are satisfied is quite narrow. In general, the growth is often far-from-equilibrium and surface energetics may not play as important a role as in the near-equilibrium growth case.

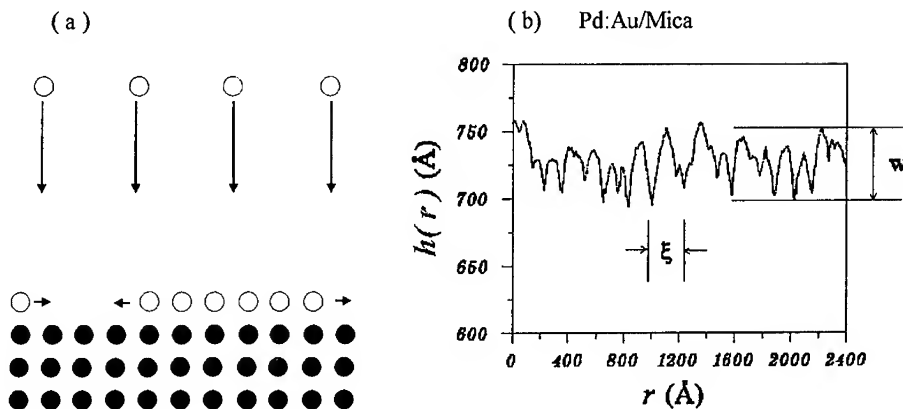


Fig. 1 (a) The growth front of a film under near-equilibrium growth conditions where energetics of surface imperfections such as atomic step edges and kinks play very important roles. (b) A cross sectional view of the morphology of a growth front (Pd:Au/Mica) under far-from-equilibrium growth conditions.

Growth under far-from-equilibrium generates random roughness at the growth front. The rough growth front results from the competition between fluctuations in the deposition of material onto the surface and the smoothing effect at the growth front due to surface diffusion. Figure 1b shows the cross section view of such a surface. Thus far a standard statistical mechanics approach to describe such a complex morphology associated with this far-from-equilibrium process has not been developed. Recently a very important dynamic scaling hypothesis [4, 5] has been proposed to describe such a far-from-equilibrium system based on the concept of self-affine fractals. In this description, both time and space scaling are considered simultaneously. This approach has generated tremendous interest both theoretically and experimentally for scientists working in thin film growth/etching as well as many diverse fields such as pattern formation, porous media, and fracture.

Both real space imaging techniques and diffraction techniques have been used to study rough surfaces and growth fronts. Real space imaging techniques include Scanning Tunneling Microscopy (STM) [6 - 12], Atomic Force Microscopy (AFM) [13, 14], Transmission Electron Microscopy (TEM) [15], Secondary Electron Microscopy (SEM), and optical imaging techniques. Examples for diffraction techniques are: electron, atom, light, and X-ray diffraction. Recent advancements in diffraction techniques [16 - 19], including both data collection and the interpretation of the data, have greatly stimulated experimental study of dynamic scaling in thin film growth fronts. Diffraction techniques are perhaps more suitable and powerful for the study of thin film growth front where parameters describing the properties of dynamic growth front such as interface width, lateral correlation length, and roughness exponent, have to be measured *in-situ* during growth. The feasibility of such a study has been demonstrated [11, 20 - 27].

## II. ROUGHNESS EXPONENT

Several parameters are required to describe the rough interface shown in Fig. 1b. First of all, the interface width  $w$  is defined as the square root of  $\langle [h(r) - \langle h \rangle]^2 \rangle$ , where  $h(r)$  is the surface height at position  $r$ .  $w$  is the "amplitude" of surface fluctuations and thus describes the property of the interface at large distances. The lateral correlation length  $\xi$  describes the "wavelength" of surface fluctuations. Two surfaces having the same interface width  $w$  and the same lateral correlation length  $\xi$  may possess very different local roughness structure as shown in Fig. 2. One therefore requires an additional parameter to describe the properties of the rough surface. The most popular way to describe the interface roughness is to use the height-height correlation function  $G(r)$ , which is defined as  $\langle [h(r) - h(0)]^2 \rangle$ . For large  $r$ , the surface height fluctuations should not be correlated and  $G(r) = 2 \langle [h(r)]^2 \rangle = 2w^2$ . Very often, for small  $r$ , the height-height correlation function has an asymptotic form,  $G(r) = (\rho r)^{2\alpha}$ , where  $\rho$  is a constant and  $\alpha$  is known as the roughness exponent, or Hurst exponent.  $\alpha$  describes how "wiggly" the local surface is and has a value of  $\leq 1$ . In Fig. 3,  $G(r)$  is plotted as a function of  $r$  in log-log scale for the surface shown in Fig. 1b. This is the surface of a Au:Pd thin film deposited on Mica. The height-height correlation function reaches a constant value (equal to  $2w^2$ ) at a large distance. This distance defines a lateral correlation length,  $\xi$ , beyond which the surface height fluctuations are not correlated. On the log-log scale, the value of  $\rho$  can be obtained from the intersection of the curve with the vertical axis, which gives  $2\alpha \log(\rho)$  at  $r = 1$  (or  $\log(r) = 0$ ).

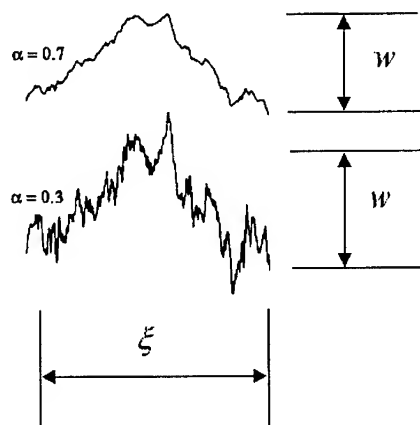


Fig. 2 Two rough surfaces having the same interface width  $w$  and lateral correlation length  $\xi$  but differing in local roughness.



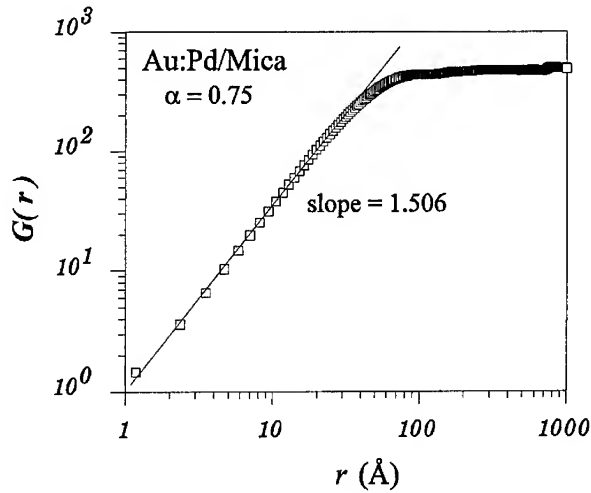


Fig. 3 The height-height correlation function  $G(r)$  measured from the surface of vacuum evaporated Pd:Au/Mica.

One notes that a rough interface having the height-height correlation function shown in Fig. 3 has the interesting characteristic that the vertical direction does not scale the same way as in the lateral direction. It is therefore not a "self-similar" but a "self-affine" surface in which the height-height correlation can be written as

$$G(r) = 2w^2 f(r/\xi), \quad (1)$$

where  $f(x) = 1$  for  $x \gg 1$ , and  $f(x) = x^{2\alpha}$ , for  $x \ll 1$ . These properties are consistent with the plot shown in Fig. 3. From Eq. (1),  $\rho$  can be written as  $\sim w^{1/\alpha}/\xi$ .  $\rho$  approximately can be treated as the average local slope of the rough surface.

### III. DYNAMIC SCALING HYPOTHESIS

For a growing interface, the height-height correlation is time dependent,  $G = G(r, t)$ . The dynamic scaling hypothesis for a growing interface assumes a height-height correlation of the form [4, 5]

$$G(r, t) = 2[w(t)]^2 f[r/\xi(t)], \quad (2)$$

where, again,  $f(x) = 1$  for  $x \gg 1$ , and  $f(x) = x^{2\alpha}$ , for  $x \ll 1$ . The interface has a power law behavior in time,  $w(t) \sim t^\beta$ . Dynamic scaling requires that  $\rho \sim w(t)^{1/\alpha}/\xi(t)$  be time independent, which means that the lateral correlation length must grow as  $\sim t^{\beta/\alpha}$ . It is important to note that although the interface width and the lateral correlation length increase with time following power laws, the local slope of the interface remains time invariant. Figure 4a shows the essential characteristics of the dynamic scaling hypothesis. As time evolves, the interface width and the lateral correlation length are shown to grow, but the intersection of the curve with the vertical axis on this log-log plot, which is related to the local slope  $\rho$  of the rough surface, does not change. The physical origin of this very interesting phenomenon is that the fluctuations and smoothing effect at the growth front have reached a balance and the local structure remains unchanged. We shall refer to this class of growth front as the type I dynamic growth, or stationary growth.

However, a recent study showed that  $\rho = \text{constant}$  is not the only kind of dynamic growth front. One can also have a case where the local slope is time dependent,  $\rho = \rho(t)$ . In this case the height-height correlation behaves like the curves shown in Fig. 4b. For large  $r$  ( $x \gg 1$ ),  $G(r, t) = 2[w(t)]^2 \sim t^{2\beta}$ . For short range ( $x \ll 1$ ),  $G(r, t) \sim [\rho(t)r]^{2\alpha}$ . Although at any time, the height-height correlation function still has a power law behavior for small  $r$  with a constant value of  $\alpha$ ,  $\rho$  is time dependent and so is the local slope of the surface. This is an interesting situation in which the fluctuations and smoothing effect cannot quite reach a balance and a stationary local slope cannot be achieved. We shall refer to this as type II dynamic growth or non-stationary growth.

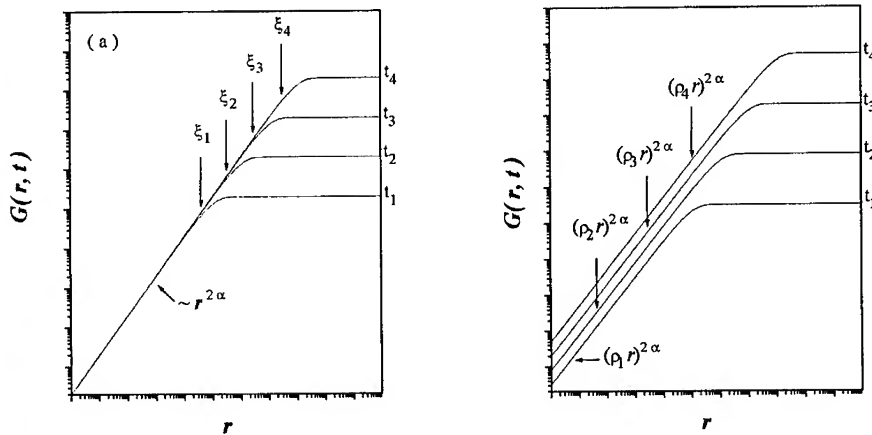


Fig. 4 (a) The time-dependent height-height correlation function  $G(r, t)$  from a type I dynamic growth front, which shows the essential characteristics of the dynamic scaling hypothesis. (b) The time-dependent height-height correlation function  $G(r, t)$  from a type II dynamic growth front. The plot of  $G(r, t)$  exhibits a time-dependent and unstable local slope  $\rho(t)$  that is different from the stable  $\rho$  shown in Fig. 4a.

#### IV. DIFFRACTION CHARACTERISTICS

Thus far, diffraction has been a very important tool for *in-situ* study of the morphology of growth fronts. All diffraction techniques involve a diffraction structure factor that is related to the morphology of the growth front. In most cases, all the important parameters related to the growth front,  $w$ ,  $\xi$ , and  $\rho$ , and therefore the exponents  $\alpha$  and  $\beta$ , can be extracted from the specularly reflected diffraction intensity (diffraction structure factor). In general, the specularly reflected intensity can be written as [16, 17]

$$I(k) \sim e^{-(k_{\perp} w)^2} \delta(k_{\parallel}) + I_{diff}(k_{\parallel}, k_{\perp}), \quad (3)$$

where  $k = k_{out} - k_{in}$  is the momentum transfer with  $k_{out}$  and  $k_{in}$  being the outgoing and incoming wavevectors, and  $k_{\parallel}$  and  $k_{\perp}$  are the momentum transfer parallel and perpendicular to the surface, respectively.  $k_{\perp} = (4\pi/\lambda)\cos\theta$  and  $k_{\parallel} = (4\pi/\lambda)\sin(\theta_{in} - \theta)$ , where  $\theta_{in}$  is the incident angle and  $\theta$  is the scattering angle with respect to the surface normal. The central sharp intensity is the  $\delta$ -component ( $\delta$  line shape) which depends on the interface width  $w$  and is used for the determination of  $w$ . The lateral correlation,  $\xi$ , is inversely proportional to the full-width-at-half-maximum (FWHM) of the diffuse part of the intensity,  $I_{diff}(k_{\parallel}, k_{\perp})$ , when  $k_{\perp}$  is small (or, the near in-phase diffraction condition for stepped surfaces). For large  $k_{\perp}$  conditions (or, near the out-of-phase diffraction condition for stepped surfaces), the FWHM of the diffuse part of the intensity (diffuse line shape) is proportional to  $\rho k_{\perp}^{1/\alpha}$ . One therefore is able to determine both  $\alpha$  and  $\rho$  by plotting the FWHM as a function of  $k_{\perp}$ .

#### V. NOISE: THE ORIGIN OF INTERFACE ROUGHNESS

The roughness of a surface growth front comes from the inherent noise that exists during the growth. The noise gives rise to fluctuations of the material arriving at the growth front in time and space. For example, in evaporation-deposition of materials onto a growth front (including molecular beam epitaxy (MBE)), atoms arriving on the surface never deposit uniformly across the surface at any time. Over the time, the growth front may become rough even it is perfectly flat initially. If we ignore the smoothing effect after the atoms have arrived at the surface, the growth front morphology can be described by the following equation:

$$\frac{\partial}{\partial t} h(r, t) = R + \eta(r, t), \quad (4)$$

where  $h(r, t)$  is the height of the growth front at the surface position  $r$  and time  $t$ , with respect to the original flat surface,  $R$  is the deposition rate, and  $\eta(r, t)$  is the noise term. The noise is random and satisfies

$$\begin{cases} \langle \eta(r, t) \rangle = 0 \\ \langle \eta(r, t) \eta(r', t') \rangle = 2D \delta(r - r') \delta(t - t'), \end{cases} \quad (5)$$

where  $D$  is a constant. Equation (4) can be reparametrized and rewritten as

$$\frac{\partial}{\partial t} h(r, t) = \eta(r, t) \quad (6)$$

after replacing  $h(r, t)$  by  $h(r, t) + Rt$  to normalize the height so that the value of  $h(r, t)$  is evaluated with respect to the average height of the surface. The solution of Eq. (6) is

$$h(r, t) = \int_0^t dt' \eta(r, t'). \quad (7)$$

The square of the interface width, which is defined as  $[w(t)]^2 = \langle [h(r, t) - \langle h \rangle]^2 \rangle$ , can then be calculated:

$$\begin{aligned} [w(t)]^2 &= \langle [h(r, t)]^2 \rangle = \int_0^t dt' \int_0^t dt'' \langle \eta(r, t') \eta(r, t'') \rangle \\ &\sim \int_0^t dt' \int_0^t dt'' \delta(t'' - t') = \int_0^t dt' = t. \end{aligned} \quad (8)$$

Note that we have used the fact that  $\langle h \rangle = 0$ . The interface width,  $w(t)$ , therefore grows as a power of time,  $t^\beta$ , with  $\beta = 1/2$ , independent of dimension. It is seen clearly that random noise can lead to the roughening of the growth front with the interface width growing as a power of time. It can also be shown from the height-height correlation that  $\xi \sim 0$  in this case. This model is, of course, not very realistic. Most growth problem would involve some kind of surface diffusion, which we shall discuss next.

## VI. EPITAXIAL GROWTH FRONTS BY EVAPORATION

There are many different ways that materials can be deposited onto the growth front. The simplest way is perhaps by evaporation. The flux of atoms arrives in the growth front at a

constant rate (except the noise, which makes it slightly non-uniform in time and space). In many classes of growth, the chance of re-evaporation and condensation is small. The smoothing effect is dominated by surface diffusion in the form of the fourth derivative of the height [28 - 33]:

$$\frac{\partial}{\partial t} h(\mathbf{r}, t) = -\kappa \nabla^4 h(\mathbf{r}, t) + \eta(\mathbf{r}, t), \quad (9)$$

where  $\kappa$  is the diffusion coefficient. The smoothing effect caused by this  $\nabla^4$  type of surface diffusion has been studied for long time and has been used to describe the kinetic of flattening of a curved surface due to heat treatment [34]. The difference presented here for the evaporation-deposition case is the addition of the noise term. Without the noise term, the surface remains flat during growth. Equation (9) does not allow void formation and therefore is a conservative growth model. The model would work well for evaporation-deposition of thin films such as low pressure MBE growth. The solution of this linear differential equation can be obtained quite simply by working in Fourier space [33]. The interface width grows as  $t^\beta$ , with  $\beta = 1/4$ . At short range, the height-height correlation function has the form  $G(r, t) \sim [\rho(t)r]^{2\alpha}$ , where  $\alpha = 1$  and  $\rho(t) \sim \sqrt{\ln(t)}$ . Obviously this belongs to type II dynamic growth and the local slope changes with time.

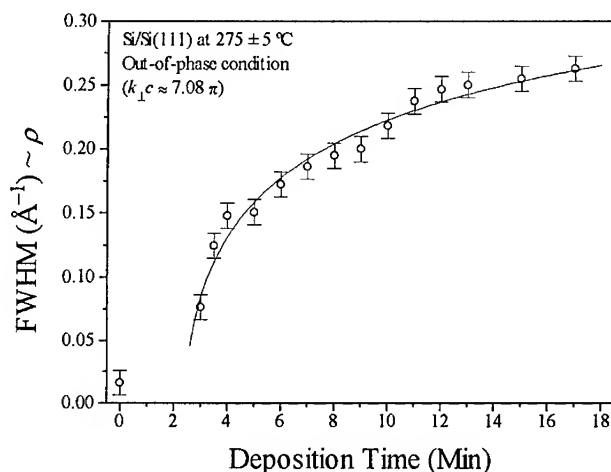


Fig. 5 The FWHM (shown as open circles) of HRLEED (00) beam line shape at an out-of-phase condition,  $k_{\perp}c = 7.08 \pi$ , is plotted as a function of the growth time. The solid curve results from the fit using the form of  $\text{FWHM} \sim \sqrt{\ln(t/\tau)}$ , where  $\tau$  is an adjustable fit parameter.

Recent MBE growth of Si on Si(111) at low substrate temperature [26] appears to belong to this type II of simple linear diffusion dynamics. Figure 5 is a plot of the FWHM ( $\sim \rho$ ) of the high-resolution low-energy electron diffraction (HRLEED) intensity profile as a function of deposition time at 275 °C substrate temperature. The electron energy is chosen such that the phase of the (00) beam is near an out-of-phase diffraction condition so that the electron wave interferes destructively from different layers of terraces separated by atomic steps. At these diffraction conditions, the intensity is most sensitive to local step (roughness) structure. The deposition rate was 7 bilayers/min and the total thickness deposited was  $\sim 370$  Å. The solid curve is a  $\sqrt{Ln(t)}$  fit of the data. The exponents  $\alpha$  and  $\beta$  were also obtained to be  $1.03 \pm 0.07$  and  $0.25 \pm 0.02$ , respectively. Interesting enough, the roughening evolution of a sputter-etched Si(111) surface [24] also behaves quite similarly in that the local slope also grows as  $\sqrt{Ln(t)}$  and  $\alpha = 1.15 \pm 0.08$ .

Type I dynamic growth can be modeled with the inclusion of a term  $\nabla^2 h$  or a nonlinear term,  $\nabla^2(\nabla h)^2$ , in Eq. (9) [29-31]. Time-invariant local structure [17] that was predicted by this model was indeed observed in some MBE experiments [21, 22, 27]. Many other interesting models were proposed in recent years [5]. However, their relevance to realistic experimental growth conditions has not been fully established.

## VII. CONCLUSION

Far-from-equilibrium growth front study is in its infancy. Model calculations for vapor deposition have been developed but not for other technologically important growth processes such as chemical vapor deposition and sputtered deposition. Only limited experimental data were available to compare with model calculations. More experimental work performed under different substrate temperatures, deposition rates, and pressures are needed to compare with theoretical predictions. Further understanding of this exciting new class of non-equilibrium phenomena would allow us not only to better control growth front morphology and therefore thin film quality but also allows testing of dynamic growth universality classes.

**ACKNOWLEDGMENT:** Work supported by NSF.

## REFERENCES

1. E. Bauer, Z. Kristallogr. **110**, 372 (1958).
2. R. Kern, G. Le Lay, and J.J. Metois, Basis Mechanisms in the Early Stages of Epitaxy, in Current Topics in Mat. Sci. **3**, 131 (North Holland, Amsterdam, 1979).
3. J.A. Venables, G.D.T. Spiller, and M. Hanbuchen, Rpt. Progr. Phys. **47**, 399 (1984).
4. F. Family and T. Vicsek, J. Phys. **A18**, L75 (1985).

5. For review, see Dynamics of Fractal Surfaces, edited by F. Family and T. Vicsek (World Scientific, Singapore, 1990).
6. M.W. Mitchell and A. Bonnell, *J. Mater. Res.* **5**, 2244 (1990).
7. J.M. Gómez-Rodríguez, A.M. Baró, and R.C. Salarezza, *J. Vac. Sci. Technol.* **B9**, 495 (1991).
8. R.S. Williams, R. Bruinsma, and J. Rudnik, in Evolution of Surface and Thin Film Microstructure, edited by H.A. Atwater, M. Grabow, E. Chason, and M. G. Lagally (*Mat. Res. Soc. Proc.* **280**, Pittsburgh, PA, 1992); E. A. Eklund, R. Bruinsma, J. Rudnik, and R.S. Williams, *Phys. Rev. Lett.* **67**, 1759 (1991).
9. J. Krim, I. Heyvaert, C. Van Haesendonck, and Y. Bruynseraede, *Phys. Rev. Lett.* **70**, 57 (1993).
10. H.-N. Yang, A. Chan, and G.-C. Wang, *J. Appl. Phys.* **74**, 101 (1993).
11. H. You, R.P. Chiarello, H.K. Kim, and K.G. Vandervoort, *Phys. Rev. Lett.* **70**, 2900 (1993).
12. G. Palasantzas and J. Krim, *Phys. Rev. Lett.*, in press.
13. W.M. Tong, R.S. Williams, A. Yanase, Y. Segawa, and M.S. Anderson, *Phys. Rev. Lett.* **72**, 3374 (1994).
14. R. Pétri, P. Brault, O. Vatel, D. Henry, E. André, P. Dumas, and F. Salvan, *J. Appl. Phys.* **75**, 7498 (1994).
15. D.J. Eaglesham, H.-J. Gossmann, and M. Cerullo, *Phys. Rev. Lett.* **65**, 1227 (1990); D.J. Eaglesham and G.H. Gilmer, in Surface disordering: Growth, roughening and phase transitions, edited by R. Jullien et al. (Nova, NY 1993).
16. For review, see H.-N. Yang, G.-C. Wang, and T.-M. Lu, Diffraction from Rough Surfaces and Growth Fronts (World Scientific, Singapore, 1993).
17. H.-N. Yang, T.-M. Lu, and G.-C. Wang, *Phys. Rev. Lett.* **68**, 2612 (1992); *Phys. Rev.* **B47**, 3911 (1993).
18. Po-zen Wong and Alan J. Bray, *Phys. Rev.* **B37**, 7751 (1988).
19. S. K. Sinha, E. B. Sirota, S. Garoff, and H. B. Stanley, *Phys. Rev.* **B38**, 2297 (1988).
20. R. Chiarello, V. Panella, J. Krim, and C. Thompson, *Phys. Rev. Lett.* **67**, 3408 (1991).
21. Y.-L. He, H.-N. Yang, T.-M. Lu, and G.-C. Wang, *Phys. Rev. Lett.* **69**, 3770 (1992).
22. H.-J. Ernst, F. Fabre, R. Folkerts, and J. Lapujoulade, *Phys. Rev. Lett.* **72**, 112 (1994).
23. C. Thompson, G. Palasantzas, Y.P. Feng, S.K. Sinha, and J. Krim, *Phys. Rev.* **B49**, 4902 (1994).
24. H.-N. Yang, G.-C. Wang, and T.-M. Lu, *Phys. Rev.* **B50**, 7365 (1994).
25. T. Salditt, T.H. Metzger, and J. Peisl, *Phys. Rev. Lett.* **73**, 2228 (1994).
26. H.-N. Yang, G.-C. Wang, and T.-M. Lu, *Phys. Rev. Lett.* **73**, 2348 (1994).
27. H. Zeng and G. Vidal, *Phys. Rev. Lett.*, in press.
28. D.E. Wolf and J. Villain, *Europhys. Lett.* **13**, 389 (1990).
29. Z.-W. Lai and S. Das Sarma, *Phys. Rev. Lett.* **66**, 2348 (1991).
30. L.-H. Tang and T. Nattermann, *Phys. Rev. Lett.* **66**, 2899 (1991).
31. A. Zangwill, D.D. Vvedensky, C.N. Luse, and M.R. Wilby, *Surf. Sci.* **274**, L529 (1992); *Phys. Rev.* **E48**, 852 (1993).
32. M. Siegert and M. Plischke, *Phys. Rev. Lett.* **68**, 2035 (1992).
33. J.G. Amar, P.-M. Lam, and F. Family, *Phys. Rev.* **E47**, 3242 (1993); J.G. Amar and F. Family, in Mechanisms of Thin Film Evolution, edited by S.M. Yalisove, C.V. Thompson, and D.J. Eaglesham (*Mat. Res. Soc. Proc.* **317**, Pittsburgh, PA, 1994).
34. W. W. Mullins, *J. Appl. Phys.* **28**, 334 (1957); **30**, 77 (1959).

## INFLUENCE OF IMPURITIES ON MECHANISMS OF GROWTH IN MOVPE GaAs

S. Nayak\*, J.M. Redwing\*\*, and J.W. Huang\*\*, M.G. Lagally\* and T.F. Kuech\*\*

\*Materials Science Program, \*\*Department of Chemical Engineering  
University of Wisconsin, Madison, WI-53706

### ABSTRACT

Atomic force microscopy (AFM) has been used to investigate the atomic-scale mechanisms of growth of GaAs by metal organic vapor phase epitaxy (MOVPE). The influence of impurities such as silicon, oxygen and carbon on the small-scale periodic structure as well as on the large-scale features has been studied. The growth front of GaAs epitaxial films grown on vicinal GaAs (100) substrates exhibits periodic structure except for the Si doped GaAs grown on semi-insulating vicinal GaAs (100) substrates. The periodicity on the surface breaks down when oxygen, silicon or carbon concentration exceeds  $10^{18}\text{cm}^{-3}$ . These impurities may preferentially attach at the step edges resulting in reduction of the mobility of the steps. At higher impurity concentrations, the motion of the growth front gets pinned on the surface resulting in a disruption of the step flow mode of growth. The wide terraces on Si doped GaAs grown on semi-insulating substrate is proposed as the kinetic limited step bunching during the step flow mode of growth.

### INTRODUCTION

The submicron device dimensions within semiconductor systems has stimulated interest in the fundamental physics of quantum structures<sup>1</sup> as well as in novel device concepts such as lateral superlattices, quantum wires, and dots<sup>2</sup>. However, the methods to fabricate these structures, and control their size in the nanometer scale rely critically on understanding of the fundamental mechanisms governing the evolution of the growth front. The concept of evolution of steps and facets on vicinal substrates under different growth conditions is extremely important in synthesizing these quantum devices. Recent investigations have focused on formation of micro-facets on GaAs and  $\text{Al}_x\text{Ga}_{1-x}\text{As}$  surfaces<sup>3-8</sup>.

The growth front morphology of molecular-beam-epitaxy (MBE)-grown GaAs has been investigated by STM<sup>6,7</sup>, AFM<sup>8</sup>, and RHEED<sup>6</sup>. The periodic or quasiperiodic morphology consisting of elongated mounds (regions of bunched steps) that is generally observed<sup>6-8</sup> has been ascribed variously to thermodynamic driving forces or kinetic limitations. The thermodynamic arguments rest on the adoption by the growth front morphology that minimizes the free energy of the surface: anisotropic step energies can lead to anisotropic shapes and steps may bunch to form specific lower-energy facets. Kinetic arguments rest on limited diffusion rates, anisotropy in diffusion, and especially the existence of barriers for atomic transport over steps. These factors cause the periodic nucleation of 2-D islands which grow into 3-D structures.

Although MOVPE growth is qualitatively different from MBE growth, similar fundamental thermodynamic driving forces and kinetic limitations must control the growth front morphology. Periodic growth front morphology has also been observed in MOVPE-grown GaAs(001)<sup>3-5</sup>. Kasu and Kobayashi<sup>3</sup> measured the angle between the facets, and suggested a thermodynamic control and the formation of microfacets with (100) and (117)<sub>B</sub> faces to minimize the surface energy as the bunched steps grown on vicinal GaAs(100) miscut toward both [110] and  $[\bar{1}10]$  were stable during prolonged annealing. Hata *et al.*<sup>4</sup> also invoked



thermodynamic arguments to explain their observation of step bunching, which occurred, however, on a vicinal surface miscut toward [010].

The work reported so far has focused on growth without deliberate incorporation of impurities in the films. This investigation has focused on the evolution of growth front morphology when oxygen, silicon and carbon are deliberately incorporated in GaAs (001) during growth. Oxygen and carbon are common, often inadvertent impurity in MOVPE growth environment<sup>9</sup>. After an evaluation of existing results on undoped GaAs in terms of thermodynamic or kinetic mechanisms, we present a model in which the evolving morphology is controlled by a modification of the kinetic parameters by the impurity.

## EXPERIMENTS

Epitaxial films were grown on semi-insulating and n-type GaAs (001) substrates with a miscut angle of  $1.95^\circ \pm 0.1^\circ$  towards [010]. Double crystal x-ray diffraction was used to confirm the miscut angles of the substrate. GaAs was grown by MOVPE at 600°C, 650°C and 700°C, using trimethyl gallium and arsine or tertiary butyl arsine at a growth rate of 50 nm/min. Diethylaluminum ethoxide (DEALO)  $((C_2H_5)_2AlOC_2H_5)$  was used to incorporate oxygen intentionally during the growth. Silicon was incorporated from silane and/or disilane. Carbon was incorporated from  $CCl_4$ . The details of the oxygen<sup>9</sup>, silicon<sup>10</sup>, and carbon<sup>11</sup> incorporation are discussed elsewhere. The oxygen, silicon and carbon concentrations were controlled over the range of  $10^{16}$ – $10^{20}$ ,  $10^{16}$ – $10^{18}$  and  $10^{17}$ – $10^{19}$  cm<sup>-3</sup> respectively. The sample structure consisted of an undoped buffer layer of GaAs, 0.1 μm thick, followed by either a 1 or 5 μm layer of doped GaAs. The impurity concentrations were determined by secondary ion mass spectrometry (SIMS) and capacitance voltage measurements. The surface morphology was investigated by AFM. The AFM was operated in a constant force mode with a wide, 100 μm length triangular commercial silicon nitride cantilever tip having a force constant of 0.58 N/m.

## RESULTS

### I. Undoped GaAs

The RMS roughness ( $\sigma$ ) of the epitaxial substrate surface prior to any deposition is less than a ( $\sigma = 0.221$  nm) monolayer when averaged over an area of  $1 \mu m^2$ . The surface has no observable structure associated with it. The surface structure of the undoped GaAs grown on n-type and semi-insulating  $2^\circ$  [010] misoriented substrates exhibits periodic structure. Figure 1(a) shows the periodic structure of the surface of 5 μm thick undoped GaAs. It has a spatial wavelength of 48 nm and an amplitude of 1.2 nm, in the direction of the substrate miscut. This miscut gives terraces with a mean width of  $\sim 8$  nm. It is clear that this periodic structure is not replicated from the substrate but develops during the growth.

### II. Silicon doped GaAs

The silicon doped GaAs samples were grown on vicinal  $\sim 2^\circ$  [010] misoriented semi-insulating and n-type substrates at the same time. The surface morphology does not depend on doping sources,  $SiH_4$  or  $Si_2H_6$  or the group V sources, arsine or tertiary butyl arsine. The morphology of the surface of the Si doped GaAs(001) grown on n-type substrates exhibits periodic structure along the [010] miscut direction. This surface structure is identical to the surface of undoped GaAs except with a smaller spatial wavelength of  $\sim 33$  nm. The periodicity decreases and the RMS roughness increases with increasing silicon concentration. Wide terraces

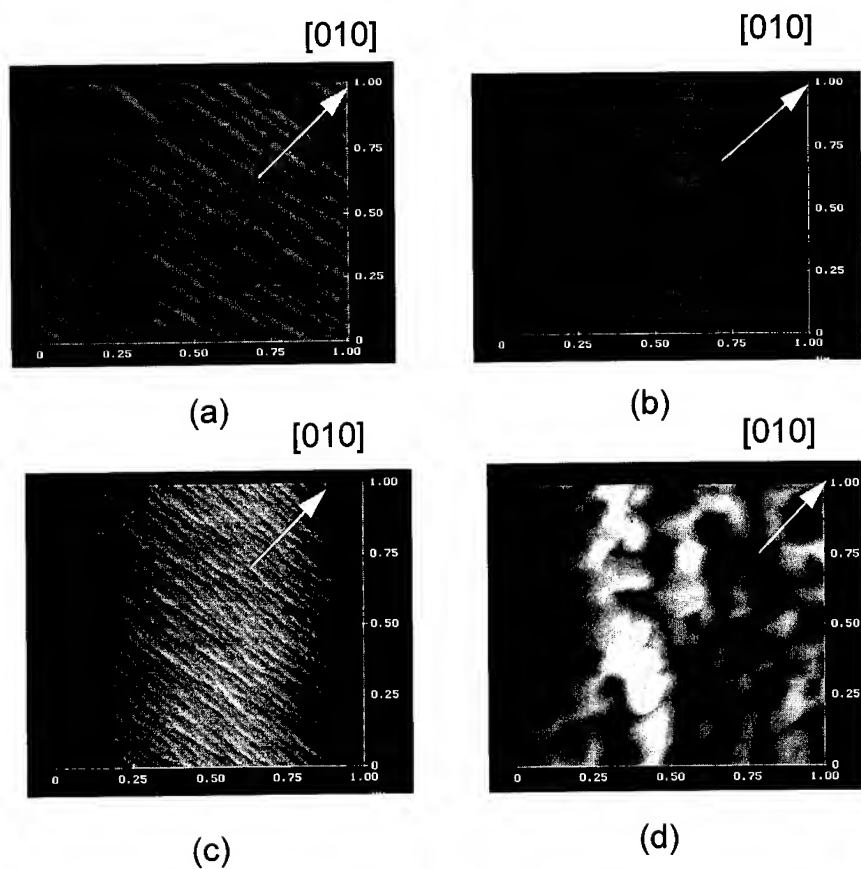


Figure 1:

- (a) The surface structure of 5 μm thick undoped GaAs grown on the above substrate with a RMS roughness of 0.313 nm. The surface is periodic along the miscut direction.
- (b) Facets of 0.4 to 0.6 μm along the miscut direction on 10<sup>17</sup> cm<sup>-3</sup> [Si] doped GaAs grown on GaAs (100) → 2 [010].
- (c) The periodic structure of 10<sup>18</sup> cm<sup>-3</sup> [O] doped GaAs along the miscut direction.
- (d) The periodicity breaks down at higher [O] 10<sup>20</sup> cm<sup>-3</sup> in GaAs.

of the order of 0.4 to 0.6  $\mu\text{m}$  are observed on  $10^{16}$  -  $10^{18} \text{ cm}^{-3}$  Si doped GaAs (001) grown on a semi-insulating substrate (shown in figure 1 (b)). These flat terraces are atomically smooth with a roughness of less than a monolayer ( $\sigma = 0.211 \text{ nm}$ ). The average width of the terraces does not decrease significantly with the increase in doping levels from  $2 \times 10^{16}$  to  $7 \times 10^{18} \text{ cm}^{-3}$ .

### III. Oxygen doped GaAs

The surface morphology of oxygen doped GaAs grown on both n-type and semi-insulating substrates, at low oxygen concentrations, exhibits a periodic structure along the misorientation direction [010]. Figure 1(c) shows the periodic structure formed on the surface of  $10^{18} \text{ cm}^{-3}$  oxygen doped GaAs. The periodicity decreases with the increase in oxygen concentration up to  $10^{18} \text{ cm}^{-3}$ . Although the qualitative features of the surface morphology are not affected by [O] concentration of less than  $10^{19} \text{ cm}^{-3}$ , quantitatively the spatial period of the surface morphology decreases, the RMS value of the roughness and the amplitude increases. At [O] concentration above  $10^{19} \text{ cm}^{-3}$  an existing new broken surface morphology consisting of 3-D clusters, evolves. Figure 1(d) shows these features, which are 0.1 - 0.2  $\mu\text{m}$  in height and corresponds to the presence of visual size haze on the surface.

### IV. Carbon doped GaAs

The surface morphology of carbon doped GaAs grown on a semi-insulating substrate exhibits a periodic structure along the miscut direction [010] when doped with carbon up to  $10^{18} \text{ cm}^{-3}$ . These features do not, however, have long-range periodicity. At higher carbon concentrations the large aperiodic mound-like structures appear on the surface. The effect of carbon doping on the morphology of GaAs is thus, similar to that of oxygen, except that at higher carbon doping (above  $10^{18} \text{ cm}^{-3}$ ) large mounds with heights on the order of  $\sim 10$ -20 nm are observed instead of isolated islands with steep edges observed for high oxygen doping.

## DISCUSSION

The principal observations are: 1) The miscut direction and feature directions are same, which is in agreement with other MOVPE studies<sup>1-3</sup>, 2) the nature of the substrates (semi-insulating or n-type) has no effect on the features observed in O and C doped GaAs, 3) the nature of the substrate does influence the surface morphology of Si doped GaAs, 4) quantitatively the spatial period of ripples observed on the surface decrease, while the RMS roughness and amplitude increase with increasing concentration of impurities, and 5) lastly, at higher concentration of O and C, there is a breakdown of the observed periodic structure.

Before suggesting a model to explain the observed behavior, we briefly evaluate the existing data in terms of possible thermodynamic or kinetic mechanisms. Both thermodynamic and kinetic arguments have merit. In any given growth situation it is likely that both play a role to a greater or lesser extent. In contrast to Si (001), GaAs(001) has a polar surface. An obvious possible cause for morphological rearrangement in GaAs to minimize free energy might be related to charge rearrangement at the surface<sup>13</sup>. In all the MOVPE data<sup>3-6</sup>, including ours, the periodic morphology is aligned along the miscut direction. The only way in which thermodynamics could accomplish this result is if there existed a step free energy that sufficiently dominated the surface free energy independent of the step orientation so that periodic morphology could form in whatever orientation the initial surface was miscut.

Kinetic limitations are much more creditable causes for large-scale periodic morphology. The periodic nucleation of islands is a direct result of a limited diffusion length, which can be

brought about by either a low substrate temperature or a high deposition rate<sup>13</sup>. On a very flat surface the nucleation is homogeneous in the sense that atoms must find each other on a terrace. If steps are present, they can act as "heterogeneous" nucleation sites that therefore lock in the direction of periodicity of the subsequently formed morphological features. Nuclei formed on steps that lie within a diffusion length of each other will tend to coalesce into one structure, leading, as for the flat surface, to a periodic morphology. The period will be smaller than that on a flat surface if barriers for crossing steps exist, because the diffusion length will be less. The morphology will be anisotropic, because in the direction in which there are no steps, the diffusion length will be larger and the separation of mounds will therefore be greater. Once such a structure forms it is difficult to "erase" it: the smoothening of a structure requires the "ripening" mechanism to be effective, in which an atom must desorb from a structure and migrate to another or migrate from the top of a structure to its base. The driving forces for ripening depend on differences of local chemical potentials (in the simple cases local curvature of the morphology). If the structures are far apart or shallow, there is little driving force and a structure, as in Ostwald ripening, simply can not reach an equilibrium configuration. For this reason, the arguments those claim an equilibrium structure of the surface as annealing has no effect, are hazardous.

An impurity mechanism proposed by Frank<sup>14</sup>, is relevant in explaining the step bunching in GaAs. The presence of an impurity directly in front of a growing step impedes the motion of step. As a result, the velocity of a step becomes a decreasing function of the density of impurities immediately in front of it. When a step segment finally moves over a given impurity, the effect of that impurity becomes weaker. Thus, impurities are essentially covered and their effect is lessened and even deactivated. The effect of one type of impurity differs from that of other. Since new impurities continually arrive from the vapor phase during growth, the motion of the steps in step flow is determined by the presence of both the active as well as covered impurities. The impurities need not be added from external sources but rather could be present in the growth environment or as defects and dislocations at the growth front or could float up like a surfactant after it is introduced. These impurities and defects on the surface may be responsible for the step bunching in MOVPE growth environments.

In MOVPE grown GaAs doped with oxygen, oxygen is known to attach strongly to the surface and preferentially incorporated at Ga terminated steps<sup>15</sup>. Under the present growth conditions on a 2° misoriented GaAs (001) substrate, for  $[O] \approx 10^{18} \text{ cm}^{-3}$ , one in eighty step sites would be associated with oxygen atom. The impact of high concentration of oxygen at the step edges can be several. Oxygen may act as a kinetic barrier to step flow impeding the motion of the steps and large scale feature across the surface, leading to step bunching. In addition, the electronic interactions between oxygen atoms at the growth front may lead to larger repulsive or attractive interactions. Repulsive interactions between the oxygen and other migrating charged species can increase the effective region over which sites for further growth will be blocked. At the highest oxygen concentration,  $[O] \sim 10^{20} \text{ cm}^{-3}$ , the regular features is finally broken into a series of small hillocks.

The large facets observed in Si doped GaAs on vicinal semi-insulating substrates are most likely meta-stable structures consisting of fifty to seventy steps, and are probably due to kinetic limited step bunching during step flow mode of growth. The difference in surface morphology obtained from Si doped GaAs grown on n-type substrates and semi-insulating

substrates, is not clear at this moment. We speculate that electronic interactions play a significant role in altering the surface morphology of Si doped GaAs. It can be predicted that oxygen has the strongest effect in pinning the motion of steps compared to silicon and carbon since the oxygen doped GaAs is rougher compared to GaAs doped with silicon and carbon at the identical conditions. Carbon most likely impedes the motion of steps but does not pin the steps as strong as oxygen does. It is important to note that oxygen and carbon are always present in growth environment. These results indicate that impurities may be responsible for step bunching in MOVPE grown GaAs even without intentional impurity incorporation.

## CONCLUSIONS

The effect of impurity incorporation on the evolution of the surface morphology of MOVPE grown GaAs was investigated in this study using AFM. It has been observed that the impact of impurities on the growth front strongly influences the mechanisms of growth on vicinal GaAs (001). The increased roughness at the growth front with oxygen incorporation is indicative of step pinning at the surface with the eventual break-up of the surface structure. Silicon incorporation in GaAs can be accomplished from various sources such as silane and disilane without affecting the morphology of the growth front. These measurements indicate that the oxygen and carbon contamination or impurity incorporation during the growth of semiconductor layers can lead to changes in the interfacial structure affecting the subsequent material properties and device design.

**Acknowledgments:-** The authors would like to acknowledge the discussions with Z. Y. Zhang, D.E. Savage and C. Teichert. This investigation was supported in by the NSF through the Materials Research Group on Chemical Vapor Deposition (DMR-9121074), the Army Research Office DAAI03-92-G-0027 and the Naval Research Laboratory NC0014-92-K-2004.

## References

1. "New Concepts in Low Dimensional Systems", edited by G. Bauer, H Heinrich, and F. Kuchar ( Springer, Berlin, 1992)
2. C. Weisbuch, J. Crystal Growth **127**, 742 (1993).
3. M. Kasu and N. Kobayashi, Appl. Phys. Lett. **62**, 1262 (1993).
4. K. Hata, A. Kawazu, T. Okana, T.Ueda, and M. Akiyama, Appl. Phys. Lett. **63**, 1625 (1993).
5. I. Ishizaki, S. Goto, M. Kishiyada, T.Fukui and H. Hasegawa, Jpn. J. Appl. Phys. **33**, 721 (1994)
6. E.J. Heller and M.G. Lagally, Appl. Phys. Lett. **60**, 2675, (1992).
7. S. L. Skala, S.T.Chou,K.y. Cheng, J.R. Tucker, and J.W. Lyding, Appl Phys. Lett. **65**, 722 (1994).
8. C. Orme, M. D. Johnson, J. L. Sudijono, K. T. Lenug, and B. G. Orr, Appl Phys. Lett. **64**, 860 (1994).
9. J. W. Huang, D. F. Gaines, T.F. Kuech, R. M. Potemski and F. Cardone, Presented at EMC conference, Santa Barbara, CA, (1993) to be published
10. J.M. Redwing, T.F. Kuech, H.Sikama and K.F. Jensen, Mat. Res. Soc. Symp. Proc. **334**, 201 (1994).
11. T.F. Kuech, G.J. Scilla and F. Cardone, J. Cryst. Grow. **93**, 550 (1988).
12. J.E. Northrup and S. Froyen, Phys. Rev. B **50**, 2015 (1994).
13. Z. Zhang, J. Detch, and H.Meitu, Phys. Rev. B **48**, 4972 (1993).
14. F.C. Frank, in " Growth and Perfection in Crystals ", edited by R. Doremus, B. Roberts, and D. Turnbull (Wiley, New York, 1958), p-411
15. S.Nayak, J.M. Redwing, J.W. Huang, T.F. Kuech and M.G. Lagally ( in preparation)

## ROUGHENING BY ION BOMBARDMENT: A STOCHASTIC CONTINUUM EQUATION

R. CUERNO<sup>†</sup> AND A.-L. BARABÁSI<sup>† ‡</sup>

<sup>†</sup> Center for Polymer Studies and Dept. of Physics, Boston University, Boston, MA 02215

<sup>‡</sup> IBM T. J. Watson Research Center, P.O. Box 218, Yorktown Heights, NY 10598

### ABSTRACT

In the context of linear cascade theory, we derive a stochastic nonlinear equation to describe the evolution and scaling properties of surfaces eroded by ion bombardment. The coefficients appearing in the equation are calculated explicitly in terms of the physical parameters characterizing the sputtering process. We find that transitions may take place between various scaling behaviors when experimental parameters such as the angle of incidence of the incoming ions or their average penetration depth, are varied.

### INTRODUCTION

The formation and development of non-equilibrium rough interfaces has attracted an enormous attention in recent years, due both to the fundamental questions that arise and to the potential technological relevance of the processes considered, ranging from growth of thin films by molecular beam epitaxy to motion of flux lines in type II superconductors [1]. A common feature of the surfaces and interfaces observed experimentally is that their roughening follows simple scaling laws. The morphology and dynamics of a rough interface can be characterized by the surface width,  $w(t, L)$ , that scales as  $w^2(t, L) = \langle [h(\mathbf{r}, t) - \bar{h}(t)]^2 \rangle = L^{2\alpha} f(t/L^z)$ , where  $\alpha$  is the roughness exponent for the interface  $h(\mathbf{r}, t)$  and the dynamic exponent  $z$  describes the scaling of the relaxation times with the system size  $L$ ;  $\bar{h}(t)$  is the mean height of the interface at time  $t$  and  $\langle \rangle$  denotes both ensemble and space average. The scaling function  $f$  has the properties  $f(u \rightarrow 0) \sim u^{2\alpha/z}$  and  $f(u \rightarrow \infty) \sim \text{const.}$  Theoretically, the exponents  $\alpha$  and  $z$  can be obtained using discrete numerical models or stochastic evolution equations. The latter approach amounts to a coarse grained description of the interface, where the interface profile  $h(\mathbf{r}, t)$  is defined over length scales at which microscopic details such as the discrete lattice structure can be ignored, but which are still detailed enough to incorporate the stochastic nature of the processes that take place on the surface. The exponents  $\alpha$ ,  $z$  characterize then the large length scale behavior of the surface profile  $h$ .

Whereas most studies of the scaling properties of rough surfaces have focused on growth phenomena, only very recently there have been a few experimental studies [2, 3, 4, 5] focusing on the dynamics and scaling behavior of surfaces eroded by ion bombardment [6]. On one side, for graphite bombarded with 5 keV Ar ions, Eklund *et al.* [2] reported  $\alpha \simeq 0.2 - 0.4$ , and  $z \simeq 1.6 - 1.8$ , values consistent with the predictions of the Kardar-Parisi-Zhang (KPZ) equation in 2+1 dimensions [7, 8]. Similarly Krim *et al.* [3] observed a self-affine surface generated by 5 keV Ar bombardment of an Fe sample, with a larger exponent,  $\alpha = 0.52$ . Meanwhile for Si bombarded with 0.5 keV Ar ions at normal incidence, Yang *et al.* [5] obtain a value of  $\alpha \simeq 1.5$ , and find that the scaling of the width  $w(L, t)$  does not follow the above form. On the other hand, it is well known that a periodic ripple structure develops for many sputter etched surfaces (see e.g. [9]). Chason *et al.* [4] have studied such morphologies for both SiO<sub>2</sub> and Ge bombarded with Xe ions at 1 keV, and found that their dynamics differs from that expected for the self-affine surfaces observed in [2] and [3].

In this work we address the large length scale behavior of ion-sputtered surfaces, aiming to understand in an unified framework the dynamics and scaling behaviors observed experimentally. We report on the derivation [10] of a nonlinear stochastic equation that describes

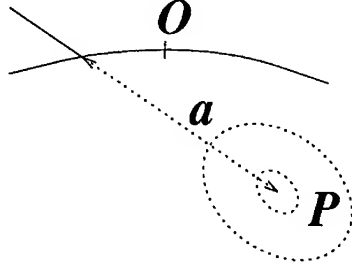


Figure 1: Following a straight trajectory (solid line) the ion penetrates an average distance  $a$  inside the solid (dotted line) after which it completely spreads out its kinetic energy. The dotted curves are equal energy contours. Energy released at point  $P$  contributes to erosion at  $O$ .

the time evolution of the surface height  $h$  as measured from an initially flat surface. We find that transitions may take place between various surface morphologies as the experimental parameters (e.g. angle of incidence, penetration depth) are varied. While at short length scales the equation describes the development of a periodic ripple structure, at larger length scales the surface morphology may be either logarithmically ( $\alpha = 0$ ) or algebraically ( $\alpha > 0$ ) rough. Note the distinction between the surface morphology as probed at different length scales. It seems that in the experiments in which the ripple structure has been observed, the scaling behavior at scales larger than the ripple wavelength has not been considered. An important conclusion of our work is to show that it is in the large length scale regime that the transitions may take place between different scaling behaviors.

## STOCHASTIC EQUATION

To derive an equation for the evolution of the surface profile, we need a model of the physical processes taking place in the system. In the case of ion-sputtering, the linear cascade theory due to Sigmund [11] has proved very successful in describing for the sputtering yield curves in a large variety of systems and experimental situations. In ion sputtering the bombarding ions penetrate the surface and transfer their kinetic energy to the atoms of the substrate by inducing cascades of collisions among them, or through other processes such as electronic excitations. Whereas most of the atoms which are actually sputtered are those located at the surface, the scattering events that might lead to sputtering take place within a certain layer of average depth  $a$ . This average value for the ion deposition depth depends on the energy of the bombarding ions, their angle of incidence, the microscopic structure of the target material and the features of the scattering processes taking place inside the sample. A convenient picture of the process is sketched in Fig. 1. According to it the ions penetrate a distance  $a$  inside the solid before they completely spread out their kinetic energy with some assumed spatial distribution. An ion releasing its energy at point  $P$  in the solid contributes an amount of energy to the surface point  $O$ , that may induce the atoms in  $O$  to break their bonds and leave the surface. Following [11, 12], we consider that the average energy deposited at point  $O$  due to the ion arriving at  $P$  follows the Gaussian distribution

$$E_D(\mathbf{r}) = \frac{\epsilon}{(2\pi)^{3/2}\sigma\mu^2} \exp \left\{ -\frac{z'^2}{2\sigma^2} - \frac{x'^2 + y'^2}{2\mu^2} \right\}. \quad (1)$$

Here  $z'$  is the distance measured along the ion trajectory, and  $x', y'$  are measured in the plane perpendicular to it;  $\epsilon$  denotes the total energy carried by the ion, and  $\sigma, \mu$  are the widths of the distribution in directions parallel and perpendicular to the incoming beam respectively. However, the sample is subject to an uniform flux  $J$  of bombarding ions: a large number of ions penetrate the solid at different points simultaneously. Thus the velocity of erosion at  $O$  depends directly on the total power  $\mathcal{E}_O$  contributed by all the ions deposited within the range of the distribution (1). If we ignore shadowing effects among neighboring points, as well as further redeposition of the eroded material, the velocity of erosion at  $O$  is given by

$$v = p \int_{\mathcal{R}} dr \Phi(r) E_D(r), \quad (2)$$

where the integral is taken over the region  $\mathcal{R}$  of all the points at which the deposited energy contributes to  $\mathcal{E}_O$ ,  $\Phi(r)$  is a local correction to the uniform flux  $J$  and  $p$  is a proportionality constant between power deposition and rate of erosion.

As noticed by Sigmund [11], and further developed by Bradley and Harper [12], this description of the sputtering process implies that the local velocity of erosion  $v$  at point  $O$  depends of the values of the surface curvatures at that point. This dependence leads to an instability, since the probability to erode at  $O$  is proportional to  $\mathcal{E}_O$ , and surface atoms will be eroded more likely if  $O$  is the bottom of a trough than if it is the peak of a crest. Still there is another main geometrical factor influencing the local velocity of erosion, and this is the dependence of the sputtering yield on the angle of incidence of the ion beam to the surface normal. This angle varies from point to point on the surface due to the local inclinations or slopes. Finally, two additional processes must be taken into account to describe the evolution of the surface. One is the stochastic nature of the sputtering process: the bombarding ions reach the surface at random positions and times. The second is the diffusion of the atoms on the surface at finite temperature [2, 4, 5].

After the above considerations we can proceed to the equation for the surface profile. The details of the calculation are given in [10], here we discuss the main results and their physical consequences. In the absence of overhangs the surface can be described by a single valued height function  $h(x, y, t)$ , measured from an initial flat configuration which is taken to lie in the  $(x, y)$  plane. The ion beam is parallel to the  $x$ - $h$  plane forming an angle  $0 < \theta < \pi/2$  with the  $h$  axis. The time evolution of  $h$  has the form

$$\begin{aligned} \frac{\partial h}{\partial t} = -v = & -v_0 + \gamma \frac{\partial h}{\partial x} + \xi_x \left( \frac{\partial h}{\partial x} \right) \left( \frac{\partial^2 h}{\partial x^2} \right) + \xi_y \left( \frac{\partial h}{\partial x} \right) \left( \frac{\partial^2 h}{\partial y^2} \right) + \\ & + \nu_x \frac{\partial^2 h}{\partial x^2} + \nu_y \frac{\partial^2 h}{\partial y^2} + \frac{\lambda_x}{2} \left( \frac{\partial h}{\partial x} \right)^2 + \frac{\lambda_y}{2} \left( \frac{\partial h}{\partial y} \right)^2 - K \nabla^2 (\nabla^2 h) + \eta(x, y, t), \end{aligned} \quad (3)$$

where the surface diffusion is represented by the  $\nabla^2(\nabla^2 h)$  term [13] with  $K$  a temperature dependent positive coefficient,  $\eta$  is Gaussian white noise with variance proportional to the flux  $J$ , and the remaining terms in (3) originate from an expansion of  $v$  in powers of curvatures and slopes, for which a number of assumptions have been made: (i) the radii of curvature at  $(x, y, h)$  are assumed much larger than the typical length scale defined in our problem, namely the average deposition depth  $a$ ; (ii) a quadratic approximation has been taken for the surface height in a neighborhood of the point  $(x, y, h)$ , and (iii) the surface is assumed to vary smoothly enough so that products of derivatives of  $h$  can be neglected for third or higher orders. In particular we would like to stress the appearance of the terms with coefficients  $\lambda_x$  and  $\lambda_y$ . These nonlinearities, usually referred to as KPZ terms, appear in the description of a great variety of growth processes. In most cases these terms appear on the basis of symmetry arguments, and describe the growth (or erosion) of a surface along the local normal direction. Here we have derived them from the physical model discussed



above, and they might be regarded as reminiscent of first-order erosion theory, in which the surface is assumed to evolve at every point along the local direction of the normal, with the refinement of a position dependent incidence angle [14].

The coefficients appearing in (3) can be computed in terms of the physical parameters characterizing the sputtering process. To simplify the discussion we restrict ourselves to the symmetric case  $\sigma = \mu$ . If we write  $F \equiv (\epsilon J p / \sqrt{2\pi}) \exp(-a_\sigma^2/2)$ ,  $s \equiv \sin \theta$ ,  $c \equiv \cos \theta$  and  $a_\sigma \equiv a/\sigma$ , we find

$$\begin{aligned} v_0 &= \frac{F}{\sigma} c, \quad \gamma = \frac{F}{\sigma} s (a_\sigma^2 c^2 - 1), \quad \xi_x = \frac{F}{2} s c \{6 + a_\sigma^2 c^2 - a_\sigma^4 s^2 c^2\}, \quad \xi_y = \frac{F}{2} s c \{2 - a_\sigma^2 c^2\}, \\ \nu_x &= \frac{F}{2} a_\sigma \{2s^2 - c^2 - a_\sigma^2 s^2 c^2\}, \quad \nu_y = -\frac{F}{2} a_\sigma c^2, \\ \lambda_x &= \frac{F}{\sigma} c \{1 + a_\sigma^2 (3s^2 - c^2) - a_\sigma^4 s^2 c^2\}, \quad \lambda_y = -\gamma \frac{c}{s}. \end{aligned} \quad (4)$$

The terms appearing in (3) reflect the asymmetry introduced between the  $x$  and  $y$  directions by the off-normal ion beam, in that (3) is invariant under the coordinate transformation  $y \rightarrow -y$  but not under  $x \rightarrow -x$ . However, for  $\theta \rightarrow 0$ ,  $\gamma = \xi_x = \xi_y = 0$ ,  $\lambda_x = \lambda_y$  and  $\nu_x = \nu_y$ , and the  $x-y$  symmetry is recovered [15]. The equation studied in Ref. [12] corresponds to the deterministic linear version of (3), i. e.  $\xi_x = \xi_y = \lambda_x = \lambda_y = \eta = 0$ .

## DISCUSSION AND SUMMARY

In the following we summarize the main conclusions concerning the scaling behavior expected from Eqn. (3), and end with some comments on both some possible verifications and limitations of its applicability. The nonlinear terms of coefficients  $\xi_x$  and  $\xi_y$  are not expected to play a significant role regarding the large distance behavior of (3), and for this reason we neglect them.

The scaling behavior depends on the relative signs of  $\nu_x$ ,  $\nu_y$ ,  $\lambda_x$  and  $\lambda_y$  [16]. The variations of these coefficients as functions of  $a_\sigma$  and  $\theta$  lead to the phase diagram shown in Fig. 2. In the following we discuss the various scaling regimes separately.

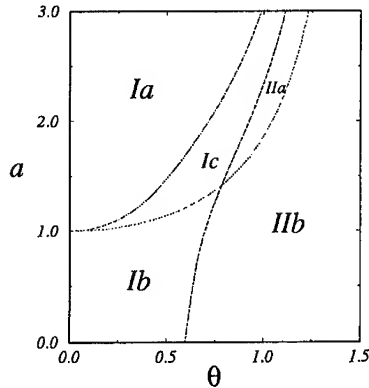


Figure 2: Phase diagram for the isotropic case  $\sigma = \mu = 1$ . Region Ia:  $\nu_x < 0$ ,  $\lambda_x < 0$ ,  $\lambda_y > 0$ ; Region Ib:  $\nu_x < 0$ ,  $\lambda_x > 0$ ,  $\lambda_y < 0$ ; Region Ic:  $\nu_x < 0$ ,  $\lambda_x > 0$ ,  $\lambda_y > 0$ ; Region IIa:  $\nu_x > 0$ ,  $\lambda_x > 0$ ,  $\lambda_y > 0$ ; Region IIb:  $\nu_x > 0$ ,  $\lambda_x > 0$ ,  $\lambda_y < 0$ .

*Region I* — For small  $\theta$  both  $\nu_x$  and  $\nu_y$  are negative. As discussed by Bradley and Harper [12] and experimentally studied by Chason *et al.* [4], a periodic structure dominates the surface morphology, with ripples oriented along the direction ( $x$  or  $y$ ) which presents the largest absolute value for its surface tension coefficient. The wavelength of the ripples is  $\lambda_c = \sqrt{2}\ell_c$ , where  $\ell_c = \sqrt{K/|\nu|}$  is a length-scale that appears due to the competition between surface tension and surface diffusion. The fact that  $\nu_x, \nu_y$  are negative reflects the geometrical instability described above, and introduces severe technical difficulties into the analysis of Eqn. (3), whether by means of dynamical renormalization group techniques (DRG) or numerical integration of the equation. A similar instability is known to occur in the Kuramoto-Sivashinsky equation describing chemical turbulence or flame front propagation [17].

The large length scale behavior  $\ell \gg \ell_c$  is expected to be different. Now both the nonlinearities  $\lambda_x, \lambda_y$  and the noise may become relevant. A DRG analysis performed for the isotropic limit of Eqn. (3) [18, 19] suggests that inside region *I*,  $\lambda_x$  and  $\lambda_y$  flow to zero. The surface is logarithmically rough, with a roughness exponent  $\alpha = 0$ . While in regions *Ia-c* the coefficients of the nonlinear terms may change sign as  $a_\sigma$  or  $\theta$  vary, we do not expect this to modify the scaling behavior.

*Region II* — For larger values of  $\theta$ ,  $\nu_x > 0$ , whereas still  $\nu_y < 0$ . Now the periodic structure associated with the instability is directed along the  $y$  direction and is the dominant morphology at scales  $\ell \sim \ell_c$ . Much less is known about the scaling behavior for large length scales. Preliminary results of a DRG calculation indicate that the surface may be stabilized by the positive  $\nu_x$  and the nonlinearities. If this is the case, surface diffusion contributes negligibly as a relaxation mechanism at these length scales, and Eqn. (3) reduces to the AKPZ equation [20, 21]. Now the scaling behavior depends on the relative signs of the nonlinearities [20]: If  $\lambda_x \lambda_y > 0$  (*IIa*),  $\alpha = 0.38$  and  $z = 1.6$ , the surface width  $w(L, t)$  increases algebraically, being characterized by the exponents of the KPZ equation in 2+1 dimensions [8]. For  $\lambda_x \lambda_y < 0$  (*IIb*), the nonlinear terms become irrelevant, and the width grows only logarithmically, i.e.  $\alpha = 0$ .

Even though several aspects of the scaling behavior predicted by (3) and (4) have still to be clarified, we believe that these equations contain the relevant ingredients for understanding roughening by ion bombardment. It is important to remark that our analysis describes the roughening process inside a small slope approximation. At later stages the slopes increase: on one side this affects the approximations made in the derivation of (3), but possibly more important is the fact that at some points on the surface the angle between the local normal and the ion beam approaches grazing incidence, where linear cascade theory [6, 11] is known to describe less accurately the sputtering processes. Finally, at these later stages additional non-linear effects such as shadowing may become relevant [22].

Summarizing the description provided by Eqns. (3) and (4), at short length scales the morphology consists of a periodic structure oriented along the direction determined by the largest in absolute value of the negative surface tension coefficients [4]. Modifying the values of  $a_\sigma$  or  $\theta$  changes the orientation of the ripples [9, 12]. At large length scales we expect two different scaling regimes. One is characterized by KPZ exponents, which might be observed in region *IIa* in Fig. 2. Indeed, the values of the exponents reported by Eklund *et al.* [2] are consistent within the experimental errors with the KPZ exponents in 2+1 dimensions. The other regime is characterized by logarithmic scaling ( $\alpha = 0$ ), which has not been observed experimentally so far. We believe that it can be experimentally tested for suitable (e.g., small) values of the angle of incidence. Moreover by tuning the values of  $\theta$  and/or  $a_\sigma$  one may induce transitions among the different scaling behaviors. For example, fixing  $a_\sigma$  and increasing the value of  $\theta$  would lead from logarithmic (regions *Ia* and *Ic*) to KPZ scaling (*IIa*), and again logarithmic scaling (*IIb*) for large enough angles. Also, the measurement of the erosion velocity may help to test the applicability of Eqn. (3). Taking

spatial and noise averages in (3), the terms contributing to the erosion velocity are the ones proportional to  $v_0$ ,  $\xi_x$ ,  $\xi_y$ ,  $\lambda_x$  and  $\lambda_y$ . In the stationary state, modifying  $\theta$  or  $a_\sigma$  changes the average yield, allowing for a comparison of the experimental yield curves with the ones predicted by (3).

We would like to acknowledge discussions, comments and encouragement by L. A. N. Amaral, K. B. Lauritsen, H. Makse and H. E. Stanley. R. C. acknowledges a postdoctoral Fellowship of the Spanish Ministerio de Educación y Ciencia.

### References

- [1] *Dynamics of Fractal Surfaces*, edited by F. Family and T. Vicsek (World Scientific, Singapore, 1991); P. Meakin, Phys. Rep. **235**, 189 (1993); T. Halpin-Healey and Y.-C. Zhang, Phys. Rep. (in press); A.-L. Barabási and H. E. Stanley, *Fractal Concepts in Surface Growth*, (Cambridge University Press, Cambridge, 1995).
- [2] E. A. Eklund, R. Bruinsma, J. Rudnick and R. S. Williams, Phys. Rev. Lett. **67**, 1759 (1991); E. A. Eklund, E. J. Snyder and R. S. Williams, Surf. Sci. **285**, 157 (1993).
- [3] J. Krim, I. Heyvaert, C. Van Haesendonck and Y. Bruynseraede, Phys. Rev. Lett. **70**, 57 (1993).
- [4] E. Chason, T. M. Mayer, B. K. Kellerman, D. T. McIlroy and A. J. Howard, Phys. Rev. Lett. **72**, 3040 (1994); T. M. Mayer, E. Chason and A. J. Howard, J. Appl. Phys. **76**, 1633 (1994).
- [5] H.-N. Yang, G.-C. Wang, and T.-M. Lu, Phys. Rev. B **50**, 7635 (1994).
- [6] *Sputtering by Particle Bombardment*, edited by R. Behrisch (Springer-Verlag, Heidelberg 1981, 1983), Vols. I, II.
- [7] M. Kardar, G. Parisi and Y.-C. Zhang, Phys. Rev. Lett. **56**, 889 (1986).
- [8] K. Moser, D. E. Wolf and J. Kertész, Physica A **178**, 215 (1991); T. Ala Nissila, T. Hjelt, J. M. Kosterlitz and O. Vemöläinen, J. Stat. Phys. **72**, 207 (1993).
- [9] G. Carter, B. Navinšek and J. L. Whitton in Vol. II of Ref. [6], pp. 231-269.
- [10] R. Cuerno and A.-L. Barabási, preprint; A.-L. Barabási and R. Cuerno, unpublished.
- [11] P. Sigmund, Phys. Rev. **184**, 383 (1969); J. Mat. Sci. **8**, 1545 (1973).
- [12] R. M. Bradley and J. M. E. Harper, J. Vac. Sci. Technol. **A6**, 2390 (1988).
- [13] C. Herring, J. Appl. Phys. **21**, 301 (1950); W. W. Mullins, J. Appl. Phys. **28**, 333 (1957); in the context of stochastic models see D. E. Wolf and J. Villain, Europhys. Lett. **13**, 389 (1990); S. Das Sarma and P. I. Tamborenea, Phys. Rev. Lett. **66**, 325 (1991).
- [14] G. Carter, in *Erosion and Growth of Solids Stimulated by Atom and Ion Beams*, edited by G. Kiriakidis, G. Carter and J. L. Whitton, (Nijhoff, Hingham, 1986) pp. 70-97; M. J. Nobes, *ibid.*, pp. 103-120.
- [15] The  $\theta = 0$  case has to be treated separately and is discussed in Ref. [10].
- [16] The terms  $-v_0$  and  $\partial_x h$  can be reabsorbed by a change of variables to a comoving frame, and do not affect the scaling properties.
- [17] Y. Kuramoto and T. Tsuzuki, Prog. Theor. Phys. **55**, 356 (1977); G. I. Sivashinsky, Acta Astronaut. **6**, 569 (1979).
- [18] R. Cuerno, K. B. Lauritsen and A.-L. Barabási (unpublished).
- [19] L. Golubović and R. Bruinsma, Phys. Rev. Lett. **66**, 321 (1991); *ibid.* **67**, 2747 (E) (1991).
- [20] D. E. Wolf, Phys. Rev. Lett. **67**, 1783 (1991).
- [21] The relevance of the AKPZ equation to sputter erosion has been suggested by R. Bruinsma in *Surface Disordering: Growth, Roughening and Phase Transitions*, edited by R. Jullien, J. Kertész, P. Meakin and D. E. Wolf (Nova Science, New York, 1992), pp. 91-94.
- [22] G. S. Bales, R. Bruinsma, E. A. Eklund, R. P. U. Karunasiri, J. Rudnick and A. Zangwill, Science **249**, 264 (1990).

## TEMPERATURE DEPENDENCE OF SURFACE MORPHOLOGY OF SILICON GROWN ON $\text{CaF}_2/\text{Si}$ BY ELECTRON BEAM ASSISTED MBE

P.O. PETTERSSON, R.J. MILES, AND T.C. MCGILL

Department of Applied Physics, California Institute of Technology, Pasadena, CA 91125

### ABSTRACT

We present the results of electron beam assisted molecular beam epitaxy (EB-MBE) on the growth mode of silicon on  $\text{CaF}_2/\text{Si}(111)$ . By irradiating the  $\text{CaF}_2$  surface with low energy electrons, the fluorine is desorbed, leaving an ordered array of F-centers behind. Using atomic force microscopy (AFM), we do not detect any surface damage on the  $\text{CaF}_2$  layer due to the low energy electron irradiation. The surface free energy of the  $\text{CaF}_2$  is raised due to the F-center array and the subsequent silicon layer is smoother. Using AFM and X-ray photoelectron spectroscopy (XPS), we find an optimal range of exposures for high temperature ( $650^\circ\text{C}$ ) growth of the silicon overlayer that minimizes surface roughness of the silicon overlayer and we present a simple model based on geometrical thermodynamics to explain this.

We observed a similar optimal range of exposures that minimizes the surface roughness for medium ( $575^\circ\text{C}$ ) and low ( $500^\circ\text{C}$ ) growth temperatures of the silicon layer. We present an explanation for this growth mode based on kinetics.

### INTRODUCTION

Integration of quantum devices such as resonant tunneling diodes with standard VLSI silicon circuitry is a way of implementing ultra dense digital memory, neural networks, and high speed analog to digital converters. To date this effort is hampered by the lack of a suitable heterojunction necessary to fabricate the quantum devices. The  $\text{Si}/\text{CaF}_2$  material system is a promising candidate for this integration since the lattice mismatch is small (0.6 % at room temperature) and the crystalline structures are similar. Consequently, the system has been studied extensively and it was found that while  $\text{CaF}_2$  grows in a two dimensional epitaxial fashion on silicon (111), silicon islands on  $\text{CaF}_2$  (see figure 1) when grown by standard molecular beam epitaxy (MBE) techniques [1]. In this paper, we report on our efforts to reduce the tendency of the silicon to island by using a technique known as electron beam assisted molecular beam epitaxy (EB MBE). This technique has been used to improve growth of both Ge [3] and GaAs [4] on  $\text{CaF}_2$ . We have reported growth of silicon on  $\text{CaF}_2$  by EB MBE at high substrate temperatures during silicon growth elsewhere [2]; here we discuss low and medium substrate temperature growth of silicon on  $\text{CaF}_2$  by EB MBE and incorporate the high temperature results for the purpose of comparison.

The EB MBE technique, where one irradiates the  $\text{CaF}_2$  surface with low energy electrons prior to depositing the silicon overlayer, relies on the fact that the electrons desorb fluorine as  $\text{F}^+$  from  $\text{CaF}_2$ . This creates a calcium rich surface with an ordered array of surface F-centers[5]. This surface should have a higher surface free energy than the normal  $\text{CaF}_2$  surface and should thus favour 2D growth or at least lower the contact angle in 3D growth of silicon on  $\text{CaF}_2$  since the reason for silicon islanding on  $\text{CaF}_2$  is the large surface free energy mismatch.

The paper is organized as follows. In the experimental section we describe the sample structure and present the LEED, AFM, and XPS data. In the discussion section we explain the high temperature results using a simple geometrical thermodynamics model. The low temperature results are explained by kinetics. In the final section, we summarize the results and suggest future directions for research in this area.

## EXPERIMENT

The sample used in the experiment has three layers: 50 nm silicon on 10 nm  $\text{CaF}_2$  on a 100 nm thick silicon buffer grown on a silicon (111) wafer. The reason for choosing a thick  $\text{CaF}_2$  layer is to prevent electron beam penetration through it. Early TEM studies showed that 10 nm is sufficient for this purpose. Since the AFM measurements were performed in air, we chose a relatively thick (50 nm) silicon overlayer to ensure that the surface features due to oxidation are about a factor of 10-50 times smaller than the features due to the electron beam exposure.

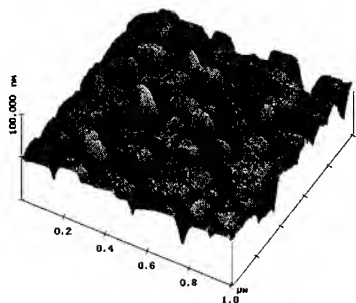


Figure 1: AFM micrograph of silicon grown on  $\text{CaF}_2(111)$  by MBE at 650 °C.

To expose the surface, we defocused the LEED beam to a spot diameter of about 4 mm and set the dose rate to 0.85  $\mu\text{A}/\text{cm}^2$  for the samples with doses ranging from zero to 1.0 mC/ $\text{cm}^2$  and 12  $\mu\text{A}/\text{cm}^2$  for the samples with doses ranging from 0.5 to 50 mC/ $\text{cm}^2$ . The LEED pattern remained the same (except the spots were larger due to the defocussing) for the doses up to 1.0 mC/ $\text{cm}^2$ . The unchanging LEED pattern shows that the surface remains ordered, indicating that the F-centers created by fluorine desorption form an ordered array [5]. For higher doses the LEED pattern lost contrast, which we interpret as a disordering of the  $\text{CaF}_2$  surface by the electron irradiation. The low temperature silicon overlayers exhibited a weak 1x1 pattern. The silicon overlayers grown at medium and high temperature all exhibited a strong 1x1 pattern although the spot size was fairly large compared to the buffer layer.

Figure 1 shows the morphology of the silicon overlayer grown at high temperature with zero electron dose. The islands are about 100-300 nm in diameter and many are hexagonal. The sides of the islands are aligned along what we believe to be the {011} directions of the substrate. The surface morphology of the zero electron dose medium temperature sample is similar to that of the zero dose high temperature sample, except that the typical island size is smaller (100 - 200 nm diameter).

Figure 2 shows the morphology of the silicon overlayer grown at low temperature with zero electron dose. Unlike the high and medium temperature samples, this sample has show

We prepared samples at three different substrate temperatures during silicon deposition. The high temperature sample was grown at 650 °C, the medium temperature sample at 575 °C, and the low temperature sample was grown at 500 °C. During  $\text{CaF}_2$  deposition the substrate temperature was kept at 700 °C for all samples. The deposition rates were 0.05 nm/s for the silicon growth and 0.04 nm/s - 0.10 nm/s for the  $\text{CaF}_2$  growth.

The silicon buffer layer exhibited the customary sharp 7x7 LEED pattern. This pattern changed to the expected 1x1 pattern after the  $\text{CaF}_2$  had been deposited. To expose the surface, we defocused the LEED beam to a spot diameter of about 4 mm and set the dose rate to 0.85  $\mu\text{A}/\text{cm}^2$  for the samples with doses ranging from zero to 1.0 mC/ $\text{cm}^2$  and 12  $\mu\text{A}/\text{cm}^2$  for the samples with doses ranging from 0.5 to 50 mC/ $\text{cm}^2$ . The LEED pattern remained the same (except the spots were larger due to the defocussing) for the doses up to 1.0 mC/ $\text{cm}^2$ . The unchanging LEED pattern shows that the surface remains ordered, indicating that the F-centers created by fluorine desorption form an ordered array [5]. For higher doses the LEED pattern lost contrast, which we interpret as a disordering of the  $\text{CaF}_2$  surface by the electron irradiation. The low temperature silicon overlayers exhibited a weak 1x1 pattern. The silicon overlayers grown at medium and high temperature all exhibited a strong 1x1 pattern although the spot size was fairly large compared to the buffer layer.

Figure 1 shows the morphology of the silicon overlayer grown at high temperature with zero electron dose. The islands are about 100-300 nm in diameter and many are hexagonal. The sides of the islands are aligned along what we believe to be the {011} directions of the substrate. The surface morphology of the zero electron dose medium temperature sample is similar to that of the zero dose high temperature sample, except that the typical island size is smaller (100 - 200 nm diameter).

Figure 2 shows the morphology of the silicon overlayer grown at low temperature with zero electron dose. Unlike the high and medium temperature samples, this sample has show

no well defined islands and the silicon overlayer appears to cover the  $\text{CaF}_2$  completely.

The surface morphology of the high temperature sample irradiated with a dose of  $1.0 \text{ mC/cm}^2$  is shown in figure 3. The islands have the same general shape as in the high temperature zero dose case, but they have coalesced to a large degree and the surface is much smoother than that of the zero dose case. The island shape changes in the medium temperature case with a an electron dose of  $1.0 \text{ mC/cm}^2$ . As you can see in figure 4, the islands have lost their hexagonal shape. The triangular shapes are due to the morphology of the underlying  $\text{CaF}_2$ . The smoothest overlayer was obtained with an electron dose of  $0.5 \text{ mC/cm}^2$  in the low temperature case, but the difference in roughness and morphology between this case and the zero dose case is small.

The high temperature and high electron dose cases can be characterized as follows. At a dose of  $10 \text{ mC/cm}^2$ , the islands are shapeless, tall and spaced far apart. The islands do not seem to have any specific crystal faces, instead their shape appears to be flattened spheres. In general, they stand about  $50 \text{ nm}$  tall with base diameter of about  $200 \text{ nm}$  and the spacing between them is about  $2.5 \mu\text{m}$ . All of these values are rough means with large (50% of mean) standard deviations. The surface between the islands does not show any specific crystalline faces either. The reason for this change in surface morphology is probably due to the  $\text{CaF}_2$  surface being randomized by the electron beam as indicated by the LEED. At a dose of  $50 \text{ mC/cm}^2$ , there are  $40 \text{ nm}$  deep triangular pinholes spaced about  $1 \mu\text{m}$  apart instead of islands. The surface between the holes also shows triangular features. Again, we think that the damage done to the  $\text{CaF}_2$  during the electron beam exposure is the reason for this change in surface morphology.

Since the histograms of the AFM micrographs acquired in the constant force mode are unimodal and gaussian-like, the root mean square (RMS) of the data is a good measure of the surface roughness. The measured roughness depends not only on the surface morphology, but also on the magnitude of the contact force, the scanning rate, and the condition of the tip. Thus, in order to ensure that the measurements were quantitatively comparable, we used a small repulsive force in the range ( $8 - 25 \text{ nN}$ ) and a slow scan rate ( $15 \text{ min/image}$ ). In order to check for tip modification, we scanned a calibration sample between the roughness measurements. Figure 5 shows that the roughness is significantly lower for the irradiated samples in the high temperature case (the lines drawn in the picture are there only to guide the eye). The roughness exhibits a broad minimum followed by an increase in roughness at  $10 \text{ mC/cm}^2$ . In the medium temperature case, the roughness also decreases with increased

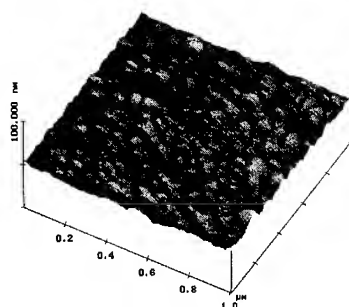


Figure 2: AFM micrograph of silicon grown on  $\text{CaF}_2(111)$  by MBE at  $500^\circ \text{C}$ .

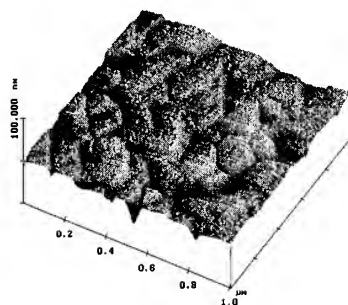


Figure 3: AFM micrograph of silicon grown on  $\text{CaF}_2(111)$  by EB MBE at  $650^\circ \text{C}$ . Dose  $1.0 \text{ mC/cm}^2$ .

electron dose. In the low temperature case, the roughness has a broad but shallow minimum around  $1.0 \text{ mC/cm}^2$ .

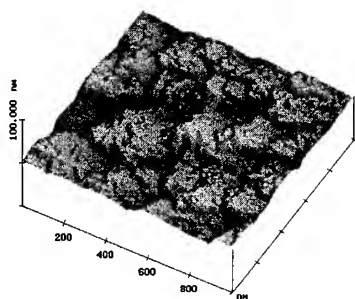


Figure 4: AFM micrograph of silicon grown on  $\text{CaF}_2(111)$  by EB MBE at  $575^\circ \text{C}$ . Dose  $1.0 \text{ mC/cm}^2$ .

calcium and fluorine peaks after sputtering. The calcium to silicon ratio is about the same for all samples before sputtering which is explained by the fact that calcium is known to surf on top of silicon [6]. The AFM micrographs show that there are valleys that probably reach down to the  $\text{CaF}_2$  layer in the zero dose case, but not in the  $1.0 \text{ mC/cm}^2$  case. Since this agrees well with the model explaining the XPS data, we conclude that the silicon almost covers the  $\text{CaF}_2$  completely in the high temperature  $1.0 \text{ mC/cm}^2$  dose case whereas the coverage is incomplete in the zero dose case.

## DISCUSSION

In the high temperature cases and in the zero dose medium temperature case, we can explain the observed crystal shape and roughness with a simple model based on geometrical thermodynamics. In this model, the electron dose creates an ordered array of F-centers that increases the surface free energy, favoring lower contact angles and a smoother surface morphology. If one assumes that the growth process is close to thermodynamic equilibrium and that the shear stress is small near the interface, the surface morphology can be determined by two conditions. The first one is that the Helmholtz surface free energy is minimized and the second one is the contact angle between the surface and the epilayer is determined by the force balance of the respective surface tensions [7]. The minimization condition determines the shape of the silicon islands and the contact angle force balance allows us to estimate the surface tensions of the interface and the irradiated  $\text{CaF}_2$  surface.

The measured surface free energies are approximately  $1240 \text{ ergs/cm}^2$  and  $450 \text{ ergs/cm}^2$  for  $\text{Si}(111)$  and  $\text{CaF}_2(111)$  respectively [8]. Thus, in the case of  $\text{CaF}_2$  growth on silicon, the surface free energy is minimized by the  $\text{CaF}_2$  covering the silicon in a 2D fashion. On the other hand, in the case of silicon growth on  $\text{CaF}_2$ , the free energy is minimized by 3D growth of the silicon on the  $\text{CaF}_2$ .

The shape of the resulting microcrystal is determined by the directional dependence of the surface free energy. By this argument, the silicon crystal should be bound by the  $\{111\}$  and  $\{100\}$  faces. However, the common crystal habit of silicon also shows  $\{113\}$  faces (see figure 6a). The presence of this face can be explained by a surface reconstruction lowering

the energy of the  $\{113\}$  surfaces [9]. Thus, we expect the shape of a silicon microcrystal on a  $(111)$  substrate to be hexagonal (see figure 6b). As one can see in figure 1, silicon does indeed form hexagonally shaped microcrystals when grown on  $\text{CaF}_2$  at high temperature. Similarly shaped microcrystals are seen in the high temperature irradiated samples as well as in the zero dose medium temperature case.

The contact angle (defined in figure 6c) between the microcrystal and the substrate is determined by the force balance at the bottom of the edge of the crystal [2]. Using measured values for the contact angle in the high temperature case one obtains an interface free energy of  $-1100 \pm 60$  ergs/cm<sup>2</sup>. Since the interface bonding has been determined to be dominated by the Si-Ca bonds [1], this implies that the Si-Ca bond energy at the interface is  $2.5 \pm 0.3$  eV which is reasonable. If we interpret the lower contact angle in the  $1.0 \text{ mC/cm}^2$  case as an increase in the surface free energy of the  $\text{CaF}_2$  surface due to induced F-centers and assume that the the Si/ $\text{CaF}_2$  interface free energy remains the same as in the zero dose case, then the F-center- $\text{CaF}_2$  surface free energy is  $520 \pm 95$  ergs/cm<sup>2</sup>. As expected, this energy is larger than the free energy of the normal  $\text{CaF}_2$  surface.

We do not see the predicted hexagonally shaped islands neither on the irradiated medium temperature samples nor on any of the low temperature samples. For the low temperature samples, the assumption that the growth process is close to thermodynamic equilibrium breaks down; in these cases the mobility is too low. Instead of forming well defined islands, the silicon forms an overlayer of polycrystalline nature as shown in figure 2. A possible explanation for the smoothening of the medium temperature irradiated sample is that small defects caused by the radiation decreases the mobility of the silicon atoms to the point where they cannot form the islanded surface of the zero dose case.

In conclusion, our model correctly predicts the observed hexagonal islands and decrease in surface roughness due to decrease in the contact angle in the high temperature cases and the medium temperature zero dose case. Furthermore, the model gives reasonable values for the Si-Ca bond energy and the free energy of the F-center- $\text{CaF}_2$  surface. At the low and medium growth temperatures the mobility of the silicon atoms is too low to form well defined microcrystals. This would explain why the resulting surfaces appears to be polycrystalline

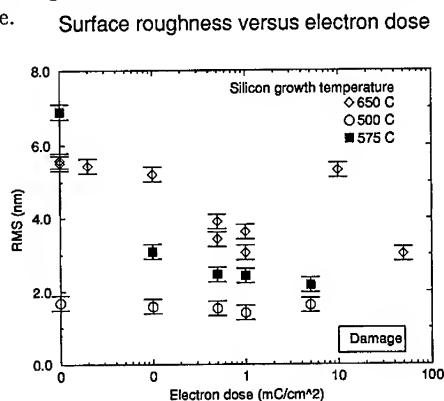


Figure 5: RMS versus electron dose.

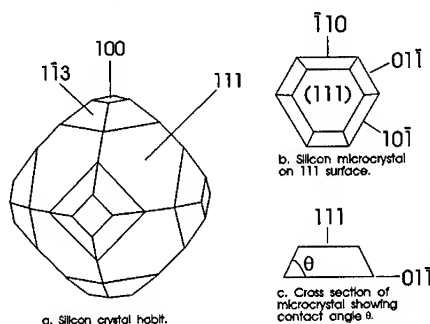


Figure 6: The silicon crystal.



in the AFM micrographs and why the LEED patterns for the low temperature case indicates that the surface might be amorphous.

### Summary

We studied the surface morphology of silicon, grown on epitaxial  $\text{CaF}_2/\text{Si}$  by electron beam assisted MBE at three different growth temperatures, using atomic force microscopy (AFM), X-ray photoelectron spectroscopy (XPS) and low energy electron diffraction (LEED). We found that the roughness of the silicon overlayer was minimized by exposing the  $\text{CaF}_2$  to an electron dose of  $1.0 \text{ mC/cm}^2$  in the high temperature case ( $650^\circ\text{C}$ ) before growing the epitaxial silicon overlayer. Contact angle measurements yielded a Si–Ca interface bond strength of  $2.5 \pm 0.3 \text{ eV}$  and a free energy of  $520 \pm 95 \text{ ergs/cm}^2$  of the irradiated  $\text{CaF}_2$  surface. The medium ( $575^\circ\text{C}$ ) and low ( $500^\circ\text{C}$ ) temperature samples showed smoother surfaces at the cost of crystalline quality. The AFM results were consistent with the LEED and XPS data. We presented a simple model based on geometrical thermodynamics which explained the data well in the high temperature case. An explanation based on kinetics was put forward for the low and medium temperature cases.

Although these results indicate that it is currently impractical to manufacture devices that require thin smooth films of silicon on  $\text{CaF}_2$  through electron irradiation of the  $\text{CaF}_2$  surface and kinetic constraints, there is some hope for this material system. The most fruitful approach would probably be to find a substance that could either lower the Si– $\text{CaF}_2$  interface free energy or passivate the silicon surface during the growth.

We are grateful to Michael W. Wang for the XPS work. This work was supported by ONR N00014-89-J-1141.

### References

- [1] Leo J. Schowalter and Robert W. Fathauer, *CRC Critical Reviews in Solid State and Materials Sciences* **15** (4), 367-421 (1989).
- [2] P.O. Pettersson, R.J. Miles, and T.C. McGill, *J. Appl. Phys.* **76** (11), 7328 (1994).
- [3] Seigo Kanemaru, Hiroshi Ishiware, and Seiji Furukawa, *J. Appl. Phys.* **63** (4), 1060 (1988).
- [4] H.C. Lee, H. Ishiware, S. Furukawa, K. Saiki, and A. Koma, *Applied Surface Science* **41/42**, 553 (1989).
- [5] Kouji Miura, Kazuhiko Sugiura, and Hiroshi Sugiura, *Surface Science Letters* **253**, L407 (1991).
- [6] M. Sasaki, H. Onoda, and N. Hirashita, *Mat. Res. Symp.* **53**, 149 (1986).
- [7] Jeffrey Y. Tsao, *Materials Fundamentals of Molecular Beam Epitaxy*, (Academic Press Inc, New York, 1992), pp. 201.
- [8] J.J. Gillman, *J. Appl. Phys.* **31**, 2208 (1960).
- [9] Gunter A. Wolff, *Intermetallic Compounds* (John Wiley & Sons, Inc., New York, 1967), pp. 85.

## VARIATIONS OF INTERFACIAL ROUGHNESS WITH EPILAYER THICKNESS AND SCALING BEHAVIOR IN $\text{Si}_{1-x}\text{Ge}_x$ GROWN ON $\text{Si}(100)$ SUBSTRATES

Z. H. MING,\* S. HUANG,\* Y. L. SOO,\* Y. H. KAO,\* T. CARNS\*\* AND K. L. WANG\*\*

\* Department of Physics, SUNY at Buffalo, Amherst, NY 14260

\*\* Electrical Engineering Department, UCLA, Los Angeles, CA 90024

### ABSTRACT

Roughness parameters of sample surface and buried interfaces in a series of thin layers of  $\text{Si}_{0.4}\text{Ge}_{0.6}$  grown on  $\text{Si}(100)$  by molecular beam epitaxy (MBE) were measured by using the technique of grazing-incidence x-ray scattering (GIXS). The strain in the layer and the critical thickness of the film were determined from x-ray diffraction of the  $\text{Si}(004)$  peak. The roughness parameters can be described by a scaling-law with an exponent  $\beta = 0.71$  for *both* the surface and interfacial roughness. Establishment of a scaling law thus allows a possibility of predicting the interfacial roughness as a function of the epilayer thickness.

### INTRODUCTION

Interfacial roughness between lattice mismatched materials is one of the important factors which limit the performance of some modern semiconductor electronic and optoelectronic devices. Variations of the interfacial roughness in multilayer semiconductors prepared under different processing conditions are closely related to the strain arising from the lattice mismatch. Measuring the changes of interfacial roughness as a function of film thickness during epitaxial growth can provide deeper insight into a physical understanding of the effects of lattice strain on interfacial morphology. The lattice strain in the layers can be determined by x-ray diffraction and the interfacial roughness can be measured by means of GIXS.

In present experiment, the surface and buried interfacial roughness in a series of thin  $\text{Si}_{0.4}\text{Ge}_{0.6}$  films grown on  $\text{Si}(100)$  by MBE were measured. The strain in the layer and the critical thickness of the films were obtained from x-ray diffraction of the  $\text{Si}(004)$  peak. The roughness parameters are found to follow a scaling-law with an exponent  $\beta = 0.71$  for *both* the surface and interfacial roughness. As the film thickness changes from below the critical thickness to above, the scaling behavior shows significant deviation, indicating a large change in the morphology of surface and interface microstructures. Physical understanding of such a scaling behavior is especially useful for predicting the interfacial roughness as a function of the epilayer thickness between lattice mismatched material systems.

Many different types of solid interfaces can be described by a self-affine surface structure as defined by Mandelbrodt in terms of fractional Brownian motion.<sup>1</sup> More recently, important progress has been made in the dynamic scaling approach; applications of these results to the study of epitaxial growth are quite successful.<sup>2-12</sup> A roughness parameter  $\sigma$  (sometimes also called interface width) can be defined to account for the root mean-square (rms) height fluctuations during the growth and

evolution of an interface. In the absence of any characteristic length scale, the roughness parameter  $\sigma$  is expected to grow with some power of time with a scaling exponent  $\beta^2$  as:

$$\sigma(t) = \sqrt{\langle [h(x, y, t) - \bar{h}]^2 \rangle_{xy}} \sim t^\beta \quad (1)$$

where  $x$  and  $y$  are the coordinates of position in the epilayer plane,  $t$  is the deposition time,  $h(x, y, t)$  is the height of surface at position  $x, y$  and time  $t$ ,  $\bar{h}$  is the mean height of the interface at time  $t$  averaged over the epilayer surface. For the case of a steady-state MBE growth in the present experiment, the deposition time is directly proportional to the epilayer thickness. Theoretical calculation of the exponent  $\beta$  will necessarily depend on the modeling of the dynamics which could capture the basic physics of epitaxial growth.

A theoretical model developed by Kardar-Parisi-Zhang (KPZ) has recently received ample attention in the study of surface relaxation/diffusion and growth dynamics.<sup>3-5</sup> In this model,  $h$  is governed by a nonlinear generalized Langevin-type equation:

$$\frac{\partial h}{\partial t} = v \nabla^2 h + \frac{\lambda}{2} (\nabla h)^2 + \eta \quad (2)$$

where  $v$  is the diffusion coefficient related to surface relaxation,  $\lambda$  is the growth velocity perpendicular to the surface and  $\eta$  represents the random noise in the incoming flux. Theoretical calculations and simulations based on the KPZ model have predicted different values for the scaling behavior of surface roughness. In the previous experimental studies of roughness scaling,<sup>6-10</sup>  $\beta$  has been found to fall in a wide range between 0.2 and 1. G.W.Collins *et al.* observed  $\beta=0.7-1.0$  for the growth of plasma polymer films at different deposition rates.<sup>6</sup> Y.-L.He *et al.* obtained  $\beta=0.22$  for Fe on Fe(001).<sup>7</sup> H.-J.Ernst *et al.* observed  $\beta=0.26$  and  $0.56$  for Cu on Cu(100) at growth temperatures of 160K and 200K, respectively.<sup>8</sup> H.You *et al.* obtained  $\beta=0.40$  and  $0.42$  for Au films grown on Si(111) at temperatures 300K and 220K, respectively.<sup>9</sup> The diversity of these measured values of  $\beta$  indicates that the growth dynamics is quite complicated for different material systems or with different surface diffusion/relaxation mechanisms.<sup>11</sup> To the best of our knowledge, there has been no prior experimental studies of this power-law scaling and exponent in heteroepitaxial growth of semiconductor compounds.

In this paper, we report results of x-ray scattering experiments to investigate the scaling behavior of interfacial roughness in compound semiconductors grown by MBE. The SiGe system was chosen for this purpose because of practical interests in this material for device applications and also in light of the fact that highly smooth interfaces with coherent strain can indeed be grown by MBE, as found in our earlier experiments.<sup>13</sup> In addition, variation of Ge concentration in the alloys can afford a means to fine-tune its lattice mismatch with the Si substrates. For the present x-ray study, Si<sub>0.4</sub>Ge<sub>0.6</sub> epilayers with varying thickness on Si(100) were used so that a coherent strain can exist in the system within a reasonable range of thickness variation below the critical thickness. It should also be noted that grazing incidence x-ray scattering measurements are uniquely suited for determining a global average of the interfacial roughness of *buried interfaces* underneath the sample surface. This method is highly accurate and nondestructive.

## EXPERIMENTAL RESULTS AND DISCUSSION

The x-ray experiments were carried out at the X3B1 beamline, National Synchrotron Light Source (NSLS), Brookhaven National Laboratory. The experimental setup and detailed procedures for the determination of interfacial roughness have been reported elsewhere.<sup>13</sup> Single layer  $\text{Si}_{0.4}\text{Ge}_{0.6}$  samples were grown on  $\text{Si}(100)$  substrates by MBE. The growth temperature of these layers was about  $500^\circ\text{C}$  at a growth pressure of  $\sim 4 \times 10^{-9}$  torr. The nominal thickness of these samples was varied in a range between 20 and 300 Å during growth, which covers both regions of pseudomorphic growth and lattice relaxation.

X-ray diffraction patterns are shown in Fig. 1. The Si (004) substrate peak is shown in the figure at the zero angle difference with a resolution-limited width. In addition, a broad peak arising from the epilayer of  $\text{Si}_{0.4}\text{Ge}_{0.6}$  is present at a lower angle. As expected, the position of the epilayer diffraction peak shows that its lattice spacing in the normal direction is larger than that of the substrate.

For the thinnest (20 Å) sample studied, the diffraction peak due to the film is, however, beyond the detection limit of our instrumentation. The film diffraction peak remains at practically the same position for films with thickness up to 120 Å. The large change of the peak position observed for the 300 Å sample shows that its lattice spacing has become smaller than the other samples, as a result of lattice relaxation. The lattice spacing in the perpendicular direction derived from these diffraction patterns are plotted in Fig. 2 as a function of layer thickness (solid squares). For comparison, the lattice constant of an unstrained (lattice relaxed)  $\text{Si}_{0.4}\text{Ge}_{0.6}$  alloy is shown in the same figure (dotted

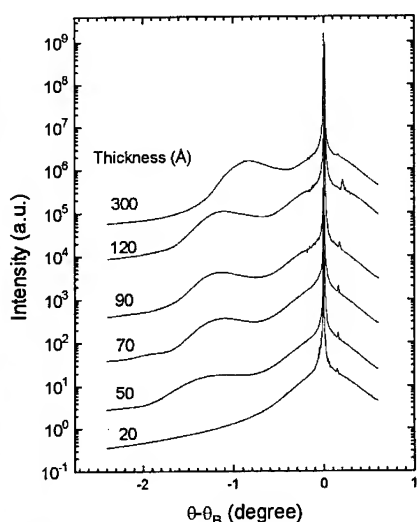


Figure 1 Measured diffraction patterns for  $\text{Si}_{0.4}\text{Ge}_{0.6}$  epilayers grown on  $\text{Si}(100)$ . The nominal thickness for each sample is indicated in the figure. The curves for different samples have been shifted vertically for the sake of clarity.

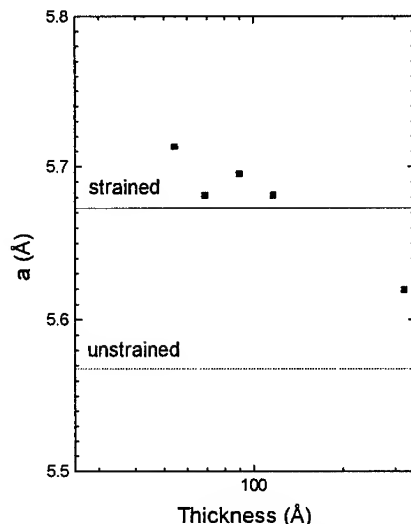


Figure 2 Lattice spacing in perpendicular direction as a function of film thickness (solid squares). The dotted line is the lattice spacing for unstrained  $\text{Si}_{0.4}\text{Ge}_{0.6}$  alloys, and the solid line is a theoretical calculation of the corresponding lattice spacing for strained  $\text{Si}_{0.4}\text{Ge}_{0.6}$  films on  $\text{Si}(100)$ .

line). Because of the anisotropic strains present in the film during pseudomorphic growth, the vertical lattice spacing is anticipated to be larger than that of the unstrained  $\text{Si}_{0.4}\text{Ge}_{0.6}$  alloy.

Commensurate growth of  $\text{Si}_{0.4}\text{Ge}_{0.6}$  strained layer on Si(100) results in a biaxial in-plane compression of the alloy lattice and a corresponding elongation normal to the interface. The strain tensor due to this tetragonal distortion takes a simple form with only two non-zero components as shown in the following:

$$\begin{aligned} e_{//} &= \left( \frac{a_0 - b}{b} \right) \\ e_{\perp} - e_{//} &= \left( \frac{1 + \mu}{1 - \mu} \right) f \end{aligned} \quad (3)$$

where  $e_{//}$  and  $e_{\perp}$  are components of the strain tensor in the directions parallel and normal to the surface,  $a_0$  and  $b$  are the lattice constants of the substrate and epilayer, respectively;  $\mu$  is Poisson's ratio and  $f$  is the lattice mismatch. A simple theoretical calculation of the perpendicular lattice spacing<sup>14</sup> for coherently strained  $\text{Si}_{0.4}\text{Ge}_{0.6}$  thin films on Si(100) based on the anisotropic strain tensor elements in Eq.(3) is also shown in Fig. 2 (solid line), where values of the elastic moduli of  $\text{Si}_{0.4}\text{Ge}_{0.6}$  used in this calculation were obtained from a linear interpolation of the tabulated values for Si and Ge.<sup>15</sup> The calculated lattice spacing in the perpendicular direction is in reasonable agreement with our experimental results for films with thickness up to 120Å. The rapid decrease in perpendicular lattice spacing of the 300Å film apparently indicates that it has already exceeded the actual critical thickness<sup>16</sup> as a result of lattice relaxation. Consequently, the tetragonal lattice distortion will be relaxed to form a cubic structure, and the vertical lattice spacing in the relaxed film becomes smaller than that of the strained films. Figure 2 shows that the critical thickness for  $\text{Si}_{0.4}\text{Ge}_{0.6}$  films on Si(100) lies somewhere between 120Å and 300Å.

The interfacial roughness parameters were determined from GIXS studies. The measured specular reflectivity data, corrected by subtracting out the longitudinal diffuse scattering background,<sup>13</sup> are shown in Fig. 3 (circles). The microstructural parameters of these samples, such as film thickness, surface and interfacial roughness can be obtained by fitting a well-established theoretical model to the experimental data as reported before.<sup>13</sup> The solid lines in this figure are theoretical calculations based on the Fresnel's laws in classical optics in which the effect of interfacial roughness has been incorporated by using a vector scattering model developed by Vidal and Vincent.<sup>17</sup> As can be seen from the close fit in Fig. 3, the theoretical calculations and experimental data are in excellent agreement.

Values of surface roughness (solid squares) and buried interfacial roughness (solid circles) deduced from the reflectivity data are shown in Fig. 4 as a function of epilayer thickness. The uncertainty in these roughness parameters is estimated to be around 1Å. The solid line in Fig. 4 is a fit of the rms surface roughness with the power-law scaling given in Eq. (1) for film thickness up to 120Å.

The value of  $\beta$  is found to be  $0.71 \pm 0.07$  for our samples. On the basis of the dynamical scaling approach,<sup>2-12</sup> this may be taken as an indication of the occurrence of kinetic roughening in the  $\text{Si}_{0.4}\text{Ge}_{0.6}$  films. It should be noted that the surface roughness of a film beyond the critical thickness cannot be described by the same power-law scaling. This result suggests that the morphology of the surface has undergone a significant change when the critical thickness is exceeded.

It is also interesting to note that the interfacial roughness of these films can be described by the same power-law scaling. The dashed line in Fig. 4 is a fit of the interfacial roughness to the same

scaling law as for the sample surface. We also obtained a *same* scaling exponent  $\beta = 0.71 \pm 0.07$ . The same scaling behavior thus indicates that similar microstructures are responsible for the rms roughness of *both* the surface and interface, most probably caused by microstructure propagation from the substrate throughout the epilayer. However, deviation from the power-law scaling behavior occurs for the interfacial roughness in the 120 Å film, before the top surface roughness shows lattice relaxation. This implies that structural changes at the interface has actually started before the film is fully relaxed, possibly resulting from the appearance of misfit dislocations at the interface which could compensate for some of the strain energy. Hence, the requirement for a smooth interface is more stringent than for the film surface. Measurements of the power-law scaling, and/or deviations thereof, could thus serve as a useful precursor for detecting microstructural changes in the interfaces.

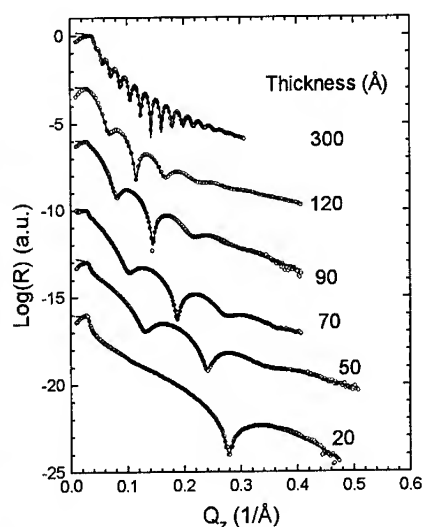


Figure 3 Results of specular reflectivity for  $\text{Si}_{0.4}\text{Ge}_{0.6}$  films on Si(100) (circles). The nominal thickness is indicated for each sample. Solid lines are theoretical calculations. The curves for different samples have been shifted vertically for the sake of clarity.

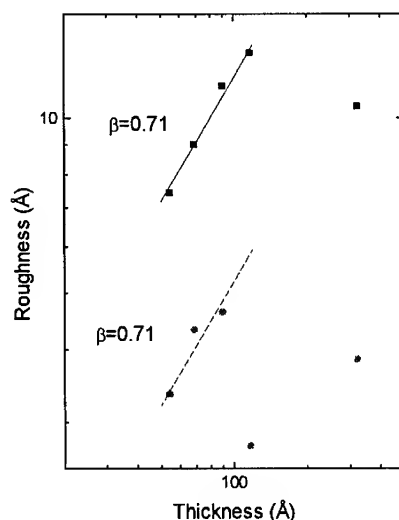


Figure 4 Results of surface roughness (solid squares) and buried interfacial roughness (solid circles) as a function of epilayer thickness. Solid line is a theoretical fit of the surface roughness to power-law scaling Eq.(1) with an exponent  $\beta = 0.71$ . Dashed line is a similar theoretical fit of the interfacial roughness to power-law scaling with the same exponent.

The value of exponent  $\beta=0.71$  measured in our experiments is invariably different from those obtained in most of the previous experiments<sup>7-10</sup> and theoretical predictions, except for the case of plasma polymer films<sup>6</sup> where values of  $0.6 < \beta < 1$  were deduced. Nonetheless, the low values of  $\beta$  below ours were mainly found in homoepitaxial growth where neither lattice mismatch nor strain is present in the films. It is believed that the coherent strain in the heteroepitaxial films studied in the present experiment should play a very important role in controlling the morphology and microstructures of the surface and interface. This view is also supported by the observed deviation of power-law scaling as the layer thickness approaches the critical thickness. Moreover, the presence of

coherent strain could also provide a pinning force during the epitaxial growth and the constituent atoms were not allowed to relax or diffuse freely. The pinning mechanisms were not explored in the theoretical predictions.

## CONCLUSIONS

In conclusion, our x-ray results have provided first evidence for power-law scaling of the rms roughness of *buried* interfaces in semiconductor heterostructures. Both the surface and interface rms roughness as a function of epilayer thickness follow the *same* scaling law with same exponent value when the films are coherently strained. When the critical thickness is exceeded, the scaling behavior of the buried interfacial roughness breaks down before the film is fully relaxed, thereby indicating a significant change in the microstructures and morphology of the buried interface.

## ACKNOWLEDGMENT

The present research at SUNY-Buffalo is supported by DOE under grant DE-FG02-87ER45283. The research at UCLA is supported by AFOSR. Research is carried out in part at the NSLS at BNL which is supported by the U.S. Department of Energy, Division of Materials Sciences and Division of Chemical Sciences. The SUNY X3 beamline at NSLS is supported by the Division of Basic Energy Sciences of the U.S. Department of Energy (DE-F02-86ER45231).

## REFERENCES

1. B.Mandelbrot, The Fractal Geometry of Nature (Freeman, New York, 1982).
2. F.Family, *Physica A* **168**, 561 (1990); and references therein.
3. M.Kardar, G.Parisi, and Y.C.Zhang, *Phys. Rev. Lett.* **56**, 889 (1986).
4. Z.W.Lai and S.Das Sarma, *Phys. Rev. Lett.* **66**, 2348 (1991).
5. J.G.Amar and F.Family, *Phys. Rev.* **A41**, 3399 (1990).
6. G.W.Collins, S.A.Letts, E.M.Fearon, R.L.McEachen, and T.P.Bernat, *Phys. Rev. Lett.* **73**, 708 (1994).
7. Y.-L.He, N.-H.Yang, T.-M.Lu, and G.-C.Wang, *Phys. Rev. Lett.* **69**, 3770 (1992).
8. E.-J.Ernst, F.Fabre, R.Folkerts, and J.Lapujoulade, *Phys. Rev. Lett.* **72**, 112 (1994).
9. D.Kessler, H.Levine, and L.Sander, *Phys. Rev. Lett.* **69**, 100 (1992).
10. H.You, R.P.Chiarelo, H.K.Kim, and K.G.Vandervoort, *Phys. Rev. Lett.* **70**, 2900 (1993).
11. J.Krug, M.Plischke, and M.Siegert, *Phys. Rev. Lett.* **70**, 3271 (1993).
12. H.-N.Yang, T.-M. Lu, and G.-C. Wang, *Phys. Rev. Lett.* **68**, 2612 (1992).
13. Z.H.Ming, A.Krol, Y.L.Soo, Y.H.Kao, J.S.Park and K.L.Wang, *Phys. Rev.* **B47**, 16373 (1993).
14. J.Hornstra and W.J.Bartels, *J. Crystal Growth*, **44**, 513(1978); P.J.Orders and B.F.Usher, *Appl. Phys. Lett.* **50**, 980 (1987).
15. N.W.Ashcroft and N.D.Mermin, Solid State Physics, p.447 (Saunders, Philadelphia, 1976).
16. R.People and J.C.Bean, *Appl. Phys. Lett.* **47**, 322 (1985).
17. B. Vidal and P. Vincent, *Appl. Opt.* **23**, 1794(1984).

## STRUCTURAL CHARACTERISATION OF IRON-COPPER MULTILAYERS USING TRANSMISSION ELECTRON MICROSCOPY

S. J. LLOYD, R. E. SOMEKH, R.E. DUNIN-BORKOWSKI AND W. M. STOBBS  
Department of Materials Science and Metallurgy, University of Cambridge, Pembroke St.,  
Cambridge CB2 3QZ, U.K.

### ABSTRACT

Coherent iron-copper multilayers of a wavelength of 2.5nm that were measured to be non-magnetic were structurally characterised using high resolution and Fresnel techniques. A measurement of the tetragonal distortion from layer to layer and as a whole would allow an assessment of the degree to which the material exhibits any anomaly in its elastic behaviour. The modelling of the distortions requires however the measurement of the abruptness of the interfaces and this requires the quantification of the Fresnel contrast. The degree to which the measurements can be obtained to the required accuracies is considered.

### INTRODUCTION

As part of a long term plan to correlate the elastic and magnetic properties of iron-copper multilayers as a function of their wavelength and Fe/Cu ratio as well as their in-plane strain our aim here has been to assess the accuracy to which a typical multilayer can be compositionally and structurally characterised. The only comparable work reported to date was that of Baxter and Stobbs [1]. These authors managed to use the same TEM techniques as we apply here to show that an admittedly somewhat longer wavelength multilayer of Cu-NiPd exhibited variations in lattice spacing of a form that could only be explained using values for the relevant elastic constants that were unrealistic for bulk material and an effectively tetragonal "strain free" state of the multilayer as a whole. It is thus worth emphasising that any elastic anomaly in the behaviour of a multilayer structure can in principle be assessed through a full characterisation of the non-stress-applied-state. In fact, since it is now commonly argued that the elastic anomalies reported at one time in abundance for such systems [2] are an artefact or at the minimum small [3], the importance of more quantitative work in the field is clear. Systems potentially exhibiting layer thickness and strain dependent magnetic properties are still more interesting and it is this which has dictated our choice of the Fe-Cu system for appraisal. That the strains could affect the magnetic properties would appear to be accepted and while it is well known that small f.c.c. Fe particles under triaxial tension in MgO can be ferromagnetic [4], there are conflicting reports of the magnetic state for variously biaxially strained Fe layer systems [5]. Neither the structure, strain or phase state of the Fe has been specifically determined by T.E.M. and it is this which has perhaps led to current confusion in the modelling of the magnetic behaviour of such systems.

### RESULTS AND DISCUSSION

The layer system examined was prepared by UHV DC magnetron sputtering by techniques described elsewhere [6]. It should be noted that this method allows the formation of coherently layered f.c.c. Fe-Cu multilayers with greater ease than they can be made using MBE techniques. This is in part because of the partial thermalisation of the adatoms in the former process which leads to a lower tendency for 3D island formation than in MBE.

A relatively low magnification image of the multilayer examined here is shown edge-on in a bright field micrograph in fig.1 with the Cu buffer layer to the left. The inset part of a diffraction pattern of the multilayer demonstrates that, given the large number of superlattice



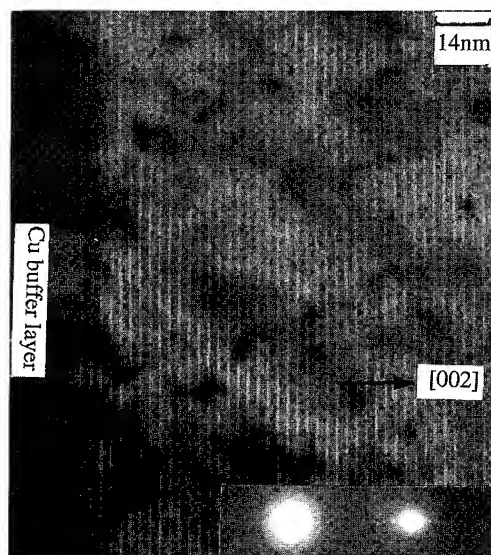


Fig.1 Bright field image of multilayer. Growth direction is [002].

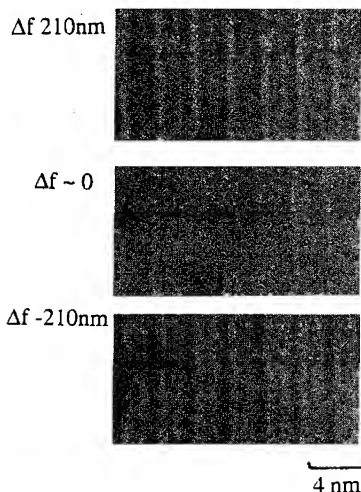


Fig.2 Bright field through focal series showing change in layer contrast.

reflections that can be seen, the quality of the multilayer is good. Interface misfit dislocations were not present and no b.c.c. reflections were in evidence. The Fe must thus be coherently strained and in the f.c.c. state. There are however changes in the contrast of the layering both on a coarse (200nm) and on a fine (~2nm) scale, and this must involve both stepping of the interfaces and a degree of local variability of the orientation and spacing of the layers. The irregularities are however at close to the monatomic layer level. The major contribution to the contrast in this image derives from the fact that it was taken at the fairly large defocus of 2 Scherzer units. The Fresnel contrast exhibited has its origins in differences between the projected forward scattering potential of the Fe and Cu layers, this leading to differences in the phase of the emergent wave which is to first order proportional both to the projected thickness and to the forward scattering potential. Changing the focus value thus allows the phase change to lead to the formation of a Fresnel fringe system, the contrast of which for a thin specimen is proportional to the phase change. The form of the Fresnel contrast can also be analysed for a single isolated layer to determine its projected abruptness, and simplistically the more abrupt the interface the more oscillations in the contrast. In fact, both the form and the magnitude of the potential difference can be determined uniquely in that these two features of the structure affect the contrast in different if not completely independent ways. Examples of the quantitative application of the approach in determining compositional profiles include [7], but the method was in fact first used quantitatively on the Cu-NiPd problem [8]. While some problems can arise in the relationship of the change in projected potential to the local composition and density (and thus in principle strain) because of dipole effects [9], we will concentrate here on the accuracy to which the profile of the potential can be obtained when the layer spacing is as low (2.5nm) as is the case for the layers of interest to us here. Beating of the Fresnel contrast due to the individual layers precludes some of the approaches which can be used in the analysis but facilitates others. It is emphasised that the abruptness of the multilayer interfaces is required to atomic accuracy if elastic calculations of the strains in relation to the lattice plane spacings are to be sufficiently accurate to demonstrate whether or not there is an anomaly in the elastic behaviour of the system.

The three 200 systematic row images shown in fig.2 are part of a through-focal series taken at 200kV with an objective aperture radius of  $1.4\text{nm}^{-1}$ . Examples of the projected profiles of these images are shown in fig.3. After averaging these over areas as marked in fig.3, and symmetrising them (the lack of symmetry is caused by the variable small local tilts from the vertical) a set of profiles was obtained as exemplified in fig.4. While the thickness of the specimen was not determined precisely because of local foil bending, this is not critical because it is the profile of the Fresnel contrast which will tell us about the degree of intermixing at the interfaces. A good profile fit for these data was obtained (using a continuum potential approach), as shown in fig.5a, for the model shown in fig.5b with repeated units of 13 atomic layers in the Cu:Fe ratio of 9:4 and two atomic layer intermixing at the interfaces. The fit is somewhat artificial since the expected changes in form as a function of the degree of intermixing were much weaker than previous studies would have suggested they should have been. The reason for this is that the small size of the aperture used cut the reciprocal space profile too near to the origin in reciprocal space, given the short wavelength and small size of the multilayer components. Better data will be obtainable using an objective aperture about a factor of two larger in size. For the more roughness-sensitive data obtained in such a way atomic multislice simulations will be required. Nevertheless the form of both the fringe width change (fig.6) and contrast (fig.7) are again very much as would be expected. Further work will be required to substantiate the point but other data we have obtained using energy filtered Fresnel imaging suggest that there is a small added degree of (near to) monatomic roughness. Given however the very low mutual solubility of Cu and Fe the layers are clearly mixed over no more than about 3 monolayers. Annoyingly the accuracy of the result we have obtained is slightly worse than has been previously achieved [1]. However the data we are currently obtaining with the GATAN GIF on the same system is of higher accuracy and very similar roughnesses have been measured to higher accuracy still [10].

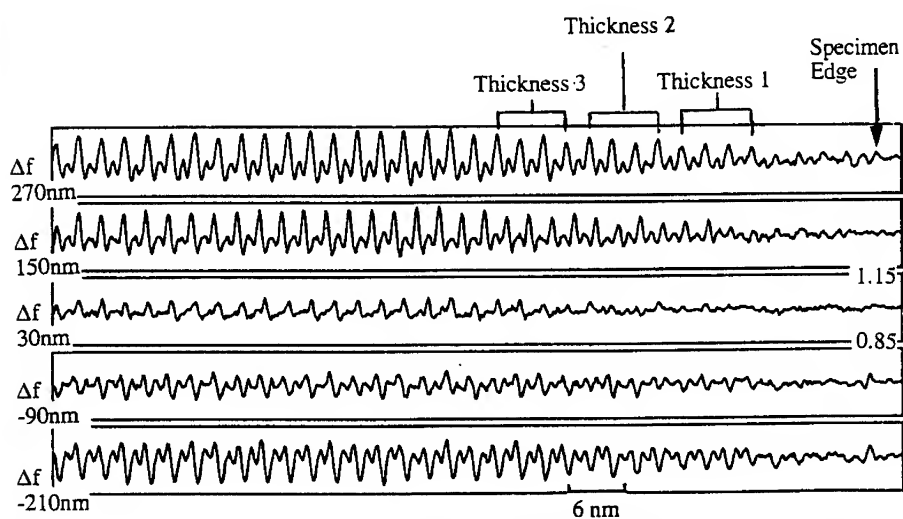


Fig. 3 Projected profiles of fresnel images for different defoci. The regions chosen for averaging are marked.

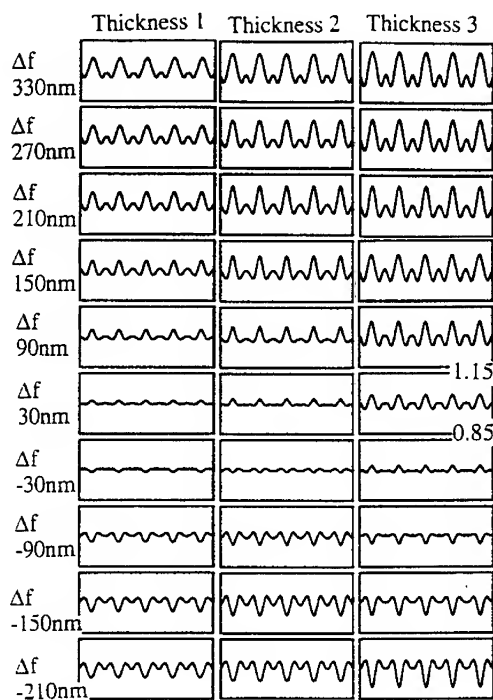


Fig.4 Experimental fringe profiles for the regions marked in fig.3 after averaging and symmetrising. The thicknesses are in the range 20-60nm

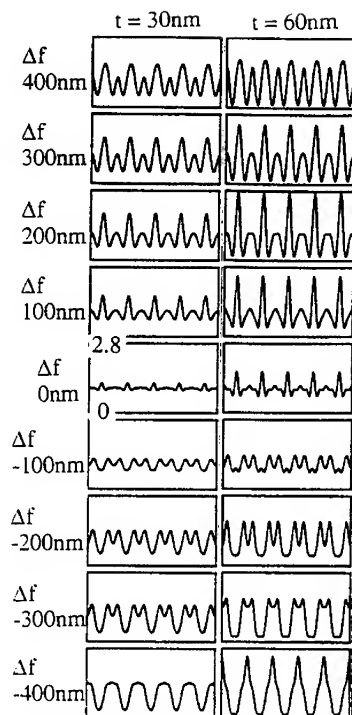


Fig.5a Simulated fringe profiles



Fig.5b Model used for simulations

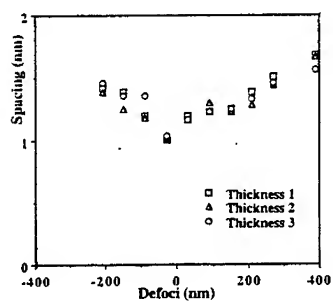


Fig.6 Experimental first fringe spacing,  $d$ , as a function of defocus

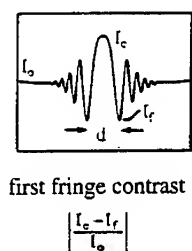


Fig.7 Experimental first fringe contrast as a function of defocus.



Fig.8.HREM image of the multilayer. The [002] layer normal is marked.

Now that we have a reasonable model for the profile of the layers we can turn to the measurement of the lattice spacings. The JEOL4000EX high resolution image shown in fig.8 was part of a of a through-focal series of a moderately thick area chosen so as to minimise the effects of stress relaxation at the foil surfaces, this causing surface corrugated distortions [11]. Before discussing the analysis of such systems we should briefly assess the simulated image formation behaviour. Image simulations were obtained by standard methods for the fully relaxed structure with compositionally abrupt interfaces. The assumption of minimisation of the strain energy is probably appropriate for the thin foil situation with a lattice spacing across the layering of 0.3604nm and spacings in the layer-plane normal direction of 0.3631nm in the Cu and 0.3563nm in the Fe. These values were obtained using the accepted anisotropic elastic constants for Cu and approximate values for f.c.c. Fe. The stress-free bulk lattice parameter for Cu was taken to be 0.3615nm while the value chosen for Fe of 0.3585 was extrapolated from high temperature data [5]. For this model the average lattice spacing in the layer plane normal direction is about 0.2% greater than perpendicular to this. The two simulations shown in fig. 9a and b at Gaussian and Scherzer defocus together with their respective fringe profiles in figs.10a and b were obtained for a thickness of 10.8nm using the appropriate imaging parameters for the microscope. The dramatic change in form that can occur, here as a function of focus, but also as a function of thickness are clear and are caused, in the main, (and as was demonstrated by artificially changing the value of  $C_s$ ) by the sensitivity of such images to the degree of transfer near to the limits of its resolution where the amplitude is spread in the layer normal direction both by the extremely small scale of the layering and its roughness. As is well known, the real danger in attempting to obtain accurate average and local fringe spacings from a system such as that examined here, and relating these to models, lies in the way fringes can be missing or doubled. This is why non axial methods can be an advantage when only spacings are required [12].

With these concerns in mind many different areas of the experimental images were digitised and the fringe profiles thus obtained were assessed by fitting procedures for each individual fringe. Examples of the fringe profiles for two individual areas so obtained, lying across the layering are shown in figs.11a and b and d and e for two different defoci. The changes in the form of the fringe profiles along the layering as a function of defocus are much smaller, as is demonstrated by the profiles for a single area in fig.11c and f. While the number of pixels/fringe at 4 was a little too low for this to be done well, local variations in the fringe spacing could not be analysed sufficiently accurately to allow a systematic trend to be revealed. Nevertheless it appears that the average spacing in the layer plane normal direction is some 4% larger than that at right angles to this. If this were true then there is indeed a large anomaly in the elastic behaviour of this multilayer system. The fringe spacing increase can be measured accurately but this is to a degree subjective in that profiles which clearly exhibited anomalous numbers of lattice fringes were not included. The difficulty here is that the increase in spacing is about half a fringe spacing! Further data will clearly be required to confirm our result and we are clear that greater accuracies can be achieved by using slightly larger apertures in the Fresnel technique to evaluate the roughness better and non axial imaging to get improved lattice fringe images.

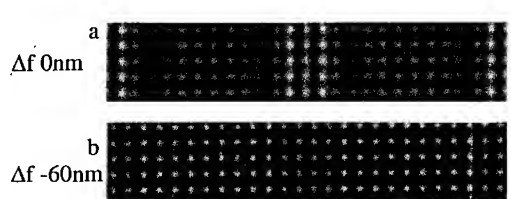


Fig.9 Simulated HREM images showing two multilayer repeats for a foil thickness of 10.8 nm

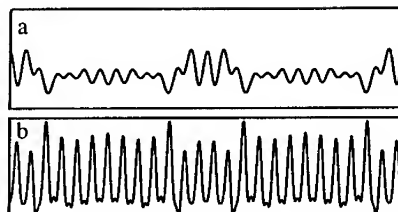


Fig.10 Projections corresponding to the images in fig.9.

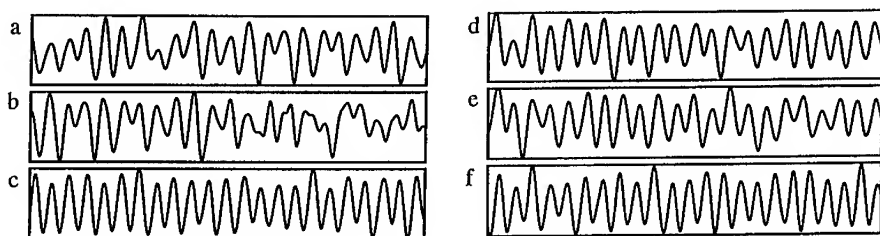


Fig.11 Experimental intensity profile across an HREM image. a, b, d and e are profiles across the layering. c and f are profiles along the layering. d-f are from the same regions as a-c but about 70 nm more underfocus.

## CONCLUSION

Our preliminary assessment of the structure and elastic properties of the coherently strained Fe-Cu multilayer structure examined suggest strongly that it has strongly anomalous elastic properties. Our evaluation has also highlighted several ways in which the measurements, both of the compositional abruptness of the interfaces and of the strains, could be improved.

We are grateful to the EPSRC for financial support.

## REFERENCES

1. C.S. Baxter and W.M. Stobbs, *Nature* **322**, 814 (1986)
2. T. Tsakalakos and J.E. Hilliard, *J. Appl. Phys.* **54**, 734 (1983)
3. E.E. Fullerton, I.K. Schuller, F.T. Parker, K.A. Svinarich, G.L. Eesley, R. Bhadra and M. Grimsditch, *J. Appl. Phys.* **73**, 7370 (1993)
4. F. Yoshizaki, N. Tanaka and K. Mihama, *J. Electron Microsc.* **39**, 459 (1990)
5. S.H. Lu, J. Quinn, D. Tian, and F. Jona, *Surface Science*, **209**, 364 (1989)
6. R.E. Somekh and C.S. Baxter, *J. Crystal Growth*, **76**, 119 (1986)
7. F.M. Ross and W.M. Stobbs, *Ultramicroscopy* **36**, 331 (1991)
8. C.S. Baxter and W.M. Stobbs, *IOPCS* (ed: G.W. Tatlock)(Hilger Bristol)**78**, 387 (1985)
9. M.O'Keefe and J.C.H. Spence, *Acta Cryst. A* **49**, 231, (1993)
10. R.E. Dunin-Borkowski, C.B. Boothroyd, S.J. Lloyd and W.M. Stobbs. To be presented at CMMP (Warwick, 1994)
11. M.M.J. Treacy, J.M. Gibson and A. Howie, *Phil. Mag. A*, **51**, 389 (1985)
12. D.J. Hall, P.G. Self and W.M. Stobbs, *J. Microsc.* **130**, 215 (1983)

## MORPHOLOGICAL EVOLUTION WITH LAYER THICKNESS IN SINGLE CRYSTAL $\text{CeO}_2(110)/\text{Si}(100)$

Tomoyasu INOUE, Yasuhiro YAMAMOTO\*, Masataka SATOH\*\* and Tetsu OHSUNA

Department of Electronic Engineering, Iwaki Meisei University, Iwaki, Fukushima 970, Japan

\*Department of Electronic Informatics, Hosei University, Koganei, Tokyo 184, Japan

\*\*Research Center of Ion Beam Technology, Hosei University, Koganei, Tokyo 184, Japan

### ABSTRACT

Surface morphology evolution of epitaxially grown  $\text{CeO}_2(110)$  layers on  $\text{Si}(100)$  substrates is studied using atomic force microscopy (AFM) and reflection high energy electron diffraction (RHEED). The surface has a faceted structure; a stripe-appearance and triangular-shape in plan- and cross-sectional views, respectively. AFM measurements clarify that as the layer thickness increases, the cross-sectional shape changes from a gable roof shape toward trapezoidal, which is consistent with RHEED analyses. The width of the facet monotonically increases with the layer thickness, while its height saturates at  $\sim 5$  nm above 600 nm in thickness, which means that the surface approaches smooth morphology. Ion channeling analyses indicate that the thicker the layer, the better the crystalline quality at the surface.

### INTRODUCTION

Epitaxial cerium dioxide ( $\text{CeO}_2$ ) layers on silicon substrates are of great interest for applications to silicon on insulator devices, miniaturized stable capacitors for ultra-large scale integration and buffer layers between silicon and high temperature superconducting materials.[1-13] We have been investigating the  $\text{CeO}_2$  epitaxial growth using electron beam evaporation in an ultra-high vacuum.[1, 3, 5-11] Although  $\text{Si}(100)$  substrates are essential for applications to microelectronics,  $\text{CeO}_2$  layers grown on  $\text{Si}(100)$  have several problems, i. e. growth with  $(110)$  orientation and low crystalline quality. We have already reported that the epitaxial growth of  $\text{CeO}_2(110)$  on  $\text{Si}(100)$  is featured as the competitive growth of  $\text{CeO}_2(110)$  under two possible configurations for long range lattice matching along  $\langle 110 \rangle$  direction in  $\text{Si}(100)$  plane, resulting in a double domain structure or a mixture of  $\text{CeO}_2[100]||\text{Si}[1\bar{1}0]$  and  $\text{CeO}_2[1\bar{1}0]||\text{Si}[1\bar{1}0]$ . [5]

Recently, it has been recognized that the step structure on  $\text{Si}(100)$  substrates cut with more than  $2.5^\circ$ -off-orientation toward  $\langle 110 \rangle$  direction leads to single crystal  $\text{CeO}_2(110)$  layer formation and significant crystalline quality improvement.[11, 13] The layer surface has a nanometer-scale-periodically corrugated structure, which consists of  $(111)$ -facets elongated toward  $\langle 110 \rangle$ . This corrugated surface itself has possibilities for certain applications, for example grapho-epitaxy.[14] On the other hand, a flat surface is preferable for planar technology. In either way, it is important to understand parameters which rule the surface structure. This paper describes surface morphological evolution of the  $\text{CeO}_2(110)$  layer surface with the layer thickness and the substrate off-orientation.

### EXPERIMENTS

Silicon substrates with off-orientation ranging  $0^\circ$  to  $15.8^\circ$  toward  $\langle 110 \rangle$  direction were prepared and chemically cleaned by four times applying immersion in  $\text{HCl}$ ,  $\text{H}_2\text{O}_2$  mixture and dilute hydrofluoric acid, each for 10 minutes.  $\text{CeO}_2$  layers of 100~720 nm in thickness were epitaxially grown by electron beam evaporation on the Si substrates heated at  $820^\circ\text{C}$ . [1] In order to maintain stoichiometry of the grown layer, an oxygen

gas was introduced into the chamber at the pressure of  $8 \times 10^{-6}$  Torr. Growth rate was 0.2~0.5 nm/s.

The epitaxially grown layers were characterized using high energy electron diffraction (RHEED), atomic force microscopy (AFM, Digital Instruments NanoScope III), high resolution transmission electron microscopy (HRTEM, JEOL JEM-4000EX) and 1.5 MeV  $^4\text{He}^+$  ion Rutherford backscattering (RBS).

## RESULTS AND DISCUSSION

### Surface Morphology Evolution with Layer Thickness

Firstly, we found that a  $\langle 110 \rangle$  incidence RHEED pattern of  $\text{CeO}_2(110)/\text{Si}(100)$  changes with the layer thickness, which should result from surface morphology evolution. Figures 1 A, B and C show RHEED patterns taken from samples A, B and C listed in Table I, respectively. Corresponding illustrations of RHEED pattern and cross-sectional shape are shown in Figs. 1 (a), (b) and (c), and (d), (e) and (f). The diamond-shaped network RHEED pattern shown in Fig. 1 A comes from two streaks at each diffraction spot, whose crossing angle is about  $71^\circ$  which is a supplementary angle of the facets.[11]

In Fig. 1 B, not only the two streaks but a vertical streak appear, resulting in a bird's footprint-like feature, which is the first finding as far as the authors know. This is explained by the facet morphology change as shown in Fig. 1 (e). This shape

Table I Samples appearing in Figs. 1 and 2.

| sample | layer thickness (nm) | substrate off-angle (deg.) |
|--------|----------------------|----------------------------|
| A      | 110                  | 5.0                        |
| B      | 460                  | 2.75                       |
| C      | 720                  | 3.0                        |

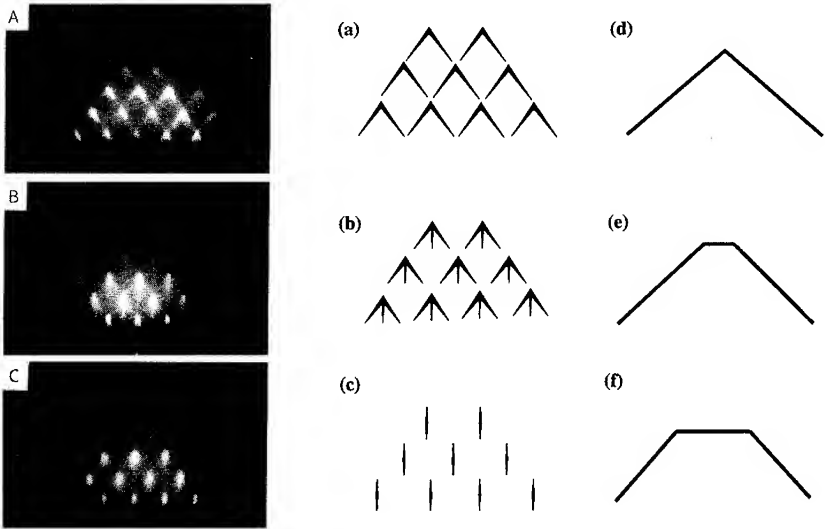


Fig. 1  $\langle 110 \rangle$  incidence RHEED patterns, where A, B and C are taken from samples A, B and C, respectively. Respective illustrations (a), (b) and (c) and predicted cross-sectional shapes (d), (e) and (f) are also shown.

causes three streaks due to both (111)-facets and a (110)-flat-top surface. The RHEED pattern entirely changes in the thicker sample (Fig. 1 C), wherein vertical streaks are dominant. This indicates that the surface is mainly consisted of flat (110) planes.

Secondly, we studied surface morphology of the  $\text{CeO}_2(110)$  layers using AFM. Figures 2 A, B and C show AFM images of sample A, B and C, respectively, below which corresponding cross-section data are shown as Figs. 2 (a), (b) and (c). The surface of thin sample A reveals facets with a quite sharp triangular shape, whereas that of thicker sample B changes to be triangle like but with somewhat flattened top. In Figs. 2 C and (c), the surface of thickest sample C shows rather trapezoidal shape. These results agree well with the RHEED analyses shown in Fig. 1.

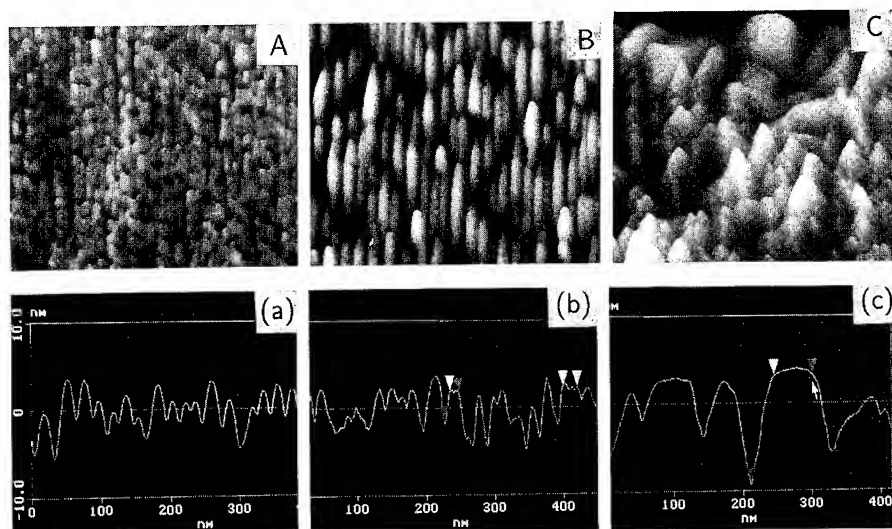


Fig. 2 AFM images of samples A, B and C, below which are respective cross-sectional profiles, (a), (b) and (c).

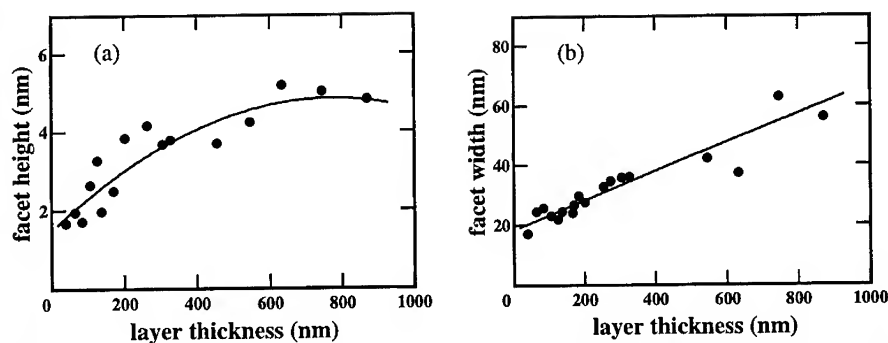


Fig. 3 Facet size as a function of layer thickness derived from AFM measurements: Facet height (a) and facet width (b).



The averaged dimension of the facets in sample A is 100~200nm in length, ~20nm in width and ~3nm in depth. Comparing carefully Figs. 2 (d), (e) and (f), it is understood that the cross-section of the facet increases with the layer thickness. Figures 3 (a) and (b) show facet height and width variations with the layer thickness, respectively. Each value was obtained from averaging more than 50 data. The facet width increases monotonically with layer thickness in the experimental range, whereas the facet height seems to saturate at ~5 nm above 600 nm. This indicates that the surface approaches smooth morphology as the layer become thicker. It is thought that adjacent facets will coalesce, so their width becomes larger as the layer growth proceeds, but their height does not increase because CeO<sub>2</sub> is deposited uniformly on not only a flattened top surface but faceted surfaces. Considerations from thermodynamical and/or crystallographic viewpoints will be needed for further understanding on this phenomenon.

#### Morphology Change with Substrate Off-angle

Comparing Figs. 2 (a), (b) and (c), it is also recognized that the facet length is significantly dependent on the substrate off-angle. The facet length of the CeO<sub>2</sub> layer on a 2.75°-off substrate (Fig. 2 (b)) is obviously longer than that on 5°-off substrate (Fig. 2 (a)). As the off-angle increased, the facet length decreases and accordingly the facet density increases as shown quantitatively in Figs. 4 (a) and (b).

This is explained as follows: The facet elongates in parallel with steps, which stretch toward CeO<sub>2</sub>(110). As reported previously, single crystal layer grows on the substrates with off-angle  $\geq 2.5^\circ$ , at which the mean terrace width corresponds to 7 times Si lattice diagonal, which is the optimum condition forming single crystal layers.[13] The relation between the theoretical mean terrace width ( $W$ ) and the off-angle ( $\theta$ ) is easily obtained as  $W = 2\sqrt{2} \tan \theta^{-1}$ , considering a bi-layer step structure.[15] It is expected that the terrace density increases as its width decreases according to above equation. The curve in Fig. 4 (a) looks like that of  $2\sqrt{2} \tan \theta^{-1}$ . This suggests that the facet length decrease is due to the increase in the terrace density and hence nucleus density.

In order to obtain high quality CeO<sub>2</sub> layers with smooth surface, smaller off-angle is preferred as far as a single crystal layer grows. It is concluded that the optimum off-angle is 2.5°, which is the same conclusion from the crystallinity characterization.[13]

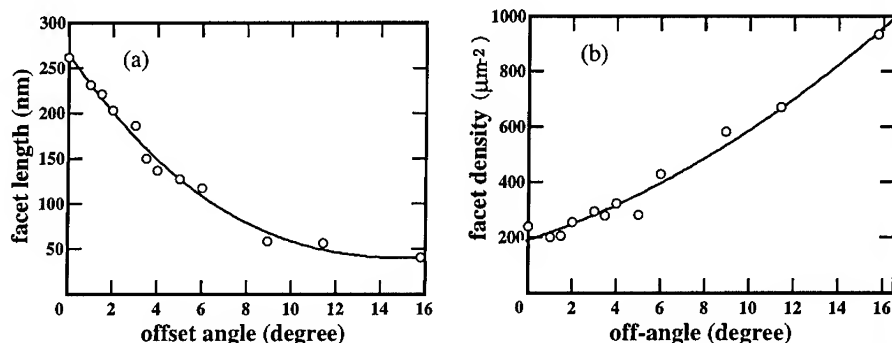


Fig. 4 Facet length (a) and facet density (b) as a function of substrate off-angle derived from AFM measurements.

### Inclination of facets

Figure 5 shows a typical cross-sectional HRTEM lattice image of the facet at the surface of a  $\text{CeO}_2(110)$  layer grown on a  $3^\circ$ -off  $\text{Si}(100)$  substrate. The vertical angle at the summit of the triangle is  $109^\circ$ , which corresponds exactly with the  $(111)$ -facet structure mentioned above. It is clearly recognized that the  $[110]$  axis of the  $\text{CeO}_2$  layer is inclined toward the substrate off-set-direction (indicated by an arrow in Fig. 5) by the same angle as the substrate off-angle. This is also confirmed by systematic RHEED measurements for various off-angles.

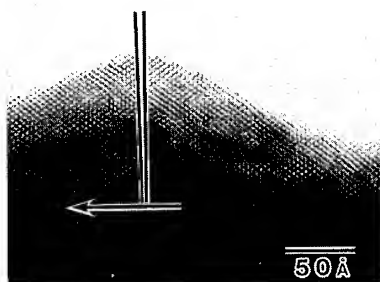


Fig. 5 A cross-sectional HRTEM image of the same sample as Fig. 4, showing the inclination of the facet. The arrow indicates the substrate-off-direction.

### Crystallinity change with layer thickness

Figure 6 shows RBS spectra taken from (a) 86-nm-thick-, (b) 170-nm-thick- and (c) 450-nm-thick-single crystal  $\text{CeO}_2(110)/\text{Si}(100)$  samples. From this figure, it is clearly understood that the defect density decreases as the  $\text{CeO}_2$  layer growth proceeds, i. e. a normalized minimum yield ( $\chi_{min}$ ) at the surface decreases with the layer thickness.  $\chi_{min}$  values of sample (a), (b) and (c) at the surface are 9.4, 4.7 and 1.8 %, respectively. The last one indicates very good crystallinity of sample (c). This significant

$\chi_{min}$  lowering at the surface is considered to be mainly due to defect reduction as the  $\text{CeO}_2$  layer growth proceeds, which is usual in hetero-epitaxy, e. g. a silicon layer on sapphire.

The crystalline quality in the vicinity of the interface, however, is not so satisfactory as that at the surface, where  $\chi_{min}$  exceeds 20 %. This is due that there are considerably many defects such as dislocations, stacking faults, micro-twins and small angle grain boundaries in the vicinity of the  $\text{CeO}_2/\text{Si}$  interface, which may correlate with the small angle misalignment of  $\text{CeO}_2[011]$  to  $\text{Si}[001]$ . [16]

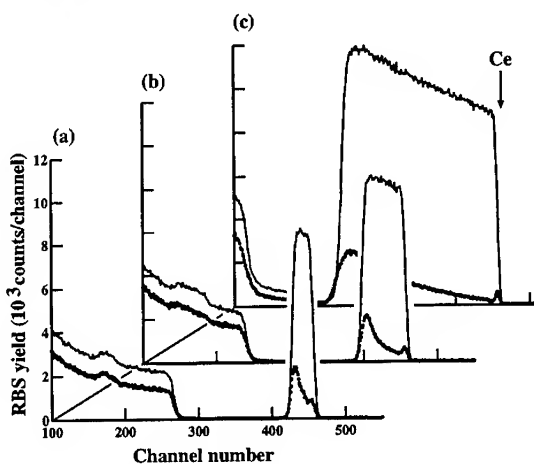


Fig. 6 RBS spectra taken from (a) 86 nm thick, (b) 170 nm thick and (c) 450 nm thick  $\text{CeO}_2(110)/\text{Si}(100)$  samples. The arrow indicates the surface of Ce spectrum.

### CONCLUSION

Surface morphology evolution of  $\text{CeO}_2(110)$  layers grown on  $\text{Si}(100)$  substrates with off-orientation was studied using RHEED, AFM, HRTEM and RBS. RHEED pattern

changed significantly with the CeO<sub>2</sub> layer thickness, which is explained by the morphology change of facets. AFM observation agreed well with the cross-sectional shape variation of the facet predicted from RHEED results. From quantitative AFM data processing, it is clearly found that the width of the facet increases monotonically with the layer thickness, whereas its height saturates at ~5nm above 600nm. Accordingly, morphology changes from a gable roof shape to trapezoidal as the layer thickness increases. It means that the surface approaches smooth morphology.

It was also found that the facet length decreases as the substrate off-angle increases, resulting in a increase in facet density. This result indicated that 2.5° is optimum substrate off-angle, which has been already recognized by the crystallinity characterization. RHEED and cross-sectional HRTEM measurements verified that CeO<sub>2</sub>[011] axis is inclined toward the substrate offset-direction by the same angle as the off-angle. RBS analyses indicated that the thicker the layer thickness, the better the crystalline quality at the surface. For further improvement, more precise control of nucleation at the early stage of the growth process will be needed.

The authors wish to thank Mr. S. Nakayama and Ms. C. Gotoh of TOYO Corp. for their aids in AFM measurements.

## REFERENCES

- [1] T. Inoue, Y. Yamamoto, S. Koyama, S. Suzuki and Y. Ueda, Appl. Phys. Lett. **56**, 1332 (1990).
- [2] M. Yoshimoto, H. Nagata, T. Tsukahara, and H. Koinuma, Jpn. J. Appl. Phys. **29**, L1199 (1990).
- [3] T. Inoue, M. Osonoe, H. Tohda, M. Hiramatsu, Y. Yamamoto, A. Yamanaka, and T. Nakayama, J. Appl. Phys. **69**, 8313 (1991).
- [4] H. Nagata, T. Tsukahara, S. Gonda, M. Yoshimoto and H. Koinuma, Jpn. J. Appl. Phys. **30**, L1136 (1991).
- [5] T. Inoue, T. Ohsuna, L. Luo, X. D. Wu, C. J. Maggiore, Y. Yamamoto, Y. Sakurai and J. H. Chang, Appl. Phys. Lett. **59**, 3604 (1991).
- [6] T. Inoue, T. Ohsuna, Y. Yamamoto, Y. Sakurai, L. Luo, X. D. Wu, C. J. Maggiore, Mater. Res. Soc. Symp. Proc. **237**, 589 (1992).
- [7] L. Luo, X. D. Wu, R. C. Dye, R. E. Muenchausen, S. R. Folton, Y. Coulter, C. J. Maggiore and T. Inoue, Appl. Phys. Lett. **59**, 2043 (1991).
- [8] T. Inoue, T. Ohsuna, Y. Yamada, K. Wakamatsu, Y. Itoh, T. Nozawa, E. Sasaki, Y. Yamamoto and Y. Sakurai, Jpn. J. Appl. Phys. **31**, L1736 (1992).
- [9] Y. Yamamoto, M. Satoh, Y. Sakurai, T. Inoue and T. Ohsuna: Jpn. J. Appl. Phys. **32**, L620 (1993).
- [10] T. Inoue, Y. Obara, Y. Yamamoto, M. Satoh and Y. Sakurai: Jpn. J. Appl. Phys. **32**, L1765 (1993).
- [11] T. Inoue, T. Ohsuna, Y. Obara, Y. Yamamoto, M. Satoh and Y. Sakurai: J. Cryst. Growth **131**, 347 (1993).
- [12] S. Yaegashi, T. Kurihara, H. Hoshi and H. Segawa, Jpn. J. Appl. Phys. **33**, 270 (1994).
- [13] T. Inoue, Y. Yamamoto, M. Satoh, T. Ohsuna, H. Myoren and T. Yamashita, Proc. Mater. Res. Soc. **341**, 101 (1994).
- [14] M. W. Geis, D. C. Flanders and H. I. Smith, Appl. Phys. Lett. **35**, 71 (1979).
- [15] D. J. Chadi, Phys. Rev. Lett. **59**, 1691 (1987).
- [16] M. Satoh, Y. Yamamoto, S. Nakajima, Y. Sakurai, T. Inoue and T. Ohsuna, Mater. Res. Soc. Symp. Proc. **312**, 309 (1993).

## SCALING ANALYSIS OF $\alpha$ - AND *poly*-Si SURFACE ROUGHNESS BY ATOMIC FORCE MICROSCOPY

T. YOSHINOBU, A. IWAMOTO, K. SUDOH AND H. IWASAKI  
The Institute of Scientific and Industrial Research, Osaka University,  
8-1 Mihogaoka, Ibaraki City, Osaka 567, Japan.

### ABSTRACT

The scaling behavior of the surface roughness of  $\alpha$ - and *poly*-Si deposited on Si was investigated by atomic force microscopy (AFM). The interface width  $W(L)$ , defined as the rms roughness as a function of the linear size of the surface area, was calculated from various sizes of AFM images.  $W(L)$  increased as a power of  $L$  with the roughness exponent  $\alpha$  on shorter length scales, and saturated at a constant value of  $\sigma$  on a macroscopic scale. The value of roughness exponent  $\alpha$  was 0.48 and 0.90 for  $\alpha$ - and *poly*-Si, respectively, and  $\sigma$  was 1.5 and 13.6 nm for 350 nm-thick  $\alpha$ -Si and 500 nm-thick *poly*-Si, respectively. The AFM images were compared with the surfaces generated by simulation.

### INTRODUCTION

The roughness of a growing surface is known to exhibit spatial and temporal scaling behaviors. The interface width of a growing surface  $W(L, t)$ , defined as the roughness observed on scale  $L$  after time  $t$  of growth, can be written as

$$W(L, t) = \begin{cases} L^\alpha & \text{for } L < L_c \\ t^\beta & \text{for } L > L_c \end{cases}, \quad (1)$$

where  $\alpha$  is the roughness exponent,  $\beta$  is the growth exponent, and  $L_c$  is the correlation length [1-4]. On scales shorter than  $L_c$ , the surface is characterized as a self-affine fractal [5,6] with the local fractal dimension  $D = 3 - \alpha$ , whereas on scales longer than  $L_c$ ,  $W(L, t)$  saturates at  $\sigma = t^\beta$ , which corresponds to the rms roughness in the conventional sense. Both  $\sigma$  and  $L_c$ , which are the characteristic lengths in vertical and horizontal directions, respectively, also grow with time.

In fact, the scaling behavior (1), or self-affine growth is generally observed for real growing surfaces of various materials [3,4,7,8]. As for the value of the

roughness exponent  $\alpha$ , however, the experimental values tend to be large compared to those given by theory and simulation. For example,  $\alpha = 0.79$  and  $0.84$  are obtained for Fe/Fe(001) [7] and CuCl/CaF<sub>2</sub>(111) [8], respectively, whereas numerical solution of the KPZ growth model [9] gives  $\alpha \sim 0.4$  [10].

Obviously, some significant features of growth in real systems, such as formation of domains [11-13], boundaries, and anisotropic growth rate *etc.*, are not taken into account in simplified models. From a material engineering point of view, *i.e.*, to predict and control the roughness evolution in real growth systems, it is necessary to investigate those specific features of growth and their dependence on the growth conditions. In our recent papers [14,15], we studied the roughness exponent in electrochemical deposition of copper, and its dependence on the growth conditions, especially on the concentration of the organic additives in the electrolyte.

In this paper, we report on the comparison between the surface roughness of  $\alpha$ - and *poly*-Si films deposited on Si substrates. The essential difference between these two materials is that *poly*-Si consists of grains of small crystals, whereas  $\alpha$ -Si has no crystal structure at all.

## EXPERIMENT

Samples of  $\alpha$ - and *poly*-Si films were deposited on Si substrates by low-pressure CVD method. The film thickness was  $350\text{nm}$  for  $\alpha$ -Si and  $500\text{nm}$  for *poly*-Si. The surface roughness of these films were measured by atomic force microscopy (AFM). AFM is suitable for scaling analysis of surface roughness, not only due to its high resolution, but also due to its wide range of measurement scales, which makes it possible to determine the roughness exponent accurately.

AFM measurements were carried out in air with SPI-3700/SPA300 from Seiko Instruments Inc. The image was acquired as numerical data of height at  $256 \times 256$  points on the surface. The area of measurement was varied from  $100 \times 100 \text{ nm}^2$  to  $20000 \times 20000 \text{ nm}^2$  so that the interface width  $W(L)$  can be calculated for a wide range of  $L$ . Following correction was applied to the data array  $h_{x,y}$  [16]. Firstly, for all  $x$  and  $y$ ,  $h_{x,y}$  was replaced with

$$h_{x,y} - \frac{1}{256} \sum_{y=1}^{256} h_{x,y} \quad , \quad (2)$$

and subsequently,  $h_{x,y}$  was replaced again with

$$h_{x,y} - \frac{1}{256} \sum_{x=1}^{256} h_{x,y} \quad . \quad (3)$$

These procedures are to remove the tilt toward the X-direction (scan direction), and to remove the tilt and the fluctuation along the Y-direction.

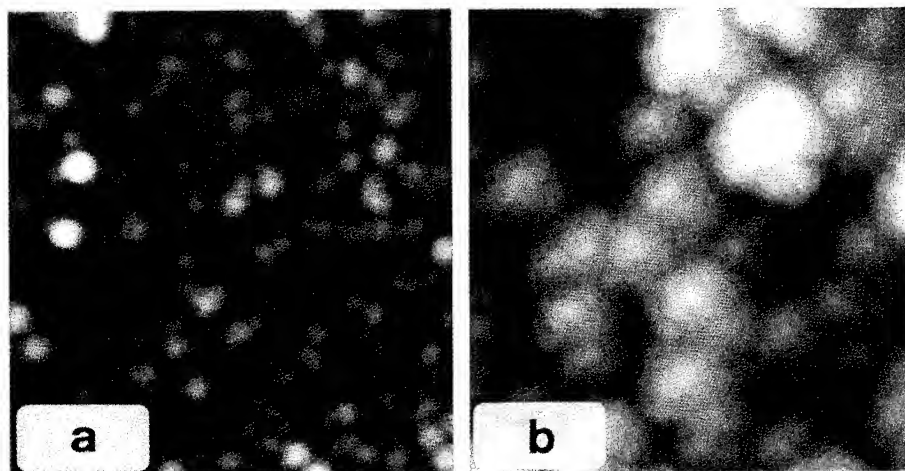


Fig.1 AFM images ( $1000 \times 1000 \text{ nm}^2$ ) of (a) $\alpha$ - and (b)*poly*-Si surfaces. The film thickness was 350nm for  $\alpha$ -Si and 500nm for *poly*-Si, respectively.

Figure 1(a) and (b) show the typical AFM images of  $\alpha$ - and *poly*-Si surfaces, respectively. Figure 1(b) shows the typical morphology of a polycrystalline film, which consists of grains. In terms of the self-affine fractal geometry, such a surface has a lower fractal dimension  $D$  since the amplitude of short-wavelength roughness within a grain is much smaller than the typical height of a grain itself. Moreover, any large structure or long-wavelength fluctuation was not observed in a wide-scan ( $20000 \times 20000 \text{ nm}^2$ ) image (not shown). Therefore, the mean grain size, which is roughly of the order of the film thickness, is the only characteristic length in the horizontal direction. This suggests that there was no external mechanism or fluctuation in the growth of *poly*-Si to form large structures, except for the horizontal spreading of grains described as  $L_c(t) \sim t^{\beta/a}$ . On the other hand, grains are not well-developed in Fig.1(a), which implies a higher fractal dimension  $D$  of  $\alpha$ -Si surface roughness.

#### INTERFACE WIDTH

The interface width  $W(L)$  was calculated by the following procedure. For each of the AFM images, the area was divided into smaller segments. The size of each segment was chosen to be  $2^n \times 2^n$  ( $n = 1 - 5$ ) pixels, and thus, the number of segments in a  $256 \times 256$  image was  $(256/2^n)^2$ . The rms roughness was calculated in each segment, and then, was averaged over the whole area. In this way, a series of  $W(L)$  was obtained from a single AFM image, and those obtained from several AFM images were combined together to cover a wide

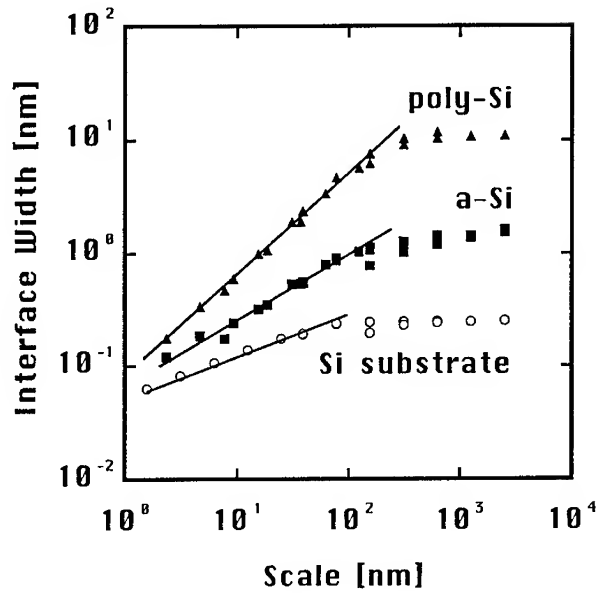


Fig.2 Interface width  $W(L)$  of the surface roughness of  $\alpha$ - and  $\text{poly-Si}$  films deposited on Si substrate.

range of length scales.

Figure 2 shows the interface width  $W(L)$  calculated from AFM images of  $\alpha$ - and  $\text{poly-Si}$  surfaces. For comparison,  $W(L)$  of the Si substrate is also shown. Each curve of  $W(L)$  is separated into two regions by the correlation length  $L_c$ . The roughness exponent  $\alpha$  calculated from the slope below  $L_c$  is 0.30, 0.48 and 0.90 for Si substrate,  $\alpha$ -Si and  $\text{poly-Si}$  surfaces, respectively.

#### COMPARISON WITH SIMULATION RESULTS

To study the dynamic scaling in the growth of grain structures, we carried out simulations. Figure 3(a) shows the surface obtained by simulation for the standard KPZ equation.

$$\frac{\partial h}{\partial t} = \nu \nabla^2 h + \frac{\lambda}{2} (\nabla h)^2 + \eta(\mathbf{r}, t) \quad . \quad (4)$$

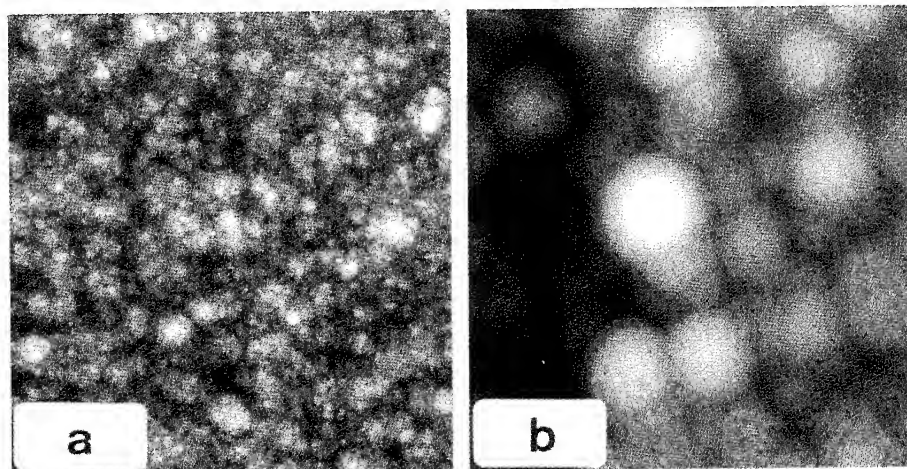


Fig.3 Topographs generated by simulation of (a)KPZ growth and (b)grain growth.

The method of simulation is the same as that described in [10], and the parameters are  $L = 256$ ,  $\epsilon = 25$  and  $\Delta\tau = 0.00025$  in their notation. Grains are not observed in Fig.3(a), and the roughness exponent  $\alpha$  of this surface is 0.40.

As a simple model of grain growth, a modified system was considered. In this system, a term proportional to  $h - \bar{h}$  was added to the right-hand side of eq. (4). This term represents the effect of preferential growth on grains that already exist. Such a growth is unstable in the sense that  $\sigma(t)$  diverges faster than  $t$  (or equivalently, the film thickness) after a finite time. Since the magnitude of the  $h - \bar{h}$  term is initially small and then increases with time, the variance from the KPZ surface becomes larger and larger, and finally the growth becomes unstable. Figure 3(b) shows a snapshot of the simulated surface. The surface has a grain structure, and the roughness exponent  $\alpha$  is calculated to be 0.90, which is equal to the value for *poly*-Si.

Considering that a grain structure is frequently seen in deposited or evaporated materials, many of the film growth in reality seem to exhibit scaling behaviors different from that of the KPZ growth. More detailed study, especially on the relation between the growth conditions and the scaling behavior, would clarify what factor is dominant in a certain class of film growth other than KPZ growth.

## SUMMARY

The scaling behavior of the surface roughness of  $\alpha$ - and *poly*-Si deposited



on Si was investigated by AFM. The interface width  $W(L)$  increased as a power of  $L$  with the roughness exponent  $\alpha$  on shorter length scales, and saturated at a constant value on a macroscopic scale. The value of roughness exponent  $\alpha$  was 0.48 and 0.90 for  $\alpha$ - and *poly*-Si, respectively. The AFM images were compared with the surfaces generated by simulation for KPZ growth and its variation which results in a grain structure.

#### ACKNOWLEDGMENT

This work was supported by a Grant-in-Aid for Scientific Research (contract No.04452092) from the Ministry of Education, Science and Culture. One of the authors (T. Y.) received financial support from Makita Scholarship Foundation.

#### REFERENCES

1. T. Vicsek, Fractal Growth Phenomena (World Scientific, Singapore, 1989).
2. J. Krug and H. Spohn, in Solids Far From Equilibrium: Growth, Morphology and Defects, ed. C. Godrèche (Cambridge University Press, Cambridge, 1990) pp. 479-582.
3. F. Family and T. Vicsek, eds., Dynamics of Fractal Surfaces (World Scientific, Singapore, 1991).
4. A. Bunde, S. Havlin, eds., Fractals in Science (Springer-Verlag, Berlin, 1994).
5. B. B. Mandelbrot, The Fractal Geometry of Nature (Freeman, New York, 1982).
6. B. B. Mandelbrot, Phys. Scr. **32**, 257 (1985).
7. Y. -L. He, H. -N. Yang, T. -M. Lu and G. -C. Wang, Phys. Rev. Lett. **69**, 3770 (1992).
8. W. M. Tong, R. S. Williams, A. Yanase, Y. Segawa and M. S. Anderson, Phys. Rev. Lett. **72**, 3374 (1994).
9. M. Kardar, G. Parisi and Y. C. Zhang, Phys. Rev. Lett. **56**, 889 (1986).
10. J. G. Amar and F. Family, Phys. Rev. **A41**, 3399 (1990).
11. G. L. M. K. S. Kahanda, X. -q. Zou, R. Farrell and P. -z. Wong, Phys. Rev. Lett. **68**, 3741 (1992).
12. L. Vázquez, R. C. Salvarezza, P. Ocón, P. Herrasti, J. M. Vara and A. J. Arvia, Phys. Rev. **E49**, 1507 (1994).
13. G. Palasantzas, Phys. Rev. **B49**, 10544 (1994).
14. H. Iwasaki and T. Yoshinobu, Phys. Rev. **B48**, 8282 (1993).
15. A. Iwamoto, T. Yoshinobu and H. Iwasaki, Phys. Rev. Lett. **72**, 4025 (1994).
16. T. Yoshinobu, A. Iwamoto and H. Iwasaki, Jpn. J. Appl. Phys. **33**, L67 (1994).

---

## PART VI

---

### **Glassy Materials Slow Relaxation and Aging**

## GLASS TRANSITION SINGULARITIES AND SLOW RELAXATION

T. ODAGAKI\*, J. MATSUI\*\* AND Y. HIWATARI\*\*

\*Kyushu University, Department of Physics, Fukuoka 812, Japan

\*\*Kanazawa University, Department of Physics, Kanazawa 920-11, Japan

### ABSTRACT

Generalized susceptibility for the binary soft-sphere mixtures is computed for the frequency range including both the  $\alpha$  and  $\beta$  peaks in a supercooled fluid phase with a super-long-time molecular dynamics simulation. It is shown that the  $\alpha$  peak has a non-Debye type frequency dependence and the  $\beta$  peak is essentially of a Debye-type. The slow dynamics is analyzed on the basis of the trapping diffusion model which takes account of two types of diffusive dynamics. With the use of the coherent medium approximation, the frequency dependence of dynamical quantities are shown to agree with the observation. The primary relaxation time is shown to exponentially diverge at a certain temperature below the glass transition point, in line with the Vogel-Fulcher equation. A unified view for the Vogel-Fulcher temperature, the glass transition temperature and the kinetic transition temperature is given on the basis of the trapping diffusion model.

### INTRODUCTION

Glass forming materials have been known for more than 3500 years since the early stage of civilization and it is 70 years since the glass transition in supercooled fluids was first observed by a thermodynamic measurement [1]. However, little has been known about the mechanism and characterization of the glass transition. In particular, there are several characteristic temperatures below and above the glass transition temperature  $T_g$  which have been identified through experimental observations: The Vogel-Fulcher temperature [2] is defined as  $T_0$  when the viscosity or the primary relaxation time measured near the glass transition temperature is well fit by  $\exp[D/(T - T_0)]$ . The Kauzmann temperature ( $T_K$ ) [3], which is supposed to be close to  $T_0$ , is defined as the temperature at which the excess entropy in the supercooled state is extrapolated to vanish. There are some evidences that there exists a characteristic temperature between the glass transition and melting temperatures where the dynamical trait begins to change [4].

The glass transition is now considered to be a change in dynamical properties of supercooled liquids. In fact, many experiments have been reported for  $\text{Ca}_{0.4}\text{K}_{0.6}(\text{NO}_3)_{1.4}$  [5-6] and other materials [7-10] which indicate that the dynamical structure factor  $S(q, \omega)$  and the generalized susceptibility  $\chi''(q, \omega) \equiv \omega \pi S(q, \omega)$  deviate from the Debye form in the supercooled liquid state in two frequency regions, which are attributed to  $\alpha$ - and  $\beta$ -dynamics in supercooled liquids.

The slow dynamics and glass transition have also been investigated by molecular dynamics (MD) simulations for soft-core systems, [11-13] Lenard-Jones systems [14-15] and ionic melts [16] in recent years. The MD simulations have revealed: (1) There is a time region

in which the intermediate scattering function shows a stretched exponential decay. (2) The dynamical trait changes at some temperature  $T_x$  above the glass transition temperature, which can be considered as a kinetic transition. (3) Two types of diffusive motions exist above and below  $T_g$  in the time scale much slower than that of the microscopic motion.

In this paper we present the dynamical properties of supercooled liquids obtained by super-long-time MD simulation and by the trapping diffusion model. We study the frequency dependence of the dynamical structure factor and the generalized susceptibility for the entire frequency region. We show that the jump motion gives rise to the  $\alpha$ -relaxation whose characteristic time appears to diverge at some point below the glass transition point, and the oscillatory-diffusive motion produces the  $\beta$ -relaxation. With the use of the trapping diffusion model, we provide a unified understanding of the characteristic temperatures which can be related to the existence of various moments of the waiting time distribution (WTD). In particular we show the the Vogel-Fulcher temperature is related to the normalizability of WTD.

## MD SIMULATION FOR BINARY SOFT-SPHERE MIXTURES

### Binary soft-sphere mixtures

We consider binary soft-sphere mixtures composed of  $N_1$  atoms of mass  $m_1$  and diameter  $\sigma_1$  and  $N_2$  atoms of mass  $m_2$  and diameter  $\sigma_2$  in a volume  $V$ , which interact through the purely repulsive soft-sphere potentials [17]:

$$v_{\alpha\beta}(r) = \epsilon \left( \frac{\sigma_{\alpha\beta}}{r} \right)^{12}, \quad (1)$$

where  $\alpha, \beta = 1$  or  $2$  denotes species indices,  $\epsilon$  is the energy unit, and we assume that  $\sigma_{\alpha\beta} = (\sigma_\alpha + \sigma_\beta)/2$ . We introduce the effective coupling constant  $\Gamma_{\text{eff}}$ :

$$\Gamma_{\text{eff}} = n^*(T^*)^{-1/4} \left( \frac{\sigma_{\text{eff}}}{\sigma_1} \right)^3, \quad (2)$$

$$\sigma_{\text{eff}}^3 = \sum_{\alpha} \sum_{\beta} x_{\alpha} x_{\beta} \sigma_{\alpha\beta}^3. \quad (3)$$

where  $n^* = N\sigma_1^3/V$  denotes the reduced number density with the total number of atoms  $N (= N_1 + N_2)$ . The reduced temperature  $T^*$  equals  $k_B T/\epsilon$ ,  $x_1 (= N_1/N)$  and  $x_2 (= 1 - x_1)$  are concentrations. Note that  $\Gamma_{\text{eff}}^4$  is inversely proportional to  $T^*$ , and thus larger  $\Gamma_{\text{eff}}$ 's correspond to lower temperatures.

### MD simulation

In the present study, we set  $\sigma_2/\sigma_1=1.2$ ,  $m_2/m_1=2.0$ , and  $x_1 = x_2 = 0.5$ . Using the constant-temperature MD techniques and the seventh-order Gear algorithm together with periodic boundary conditions, we have carried out MD simulations with  $N=500$  particles in a cubic cell. Some runs for a larger system size with  $N = 4000$  were also carried out, but no significant difference between both system sizes was found. In the MD simulation, we truncated the pair potential (1) at the distance  $r/\sigma_{\alpha\beta}=3.5$ . The microscopic time scale is chosen to be

$$\tau = \left( \frac{m_1 \sigma_1^2}{\epsilon} \right)^{1/2}, \quad (4)$$

which is of the order of  $10^{-13}$  sec, if we use the parameters suitable for Ar in Eq. (4). The equation of motions were solved numerically with a time mesh of the order of  $0.01\tau$ .

We quenched the system from an equilibrium state at  $\Gamma_{\text{eff}} = 0.8$  to  $\Gamma_{\text{eff}} = 1.50$  and carried out MD simulation at  $\Gamma_{\text{eff}} = 1.50$ , starting with the final configuration obtained by the quenching MD simulation. Note that  $\Gamma_{\text{eff}} = 1.50$  corresponds to a supercooled fluid state, namely the coupling constant (temperature) lower (larger) than  $\Gamma_{\text{eff}} = 1.58$  (glass transition point), and larger (lower) than  $\Gamma_{\text{eff}} = 1.45$  (kinetic transition point) which is between the melting point  $\Gamma_{\text{eff}} = 1.15$  and the glass transition point.

The Laplace transform,  $G(\mathbf{q}, \omega)$ , of the intermediate scattering function  $F(\mathbf{q}, t)$  is defined by

$$G(\mathbf{q}, \omega) = \int_0^\infty F(\mathbf{q}, t) e^{-i\omega t} dt, \quad (5)$$

where

$$F(\mathbf{q}, t) = \left\langle \sum_j \exp i\mathbf{q} \cdot [\mathbf{r}_i(t + t_0) - \mathbf{r}_j(t_0)] \right\rangle_{i, t_0}. \quad (6)$$

The averages are taken over the configuration of atoms  $\{\mathbf{r}_i\}$  and the initial time  $t_0$ . It is known that the generalized susceptibility  $\chi(\mathbf{q}, \omega)$  is related to  $G(\mathbf{q}, \omega)$  through

$$\chi'(\mathbf{q}, \omega) = 1 + \omega G''(\mathbf{q}, \omega), \quad (7)$$

$$\chi''(\mathbf{q}, \omega) = \omega G'(\mathbf{q}, \omega), \quad (8)$$

where  $\chi(\mathbf{q}, \omega) = \chi'(\mathbf{q}, \omega) + i\chi''(\mathbf{q}, \omega)$ ,  $G(\mathbf{q}, \omega) = G'(\mathbf{q}, \omega) + iG''(\mathbf{q}, \omega)$ , and the dynamical structure factor is given by  $S(\mathbf{q}, \omega) = G'(\mathbf{q}, \omega)/\pi$ . We computed  $G(\mathbf{q}, \omega)$  from the formula

$$G(\mathbf{q}, \omega) = \frac{1}{t_{\text{max}}} \left\langle \sum_j \int_0^{t_{\text{max}}} dt_0 e^{i\mathbf{q} \cdot \mathbf{r}_i(t_0)} e^{-i\omega t_0} \int_0^{t_0} dt e^{-i\mathbf{q} \cdot \mathbf{r}_j(t)} e^{i\omega t} \right\rangle_i, \quad (9)$$

where  $\langle \dots \rangle$  means an average over the configuration of atoms  $\{\mathbf{r}_i\}$  and  $t_{\text{max}}$  is the total time step of the simulation [18]. The self part  $G_s(\mathbf{q}, \omega)$  of  $G(\mathbf{q}, \omega)$  is obtained by setting  $i = j$  in Eq. (9).

We show in Fig. 1 (open and closed circles) the frequency dependence of the imaginary part of the self part of  $G(\mathbf{q}, \omega)$ , i.e.  $G'_s(\mathbf{q}, \omega) = \pi S(\mathbf{q}, \omega)$ . The imaginary part of the self part of the generalized susceptibility  $\chi''_s(\mathbf{q}, \omega)$  is shown in Fig. 2 (open and closed circles). In Figs. 1 and 2, the results are shown for frequencies where the data are not affected by the time mesh or the length of simulation.

In order to see a frequency dependence of  $S_s(\mathbf{q}, \omega)$  in terms of a power-law formula, we computed the logarithmic derivative  $\sigma$

$$\sigma = -\frac{\partial \ln S_s(\mathbf{q}, \omega)}{\partial \ln \omega}, \quad (10)$$

which is shown in Fig. 3. The effective exponent  $\sigma$  takes a plateau value about  $\sigma \sim 1.5$  in the high frequency side of the  $\alpha$  peak. This value of  $\sigma$  gives the approximate value of the stretched exponential (KWW) exponent  $\beta \sim 0.5$ , which differs from a usual Debye value  $\beta = 1$ . The exponent  $\sigma$  becomes a plateau between the  $\beta$ -minimum and the  $\beta$ -peak, which indicates that a power law decay of  $S_s(\mathbf{q}, \omega)$  exists beyond the  $\alpha$ -decay region.

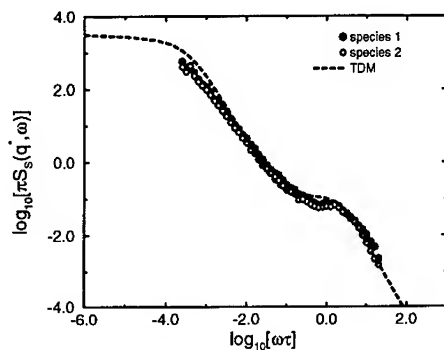


Fig. 1.  $G'_s(\mathbf{q}, \omega)$  vs.  $\omega$  in log-log scales. The reduced wavenumber  $q^*(=qL/2\pi)$ ,  $L$  being the side length of the cubic simulation cell, is equal to 8.0. Circles (open circles: species 1 and closed circles: species 2) are the results of the numerical simulation. The broken curve is the result obtained by the trapping diffusion model.

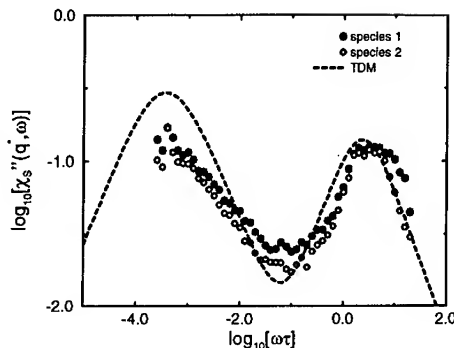


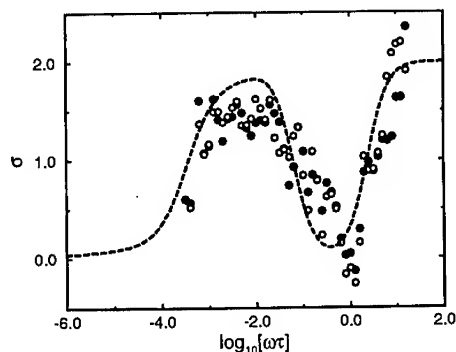
Fig. 2. The imaginary part of the generalized susceptibility (self part)  $\chi''_s(\mathbf{q}, \omega)$  vs.  $\omega$  in log-log scales. The symbols are the same as in Fig. 1.

Figure 4 shows the Cole-Cole plot of the generalized susceptibility. The  $\beta$ -peak appears as a semi-circle with the center on the real axis, indicating the  $\beta$ -process is the Debye relaxation.

## TRAPPING DIFFUSION MODEL

### Model

According to MD simulation [11,13], an atom appears to perform two kinds of diffusive motions if the rapid oscillatory motion is averaged out: one is a motion bound within a local area with deviation about 10–20% of the mean interatomic distance (we call it the *stray motion*) and the other is a *jump motion* with jump distance in the order of the mean interatomic distance. From the observation we can assume that the jump rate distribution is sharply peaked for the faster motion and is a power-law function for the slower motion. Noting that the distribution of the number of neighboring atoms is also sharply peaked, we arrive at the following mesoscopic phenomenological model: An atom at a given site  $s$  performs a stray motion between  $s$  and neighboring positions  $\{\mathbf{u}_s\}$  ( $|\mathbf{u}_s|$  is of the order of 10–20% of the average interatomic distance) with a constant jump rate  $w_b$ . Occasionally, it makes a long jump motion to site  $s'$  with jump rate  $w_s$ . The jump rate for this motion is assumed to depend only on the origin of the jump and not on the destination of the jump, because a structural relaxation following the jump will eliminate the correlation between forward and backward jumps. We further assume that the distribution of site  $\{s\}$  will not be important and sites  $\{s\}$  form a regular lattice, which can be conveniently assumed to be a simple cubic lattice. Consequently, we describe the motion of a tagged atom by the



**Fig. 3.** The effective exponent  $\sigma$  is plotted against  $\log \omega$ .  $S_s(\mathbf{q}, \omega)$  obeys a power-law decay when  $\sigma$  is approximately constant. The symbols are the same as in Fig. 1.

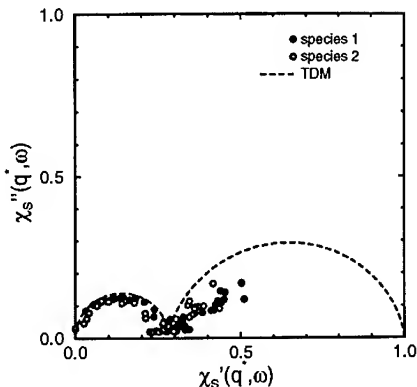


**Fig. 4.** Cole-Cole plots of  $\chi_s(\mathbf{q}, \omega)$ , i.e.  $\chi_s''(\mathbf{q}, \omega)$  vs.  $\chi_s'(\mathbf{q}, \omega)$ . The symbols are the same as in Fig. 1. At least two relaxation modes are seen; a semi-circle near the origin represents the  $\beta$  relaxation, and the other in the right side, representing the  $\alpha$  relaxation, appears to differ from a semi-circle. The broken curve is the result obtained from the trapping diffusion model.

following trapping master equation [19].

$$\begin{aligned} \dot{P}(s, t|s_0, 0) &= \sum_{s'} w_{s'} P(s', t|s_0, 0) + \sum_{u_s} w_b P(s + u_s, t|s_0, 0) \\ &- \{ \sum_{s'} w_s + \sum_{u_s} w_b \} P(s, t|s_0, 0), \end{aligned} \quad (11)$$

$$\dot{P}(s + u_s, t|s_0, 0) = w_b P(s, t|s_0, 0) - w_b P(s + u_s, t|s_0, 0), \quad (12)$$

where  $P(\mathbf{x}, t|s_0, 0)$  denotes the probability that the tagged atom is at  $\mathbf{x}$  at time  $t$  when it was at  $s_0$  at time  $t = 0$ , the summation for  $s'$  is taken over nearest neighbors of site  $s$ . Introducing the Laplace transformation  $\tilde{P}(\mathbf{x}, u|s_0) = \int_0^\infty e^{-ut} P(\mathbf{x}, t|s_0, 0) dt$  and decimating  $\tilde{P}(s + u_s, u|s_0)$  from the Laplace transform of Eqs. (11) and (12), we find

$$[u + \sum_{u_s} \{w_b - \frac{w_b^2}{u + w_b}\}] + \sum_{s'} w_s \tilde{P}(s, u|s_0) - \sum_{s'} w_{s'} \tilde{P}(s', u|s_0) = \delta_{s, s_0}. \quad (13)$$

We denote by  $z'$  the number of sites to which the tagged atom can stray and set  $u' \equiv u + z'w_b u/(u + w_b)$ . Then Eq.(13) reduces to

$$[u' + \sum_{s'} w_s] \tilde{P}(s, u|s_0) - \sum_{s'} \tilde{P}(s', u|s_0) = \delta_{s, s_0}, \quad (14)$$

which is nothing but the master equation for the trapping diffusion process. As we discussed above, jump rate  $\{w_s\}$  can be assumed to obey the power-law distribution

$$\Phi(w_s) = \begin{cases} \frac{p+1}{w_0^{p+1}} w_s^p & (0 \leq w_s \leq w_0) \\ 0 & (\text{otherwise}) \end{cases} \quad (15)$$

where  $\rho$  is a parameter of the model which represents the thermodynamic state of the system. In fact, from a comparison of the waiting time distribution we found [20]

$$\rho = 398[\Gamma_g - \Gamma_{\text{eff}}]^3, \quad (\Gamma_{\text{eff}} \leq \Gamma_g). \quad (16)$$

Equation (14) can not be solved analytically since  $\{w_s\}$  are random. We employ the coherent medium approximation for the master equation [19]. Namely, we find a  $u$ -dependent coherent jump rate  $w_c(u)$  by the condition

$$\int_0^\infty \frac{w_s - w_c}{w_c + (w_s - w_c)(1 - u'P_{nn})} \Phi(w_s) dw_s = 0. \quad (17)$$

Here,  $P_{nn} = \tilde{P}_c(s_0, u|s_0)$ , and the coherent Green function  $\tilde{P}_c(s, u|s_0)$  satisfies Eq.(14) where all  $w_s$  are replaced by  $w_c(u)$ . When we need numerical calculation we approximate  $P_{nn}$  by  $2\{u' + zw_c + [u'(u' + 2zw_c)]^{1/2}\}^{-1}$ . As we have shown already [21], there exists a glass transition at  $\rho = 0$ , where the diffusion constant vanishes below  $\rho = 0$ . We have also shown that the transition at  $\rho = 0$  can be understood as a change of dynamics from Gaussian to non-Gaussian [21].

#### Dynamical structure factor and generalized susceptibility

The self-part of the dynamical structure factor  $S_s(\mathbf{q}, \omega)$  and the generalized susceptibility  $\chi_s(\mathbf{q}, \omega)$  are given by

$$S_s(\mathbf{q}, \omega) = \frac{1}{\pi} \text{Re} \left[ 1 + \frac{w_b \beta(\mathbf{q})}{w_b + i\omega} \right] \sum_s e^{iq(s-s_0)} < \tilde{P}(s, i\omega|s_0) >, \quad (18)$$

and

$$\chi_s(\mathbf{q}, \omega) = 1 + i\omega \left[ 1 + \frac{w_b \beta(\mathbf{q})}{w_b + i\omega} \right] \sum_s e^{iq(s-s_0)} < \tilde{P}(s, -i\omega|s_0) >. \quad (19)$$

Here the angular brackets  $< \dots >$  denotes an ensemble average and  $\beta(\mathbf{q}) = \sum_u e^{iqu}$  is assumed to be real and independent of  $s$ . In the coherent medium approximation we approximate the ensemble average by

$$< \tilde{P}(s, u|s_0) > = \tilde{P}_c(s, u|s_0). \quad (20)$$

In order to obtain the frequency dependence of  $S_s(\mathbf{q}, \omega)$  and hence  $\chi_s(\mathbf{q}, \omega)$  we solved the self-consistent non-linear equation (17) numerically. The broken lines in Figs. 1 – 3 show the frequency dependence of  $S_s(\mathbf{q}, \omega)$ ,  $\chi_s''(\mathbf{q}, \omega)$  and  $\sigma$ , respectively. The Cole-Cole plot for the present model is shown by the broken curve in Fig. 4. In these plot, we set  $\rho = 0.2038$ , which corresponds to  $\Gamma = 1.50$  via Eq. (16),  $b/a = 0.14$ ,  $qa/2\pi = 5.88$  and  $w_b/w_0 = 20$  to get the best fit. The agreement is excellent, which indicates strongly the validity of the trapping diffusion model.

#### Relaxation time for the $\alpha$ -process

We define the relaxation time  $\tau_\alpha$  by

$$\tau_\alpha = \frac{2\pi}{\omega_{\text{max}}}, \quad (21)$$



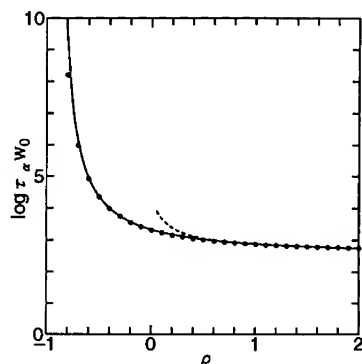


Fig. 5. The  $\alpha$ -relaxation time  $\tau_\alpha$  is shown as a function of  $\rho$ . The solid circles are obtained from the trapping diffusion model. The solid curve is a fit to the data by Eq. (22) and the dashed curve is a fit for  $\rho \geq 1$  by a curve in proportion to  $D^{-1}$ .

where  $\omega_{\max}$  is the frequency at which  $\chi''_s(\mathbf{q}, \omega)$  takes its maximum. We show by the solid circles in Fig. 5 the  $\rho$ -dependence of  $\tau_\alpha$  obtained by the present model. It is interesting to note that for  $\rho \geq 1$   $\tau_\alpha$  is closely related to the inverse of the diffusion constant  $D = \rho/(\rho+1)$ . In fact the dashed curve in Fig. 4 showing  $374(\rho+1)/\rho$  is an excellent fit of  $\tau_\alpha$  for  $\rho \geq 1$ . The observed relaxation time deviates from this behavior when  $\rho \leq 1$ . We can fit the entire dependence of  $\tau_\alpha$  on  $\rho$  by

$$\tau_\alpha^{\text{fit}} = 99 \exp \left[ 1.15 \left( \frac{\rho+2}{\rho+1} \right)^{1.4} \right], \quad (22)$$

which is shown by the solid curve in Fig. 4. Equation (22) indicates that  $\rho = -1$  appears as the Vogel-Fulcher point where  $\tau_\alpha$  diverges. In fact, we can make a detailed analysis of the self-consistent equation (17) in the low frequency limit and it is straightforward to show that for  $-1 < \rho < 0$  the low frequency behavior of  $\chi''_s(\mathbf{q}, \omega)$  is essentially determined by  $[1 + (-i\omega\tau_\alpha)^{1+\rho}]^{-1}$  which is identical to the Cole-Cole susceptibility. The relaxation time  $\tau_\alpha$  is given by

$$\frac{\tau_\alpha w_0}{2\pi} = (1+z') \left[ \frac{C^\rho \sin[\pi(1+\rho)]}{\alpha(\mathbf{q}) \pi(1+\rho)} \right]^{1/(1+\rho)}, \quad (23)$$

where  $C$  is a constant of the order of  $10^{-1}$  and

$$\alpha(\mathbf{q}) = z - \sum_{\substack{\mathbf{s} \\ \in \text{N.N. of } \mathbf{s}_0}} \exp[i\mathbf{q}(\mathbf{s} - \mathbf{s}_0)]. \quad (24)$$

Since the quantity in  $[\dots]$  in Eq. (23) takes a finite value larger than unity for the wave vectors we are concerned with, the relaxation time  $\tau_\alpha$  diverges exponentially at  $\rho = -1$ .

## CONCLUSIONS

In this paper, we first showed by MD simulation for the binary soft-sphere mixtures that (1) the  $\alpha$  peak as well as the  $\beta$  peak exists in the generalized susceptibility  $\chi''(\mathbf{q}, \omega)$ , (2) the  $\alpha$  relaxation exists for temperatures significantly lower than the kinetic transition temperature ( $\Gamma_X = 1.45$ ) and the mode coupling glass transition temperature ( $\Gamma_C = 1.32$ ) [22], and (3) the  $\beta$ -relaxation is essentially a Debye-type relaxation.

We have also presented the trapping diffusion model for the glass transition constructed on the basis of the observation for the mesoscopic dynamics in supercooled fluids. We showed that  $\alpha$ -relaxation observed in a certain time window is due to the jump motion and  $\beta$ -relaxation is due to the stray motion. We also showed that the relaxation time for the  $\alpha$ -process diverges at  $\rho = -1$  not at  $\rho = 0$  where the glass transition takes place in line with the Vogel-Fulcher behavior.

We can understand these characteristic temperatures from the waiting time distribution (WTD) of the jump motion. For  $\rho \leq -1$ , WTD is not be normalizable, which means that atoms cannot make any jump forever. For  $-1 < \rho \leq 0$ , the mean waiting time diverges and the system is in an anomalous diffusion regime, where the dynamics becomes non-Gaussian and the Kohlrausch-William-Watts (KWW) relaxation is expected in the long time limit. When  $0 < \rho \leq 1$ , the fluctuation of waiting time diverges and the dynamics is in a sub-anomalous regime, where the KWW relaxation is expected in the finite time domain though the dynamics is Gaussian. As we have already shown elsewhere [19], we expect to see the glass transition at  $\rho = 0$  and a kinetic transition at  $\rho = 1$ . We can also give a heuristic model which shows that  $\rho = -1$  corresponds to the Kauzmann temperature [23]. The trapping diffusion model thus provides an excellent phenomenological description of slow dynamics and gives a unified understanding of the singularities observed in supercooled fluids around the glass transition point.

Finally, we would like to mention to the mode coupling model of the glass transition. According to the mode coupling theory (MCT) [24], a supercooled liquid undergoes structural arrest at a certain temperature above the observed glass transition point. In this approach, this structural arrest or an ergodic-nonergodic transition is considered as the ideal glass transition, and the Vogel-Fulcher and glass transition points are considered to be artifacts of the data analysis. Although some experiments [6,10] seem to be well explained by MCT, some predictions of MCT have been shown to contradict to experiments or MD simulations. For example, the KWW exponent  $\beta$  is shown not to be constant as a function of temperature [25], in contrast to the prediction of the mode coupling theory. Furthermore, recent extensive analysis of experiments revealed that the hopping motion plays a significant role in determining the relaxations [26]. Therefore the description of atomic dynamics based on the localized picture seems to be important to understand the slow dynamics and the glass transition, which is effectively provided by TDM.

## ACKNOWLEDGEMENT

This work was supported in part by the Grant-in-Aid for Scientific Research from Ministry of Education, Science and Culture.

## REFERENCES

- [1] G. E. Gibson and W. F. Giaque, *J. Am. Chem. Soc.* **40**, 93 (1923).
- [2] H. Vogel, *Phys. Zeit.* **22**, 641 (1921); G. S. Fulcher, *J. Am. Cer. Soc.* **8**, 339 (1925).
- [3] W. Kauzmann, *Chem. Rev.* **43**, 219 (1948).
- [4] G. P. Johari and M. Goldstein, *J. Chem. Phys.* **53**, 2372 (1970); C. A. Angell, *J. Phys. Chem. Solids* **49**, 863 (1988).
- [5] F. Mezei, W. Knaak, and B. Farago, *Phys. Rev. Lett.* **58**, 571 (1987); W. Knaak, F. Mezei, and B. Farago, *Europhys. Lett.* **7**, 529 (1988).
- [6] N. J. Tao, G. Li and H. Z. Cummins, *Phys. Rev. Lett.* **66**, 1334 (1991); G. Li, W. M. Du, X. K. Chen, H. Z. Cummins and N. J. Tao, *Phys. Rev. A* **45**, 3867(1992).
- [7] G. Li, W. M. Du, A. Sakai and H. Z. Cummins, *Phys. Rev. A* **46**, 3343 (1992).
- [8] D. L. Sidebottom, R. Bergmann, L. Börjesson and L. M. Torell, *Phys. Rev. Lett.* **68**, 3587 (1992); **71**, 2260 (1993).
- [9] W. van Megen and S. M. Underwood, *Phys. Rev. E* **47**, 248 (1993).
- [10] J. Coleméro, A. Arbe and A. Alegría, *Phys. Rev. Lett.* **71**, 2603 (1993); E. W. Fischer, *Physica A* **201**, 183 (1993); J. Wuttke, J. Hernandez, G. Li, G. Goddens, H. Z. Cummins, F. Fujara, W. Petry and H. Sillescu, *Phys. Rev. Lett.* **72**, 3052 (1994).
- [11] H. Miyagawa, Y. Hiwatari, B. Bernu, and J. P. Hansen, *J. Chem. Phys.* **88**, 3879 (1988).
- [12] G. F. Signorini, J. L. Barrat, and M. L. Klein, *J. Chem. Phys.* **92**, 1294 (1990).
- [13] H. Miyagawa and H. Hiwatari, *Phys. Rev. A* **44**, 8278 (1991).
- [14] G. Wahnström, *Phys. Rev. A* **44**, 3752 (1991).
- [15] W. Kob and H. C. Andersen, *Phys. Rev. Lett.* **73**, 1376 (1994).
- [16] H. Miyagawa, Y. Hiwatari and S. Itoh, *Prog. Theor. Phys. Suppl.* **103**, 47 (1991).
- [17] B. Bernu, Y. Hiwatari and J. P. Hansen, *J. Phys. C* **18**, L371 (1985); B. Bernu, J. P. Hansen, Y. Hiwatari and G. Pastore, *Phys. Rev. A* **36**, 4891 (1987); G. Pastore, B. Bernu, J. P. Hansen and Y. Hiwatari, *Phys. Rev. A* **38**, 454 (1988).
- [18] J. Matsui, H. Miyagawa, T. Muranaka, K. Uehara, T. Odagaki and Y. Hiwatari, *Mol. Sim.* **12**, 305 (1994); J. Matsui, T. Odagaki and Y. Hiwatari, *Phys. Rev. Lett.* **73**, 2452 (1994).
- [19] T. Odagaki, J. Matsui and Y. Hiwatari, *Phys. Rev. E* **49**, 3150 (1994).
- [20] T. Odagaki and Y. Hiwatari, *J. Phys.: Cond. Matt.* **3**, 5191 (1991).

- [21] T. Odagaki and Y. Hiwatari, Phys. Rev. A **41**, 929 (1990); A **43**, 1103 (1991).
- [22] J. L. Barrat and A. Latz, J. Phys. : Cond. Matt. **2** 4289 (1990).
- [23] T. Odagaki, J. Matsui and Y. Hiwatari, unpublished.
- [24] W. Götze, in Liquids, Freezing and the Glass Transition, edited by J. P. Hansen *et al* (North Holland, Amsterdam, 1991), 287; W. Götze and L. Sjögren, Rep. Prog. Phys. **55**, 241(1992).
- [25] S. Kambayashi and Y. Hiwatari, J. Phys. Soc. Japan, **56**, 2788 (1987).
- [26] H. Z. Cummins, W. M. Du, M. Fuchs, W. Götze, S. Hildebrand, A. Latz, G. Li, and N. J. Tao, Phys. Rev. E **47**, 4223 (1993); H. Z. Cummins, G. Li, W. M. Du and J. Hernandez, Physica A **204**, 169 (1994).

## AGING AND GLASSY DYNAMICS IN COMPLEX SYSTEMS: SOME THEORETICAL IDEAS

Jean-Philippe BOUCHAUD

Service de Physique de l'Etat Condensé, Commissariat à l'Energie Atomique, Orme des  
Merisiers, 91191 Gif-sur-Yvette CEDEX, France

### ABSTRACT

We discuss some recent experimental results on the non-stationary dynamics of spin-glasses, which serves as an excellent laboratory for other complex systems. Inspired from Parisi's mean-field solution, we propose that the dynamics of these systems can be thought of as a random walk in phase space, between traps characterized by trapping time distribution decaying as a power law. The average exploration time diverges in the spin-glass phase, naturally leading to time-dependent dynamics with a characteristic time scale fixed by the observation time  $t_w$  itself (aging). By the same token, we find that the correlation function (or the magnetization) decays as a stretched exponential at small times  $t \ll t_w$  crossing over to power-law decay at large times  $t \gg t_w$ . Finally, we discuss recent speculations on the relevance of these concepts to real glasses, where quenched disorder is a priori absent.

Keywords: Aging, slow dynamics, spin-glasses, glasses.

One of the most striking features of glassy dynamics is the *aging* phenomenon [1,2], that is, the fact that most physical properties strongly depend on the history of the sample, in particular the time  $t_w$  elapsed since the quench from high temperature into the glass phase. For example, the a.c. susceptibility of a spin-glass at a frequency  $\omega$  decays towards its equilibrium value as  $(\omega t_w)^{x-1}$ , where  $x$  is an exponent less than 1. In fact, the full response function  $R(t, t')$  does not depend on the *difference*  $t - t'$ , as in usual equilibrium dynamics, but rather on the *ratio*  $\frac{t}{t'}$ . Since the equilibration time is infinite, the only relevant time scale can only be the experimental time itself. In this sense, time translation

invariance is broken. Similar effects were observed in other contexts, such as the mechanical or dielectric properties of various glasses [2].

The theoretical investigation of this peculiar type of dynamics is only quite recent, but extremely active [3]. An immediate formal difficulty is that the usual time Fourier transform is useless and one must keep two-time functions all along. Furthermore, the fluctuation-dissipation theorem is no longer valid, and some interesting suggestions for a generalised form of this theorem have been discussed [3]. Several phenomenological descriptions have been suggested, based in particular on the idea of 'coarsening' of domains [4,5]. A simple picture, based on mean-field solutions of the spin-glass problem, was proposed in [6]. A remarkable result found within these mean-field theories [7] is that the (free-)energy distribution of the low-lying states is *exponential*:

$$P(\epsilon) = \frac{x}{T} \exp\left[-\frac{x|\epsilon|}{T}\right], \quad \epsilon < 0 \quad (1)$$

with a certain number  $x$  which happens to be  $\leq 1$  in the whole spin-glass phase. For example,  $x = \frac{T}{T_g}$  in the Random Energy Model, where  $T_g$  is the glass transition temperature.

Now it is reasonable to assume that the energy barrier  $\Delta$  that the system will have to cross in order to leave a particular metastable state is related to  $\epsilon$ ; the simplest possibility is that  $\Delta = -\epsilon$ . The time spent in a certain metastable state is thus given by  $\tau = \tau_0 \exp[\frac{\Delta}{T}]$ . An 'exponential conspiracy' then comes into play and transforms the exponential distribution (1) into a power-law distribution  $P(\tau) \propto \frac{\tau^x}{\tau^{1+x}}$  for these 'trapping' times, where the traps should be thought of as deep valleys in phase space.

The key point to notice is that the probability to *observe* the system in a given trap is not simply  $P(\tau)$  since it is *a priori* more probable to find the system in a state in which it remains for a long time. The naive guess is that the probability to observe the system in a given trap is  $\mathcal{P}(\tau, t_w) \propto \tau P(\tau)$ . However, when the index  $x$  is less than 1, the integral  $\int_0^\infty d\tau \tau P(\tau)$  diverges, and  $\mathcal{P}$  would not be normalizable!

The regularization comes from the experimental time scale  $t_w$  itself: as usual for broadly distributed events [8], the sum of the  $N$  successive trapping times is of the order of the largest (rarest) one encountered, itself being of order  $t_w$ . More precisely, one can

show that:

$$\mathcal{P}(\tau, t_w) = \frac{\tau_0^{x-1}}{\tau^x} g\left(\frac{\tau}{t_w}\right) \quad \text{for } x > 1 \quad (2-a)$$

$$\mathcal{P}(\tau, t_w) = \frac{t_w^{x-1}}{\tau^x} g\left(\frac{\tau}{t_w}\right) \quad \text{for } x < 1 \quad (2-b)$$

where  $g(u)$  is a certain cut-off function. Note that for  $x < 1$ , the microscopic time  $\tau_0$  *totally disappears* from  $\mathcal{P}(\tau, t_w)$ :  $t_w$  is the only relevant time scale for the dynamics, as observed experimentally. Furthermore, the relaxation function is expected (from Eq. (2-b)) to decay as  $1 - (\frac{t}{t_w})^{1-x}$  for  $t \ll t_w$ , corresponding to the relaxation of 'fast' traps  $\tau < t$ , and as  $(\frac{t_w}{t})^x$  for  $t \gg t_w$ , corresponding to the fraction of very 'deep' traps still surviving after time  $t$ . Such a behaviour is indeed observed in many glassy systems: the initial decay  $1 - (\frac{t}{t_w})^{1-x}$  is better known as a *stretched exponential*  $\exp -(\frac{t}{t_w})^{1-x}$ .

A somewhat more refined version of this simple picture, inspired by Parisi's hierarchical 'replica symmetry broken' solution of the SK model [7], is needed to account for the data in a quantitative manner [9]. In particular, the  $(\omega t_w)^{x-1}$  behaviour of the a.c. susceptibility mentioned above is obtained. More subtle aspects, such as temperature cycling experiments, revealing spectacular *memory effects* [10], or the 'second noise spectrum' measured by Weissmann et al. [11] can also be accounted for very naturally within this framework [9].

The basic remark of Fisher, Huse, Koper and Hilhorst [4] that the flipping spins are clustered somewhere in space and that the time scales should grow with the size of these clusters seems however unavoidable. How can this be reconciled with the above picture and 'replica symmetry breaking'? Of course, a proper replica (or dynamical) theory in finite dimension is needed to answer completely this question. Such a theory is not yet available for spin glasses, but has been worked out for the simpler problems of manifolds in random media [12] (i.e. polymers, surfaces, vortex lattices. etc..). One basically finds that the order parameter function  $q(x)$  becomes  $L$  (scale) dependent, with a characteristic value of  $x(L)$  varying as  $L^{-\theta}$ : small scales correspond to large  $x$ . From Eq. (1) and the interpretation of  $x(L)$ , one thus sees that the energy distribution for the excitations ('droplets') of scale  $L$  has the form:

$$\rho(f, L) = \frac{1}{f_0 L^\theta} \exp\left(-\frac{|f|}{f_0 L^\theta}\right) \quad (3)$$

showing, as postulated by Fisher and Huse, that the energy scale grows as  $L^\theta$ . At this stage, an important difference with Fisher and Huse is the exponential form of the distribution. Interestingly, Eq. (3) means, within our interpretation, that there is a spin-glass transition temperature  $T_g(L)$  associated with each scale, defined through  $x(L, T_g(L)) = 1$ . The infinite sequence of micro-phase transitions suggested in [1,10] thus corresponds to a progressive ‘weak ergodicity breaking’ (in the sense that  $x(L)$  crosses 1) of smaller and smaller length scales (faster and faster degrees of freedom).

The idea has recently emerged [14,13] that a ‘true’ glass is a system in which disorder is ‘self-induced’ – and is thus in some sense rather close to other ‘quenched’ disordered systems, such as spin glasses. A natural idea is that the glass transition is defined by the temperature at which the relaxation time spectrum loses its first moment, and is thus *essentially dynamical*. Exactly this scenario seems to underlie the glass transition in hard sphere systems [15]: the trapping time distribution for a ‘tagged’ particle within the cage formed by its neighbours decays as  $\tau^{-1-x}$  with  $x$  crossing 1 at the glass transition\*. This suggests, as noticed in [15], that the motion of a tagged particle is subdiffusive [8] ( $R^2(t) \propto t^x$ ) in the glass phase, but more importantly that aging effects should be present, in particular in the dynamical structure factor. To the best of our knowledge this has not been reported; the experimental procedure is however not straightforward since one cannot average over sequences corresponding to different waiting times, as is usually done since one implicitly assumes time translation invariance. Furthermore, the long time ‘interrupted aging’ regime [6] should be avoided.

---

\*Note that the persistence of a power-law distribution of relaxation times *above the glass temperature* and thus with  $x > 1$  has also been reported in dipolar glasses (see [16])



In summary, we have proposed a simple model in which aging occurs because of the very broad nature of the relaxation time distribution. Correspondingly, the 'equilibrium' state is non-normalizable and thus equilibrium is never fully achieved : only a time dependent, partial equilibrium is reached. <sup>†</sup> This is what we have called 'weak ergodicity breaking' [6]. It would be interesting to perform careful experiments to detect these aging effects in the dynamical structure factor of glass forming liquids. It also suggests that the mode coupling theory developed to describe the glass transition should not be formulated *a priori* in a time translational invariant way.

*Acknowledgments* I wish to thank many people for sharing with me their insights on the aging problem, in particular L. Cugliandolo, D. S. Dean, S. Franz, J. Hammann, J. Kurchan, M. Mézard, H. Rieger, M. Ocio and E. Vincent.

## REFERENCES

- [1] for a review, see: E. Vincent, J. Hammann, M. Ocio, p. 207 in "Recent Progress in Random Magnets", D.H. Ryan Editor, (World Scientific Pub. Co. Pte. Ltd, Singapore 1992)
- [2] L.C.E. Struick, "Physical Aging in Amorphous Polymers and Other Materials" (Elsevier, Houston, 1978)
- [3] L. Cugliandolo, J. Kurchan, Phys. Rev. Lett. **71** 173 (1993), S. Franz, M. Mézard, Europhys. Lett. **26** 209 (1994), Physica **A209** 1 (1994), L. Cugliandolo, J. Kurchan, J. Phys. A **27** 5749 (1994), H. Rieger, preprint (cond-mat, October 94)
- [4] D.S Fisher, D.A. Huse, Phys. Rev. Lett **56**, 1601 (1986), Phys. Rev. **B 38**, 373 (1988), G.J. Koper, H.J. Hilhorst, J. Physique (France) **49** 429 (1988)

---

<sup>†</sup>Another interesting example where this mechanism operates is in a particular 'subrecoil laser cooling' scheme [17]

- [5] A. J. Bray, *Theory of phase ordering kinetics*, to appear in Adv. Physics (1994)
- [6] a- J.P. Bouchaud, J. Physique I (France) 2, 1705 (1992) , b- J.P. Bouchaud, E. Vincent, J. Hammann, J. Physique I (France) 4, 139 (1994)
- [7] M. Mézard, G. Parisi, M.A. Virasoro, "Spin Glass Theory and Beyond", (World Scientific, Singapore 1987), B. Derrida, Phys. Rev. B 24, 2613 (1981), D.J. Gross, M. Mézard, Nucl. Phys. B240 431 (1984).
- [8] J.P. Bouchaud, A. Georges, Phys. Rep. 195 127 (1990)
- [9] J.P. Bouchaud, D.S. Dean, 'Aging on Parisi's tree', submitted to J. Physique I
- [10] J. Hammann, M. Lederman, M. Ocio, R. Orbach, E. Vincent, Physica A 185, 278 (1992), F. Lefloch, J. Hammann, M. Ocio, E. Vincent, Europhys. Lett 18, 647 (1992)
- [11] G. B. Alers, M. B. Weissmann, N.E. Isrealoff, Phys. Rev. B 46, 507 (1992), M. B. Weissmann, N.E. Isrealoff, G. B. Alers, Journal of Magn. Magn. Mat. 114, 87 (1992), and M. B. Weissmann, Rev. Mod. Phys., July 1993.
- [12] M. Mézard, G. Parisi, J. Physique I 1 809 (1991), J.P. Bouchaud, M. Mézard, J. Yedidia, Phys. Rev B 46 14 686 (1992)
- [13] J.P. Bouchaud, M. Mézard J. Phys. I France 4 1109 (1994), E. Marinari, G.Parisi, F.Ritort, *Replica Field Theory for Deterministic Models: Binary Sequences with Low Autocorrelation I and II* preprint cond-mat/9406074, L. F. Cugliandolo, J. Kurchan, G.Parisi, F.Ritort, *Matrix Models as solvable Glass Models* to appear in Phys. Rev. Lett., S. Franz, J. Hertz, *Glassy transition and aging in a model without disorder* preprint cond-mat/9408075, T. Blum, J. Doherty, M.A. Moore, J.P. Bouchaud, P. Claudin, *Glassy solutions of the KPZ equation*, submitted to Phys. Rev. Lett.
- [14] T. Kirkpatrick, D. Thirumalai, J. Phys. A 22 L149 (1989)
- [15] T. Odagaki, J. Matsui, Y. Hiwatari, Physica A 204 464 (1994).

- [16] P. Doussineau, Y. Farssi, C. Frénois, A. Levelut, J. Toulouse, S. Ziolkiewicz, J. Phys. I (France) 4 1217 (1994). The dielectric properties of  $K_{1-y}Li_yTaO_3$  in the high temperature phase are well described by an power law distribution of relaxation time with  $x \simeq \frac{T}{T_g} > 1$ .
- [17] F. Bardou, J.P. Bouchaud, O. Emile, A. Aspect, C. Cohen-Tannouji, Phys. Rev. Lett 72 203 (1994)

## SLOW RELAXATION IN POLYMERIC GLASSES BY TWO-DIMENSIONAL NMR

ALAN A. JONES, P. T. INGLEFIELD, Y. H. CHIN AND C. ZHANG  
Carlson School of Chemistry, Clark University, Worcester, Ma. 01610

### Introduction

A variety of relaxation and recovery experiments on polymeric glasses indicate a complex response in either the time or frequency domain<sup>1</sup>. The behavior is far from that seen in simple liquids where relaxation can be characterized in terms of exponential decay and a single time constant or rate. A variety of more complicated mathematical functions have been employed in an attempt to match the observed relaxation behavior of polymeric glasses<sup>1</sup>. One of the more successful mathematical forms is the stretched exponential correlation<sup>2</sup> function which can be used to characterize experimental observations obtained from mechanical, dielectric, thermodynamic and spectroscopic investigations<sup>3</sup>.

The experimental results can be thought of in terms of a distribution of exponential correlation times and indeed a mathematical form can be given for the distribution of exponential correlation times corresponding to the stretched exponential function or other functions which are used to interpret experimental results. If one thinks in terms of such a distribution, the time scales can be divided into faster and slower components<sup>4</sup>. This can be done if there is a characteristic time scale of the experiment which allows for a discussion of "slow relaxation" though slow relaxation can also be viewed in another context, aging. If a glass near the apparent glass transition is shifted to a new temperature system, volume changes. There may be very rapid volume fluctuations but there will also be a slow evolution of volume towards a final state which is often discussed as the process of aging.

NMR spectroscopy has contributed significantly to the development of an understanding of relaxation in glasses over the past decade. NMR is most sensitive to local magnetic interactions over a distance scale of Angstroms or nanometers and is particularly useful in monitoring reorientation in glasses over this distance scale. The NMR experiment is usually performed under a steady state condition where the dynamics of the glass is not expected to be evolving though it is always questionable whether this is actually achieved. In addition, there is no perturbation of

the glass from a steady state in an NMR experiment. The nuclear spin system is only weakly coupled to the glass and can serve as a probe which does not perturb the system. In the case of a typical mechanical or thermodynamic experiment, the macroscopic system may be perturbed. Thus in the NMR experiment the molecular reorientation can be studied which takes place in the glass at a given temperature as a result of thermal energy associated with that temperature.

#### Heterogeneous Relaxation

One key result of carbon-13 and deuterium NMR experiments on glasses in the last fifteen years is to clearly demonstrate that the complex time response of a glass is heterogeneous<sup>5-7</sup>. This means that over the time scale of measurement, say one second, the reorientational motion which might have an average time scale of milliseconds also has a distribution of time scales extending over a few decades. The distribution is primarily associated with different spatial locations in the glassy sample having different time scales of relaxation. The different time scales at the various locations in the sample are not interchanged during the overall time scale of the experiment, one second in the example chosen. Thus NMR sees different reorientational time scales in different spatial regions of the glass and during the time scale of the experiment the time scale of motion in a particular region doesn't change.

In carbon-13 NMR heterogeneous relaxation manifests itself as a non-exponential relaxation time in a  $T_{1\rho}$  experiment<sup>5</sup> and as a superposition of broad and narrow lines in carbon-13 and deuterium line shape experiments<sup>7</sup>. If molecular reorientation were homogeneous, that is, the same at all spatial locations in the sample, but characterized by a nonexponential correlation function, exponential decay would be seen in the spin relaxation experiments and the line shape would be a single line shape not a superposition of line shapes.

The experimental manifestation of heterogeneous relaxation can be changed by a shift in temperature so that rapid spatial exchange of time constants occurs during the time scale of the experiment. Thus the same measurement of a carbon-13  $T_{1\rho}$  at a higher temperature will appear exponential. There will also be an intermediate regime where the relaxation is only partially averaged over spatial locations.

The interpretation of these NMR relaxation experiments in terms of the stretched exponential is complicated by the degree to which the

spatial inhomogeneity of relaxation affects the data. In one of the more conceptually useful derivations of the stretched exponentially, diffusing defects are imagined to pass over a distribution of energy barriers leading to relaxation which displays stretched exponential behavior<sup>8-10</sup>. In a polymeric glass the defect could either be an intramolecular conformation in the chain backbone or an intermolecular high free volume region. Either of these defects could be imagined to diffuse through the glass leading to relaxation. If the time scale of the experiment is long so that these defects relax all regions, then the connection between this derivation and the observed relaxation would seem to be valid.

In an NMR experiment where inhomogeneous relaxation is observed, local regions are observed to relax at different rates. In a defect region could be identified with fast relaxation and a non-defect regions with slow relaxation. However during the course of the NMR experiment there is at least some prospect of exchange of fast relaxing and slow relaxing regions. This has been clearly identified in a multidimensional NMR experiment<sup>11</sup> where a slowly relaxing region eventually evolved into faster relaxing regions. In a two-dimensional NMR experiment there are two axes labeled by frequency which corresponds to orientation. One axis is the orientation at an arbitrary time zero and the second axis is the orientation at specific time,  $t$ , later. In this experiment a wide variety of reorientational correlation times are required to simulate the observed pattern including fast relaxing and slow relaxing components. In a three dimensional experiment, the slow relaxing components were monitored to see if they remained slow. On a time scale corresponding to the longer correlation times of the distribution of correlation times some of the slowly relaxing components became fast relaxing. Conceptually this is consistent with the idea of fast relaxing defects moving through the glass but a quantitative interpretation of relaxation in a particular experiment will be some mix of homogeneous and inhomogeneous relaxation. The mix will change with the time scale of the experiment and with temperature, but whatever the mix the stretched exponential correlation function can be used to fit the relaxation data. In so much as the relaxation is inhomogeneous or a mix between inhomogeneous, the derivation from a picture of defect diffusion is inappropriate for application to this experiment and this system.

The exchange of fast relaxing and slow relaxing regions seems to take place at the slow end of the general distribution of relaxation times. Thus a given NMR experiment is sensitive to both fast and slow processes and the processes are intertwined. Trying to separate slow relaxation from fast relaxation in an NMR experiment seems likely to be arbitrary and artificial. However, various aspects of the fast and slow relaxation

regions can be measured and changes in the composition of the glass can be used to introduce either fast or slowly relaxing regions.

#### Size of Defects or Fast Relaxing Regions

In a particular glassy polycarbonate just below the glass transition temperature, the proton line shape is simple and consists of a broadened Pake doublet<sup>12</sup>. As the glass transition region is traversed, the line shape changes to a composite line consisting of the broadened Pake plus a narrow Lorentzian line shape. The narrow line shape is associated with high mobility and the fraction of polymer with high mobility represented by the narrow component follows the Vogel-Tamman-Fulcher relationship as temperature is raised.

The size of the high mobility regions can be measured using the proton line shape and monitoring proton spin diffusion from the mobile region to the less mobile region<sup>13</sup>. At 30 degrees above the glass transition temperature, the mobile region has a radius of 30 Angstroms and comprises about 12 per cent of the glass. As temperature is increased, the size of the mobile region grows. If one extrapolates to the glass transition temperature, the radius of the high mobility region is approximately 10 Angstroms and comprises only about 1 percent of the glass. A region of this size contains only a small fraction of the polymer chain and indeed is close to the dimensions of the repeat unit. Thus it would seem that the mobile regions could be considered defects at temperatures near the glass transition and the defect corresponds to a few mobile repeat units. The question of whether these repeat units belong to one chain or involve several chains remains open; or stated in another fashion, whether these defects are intramolecular or intermolecular in nature.

#### Multicomponent Glasses

One approach available to study localized mobile regions in a glass is to modify the chemical constituents of the glass. The systems discussed thus far have been polymeric glasses consisting of high molecular weight polymers composed of identical repeat units. NMR has been used to study

two types of chemical modifications of this basic system: first mixed glasses of a high molecular weight polymer plus a low molecular weight diluent and secondly mixed glasses consisting of two miscible high molecular weight polymers.

The addition of a low molecular weight compound with an intrinsically low glass transition temperature to a polymeric glass of higher glass transition temperature might be viewed as a method for increasing the number of mobile defects in a polymer glass. Such systems are of significant practical interest since many technological applications of polymeric glasses involve the addition of low molecular weight compounds and these are also ideal systems for study by NMR since the diluent and the polymer can frequently be distinguished spectroscopically allowing for independent monitoring of the mobility of each component.

Typical bulk properties of polymer/diluent systems can be briefly summarized by introducing some polymer science nomenclature for these systems. The glass transition of such mixed glasses is lowered relative to the pure polymer but the modulus of the system can either be lower or higher which is referred to as plasticized or antiplasticized respectively<sup>14-15</sup>. The lowering of the glass transition by the addition of a low molecular weight, low glass transition temperature compound seems intuitively reasonable. However, the possibility of either increasing or decreasing the modulus is more difficult to rationalize. A higher modulus or antiplasticized system would generally be associated with a more rigid, less mobile system which is difficult to mesh with the addition of a low glass transition temperature component. However the increase in modulus in an antiplasticized system is associated with a reduction of sub-glass transition motions not a reduction in glass transition motions. Thus in an antiplasticized glass, glass transition motions are enhanced and sub-glass transition motions are suppressed. In a plasticized glass both types of motions are enhanced. As we shall see these generalizations are not so easily applied as concentrations, temperatures and frequencies of observation are varied.

The dynamics and structure of one type of polymer diluent systems has been studied in detail by NMR with considerable mechanical and thermal characterization information available as well<sup>15-18</sup>. The system consists of polycarbonate (BPA-PC) as the polymeric host and trioctyl phosphate (TOP) as the diluent. The systems are optically clear and homogeneous down to the level of molecular dimensions. The thermal glass transition temperature of the polymeric host is 160°C while that of the diluent is -134°C. As the content of the TOP in the mixed glass is raised the thermal glass transition temperature is lowered so that by the time a concentration of 15 weight percent TOP is reached the transition



temperature is 74°C. The glass transition in the polymer or in the pure diluent is associated with the onset of rotational mobility. In the mixed glasses, the rotational dynamics of the TOP was determined from the solid state phosphorous-31 line shape. At temperatures as low as 50° below the thermal glass transition temperature, the presence of rapidly rotating TOP was observed<sup>16-17</sup>. However the rotational mobility of the diluent was bimodal with both rapidly rotating and rotationally restricted molecules present. The rotationally restricted molecules were actually only observed to execute rotation over a limited solid angle. The ratio of rapidly rotating to restricted molecules was both temperature and concentration dependent with the presence of molecules with restricted rotational character persisting until the thermal glass transition temperature is reached.

The concentration dependence of the ratio of mobile to less mobile molecules was explained by a lattice model and nearest neighbor contacts<sup>16-17</sup>. Diluent molecules in contact with other diluent molecules had considerable rotational freedom below the glass transition while those surrounded by polymer did not achieve rotational mobility until the thermal glass transition temperature. The size of the mobile diluent regions<sup>18</sup> was measured by a proton spin diffusion experiment which confirmed that rotational freedom existed over a domain of about 10 to 15 Angstroms and contained only a couple of diluent molecules in agreement with the lattice explanation.

It would appear that in one sense, the introduction of mobile diluent molecules distributes mobile defects throughout the glass. These defects do introduce mobility into the immediately adjacent polymer units<sup>17-18</sup> but these defects do not diffuse or redistribute themselves on the time scale of the distribution of reorientational relaxation times as was observed at the glass transition in pure polymer<sup>11</sup>. Thus these defects appear to have their own glass transition which is defined as the onset of rotational mobility for the purposes of this discussion. The rotational mobility of the defects is not fully coupled to the remaining polymeric glass so that the rotational mobility of the latter component occurs at a significantly higher temperature. The remaining polymeric glass does contain isolated diluent molecules and does have a lower glass transition than pure polymer. Thus the isolated diluent molecules change the nature of the dynamics of the glass transition but do not exist as highly mobile defects with a well separated rate of rotational motion. The diluent molecules in contact with other diluent molecules do behave as mobile defects with a rotational mobility at least partially independent of the surrounding glass. The behavior of the bulk mixed glass material shows only one thermal glass transition temperature in a conventional

differential scanning calorimetry experiment but two mechanical loss peaks can be observed for these systems<sup>15</sup>. A lower temperature loss associated with mobility of the diluent-diluent contacts is quite distinct from the loss associated with the onset of rotational mobility of the polymer.

The glass transition has been studied in a second class of mixed polymeric glasses, polymer blends. The same polycarbonate originally employed in the proton line shape study which indicated the presence of heterogeneous relaxation through composite line shape consisting of broad and narrow components can be blended with poly(methyl methacrylate) (PMMA)<sup>19</sup>. The PMMA has a glass transition temperature which is about fifty degrees lower than the polycarbonate and the blend shows only a single thermal and mechanical transition. The mobility of the polycarbonate in the blend can be monitored independently from the PMMA if deuterated PMMA is blended with the polycarbonate. In that case, the proton line shape originates almost entirely from the polycarbonate component of the mixed glass.

As discussed above, pure polycarbonate has a proton line shape consisting of a broad Pake component plus a narrow Lorentzian component in the vicinity of the thermal glass transition. In the blend with deuterated PMMA, the proton line shape of the polycarbonate consists of the same two components. The aspect that changes is that the temperature at which the narrow Lorentzian component appears. This temperature is lowered as the content of PMMA is raised in the blend. Thus the PMMA with the intrinsically lower glass transition temperature has modified the onset of rotational mobility and thus the glass transition of the higher glass transition component. The initial growth of the mobile fraction of the polycarbonate,  $\delta$ , continues to follow the Vogel-Tamman-Fulcher equation

$$\delta = \delta_0 \exp(-B / (T-T_0)) \quad (1)$$

with the parameters  $B$  and  $T_0$  decreasing as the PMMA content is raised.

To establish the time scale of motion specific to each of the two components of a polymer blend, a series of two-dimensional NMR experiments<sup>20-21</sup> were performed on isotopically labeled blends of a different system: poly(styrene) (PS) and poly(2,6-dimethyl-1,4-phenylene oxide) (PXE). The proton NMR measurement just discussed indicates that the mobility of the lower glass transition temperature component of the polymer blend induces the onset of rotational mobility in the higher glass transition component at lower temperatures. One assumes complimentary

changes by the high glass transition component on the low glass transition component and the two-dimensional NMR experiments allows for the establishment of the time scale of rotational motion for each of the two components. The bimodal motion of the diluent in a polymer represents an extreme case where a fraction of the low glass transition component undergoes rotation one hundred degrees below the onset of comparable mobility in the high glass transition component.

In the polymer blend studied, PXE has a glass transition as a pure polymer which is over 100 degrees higher than PS. The thermal and mechanical data on the bulk blend show only a single intermediate glass transition which is slightly broader than the pure materials. The two-dimensional NMR study indicates a bimodal distribution of relaxation times for both the PXE and the PS components in a 75 wt % PS/ 25 wt % PXE blend. The actual distribution of correlation times is shown in Figure 1 at a temperature near the glass transition. What is particularly striking about the distributions in Figure 1 is that the bimodal distribution for each component is very nearly the same. The relative weighting of the two modes in the distribution was related to the nearest neighbor environment of the repeat unit being observed. Thus for instance it was found that the rate of rotational motion of a PXE unit surrounded by PS units was essentially the same as PS unit surrounded by PS units.

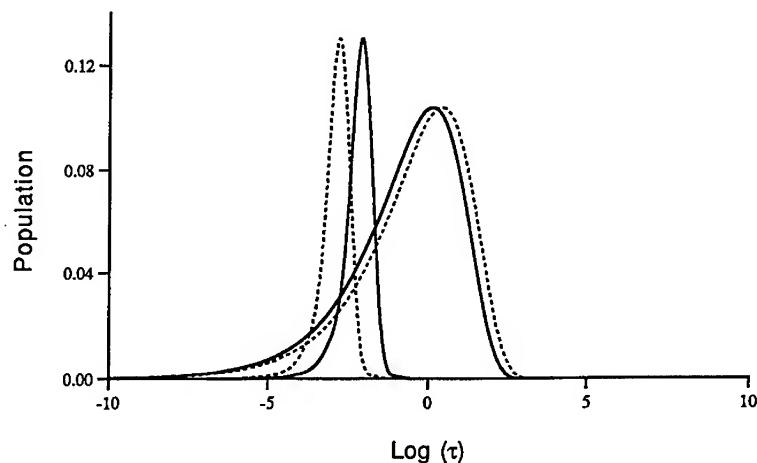


Fig 1. Population of exponential correlation times versus the logarithm of the correlation time. The distribution of correlation times for PS (dashed line) and PXE (solid line) in the 75/25 blend is shown near the glass transition.

The local intermolecular environment was the determining factor in the modal character of the distribution of correlation times with only a small residual contribution from the intrinsic glass transition temperature of the pure polymer for the type or repeat unit being observed. Furthermore, the glass transitions of the two components as indicated by rotational mobility is very nearly merged in time and temperature in spite of the fact that they are initially separated by over one hundred degrees. The merging of the rotational dynamics in this mixed glass composed of polymers is quite different from the well separated time scales for rotational mobility in the mixed glass composed of a low molecular weight compound and a polymer. The more nearly merged dynamics of this polymer blend is attributed to the cooperative nature of the rotational motion in this system as opposed to a lesser degree of cooperativity observed in the diluent-polymer system. In the polymer-polymer system the lower glass transition material, PS, does not introduce mobile defects into the higher glass transition material when they are blended. Rather there is a shift in the cooperative dynamics of both materials in the blend to an intermediate situation.

Proton spin diffusion studies have also been performed on the PS/PXE blend to determined structure in this system<sup>22</sup>. The structural interpretation from spin diffusion matches the local view of structure developed to interpret the glass transition dynamics. From the view of both dynamic and structure determinations, the blend is very homogeneous down to near repeat unit scale; and at that scale structure and dynamics can be understood on the basis of simplistic nearest neighbor considerations. The heterogeneity of the glass transition is increased modestly by the presence of quite localized concentration variations of materials with very different intrinsic rotational dynamics but the cooperativity in the system very nearly merges the dynamic behavior of the two components. Not all polymer blends appear to have this level of merging of dynamics and it remains to establish the factors which determine the level of cooperativity.

### Summary

NMR has provided detailed information of the structure and dynamics of polymeric glasses in the vicinity of the glass transition. The heterogeneity of the dynamics is a key feature with slow and fast relaxing spatial regions clearly defined. The evolution or interchange of these

regions occurs on a slower time scale than the average relaxation time. The size and quantity of the fast relaxing regions allows them to be viewed as defects at the onset of the glass transition. The stretched exponential correlation function can describe the distribution of relaxation times but the heterogeneous character of the relaxation is not easily meshed with derivations of this correlation function based on defects. Modifications of the composition of the glass can produce additional spatial heterogeneity or defects but it is not fully comparable to the heterogeneity seen in a simple, pure polymeric glass.

## References

1. N. G. McCrum, B. E. Read, and G. Williams, Anelastic and Dielectric Effects in Polymeric Solids, ( John Wiley and Sons, New York, 1967).
2. G. Williams and D. C. Watts, Trans. Faraday Soc. **66**, 80 (1970).
3. Relaxations in Complex Systems, edited by K. L. Ngai and G. B. Wright, (North Holland, Amsterdam, 1991).
4. E. Roessler and M. Taupitz, Disorder Effects on Relaxation Processes, edited by Richert and Blumen (Springer-Verlag, Berlin, 1994) pp, 361-383.
5. J. Schaefer, E. O. Stejskal, and R. Buchdahl, Macromolecules **10**, 384 (1977).
6. J. I. Kaplan and A. N. Garroway, J. Magn. Res. **49**, 464 (1982).
7. H. W. Spiess, Colloid. Polym. Sci. **261**, 13 (1983).
8. M. F. Shlesinger and M. F. Montroll, Proc. Natl. Acad. Sci. U. S. A. **81**, 1280 (1984).
9. M. F. Shlesinger, J. Stat. Phys. **36**, 639 (1984).
10. A. Blumen, G. Zumdofen and J. Klafter, J. Phys. Rev. B **30**, 5379 (1984).
11. K. Schmidt-Rohr and H. W. Spiess, Phys. Rev. Lett. **66**, 3020 (1991).
12. K.-L. Li, P. T. Inglefield, A. A. Jones, J. T. Bendler and A. D. English, Macromolecules, **21**, 2940 (1988).
13. K.-L. Li, A. A. Jones, P. T. Inglefield and A. D. English, Macromolecules **22**, 4198 (1989).
14. W. J. Jackson and J. R. Caldwell, Adv. Chem. Ser. **No.48** 185 (1965).
15. R. P. Kambour, J. M. Kelly, and B. J. McKinley, J. Polym. Sci. Polym. Phys. **27**, 1979 (1989).
16. B. J. Cauley, C. Cipriani, K. Ellis, A. K. Roy, A. A. Jones, P. T. Inglefield, B. J. McKinley and R. P. Kambour, Macromolecules **24**, 403 (1991).

17. Y. Liu, M. M. Turnbull, A. A. Jones, P. T. Inglefield, and R. P. Kambour, *Solid State NMR* **2**, 289 (1993).
18. Y. Liu, P. T. Inglefield, A. A. Jones and R. P. Kambour, *Mag. Reson. Chem.*, to appear.
19. J. S. Chiou and D. R. Paul, *J. Appl. Polym. Sci.* **33**, 2935 (1987).
20. Y. H. Chin, C. Zhang, P. Wang, A. A. Jones and P. T. Inglefield, *Macromolecules* **25**, 3031 (1991).
21. Y. H. Chin, P. T. Inglefield, and A. A. Jones, *Macromolecules* **26**, 5372 (1993).
22. D. L. VanderHart, *Macromolecules* **27**, 2837 (1994).

## CHARACTERIZING FRACTAL AND HIERARCHICAL MORPHOLOGIES BEYOND THE FRACTAL DIMENSION

Raphael Blumenfeld<sup>\*</sup> and Robin C. Ball<sup>\*\*</sup>

<sup>\*</sup> CNLS and the Theoretical Division, MS B258, Los Alamos National Laboratory, Los Alamos, NM 87545, USA.

<sup>\*\*</sup> Cavendish Laboratory, Madingley Road, Cambridge CB3 0HE, UK.

### ABSTRACT

We present a novel correlation scheme to characterize the morphology of fractal and hierarchical patterns beyond traditional scaling. The method consists of analysing correlations between more than two-points in *logarithmic coordinates*. This technique has several advantages: i) It can be used to quantify the currently vague concept of morphology; ii) It allows to distinguish between different signatures of structures with similar fractal dimension but different morphologies already for relatively small systems; iii) The method is sensitive to oscillations in logarithmic coordinates, which are both admissible solutions for renormalization equations and which appear in many branching patterns (e.g., noise-reduced diffusion-limited-aggregation and bronchial structures); iv) The method yields information on corrections to scaling *from the asymptotic behavior*, which is very useful in finite size analysis. Markovian processes are calculated exactly and several structures are analyzed by this method to demonstrate its advantages.

### Introduction

The last two decades have seen a growing realization that hierarchical and fractal structures are all too common in nature. This begs the question what is it that makes these structures optimal for so many applications. The first step towards understanding this question is through an intelligent characterization. At present, the main tool used for this purpose is the measure of the fractal dimension or the scaling of various properties of media with such constructions. We claim that this characterization provides insufficient

information about the system and propose a better suited correlation scheme that can distinguish between structures via signatures that go beyond simple scaling.

A massive system is said to be fractal, or scale-invariant, if under the transformation  $r \rightarrow r' = \lambda r (\lambda > 1)$  the structure maps onto itself in the form  $m \rightarrow m' = \lambda^D m$ , where  $m$  is the mass. The power  $D$  is the fractal dimension, or scaling exponent, whenever it does not coincide with the (integral) Euclidean dimension,  $d$ , in which the structure is embedded. In finite systems, with upper and lower cutoff scales on the fractal behavior, the transformation has to be accompanied by an appropriate coarse-graining of the fine details and the mapping is onto a subset of the original system. The transformed structure can be either an exact, or a statistically similar, replica of the pre-transformed system. The latter is usually the case in nature.

To understand why scaling is the roughest possible description, consider the  $n$ -point correlation functions (CFs) of a fractal construction consisting of isotropically-distributed mass,  $\Phi(\mathbf{r})$ . The one-point CF is

$$\langle \Phi(\mathbf{r}) \rangle = \text{Const.} \equiv \Phi_1, \quad (1)$$

which is simply the average density. The two-point CF is

$$\langle \Phi(\mathbf{r})\Phi(\mathbf{r}') \rangle = \Phi_2(\mathbf{r} - \mathbf{r}') = \Phi_1 C_2(|\mathbf{r} - \mathbf{r}'|), \quad (2)$$

where  $C_2 = A|\mathbf{r} - \mathbf{r}'|^{d-D}$ . This immediately shows that the two-point CF can yield no detailed information on the system because it reduces to just two constants, the coefficient  $A$  and the codimension  $d - D$ . The culprit that robs this CF of its structural information is the additional symmetry of dilational invariance. In general, every added symmetry inevitably reduces the number of variables that describe a system and therefore the codimension and the fractal dimension constitute level of description that is equivalent to the average density in the traditional translational invariant structures. Since all the spectral analyses relate to the two-point CF in some way or another it follows that the



scaling exponents found in measurements are at the same level of characterization. Thus the natural way to refine the description is by climbing to higher CFs. In particular, let us consider the three-point CF,

$$\Phi_3(\mathbf{r}, \mathbf{r}', \mathbf{r}'') = \Phi_1 C_3(\mathbf{r} - \mathbf{r}', \mathbf{r} - \mathbf{r}'') = \Phi_1 C_3 \left( \frac{|\mathbf{r} - \mathbf{r}'|}{|\mathbf{r} - \mathbf{r}''|} \right). \quad (3)$$

The r.h.s. of expression (2) is reached by successive applications of translational invariance, isotropy and dilational invariance. We find it convenient to represent  $C_3$  in the form

$$C_3 = C_2(|\mathbf{r} - \mathbf{r}'|) C_2(|\mathbf{r} - \mathbf{r}''|) \mathcal{L} \left( \log \frac{|\mathbf{r} - \mathbf{r}'|}{|\mathbf{r} - \mathbf{r}''|} \right). \quad (4)$$

As will become apparent below, the use of logarithmic coordinates allows to use insight from two-point CFs in traditional systems. Other than quantifying the morphology of such structures, the method that we propose enjoys several advantages: 1) It can distinguish between structures that have a very similar fractal dimension already from relatively small sizes. This alleviates the need to analyze large systems in order to discriminate between the fractal dimensions to a sufficient accuracy. An demonstration of this is given below. 2) The scheme is sensitive to scale-invariant side-branching, which appear in many aggregation, and stochastic interface growth, processes.

### The method

Given a set of unit mass points in  $d$ -dimensions

$$\Phi(\mathbf{r}) = \frac{1}{N} \sum_{n=1}^N \delta(\mathbf{r} - \mathbf{r}_n),$$

choose an arbitrary point,  $j$  as an origin and construct shells around it that are of equal width in the *logarithm* of the distance from this point,  $\rho = \log |\mathbf{r} - \mathbf{r}_j|$ . Each shell is now indexed by its logarithmic distance from the origin,  $\rho$ . Summing over all the mass within a particular shell one obtains the shell's mass,  $\delta S(\rho)$ . Averaging over all possible origins (denoted by  $\langle \rangle_j$ ) and normalizing by the volume of the shell,  $\delta V(\rho)$ , one obtains the two-point CF,

$$C_2(\rho) = \frac{\langle \delta S(\rho) \rangle_j}{\delta V(\rho)} \sim e^{-(d-D)\rho}, \quad (5)$$

which scales as discussed above. The three-point CF corresponds in these variables to an average over all origins of the mass in the  $\rho$ -th shell times that in the  $\rho'$ -th shell,  $\langle \delta S(\rho) \delta S(\rho') \rangle_j$ . Normalized correctly this defines a new correlation matrix

$$M(\rho, \rho') = \frac{\langle \delta S(\rho) \delta S(\rho') \rangle_j}{\langle \delta S(\rho) \rangle_j \langle \delta S(\rho') \rangle_j} . \quad (6)$$

It is straightforward to see that for scale-invariant structures (whether fractal or hierarchical) the matrix  $M$  depends only on the absolute 'distance' in the logarithmic coordinates

$$M(\rho, \rho') = M(|\rho - \rho'|) .$$

The matrix  $M$  defines a surface in the  $\rho - \rho'$  plane which can be contour-plotted. For fractal systems the dependence on  $|\rho - \rho'|$  means that in such a contour plot the contours must consist of lines that lie in parallel to the diagonal,  $\rho = \rho'$ . An average over all occurrences of a given value  $\lambda = |\rho - \rho'|$  gives the function  $\mathcal{L} = \mathcal{L}(|\rho - \rho'|)$  defined above

$$\mathcal{L}(\lambda) = \int d\rho d\rho' M(\rho, \rho') \delta(|\rho - \rho'|) .$$

This function we term a lacunarity function because for  $\lambda = 0$  it coincides with the lacunarity parameter defined by Mandelbrot and coworkers on fractals.<sup>(1),(2)</sup>

### Applications and advantages

**I. Unrestricted branched polymers:** These structures can be analyzed exactly because they can be modelled by a Markovian brownian walk. Although detailed, the algebra is straightforward and one can calculate the lacunarity function explicitly<sup>(3)</sup>

$$\mathcal{L} = \frac{1}{2} + \cosh \frac{(d-D)\lambda}{2} [2 \sinh(\lambda)]^{(D-d)/2} \frac{P_\nu^\mu(\coth \lambda)}{P_{-\mu}^\mu(\coth \lambda)} , \quad (7)$$

where  $\mu = 1 - d/2$ ,  $\nu = D/2 - 1$  and  $P_a^b(x)$  is the associated Legendre polynomial. The resulting plot of  $\mathcal{L}$  against  $\lambda$  is smooth and shows no interesting features, as can be expected from a Markovian process.

**II. SAW, DLA and CCA:** We have constructed numerically cluster-cluster-aggregates (CCA) and self-avoiding-walks (SAW) in two dimensions. The two processes are known to lead to structures that have a very similar fractal dimension:  $D_{SAW} = 1.35$  and  $D_{CCA} = 1.42$ . But despite the similar scaling the morphologies are completely different. By first measuring the fractal dimensions for structures of 4096 particles we made sure that this quantity cannot distinguish between the systems. Our measurements gave:  $1.1 \leq D_{SAW} \leq 1.5$  and  $1.3 \leq D_{CCA} \leq 1.6$ . Then we applied our scheme for these very structures and measured the lacunarity function. We found that there are distinguishable differences between the two functions. Specifically, for CCA  $\mathcal{L}$  shows a signature that could be traced to the process of doubling the cluster mass in stages. this signature was absent in the SAW and demonstrates that the structure could be separated already on this scale.

We have also applied this scheme to analyze diffusion-limited-aggregates (DLA) that were constructed by P. Meakin. We find that the lacunarity function decays in this system much slower than in both SAW and CCA. This may bear on recent observations that correlations die slowly in DLA.<sup>(4)</sup>

**III. Disordered Cantor sets:** our scheme is very sensitive to periodic oscillations on logarithmic scales. Examples of such oscillations occur in branching structures, such as, noise-reduced DLA,<sup>(5)</sup> cracking patterns,<sup>(6)</sup> bronchial trees<sup>(7)</sup> and tree-structures in general. To demonstrate the sensitivity of this technique to such oscillations we constructed disordered Cantor sets and measured their lacunarity functions. For example, the exact triadic Cantor set would give rise to sharp peaks at a periodicity that corresponds to integral multiples of  $\Delta\lambda = \log 3$ . By introducing disorder we ascertained that the original structure could not be discerned by the eye. Yet, the lacunarity function picked easily the original periodicity, although the peaks were damped by the disorder.

## Conclusion

To conclude, we propose this new technique as a tool to distinguish between fractal and scale-invariant structures with different morphologies, regardless of whether the fractal

dimensions are similar or not. The use of logarithmic variables allows to employ insight gained from traditional pair correlations statistics. This insight can be used once traditional distances are replaced by ratios of scales and the usual two-point CF is replaced by the three-point CF in logarithmic coordinates. We demonstrated that the method is sensitive to structural signatures already for small systems and to periodicity on logarithmic scales. An advantage that we have not elaborated on here is that the method has also been found to yield the corrections to scaling from the asymptotic behavior.<sup>(3)</sup> Traditional measurements of such corrections are carried out for small size system, where the error bars are usually large, therefore this feature of  $\mathcal{L}$  is significant in that the error bars are far smaller in the asymptotic large-scale regime. This scheme have been recently applied to analysis of the roughness of fracture surfaces,<sup>(8)</sup> and structure of porous media.<sup>(9)</sup>

## REFERENCES

1. B. B. Mandelbrot, *The fractal geometry of nature* (San Francisco: Freeman, 1982).
2. B. B. Mandelbrot, C. R. Acad. Sci. Ser. A **288**, 81 (1979); Y. Gefen, B. B. Mandelbrot and A. Aharony, Phys. Rev. Lett. **45** 855 (1980); Y. Gefen, A. Aharony and B. B. Mandelbrot, J. Phys. A **17**, 1277 (1984); R. Blumenfeld and B. B. Mandelbrot, unpublished.
3. R. Blumenfeld and R.C. Ball, Phys. Rev. E **47**, 2298 (1993).
4. B. B. Mandelbrot, Fractals, xxxx (1993).
5. R. C. Ball, P. W. barker and R. Blumenfeld, Europhys. Lett. **16**, 47 (1991).
6. R. C. Ball and R. Blumenfeld, Phys. Rev. Lett. **65**, 1784 (1990).
7. M. F. Shlesinger and B. J. West, Phys. Rev. Lett. **67**, 2106 (1991).
8. V. Y. Milman, R. Blumenfeld, N. A. Stelmashenko and R. C. Ball, Phys. Rev. Lett. **71**, 204 (1993); V. Y. Milman, N. A. Stelmashenko and R. Blumenfeld, to appear in Prog. Mater. Res. (1994).
9. R. Held and R. Blumenfeld, in preparation.

## CONCENTRATION INFLUENCE ON DIFFUSION LIMITED CLUSTER AGGREGATION

ST.C. PENCEA\* AND M. DUMITRASCU\*\*

\*Romanian Academy, Institute of Physical Chemistry, Department of Colloids, Spl. Independentei 202, 79611 Bucharest sect. 6, Romania

\*\*Biotehnos SA, Department of Automation, Str. Dumbrava Rosie 18, Bucharest sect. 2, Romania

### ABSTRACT

Diffusion-limited cluster aggregation has been simulated on a square two dimensional lattice. In order to simulate the brownian motion, we used both the algorithm proposed initially by Kolb *et al.* and a new algorithm intermediary between a simple random walk and the ballistic model.

The simulation was performed for many values of the concentration, from 1 to 50%. By using a box-counting algorithm one has calculated the fractal dimensions of the obtained clusters. Its increasing vs. concentration has been pointed out. The results were compared with those of the classical diffusion-limited aggregation (DLA).

### INTRODUCTION

Since Witten and Sander proposed DLA as a model which describes a large number of fractal patterns [1], considerable studies concerning this subject have been done. The classical DLA model [1,2] supposes that the growth of the aggregate starts from an incipient center. The center could be either a unique point, as initially proposed by Witten and Sander, or a whole surface, as in surface deposition models. Further, successive random walk particles stick themselves to the center, causing the growth.

Nevertheless, there are many aggregation phenomena in which such a starting center does not exist. An example is the colloidal aggregation, phenomenon occurred in a cooled solution of colloids. The start configuration is, then, the one of a homogeneous solution, where no aggregation center exists. In this case the aggregation centers are not apriori determined, but formed by the sticking of the elementary particles and could eventually move. Such simulations were performed initially by Meakin [6] and Kolb *et al.* [7], in the limit of zero concentration, and were followed by a large number of studies (see [8] for further references).

Our work consists mainly in implementing two algorithms that simulate such an aggregation in solution, at different concentrations between 0 and 50%. The obtained structures were then investigated as fractals. We limited ourselves to the calculus of the fractal dimension, using a box-counting algorithm.

## AGGREGATION ALGORITHMS

In all cases, the start distribution was generated by randomly choosing the positions of the elementary particles on the lattice, according to the given concentration of the aggregating particles. Afterwards one identified the clusters as free particles or groups of nearest-neighbor connected particles. The start configuration was then successively modified by simulating the brownian motion of the rigid and non-rotating clusters. When two (or more) clusters meet each other, they stick together and form a greater one. We were not concern about the sticking mechanism, and considered the sticking probability equal to 1.

Attempting to give a realistic description, one could generate the brownian motion in several ways described below.

The simplest manner is to move at each step a randomly selected cluster to a randomly chosen nearest-neighbor position. We have used it only in few cases, and we mention it only because it is very similar to the "random walk" of the elementary particle in classical DLA: neither the temperature [3], nor the cluster masses does influence the aggregation process.

Instead, following the algorithm proposed initially by Kolb *et al.*, we considered an improved set of rules: the selected cluster has been moved only if a random variable, whose spectrum is the interval [0,1], is lower than  $1/\sqrt{N}$ , where  $N$  is the number of elementary particles that build the cluster. This approach correctly describes the mean displacement of the cluster as being proportional to the inverse of the mass' square root, but also does not take into account the temperature. In fact, it corresponds to that temperature  $T_0$  at which the mean displacement of a uniparticle cluster equals the lattice unity. We restricted ourselves to this case, despite the fact that one could introduce a temperature dependence, for instance by using a treshold of the form  $\sqrt{(T/T_0)}/N$  instead of the previous one. Further in this paper we will denote this algorithm as nearest-neighbor algorithm (NNA).

We proposed another method to obtain the new position of the cluster by generating a displacement vector. The components of the displacement vector were calculated using the formula:

$$\Delta R_{x,y} = \alpha \cdot \text{Erf}^{-1}(2rnd - 1) \quad (1)$$

where  $rnd$  is a randomly chosen variable between 0 and 1,  $\text{Erf}^{-1}$  represents the inverse of the error function

$$\text{Erf}(x) = \frac{2}{\sqrt{\pi}} \int_0^x \exp(-y^2) \cdot dy \quad (2)$$

and

$$\alpha = \Delta t \cdot \sqrt{\frac{2kT}{M}} \quad (3)$$

In Eq. (3)  $M$  is the mass of the cluster,  $T$  - the temperature, and  $k$  - the Boltzman constant. If on his linear trajectory the moved cluster meets another one, it stops and sticks to this.

Our algorithm is noticeable because one can adjust the motion of the cluster from repaus (corresponding to  $\alpha = 0$ ) to the ballistic motion ( $\alpha \rightarrow \infty$ ). It will be called the long-displacement algorithm (LDA).

Fig. 1 presents some results of a simulation which uses LDA at a concentration of 10%. The aggregation started from a randomly chosen configuration (Fig. 1.a). Figs. 1.b and 1.c represent successive images of the bidimensional solution during the aggregation process, until the unicluster configuration is reached (Fig. 1.d).

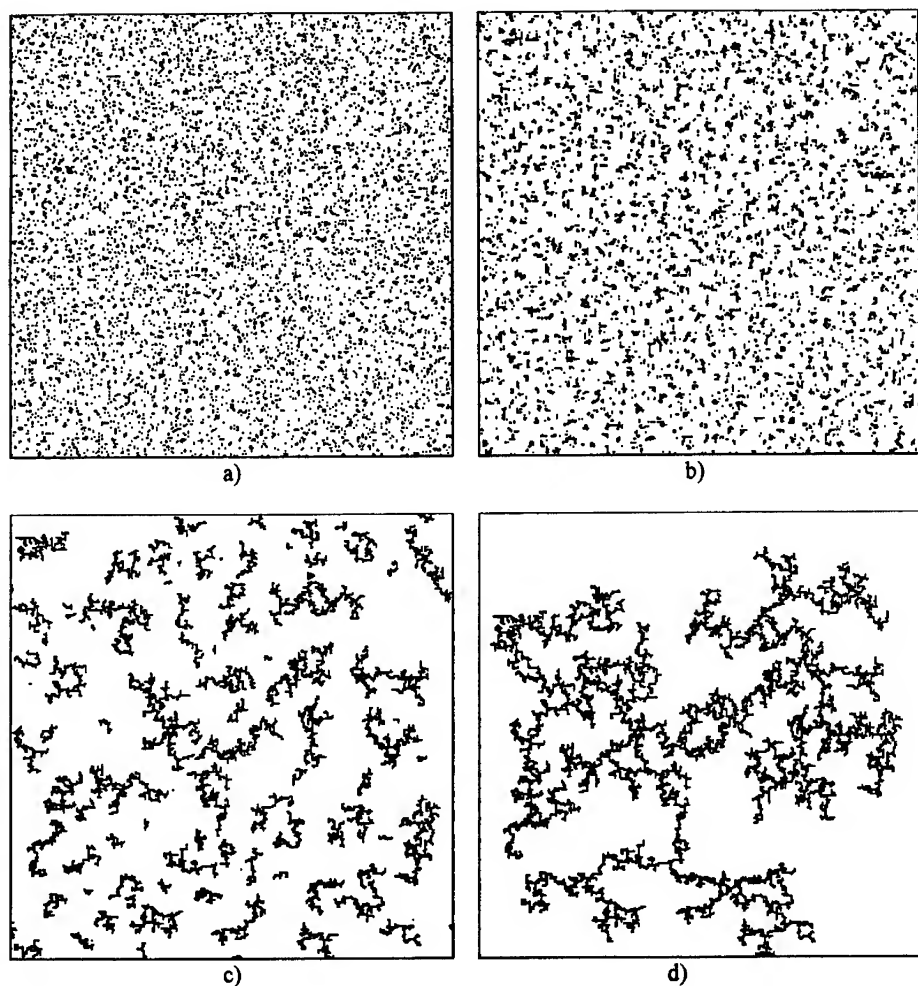


Figure 1. Successive stages of a simulated aggregation process. This simulation was performed on a 300x300 lattice using the LDA. a) Start configuration; b) Incipient aggregation; c) Advanced aggregation; d) Final cluster.

## RESULTS

One has performed many simulations using both algorithms described above. The concentration of the aggregating phase took different values from 1 to 50%. The speed of the simulated aggregation process depends on both concentration and algorithm. At low concentrations, the nearest-neighbor algorithm generated only configurations with small clusters (built from only a few particles). This is due to the small probability that a cluster meets another one in his very neighborhood. In order to obtain greater aggregates one should either increase dramatically the computation time or use LDA. In the last case, one has to choose a parameter  $\alpha$  large enough that the displacement vector has usually a magnitude of several lattice steps. Such a displacement corresponds to a greater probability that the moved cluster meets another one, and the aggregation velocity increases significantly. At higher concentrations, the meeting probability becomes significant even for one-step movements, so that NNA, which is simpler than LDA, is also faster.

Figs. 2 and 3 represent several final configurations obtained for different values of the concentration, using LDA and NNA, respectively.

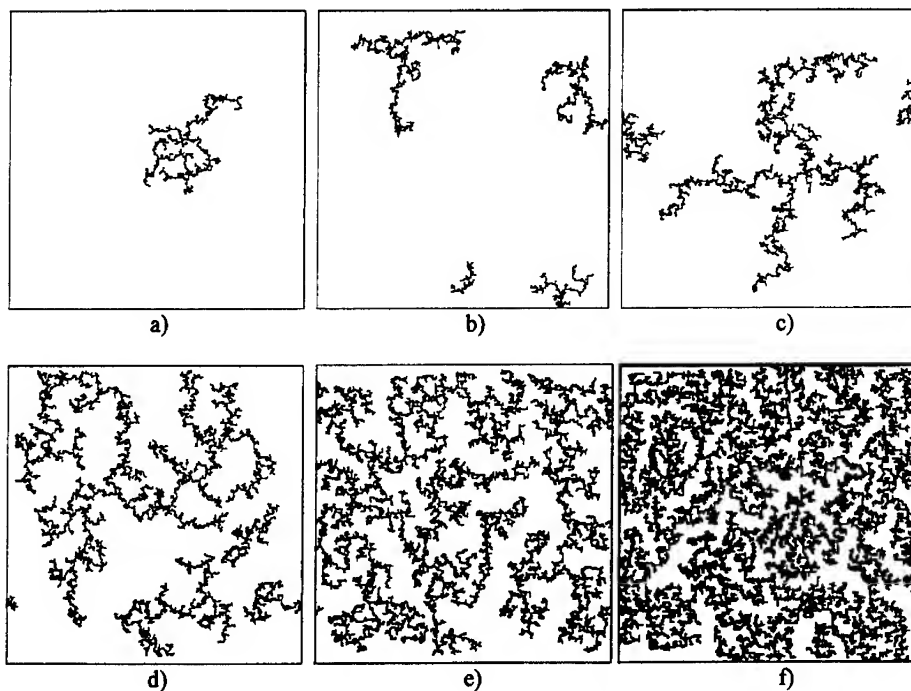


Figure 2. Configurations resulted for different values of the concentration using the LDA. Concentrations and lattice dimensions are, respectively: a) 1%, 400; b) 2%, 400; c) 4%, 400; d) 8%, 400; e) 16%, 200; f) 32%, 200.



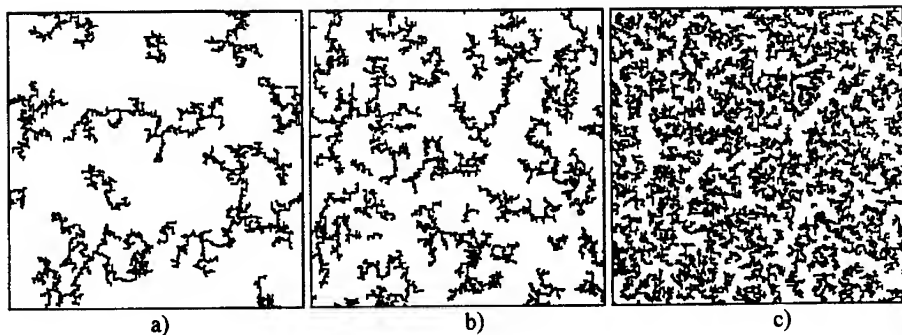


Figure 3. Configurations resulted for different values of the concentration using the NNA. In all cases the lattice dimension is 200. Concentrations are: a) 10%; b) 16%; c) 32%.

Further we used a classical box-counting algorithm to investigate the fractal dimension of the clusters we had obtained. Fig. 4 shows the concentration dependence of the fractal dimensions calculated for several clusters, including those presented in Figs. 1.d, 2 and 3.

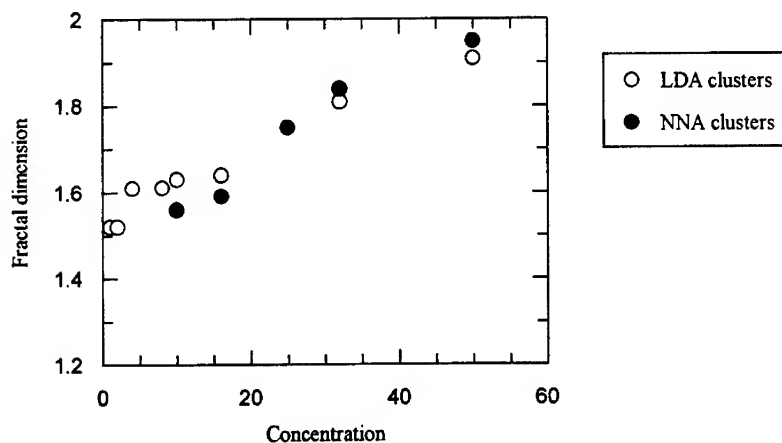


Figure 4. Concentration dependence of fractal dimensions, for clusters generated by using both LDA and NNA.

## CONCLUSIONS

The differences between the fractal dimensions of the clusters obtained by NNA and LDA, respectively, are smaller than experimental errors (about 5%). So, we could preliminary conclude that the aggregation algorithm does not affect significantly the

scale-invariant properties of the clusters, despite the fact that the motion of the clusters is strongly determined by the algorithm. Even simulations performed by using random movements to a nearest-neighbor position present results similar to those shown in Fig. 4.

In Fig. 4 one could also observe that the fractal dimension increases with concentration, as before expected. At low concentrations, because the diffusing clusters are greater than a single particle, the branches of the cluster screen stronger the center, producing a fractal dimension smaller than those of DLA clusters [2,6].

Under the percolation threshold [9] we observed that the fractal dimension did hardly if ever depend on concentration.

At higher concentrations, the growth of some clusters occurs quickly enough that other smaller clusters are captured by the grown branches and they will stick to the inner part of the greater clusters. Then a higher fractal dimension will result.

If we consider in Fig. 4 a logarithmic scale for the concentration, we could point out a change in slope at a concentration of about 16%. We notify that this concentration corresponds to a fractal dimension similar to that of classical DLA [2]. Moreover, at this concentration the final cluster reaches the margins of the lattice and a "bicontinuous" phase appears. This hypothesis is very attractive; however, it should be considered very cautiously.

## REFERENCES

1. T.A. Witten and L.M. Sander, Phys. Rev. Lett. **47**, 1400 (1980); Phys. Rev. B **27**, 5696 (1983).
2. P. Meakin, Phys. Rev. A **27**, 1495 (1983).
3. H.E. Stanley, A. Bunde, S. Halvin, J. Lee, E. Roman and S. Schwartz, Physica A **168**, **23** (1990).
4. P. Meakin, H.E. Stanley, A. Coniglio and T.A. Witten, Phys. Rev. A **32**, 2364 (1985).
5. J. Nittman and H.E. Stanley, Nature **321**, 663 (1986).
6. P. Meakin, Phys. Rev. Lett. **51**, 1119 (1983).
7. M. Kolb, R. Botet and R. Jullien, Phys. Rev. Lett. **51**, 1123 (1983).
8. T. Wicsek, *Fractal Growth Phenomena*, 2nd ed., World Scientific Publishing Co. Pte. Ltd., Singapore, 1992.
9. The percolation threshold depends on the lattice dimension, because the clusters are fractals. At any given concentration, when the lattice dimension increases, the fractal dimension remains quite constant, until that lattice dimension at which percolation firstly occurs. Above this dimension we expect that the fractal dimension will obviously increase with the dimension of the lattice, having a limit equal to 2 for an infinite lattice. Please note that at concentration greater or equal to 50% one must observe incipient percolation even for small lattices. The first author wishes to thank A.E. Gonzales and T. Odagaki for their comments who gave a new light on our conclusions.

## LASER SCANNING OF NATURAL AND ARTIFICIAL SNOW PACKS

KAZUHIKO ITAGAKI,\* G.E. LEMIEUX\* AND NINA JI\*

\*USA CRREL, 72 Lyme Road, Hanover, NH 03755 U.S.A.

### ABSTRACT

In an effort to numerically describe a snow pack as a disordered aggregate of irregularly shaped particles, a new optical analysis system was conceived. The system measures light transmission through snow samples impregnated with an opaque fluid. The analysis of the results is presented.

### INTRODUCTION

The physical properties of snow are a complex function of various parameters, such as density, particle size, age and moisture content. The global structure and local texture are important factors, affecting mechanical, electrical and optical properties. Quantitatively characterizing snow would benefit many research areas.

Bonds between snow particles are one of the basic factors controlling the properties of a snow pack. Thin sectioning has been used to gain two-dimensional information<sup>1,2</sup> and has been applied to the study of many snow properties.<sup>3,4,5</sup> However, this method does not provide the three-dimensional information that is needed to completely understand snow properties. To gain three-dimensional information, researchers have attempted to make a series of cross sections and then reconstruct them.<sup>6</sup> This method is very time-consuming and, even so, did not yield numerical information. Automation of the method may be difficult and expensive.

### SCANNING SYSTEM AND SAMPLE

We conceived and tested a novel optical method using natural snow and an artificial model snow pack.<sup>7</sup> Since snow particles are transparent, light can be transmitted through the particles and the bonds between them. When the snow is immersed in an opaque fluid, light can only be transmitted between connected grains through their bonds. If there is no bond between grains, light will not be transmitted to the next grain. Scanning through the snow immersed in the opaque fluid and recording the emergence and deflection of light, we should be able to obtain certain information on the structure, such as the number of bonds and the extent of connected grains.

A combination of off-the-shelf items—He-Ne laser, video camera, video recorder and X-Y positioner—constitute the scan system (Fig. 1). Although this simple system seems to have great potential for examining snow structure and texture, several areas still need improvement and development.

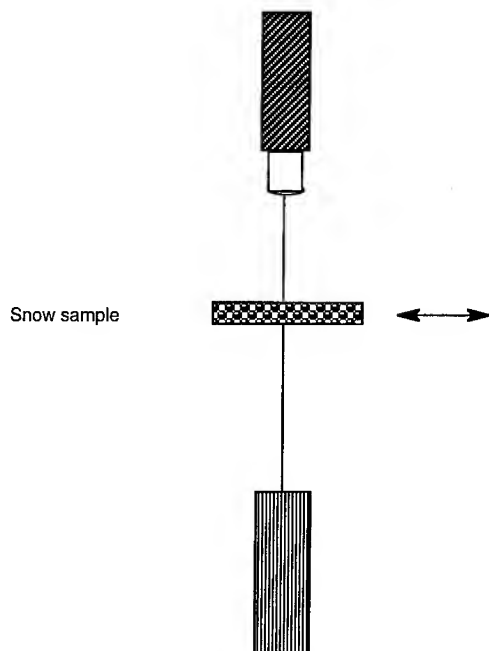


Figure 1. Schematic diagram of the snow scan system.

sitions of the laser and the video camera are fixed, point of beam entry relative to the camera is fixed. Deviation of the beam, readily measured on the video screen, could provide more information but we left that for future studies.

## RESULTS

The intensity of the transmission of the laser beam through the impregnated snow pack provides information on connecting snow particles. Both natural and artificial impregnated snow packs of various ages were scanned, and the intensity of the emerging light spots was recorded by the video camera and VCR. After each scan was completed, the sample was thinned by microtome. Very few light spots emerged from the thicker fine-grained snow samples, so we had to remove a layer from such samples before useful data could be obtained.

Since the emerging light intensity ( $I$ ) indicates the tortuosity of the light path, we measured light intensity straight above its entrance, assuming that the entering light intensity remains constant. Direct measurement of light intensity in real time may be preferable because of the nonlinearity of video recording. However, much other information can be stored on the video tape before the sample is thinned down for the next scan. Later, the video tape was played and the light intensity of the video images was measured.

The field size of the image displayed on the video screen was  $8 \times 6$  mm, with 1 mm between scan lines. The He-Ne laser beam width at the entrance was 0.5 mm. The transmitted light

A natural snow pack was sampled on 1 February 1994; it was granular, undisturbed snow near the USA CRREL building at Hanover, New Hampshire. A cube of snow, about 30 cm above the first sample, was brought into a CRREL coldroom and three samples were made from it after aging. The artificial snow was produced by sifting old, crushed snow through a no. 16 sieve (1.190 mm) into four  $7 \times 7 \times 5$ -cm cardboard boxes. These snow samples were stored in a coldroom in a larger Styrofoam box that was filled with snow under isothermal conditions to prevent sublimation. The samples were immersed in an opaque fluid (dimethyl phthalate solution of methylene blue) at dates selected earlier. Each sample was then mounted on a glass plate and thinned down by a microtome to the desired thickness (6 mm or less) and scanned by well-collimated laser beam. Since the po-

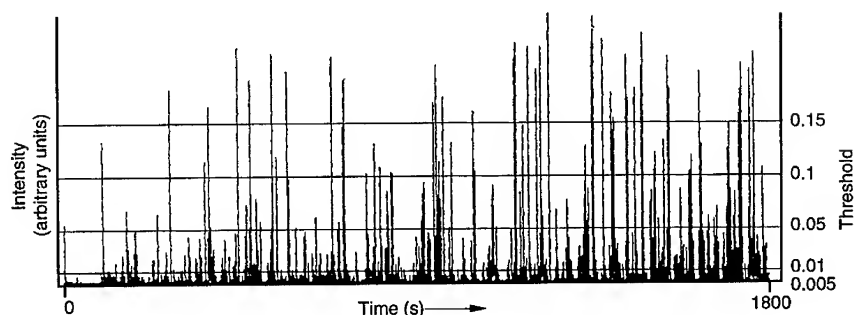


Figure 2. Emerging light intensity with time (sample 12-2).

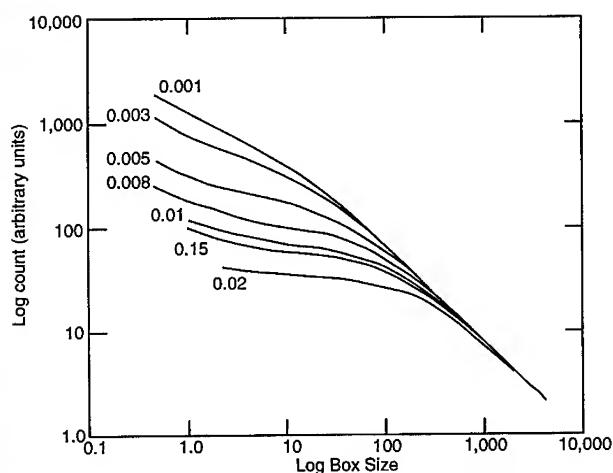


Figure 3. Box count curve with various threshold values.

intensity within a 1-mm circle just above the light beam's entrance point was measured by a photo-multiplier tube. Then, the photo-multiplier output current was measured by an HP3457A digital multimeter and the data were recorded on a floppy disk of the HP 9020 desktop computer. An example of emerging light intensity plotted with time is shown in Figure 2. Later, box counting was done on the signal intensity above the threshold. For the current method of analysis, light intensity was measured directly above the beam's entrance. Since mea-

surement was made only directly above the light entrance, there is no interference from a neighboring pass. Therefore, we did one-dimensional box counting along the line of the scan as a function of the threshold intensity and the thickness.

## ANALYSIS

The slopes of the box counts are generally composed of two regions. With the larger box sizes, we would always find emergence of light within the box, so the slope of  $\log(\text{box size})$  vs.  $\log(\text{number of boxes})$  would be  $-1$  until the box size became small enough to find sufficient empty boxes to change the slope. With a finite number of data points and limited time resolution (0.2 s), such behavior can be expected. In the smaller box sizes, the slope systematically become lower with the increase in threshold (Fig. 3).

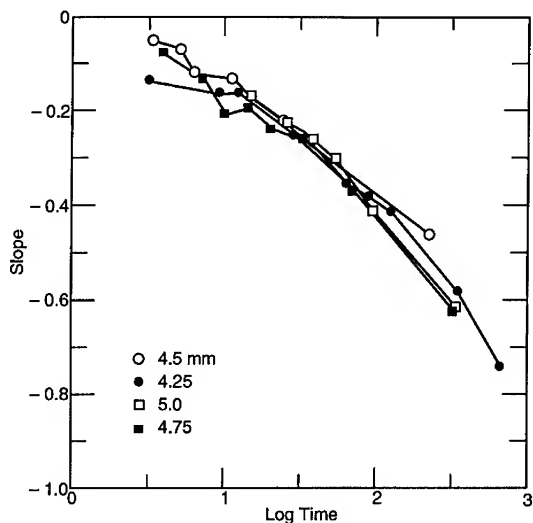


Figure 4. Curves of  $\log(TTime)$  vs. slope of box count for various sample thicknesses show a linear relationship and are close to each other.

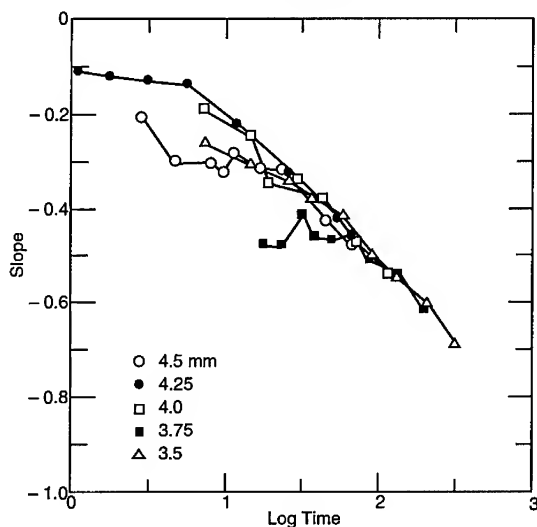


Figure 5. Sometimes  $\log(TTime)$  vs. slope of box count is composed of two linear parts. Note that all curves have a common slope at their low ends.

The total time (the cumulative time above a threshold,  $TTime$ ), which is also a function of the threshold and the sample thickness, is an indicator of the number of light paths. Interestingly,  $\log(TTime)$  vs. slope tended to be linear. As shown in Figure 4, there was little deviation from a common trend for a particular sample thinned down to various thicknesses. Under a condition that is unclear to us at this time, the  $\log(TTime)$  vs. slope relation exhibited two distinct linear components (Fig. 5). Notice that most curves indicated two linear parts, particularly the 4.25-mm-thick sample, which showed two pronounced straight lines. Since this particular sample was well aged and had a large grain size, two such linear components may indicate the texture of the aged snow.

The  $\log(TTime)$  vs. slope relationship seems to be related to the age and morphology of the samples. As the sample is aged, the slope of  $\log(TTime)$  vs. slope for artificially made snow tended to decrease. We noted a slight thickness dependency of the slope as the samples were thinned down; this may indicate deviation from homogeneity in the sample.

## DISCUSSION

There are many possible ways to analyze the video images to gain information on the structure of natural and artificially grown snow packs and on the effect of metamorphosis. Deflection of light emergence relative to its entrance point, as well as the overall light emergence distribution, can be examples.

To use our results for the analysis of snow strength and other properties, we need a fundamental understanding of how to quantify snow characterization. Snow density and strength are related to connectivity and coordination number. The laser scan method described above, as well as the other techniques, could yield information on connectivity and coordination number.

Other types of radiation, such as ultrasonic techniques and X-ray scattering and absorption methods, have been used to characterize colloids. The same techniques may be applicable to snow. These approaches would not need much development, but just adjusting the frequency and selecting the proper media.

The ultrasonic technique also allows us to use either longitudinal or transversal waves. Since transversal waves cannot transmit in a fluid, the connectivity of solid particles, such as found in snow, could be better studied using transversal waves. However, ultrasonic scanning needs a coupling fluid. Scanning with a thin layer of fluid between the ultrasonic transducer and the delicate structure of snow may be a difficult problem.

The propagation of light in our technique can be regarded as a special case of the percolation process. All of the particles are connected to the others so that the structure can be called "Complete," otherwise the particles are still falling because there are no connections. The output light intensity depends on the tortuosity and the length of light paths. As the snow samples were thinned down, the light paths became straighter and their number increased. However, the effect of thickness seems minor on the  $\log(TTime)$  vs. slope of box count curve for one particular set of samples.

## CONCLUSION

A simple optical system built using off-the-shelf components—a He-Ne laser, a video camera-recorder combination and an X-Y scanning device—seems to have considerable potential for snow structure studies. In the course of the data analysis, we found the interesting relationship of  $\log(TTime)$  vs. slope of box count to be nearly linear, though the reason why this is so is unclear at this time. However, the observations indicated that the slope and location of the  $\log(TTime)$  vs. slope of box count curves are closely tied to the snow pack texture. With the proper theoretical development, this could be one of the parameters used in a numerical description of snow pack texture and structure.

---

## REFERENCES

1. H. Shimizu. *Low Temperature Science*, A17, pp. 81–86 (1958)
2. S. Kinoshita and G. Wakahama. *Low Temperature Science*, A18, pp. 77–96 (1959)
3. G. Wakahama. *Low Temperature Science*, A19, pp. 73–96 (1960a)
4. G. Wakahama. *Low Temperature Science*, A19, pp. 37–72 (1960b)
5. S. Kinoshita. *Low Temperature Science*, A19, pp. 111–118 (1960)
6. J. Huse, K. Tusima and K. Tusima. Preprint for Japanese Society of Snow and Ice 1985 meetings 185 (1985)
7. K. Itagaki and G.E. Lemieux. *Annals of Glaciology*, 18, pp. 7–10 (1993)



## ELASTIC AND LATTICE DYNAMICAL PROPERTIES OF METALS STUDIED BY N-BODY POTENTIAL

YOSHIAKI KOGURE, O. KOUCHI AND M. DOYAMA

The Nishi Tokyo University, Uenohara, Kitatsurugun, Yamanashi 409-01, Japan

### ABSTRACT

Higher order elastic constants and phonon dispersion relation have been calculated by using the n-body potential based on the embedded atom method. Results of second- and third-order elastic constants for Cu, Ag, and Au crystal were compared with the experimental data and the Cauchy discrepancy was discussed. A result of phonon dispersion relation for Cu crystal was also shown.

### INTRODUCTION

The atomic interaction in metals has non-central characters due to the existence of conduction electrons, and can be expressed by a n-body potential. Recently, the embedded atom method (EAM) potentials have been developed by many authors [1-5] and extensively been applied on the molecular dynamics simulations. The choice of the potential function is very important because it influences on the final results. We are now developing a method to characterize the potential function by calculating various properties of materials. By using the EAM potential the third-order elastic constants and the phonon dispersion relation of the noble metals have been calculated in this paper. The third order elastic constants represent a measure of crystal anharmonicity, which is related to the thermal expansion, high temperature thermal conductivity, defect-phonon interaction, and many other mechanical and thermal properties in the crystals. The third-order elastic constants in many kinds of materials have been measured by the ultrasonic methods under stress conditions[6-8]. We have applied the results on the calculations of the defect-phonon scattering [9] and the thermal conductivity [10]. It is interesting to see how the EAM potential reproduces the third-order elastic constants. It could be a way to characterize the potential.

### CALCULATION OF HIGHER ORDER ELASTIC CONSTANTS

The total internal energy  $E_i$  for an atom  $i$  in metals consists of two terms due to the EAM.

$$E_i = F(\rho_i) + \frac{1}{2} \sum_{j \neq i} \phi(r_{ij}). \quad (1)$$

The first term  $F(\rho)$  in RHS is the energy to embed atom  $i$  to the electron density  $\rho$  and  $\rho$  is expressed as a sum of the electron density of the other atom  $j$ .

$$\rho_i = \sum_{j \neq i} f(r_{ij}) \quad (2)$$

The second term  $\phi(r_{ij})$  in RHS of eq. (1) corresponds to the two body interaction, which mainly contributes to the repulsive force between the two ions. A variety of functional forms for  $F(\rho)$ ,  $f(r)$ ,  $\phi(r)$  have been proposed, and here we adopt the potential function developed by Oh and Johnson [4], because it is rather simple and is easily applicable to molecular dynamics simulations[11]. Following to the Oh-Johnson's potential the functions  $f(r)$  and  $\phi(r)$  are expressed by combinations of exponential functions and  $F(\rho)$  is a power functional form. The potential function contains seven parameters (except the cut off distance  $r_c$ ), and these can be determined from the experimental values of the cohesive energy, the bulk modulus, the lattice parameter (through the mechanical equilibrium condition), the shear modulus, and the unrelaxed vacancy formation energy.

#### Second-order elastic constants

The second-order elastic constants is obtained as the second-order derivative of the total internal energy  $E$  by the elastic strain  $\eta_{ij}$ , which can be written in the tensor expression as,

$$c_{pqrs} = \frac{1}{\Omega} \frac{\partial^2 E}{\partial \eta_{pq} \partial \eta_{rs}} = c_{pqrs}^F + c_{pqrs}^\phi, \quad (3)$$

here  $\Omega$  is the atomic volume,  $c_{pqrs}^F$  and  $c_{pqrs}^\phi$  are the contribution from the electron density and the two-body interaction, respectively. Each term is expressed as,

$$c_{pqrs}^F = \left( \frac{\partial^2 F}{\partial \rho^2} \right) \left( \sum_j \frac{x_r x_s}{r} \frac{\partial f}{\partial r} \right) \left( \sum_{j'} \frac{x_p x_q}{r} \frac{\partial f}{\partial r} \right) + \left( \frac{\partial F}{\partial \rho} \right) \sum_j x_p x_q x_r x_s \left( \frac{1}{r^3} \frac{\partial f}{\partial r} + \frac{1}{r^2} \frac{\partial^2 f}{\partial r^2} \right), \quad (4)$$

and

$$c_{pqrs}^\phi = \frac{1}{2} \sum_j x_p x_q x_r x_s \left( \frac{1}{r^3} \frac{\partial \phi}{\partial r} + \frac{1}{r^2} \frac{\partial^2 \phi}{\partial r^2} \right) \quad (5)$$

Here,  $x_p$  ( $p = 1, 2, 3$ ) is the  $p$ -th component of the position vector  $\mathbf{r}$ . There are three independent elastic constants;  $c_{11}, c_{12}, c_{44}$ , for the cubic crystals, and the Cauchy relation is expressed as,

$$c_{12} = c_{44}. \quad (6)$$

The temperature effects are not included in above expressions, but the effects are more or less a few percents and are not important for the present purpose.

#### Third-order elastic constants

The expressions for the third-order elastic constants can be derived by a similar manner by taking the third order derivative.

$$C_{pqrstu} = \frac{1}{\Omega} \frac{\partial^3 E}{\eta_{pq} \eta_{rs} \eta_{tu}} = C_{pqrstu}^F + C_{pqrstu}^\phi. \quad (7)$$

Where, the two components,  $C_{pqrstu}^F$  and  $C_{pqrstu}^\phi$  are as follows.

$$\begin{aligned} C_{pqrstu}^F = & \left( \frac{\partial^3 F}{\partial \rho^3} \right) \left( \sum_j \frac{x_t x_u}{r} \frac{\partial f}{\partial r} \right) \left( \sum_{j'} \frac{x_r x_s}{r} \frac{\partial f}{\partial r} \right) \left( \sum_{j''} \frac{x_p x_q}{r} \frac{\partial f}{\partial r} \right) \\ & + \left( \frac{\partial^2 F}{\partial \rho^2} \right) \left[ \sum_j x_r x_s x_t x_u \left( \frac{1}{r^3} \frac{\partial f}{\partial r} + \frac{1}{r^2} \frac{\partial^2 f}{\partial r^2} \right) \right] \left( \sum_{j'} \frac{x_p x_q}{r} \frac{\partial f}{\partial r} \right) \\ & + \left( \frac{\partial^2 F}{\partial \rho^2} \right) \left[ \sum_j x_p x_q x_t x_u \left( \frac{1}{r^3} \frac{\partial f}{\partial r} + \frac{1}{r^2} \frac{\partial^2 f}{\partial r^2} \right) \right] \left( \sum_{j'} \frac{x_r x_s}{r} \frac{\partial f}{\partial r} \right) \\ & + \left( \frac{\partial^2 F}{\partial \rho^2} \right) \left[ \sum_j x_p x_q x_r x_s \left( \frac{1}{r^3} \frac{\partial f}{\partial r} + \frac{1}{r^2} \frac{\partial^2 f}{\partial r^2} \right) \right] \left( \sum_{j'} \frac{x_t x_u}{r} \frac{\partial f}{\partial r} \right) \\ & + \left( \frac{\partial F}{\partial \rho} \right) \left[ \sum_j x_p x_q x_r x_s x_t x_u \left( \frac{1}{r^5} \frac{\partial f}{\partial r} + \frac{3}{r^4} \frac{\partial^2 f}{\partial r^2} + \frac{1}{r^3} \frac{\partial^3 f}{\partial r^3} \right) \right], \end{aligned} \quad (8)$$

and

$$C_{pqrstu}^\phi = \frac{1}{2} \left[ \sum_j x_p x_q x_r x_s x_t x_u \left( \frac{1}{r^5} \frac{\partial \phi}{\partial r} + \frac{3}{r^4} \frac{\partial^2 \phi}{\partial r^2} + \frac{1}{r^3} \frac{\partial^3 \phi}{\partial r^3} \right) \right]. \quad (9)$$

There are six independent elastic constants for cubic crystals. These are  $C_{111}$ ,  $C_{112}$ ,  $C_{123}$ ,  $C_{144}$ ,  $C_{155}$ , and  $C_{456}$ . The Cauchy relations are expressed as,

$$C_{112} = C_{155}, \quad C_{123} = C_{144} = C_{456}. \quad (10)$$

The second- and the third-order elastic constants for Cu, Ag, and Au crystals were calculated and the results were summarized in Table I, where the contributions from  $F(\rho)$  and  $\phi(r)$  were separately shown. The experimental values  $c_{\text{exp}}$  and  $C_{\text{exp}}$  by Hiki *et al.*[7] were also shown for the comparison.

It is seen that the contributions from two body interaction,  $c^\phi$  and  $C^\phi$ , satisfy the Cauchy relations, but the deviations are seen in the contributions from the embedded function,  $c^F$  and  $C^F$ .

## PHONON DISPERSION RELATION

When the interaction potential is known the phonon dispersion relation ( $\omega$  -vs.-  $q$ ) can be calculated by the D-matrix method of the lattice dynamics. As the number of atoms in the unit cell of fcc crystal is one, the D-matrix consists of  $3 \times 3$  matrix elements [12].

$$D_{\alpha\beta}(q) = \frac{1}{m} \sum_l \Phi_{\alpha\beta}(0, l) \exp(iq \cdot r(l)), \quad (11)$$

Table I. Elastic constants calculated by EAM potential.

(a) Cu

|           | $C^F$  | $C^\phi$ | $C$    | $C_{\text{exp}}$ |
|-----------|--------|----------|--------|------------------|
| $c_{11}$  | -1.699 | 3.432    | 1.733  | 1.684            |
| $c_{12}$  | -0.417 | 1.618    | 1.202  | 1.214            |
| $c_{44}$  | -0.880 | 1.618    | 0.738  | 0.754            |
| $C_{111}$ | 2.514  | -12.413  | -9.898 | -12.71           |
| $C_{112}$ | 1.134  | -5.179   | -4.044 | -8.14            |
| $C_{123}$ | 0.039  | -0.053   | -0.014 | -0.50            |
| $C_{144}$ | -0.355 | -0.053   | -0.407 | -0.03            |
| $C_{155}$ | 0.753  | -5.179   | -4.426 | -7.80            |
| $C_{456}$ | 0.112  | -0.053   | 0.059  | -0.95            |

(b) Ag

|           | $C^F$  | $C^\phi$ | $C$    | $C_{\text{exp}}$ |
|-----------|--------|----------|--------|------------------|
| $c_{11}$  | -3.115 | 4.370    | 1.256  | 1.240            |
| $c_{12}$  | -1.068 | 2.002    | 0.935  | 0.934            |
| $c_{44}$  | -1.545 | 2.002    | 0.458  | 0.461            |
| $C_{111}$ | 6.758  | -14.145  | -7.387 | -8.43            |
| $C_{112}$ | 2.573  | -5.410   | -2.836 | -5.29            |
| $C_{123}$ | -0.250 | -0.113   | -0.363 | 1.89             |
| $C_{144}$ | -0.422 | -0.113   | -0.534 | 0.56             |
| $C_{155}$ | 2.409  | -5.410   | -3.000 | -6.37            |
| $C_{456}$ | 0.166  | -0.113   | 0.053  | 0.83             |

(c) Au

|           | $C^F$  | $C^\phi$ | $C$     | $C_{\text{exp}}$ |
|-----------|--------|----------|---------|------------------|
| $c_{11}$  | -1.293 | 3.160    | 1.867   | 1.86             |
| $c_{12}$  | 0.100  | 1.470    | 1.571   | 1.57             |
| $c_{44}$  | -1.052 | 1.470    | 0.419   | 0.420            |
| $C_{111}$ | -0.833 | -10.825  | -11.657 | -17.29           |
| $C_{112}$ | 0.369  | -4.340   | -3.971  | -9.22            |
| $C_{123}$ | -1.541 | -0.064   | -1.604  | -2.33            |
| $C_{144}$ | -1.306 | -0.064   | -1.370  | -0.13            |
| $C_{155}$ | 0.622  | -4.340   | -3.718  | -6.48            |
| $C_{456}$ | 0.113  | -0.064   | 0.049   | -0.12            |

(in units of 100 GPa)

and

$$\Phi_{\alpha\beta}(0, l) = \frac{\partial^2 E}{\partial u_{\alpha}(l) \partial u_{\beta}(l)}. \quad (12)$$

Where  $E$  is the total internal energy given by eq.(1),  $u_{\alpha}(l)$  is the  $\alpha$  component of the displacement of the atom in the  $l$ -th unit cell,  $q$  is the propagation vector of a phonon, and  $m$  is the atomic mass. The dispersion relation can be determined by solving the determinantal equation,

$$| D_{\alpha\beta}(q) - \omega^2 \delta_{\alpha\beta} | = 0 \quad (13)$$

A result of calculation of the phonon dispersion relation for copper crystal is shown in figure 1. There are three acoustic (1 longitudinal + 2 transverse) and no optical phonon modes in the fcc crystal. The solid circles in the figure shows the experimental result by the neutron inelastic scattering [13]. The calculation shows some deviation from the experimental value at the zone boundary, but over all agreement between the calculation and the experiment is satisfactory.

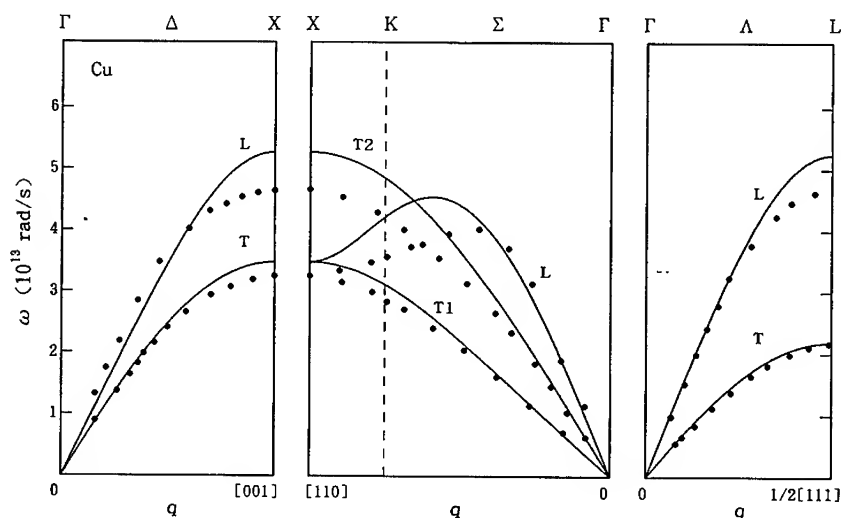


Fig. 1. Phonon dispersion relation calculated from the EAM potential. The solid circles show the experimental data by the neutron inelastic scattering[13].

## DISCUSSION

Recently, the method of molecular dynamics simulation have widely been used in the field of the solid state physics and the material science. For a simulation of a large scale atomic system, a simple and reliable interatomic potential is required to reduce the computational time. Usually the potential parameters are determined mostly in a equilibrium state of a perfect crystal. On the contrary the configuration of atoms in the course of simulation may be heavily disturbed and the potential must work at such a condition. The anharmonicity is a deviation from the linear elasticity and the effects becomes appreciable when the displacement of atoms becomes large. The phonon dispersion effects becomes remarkable at high frequency (short wave length) vibration of atoms. Although the EAM potential we adopted in this study is not include the anharmonicity and dispersion effects in the process of parameter determination, the reproducibilities of the experimental data are reasonable. We could make include the third order elastic constant and/or zone boundary phonon frequency to the potential parameters, but it may make the potential more complicated. We are also studying another potential functions. After the examination of variety of functions, a new simple and reliable potential function may be realized.

## REFERENCES

1. M. S. Dow and M. I. Baskes, Phys. Rev. B **29**, 6443 (1984)
2. M. W. Finnis and J. E. Sinclair, Philos. Mag. A **50**, 45 (1984)
3. S. M. Foiles, M. I. Baskes and M. S. Daw, Phys. Rev. B **33**, 7983 (1986)
4. D. J. Oh and R. A. Johnson, J. Mater. Res. **3**, 471 (1988)
5. R. A. Johnson and D. J. Oh, J. Mater. Res. **4**, 1195 (1989)
6. H. J. McSkimin, P. Andreach, Jr., J. Appl. Phys. **35**, 3312 (1964)
7. Y. Hiki and A. V. Granato, Phys. Rev. **144**, 411 (1966)
8. E. J. R. Drabble and R. E. B. Strathern, Proc. Phys. Soc. **92**, 1090 (1967)
9. Y. Kogure and Y. Hiki, J. Phys. Soc. Jpn. **36**, 1597 (1974)
10. Y. Kogure and Y. Hiki, J. Phys. Soc. Jpn. **38**, 471 (1975)
11. Y. Kogure and M. Doyama, Proc. IUMRS-ICAM-93, in press.
12. G. P. Srivastava, *The physics of Phonons* (Adam Hilger, Bristol, 1990) p. 20.
13. G. Nilsson and S. Rolandson, Phys. Rev. B **7**, 2393 (1973)

## MICROSTRUCTURAL CHANGES OF WELDED Zn-Al ALLOY

YAO HUA ZHU

Instituto de Investigaciones en Materiales, UNAM  
Apdo.P.70-360, Mexico D.F.04510, Mexico

### ABSTRACT

Extruded eutectoid Zn-Al alloy was welded by a melt of the same eutectoid alloy. Two different microstructures were observed in the joint part and the bulk of the welded alloy. Typical dendritic structure of as cast Zn-Al alloy was observed in the joint part of the welded alloy. The bulk of the welded Zn-Al alloy appeared as fine grain structure. Two different metastable phases  $\eta'_T$  decomposed from  $\eta'_S$  of chilled as cast state and  $\eta'_E$  of extruded state were found to be unstable during early stage of ageing. A four phase transformation occurred after the decompositions of these two metastable phases of  $\eta'_T$ . Microstructures of both joint part and bulk of the welded alloy were investigated parallelly during ageing processes.

### INTRODUCTION

Welding processes appear as an important method in metal and alloy productions. It has been interested in Zn-Al alloy production especially. Because of cast defects, such as underneath shrinkage and porous holes, the alloy products need to be repaired and welding becomes a good way for the repairing. Also for the large products, it would be convenient to join several small die castings which are produced in high volume and high speed. Unfortunately very little has been done on joining of zinc and zinc-aluminium alloys. The present study will discuss microstructures and ageing characteristics of the welded eutectoid Zn-Al alloy, based on the systematic investigations on cast and extruded Zn-Al alloys(1-3).

### EXPERIMENTAL

Two extruded Zn-Al alloy rods of 25 mm diameter were welded using alloy wire of the same eutectoid composition( Zn76Al22Cu2 in wt% ), as shown in fig.1. The tungsten - inert gas (TIG) process was used for welding. Three specimens were cut from separately the extruded bulk part,

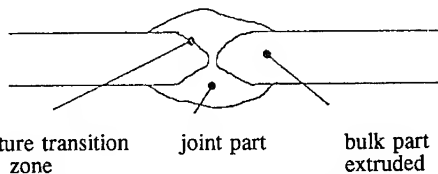


Fig. 1 Schematic of the welded eutectoid Zn-Al alloy

joint part and the structure transitional zone. General studies of the metallurgical structure were made on conventionally ground and polished specimens in the SEM using back scattered electron imaging to show atomic number contrast. For comparison, scanning electron microscopy

observations were respectively carried out on 290°C extruded eutectoid Zn-Al alloy and chilled as cast eutectoid Zn-Al alloy.

Phase identification and transformation studies were carried out on flat specimen using Philips X-ray diffractometer. Nickel filter and Cu  $K_{\alpha}$  radiation was applied within the diffraction angle range from 35° to 38°.

Microstructural changes of the welded alloy specimens both from bulk part and the joint part were studied during isothermal holding at 91°C and 150°C using X-ray diffraction technique.

## RESULTS

### 1, Microstructure of welded eutectoid Zn-Al alloy:

#### a, X-ray diffraction results:

The X-ray diffraction examinations were carried out on specimens of both the joint part and bulk part of the welded alloy. As shown in figs.2 and 3, both parts of the alloy consisted of three phases of  $\eta'_T$ ,  $\alpha$  and  $\epsilon$ . The phases of  $\eta'_T$  and  $\epsilon$  were of hexagonal close packed structure and the  $\alpha$  phase was of face center cubic structure. The diffraction peaks of  $\alpha$  and  $\epsilon$  phases appeared at the same  $2\theta$  angles in both parts of the alloy. The diffraction peaks of  $\alpha$  phase from crystal planes of (111) and (200) were respectively at  $2\theta$  angles 38.5° and 44.8°. The diffraction peaks of  $\epsilon$  phase from planes of (10 $\bar{1}0$ ), (0002) and (10 $\bar{1}1$ ) were respectively at  $2\theta$  angles 36.7°, 42.1° and 43.3°.

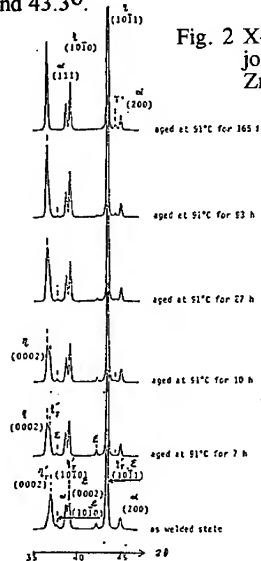


Fig. 2 X-ray diffractograms of the joint part of welded eutectoid Zn-Al alloy

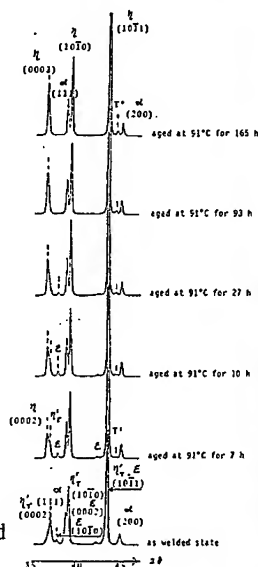


Fig. 3 X-ray diffractograms of the bulk part of welded eutectoid Zn-Al alloy

The diffraction peaks of  $\eta'_T$  and  $\epsilon$  phases from crystal planes (10 $\bar{1}1$ ) were well overlapped at  $2\theta$  angle 43.3°. Both  $\eta'_T$  phases were metastable phases derived from cast state of  $\eta'_S$  in the joint part and extruded state of  $\eta'_E$  in the bulk part of the welded alloy during welding. It was noticed that the diffraction peak of  $\eta'_T$  phase in the joint part appeared at different  $2\theta$  angles compared with that in the bulk part of the alloy. The diffraction peak of (0002) planes of the  $\eta'_T$  phase in the



joint part of the alloy was at  $2\theta$  angle  $36.9^\circ$ , while that of  $\eta'_T$  phase in the bulk part of the alloy was at  $36.8^\circ$ .

#### b, SEM observations:

Based on the X-ray diffraction identifications of the phases, the SEM observations were carried out on the joint part and the bulk part of the welded alloy and the structure transitional zone.

In the joint part of the welded alloy, typical dendritic structure of as cast eutectoid Zn-Al alloy was observed, as shown in fig.4a. The first solidified  $\alpha$  phase appeared as the core of the dendrite and surrounded by decomposed  $\beta'_S$  phase region. The decomposed  $\beta'_S$  phase region consisted of three phases ( $\alpha'_T$ ,  $\epsilon$  and  $\eta$  phases), and therefore the X-ray diffraction peak of  $\beta'_S$  phase did not appear on the X-ray diffractograms in fig.3. The interdendritic region consisted of  $\epsilon$  and  $\eta'_E$  phases.

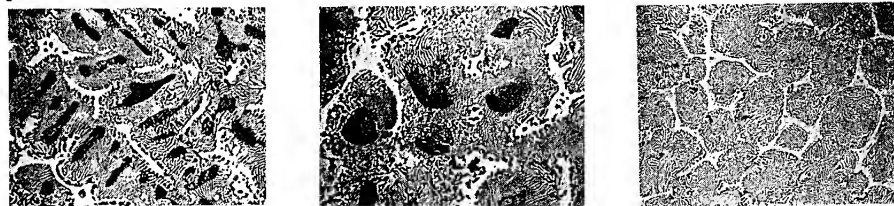


Fig. 4 Scanning electron micrographs of the welded eutectoid Zn-Al alloy:  
a) joint part b) transition zone c) bulk part

It was also found that the dendritic fragments had broken away from the growing interface or simply from melted-off dendrite arms due to turbulence in the weld pool, as shown in fig.4a. The dendritic structure in the joint part of the welded alloy tend to be on a finer scale ( about 30-50  $\mu\text{m}$  ) than in cast eutectoid Zn-Al alloy ( about 150  $\mu\text{m}$  ).

The bulk part of the welded alloy appeared as fine grain structure, as shown in fig.4c. The diameter of the grains was between 15-20  $\mu\text{m}$ . Inside the grain lamellar structure consisted of  $\alpha$ ,  $\epsilon$  and  $\eta'_T$ . The white inter-grain region was the  $\eta'_T$  phase.

In the transition zone, the microstructure changed gradually from the dendritic structure in the joint part to the fine grain structure in the bulk part of the welded alloy, as shown in fig.4b. The lamellar structure in the decomposed  $\beta'_S$  phase region gradually invaded into  $\alpha$  phase particle, as shown in fig.5. The welded alloy at the transition zone received the most severe thermal cycle and the grain in this zone tended to grow and became relatively coarse. The weld microstructure was thus inherently coarse grained.

#### 2, Phase transformation during isothermal holding:

Phase transformations of both the bulk part and the joint part of the welded alloy were parallelly examined after ageing at  $91^\circ\text{C}$  for 7 h, 10 h, 27 h, 92.5 h, 164 h by using the X-ray diffraction technique. The X-ray diffractograms are shown in figs.2 and 3. It was found that the both metastable  $\eta'_T$  phases decomposed at early stage of ageing. The diffraction peaks of crystal planes (0002) of the  $\eta'_T$  phases shifted gradually from lower  $2\theta$  angles from  $36.9^\circ$  and  $36.8^\circ$  respectively for the joint part and the bulk part of the alloy. The diffraction peaks of crystal plane of (10 $\bar{1}$ 1) were well overlapped and did not change their  $2\theta$  angle positions, as observed previously.(2 and 3 )

After 7 h ageing at 91°C T' phase occurred in both parts of the welded alloy. Furthering ageing, the  $\alpha$  and  $\varepsilon$  phases decreased in their diffraction peak heights, meanwhile the diffraction peaks of T' and  $\eta$  increased in heights. The four phase transformation,  $\alpha + \varepsilon \rightarrow T' + \eta$  (1-9), occurred. After 93 h ageing at 91°C, the  $\varepsilon$  phase vanished in the bulk part of the alloy and disappeared in the joint part of the alloy after 165 h ageing at 91°C, as shown in the the X-ray diffractograms figs.2 and 3. No more phase transformation was observed afterwards.

## DISCUSSION

### 1, Microstructures of welded eutectoid Zn-Al alloy:

In the 290°C extruded eutectoid Zn-Al alloy, the  $\alpha$  phase, appeared as dark particles, were surrounded by the decomposed  $\beta'_s$  phase of lamellar structure, and the  $\eta'_E$  appeared as white particles, as shown in fig.6. According to the phase diagram of the ternary Zn-Al-Cu alloy(10-12),  $\alpha$  phase is unstable at higher temperature, instead  $\beta$  phase is more stable and vice versa the  $\beta$  phase is unstable at lower temperature for the chemical composition of the eutectoid Zn-Al alloy being tested. During welding, the bulk part of alloy was heated up to high temperature close to the melting point, therefore the particle  $\alpha$  phase disappeared. Original extruded alloy stored high energy during extrusion. With this storage energy, it was facile to form fine grain structure when the alloy reached high temperature during welding. The zinc rich  $\beta$  phase formed as fine grain structure. The  $\eta'_E$  phase changed to the metastable  $\eta'_T$  phase appeared as the inter-grain region.

Fig. 5 Scanning electron micrograph of the transition zone, showing the gradual structure change X1750

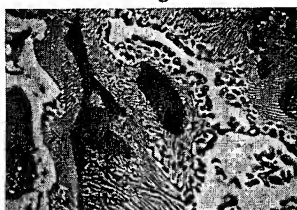


Fig. 6 Scanning electron micrograph of the 290°C extruded eutectoid Zn-Al alloy X500

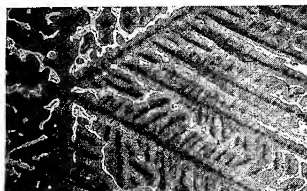


Fig. 7 Scanning electron micrograph of the chilled as cast eutectoid Zn-Al alloy X175

Since the temperature of the melt pool is so high and the base material is such a efficient heat sink there is initially a steep temperature gradient in the liquid and consequently the degree of constitutional super cooling is low. During air cooling after welding, this  $\beta$  phase became supersaturated, nominated as  $\beta'_s$  phase and decomposed (1,2,5 and 7). The fine grains got coarsened. The general coarseness of the microstructure is characteristic of the coarsened lamellar structure of the alloy. As shown in fig.4c, coarsened lamellar structure formed inside the fine grain structure in the bulk of the welded alloy.

According to the X-ray diffraction results, the  $\beta'_s$  phase had completely decomposed and both  $\alpha$  and  $\varepsilon$  phases appeared at the same diffraction  $2\theta$  angles in both the extruded and welded eutectoid alloys (1-3). Only the diffraction peak from (10 $\bar{1}$ 0) planes of  $\eta'_E$  phase at  $2\theta$  angle 36.9° shifted to the diffraction peak from (10 $\bar{1}$ 0) planes of the metastable  $\eta'_T$  phase in the bulk part of the welded alloy at  $2\theta$  angle 36.8°.

In the joint part of the welded alloy, the  $\eta'_T$  phase was derived from the as solidified  $\eta'_s$  phase in the chilled as cast eutectoid Zn-Al alloy. Compared with the chilled as cast eutectoid Zn-Al

alloy, the  $\beta'_s$  phase had completely decomposed into three phases,  $\alpha'_T$ ,  $\epsilon$  and  $\eta$ , and the  $\eta'_s$  phase decomposed to the metastable  $\eta'_T$  phase in the joint part of the welded alloy. The X-ray diffraction peak from (10 $\bar{1}$ 0) planes of the  $\eta'_s$  phase at  $2\theta$  angle  $37.1^\circ$  shifted to  $36.9^\circ$ . The decomposed  $\beta'_s$  phase region became coarsened lamellar structure.

Compared with the typical dendritic structure of the chilled as cast eutectoid Zn-Al alloy, as shown in fig.7, the dendrites in joint part of the welded alloy became smaller because of turbulence in the weld pool during welding and also the comparatively high solidification rates of weld alloy where the bulk part of the welded alloy became a sufficient heat sink.

## 2, Phase transformation during isothermal holding:

The metastable phases  $\eta'_T$  derived from  $\eta'_s$  phase of the chilled as cast state, during air cooling, and decomposed during isothermal holding. Al and Cu precipitated from the  $\eta'_T$  phase. The X-ray diffraction results showed that diffraction peaks of  $\alpha$ ,  $\epsilon$  and  $\eta$  phases increased in height in the early stage of isothermal holding, as shown in figs. 2 and 3. During prolonged ageing,  $\alpha$  and  $\epsilon$  phases decreased, meanwhile  $T'$  and  $\eta$  phases increased, the changes of X-ray diffraction intensities of those phases are shown in figs. 2 and 3. As discussed in the systematic studies (1-9), A four phase transformation,  $\alpha + \epsilon \rightarrow T' + \eta$ , occurred after decomposition of  $\eta'_T$  phase. The X-ray diffraction intensities of  $\alpha$ ,  $\epsilon$ ,  $T'$  and  $\eta$  phases are plotted against  $\ln t$  ( $t$ : ageing time) as shown in fig. 8.

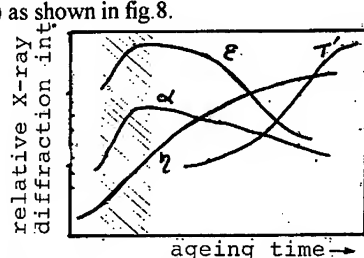


Fig. 8 Relative x-ray diffraction intensity changes of  $\alpha, \epsilon, \eta, T'$  phases in the joint part of the welded alloy during ageing at  $91^\circ\text{C}$

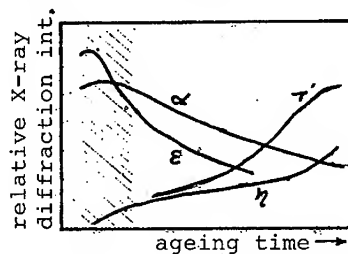


Fig. 9 Relative x-ray diffraction intensity changes of  $\alpha, \epsilon, \eta, T'$  phases in the bulk part of the welded alloy during ageing at  $91^\circ\text{C}$

In the bulk part of the welded eutectoid Zn-Al alloy, the  $\eta'_E$  phase in the original extruded alloy transformed to the metastable  $\eta'_T$  phase during welding at higher temperature. Microstructure appeared as fine grain structure, as shown in fig.4c. During isothermal holding, the  $\eta'_T$  phase decomposed into  $\alpha$ ,  $\epsilon$  and  $\eta$  phases, similar with the  $\eta'_T$  phase in the joint part of the alloy. The X-ray diffraction of  $\alpha$ ,  $\epsilon$  and  $\eta$  phases increased in intensity as shown figs. 2 and 3. During prolonged ageing both of diffraction intensities of  $\alpha$  and  $\epsilon$  phases decreased, meanwhile diffraction intensities of  $T'$  and  $\eta$  phases increased. The four phase transformation occurred. The X-ray diffraction intensities curves of  $\alpha$ ,  $\epsilon$ ,  $T'$  and  $\eta$  phases are shown in fig.9. The phase transformation of  $\alpha$ ,  $\epsilon$ ,  $T'$  and  $\eta$  phases are clearly shown. In the early stage of ageing, decomposition of  $\eta'_T$  phase occurred and followed by the four phase transformation,  $\alpha + \epsilon \rightarrow T' + \eta$ .

The shadow regions in Figs. 8 and 9 implies that the overlappings of the decomposition of the  $\eta'_T$  phases and the four phase transformation and also the decomposition of the  $\eta'_T$  phases and the four phase transformation occurred in the bulk part of the welded alloy were more rapid than that in the joint part of the welded alloy.

Though the phase transformations occurred in both joint part and bulk part of the welded alloy were similar to start with the decomposition of the metastable  $\eta'$ T phases, followed by a four phase transformation, the metallurgical characteristics were different. In the joint part of the alloy, those two stage of phase transformation occurred based on the typical as cast dendritic structure, while the similar phase transformations in the bulk part were carried out in the fine grain structure which derived from a thermal-mechanical treatment, i.e. hot extrusion.

## CONCLUSIONS

- 1, The welded eutectoid Zn-Al alloy consisted of three parts metallurgically, i.e. the bulk part of the alloy ( i.e. originally hot extruded rod ), joint part of the alloy and the structure transition zone. The bulk part appeared as fine grain structure of 15-20  $\mu\text{m}$  diameters. The joint part was characteristic of a typical dendritic structure of 30-50  $\mu\text{m}$  dendrites, smaller than that in as cast eutectoid Zn-Al alloy. In the transition zone, the structure changes from the dendritic structure to fine grain structure were clearly observed.
- 2, Both bulk part and joint part of the welded alloy consisted of three phases  $\eta'$ T,  $\alpha$  and  $\epsilon$ . The  $\eta'$ T phases in both parts were metastable phases.
- 3, During isothermal holding, the phase transformations occurred in both bulk part and joint part of the welded alloy were similar to start with the decomposition of the metastable  $\eta'$ T phases, followed by a four phase transformation,  $\alpha + \epsilon \rightarrow T' + \eta$ .
- 4, The metallurgical characteristics of the phase transformation were different. In the joint part of the alloy, those two stages of phase transformations occurred based on the typical as cast dendritic structure, while the similar phase transformations in the bulk part of the alloy were carried out in the fine grain structure, which derived from original thermal-mechanical treatment, i.e. hot extrusion.

## ACKNOWLEDGEMENTS

The author is grateful to Leticia Baños and antonio Caballero for their helps in the experimental work.

## REFERENCES

- 1, Y.H.ZHU, Chin.J.Met.Sci.Technol.Vol.6,1990 125
- 2, Y.H.ZHU,G.TORRES-VILLASEÑOR and C.PIÑA, J.Mater.Sci. 29,1994 1549
- 3, Y.H.ZHU and F.E.GOODWIN,J.Mater.Sci.Technol.,Vol.10,1994,121
- 4, Y.H.ZHU and S.MURPHY,Cin.J.Met.Sci.Technol.Vol.65,1987,261
- 5, Y.H.ZHU,B.YAN and W.HUANG, Symp.Proc.Zn-Al Casting Alloys,Toronto Canada,1986,23
- 6, Y.H.ZHU,W.HUANG and B.YAN,Shanghai Metals (Nonferrous Fascicule) Vol.9,1988,1
- 7, Y.H.ZHU and F.E.GOODWIN, J.Mater.Res. Vol.8,No.12,1993,3043
- 8, J.KROL and K.WEGREZYN, Archiwum Hutnictwa,1971,17,119
- 9, R.CIACH,J.KROL and K.WEGREZYN, Bulletin de LACADEMIE Polonais des Science serie desSciences Techniques,1969,17(4),341
- 10, S.MURPHY,Z.Metallkde 71,1980,96
- 11, Y.H.ZHU and S.MURPHY,Chin.J.Met.Sci.Technol.,vol.2,1986,105
- 12, Y.H.ZHU,Chin.J.Met.Sci.Technol., Vol.5,1989,113

## FRACTURE AND FRACTALS IN GLASSES

ELENA A. CHECHETKINA

Institute of General and Inorganic Chemistry, Leninsky Pr. 31,  
Moscow 117907, Russia

### ABSTRACT

Original model of bond waves is applied to the problem of fracture in glasses when considering it from the fractal point of view. Bond waves are assumed to be traveling above  $T_g$ , the glass transition temperature, and frozen in solid material ( $T < T_g$ ), and just along the stopped wavefronts (WF) populated with weakened bonds the fracture occurs. Crack, initiating at a given WF, then develops along WF's belonging to this system (a given bond wave) and/or another set (coexisting bond wave), and may oscillate between them. The arising surface represents a natural fractal whose fractal dimension depends on the mode of bond waves' interaction and their arrangement relatively to the crack direction.

### INTRODUCTION

Particular fracture (often termed conchoidal fracture) is an inherent attribute of amorphous solids including glasses: prior to early 1900's, before the X-ray analysis advent, a solid was characterized as amorphous by means of fractography. Really, even by eye or, better, by microscope one may differ confidently enough monocrystal (usually regular steps with regular triangles, etc. on them) or polycrystal (grainy surface) from glass (smooth "mirror" areas together with wavy steps and equidistant lines on their surface). Fractography of glass describes a number of features which display in a more or less extent depending on a sample: bulk glass (rib marks, Wallner lines, etc. [1]) or fiber (mirror, mist, hackle [2]) and its prehistory. However, the question of whence these features and why they are sensitive to the preparing conditions remains open.

On the other hand, one may observe the self-similarity at different scales at the glass fracture surface, e.g. small conches developing on the large ones. In addition, some of the surfaces are suspiciously similar to mathematical fractal sets (see e.g. photos 69-73 and 79-88 in [3]). Thus, one may consider the fracture surface of glass as a natural fractal, and with a better reason than in the case of polycrystalline metals [4] or rocks [5].

Usually, there are two approaches to investigate fractals, first, construction of artificial fractal sets [3] and, second, description of natural fractals by means of their fractal dimension [4,5]. Here the attempt of the third kind is made: we will try to understand what is the origin of "glassy" fractals and how one may form them under real experimental conditions. The central idea is self-organization of chemical bonds that leads to dynamical substructure in the form of bond wave.

## BOND WAVE(S) IN AMORPHOUS MEDIUM

Amorphous not means "formless" just because one may observe the well defined shapes on fracture surfaces [1,2]. Furthermore, a widespread opinion that amorphous solid is characterized only by short-range order (SRO) in contrast to crystal possessing long-range order (LRO) became antiquated: it is evident now that glasses and some other amorphous solids and liquids possess the so called medium-range order (MRO). The most prominent evidence of MRO is the first sharp diffraction peak (FSDP) whose nature remains unclear up to now (see [6] as review). The author opinion about the origin of FSDP was stated in frames of two models named synergetic model [7] and modified layer model [8] of FSDP. Their general points are:

(i) FSDP is a true Bragg reflex from real internal layers of the  $d=2\pi/Q_1$  thickness (where  $Q_1$  is the FSDP position), the  $2\pi/Q_1$  "oscillations" of FSDP described recently [9] being simply the higher-order reflections from the layers;

(ii) The layers are formed by means of special bonds named *alternative bonds* (AB) in contrast to *main bonds* (MB), the latter being forming both crystalline lattice and random amorphous network of a substance but not the structure regions responsible for MRO;

(iii) A possible nature of AB may be evaluated by means of the  $d$  vs  $r_1$  relations (where  $r_1$  is the first interatomic distance or the SRO dimension) which are specific for every group of amorphous substances (glasses, amorphous metals, KSn melt, etc.) [10]. For glasses, in which MB are ordinary two-centre covalent bonds, the three-centre bonds (TCB) seems to be the most appropriate candidate for AB. Note that TCB as characteristic bonding state in glasses was introduced by Dembovsky as long ago as 1981 [11];

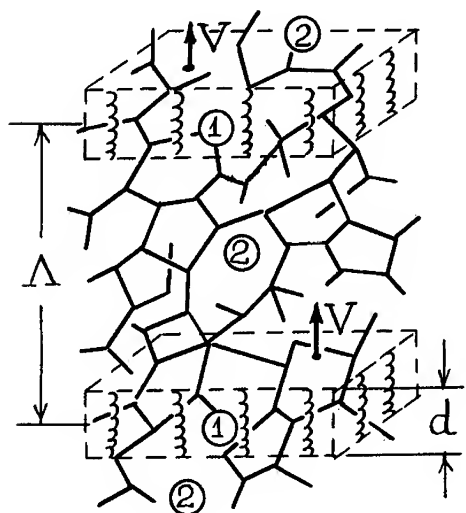


Fig.1

Amorphous structure with reflecting layers (1) and amorphous tissue (2) between them. Solid segments represent MB and springs - AB. This is a minimal fragment consisting of two wavefronts/layers which belong to the plane bond wave of  $\Lambda$  wavelength.  $V$  is the wave velocity (at  $T > T_g$ ). In solid ( $T < T_g$ )  $V$  should be replaced by the unit vector  $n$ , the  $n$  direction being the same as the  $V$  direction before freezing.

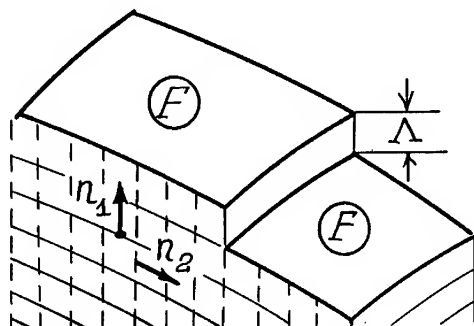


Fig.2

Elementary step on fracture surface of glass whose substructure represents two frozen bond waves, each of the  $\Lambda$  wavelength.

(iv) The origin of reflecting layers is not only bond instability or "bond option" after Ovshinsky [12] but also the spatiotemporal correlation of elementary acts  $MB \leftrightarrow AB$  which gives rise to bond wave shown conditionally in fig.1;

(v) Characteristic (but not compulsory!) isotropy of amorphous solids observed at macroscopic scale points to several bond waves coexisting before freezing.

Thus, we obtain not only MRO that exists in the limits of reflecting layers "1" in fig.1 but also particular LRO with the period  $\Lambda$  and corresponding substructure ( $\Lambda$ -lattice) representing a set of the layers belonging to one and the same bond wave. Since AB are weaker than MB (otherwise they would be the main bonds in a substance) the TCB-layers in glass may play a role of cleavage planes in monocrystal and, therefore, fracture is able to visualize  $\Lambda$ -lattice(es) as it is shown in fig.2. Curved and complex shapes of real fractures indicate that (i) the plane bond waves does not realize in general case, (ii) fracture may transfer from one set (wave) to another.

#### INFORMATION FIELDS FOR BOND WAVE

To characterize the bond wave originated substructure of a glass-forming melt or glass one should know the following parameters: number of coexisting bond waves ( $N=1,2,\dots$ ), population of wavefront with alternative bonds ( $\rho_{AB}$ ), velocity and direction ( $V_1, V_2, \dots$ ) or -in glass- the direction ( $n_1, n_2, \dots$ ), and wavelength ( $\Lambda_1, \Lambda_2, \dots$ ). In case of  $N=1$  the scale parameters  $\rho_{AB}$  and  $\Lambda$  depends on temperature if the bond exchange is a thermally activated process; in this case heating increases concentration of AB and, therefore, increases  $\rho_{AB}$  at  $\Lambda=\text{const}$  or decreases  $\Lambda$  at  $\rho_{AB}=\text{const}$ . However, because self-organization occurs only in open systems which interacts with its surrounding not only by energy (mass) exchange but also by information exchange [13], then in order to obtain bond wave(s) there needs information field(s) which determine the number of bond waves and their direction of spreading.

### Temperature Gradient

Under ideal adiabatic conditions, i.e. in a closed system, self-organization is absent: in our case this means chaotic bond exchange instead of bond wave. Let open a system under consideration, i.e. glassforming melt, by introduction of thermal flow through it. At a critical value of  $\text{grad}T$  the bond wave appears and its wavefronts, being a more ordered and so "cold" formations, will move to "hot" direction, i.e.  $V \propto \text{grad}T$ . Note that  $\text{grad}T$  always presents when glass making both at the stage of melt cooling ( $T > T_g$ ) and glass article forming ( $T \approx T_g$ ).

### Mechanical Stress

While a piece of glass may be obtained by cooling merely, the glass article (bottle, fiber, etc.) - only by means of joint action of temperature and stress (S). To clear the S influence on the bond wave let us consider experiments of Donnadieu [14]. She observed that the silica glass samples fractured after plastic deformation demonstrate regular sets of planes parallel to the stress plane: the big steps of  $h \approx 1-2 \mu$  and "river pattern" with  $h \approx 100 \text{ \AA}$ . In addition, the "family of empty disks" with  $d \approx 20-100 \mu$  sometimes displays on fracture surface. It means:

Fig.3a-b: reorientation of initial bond waves  $n_1, n_2$  (a) in the field direction ( $n \parallel S$ ) and forming of dynamic blocks whose dimension  $M$  depends on deformation conditions ( $T, S$ ). Fig.3c: wavefronts which participate in the sub- $T_g$  flow are destroyed partially and may split after thermal shock ( $1000/1200^\circ\text{C} \rightarrow 20^\circ\text{C}$ ).

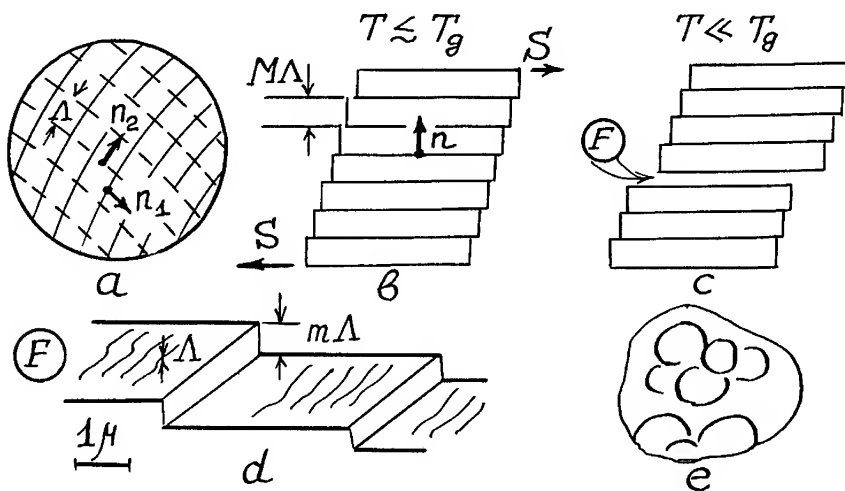


Fig.3

Model of plastic flow (a,b) and afterflow spontaneous fracture (c) proposed for explanation of experimental data [14] (d,e).



Fig.3d: fracture reveals the second family of blocks with  $m \ll M$ , which was also formed during deformation; this set gives large steps while tiny steps seems to visualize neighbouring wavefronts, i.e.  $h=\lambda$ . Fig.3e: the process of reorientation ( $n_{1,2} \rightarrow n$ ) was not completed, and we see the result of interaction between primary ( $n_1, n_2$ ) and secondary ( $n$ ) waves.

### Magnetic Field

The fact that magnetic field can modify internal structure of glass was revealed in our viscosity ( $\eta$ ) experiments [15,16], in which a rather weak field ( $H \approx 2000e$ ) decreased  $\eta$  when  $H \parallel \vec{\omega}$ , where vector  $\vec{\omega}$  is velocity of the indenter immersion into a softening Se glass, or increased  $\eta$  when  $H \perp \vec{\omega}$ , and up to 2-3 times in "resonant conditions" ( $f=50Hz$ ,  $T=49^\circ C$ ). In addition, the  $As_2S_3$  and  $As_2Se_3$  glasses prepared in the presence of the field was shown to differ in optical and mechanical properties from their non-field analogues [17]. It is seen in fig.4 that fracture modes in these glasses differ too.

As soon as the act of bond exchange  $MB \leftrightarrow AB$  proceeds as initially one-electron process [18] it is sensitive to magnetic field, as well as bond wave considered as cooperative bond exchange. Resonance [16] means that the field frequency  $f$  fit to the bond wave frequency  $V(T)/\lambda(T)$  at a given temperature  $T$ . It follows from the character of  $\omega$  change under the field action [15,16] that  $V \parallel H$ , what is confirmed by the fracture mode FHH in fig.4. The complex fracture mode in non-field sample (marked T) reflects the complexity of thermal field ( $\Sigma grad T$ ) existing during solidification, i.e. coexistence of different bond waves, each of  $V_i \parallel grad T_i$ , that are frozen in glass.

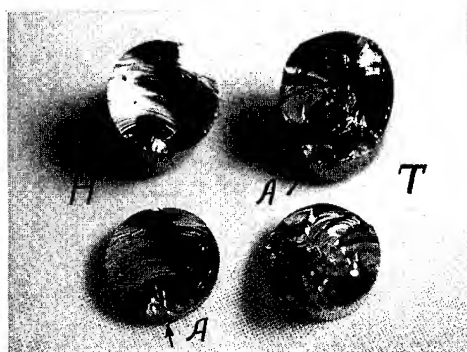


Fig.4

Fracture modes for a pair of  $As_2S_3$  samples, one (H) prepared in magnetic field ( $H=2400e$ ,  $480^\circ C$ , 1h; cooling 10min to room temperature under the field). Glasses were fractured by blow on the knife blade arranged at points A parallel to the sample bottom.

### Complex Fields

In general case there may be two and more information fields (e.g.  $grad T$  and  $S$  during fiber drawing) and the question is does they form two/more independent bond waves (soliton behavior), or one wave with somewhat averaged parameters, or two/more waves interacting with each other.

## DISCUSSION

We have saw that even in the simple case of specially created single plane bond wave (fig.3b-d) crack does not spread along one and the same wavefront and the structure realized is hierarchical: at least three sets  $MA-mA-A$  coexist and simultaneously revealed by fracture. Thus, the fractal dimension is  $D > 2$  and depends both on internal structure [e.g.  $D(H) < D(T)$  in fig.4], being increasing in complex information fields, and on the mode of destruction including direction of stress relatively to the wave(s) direction. The latter may be excluded by using other experimental methods of investigation of fractals [19] (see e.g. [20] for glasses), however, fracture is the most simple and obvious among them.

## ACKNOWLEDGEMENTS

This work was supported by Russian Foundation for Basic Research Grant No.93-03-456 and ISF Grant No.4225/5.

## REFERENCES

1. H.Rawson, Properties and Applications of Glass (Elsevier, Amsterdam, 1980), p.147.
2. S.R.Choi and J.E.Ritter, Phys. Chem. Glass. 32, 79 (1991).
3. H.O.Peitgen and P.H.Richter, The Beauty of Fractals (Springer, Berlin, 1986).
4. B.B.Mandelbrot, D.E.Passoja and A.J.Pauling, Nature 308, 721 (1984).
5. C.Y.Poon, R.S.Sayles and T.A.Jones, J.Phys.D:Appl.Phys. 25, 1269 (1992).
6. S.R.Elliott, J.Phys.:Cond.Matt. 4, 7661 (1992).
7. E.A.Chechetkina, Sol. St. Comm. 87, 171 (1993).
8. E.A.Chechetkina, Sol. St. Comm. 91, 101 (1994).
9. P.S.Salmon, Proc. R. Soc. Lond. A445, 351 (1994).
10. E.A.Chechetkina, J.Phys.:Cond.Matt. 5, L527 (1993).
11. S.A.Dembovsky, Mater. Res. Bull. 16, 1331 (1981).
12. S.R.Ovshinsky, J. Non-Cryst. Solids 75, 161 (1985).
13. H.Haken, Information and Self-Organization (Springer, Berlin, 1988).
14. P.Donnadieu, J.Non-Cryst.Sol. 105,280 (1988); 111, 7 (1989).
15. S.A.Dembovsky, S.A.Kozuykhin and E.A.Chechetkina, Mater. Res. Bull. 17, 801 (1982).
16. S.A.Dembovsky, E.A.Chechetkina and S.A.Kozuykhin, Pis'ma Zh. Eksper. Teor. Fiz. 41, 74 (1985).
17. E.A.Chechetkina, S.A.Dembovsky, S.A.Kozuykhin, V.G.Podkopaev and V.A.Sidorov, in Amorphous Semiconductors'84 (Bulg. Acad. Sci., Gabrovo, 1984), v.1, p.74.
18. S.A.Dembovsky and E.A.Chechetkina, Phil.Mag. B53,367 (1986).
19. J.K.Kjems, in Fractals and Disordered Sysytems, edited by A.Bunde and S.Havlin (Springer, Berlin, 1991), p.263.
20. A.Fontana, F.Rocca, M.P.Fontana, B.Rosi and A.J.Dianoux, Phys. Rev. B41, 3778 (1991).

---

## PART VII

---

### **Complex Materials**

## COOPERATIVE STRATEGIES AND GENOME CYBERNETICS IN FORMATION OF COMPLEX BACTERIAL PATTERNS

ESHEL BEN-JACOB\*, OFER SHOCHET\*, INON COHEN\*, ADAM TENENBAUM\*,  
ANDRAS CZIRÓK\*\* AND TAMAS VICSEK\*\*.

\* School of Physics and Astronomy, Raymond & Beverly Sackler Faculty of Exact Sciences,  
Tel-Aviv University, Tel-Aviv 69978, ISRAEL

\*\* Department of Atomic Physics, Eötvös University, Budapest, Puskin u 5-7, 1088 Hungary

### ABSTRACT

We present a study of interfacial pattern formation during growth of bacterial colonies. Growth of bacterial colonies bears similarities but presents an inherent additional level of complexity in comparison with non-living systems. In the former case, the building blocks themselves are living systems, each with its own autonomous self-interest and internal degrees of freedom. The bacteria have developed sophisticated communication channels, which they utilize when growth conditions are tough. Here we present a non-local communicating walkers model to study the effect of local bacterium-bacterium interaction and communication via chemotaxis signaling. We demonstrate how communication enables the colony to develop complex patterns in response to adverse growth conditions. This self-organization of the colony, which can be achieved only via cooperative behavior of the bacteria, may be viewed as the outcome of an interplay between the micro-level (the individual bacterium) and the macro-level (the colony). Some qualitative features of the complex morphologies can be accounted for by invoking ideas from pattern formation in non-living systems together with a simplified model of chemotactic "feedback".

### INTRODUCTION

Typically, bacterial colonies are grown on substrates with a high nutrient level and intermediate agar concentration. Under such "friendly" conditions, the colonies develop simple (almost structureless) compact patterns with smooth envelope. This behavior fits well the contemporary view of the bacterial colonies as a collection of independent unicellular organisms (or non-interacting "particles", if borrowing terminology from physics). However, in nature, bacterial colonies regularly must cope with hostile environmental conditions[1]. What happens if we create hostile conditions in a petri dish by using, for example, a very low level of nutrients or a hard surface (high concentration of agar), or both? The bacteria reproduction rate, which determines the growth rate of the colony, is limited by the level of nutrients concentration available for the bacteria. The latter is limited by the diffusion of nutrients towards the colony. Hence, the growth of the colony resembles diffusion limited growth in azoic systems. From the study of diffusive patterning in azoic systems we understand that a diffusion field drives the system towards decorated (on many length scales) irregular fractal shapes. Moreover, we now understand how the competition between the actions of the diffusion field and the microscopic effects (surface tension and surface kinetics) determines the evolved pattern[2, 3]. The microscopic effects, when present, compete with the diffusive instability and channel it towards regular and less decorated structures. Generally speaking, the morphology changes from fractal-like[4], when the diffusive instability

dominates the growth, to compact[5] when the diffusive instability is weaker than the action of the microscopic effects.

In view of the above, one would naively expect that whenever bacterial colonies are grown on very low-nutrient agar (diffusion limited) branching will occur (rather than compact growth) to facilitate the colony's access to food. Indeed, bacterial colonies develop patterns reminiscent of those observed during growth in azoic systems [6, 7, 8, 9] such as solidification from a supersaturated solution, liquid-crystal solidification, electro-chemical deposition etc.[2]. We believe that the complex patterning of bacterial colonies is not merely an additional example (albeit more involved) of spontaneous emergence of patterns, that may be explained according to the theory of patterning in azoic systems, but that it leads to a new understanding required for biological systems.

We will show that by comparing the formation of patterns in the two worlds we can identify both the common principles and the features unique to bacterial colonies. An additional level of complexity is involved in bacterial colonies, since the building blocks themselves are living systems, each having its own autonomous self-interest and internal degrees of freedom. At the same time, efficient adaptation of the colony to adverse growth conditions requires self-organization on all levels – which can be achieved only via cooperative behavior of the bacteria. This may be viewed as the action of a singular interplay[8, 9] (singular perturbation or regulation and singular feedback or control) between the micro-level (the individual bacterium) and the macro-level (the colony) in the determination of the emerging pattern. In general, as growth conditions worsen, a more complex global structure is observed together with a higher micro-level organization.

To achieve this, the bacteria have developed sophisticated communication channels on all levels[1, 10, 11, 12, 13]: from direct (by contact) bacterium-bacterium physical interaction and chemical interaction, through indirect physical and chemical interactions via marks left on the agar surface and chemical (chemotactic) signaling, to genetic communication via exchange of genetic material. The communication enables each bacterium to be both actor and spectator (using Bohr's expressions) during the complex patterning. The bacteria developed a particle-field duality: each of the bacterium is a localized (moving) particle which can produce a chemical and physical field around itself. For researchers in the pattern formation field, the above communication regulation and control mechanism opens a new class of tantalizing complex models exhibiting a much richer spectrum of patterns than the models for azoic systems.

An additional level of complexity arises from the potential of the individual bacterium to perform inheritable genetic metamorphoses in response to the growth conditions[8, 9]. Indeed, as the bacteria are exposed to more adverse growth conditions, new modes (mutations), with more sophisticated communication strategies enabling a more complex behavior, were observed. Hence, pattern selection during complex patterning is directly related to the issue of genome cybernetics, as the colony organization (being the environment) can directly affect the genetic metamorphosis of the individual and vice-versa[8, 9].

## EXCITATION OF THE MOTILE MODE : phase $T$

We have started our experimental endeavor with *Bacillus subtilis* 168 ( $B168$ ). The bacterial colonies were grown on standard petri-dishes covered with a thin layer of substrate (see ref [8, 9] for details). The growth conditions varied from an extremely poor level of nutrients to a rich mixture and from a soft substrate to a very hard one. The typical growth patterns were compact with a rough interface, reflecting the fact that the  $B168$  bacteria are

nonmotile. Can the bacteria develop mobility, or change the nature of the reproduction?

Seeking experimental answers to the above questions, Ben-Jacob *et al.* [8, 9, 14] have performed experiments in which numerous numbers of colonies of the *Bacillus subtilis* 168 were grown under a wide range of adverse conditions for a long time. Occasionally, bursts of spectacular new modes of growth exhibiting branching patterns were observed (Phase T, Cf. [8, 9]). These new branching modes were shown to be inheritable, i.e. inoculation of bacteria (and even single bacterium after dilution in liquid) from the new bursting mode led again to a branching colony. The branching colonies propagate much faster than the original *Bacillus subtilis* 168 colonies, indicating that a genetic change took place as a strategy for better adaptation to the environment.

The colonies of phase T adopt various shapes as the growth conditions are varied (Fig. 1). The patterns are compact for high pepton levels and become more ramified at low pepton levels, in agreement with the results of references [15, 6, 16, 17]. Surprisingly, at even lower pepton levels the colonies again adopt a more organized (well defined circular envelope) dense structure.

Microscope studies reveal that the bacteria perform a random-walk-like movement within a well defined envelope [18, 14]. The latter is formed presumably by chemicals which are excreted by the bacteria and/or by fluid drawn by the bacteria from the agar. The envelope slowly propagates, as if by the action of an effective internal pressure produced by the collective movement of the bacteria.

## MODELING THE GROWTH : THE COMMUNICATING WALKERS MODEL

We adopted the approach of generic modeling for the bacterial complex patterning.

A single colony may consist of  $10^{10}$  bacteria. Hence, it is impractical to deal with modeling of a single bacterium. Instead we chose to represent the bacteria by walkers, each of which should be viewed as a mesoscopic unit (course graining of the colony) and not as an individual bacterium. In our simulations, each walker represents about  $10^4 - 10^5$  bacteria.

Each walker is described by its location  $\vec{R}_i$  and an internal degree of freedom ("internal energy"  $E_i$ ), which affects its activity. The walker loses "internal energy" at a constant rate. To increase the internal energy, it consumes nutrients at a fixed rate if sufficient food is available. Otherwise, it consumes the available amount. When there is not enough food for an interval of time (causing  $E_i$  to drop to zero), the walker becomes immotile and remains in this state. With sufficient food  $E_i$  increases, and when it reaches some threshold, the walker divides into two (reproduction).

As in the experiments, we start the simulations with a uniform distribution of nutrients. For simplicity, we assume a single component of "food" whose concentration is  $c(\vec{r})$ . As the walkers consume the food,  $c(\vec{r})$  decreases around the colony and there is diffusion of nutrients towards the colony. Nutrients diffusion is handled by solving the diffusion equation for  $c(\vec{r})$  on a triangular lattice.

The walkers perform off lattice random walk within an envelope that is defined on the triangular lattice. At each time step, each of the active (motile) walkers moves a step of size  $d$  (which is shorter than the lattice size) and at an angle  $\Theta$ , uniformly chosen from the interval  $[0, 2\pi]$ . If the step crosses the envelope, the step is not performed and a counter on the appropriate segment of the envelope is increased by one. When a segment counter reaches  $N_c$  the envelope segment propagates one lattice step and additional lattice cell is added to the colony. This requirement (of  $N_c$  hits) represents the local communication or cooperation

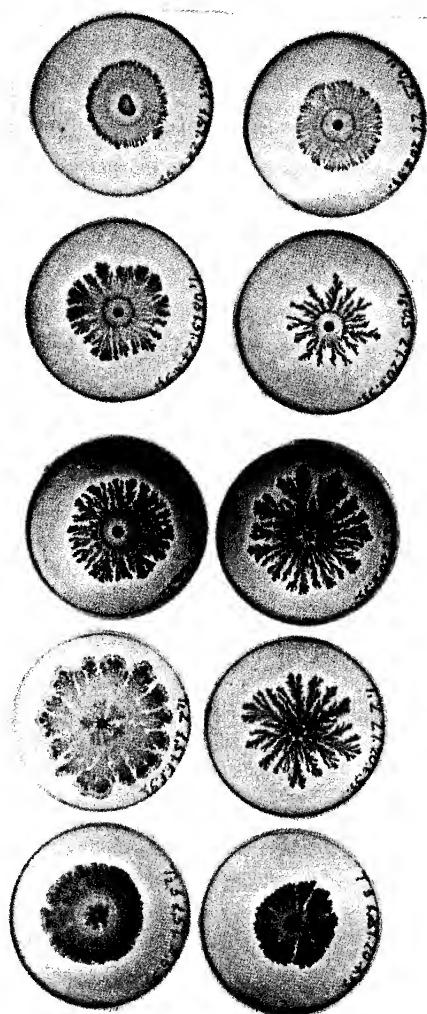


Fig. 1. Example of the morphology diagram of Phase T as function of pepton level (increasing from top to bottom) and for two values of agar concentration. (1.5% (left column); 2.0% (right column)).

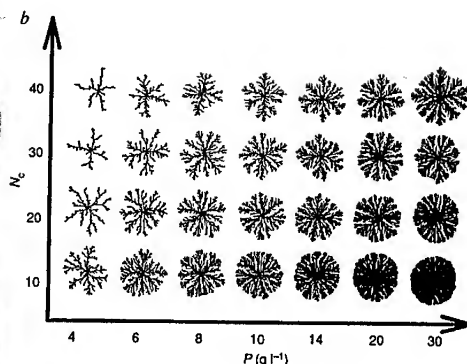


Fig. 2. Results of numerical simulations of the communicating walkers model. The patterns are organized as function of pepton level  $P$  (the initial value of  $c$ ) and  $N_c$  (corresponds to the agar concentration). The typical system size is  $600 \times 600$  and the typical number of the walkers is  $10^5$ . Hence each walker represents about  $10^4$  bacteria. The observed patterns are compact for high pepton levels and become ramified for low pepton levels. For the same pepton level, the patterns are more branching for higher  $N_c$ . Both are consistent with experimental observations. Note that the fractal dimension becomes much smaller than the DLA fractal dimension. It reflects the fact that the envelope propagation has non trivial dependence on the gradient of the nutrients diffusion field.

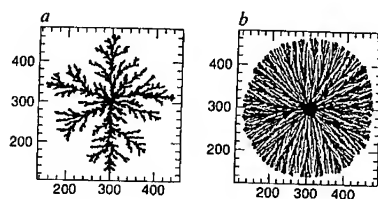


Fig. 3. Effect of chemotaxis signaling: (a) In the absence of chemotaxis for  $P = 10$  and  $N_c = 40$ . (b) In the presence of chemotaxis (for the same values of  $P$  and  $N_c$ ). The pattern becomes denser with radial thin branches and well defined circular envelope, in agreement with experimental observations.

in the behavior of the bacteria. Note that, to a first approximation,  $N_c$  represents the agar concentration, as more "collisions" are needed to push the envelope on a harder substrate. for more details see ref [18, 14].

Results of numerical simulations of the model are shown in fig. 2. As in the growth of bacterial colonies, the patterns are compact at high pepton levels and become fractal with decreasing food level. The results capture some of the observed features but not the ability of the bacteria to develop organized patterns at very low pepton levels. Does chemotactic signaling provide the colony with the means to do so? Generally, chemotaxis means movement of the bacteria in response to a gradient of certain chemicals field [19, 13, 20]. Ordinarily, the movement is along the gradient either in the opposite direction or in the gradient direction. The chemotactic response may be to an external field or to a field produced directly or indirectly by the bacteria. The latter case can be referred to as chemotaxis signaling or chemotaxis communication. Moreover, it is well known that excretion of the chemotaxis material can be triggered by exerting stress on the microorganisms. Such non-local communication enables each bacterium to obtain information about and respond to the state of the colony as a whole.

We include a simple version of chemotaxis communication to reveal the generic features. Each of the stationary walkers produces a communication chemical at a fixed rate, and each of the active walkers consumes the chemical at a fixed rate. The movement of the active bacteria changes from pure random walk (equal probability to move along any direction) to a random walk with a bias along the gradient of the communication field (higher probability to move in the direction of the signaling material). In Fig. 3 we show that indeed, the inclusion of such chemotaxis signaling produces the desired phenomena: the patterns change from fractal to a dense structure with thin branches and a well defined circular envelope.

## IMPOSED ANISOTROPY

We have studied the effect of imposed four-fold lattice anisotropy on the growth of the bacterial colonies. In Fig. 4 we show simulations of the communicating walkers model in the presence of four-fold lattice anisotropy. The anisotropy is included via a four-fold net of lines, along which  $N_c$  is of lower value. The results show a clear concave-to-convex transition as a function of pepton level. Chemotaxis signaling has been included in the simulations shown in Fig. 5. In the absence of such signaling, the concave-to-convex transition fades away.

To test the above predictions, we developed a method of "agar stamping" that induces modulation on the agar surface [21]. A clear concave-to-convex transition is observed. The qualitative agreement with the model's predictions indicates again the role of repulsive chemotaxis signaling. The results also suggest that morphology transitions occur and hence a morphology selection principle acts during growth of the bacterial colonies.

In Fig. 6 we show typical growth patterns observed in the presence of imposed 6-fold anisotropy. The patterns exhibit a tantalizing similarity to the shapes of real snowflakes. Each morphology consists of six main arms with dendrites. At high pepton levels, the patterns are denser and the effect of the anisotropy fades away. At very low pepton levels, the patterns become denser again and maintain the six-fold symmetry, in agreement with the simulations when repulsive chemotaxis is included.

The observations demonstrate that singular perturbation does play a role during growth of bacterial colonies. The modulations on the agar surface break the symmetry in the dynamics over just a small regime of the advancing front, in the immediate vicinity of the ridge. Yet,



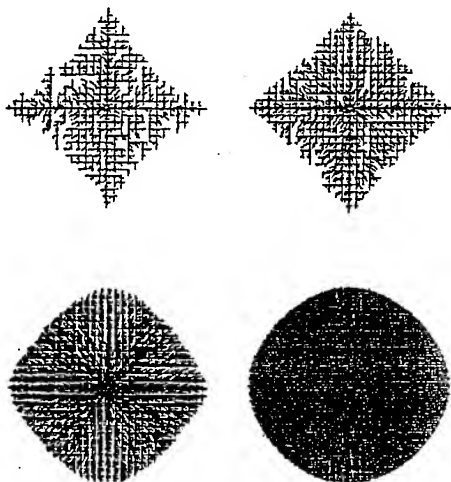


Fig. 4. Patterns produced by the "communicating walkers" model in the presence of lattice four-fold anisotropy and with chemotaxis signaling. The simulations are for  $N_c=20$ . (a)-(d) are for  $P=10;15;35$  and  $75$  respectively. Note that the envelope shows a transition from concave to convex shape.

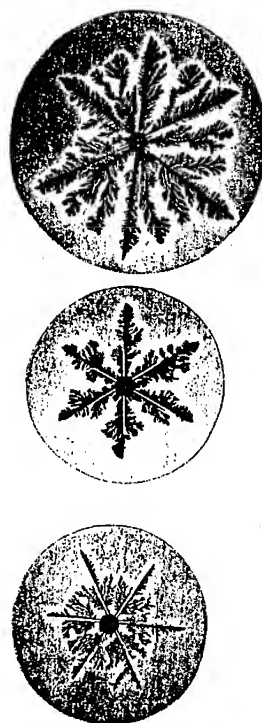


Fig. 6. "Bacterial snowflake" : The effect of imposed six-fold anisotropy. The anisotropy is introduced using the "stamping" method described in the text.

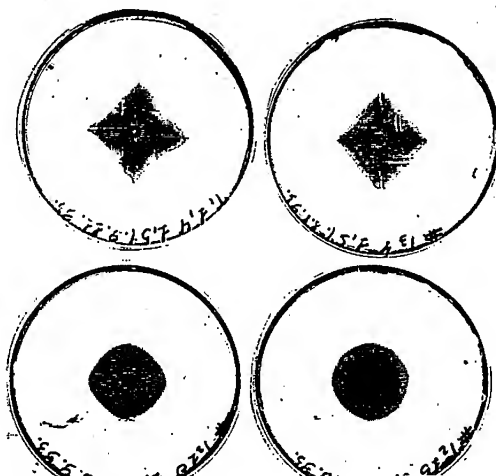


Fig. 5. Patterns observed during growth in the presence of imposed four-fold anisotropy for 1.5% agar. (a); (b); (c) and (d) are for pepton levels 1.4; 4; 10 and 15 g/l respectively. Note the similarity to the model predictions shown in Fig. 4.

this broken symmetry is sufficient to change the original tip-splitting growth into dendritic growth.

### Chiral growth: Phase C

During growth of the branching mode on low nutrient soft agar (easier mobility), bursts (inheritable) of new patterns which overgrow the branching ones are observed [8, 9]. The new patterns consist of thinner branches all having the same handedness of twisting (fig 7). We name this type of growth chiral growth, and refer to the new inheritable phase as phase C.

The chiral growth appears to be a fairly sophisticated tactics. Are new features needed in order to explain this behavior? In phase C the bacteria are much longer. Hence each bacterium has a well defined orientation. The bacteria should no longer be modelled as random walkers, for there is no side movement; only forward and backward motion is observed, with a weak twist. There must also be a strong direct bacteria-bacteria interaction, as the bacteria are attracted to move alongside each other.

Following our microscopic observations of the bacterial movements, we propose to include the following additional novel features to model the chiral growth: (i) Each walker has a well defined orientation  $\Theta_i$ . (ii) There is a bacterium-bacterium co-alignment (orientational interaction): the walkers sense the local mean orientational field  $\Phi(\vec{r}_i)$ , and a magnetic like interaction acts on each walker to orient  $\Theta_i$  along the direction of  $\Phi(\vec{r}_i)$ . (iii) There is a stochastic rotation  $\eta$ , and a fixed rotation  $Ch$  representing the level of microscopic chirality of the movement. We assume that the bacterial tumbling [22] is due to a rotation with the same handedness. Due to the orientational interaction, the tumbling is always much smaller than  $360^\circ$ . Therefore it may be presented as a combination of  $Ch$  and  $\eta$ .

Results of the numerical simulations of the model are shown in Fig. 8. A crucial test of a model is its predictive power. For example, we assume that the strength of the stochastic rotation is related to the length of the bacteria ( $\sigma$ , the standard deviation, is larger for shorter bacteria). In Fig. 9 we show that, as  $\sigma$  is increased, the chiral nature of the pattern disappears and it becomes tip-splitting. Typically, *Bacillus subtilis* bacteria are shorter when grown on a rich substrate. Hence we predicted that growth on high nutrient agar will change the pattern to tip-splitting, and this prediction was supported by our observations.

### The vortex mode

Growth of the bacteria on soft agar led to the complex chiral behavior. Bacteria grown on hard agar adopt yet another tactic, as is demonstrated by the vortex mode reported by Ben-Jacob *et al.* [8, 9].

In fig. 10 we show examples of the vortex colonies. These colonies spread via leading droplets (the darker dots) that leave behind on the agar a clear trail filled with bacteria. Each droplet consists of many bacteria that spin around a common center (hence named vortex) at typical velocities of 1-10  $\mu\text{m}$  per second (the velocity is very sensitive to the growth conditions). Depending on the growth conditions, the number of bacteria in a vortex can vary from a mere few to millions. Within a given colony, both clockwise and anti clockwise vortices are observed. The vortices also vary from being one layered to many layered. Usually, the pioneering droplets are the larger ones, and smaller droplets "explore" the empty areas left behind the advancing front.

If we take the micro-level (individual bacterium) view point, we notice the following: there is a very high level of correlation, as all the bacteria in the vortex move together. The

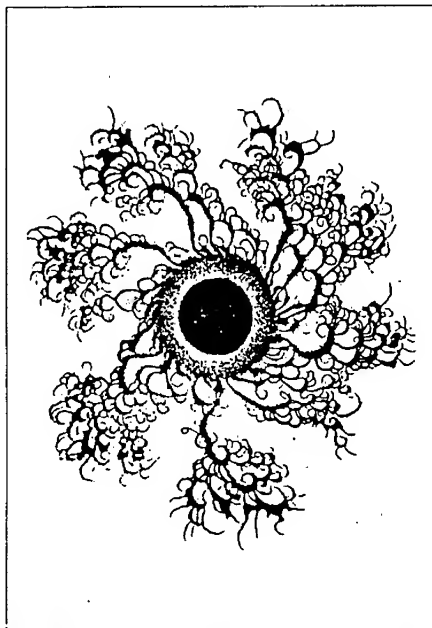


Fig. 8. Example of chiral pattern produced by the model when orientation correlation is included ( $P = 2, N_c = 5$ ).

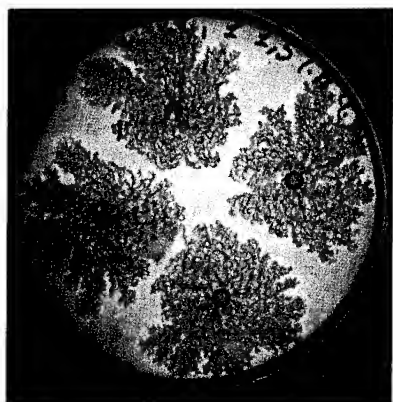
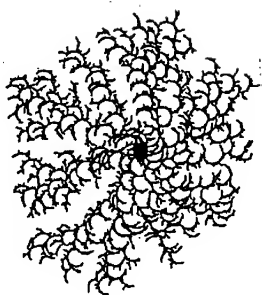


Fig. 7. Example of chiral developed during growth of phase  $C$ . (a) a single colony. (b) four colonies on a single petri dish demonstrate the reproducibility of the growth.

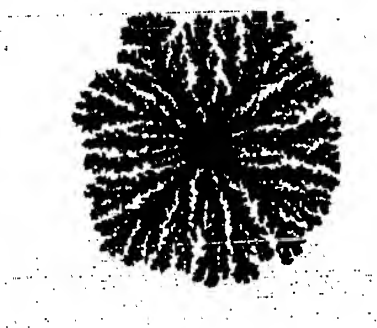


Fig. 9. Tip splitting growth of the same model when the standard deviation of  $\eta$  is large ( $= \pi/2$ ).



Fig. 10. Examples of vortex colonies (the preferred mode on hard agar) for different growth conditions. Each branch is formed by a spinning droplet of many bacteria all moving together in very high level of coordination.

motion reminds one of the coordinated motion of many schools of eucaryotes (e.g. schools of insects, squids, various types of fishes etc.) [23].

## DISCUSSION

In ref [9] we have shown that the growth of bacteria colonies requires a high level of organization leading to complex pattern formation. During growth the patterns undergo transitions from compact growth to tip-splitting (phase  $T$ ) and from phase  $T$  to phase  $C$ , as well as transitions from  $B168$  to the vortex mode. The main challenge is to elucidate the genetic basis of these fascinating transitions. We have presented an hypothesis describing a cybernetic capacity for  $B168$ , which reflects regulation of three levels of organism interactions: the cybernator, the bacterium and the colony. The 'interest' of the cybernator serves the purposes of the colony by re-adjusting appropriately the single bacterium. The cybernator provides a singular feedback mechanism, as the colony uses it to induce changes in the single bacterium, thus leading to a consistent adaptive self-organization of the colony.

As we have said in ref [8] "... the colony organization can directly affect the genetic metamorphosis of the individuals". To emphasize the special nature of the phase determination and to distinguish it from ordinary reversible phenotypic adaptation, we refer to it as genome adaptation. The present existence of such a potential for genome adaptation means that it had to be developed (acquired) by the genome in the past. Hence, if we accept genome adaptation, it directly implies the possibility of genome learning. The latter requires the following elements: (1) Exposure of the bacteria to alternating environmental conditions (e.g. alternating between conditions for which phases  $C$  and  $T$  are preferred). (2) Memory of the environmental variations. (3) Means for problem solving by the genome according to the collected and processed information (both internal and external). (4) Means for genome reorganization (natural genetic engineering) according to the solution for the problem. Thus, the genome may be viewed as a learning cybernetic unit.

During the last decade we have learned that, as an azoic system is driven away from equilibrium, a singular interplay between the two levels determines the self-organization of the entire system. Hence, the interplay may be viewed as balancing between the constraints that each level imposes on the other one. It is tempting to introduce the concept of complexity as a quantitative measure of the interplay. At present, we lack a definition of complexity, and it is not clear whether indeed such a new real variable does exist - real in the sense that a measurement of the variable can be defined. Cybernetics suggests that, to maintain singular interplay between the level of the individual bacterium and the colony, it is necessary to have a regulating channel to a level below that of the individual bacterium. If correct, it implies that more than two levels are required to describe the interplay in the colony. Hence, instead of applying concepts of statistical mechanics to the genome and to the evolution process, we might use the lesson learned from the bacterial colonies as a hint for the development of the concept of complexity in the description of azoic systems driven out of equilibrium.

## ACKNOWLEDGMENTS

We have benefited from conversations with David Gutnick, David Kessler and Herbert Levine. We thank Inna Brainis for technical assistance. This research was supported in part by a grant from the G.I.F., the German-Israeli Foundation for Scientific Research and Development, the BSF Grant 92-00051/2 and the Hungarian Research Foundation Grant No. T4439.

## References

- [1] R.Y. Stainer, M. Doudoroff and E.A. Adelberg, *The Microbial World* (Prentice-Hall, Inc., N.J. 1957).
- [2] E. Ben-Jacob and P. Garik, *Nature* 343 523-530 (1990).
- [3] E. Ben-Jacob, "From snowflake formation to the growth of bacterial colonies. Part I: Diffusive patterning in non-living systems", *Contemporary Physics* 34 (1993) 247.
- [4] T. Vicsek, *Fractal Growth Phenomena* (World Scientific, New York, 1989).
- [5] M. Eden, in: Proc. 4th Berkeley symp. on Mathematical Statistics and Probability, vol 4, F. Neyman, ed. (University of California Press, Berkeley, 1961) 223.
- [6] H. Fujikawa and M. Matsushita, *J. Phys. Soc. Jap.*, 58 3875-3878 (1989).
- [7] M. Matsushita and H. Fujikawa, *Physica A* 168 (1990) 498.
- [8] E. Ben-Jacob, H. Shmueli, O. Shochet, and A. Tenenbaum. *Physica A* 187 378-424 (1992).
- [9] E. Ben-Jacob, A. Tenenbaum, O. Shochet and O. Avidan, *Physica A* 202 1-47 (1994).
- [10] J. Adler, *J. Gen. Microbiol.* 74 (1973) 77.
- [11] M. Silverman and M. Simon *Proc. Natl. Acad. Sci.* 74 (1977) 3317.
- [12] P. Devreotes, *Science* 245 (1989) 1054.
- [13] J.M. Lackie Ed, *Biology of the chemotactic response*, (Cambridge Univ. Press 1981).
- [14] E. Ben-Jacob, O. Shochet, A. Tenenbaum, I. Cohen, A. Czirók and T. Vicsek, *Fractals* 2-1 15 (1994).
- [15] A.L. Cooper, *Proc. Roy. Soc. B* 171 175-199 (1968).
- [16] H. Fujikawa and M. Matsushita, *J. Phys. Soc. Jap.*, 60 88-94 (1991).
- [17] J. Schindler and T. Rataj, *Binary* 4 66-72 (1992).
- [18] Ben-Jacob E., Shochet O., Tenenbaum A., Cohen I., Czirók A. and Vicsek T. *Nature* 368 46-49 (1994).
- [19] J. Adler, *Science*, 166 1588-1597 (1969).
- [20] H.C. Berg and E.M. Purcell, *Biophysical Journal* 20 193-219 (1977).
- [21] E. Ben-Jacob, O. Shochet, A. Tenenbaum, I. Cohen, A. Czirók and T. Vicsek, submitted to *Phys. Rev. E*.
- [22] H.C. Berg, *Nature* 254, 389-392 (1975).
- [23] T. Vicsek, A. Czirók, E. Ben-Jacob, I. Cohen, O. Shochet and A. Tenenbaum, *Phys. Rev. Lett.* (in press).

## OPTICAL PROPERTIES OF FRACTAL NANOCOMPOSITES

V. A. MARKEL, E. B. STECHEL\*, W. KIM, R. ARMSTRONG AND VLADIMIR SHALAEV

Department of Physics, New Mexico State University, Las Cruces, New Mexico 88003

\* Sandia National Laboratories, Albuquerque, New Mexico 87185.

### ABSTRACT

Optical processes in nanostructured fractal composites are shown to be strongly enhanced. The enhancement occurs because of a localization of dipolar eigenmodes in subwavelength areas.

Composite materials constituted of tens-of-nanometer-sized particles possess fascinating electromagnetic properties and they are likely to become ever more important with the miniaturization of electronic components. Fractal structures are very prevalent in composites. The emergence of fractal geometry was a significant breakthrough in the description of irregularity [1]. Fractal objects (fractals) do not possess translational invariance and, therefore, cannot transmit ordinary waves [2,3]. Accordingly, dynamical excitations such as vibrational modes, known as fractons, tend to be localized in fractals [3]. Formally, this is a consequence of the fact that plane running waves are not eigenfunctions of the operator of dilatation symmetry (scale-invariance) characterizing fractals. The efficiency of fractal structures in damping running waves is probably the key to a "self-stabilization" of many of the fractals found in nature [2].

The localization of optical eigenmodes can lead to a dramatic enhancement of many optical effects in fractals [4-6]. The theory of optical excitations in fractal clusters and percolation systems has been intensively developing during the last decade, in particular, by Berry [7], Stroud [8], Bergman [9], Fuchs and Claro [10], Devaty [11], Brouers [12], Niklasson [13], and by Stockman, Markel and Shalaev [4-6, 14-23]. One of the most fascinating optical properties of fractals is a strong localization (in regions smaller than the wavelength  $\lambda$ ) of the dipolar eigenmodes [6, 8, 12, 14-17, 24]. Localized modes concentrate electromagnetic energy in areas smaller than the diffraction limit of conventional optics ( $\sim \lambda$ ) acting, to some extent, as antennas or as the "near-field lenses". Such modes produce high-local-field zones resulting in strong enhancement of optical processes (especially, nonlinear ones which are proportional to the local field strengths to a high power). In fractal aggregates composed of metal nanoparticles and in rough self-affine films the modes are associated with localized surface plasmon (LSP) oscillations. Direct experimental observation of the strongly localized optical modes in fractal silver aggregates has been recently reported [24].

As shown previously [4-6, 15-23], resonant excitation of strongly localized optical modes in fractals results in a huge enhancement of resonant Rayleigh [16], Raman [18] and, especially, nonlinear light scattering [21-23]. We have also predicted recently that, in addition to localization of light-induced dipole excitations, fractality can result in Anderson localization (trapping) of the light itself within a range of the order of a wavelength [19].

An important property of the interaction of light with fractals is the very strong frequency and polarization dependence of the spatial location of light-induced dipole modes [6, 22, 24]. Such frequency-spatial and polarization-spatial selectivity of the interaction can find applications in the recording and processing of optical information. This selectivity arises because the fractal morphology provides localization of optical modes on different sections of an object with random local structure and because of the tensor character of the dipole (or, multipole, in a general case) interactions between particles forming the fractal object.

A well-known example of a fractal aggregate of particles is a metal colloid cluster. In particular, fractal aggregates of silver colloid particles can be produced from a silver sol generated by reducing silver nitrate with sodium borohydride. Addition of an adsorbate (e.g., phthalazine) promotes aggregation and fractal colloid clusters form. This aggregation can be described as follows. A large number of initially isolated silver nanoparticles execute random walks in the solution. Encounters with other nanoparticles result in their sticking together, first to form small groups, which then aggregate into larger formations, and so on. This is the so called cluster-cluster aggregation model, which results in clusters having fractal dimension  $D \approx 1.78$ . Cluster-cluster aggregation can be

easily modeled in a computer, which provides excellent simulation of the empirically observed structures.

The number of particles,  $N$ , in a fractal aggregate is given by  $N = (R_c/R_0)^D$ , where  $R_c$  is the radius of gyration of the cluster and  $R_0$  is a typical separation between neighbor monomers. For silver colloid fractal clusters one typically has  $R_0 \sim 10\text{nm}$ ,  $R_c \sim 1\mu\text{m}$  and  $D \approx 1.78$ . Note that each section of a fractal composite contains holes comparable in size to the section itself. Such a structure is statistically self-similar, i.e., it possesses a scale-invariance property. The positions of particles in a cluster are correlated so that the pair correlation function has a power-law dependence:  $g(r) \propto r^{D-d}$ , where  $d$  is the dimension of the embedding space ( $d = 3$  in the case under consideration). The mean density of a fractal cluster  $\rho \sim N/R_c^d \propto R_c^{D-d} \rightarrow 0$  when  $R_c \rightarrow \infty$  since  $D < d$ . Thus, the larger a fractal cluster, the smaller its mean density. This is because holes in a fractal composite are presented in all scales from the minimum ( $\sim R_0$ ) to the maximum ( $\sim R_c$ ).

Metallic particles constituting a nanocomposite are polarizable and possess an optical resonance with high quality-factor  $Q : Q \gg 1$ . This resonance is associated with plasmon oscillations within the spherical particles. Light-induced dipole-dipole interactions between the polarizable particles in the aggregate are determined by the complex polarizability  $\chi_0$  of an isolated monomer. For a spherical monomer (in vacuum)  $\chi_0 = R_m^3(\epsilon - 1)/(\epsilon + 2)$ , where  $R_m$  is the monomer radius, and  $\epsilon = \epsilon' + i\epsilon''$  is the dielectric constant of the metal. Defining  $X \equiv -\text{Re}[\chi_0^{-1}]$ , and  $\delta \equiv -\text{Im}[\chi_0^{-1}]$ ,  $X$  plays the role of a spectral variable and  $\delta$  expresses the dielectric losses. At the resonant frequency  $\omega_0$  one has  $\epsilon'(\omega_0) = -2$  and  $X(\omega_0) = 0$ . In the vicinity of the localized surface plasmon (LSP) resonance,  $X \propto \omega - \omega_0$  where  $\omega$  is the frequency of light. The quality factor is determined by  $Q = (R_0^3\delta)^{-1} = (R_0/R_m)^3|\epsilon - 1|^2/3\epsilon'' \sim |\epsilon - 1|^2/3\epsilon''$ .

An external optical field induces transitional dipole moments on the particles, and strong dipole interactions lead to a renormalization of the problem, from one of  $N$  dipoles in a cluster to one of  $3N$  collective dipolar eigenmodes. These modes in the case of silver fractal nanocomposites cover a wide spectral range, from approximately 340 nm to 1000 nm, i.e., the visible and near-infrared parts of the spectrum. Thus, while the LSP resonance of an isolated silver particle peaks (in water) at 400 nm, a fractal nanostructured aggregate resonates at an almost continuous set of frequencies in a broad spectral range and, accordingly, can provide enhancement at all these frequencies. These resonances are shifted mostly to the red-wavelength part of the spectrum where the quality-factor  $Q$  for metal nanocomposites is significantly larger than that at the near uv resonance of an isolated spherical particle. (For silver,  $Q \sim 10$  at the uv resonance of an isolated particle, and  $Q \sim 10^2$  at the collective plasmon resonances of a fractal nanocomposite in the visible and ir ranges [18]).

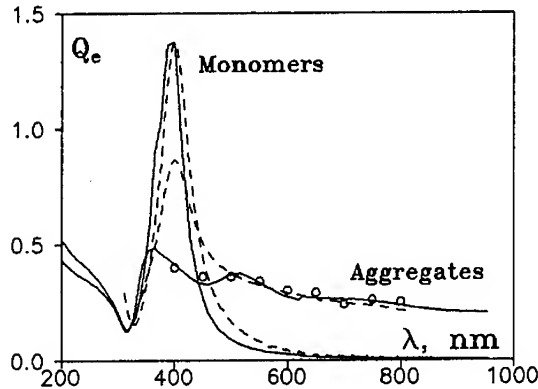


Fig. 1: Extinction spectrum of silver colloid fractal aggregates (dashed lines - experiment; circles and solid lines - simulations).



In Fig. 1 we present the results of our numerical simulations of the extinction spectrum of isolated silver monomers and their fractal aggregates compared with experimental data. Clearly, the aggregation results in a large tail in the red and near infra-red part of the spectrum. In the case of fractal composites the simulations have been performed for 10 clusters of 500 particles each (the solid line with a large wing) and for 4 clusters of 10,000 particles each (circles). As follows from the figure the simulations describe well the experimental data in the wing of the absorption spectrum associated with localized optical modes of fractal nanocomposites. The discrepancy in the central part of the spectrum (which is mostly due to delocalized modes) occurs because in the experiments a number of particles remained nonaggregated in solution and led to additional (not related to fractal aggregates) absorption at 400 nm.

The strong localization of the eigenmodes results in accumulation of electromagnetic energy in areas smaller than the wavelength. These "hot zones" are characterized by very high local fields. Note that these local fields are strongly fluctuating in space so that  $\langle |E_{loc}|^2 \rangle \gg \langle |E_{loc}| \rangle^2$  [6, 14] ( $\langle \dots \rangle$  denotes averaging over the ensemble of clusters).

The localization of the eigenmodes is characterized by a coherence length  $L_X$  of the eigenmodes defined by [14, 17]

$$L_X^2 = \frac{\langle \sum_n \delta(X - w_n) \{ \sum_i (i\alpha | n)^2 r_i^2 - [\sum_i (i\alpha | n)^2 \tilde{r}_i]^2 \} \rangle}{\langle \sum_n \delta(X - w_n) \rangle}$$

where  $(i\alpha | n)$  and  $w_n$  are the eigenfunctions and eigenvalues of the dipole-dipole interaction operator,  $\hat{W}$ , between particles in a cluster. This definition has a clear quantum-mechanical analogy with  $(i\alpha | n)$  as the wave function. In Fig. 2 we plot  $L_X$  against  $X$ . According to the figure, the localization increases for larger values of  $|X|$ , i.e., for larger detuning from the resonance of an isolated particle given by  $X = 0$ . The most localized modes have linear dimensions which are of the order of the particle size.

The increase of the localization with increasing  $|X|$  leads to the higher local intensity associated with the modes and, as a result, to larger enhancements. As shown in previous papers, the enhancement of optical processes, such as Raman scattering and DWFm, significantly increases towards larger values of  $|X|$  [6, 18, 23]. Note also that fluctuations are very strong and increase toward the center  $X = 0$ . These are long-range fluctuations near the critical point,  $X = 0$ , which ultimately provide the scaling of optical excitations similar to a phase transition [14, 15]. Thus, the point  $X = 0$  plays a role similar to the phase transition point in phase transition theory.

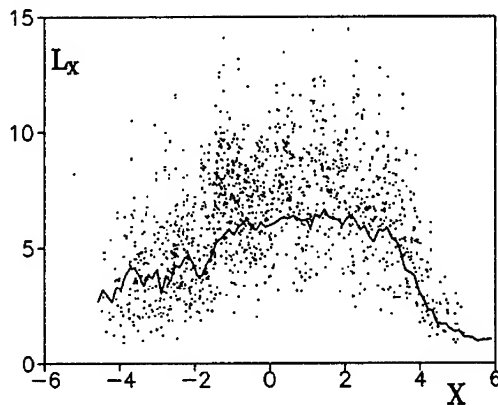


**Figure 2:** The localization length  $L_X$  of eigenmodes versus their eigenvalue  $a^3 X$  for the cluster-cluster aggregate, CCA, with  $N = 500$  particles. (The diameter of a particle,  $a$ , is equal to unity). The dependence  $L_X$  averaged over an interval of  $a^3 \Delta X = 0.02$  for ten CCAs is shown by the solid line.

The property of fractal nanocomposites to produce high-field areas can be utilized for controlling some optical characteristics, such as light absorption and scattering, of various optical materials. This can be achieved by adding into a material a certain amount of metal nanocomposites and thereby improving its optical sensitivity. The same property is of importance in high resolution spectroscopy also and, especially, in the nonlinear case. The huge enhancement of a number of linear and nonlinear optical effects observed in metal colloid clusters and on rough surfaces is in a large part due to the high-field zones.

As already mentioned, spatial locations of the regions of high local field strongly depend on the frequency and polarization of light. The ability to distinguish optical frequencies and polarizations is one of the most interesting, and potentially useful, properties of fractal nanocomposites. We envision applications in optical signal processing and optical data storage based on this unique property. For example, one may wish to demultiplex, i.e., to spatially separate and detect, a set of optical communication channels which are distinct from each other only by their carrier frequency. Another possibility, in the realm of optical data storages, is to photomodify the absorption spectrum of a small region of a cluster, thereby creating a frequency- or polarization-addressable optical data bit. Our preliminary experiments on frequency- and polarization-selective photomodification of fractal clusters [22] support these expectations.

It is worth comparing fractal nanocomposites with other inhomogeneous media and, specifically, with a medium having the same volume fraction of metal particles which, however, are randomly distributed in a three-dimensional space. This is, of course, different from a fractal nanocomposite where the positions of particles are correlated, so that  $g(r) \propto r^{D-d}$  with  $D < d$ . The volume fraction  $p$  of particles in a fractal cluster is very small,  $p \ll 1$ , (in fact,  $p \rightarrow 0$  at  $R_c \rightarrow \infty$ ). For a random inhomogeneous media with  $p \ll 1$  and  $D = d$  (we refer it as "gas" of particles), one can apply the well-known Maxwell-Garnett theory [9] which predicts only one resonant frequency close to the resonance of an isolated particle at  $X(\omega) = 0$ . In fractals, however, in spite of the fact that the mean density is asymptotically zero, there is a high probability of finding a number of particles close to any particular one. (The pair correlation function,  $g(r) \propto r^{D-d}$ , increases with the decrease of a distance  $r$  between the particles). Thus, in fractals there is always a strong interaction of a particle with others distributed in its random neighborhood. As a result, there exist localized eigenmodes which are oriented spatially in different parts of a cluster, with the location depending on the eigenfrequency and polarization characteristics of the mode. As mentioned above, some of these modes are significantly shifted to the red part of the spectrum and therefore their quality factors are much larger than at  $X(\omega) = 0$ , for a non-interacting particle. (As follows from the Drude formula,  $Q \propto \lambda$  in the infrared part of the spectrum [18]). Thus, the dipole-dipole interaction of particles composed into a fractal cluster "generates" a wide spectral range of resonant modes with improved quality-factors and with spatial locations which are very sensitive to the frequency and polarization of the excited field.

The other medium with which to compare fractal composites is a close-packed 3-dimensional aggregate of metal nanoparticles (the volume fraction occupied by metal particles in this case is  $p \sim 1$ ). Since the dipole-dipole interaction for 3-dimensional structures is long-range, one expects that eigenmodes in this case are delocalized over the whole sample. Accordingly, fluctuations of local fields ( $\propto 1/\sqrt{N}$ ) are much smaller than in the case of localized dipolar modes in a fractal aggregate. Because the strong fluctuations of local fields are primarily responsible for high values of optical nonlinear response, the nonlinear susceptibilities of a random close-packed aggregate are significantly smaller than those of a fractal aggregate. Thus in both considered cases of non-fractal composites, a "gas" of particles and a close-packed aggregate, the enhancement of optical processes is expected to be much smaller than for a fractal nanocomposite.

In Fig. 3, we present the results of numerical simulations for the enhancement of local field intensities,  $G = \langle E^2 \rangle / (E^{(0)})^2$  ( $E$  and  $E^{(0)}$  are the local random field and the external driving field, respectively). Clearly, the enhancement of local fields in fractal composites (cluster-cluster aggregates, CCA) achieves much larger values than for the case of non-fractal silver composites (either a "gas" of silver particles with the same, as in the CCA,  $p$  or a close-packed random aggregate of silver spherules). Note also that for fractal composites  $G$  strongly increases with increasing wavelength  $\lambda$ . This occurs because of two basic reasons: first, localization of eigenmodes in fractals increases with  $\lambda$  and, second, the mode quality-factor ( $Q \sim |\epsilon - 1|^2 / 3\epsilon''$ ) also increases

for the eigenmodes located towards the red part of the spectrum.

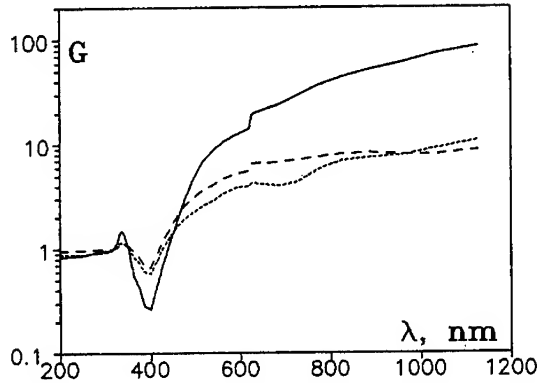


Fig. 3: Enhancement factors,  $G$ , of the local field intensities plotted against  $\lambda$  for the fractal composite (solid line), "gas" of particles with the same as for the fractal aggregate volume fraction of metal (short-dashed line), and the close-packed aggregate of particles (long-dashed line). The local intensities in all cases were averaged over ensemble of random aggregates with  $N \approx 500$  in each cluster.

Clearly, the enhancement of nonlinear optical processes will be especially strong since the generated intensity in this case is proportional to a high power of the local field. The enhancement factor  $G$  for an optical process  $\propto E^n$  can be estimated as [7]:  $G \sim \langle |E/E^{(0)}|^n \rangle \sim [Q(\lambda)]^{n-1} F(\lambda)$ , where  $F(\lambda)$  is a smooth function of the wavelength which is of the order of unity. In particular, for degenerate four-wave mixing, DFWM, (when the generated amplitude is enhanced as well as the driving field) the theory predicts the giant enhancement  $G \propto Q^6$  [23]. The nonlinear polarization  $P_{NL}$  for DFWM of waves with amplitudes  $E^{(0)}$  and  $E_1^{(0)}$  can be presented as  $P_{NL} = \chi_{FC}^{(3)} [E^{(0)}]^2 E_1^{(0)*}$  where  $\chi_{FC}^{(3)} = \chi^{(3)} G^{1/2}$  is the effective nonlinear susceptibility of a fractal composite ( $\chi^{(3)}$  is the nonlinear susceptibility of nonaggregated particles).

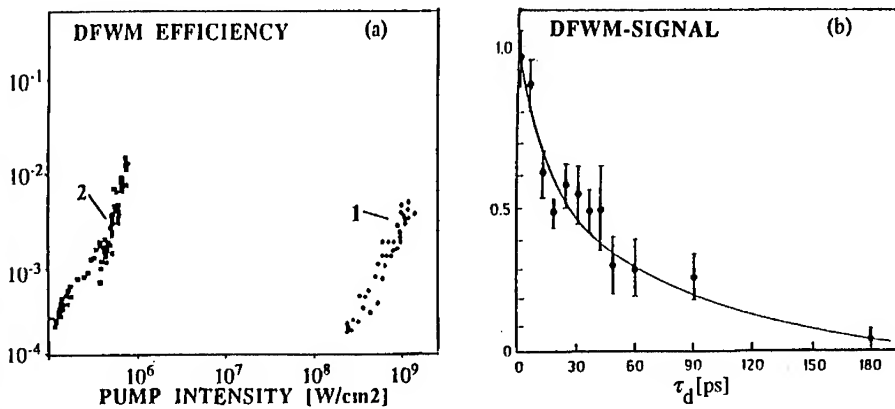


Fig. 4: a) DFWM efficiency vs pump intensity for silver particles which are isolated (1) and aggregated into fractal composites (2) ( $\lambda = 532$  nm); b) DFWM signal vs the time delay of one of the pumps ( $\lambda = 540$  nm; pulse duration is  $\tau \approx 30$  ps). Taken from [21] and [22].

In Fig. 4a we plot the experimental data for conversion efficiency  $\eta = I_s/I_1 \propto I_0^2$  ( $I_s, I_1$  and  $I_0$  are the intensities of the DFWM signal, probe beam and pump beam, respectively). The conventional scheme for observation of optical phase conjugation (OPC), with two oppositely directed pump beams and a probe beam directed at small angle with respect to the pumps, was used in the experiment. As follows from the figure, similar values of  $\eta$  can be obtained in silver particles aggregated into fractals at pump intensities  $\sim 10^3$  less than in the case of non-aggregated, isolated, particles. Since  $\eta \propto I_0^2$  the enhancement factor for silver fractal composites is  $G \sim 10^6$ . The measured value of the nonlinear susceptibility is very large  $\chi_{FC}^{(3)}(-\omega, \omega, \omega; -\omega) \sim 10^{-5}$  e.s.u. Rapid nonlinear response of fractal nanocomposites was tested in the OPC scheme when one of the input pulses was delayed by moving the mirror that reflected the input beam back to the sample. As follows from Fig. 4b the DFWM signal is twice decreased with the time delay  $\tau_d$  increasing up to 30 ps, which coincides with the pulse duration. Hence, the relaxation time of the nonlinear response does not exceed  $10^{-11}$  s. Such a large nonlinear susceptibility  $\chi_{FC}^{(3)} \sim 10^{-5}$  e.s.u. with the time of nonlinear response  $\leq 30$  ps is, to our knowledge, a world record and it indicates that fractal metal nanocomposites possess high potential in various applications (e.g., as optical switches).

#### REFERENCES

- [1] B. B. Mandelbrot, *The Fractal Geometry of Nature* (Freeman, San Francisco, 1982).
- [2] B. Sapoval, *Fractals* (Aditech, Paris, 1990).
- [3] *Fractals & Disorder*, Editor: Armin Bunde, (North-Holland, 1992); S. Alexander & R. Orbach, *J. Phys. (Paris) Lett.* **43**, L1625 (1982).
- [4] V. M. Shalaev, M. I. Stockman, *Zh. Eksp. Teor. Fiz.* **92**, 509 (1987) [*Sov. Phys. JETP* **65**, 287 (1987)]; *Z. Phys. D-Atoms, Molecules and Clusters*, **10**, 71 (1988).
- [5] A. V. Butenko, V. M. Shalaev, M. I. Stockman, *Zh. Eksp. Teor. Fiz.* **94**, 107 (1988) [*Sov. Phys. JETP* **67**, 60 (1988)]; *Z. Phys. D - Atoms, Molecules and Clusters*, **10**, 81 (1988).
- [6] V. M. Shalaev, et al., *Physica A* **207**, 197 (1994); *Fractals* **2**, 201 (1994).
- [7] M. V. Berry and I.C. Percival, *Optica Acta* **5**, 577 (1986).
- [8] I. H. Zabel & D. Stroud, *Phys. Rev. B* **46**, 8132 (1992); X. Zhang and D. Stroud, *Phys. Rev. B* **48**, 6658 (1993); X. Zhang and D. Stroud, *Phys. Rev. B* **49**, 944 (1994); P. M. Hui, D. Stroud, *Phys. Rev. B* **49**, 11729 (1994).
- [9] D. J. Bergman and D. Stroud, *Physical Properties of Macroscopically Inhomogeneous Media*. In: *Solid State Physics*, volume 46, p. 147. (Academic Press, Inc. 1992).
- [10] F. Claro, R. Fuchs, *Phys. Rev. B* **44**, 4109 (1991); K. Ghosh & R. Fuchs, *Phys. Rev. B* **38**, 5222 (1988).
- [11] R. P. Devaty, *Phys. Rev. B* **44**, 593 (1991).
- [12] F. Brouers, et al., *Phys. Rev. B* **49**, 14582 (1994); **47**, 666 (1993).
- [13] G. A. Niklasson, *J. Appl. Phys.* **62**, R1 (1987).
- [14] V. A. Markel, L. S. Muratov, M. I. Stockman, and T. F. George, *Phys. Rev. B* **43**, 8183 (1991); M. I. Stockman, et al., *Phys. Rev. Lett.* **72**, 2486 (1994).
- [15] M. I. Stockman, T. F. George, and V. M. Shalaev, *Phys. Rev. B* **44**, 115 (1991).
- [16] V. M. Shalaev, R. Botet, and R. Jullien, *Phys. Rev. B* **44**, 12216 (1991); **45**, 7592(E) (1992).
- [17] V. M. Shalaev, R. Botet, A. V. Butenko, *Phys. Rev. B* **48**, 6662 (1993).
- [18] M. I. Stockman, V. M. Shalaev, M. Moskovits, R. Botet, and T. F. George, *Phys. Rev. B* **46**, 2821 (1992).
- [19] V. M. Shalaev, M. Moskovits, A. A. Golubentsev, and S. John, *Physica A* **191**, 352 (1992).
- [20] V. M. Shalaev, R. Botet, *Phys. Rev. B* **50** (1994).
- [21] S. G. Rautian, V. P. Safonov, P. A. Chubakov, V. M. Shalaev, M. I. Stockman, *Pis'ma Zh. Eksp. Teor. Fiz.* **47**, 243 (1988) [*JETP Lett.* **47**, 243 (1988)].
- [22] A. V. Butenko, et al., *Z. Phys. D Atoms, Molecules and Clusters*, *Nonlinear optics of metal fractal clusters*, **17**, 283 (1990); A. V. Karpov, et al., *Pis'ma Zh. Eksp. Teor. Fiz.* **48**, 528 (1988) [*JETP Lett.* **48**, 571 (1988)].
- [23] V. M. Shalaev, M. I. Stockman, & R. Botet, *Physica A* **185**, 181 (1992).
- [24] D. P. Tsai, J. Kovacs, Z. Wang, M. Moskovits, V. M. Shalaev, J. Suh, and R. Botet, *Photon STM Images of Optical Excitations of Fractal Metal Colloid Clusters*, *Phys. Rev. Lett.* **72**, 4149 (1994).

## NON UNIVERSAL SCALING LAW EXPONENTS IN THE ac DIELECTRIC RESPONSE OF POLYMER-CARBON BLACK COMPOSITES

P.HAKIZABERA\*, R.DELTOUR\*, F.BROUERS†

\*Physique des Solides, Université Libre de Bruxelles CP233, B1050 Belgium

†Etude Physique des Matériaux, Université de Liège B5, B4000 Belgium

### ABSTRACT

We report experimental and theoretical results concerning the ac properties of polymer-carbon black (CB) composites. For these materials, the theory of percolation has to be generalised to account for the complex structure of the CB and the observation that tunnelling plays an important role close to the percolation threshold. We have extended a model of Balberg [1] relating the non-universality of the exponent  $t$  to the CB morphology, to interpret the non universality of the dynamic scaling exponents  $t/(s+t)$  and  $s/(s+t)$  in the critical ac regime observed in these composites

### 1. INTRODUCTION

The electrical properties of polymer-carbon black (CB) composites have been extensively studied but only a small part of these works are dealing with ac conductivities [2]. The percolation theory has been applied to polymer-CB composites [1-5]. Indeed close to the percolation threshold  $p_c$  the effective dc electrical conductivity and dielectric constant vary as power laws  $\sigma_e(0) = \sigma_m |p - p_c|^t$  above  $p_c$  and  $\epsilon_e(0) = \epsilon_a |p - p_c|^{-s}$  below and above  $p_c$  while over a few orders of magnitude the ac quantities  $\sigma_e(\omega)$  and  $\epsilon_e(\omega)$  vary with the frequency respectively as  $\omega^u$  and  $\omega^{u-1}$ . However, it appears that the classical theory of percolation [6,7] cannot account qualitatively for some of the experimental results. The measured exponents  $t$ ,  $s$  and  $u$  may be quite different from the theoretical values and the conductivity has often an exponential behavior for  $p < p_c$ . The theory has to be modified or generalized to account for the complex geometry and the structure of CB aggregates. It is also clear that a proper description of the electrical behavior of CB-polymer composites cannot neglect tunnelling mechanisms between aggregates [1,4,8-14]

A few years ago, Balberg [1] interpreted the non-universality of the conductivity critical exponent  $t$  observed in some of these CB-polymer composites by introducing explicitly the effect of tunnelling on the distribution of network resistors representing the percolating system. Using this model he was able to establish a correlation between the CB structure and the deviation from universality of the exponent  $t$ . High structured CB are formed of large and complicated particles known as aggregates while smaller and geometrically simpler aggregates are called "low-structure" blacks. The morphologic analysis of these various CB indicates that the inter-particle tunnelling distances (between the two closest points of adjacent particles) of high structured blacks have a distribution which is much narrower than the one of low structure blacks. A narrow distribution can be represented by a resistor network with equal average resistors. Such a system is known to exhibit a universal behaviour. In CB formed of aggregates with a lower degree of structure the exponential distribution is wide enough so that the non universality in these composites can be predicted quantitatively.

In this paper we report the results of a experimental and theoretical investigation of the relation between the values of the critical exponents and the morphology of the CB dispersed in polystyrene for dc and ac conductivity and dielectric constants. As far as the dc exponent  $t$

is concerned our results are in agreement with those of Balberg who studied CB-PVC composites. Moreover we have observed that the dc dielectric critical exponent  $s$  may also depend on the morphology. More precisely the existence of tunnelling conduction gives rise to two percolation thresholds the first  $p_{c\sigma}$  when the conduction starts to increase noticeably and the second  $p_{ce}$  when the percolating clusters start to have direct contact and the dielectric constant becomes very large. To account for these new results we have found that if we assume an exponential variation of the dielectric constant in the contact region, the exponent  $s$  may be also non universal close to  $p_{ce}$ . In that case, the non universal  $t_{nu}$  and  $s_{nu}$  are related to each other. The ac properties of a large number of these composites have been measured in the range  $10^3 - 10^8$  Hz. The experimental details and the statistical analysis of the data are discussed in [11]. It appears from theory and experiment that the dynamical exponent  $u$  which is relevant in the range  $10^5 - 10^7$  Hz can be calculated in the non-universal conditions and that for  $p_{c\sigma} < p < p_{ce}$  it is given by  $u_{nu} = \frac{t_{nu}}{t_{nu} + s_{nu}}$  generalising simply the percolation theory expression. These scaling exponents appear to be in good agreement with experimental data. If our results are confirmed impedance spectroscopy could provide a simple method to characterize the morphology of CB-polymer composites.

## 2. NON-UNIVERSAL EXPONENTS AND MORPHOLOGY.

Various models have been introduced to deal with non-universal percolation systems. In the most popular, the Swiss cheese model [12], the conductance through the narrow channels of width  $\delta$  between random empty spheroids is assumed to be distributed according to the power law  $\sigma = \sigma_0 \delta^m$  where  $\delta$  is the channel width. In that case one can show that the conductance distribution function is given by

$$f(\sigma) \approx (1 - \alpha) \sigma_0^{1-\alpha} \sigma^{-\alpha} = C \sigma^{-\alpha} \quad \text{with} \quad \alpha = 1 - 1/m \quad (2)$$

When  $0 < \alpha < 1$  ( $m > 1$ ) an effective medium theory argument leads to the conclusion that the exponent  $t$  is non-universal and is given by

$$t(\alpha) = t_{un} - \frac{\alpha}{1 - \alpha} \quad (3)$$

The Swiss-cheese model is not appropriate in the case of CB dispersed in polymers. For that reason, Balberg[1] has introduced a continuous percolation model to account for a possible non-universal behaviour in CB-polymer composites. This model makes use of the correlation between the distribution function of the inter particle distances  $h(r)$  (which depends on the morphological structure of the conducting aggregates) and the distribution  $g_t(\sigma)$  of the tunnelling conductance  $\sigma = \sigma_0 \exp(-r/\lambda_T)$ . Here  $\lambda_T$  is the tunnelling constant which is of the order of 10-20 Å. for CB. In order to see whether tunnelling can yield a non-universal behaviour, one has to determine the conductance distribution of the equivalent network  $g_t(\sigma)$ . In the Balberg's model, one considers a distribution function of the inter particle distance given by  $h(r) = (r/a) \exp(-r/a)$  with  $\langle r \rangle = 2a$ . Using the relation  $g_t(\sigma) = h(r) (dr/d\sigma)$  one gets easily the following expression for the conductance distribution

$$g_t(\sigma) = g_0 \ln(\sigma/\sigma_0) \sigma^{-\alpha} \text{ with } \alpha = 1 - \lambda_T/a \text{ and } g_0 = (\lambda_T/a)^2 \sigma_0^{\alpha-1} \quad (3)$$

If  $\lambda_T < a$ , i.e.  $0 < \alpha < 1$ , the distribution is dominated by the power function  $\sigma^{-\alpha}$ . Such a distribution is well known to yield a non-universal behaviour as in the Swiss-cheese model ( $m \equiv a/\lambda_T$ ). The non universality occurs when the conductance decays faster than the probability  $h(r)$ . If the inter-cluster capacitance varies linearly with  $r$ , in that model the exponent  $s$  is universal.

To account for non-universal values of  $s$  one has to assume a non-conventional variation of the permittivity in the contact region between carbon black aggregates conductivity of the form  $\epsilon \approx \epsilon_c^0 e^{+\pi/\lambda_T}$  expressing the decrease of the intergranular capacity as the tunnelling conduction increases in the contact region close to the percolation threshold. The presence of such fluctuations is suggested by the results of a Maxwell-Wagner calculation of the coupling between normal and tunnelling contacts in CB-polymer composites [13] and the fact that the effective dielectric constant close to percolation threshold is inversely proportional to the effective tunnelling conductivity [14]. These fluctuations linked to the exponential variation of the tunnelling conductivity lead to the possibility of a non-universal variation of the critical exponent  $s$ . Indeed an argument analogous to the one used in the derivation of the conductivity distribution function  $g_t(\sigma)$  yields the following expression for the dielectric constant distribution function  $f(\epsilon)$ :

$$f(\epsilon) = f_0 \ln(\epsilon/\epsilon_c^0) \epsilon^{-\beta} \text{ with } \beta = 1 + \lambda_T/a \text{ and } f_0 = (\lambda_T/a)^2 (\epsilon_c^0)^{\lambda_T/a} \quad (4)$$

As in the case of the conductivity, this will lead to non universal critical exponents of the dielectric constant close to the percolation threshold. In that situation, the expression of the non-universal  $s$  exponent has been calculated more than a decade ago by Kogut and Straley [15]

$$s = s_{un} \text{ for } \beta > 2 \text{ and } s = s_{un} + \frac{2-\beta}{\beta-1} \text{ for } 1 < \beta < 2 \quad (\beta + \alpha = 2) \quad (5)$$

The quantities  $\alpha$  and  $\beta$  depend both on the ratio  $\lambda_T/a$  and therefore the non universal exponents  $s_{nu}$  and  $s_{un}$  are not independent. Since we expect non universal exponents in the frequency dependence of  $\sigma_e(\omega)$  and  $\epsilon_e(\omega)$ , we start from the general two variables scaling law [7]

$$\left[ \frac{\epsilon_e^*}{\epsilon_c^*} \right]^a = [p - p_d]^b \Phi_{\pm} \left[ \frac{(\epsilon_p^*/\epsilon_c^*)^a}{[p - p_d]^{b+c}} \right] \text{ where the analytical function } \Phi_{\pm}(z) = A_{\pm} + B_{\pm}z + C_{\pm}z^2 + \dots$$

near  $z=0$  and is expected to vary as  $\Phi(z) \sim z^{b/(b+c)}$  for  $z \gg 1$ .

The exponents  $a$ ,  $b$  and  $c$  are given by the three conditions

- i)  $\text{Re}[\sigma_e(\omega=0)]$  varies as  $[p - p_c]^{l(\alpha)}$  for  $p > p_c$
- ii)  $\text{Re}[\epsilon_e(\omega=0)]$  diverges as  $[p - p_c]^{-s(\beta)}$  for  $p < p_c$

iii)  $\text{Re} [\epsilon_c(\omega)]$  varies with  $\omega$  as  $\omega^{\beta-1}$  for  $p < p_c$  for frequencies lower than the dynamical cross over frequency. Above that frequency, the usual analysis [7] yields the following results

$\text{Re} [\sigma_c^*] \sim \omega^{u(\alpha)}$       $\text{Re} [\epsilon_c^*] \sim \omega^{u(\alpha)-1}$      .     Using Eqs (2-5) one has

$$u(\alpha) = \frac{(1 - \alpha) t_{un} + \alpha}{(1 - \alpha) (t_{un} + s_{un}) + 2\alpha} \quad (6)$$

The 3d values of  $t_{un}$  and  $s_{un}$  are respectively  $1.95 \pm 0.05$  and  $0.75 \pm 0.4$ . The expression (6) is valid in the region  $0 < \alpha < 1$ . When  $\alpha \rightarrow 0$  i.e when  $\lambda_t/a \approx 1$ , the dynamical scaling exponent  $u$  tends to the universal percolation value  $u_{un} = 0.72 \pm 0.06$ . When  $\alpha \rightarrow 1$ ,  $\lambda_t/a \rightarrow 0$ . This corresponds to the two possible limits  $\lambda_t \rightarrow 0$  or  $a \rightarrow \infty$ . In both cases, the exponent  $u$  tends towards its mean field theory  $u = 0.5$  since this corresponds to situations far from the percolation threshold conditions.

In the Table we report the experimental and theoretical values of the dynamical exponents  $u$  [13]. The degree of CB structure decreases from top to bottom. The experimental values are calculated from the slope  $\log [\epsilon(f=\omega/2\pi)]$  or  $\log [\sigma(f)]$  versus  $\log f$  in the dynamical region. The calculated  $u(\alpha)$  are obtained from  $t(\alpha) - t_{un} = \alpha / (1 - \alpha)$  where the  $t(\alpha)$  are the experimental values of the conductivity critical exponents. The experimental results are in good agreement with the proposed of correlation between the CB morphology and the non universality of percolation exponents as proposed by Balberg [1].

TABLE     MEASURED AND CALCULATED DYNAMICAL EXPONENT  $u$

| Carbon black<br>COMPOSITES                      | exp.results<br>close to $p_{c_e}$ | theor. results<br>$u[t_{nu}, s_{nu}]$ | theor.results<br>$u[t_{nu}, s_{un}]$ |
|---|-----------------------------------|---------------------------------------|--------------------------------------|
| KBEC<br>noncrushed<br>$\alpha = 0$              | $0.67 \pm 0.02$                   | $0.72 \pm 0.06$                       | $0.72 \pm 0.06$                      |
| KBEC<br>crushed<br>$\alpha = 0.3 \pm 0.1$       | $0.62 \pm 0.02$                   | $0.67 \pm 0.08$                       | $0.76 \pm 0.04$                      |
| XC72<br>$\alpha = 0.54 \pm 0.06$                | $0.60 \pm 0.02$                   | $0.61 \pm 0.15$                       | $0.81 \pm 0.02$                      |
| N550<br>non crushed<br>$\alpha = 0.62 \pm 0.06$ | $0.60 \pm 0.02$                   | $0.60 \pm 0.14$                       | $0.83 \pm 0.03$                      |
| N550<br>crushed<br>$\alpha = 0.71 \pm 0.06$     | $0.58 \pm 0.02$                   | $0.585 \pm 0.15$                      | $0.84 \pm 0.04$                      |



The two Figures illustrate the many results reported in [13]. In Fig.1 we show the conductivity dispersion curves  $\log [\sigma(f)]$  versus  $\log [f]$  of Ketjenblack CB-polystyrene composite for  $p \approx p_{c\sigma}$  (open symbols) and for  $p \approx p_{ce}$  (close symbols) and  $\log [\epsilon(f)]$ . In the latter case, the scaling discussed in this paper is observed in a region covering 3 decades around  $10^6$  Hz (Full line indicates a slope of 0.60). For lower frequencies an other scaling with  $u$  slightly smaller than 1 seems to govern the behaviour of the ac conductivity. This phenomenon should be related to a new tunnelling scaling introduced recently [14]. In Fig.2, we show the dielectric constant dispersion curves  $\log [\epsilon(f) - \epsilon(\infty)]$  versus  $\log [f]$  of N550(CB)-polystyrene composites for concentrations for  $p > p_{c\sigma}$  and close to  $p_{ce}$  (the full line indicates a slope of -0.40).

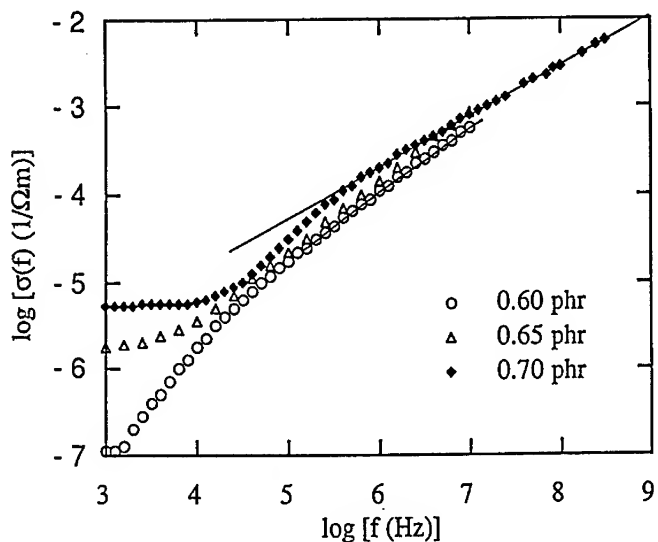


FIG 1.  $\log [\sigma(f) (1/\Omega m)]$  versus  $\log [f (Hz)]$  for PS-crushed Ketjenblack close to  $p_{c\sigma}$  (open symbols) and close to  $p_{ce}$  (closed symbols). Full line indicates a slope of 0.60.

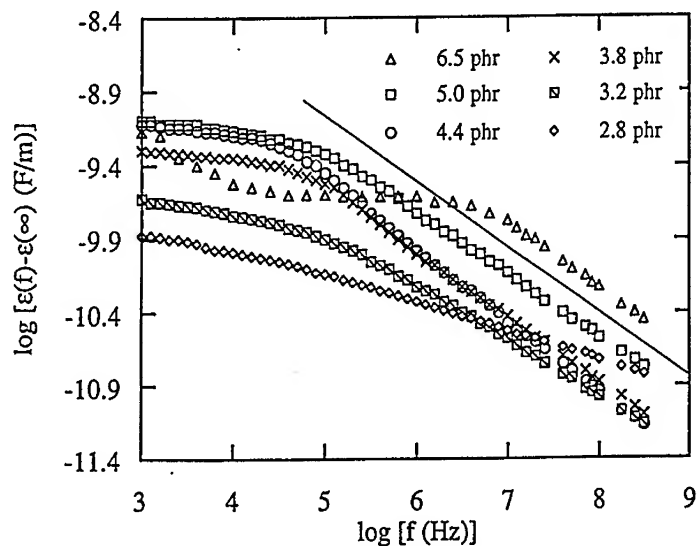


FIG 2.  $\log [\epsilon(f) - \epsilon(\infty) \text{ (F/m)}]$  versus  $\log [f \text{ (Hz)}]$  for PS-crushed N550 above  $p_{c0}$ . Full line indicates a slope of -0.40 .

## REFERENCES

- 1) I.Balberg, Phys.Rev. Lett. 59, 1305 (1987)
- 2) H.Kawamoto in Carbon Black-Polymer Composites, edited by E.K.Sichel (Dekker, New York 1982)
- 3) F.Carmona, F.Barreau, P.Delhaes, and R.Canet J.Phys.Lett., 41, L-534 (1980)
- 4) I.Balberg and S.Bozowski, Solid State Commun.,44, 551 (1982)
- 5) K.T.Chung, A.Sabo, and A.P.Pica, J.Appl.Phys. 53, 6867 (1982)
- 6) D. Stauffer and A. Aharony, Introduction to Percolation Theory (Taylor and Francis, Philadelphia, 1991) and references herein
- 7) J.P. Clerc, G. Giraud and J.M. Luck, Adv. Phys. 39, 191 (1990) and references herein
- 8) B.Abeles, P.Sheng, M.D.Coutts, and Y.Arie, Adv.Phys. 24, 407 (1975)
- 9) E.K.Sichel and J.I.Gittelman, J.Electron. Mater. 11, 699 (1982)
- 10) P.Sheng and J.Klafter Phys.Rev. B27, 2583 (1983)
- 11) P.Hakizabera Thèse de Doctorat, Université Libre de Bruxelles 1993.
- 12) S.Feng, B.I.Halperin and P.N.Sen Phys.Rev.B35 197 (1987)
- 13) P.N.Sen, J.N.Roberts and B.I.Halperin Phys.Rev. B32, 3306 (1985)
- 14) P.M.Kogut and J.P.Straley, J.Phys.C:Solid St.Phys. 12 2151(1979)
- 14) A.Sarychev and F.Brouers, Phys.Rev.Lett. 73,2895 (1994).

## TWO-LENGTH-SCALE STRUCTURE IN SOME COMPUTER-GENERATED AGGREGATES GROWN BY DIFFUSION-LIMITED AGGREGATION

PAUL W. SCHMIDT,\* GIUSEPPE PIPITONE,\*<sup>\*\*\*</sup> M. A. FLORIANO,\*\* E. CAPONETTI,\*\* AND R. TRIOLO,\*\*

\*Department of Physics and Astronomy, University of Missouri--Columbia, Columbia, MO 65211 USA

\*\*Dipartimento di Chimica Fisica, Università di Palermo, Via Archirafi, 26, 90123 Palermo, Italy

<sup>\*\*\*</sup>Permanent Address: Dipartimento di Chimica Fisica, Università di Palerermo, Via Archirafi, 26, 90123 Palermo, Italy

### ABSTRACT

The properties of some aggregates "grown" on a computer by diffusion-limited aggregation have been investigated. Calculations showed that the intensity of the small-angle x-ray and neutron scattering from the aggregates was proportional to  $q^{-D}$  for  $qL \gg 1$ , where  $D > 0$ ,  $L$  is a length that characterizes the large-scale structure of the aggregate,  $q = 4\pi\lambda^{-1}\sin(\theta/2)$ ,  $\lambda$  is the wavelength, and  $\theta$  is the scattering angle. The magnitude of the exponent  $D$  was appreciably smaller than the fractal dimensions that many simulations have shown to be typical of the mass fractal aggregates grown by diffusion-limited aggregation. The calculations suggest that the aggregates have structure on *two* different characteristic-length scales.

### INTRODUCTION

Both computer simulations<sup>1-3</sup> and x-ray and neutron small-angle scattering experiments<sup>4-6</sup> have made many important contributions to the present understanding of the properties of mass-fractal aggregates. To the best of our knowledge, however, only Pearson and Anderson<sup>3a</sup> and Amar, Family, and Lam<sup>3b</sup> have published calculations of the small-angle scattering from fractal structures grown in computer simulations.

Because we believe that there is a need for more investigations of the small-angle-scattering intensity from computer-generated aggregates, we have recently studied some aggregates generated by diffusion-limited aggregation (DLA) and have computed the intensity expected from these aggregates. As we explain in this report, we believe that our results provide further insight into the relation between the intensity of the small-angle scattering and the structure of DLA aggregates. Our calculations suggest that the structure of the aggregates on length scales of the order of magnitude of the maximum diameter of the aggregate is different from the structure on length scales not much larger than the average distances between neighboring particles in the aggregate. (The maximum diameter is defined to be the largest distance separating two points in the aggregate.)

In the next section, we describe the processes by which our aggregates were grown. Next, we review some of the most important characteristics of the small-angle scattering from mass-fractals. We conclude by discussing some of the implications of our results.

### GENERATION OF THE AGGREGATES

We used a DLA aggregation processes similar to some<sup>2,7,8</sup> that others have recently employed. The aggregates were grown on cubic lattices with a lattice constant  $a$  and with  $n$  sites on one side of the lattice. The lattice thus contained  $n^3$  sites. For 15 lattices,  $n$  was equal to 101. (Our simulation process requires that the lattice must have an odd number of lattice points on each side of the cube.) As we later decided that a larger lattice might be desirable, we also made one simulation in  $n = 201$  lattice points. The computing time required for  $n = 201$ , however, was so long that we simulated only one of the larger lattices.

All particles in the simulation were classed as either "sticky" or mobile. A sticky particle was defined to have the property that if a mobile particle moved to a lattice site adjacent to a sticky

particle, the mobile particle then became sticky. Before the simulation began, all particles except the central sticky particle were mobile.

Before the beginning a simulation, a sticky particle was placed at the center of the lattice, and  $v = \eta n^3$  particles, where  $0 < \eta < 1$ , were put on non-central lattice sites selected at random. (The central sticky particle played the role of the seed in the growth of a real crystal.) At each step of the simulation a lattice site was randomly selected  $n^3$  times. If the site that was elected either was empty or was occupied by an aggregated (sticky) particle, nothing was changed. If a site containing a mobile particle was selected, one of the six lattice sites adjacent to the latter site was chosen at random. (All of these adjacent sites were a distance  $a$  from the mobile particle.) If the site was already occupied, nothing was changed, but if an empty site was selected, the mobile particle moved to the site and occupied it. If the mobile particle moved to a site one lattice distance away from a sticky particle, the mobile particle became sticky and was incorporated into the aggregate. Once a particle became part of the aggregate, it was never moved again.

For  $n = 101$ , we made three simulations with each of the  $v$  values 0.050 0.075, 0.100, 0.125, and 0.150. Thus there were fifteen simulations with  $n = 101$ . We also made one simulation with  $n = 201$  and  $\eta = 0.10$ . As we mentioned, because of the long computation time necessary for the  $n = 201$  simulation, we performed only one simulation with  $n = 201$ .

After each step, we calculated the number  $N$  of particles in an aggregate and the radius of gyration  $R_g$ , where

$$R_g = \left[ \frac{1}{N} \sum_{i=1}^N r_i^2 \right]^{1/2}, \quad (1)$$

where  $r_i$  is the distance of particle  $i$  from the center of mass of the aggregate. Since all particles were identical, the mass  $M$  of the aggregate was proportional to  $N$ . We therefore found it was convenient to choose the mass unit to be the mass on one of the particles. In these units,  $N$  is equal to the mass of the aggregate.

For  $n = 101$ , the simulation was stopped as soon as the radius of gyration had grown to a value in the interval  $33.67 a \leq R_g \leq 33.76 a$ . We used the radius of gyration as the characteristic length of the aggregate. For the  $n = 201$  aggregate,  $R_g$  was  $67.01 a$ .

Because of the relatively small number of particles in the simulations with  $n = 101$ , there were some differences in quantities calculated for different aggregates that had the same value of  $\eta$ . We therefore computed the average of the calculations of a quantity for each value of  $\eta$ . Table I shows the number  $N$  and the radius of gyration  $R_g$  of particles in the 16 DLA aggregates.

**Table I - Vales of  $n$ ,  $\eta$ ,  $N$  and  $R_g$**

| n   | $\eta$ | N         |       |       | $R_g$     |       |       |
|-----|--------|-----------|-------|-------|-----------|-------|-------|
|     |        | Aggregate |       |       | Aggregate |       |       |
|     |        | A         | B     | C     | A         | B     | C     |
| 101 | 0.050  | 25529     | 28057 | 26846 | 33.67     | 33.67 | 33.68 |
| 101 | 0.075  | 30197     | 29878 | 29016 | 33.69     | 33.68 | 33.68 |
| 101 | 0.100  | 34241     | 36031 | 34680 | 33.70     | 33.68 | 33.71 |
| 101 | 0.125  | 41118     | 41805 | 41150 | 33.72     | 33.68 | 33.73 |
| 100 | 0.150  | 47216     | 48381 | 47630 | 33.70     | 33.73 | 33.76 |
| 201 | 0.100  | 276144    |       |       | 67.01     |       |       |

Note: For  $n = 101$ , the three aggregates A, B and C were generated for each  $\eta$ .

From the simulations we obtained the coordinates of all the  $N$  particles in an aggregate. From these coordinates it was possible to compute properties of the aggregates.

Although the simulation technique was straightforward, it required a large amount of memory, and computing times were often quite long.

To verify the correctness and reliability of the simulation process and our other calculations, we also generated one aggregate by a true self-avoiding walk (TSAW).<sup>3a,9</sup> For the TSAW, the fractal dimension is 2.<sup>3a,10</sup> In this aggregation process, a particle was placed at each site in a cubic lattice that was visited by a random walk that was subject to the restriction that no site could be visited more than once. There were 11958 particles in this aggregate.

We used two methods to calculate the fractal dimension  $D$  of each mass-fractal aggregate. First, we employed the equation<sup>11</sup>

$$R_g = r_m N^{1/D}, \quad (2)$$

where  $r_m$  is a constant. We also computed  $D$  by the box-counting technique,<sup>9</sup> in which the space surrounding the aggregate is divided into cubic cells, or boxes, with side  $\epsilon$ . The number  $N_b(\epsilon)$  of boxes that intersect the aggregate is evaluated as a function of  $\epsilon$ . Then<sup>12</sup>

$$N_b(\epsilon) = n_b \epsilon^{-D}, \quad (3)$$

where  $n_b$  is a constant.

The  $D$  values obtained with Eq. (3) tended to increase with  $\eta$ . For example, for DLA aggregates with  $n = 101$ ,  $D$  was about 2.7 for  $\eta = 0.050$  and 3.15 for  $\eta = 0.200$ . (As  $D$  values greater than 3 have no meaning, we expect that the latter result may have been due to some artifact in our numerical techniques.)

As can be seen in Figs. 1 and 2, for both the DLA aggregates and the aggregate from the TSAW, there are *two* linear regions in the logarithmic plots of  $N_b(\epsilon)$ . For both types of aggregate, the exponent calculated from the linear region at larger  $\epsilon$  was in good agreement with the  $D$  values given by other workers. For  $n = 101$ , values of  $D$  from box counting changed from about 2.2 to 2.5 as  $\eta$  increased from 0.050 to 0.200. For the DLA aggregate with  $n = 201$ , for which  $\eta$  was 0.100, the value of  $D$  calculated from the box-counting plot for this aggregate for  $6a < \epsilon < 15a$  is 2.6. This value is not appreciably larger than those found in other simulations of DLA aggregates.<sup>2,7</sup>

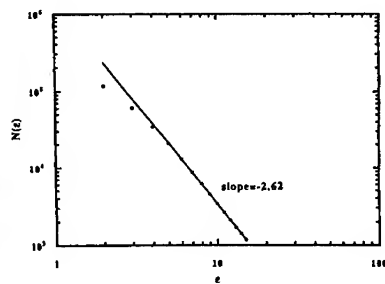


Figure 1. The dependence of  $N_b(\epsilon)$  on  $\epsilon$  for the 201 DLA aggregate.

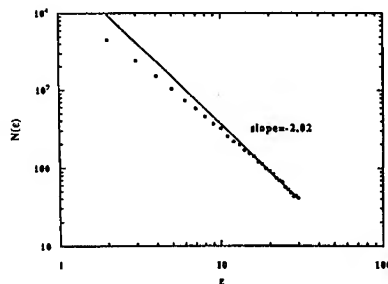


Figure 2. The dependence of  $N_b(\epsilon)$  on  $\epsilon$  for the TSAW aggregate.

Just as in Fig. 1, there are two linear regions in Fig. 2, which is a plot of  $N_b(\epsilon)$  for the TSAW aggregate. The exponent in the region for  $15a \epsilon < 30a$  is essentially equal to the  $D$  value for the TSAW.<sup>3,10</sup>

## CALCULATION OF THE SCATTERED INTENSITY

The scattered intensity  $I(q)$  from a system of  $N$  scatterers can be expressed<sup>13</sup>

$$I(q) = I_e \sum_{i=0}^N \sum_{j=0}^N n_i n_j \frac{\sin q r_{ij}}{q r_{ij}}, \quad (4)$$

where  $I_e$  is the scattered intensity from one electron,  $n_i$  and  $n_j$  are the numbers of electrons in scatterers  $i$  and  $j$ , respectively,  $r_{ij}$  is the distance between scatterers  $i$  and  $j$ ,

$$q = \frac{4\pi \sin(\theta/2)}{\lambda}, \quad (5)$$

$\lambda$  is the x-ray wavelength, and  $\theta$  is the scattering angle. In Eq. (5), all of the scatterers are assumed to be points. Therefore the  $n_i$  are independent of  $q$ .

If all of the scatterers are identical, and if each scatterer contains  $n$  electrons, Eq. (4) becomes

$$I(q) = n^2 I_e \sum_{i=0}^N \sum_{j=0}^N \frac{\sin q r_{ij}}{q r_{ij}}. \quad (6)$$

Equations (4) and (6) are exact.

As the coordinates of all the particles in an aggregate were recorded during each simulation, and since all particles in an aggregate were identical, the exact scattered intensity could be calculated by evaluating the  $r_{ij}$  from the coordinates of an aggregate and substituting these  $r_{ij}$  into Eq. (6).

Equations (4) and (6) can be rearranged to make them easier to evaluate. In calculations of  $I(q)$  that use these equations, many values of  $r_{ij}$  almost always are equal. For example, for the aggregates with  $n = 101$ , there are about  $3.8 \times 10^{10}$  values of  $r_{ij}$ , but in our largest aggregate for  $n = 101$  there were only there were only about  $3.5 \times 10^4$  different  $r_{ij}$ . When we denote the different  $r_{ij}$  by the distances  $d_k$ , Eq. (6) becomes

$$I(q) = n^2 I_e \sum_{k=0}^{K_{\max}} G_k \frac{\sin q d_k}{q d_k}, \quad (7)$$

where  $k_{\max}$  is the value of  $k$  corresponding to the largest  $d_k$ , and  $G_k$  is the number of times the distance  $d_k$  occurs in the double sum in Eqs. (4) and (6). (The  $d_k$  are defined so that they of  $d_k$  increases when  $k$  becomes larger. Thus the largest  $d_k$  is obtained for  $k = k_{\max}$ .)

The  $I(q)$  curves for the  $\eta = 201$  DLA aggregate and the TSAW aggregate are shown in Figs. 3 and 4, respectively. The unit of  $q$  in these plots is  $a^{-1}$ . In other words, the intensities are plotted as functions of the dimensionless quantity  $qa$ .

When  $qd_k$  never exceeds 1 in any of the terms in the sum in Eq. (7),  $I(q)$  can be approximated by the expression

$$I(q) \approx I(0) e^{-(qR_g)^2/3}, \quad (8)$$

where the radius of gyration  $R_g$  is given by Eq. (1).<sup>14</sup>

During one simulation for  $n = 101$  and  $\eta = 0.10$ , we interrupted the simulation every 100 steps during the 591 steps of the calculation. Each time the simulation was interrupted, we calculated an intensity curve, and from the part of this curve for  $q$  less than about 0.05 we found  $R_g$  at that stage of the simulation. At the end of the calculation, we computed another intensity

curve, and from this curve found the radius of gyration of the aggregate. All of the  $R_g$  values from the intensity curves agreed within 0.4% with the corresponding  $R_g$  values from the coordinates. We believe that the agreement of the two independent calculations of  $R_g$  demonstrates the consistency and reliability of our calculations.

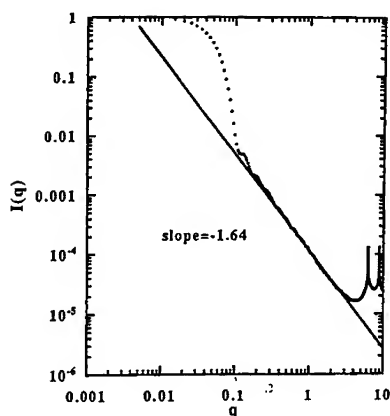


Fig. 3. The intensity  $I(q)$  calculated from Eq. (7) for the  $\eta=201$  DLA aggregate.

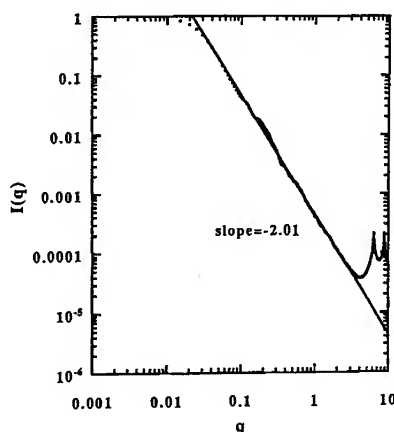


Fig. 4. The intensity  $I(q)$  calculated from Eq. (7) for the TSAW aggregate.

## DISCUSSION

A fundamental property of an aggregate with radius of gyration  $R_g$  is that the intensity  $I(q)$  from the aggregate has the approximate form<sup>4</sup>

$$I(q) = I_0 q^{-D} \quad (9)$$

when  $qR_g \gg 1$ . [In Eq. (9),  $I_0$  is a constant.] However, Eq. (9) does not apply when  $q$  is so large that the inequality  $qa < 1$  no longer is satisfied, where  $a$  is the average distance between neighboring particles in the aggregate. This limit therefore applies to aggregates grown on lattices if  $a$  is the lattice spacing. Thus Eq. (9), which gives the small angle scattering that has been found to be characteristic of mass-fractal aggregates, applies only when  $q$  satisfies *both* of the inequalities  $1 < qa$  and  $qR_g \gg 1$ .

These limits can be seen in both Figs. 3 and 4. In both plots here is a power law only for  $0.1 < q < 2$ . The maxima at  $q \approx 6$  and  $q \approx 9$  are due to the two lowest-order Bragg reflections for cubic lattice. These reflection occur for  $qa = \pi$  and for  $qa = 2^{1/2}\pi$ . The presence of these maxima is another demonstration of the consistency of our calculations.

In Fig. 4, the value of the slope is about 2.0, and thus is in good agreement with the prediction of Ref. 10 that the fractal dimension is 2 and also with the  $D$  value from Fig. 2.

However, the exponent of the power law in Fig. 3 has a magnitude 1.64, rather than the value 2.6 that is typical of a mass fractal with fractal dimension of 2.6 as might have been expected from the exponent for larger  $\epsilon$  in Fig. 1. Other workers<sup>3a,3b,15,16</sup> have found similar differences. We point out, however, that the fractal dimensions from Eq. (2) and Fig. 1 are in reasonable agreement.

Nevertheless, since *both* Figs. 1 and 2 have two linear regions, we are tempted to suggest that in both the DLA and TSAW aggregates, the structure is different on large and small length scales. Figures 3 and 4 show that although the small-length-scale structure determines the

scattered intensity for the DLA aggregates, in the TASW aggregate the scattering is produced mainly by structure on larger length scales. Further study is necessary to determine the conditions under which such differences are found. Since Ref. 16 considers aggregates not grown on lattices, as well as those generated on lattices, the effect does not appear to be due only to the lattice.

Close examination of Fig. 3 shows that in the neighborhood of  $q = 0.1$ , the intensity rises above the straight line. In this region the average magnitude of the oscillations in the intensity decays by a power-law with  $n$  exponent of magnitude about 2.65 [*i. e.*, with the exponent predicted by Eq. (9)]. We believe that this scattering comes from the structure that produces the large- $z$  linear region in Fig. 1. The intensity in this region of  $q$  is modulated by oscillations that, according to our unpublished calculations, are caused by the cubic symmetry of the lattice. As the analogous region of oscillations is barely detectable in the  $I(q)$  curve for the aggregate for which  $\eta = 0.1$  and  $n = 101$ , we expect that the oscillatory power-law region in Fig. 3 would have extended over a wider interval of  $q$  if  $n$  had been larger than 201. Calculations with larger lattices, however, would be difficult, because when  $n$  is doubled, the number of particles increases by a factor of 8, and there are about  $8^2$  times as many interparticle distances.

Perhaps the presence of structure on two length scales in DLA aggregates might have been noticed earlier if scattered intensities had been calculated for some of the aggregates produced in the first simulations. Our investigation suggests that such calculations would be useful and perhaps could help explain the nature and the source of the effects that we have observed. We point out that once the coordinates of the particles in an aggregate have been calculated in a simulation, the additional effort needed to compute the scattered intensity is relatively small.

## ACKNOWLEDGEMENTS

Acknowledgements for support of this research are made to the Ministero della Università e della Ricerca Scientifica, to the Consiglio Nazionale delle Ricerche, and to the Donors of the Petroleum Research Fund, administered by the American Chemical .

## REFERENCES

1. P. Meakin, Phys. Rev. A **27**, 1495 (1983).
2. P. Meakin and J. M. Deutch, J. Chem. Phys. **80**, 2115 (1984).
3. (a) A. Pearson and R. W. Anderson, Phys. Rev. B **9**, 5865 (1993).  
(b) J. Amar, F. Family, and P. M. Lam, Phys. Rev. B **50**, 8792 (1994).
4. T. Freltoft, J. K. Kjems, and S. K. Sinha, Phys. Rev. B **33**, 269 (1986).
5. G. Dietler, C. Aubert, D. S. Cannell, and P. Wiltzius, Phys. Rev. Lett. **57**, 3117 (1986).
6. R. Vacher, T. Woignier, J. Pelous, and E. Courtens, Phys. Rev. B, **37**, 6500--6503 (1988).
7. M. Matsuhita, K. Honda, H. Toyoki, Y. Hayakawa, and H. Kondo, J. Phys. Soc. Japan **55**, 2618 (1986).
8. M. B. Amar, J. Physique I **3**, 353 (1993).
9. T. Vicsek, in *Fractal Growth Phenomena*, (World Scientific, 1992), Section 5.4.
10. Reference 9, p. 121 and p. 125.
11. P. Pfeifer and M. Obert, in *The Fractal Approach to Heterogeneous Chemistry*, edited by D. Avnir, (Wiley, Chichester, England, 1989), Eq. (17), p. 22.
12. Reference 11, Section B1, pp. 14-16.
13. A. H. Compton and S. K. Allison, *X-Rays in Theory and Experiment*, Van Nostrand, New York, 1935, Eq. (3.55), p. 159.
14. A. Guinier, G. Fournet, C. B. Walker, and K. L. Yudowitch, *Small-Angle Scattering of X-Rays*, Wiley, New York, 1955, , Eq. (39) and Sect. 2.1.3.1, pp. 24-28.
15. P. Meakin, private communication.
16. H. X. Zhang, Sheng Jun, and H. G. Wang, Paper P4.22 presented at the 1993 Fall meeting of the Materials Research Society.



## KINETIC AND EQUILIBRIUM CLUSTER-SIZE DISTRIBUTIONS OF ANTIBODY-ANTIGEN-INDUCED COLLOIDAL AGGREGATION

DERIN A. SHERMAN AND RICHARD J. COHEN

Harvard-MIT Division of Health Sciences and Technology, Cambridge, MA

### INTRODUCTION

Our colloidal system is composed of antigens covalently coupled to polystyrene microspheres. When monoclonal antibodies are added to solution, they reversibly bind to the antigens causing aggregation. Unlike many other similar systems, our system is thermodynamically reversible: the aggregates will dissociate in the presence of free antigen, and the aggregation process reaches a state of thermodynamic equilibrium. This system is of interest as it can be used to model many different chemical, physical and biological processes. In particular, this system can be used to quantify the interactions between the biomolecules attached to the microspheres<sup>1</sup> and also to explore the statistical mechanics of reversible particle aggregation.

We used our measurements of the cluster-size distribution together with the reversible aggregation equation

$$\frac{dC_n}{dt} = \frac{1}{2} \sum_{i+j=n} [K_{ij}C_iC_j - F_{ij}C_n] - \sum_{i=1}^{\infty} [K_{ni}C_nC_i - F_{ni}C_{n+i}] \quad (1)$$

to determine the behavior of the aggregation kernel ( $K_{ij}$ ) and the fragmentation kernel ( $F_{ij}$ ). In the limit that  $F_{ij}$  vanishes, the aggregation process is irreversible and equation (1) is known as the Smoluchowski coagulation equation. In this limit, the solutions to equation (1) are known to exhibit dynamic scaling<sup>2</sup>. By adjusting the concentrations of microspheres and antibodies, we were able to achieve dynamic scaling and thus determine the critical exponents of the aggregation kernel.

The aggregation and fragmentation kernels are not independent of one another, and are related via detailed balance

$$\frac{K_{ij}}{F_{ij}} = \frac{C_{i+j}(t = \infty)}{C_i(t = \infty)C_j(t = \infty)}. \quad (2)$$

We were able to measure the equilibrium cluster-size distribution,  $C_n(t = \infty)$ , and thus determine the fragmentation kernel from our measurements of  $K_{ij}$ .

### EXPERIMENTAL METHODS AND TECHNIQUE

#### Antibodies, Antigens, and Microspheres

The antibody-antigen-microsphere system is ideal for our studies for the following reasons. First, the antibodies used are bivalent: each antibody has two binding sites, each specific to the same antigen. Thus one antibody molecule can be used to form a discrete rigid bond between two antigen-coated microspheres. Second, the antibodies used are monoclonal: unlike antibodies found in animals, our antibodies are all chemically identical. Third, the technology required to produce our system is both robust and cheap: many medical diagnostic tests, such as the latex test and the home pregnancy test, rely on microspheres coated by suitable biomolecules. Fourth, the microspheres used are extremely uniform; thus, each can be treated as being chemically identical. Fifth, the large charge

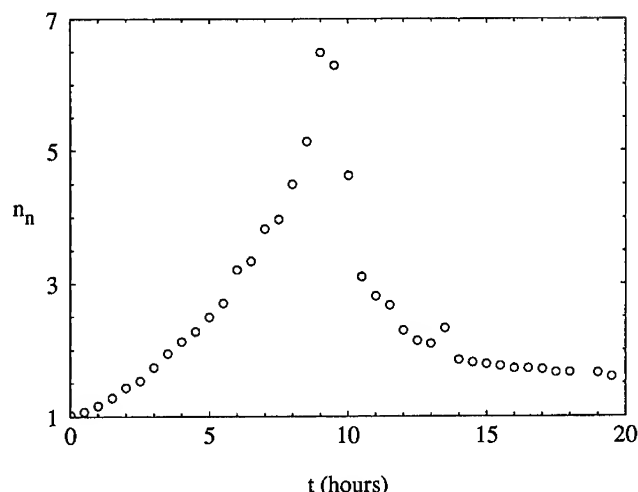


Figure 1: Clusters fragment when a large excess of free antigen is added to the solution after 10 hours of aggregating. The rapid decrease in the number average,  $\bar{n}_n$ , clearly shows cluster breakup.

on the microspheres prevents them from getting close enough to bind irreversibly. This is demonstrated in Figure 1, which shows a remarkable amount of cluster break-up after a large excess of free antigen was added to the solution of antibodies and coated microspheres. The excess free antigen was able to compete for the antibodies more effectively than the small quantity of bound antigen, so the antibodies ceased to cross-link the antigen-coated microspheres. Note that there is a small amount of non-antibody-antigen-induced colloidal aggregation which is not reversible. This "non-specific" aggregation was present to some degree in all our samples, but was always a small factor in the total aggregation process. Finally, our ability to measure the cluster-size distribution using particle counting techniques depends only on the physical characteristics of the microspheres and is unaffected by the nature of the specific biomolecules used to instigate aggregation. This means that we can readily alter our system to study a wide range of biomolecular interactions under a wide range of operating conditions.

We used 360 nm diameter carboxylate-modified microspheres (lot number 10-31-10) provided by Interfacial Dynamics Corporation (Portland, OR). The antigen used was 2,4-dinitrophenyl (DNP) conjugated with lysine to form  $\epsilon$ -N-DNP-L-lysine (DNP-lysine). The monoclonal antibody used was 2A1 (IgG1) against the DNP group. The details of the antibody, antigen, and sphere preparation are discussed in reference 1. Approximately 5000 antigens were covalently coated to each microsphere. The number of antibodies bound to each sphere was varied over a range of 1% to 10% of the number of antigens, and the microsphere concentration was varied over a range of  $10^8 \text{cm}^{-3}$  to  $10^{10} \text{cm}^{-3}$ .

### Single-particle light scattering

We utilized an optical pulse particle size analyzer to study microsphere aggregation. In our apparatus, the microsphere clusters flowed single-file through a hydrodynamically focused flow cell illuminated by a focused laser beam. Light scattered at very small angles

by the clusters was collected and measured using a photomultiplier tube. Since the microspheres were uniform, the intensity of light scattered by an  $n$ -mer was proportional to  $n^2$  regardless of the orientation of the cluster or the configuration of the  $n$  microspheres which constitute the cluster. The optical pulse analyzer is described in detail in reference 3.

The cluster-size distribution is determined by injecting a known volume of sample into the instrument, and then assembling a histogram of scattered light intensities. Using our instrument, clusters of sizes up to 15 were easily resolvable, and we routinely measured cluster sizes as large as 30. In addition, although we were not able to measure the sizes of the largest cluster, we were able to count them; thus, we measured the zeroth moment of the cluster-size distribution. Since our system did not gel, we were able to measure  $\bar{n}_n$  even when the average cluster size was much greater than 30. It is important to note that we were able to accurately measure  $C_n(t)$  for  $n < 30$  even when  $\bar{n}_n \gg 30$ .

## RESULTS

### Initial kinetics

Our initial studies focused on the aggregation kinetics. When high concentrations of antibodies were used (approximately 10% of antigens bound) then the equilibrium values of  $\bar{n}_n$  was on the order of 100 or more. Even with 10% antigen occupancy, the measured value of  $K_{11}$  was less than 1% of the rate of dimerization for a diffusion-limited cluster aggregation (DLCA) process. We therefore concluded that this process was a reaction-limited cluster aggregation (RLCA) process.

When the equilibrium value of  $\bar{n}_n$  is high, it is possible to probe dynamic scaling of the aggregating system before it reached equilibrium. The dynamic scaling ansatz

$$C_n(t \rightarrow \infty) \rightarrow s^{-2}(t)\phi(x = n/s) \quad (3)$$

relates the time-dependent cluster-size distribution,  $C_n(t)$ , to a time-independent cluster-size distribution,  $\phi(x)$ , via an "average cluster-size,"  $s(t)$ , which is proportional to  $\bar{n}_w$  for non-gelling systems. In our system,  $s(t)$  showed initial exponential growth, as shown in Figure 2, followed by a leveling off at the equilibrium value. Exponential growth is a characteristic of aggregation kernels with  $\lambda = 1$  where the two critical exponents  $\lambda$  and  $\mu$  are defined by the following equations:

$$\begin{aligned} K_{ai,aj} &\sim a^\lambda K_{ij} \\ K_{i \ll j} &\sim K_0 \left(\frac{i}{j}\right)^\mu j^\lambda. \end{aligned}$$

In addition, we were able to demonstrate dynamic scaling in our system long before equilibrium was reached. Figure 3 shows how the cluster-size distribution measured at different times are related to one another via the time-independent cluster-size distribution. Note that there are no free parameters required to "fit" the individual measurements of  $C_n(t)$  to create the plot of  $\phi(x)$ : once  $C_n(t)$  is measured, the value of  $\phi(x)$  is automatically determined. Since the scatter plot clearly shows the data collapsing onto a single curve, we conclude that dynamic scaling is present in our system.

We found that  $\phi(x \ll 1) \sim x^{-\tau}$  with  $\tau$  ranging between 1.35 and 1.78. Both of these observations are consistent with a kernel described by exponents  $\lambda = 1$  and  $\mu = 0$ . Other investigators have measured these exponents in other RLCA systems<sup>4</sup>, but not all RLCA system appear to have these exponents<sup>5</sup>. Our system could be very closely approximated by the sum kernel,  $K_{ij} \sim i + j$ , which shares the same exponents as our system.

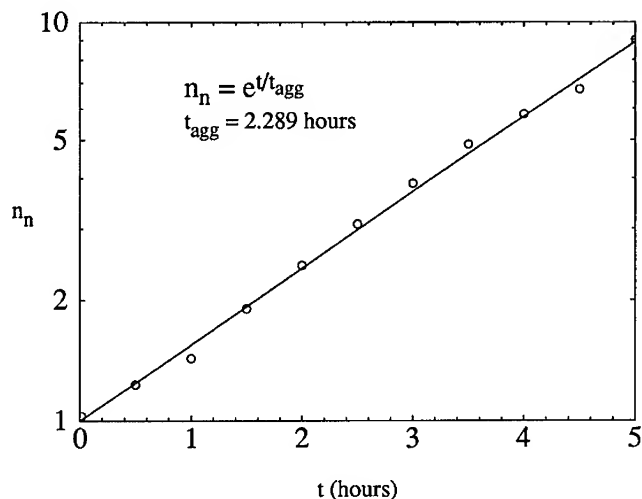


Figure 2: Initial temporal growth is exponential

## Equilibrium

The most dramatic feature of our work is that the system is reversible unlike most colloidal polystyrene systems which bind irreversibly when particles fall into the attractive DLVO potential well. Because our spheres were highly charged (0.5 to 3.0 nm<sup>2</sup> per charge group), the majority of spheres were not able to get close enough to bind via Van der Waals forces. We initially expected to see an equilibrium cluster-size distribution with a value of  $\tau = 2.5$ . This is a characteristic of Flory RA<sub>f</sub> polymer systems in which all active sites on a polymer can bind to any other active site on any other polymer<sup>6</sup>. However, we were surprised to see that the equilibrium distribution was well-described by the sum kernel, which is characteristic of a Flory ARB<sub>f-1</sub> system. This agreement is shown in Figure 4.

## DISCUSSION

Our system would be expected to behave like a Flory ARB<sub>f-1</sub> system if there was only one antibody per microsphere; however, there were several hundred antibodies and several thousand antigens per microsphere. The reason for the  $\tau = 1.5$  distribution can be found by considering the RLCA aggregation and fragmentation processes separately. Ball and colleagues<sup>7</sup> have presented a very clear geometric argument explaining the cause of the critical exponents  $\lambda = 1, \mu = 0$ . Their argument is based on the self-adjustment of the fractal dimension of the RLCA clusters. They note that when a small  $i$ -mer interacts with a large  $j$ -mer, the  $j$ -mer can be treated as  $j/i$  blobs each of mass  $i$ , therefore constraining  $\lambda - \mu = 1$ . In addition, Ball and colleagues note that  $\lambda$  depends upon the fractal dimension of the clusters. When  $\mu < 0$ ,  $C_n$  is monodisperse and the clusters which form have a large reaction surface, which raises the value of  $\lambda$ . When  $\mu > 0$ , the solution is dominated by small clusters which can easily penetrate and bind to large clusters, thus increasing the fractal dimension and lowering both the reaction surface and  $\lambda$ . Therefore, the critical point  $\lambda = 1, \mu = 0$  acts as an attractor which stabilizes both the RLCA exponents as well

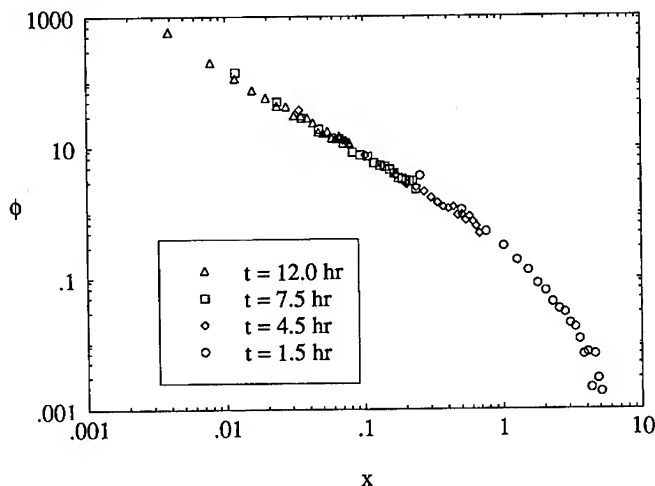


Figure 3: The time-independent cluster-size distribution,  $\phi(x)$ , demonstrates dynamic scaling. When  $C_n(t)$  are rescaled according to the dynamic scaling ansatz, all the points collapse onto a single curve.

as the fractal dimension.

The main assumptions that Ball and colleagues make about RLCA processes are that all possible cluster combinations are equally valid, and that the cluster sticking probability is close to zero. We used these same assumptions about RLCA systems to determine the form of the RLCA fragmentation kernel. First, if all cluster configurations are allowed, and all are equally probable, then the number of ways in which an  $n$ -mer can be constructed from  $n$  distinguishable monomeric sub-units is equal to  $W_n$ , where

$$W_n = n^{n-2}. \quad (4)$$

We assumed that all bonds were equal and had a probability  $F_0$  of breaking during a unit time period. Furthermore, because the system was reaction-limited, sub-clusters would not recombine after the bond between them broke. With these assumptions, we arrived at the RLCA fragmentation kernel:

$$F_{ij} = F_0 ij \frac{W_i W_j (i+j)!}{W_{i+j} i! j!}. \quad (5)$$

This fragmentation kernel has the property that

$$\frac{1}{2} \sum_{i+j=n} F_{ij} = (n-1)F_0. \quad (6)$$

The left-hand side of equation (6) is equal to the total rate at which an  $n$ -mer dissociates. The factor of  $1/2$  accounts for double-counting. The factor of  $n-1$  is equal to the total number of bonds in an acyclic  $n$ -mer. Therefore, equation (6) is merely a mathematical recapitulation of our original hypotheses concerning RLCA fragmentation: all bonds are equivalent, and all cluster configurations are equally probable.

We refer to the conjunction of the RLCA fragmentation kernel and the sum kernel as the "reversible sum kernel." The reversible sum kernel has the property that it preserves the

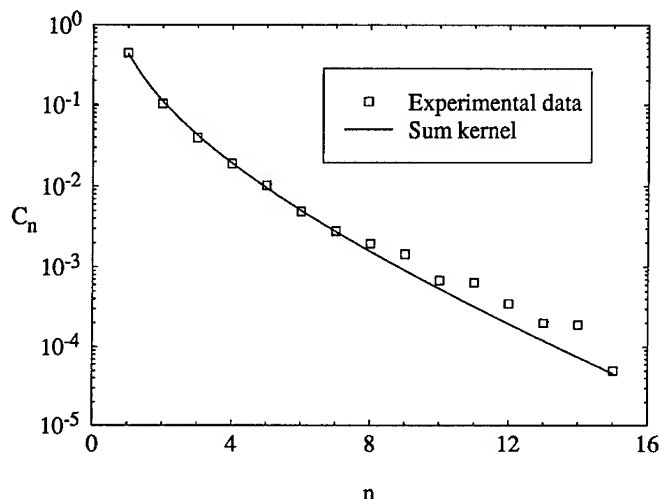


Figure 4: The equilibrium cluster-size distribution is well described by the sum kernel.

same cluster-size distribution as the sum kernel when the initial conditions are monomeric. This behavior was first described in detail by van Dongen and Ernst<sup>8</sup>. Using the condition of detailed balance, they construct a recursion relation for  $C_n(\infty)$ . The solutions to the recursion relation are identical to the sum kernel with monomeric initial conditions.

The reason why we saw an equilibrium value of  $\tau \approx 1.5$  is due to the fact that the bonds were rigid and therefore clusters could only interact at "the surface" rather than deeply interpenetrating. Thus, we concluded that the same factors which kept  $\lambda = 1$  for purely kinetic aggregation continued to hold for equilibrium. If the bonds were not rigid, or equivalently, if the clusters could interpenetrate, then the total available reaction surface would be much larger, and both the values of  $\lambda$  and  $\tau$  would be much larger than those observed. In particular, if the clusters could have freely interpenetrated, then  $\lambda = 2$  and  $\tau = 2.5$ , corresponding to Flory  $RA_f$  polymers.

## REFERENCES

1. Y.K. Sykulev, D.A. Sherman, R.J. Cohen, H.N. Eisen, *Proc. Nat. Acad. Sci.* **89**, 4703 (1992)
2. P.G.J. van Dongen and M.H. Ernst, *Phys. Rev. Lett.* **54**, 1396 (1985)
3. D.A. Sherman, PhD thesis, MIT, 1994
4. G.K. von Schulthess, G.B. Benedek, R.W. DeBlois, *Macromolecules* **13**, 939 (1986)
5. M.L. Broide and R.J. Cohen, *Phys. Rev. Lett.* **64**, 2026 (1990)
6. P.J. Flory, *Principles of Polymer Chemistry* (Cornell University Press, Ithica, NY, 1953)
7. R.C. Ball, D.A. Weitz, T.A. Witten, F. Leyvraz, *Phys. Rev. Lett.* **58**, 274 (1987)
8. P.G.J. van Dongen and M.H. Ernst, *J. Stat. Phys.* **37**, 301 (1984)

## PROPERTIES OF CONDUCTING POLYMER INTERCONNECTS

CORRINE L. CURTIS, GRACE M. CREDO, JASON E. RITCHIE, AND  
MICHAEL J. SAILOR

University of California, San Diego, Department of Chemistry, La Jolla, CA  
92093-0358

### ABSTRACT

The possibility of using conducting polymer dendrites as electrical connections has been explored. AC electropolymerization of dendritic conducting polymers can be used to connect two different platinum wires. The polymerization conditions were varied in order to improve morphology, strength, conductivity, and to shorten the time needed to make connections. The variables involved in this study include electrolyte and monomer concentrations and the type of conducting polymer used (3-methylthiophene and aniline). Another area of study has been the exploitation of the inherent doping and undoping properties associated with conducting polymers to store information in the connections in the form of a resistance value. To this end, the connections were doped to known conductivity values and the persistence of conductivity was monitored over time.

### SYNTHESIZING POLYMER CONNECTIONS

One major field of research in materials science is the fabrication of micro- and nanoscale devices. Some examples include semiconductor microelectronic devices and molecular recognition sensors. One aspect of this burgeoning area that has not been extensively studied is the problem of "wiring up" small devices so that they can communicate with the macroscopic world. To this end we have been developing methods to electrically connect one or more sets of Pt wires with the conducting polymers poly(3-methylthiophene),<sup>1</sup> polypyrrole,<sup>2</sup> and polyaniline. The procedure involves cycling the potential of the Pt wires that are to be connected between two extremes; at one extreme the polymer dendrites are actually growing and at the other extreme they are in a nonconductive state. When the fibers from one wire grow to touch polymer from the other, the polymer connection acts as an electrical shunt. We hypothesize that the polymer connection then remains conductive and is reinforced.

### Poly(3-methylthiophene) and Tetrabutylammonium Tetrafluoroborate Concentration Studies

We wished to explore electropolymerization parameters such as electrolyte and monomer concentrations and scan rate to determine conditions which favored production of dendritic, well-defined connections. The concentrations of 3-methylthiophene (3MT) and tetrabutylammonium tetrafluoroborate (TBAF, the electrolyte) have a large effect on the polymer connection's morphology. Uniform films or cauliflower polymer growth was observed with 3MT concentrations of 0.17 M 3MT or greater at a scan rate of 100 mV/sec (Figure 1A).

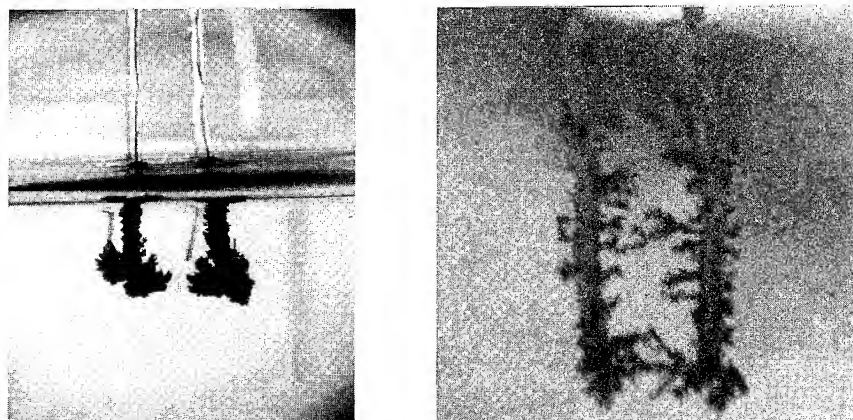


Figure 1A (left): This is an example of cauliflower morphology and was synthesized from a water- and oxygen-free acetonitrile solution containing 0.17 M 3MT and 0.12 M TBAF. The Pt wires are approximately 2 mm apart. Figure 1B (right): This is an example of dendritic morphology and was synthesized from a water- and oxygen-free acetonitrile solution containing 0.09 M 3MT and 0.12 M TBAF. The Pt wires are approximately 1 mm apart.

No clear-cut division between film-like growth and dendritic growth was consistently observed. However, above 0.34 M 3MT, the polymer's morphology was predominantly film-like. Below 0.09 M 3MT, very fine, dendritic polymer strands could be seen (Figure 1B). In these experiments 0.12 M TBAF was used. If the electrochemical cell was exposed to oxygen, no polymer was formed at the lowest monomer concentrations. At and above 0.17 M 3MT, oxygen-free and oxygen-containing solutions produced the same polymer morphologies. Similar results were seen with constant monomer concentration (0.17 M) and varying the concentration of TBAF. Uniform polymer growth was observed at concentrations equal to or greater than 0.12 M TBAF. The cauliflower polymer morphology was observed at TBAF concentrations between 0.12 M and 0.07 M (Figure 1A). Dendritic fibers were observed at concentrations equal to and less than 0.07 M TBAF (Figure 1B).



At the lower concentrations the electropolymerization rate is presumably diffusion limited. The dendritic polymer growth that results from this diffusion-limited condition is similar to what is seen in metal deposition and other diffusion-limited electropolymerization systems.<sup>3, 4</sup>

A "standard" polymerization with 0.17 M 3MT and 0.12 M TBAF takes on average 20 minutes to span a 2 mm electrode gap. The polymer connection created from the above solution is usually mechanically stable enough to remove from the polymerization solution. At lower salt and monomer concentrations, the connection process takes greater than 3 hours and the small dendrites usually fall off when the electrode system is removed from solution. At higher salt and monomer concentrations, a dense connection that is very mechanically stable can usually be formed in a couple of minutes.

### Polyaniline

Polyaniline is a novel conducting polymer because its conductivity depends not only on its oxidation state, but also on its level of protonation.<sup>5</sup> Polyaniline is usually electropolymerized in an aqueous solution containing an acid as electrolyte and aniline as the monomer.<sup>5</sup> We wish to make connections using this polymer because changing the solution pH will change the connection's conductivity. The pH effect is an interesting, additional variable in electropolymerization that we wish to explore with regard to the construction of polymer connection networks.

We synthesized the polyaniline using the same AC electropolymerization technique as described above for poly(3-methylthiophene). One modification that had to be made was the initial deposition of a polyaniline layer (at 0.65 or 0.70 V vs. SCE) on both working electrodes. If this base polymer layer was not created, no polymer would be observed to grow. Other modifications that were made included adjusting the voltage range to -0.20 to 0.65 or 0.70 V vs. SCE. This was necessary because it is known that successive potential cycles of polyaniline positive of 0.70 V lead to polymer degradation.<sup>5</sup> The effect of scan rate was also explored. Scan rates between 300 and 600 mV/sec produced polyaniline connections between 2 Pt wire electrodes separated by 2 mm in 5 hours or more. So far we have focused on two different acids for the synthesis of polyaniline: hydrochloric and perchloric acid. Specifically, we have used 0.50 to 1.70 M HCl with 0.10 to 0.70 M aniline and 1.3 to 1.8 M HClO<sub>4</sub> with 0.30 to 0.61 M aniline. At concentrations of aniline greater than 0.70 M, aniline solubility becomes a problem in our systems. No polymer connections were observed to form from solutions containing less than 0.08 M aniline. Under these conditions, the measured current dropped and approached zero as electropolymerization progressed. We hypothesize that at lower aniline concentrations, the

concentration of impurities is high enough to interfere with electropolymerization.

We have not yet been able to obtain fibrous polymer growth for polyaniline similar to that observed with the poly(3-methylthiophene) system. Figure 2A is a scanning electron micrograph of one polyaniline-coated Pt working electrode prepared with 1.3 M  $\text{HClO}_4$  and 0.58 M aniline and electropolymerized for 2.5 hours.

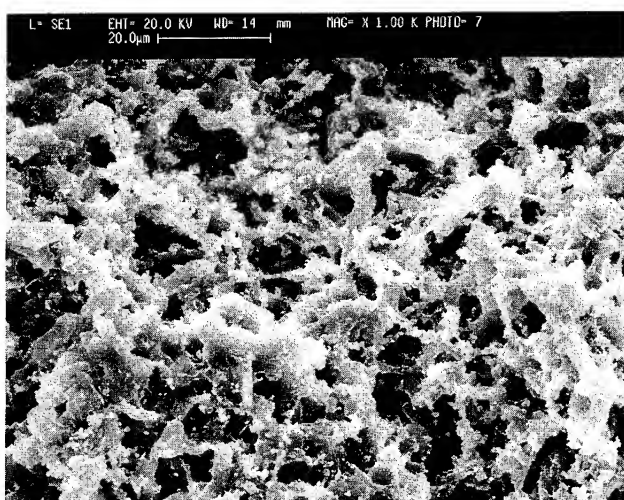


Figure 2A: An example of the polyaniline morphology typically observed under the reaction conditions. Polyaniline was synthesized from an aqueous solution of 1.3 M  $\text{HClO}_4$  and 0.58 M aniline.

#### Poly(3-methylthiophene) Doping and Undoping Studies

Many studies of the conduction process and doping and undoping of conducting polymers have been performed.<sup>6</sup> Because poly(3-methylthiophene) has a conductivity range spanning eight orders of magnitude, a polymer connection such as those described in this work could potentially be used for data storage. To study the stability of conductivity of the poly(3-methylthiophene) connection, the resistance of the doped polymer connection was measured over time. In one experiment, the polymer connection was kept in its original, salt- and monomer-containing polymerization solution for almost 5 days and its resistance measured periodically. The connection lost 50% of its conductivity within 40 hours. In a second experiment, the polymer connection was removed from the polymerization solution and placed in a fresh water- and oxygen-free

acetonitrile solution for over 6 days. Under these conditions, the polymer connection lost 50% of its conductivity within 15 hours. Thus the resistance of the polymer connection increases faster in the salt-free solution than in the salt-containing solution. This is consistent with a concentration gradient-driven polymer undoping process, as has been previously observed for polypyrrole films.<sup>7</sup> To demonstrate reading and writing of conductivity information into polymer connections, a poly(3-methylthiophene) connection was doped to a resistance of 500 ohms and its resistance monitored for 1 day. The connection was then undoped or doped as shown below and its resistance measured as a function of time (Figure 3). As can be observed from the graph, the polymer connection's resistance is stable for storage times on the order of tens of hours.

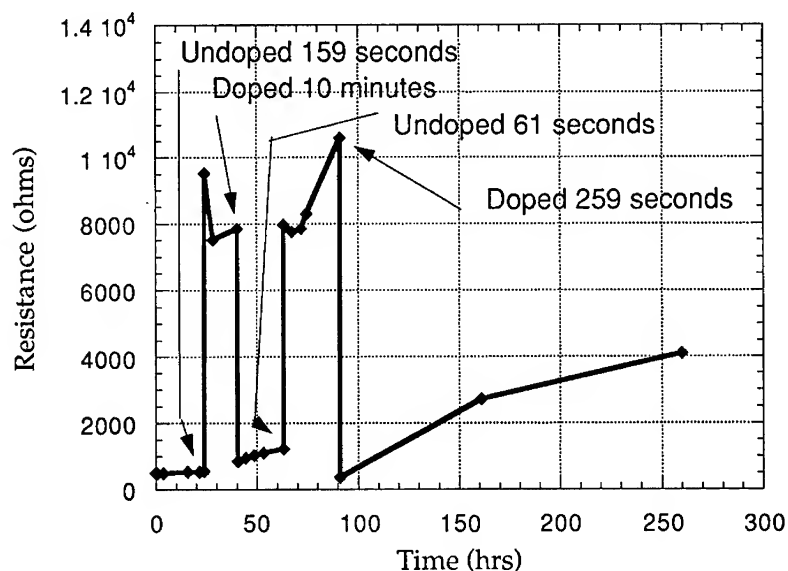


Figure 3: Resistance vs. time of a poly(3-methylthiophene) connection run through 4 conductivity state changes. Throughout the course of the experiment, the connection was held in a salt- and monomer-containing solution.

### Conclusions

We have explored the properties of connecting 2 Pt working electrodes with conducting polymers synthesized from poly(3-methylthiophene) and polyaniline. By varying the concentration of poly(3-methylthiophene) and the electrolyte, tetrabutylammonium tetrafluoroborate, different polymer

the electrolyte, tetrabutylammonium tetrafluoroborate, different polymer morphologies could be obtained. The most dendritic polymer strands were created at concentrations of 3MT equal to or less than 0.09 M with a TBAF concentration of 0.12 M. Very fine, dendritic polymer strands were also observed at concentrations equal to and less than 0.07 M TBAF with a 3MT concentration of 0.17 M. Polyaniline connections with morphologies similar to the poly(3-methylthiophene) system have not yet been obtained in our system. We have also explored the diffusion of dopants out of poly(3-methylthiophene) connections in two different solutions. One solution consisted of the water- and oxygen-free acetonitrile, and the other consisted of TBAF and monomer in acetonitrile. The connection stored in the salt- and monomer-free solution undoped faster than the polymer connection stored in the salt- and monomer-containing solution, consistent with prior observations.<sup>7</sup> The process of storing and erasing conductivity information into these polymer connections was demonstrated.

#### Acknowledgments

The authors would like to thank Vincent V. Doan and Beatrice K. Chinh for providing the scanning electron microscope images.

#### References

1. C.L. Curtis, J. E. Ritchie, M. J. Sailor, *Science* **262**, 2014 (1993).
2. M. J. Sailor, C. L. Curtis, *Adv. Mater.* **6**, 688 (1994).
3. R. M. Brady, R. C. Ball, *Nature* **309**, 225 (1984).
4. J. H. Kaufman, A. I. Nazzari, O. R. Melroy, A. Kapitulnik, *Physical Review B* **35**, 1881 (1987).
5. W. -S. Huang, B. D. Humphrey, A. G. MacDiarmid, *J. Chem. Soc., Faraday Trans. 1* **82**, 2385 (1986).
6. G. Tourillon, in Handbook of Conducting Polymers, edited by T. A. Skotheim (Marcel Dekker, Inc., New York, 1986), pp. 293-350.
7. R. M. Penner, L. S. V. Dyke, C. R. Martin, *J. Phys. Chem.* **92**, 5274 (1988).

# STRUCTURE FACTOR SCALING IN FRACTAL AGGREGATION OF COLLOIDAL CLUSTERS

Guillermo Ramírez-Santiago and Agustín E. González

*Instituto de Física, Universidad Nacional Autónoma  
de México, Apdo Postal 20-364, México, 01000 D. F.*

## ABSTRACT

We report the observation of spatial ordering of clusters that leads to a spinodal-type scaling of the structure factor  $S(q)$ , in the 3D simulations of diffusion-limited colloid aggregation. We are able to clearly identify the peak in  $S(q)$  as arising from the correlation between particles belonging to nearest neighbor clusters. The  $S(q)$  has a terminal shape that corresponds to a close-packing of the clusters after gelation, in a concentration range larger than the one found in recent experiments.

PACS numbers: 02.70.-e, 05.40.+j, 64.60.Qb, 81.10.Dn

## Introduction.

Aggregation phenomena has been an area of active research during the past decade [1]. In the particular case of colloidal dispersions, researchers have identified two limiting regimes of the irreversible aggregation [2], according to the value of the bonding probability between colloidal particles upon encounters. If this value is one, the aggregation is limited by the time taken for the particles to diffuse before they meet and is termed *diffusion limited* (DLCA). If, on the other hand, this probability is close to zero, the aggregation is limited by the time taken for the particles to react and form a single entity and is named *reaction limited* (RLCA). In this paper we concentrate on the study of the DLCA regime.

Recent experimental studies [3-5] in the high concentration regime have shown that during a DLCA process the distribution of the scattered intensity of light displays a pronounced peak at a finite  $q$  vector. The position  $q_m$  of the peak shifts to smaller values while the peak intensity increases, as the time goes on. Experimentally [3] it has also been found that  $S(q)$  shows a saturation effect after a certain aggregation time, that is, the subsequent  $S(q)$  curves show approximately the same peak position and height.

As pointed out in ref. 3, there is a wide variety of systems that show a similar behavior in their corresponding light, neutron or x-ray scattered intensity, suggesting that there are some universal features. In the later stages of the aggregation process, the scattered intensity in all those systems scales according to the universal law,

$$S(q, t) = q_m^{-d}(t) F(q/q_m(t)), \quad (1)$$

with the value of  $d$  depending on the specific system under study. For DLCA  $d = d_f \approx 1.8$ , is the fractal dimension of the clusters.

To investigate the physical origin of the peak in  $S(q)$  observed in the experiments we have carried out extensive numerical simulations of DLCA processes. For instance, we would like to clearly identify in  $S(q)$  the points that correspond in real space to the nearest-neighbor cluster distance, the depletion region and the size of the denser core. We also would like to find out if the gelation time and the onset of the saturation effect occur simultaneously, all this as a function of concentration.

The approach we follow is to first evaluate the particle-particle correlation function,  $g(r)$ . To this end, the simulation is momentarily stopped at predetermined times to obtain a histogram, giving the number of pairs of particles located within the spherical shells of radii  $r$  and  $r + \delta r$ , regardless that the particles belong to the same or to different clusters. We calculated the  $g(r)$  from this histogram using the formula

$$g(r) = \frac{\text{density of pairs in } (r, r + \delta r)}{\text{average density of pairs}}. \quad (2)$$

The scattering function  $S(q)$  is easily obtained from  $g(r)$  by Fourier transformation, yielding [6]

$$S(q) = 1 + \frac{4\pi\rho}{q} \int_0^\infty r \sin(qr) (g(r) - 1) dr. \quad (3)$$

### Algorithm.

Here we briefly describe the DLCA algorithm used in the present work. We consider a three dimensional cubic lattice with periodic boundary conditions, where at some intermediate time a collection of clusters formed of nearest neighbor lattice cells, representing the colloidal particles, diffuse randomly. A cluster is chosen at random and moved one lattice spacing in a random direction only if a random number  $x$ , uniformly distributed in the interval  $[0, 1]$ , satisfies the condition  $x < D(s)/D_{\max}$ , where  $D(s) \sim s^{-\frac{1}{d_f}}$  is the diffusion coefficient for the selected cluster of size  $s$  and  $D_{\max}$  is the maximum diffusion coefficient for any cluster in the system. After each cluster has been selected the time is increased by  $1/(N_c D_{\max})$ , with  $N_c$  the number of moving clusters in the system at that time, regardless if the cluster is actually moved. If the cluster attempts to invade the lattice cells occupied by another cluster, the move is rejected and the moving cluster either sticks and merges to the other with probability  $P_0$  or remains side by side to the other with probability  $1 - P_0$ . For DLCA processes one has  $P_0 = 1$ . This algorithm has been applied successfully to demonstrate dynamic scaling in the simulations of colloidal aggregation [7].

### Results.

To check the picture of close packed clusters [4,5,8] and determine the terminal  $q_m$ , we carried out simulations for 10 different concentrations ranging from 0.0050 to 0.08 in volume fraction  $\phi$ . We found that for this concentration range,  $N_0 \approx 100\,000$  particles is the optimum number of particles that yields a good statistics for the evaluation of  $g(r)$ ,

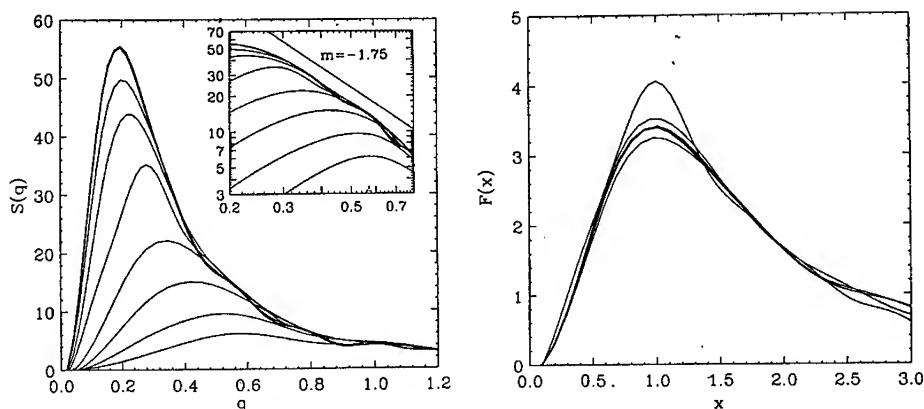


Fig. 1. Left: The scattering function  $S(q)$  for ten different times (see text), for a simulation with  $\phi = 0.04$ . The high- $q$  behavior of these curves is shown in the inset, in a double logarithmic scale. Right: A plot of  $F \equiv q_m^{d_f}(t) S(q, t)$  vs.  $x \equiv q/q_m(t)$  for the curves corresponding to the last six times on the left.

and still can be handled in a reasonable time with the Cray Y-MP4/464 supercomputer at UNAM.

We define the onset of gelation as the first time for which a cluster spans the box, regardless of the direction at which such spanning occurs. Whenever a cluster spans the lattice it is automatically frozen and becomes part of the "infinite" network. However, the non-spanning clusters keep moving around and eventually stick to the infinite network. We found that for low concentrations and relatively small boxes, it may happen that the simulation ends up with a single non-spanning cluster. We systematically tried to avoid that by choosing boxes of size such that their linear dimension  $L$  embraces several terminal clusters (see below). The simulation was terminated when no moving clusters were found in the system.

In fig. 1 (left) we show the scattering functions for a simulation with  $\phi = 0.04$  at ten different times, namely, 90, 148, 245, 403, 665, 1 097, 1 808, 2 981, 4 915 and 6 634. The last four times correspond to states after the occurrence of gelation, that took place at  $t = 1 212$ . Note that the curves corresponding to the last three times are almost indistinguishable (top curve in the figure). After some initial time the curves start to develop a peak that increases in height and whose position  $q_m$  moves to the left, in complete accord with the experimental results [3-5]. Similar results are obtained for all the other concentrations studied. Among the important features to note in that figure is that all the curves merge into one single curve for high values of  $q$ . Moreover, in the inset of the same figure we show that the high- $q$  dependence of these curves obeys the power law  $q^{-1.75}$ , where the

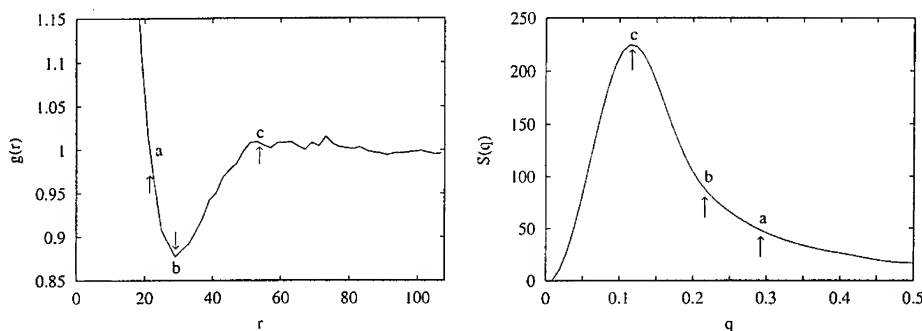


Fig. 2. The particle-particle correlation function  $g(r)$  (left) and the scattering function  $S(q)$  (right) for a  $\phi = 0.01$  simulation, corresponding to the time  $t = 13\,360$ . Point  $c$  is defined in  $S(q)$  as the peak position, while points  $a$  and  $b$  are defined in  $g(r)$  as the size of the denser core and the minimum position, respectively.

exponent  $d_f = 1.75 \pm 0.11$  gives an estimate of the fractal dimension of the clusters [3-5]. We tried to scale our data according to Eq. (1). In Fig. 1 (right) we show the results of a scaling analysis;  $F = q_m^{d_f}(t) S(q, t)$  versus  $x = q/q_m(t)$  for the last six times. We see that for these times the collapsing of the data is indeed very good. However, for earlier times the data did not scale very well. In this scaling analysis  $d_f$  was used as an adjustable parameter and the best collapse of the data occurred for  $d_f = 1.70$ , giving us another independent estimate of the fractal dimension. In this case it was found that a variation of  $d_f$  by 10% leads to a noticeable degradation of the scaling.

In Fig. 2 are shown the  $g(r)$  (left) and  $S(q)$  (right) curves, corresponding to a simulation with  $\phi = 0.01$  at the time  $t=13360$ . The  $g(r)$  exhibits the following general features: for small distances it is quite large indicating that any particle is highly correlated with many others, mainly belonging to the same cluster. At longer distances there appears a minimum in  $g(r)$ , that corresponds to the depletion region [3-5]. At even longer distances  $g(r)$  increases again, showing the correlations between particles belonging to nearest-neighbor clusters. At earlier or later times there is a similar situation except that the minimum and nearest neighbor positions move to the left or to the right, respectively. The points  $a$  and  $b$  are defined in  $g(r)$  as the size of the denser core (defined here as the point at which  $g(r)$  crosses one) and the minimum position, respectively. Point  $c$  is defined in  $S(q)$  as the peak position. In the figure we can see that  $q_m(t) \approx 0.117$ , which corresponds to a distance  $2\pi/q_m \approx 53.7$  that lies precisely in the nearest-neighbor region of  $g(r)$ , as mentioned before.

We found that unlike the gelation times that can be obtained exactly, the saturation times can only be roughly estimated. These quantities were obtained from the simulations for the following volume fractions:  $\phi = 0.005, 0.0065, 0.008, 0.01, 0.013, 0.02, 0.03, 0.04$



and 0.06. The resulting gelation times were, 109 098, 80 822, 26 903, 22 026, 14 765, 6 003, 2 441, 1 212 and 545, while the saturation times were approximately 300 000, 180 000, 170 000, 100 000, 40 000, 13 000, 5 000, 3 000 and 1 100. The saturation time – for which  $q_m$  does not change appreciably anymore – is assumed to be the onset of formation of a close packed structure of terminal clusters, of which the infinite network is made. The consistently smaller values for the gelation times indicate that, at the gelation threshold, *we have an infinite network made of terminal clusters plus some holes*, where a number of finite cluster reside that have not reached the size of a terminal cluster.

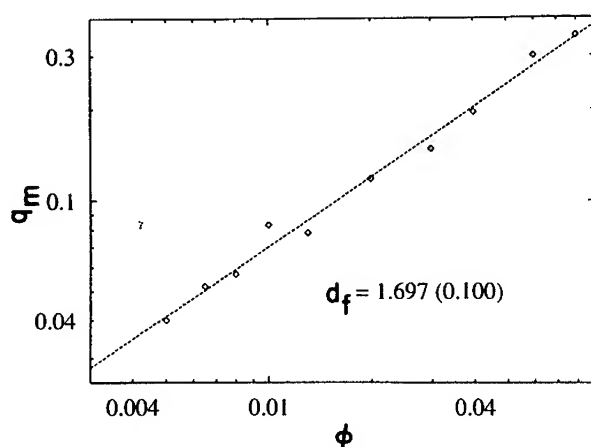


Fig. 3. A double logarithmic plot of the terminal  $q_m$  vs.  $\phi$  for the ten different concentrations studied. the straight line is the best fit to the data.

To obtain an analytical estimate of the terminal  $q_m$  [8] we consider a close packed structure of  $n$  monodisperse terminal clusters of size  $R$  and containing  $N$  particles each in the volume  $V$  of the system. In general, the cluster volume fraction  $\phi_c$  is  $(n \frac{4\pi}{3} R^3)/V$ . Considering that  $n = N_0/N$  and  $N = (R/a)^{d_f}$ , we find  $\phi_c \sim \phi a^{d_f-3} R^{3-d_f}$ . As at saturation  $\phi_c \approx 1$ , and  $q_m \sim 1/R$ , we find  $q_m \sim a^{-1} \phi^{\frac{1}{3-d_f}}$ . In Fig. 3 we see a log-log plot of the terminal  $q_m$  versus  $\phi$  for the ten concentrations studied, to test this equation. All the points stay closely on a straight line, giving us another independent estimate of the fractal dimension  $d_f = 1.70 \pm 0.10$ . It is important to note that this picture of close packed terminal clusters works well, even at concentrations as high as 0.08 in volume fraction. This is in contrast with the results of Ref. 4 where, after  $\phi \approx 0.01$ , a clear deviation from the above law was observed.

### Summary.

Our main results can be summarized as follows: (a) we are able to clearly relate the peak in the structure factor to the nearest-neighbor cluster distance; (b) we find that the gelation time is of the same order of magnitude, although consistently smaller than the time for the onset of saturation and (c) the picture of close packed clusters to determine the terminal  $q_m$  is extended in concentration well beyond the point it was originally assumed [4]. We believe that more experimental and numerical work is needed to ascertain these results.

This work was partially supported by CONACYT grant 4906-E. GRS was also partially supported by DGAPA grant IN103294 while AEG was also partially supported by the CRAY Research grant SC100394. The authors thank the committee at DGSCA-UNAM for granting them a generous amount of CPU time on the Cray Y-MP supercomputer.

### References

- [1] Kinetics of Aggregation and Gelation, edited by F. Family and D. P. Landau (Elsevier, Amsterdam, 1984).
- [2] D. A. Weitz and J. S. Huang, in Ref. 1, p. 19.
- [3] M. Carpineti and M. Giglio, Phys. Rev. Lett. **68**, 3327 (1992).
- [4] J. Bibette, T. G. Mason, H. Gang and D. A. Weitz, Phys. Rev. Lett. **69**, 981 (1992).
- [5] M. Carpineti and M. Giglio, Phys. Rev. Lett. **70**, 3828 (1993).
- [6] R. O. Watts and I. J. McGee, Liquid State Chemical Physics, (Wiley, New York, 1976).
- [7] A. E. González, Phys. Rev. Lett. **71**, 2248 (1993).
- [8] G. Dietler, C. Aubert, D. S. Cannell and P. Wiltzius, Phys. Rev. Lett. **57**, 3117 (1986).

## HOT CORROSION MECHANISM OF SILICON NITRIDE BASED CERAMICS EXPOSED TO COAL SLAG CONTAINING POTASSIUM SULFATE

Z.B. YU, W.H. LI, N.F. LI\*

Shandong R&D Institute of Industrial Ceramics, Zibo, Shandong, 255031, China

\*Wuhan University of Technology, Wuhan, Hubei, 430070, China

### ABSTRACT

The corrosion of three kinds of silicon nitride based ceramics by static liquid potassium sulfate-coal slag immersion was investigated at high temperatures. The reaction kinetics between silicon nitride based ceramics and coal-slag-potassium sulfate was investigated, different kinetic curves were obtained at different temperatures, it was  $1-(1-a)^{1/3}=kt$  at 1350°C and  $a=kt^2$  at 1400°C. Phase composition, microstructure of the materials before and after corrosion were studied by XRD, SEM/EDAX, and EPMA etc, which lead to the following detailed corrosion mechanism: (1) oxidation of silicon nitride based ceramics by potassium salt and oxygen in air simultaneously and formation of silicon dioxide. (2) melting of as-formed silica by potassium sulfate or K-contained silicate and resulting in a silicate melt  $Me-K_2O \cdot xSiO_2$ , and (3) formation of a protective silica layer below the silicate melt.

### INTRODUCTION

In recent years, there has been considerable interest in using high-efficiency energy conversion system to produce electricity from coal. The MHD generator is one of new technologies of generating electricity, it can remarkably improve the thermal efficiency and reduce the environment pollution. Due to the severe working condition for the channel in coal-fired MHD generator, it requires the insulation material must have the following characters: (1) oxidation resistance, (2) high temperature capability, (3) high temperature gases and liquid corrosion resistance to the fluxing effects of coal slag and fuel seeds such as alkali sulfate, (4) good thermal shock resistance, and (5) high thermal conductivity and electric insulation. The corrosion is one of the major effects on the lifetime of the channel. Although engineering ceramics such as  $Si_3N_4$  and SiC have many excellent physical properties, the potential application of ceramics in such system is very dependent upon their resistance to corrosion environment produced during combustion [1]. The effects of corrosion in various potassium salts on  $Si_3N_4$ , SiC, AlN and sialon [2,3] has been found to be a function of salt/environment chemistry and the material composition. Similar effects were noted in coal slag environments for SiC and  $Si_3N_4$  ceramics [1,4]. It is important to address the hot corrosion problem especially hot corrosion mechanism for these materials in order to improve their properties. D.S. Fox et al [5] did great work on this aspect, they employed the film method and discussed the corrosion mechanism of various  $Si_3N_4$  ceramics in pure  $Na_2CO_3/Na_2SO_4$ . The purpose of this paper is to report on the chemical mechanism of corrosion for  $Si_3N_4$ -based ceramics exposed to coal slag containing potassium sulfate.

### EXPERIMENTAL PROCEDURES

The materials used in this study are listed in Table I.

Table I Materials

| Designation | Material                                  | Additives  |
|-------------|---|--|
| S101        | Si <sub>3</sub> N <sub>4</sub> ( MA )     | MgO, Al <sub>2</sub> O <sub>3</sub> , ZrO <sub>2</sub>       |
| S401        | Si <sub>3</sub> N <sub>4</sub> - BN       | MgO, Al <sub>2</sub> O <sub>3</sub> , ZrO <sub>2</sub>       |
| S406        | Si <sub>3</sub> N <sub>4</sub> - BN - AlN | MgO, Al <sub>2</sub> O <sub>3</sub> , ZrO <sub>2</sub> , AlN |

All materials were hot-pressed in a graphite die at the temperature range of 1750°C to 1800°C, at 15 to 30 MPa, for 0.5 to 2 hours in N<sub>2</sub> atmosphere. These materials were cut into 10 by 8 by 4 mm. The surface of the specimens were finished and the edges bevelled by diamond to 1 μm. The samples were cleaned by distilled water and alcohol. The corrosion medium employed is Datong ash plus 20% of K<sub>2</sub>O ( added in the form of K<sub>2</sub>SO<sub>4</sub>).

In each experiment, a weighed sample and the powdered corrosion medium were put into a test crucible of highly purified alumina, 35 mm in diameter and 50 mm long, then placed in an electric furnace regulated at the temperatures of 1350°C and 1400°C respectively for 1 to 250 hours. The experiment was conducted in air atmosphere. After maintaining the desired temperature & time, the crucible was removed from the electric furnace and cooled quickly to room temperature and weighed with a Shimadzu - LIBOROR electronic balance ( EB-2800 type ). Phase composition and microstructure of the materials before and after corrosion were studied by X-ray diffraction analysis (XRD), scanning electron microscopy (SEM) with energy-dispersive spectrometry (EDS), and electron microprobe analysis (EMPA). The microprobe was also equipped with a wavelength dispersive spectrometer which allowed oxygen mapping. Cross section were polished to 1 μm and sputtered the coating of carbon on the corroded samples.

## EXPERIMENTAL RESULTS

### Corrosion kinetics of the materials

The time dependence of the degree of the weight loss of the three kinds of Si<sub>3</sub>N<sub>4</sub> based ceramics immersed in coal slag - potassium sulfate melts at 1350°C and 1400°C exposed to air is shown in Fig.1 and Fig.2. As can be seen from Fig.1 and Fig.2, materials with different kinds of additives have different properties of corrosion resistance, the effect of temperature on the corrosion of the materials is very serious, and different kinetic curves were obtained at different temperatures, it was  $1-(1-a)^{1/3}=kt$  at 1350°C, this means that the surface chemical reaction controlled shrinking core model could describe the relation very well between time and weight loss rate of Si<sub>3</sub>N<sub>4</sub>- based ceramics in coal slag containing potassium sulfate exposed to air at the temperature of 1350°C. However, it was  $a=kt^2$  at 1400°C, which means the corrosion is much intensified at 1400°C than that at 1350°C.

### XRD analysis on the surface of the materials

The XRD analysis results of the surface of the silicon nitride based ceramics before and after corrosion are listed in Table II.

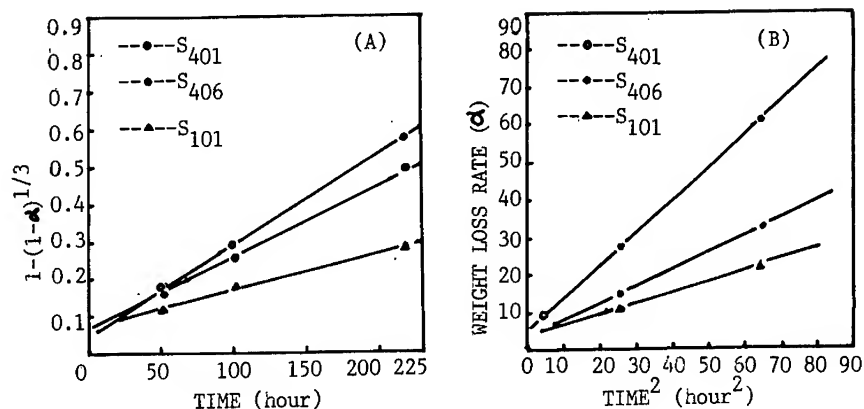


Fig.1 Relationship between weight loss rate and time at 1350°C. Fig.2 Relationship between weight loss rate and time at 1400°C.

Table II XRD analysis results before and after the corrosion of the material

| Designation | Before corrosion   | corrosion 1400°C, 1 hr.  | corrosion 1400°C, 5 hr.  |
|-------------|--|--|--|
| S101        | Si <sub>3</sub> N <sub>4</sub> (s)                                   | Si <sub>3</sub> N <sub>4</sub> (s)                                   | Si <sub>3</sub> N <sub>4</sub> (s)                                   |
|             | Si <sub>2</sub> N <sub>2</sub> O (v.w)                               | Si <sub>2</sub> N <sub>2</sub> O (w)                                 | Si <sub>2</sub> N <sub>2</sub> O (m)                                 |
|             | ZrO <sub>2</sub> (v.w)   | ZrO <sub>2</sub> (v.w)   | ZrO <sub>2</sub> (v.w)   |
|             | Tridymite (v.w)  | Tridymite (w)  | Tridymite (w)  |
| S401        | Si <sub>3</sub> N <sub>4</sub> (s)                                   | Si <sub>3</sub> N <sub>4</sub> (s)                                   | Si <sub>3</sub> N <sub>4</sub> (s)                                   |
|             | BN (s)   | BN (s)   | BN (s)   |
|             | ZrO <sub>2</sub> (v.w)   | ZrO <sub>2</sub> (v.w)   | ZrO <sub>2</sub> (v.w)   |
|             |  | Tridymite (v.w)  | Tridymite (v.w)  |
| S406        | Si <sub>3</sub> N <sub>4</sub> (s)                                   | Si <sub>3</sub> N <sub>4</sub> (s)                                   | Si <sub>3</sub> N <sub>4</sub> (s)                                   |
|             | BN (s)   | BN (s)   | BN (s)   |
|             | Si <sub>3</sub> Al <sub>2.67</sub> N <sub>4</sub> O <sub>4</sub> (m) | Si <sub>3</sub> Al <sub>2.67</sub> N <sub>4</sub> O <sub>4</sub> (m) | Si <sub>3</sub> Al <sub>2.67</sub> N <sub>4</sub> O <sub>4</sub> (m) |
|             | Tridymite (v.w)  | Tridymite (v.w)  | Tridymite (v.w)  |

s: strong, m: middle, w: weak, v.w: very weak

The results show that the corrosion of silicon nitride based ceramics is accompanied by the formation of Si<sub>2</sub>N<sub>2</sub>O (only for S101) and tridymite, and its content will increase with the increase of temperature and time.

## Microstructure analysis of the cross section of silicon nitride based ceramics

### SEM / EDAX analysis

Fig.3 is the SEM morphology of the polished cross section of S401 and S406 after corrosion at 1400°C for 1 hour.

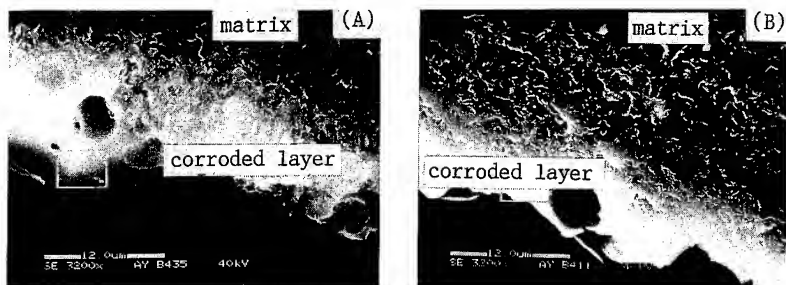


Fig.3 SEM morphology of cross section of  $\text{Si}_3\text{N}_4$  based ceramics  
( A ) S401 , ( B ) S406

Fig.3 indicates that the microstructure of S401 is similar to that of S406, it can be divided into three parts: corrosion layer, transition layer and the matrix. Some regions appear very porous in the corrosion layer, a large bubble is clearly evident. There may be some type of composition change in the vicinity of the bubble, but it was not possible to determine this by EDAX or XRD[5]. The corrosion layer of S406 is denser than that of S401. Micro-area composition analysis was conducted by EDAX within an area of 6 by 4  $\mu\text{m}$  for the corrosion layers, the results are shown in Fig.4.

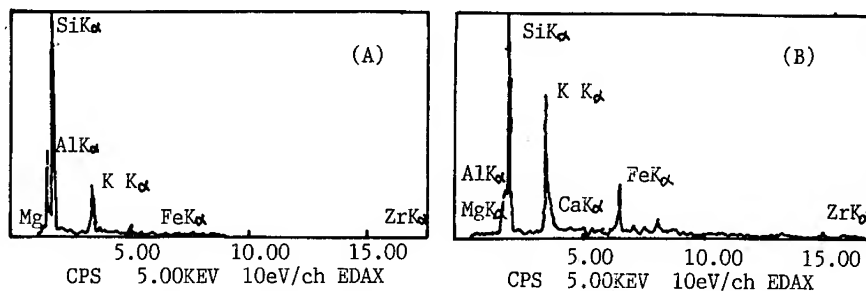


Fig.4 EDAX analysis of the corrosion layer (A) S406 , (B) S401

The element contents of the corrosion layer tested by EDAX is listed in Table III. It can be seen from the Fig.4 and the Table III, the corrosion layer mainly contains the metal elements of Si, Al, K, Fe and small amount of Mg, Ca and Zr. Considering the possible formation of some compounds in the corrosion layer, the content of Si, Al, K was normalized and got a new result as following

Table III Element contents of corrosion layer tested by EDAX

| Designation      | Elements |       |       |       |      |       |       |
|------------------|----------|-------|-------|-------|------|-------|-------|
|                  | Mg       | Al    | Si    | K     | Ca   | Fe    | Zr    |
| S <sub>401</sub> |          | 5.69  | 37.11 | 28.52 | 1.58 | 17.67 | 9.417 |
| S <sub>406</sub> | 1.901    | 19.95 | 58.86 | 17.67 |      |       | 1.61  |

Si:52%, Al:8%, K:40% for S<sub>401</sub>, which is equivalent to 27.5% KAlSiO<sub>4</sub> and 72.5% K<sub>2</sub>O·3.37SiO<sub>2</sub>; and Si:61%, Al:21%, K:18% for S<sub>406</sub>, which is equivalent to 43% KAlSiO<sub>4</sub>, 12% 3Al<sub>2</sub>O<sub>3</sub>·2SiO<sub>2</sub> and 45% SiO<sub>2</sub>.

#### Electron microprobe analysis

Results of X-ray scanning by electron probe in depth direction from the corroded surface on the cross section of S<sub>401</sub> and S<sub>406</sub> are shown in Fig.5.

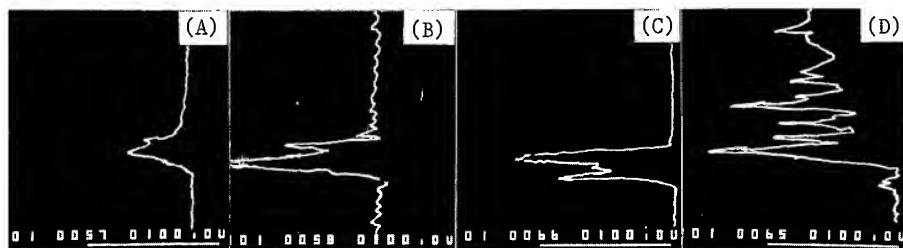
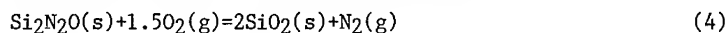
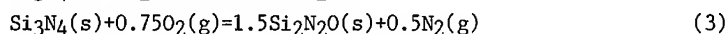
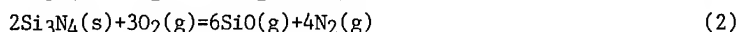
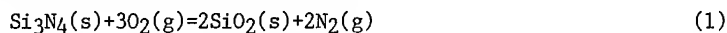


Fig.5 Results of the X-ray scanning by EPMA in depth direction  
S<sub>401</sub>: (A) K, (B) O ; S<sub>406</sub>: (C) K, (D) O

The results indicated that the depth of element O is larger than that of element K. Combined with the results of EDAX, the corrosion microstructure features of Si<sub>3</sub>N<sub>4</sub> based ceramics could be described as a multilayer structure, the first layer is K-silicate melt containing the elements of Fe, Zr, Mg; the second layer is a thin film of silica, and the last is silicon nitride matrix.

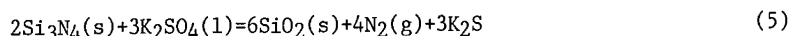
#### DISCUSSION

Under the present study condition, the oxidation of the materials is inevitable and may occur by the following reactions:

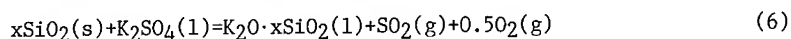


T.Sato et al [2] had given the relationship between  $\Delta G_T^\circ$  and T for reaction (1) to (3), and pointed out that all the reactions is possible, and reaction (1)

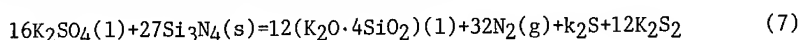
is prior to the others, based on the thermodynamic data.  $\text{Si}_3\text{N}_4$  based ceramics can also be oxidized by  $\text{K}_2\text{SO}_4$ , because  $\text{K}_2\text{SO}_4$  has a strong oxidation ability at high temperature, the reaction is shown as following:



The  $\text{SiO}_2$  as-formed could react with  $\text{K}_2\text{SO}_4$  further to form  $\text{K}_2\text{O} \cdot x\text{SiO}_2$ :



In addition, Sato et al [2] obtained a quantitative reaction between  $\text{Si}_3\text{N}_4$  and  $\text{K}_2\text{SO}_4$  to form a stoichiometry compound  $\text{K}_2\text{O} \cdot 4\text{SiO}_2$ .



Therefore, three possible corrosion processes of silicon nitride based ceramics could be raised: (1) oxidized only by  $\text{O}_2$  in air to form silica which then was reacted completely by  $\text{K}_2\text{SO}_4$  to form  $\text{K}_2\text{O} \cdot x\text{SiO}_2$ ; (2) reacted quantitatively with  $\text{K}_2\text{SO}_4$  to form a stoichiometry compound  $\text{K}_2\text{O} \cdot 4\text{SiO}_2$ , (3) oxidized by  $\text{K}_2\text{SO}_4$  and  $\text{O}_2$  in air simultaneously to form silica and the silica was melted by  $\text{K}_2\text{SO}_4$ . However, based on the experiment results, the first process and the second are not true, because the corrosion kinetics obtained in present study does not agree with the parabolic law, and the corrosion products are not the stoichiometry compound as expected either. The third is feasible, as shown in XRD analysis (see Table I), tridymite occurred on the surface of the corroded samples. Furthermore, the results of EPMA also showed that there was a thin silica layer beneath the K-contained silicate on the surface of the materials. Therefore, the hot corrosion mechanism of silicon nitride based ceramics immersed in coal slag containing  $\text{K}_2\text{SO}_4$  could be described as following: (1) Oxidation of  $\text{Si}_3\text{N}_4$  based ceramics by potassium salt and  $\text{O}_2$  in air simultaneously and formation of silica. (2) Melting of as-formed silica by  $\text{K}_2\text{SO}_4$  or K-contained silicate and resulting in a silicate melt, and (3) Formation of a protective silica layer below the silicate melt.

#### SUMMARY

The materials as-prepared have a good corrosion resistance to coal slag containing  $\text{K}_2\text{SO}_4$  except  $\text{S}_{401}$ . Different corrosion kinetic curves were obtained, it was  $1-(1-a)^{1/3} = kt$  at  $1350^\circ\text{C}$  and  $a = kt^2$  at  $1400^\circ\text{C}$ . The corrosion process includes three stages: (1) Oxidation of silicon nitride based ceramics by  $\text{K}_2\text{SO}_4$  salt and  $\text{O}_2$  in air simultaneously and formation of silica, (2) Melting of as-formed silica by  $\text{K}_2\text{SO}_4$  or K-contained silicate and resulting in a silicate melt, and (3) Formation of a protective silica layer below the silicate melt.

#### REFERENCE

1. P.F. Becher, J. Mater. Sci. 19, 2805 (1984).
2. T. Sato, Y. Yoiike, T. Endo, M. Shimada, J. Mater. Sci. 23, 1405 (1988).
3. T. Sato, Y. Kanno, T. Endo, M. Shimada, yogyo-kyokai shi, 94[1], 134 (1986).
4. M.K. Ferber, V.J. Tennery, Am. Ceram. Soc. Bull. 62(2), 236 (1983).
5. D.S. Fox, N.S. Jacobson, J. Am. Ceram. Soc. 71(2), 128 (1988).



---

## PART VIII

---

### Granular Materials

## The Scientist in the Sandbox: Complexity and Dynamics in Granular Flow

R. P. Behringer

Department of Physics and Center for Nonlinear and Complex Systems  
Duke University

Granular materials exhibit a rich variety of dynamical behavior, much of which is poorly understood. Fractal-like stress chains, convection, a variety of wave dynamics, including waves which resemble capillary waves, and fractional Brownian motion provide examples. Although granular materials consist of collections of interacting particles, there are important differences between the dynamics of a collections of grains and the dynamics of a collections of molecules; in particular, the ergodic hypothesis is generally invalid for granular materials, so that ordinary statistical physics does not apply. Nonlinear Dynamics, Mathematics, Molecular Dynamics, and Condensed Matter Physics as well as traditional Engineering fields have all contributed to recent insights for these phenomena.

PACS numbers: 47.35.+i, 47.50.+d 62.90.+k

Granular materials<sup>1-4</sup> are collections of macroscopic particles or grains typically having inelastic interactions and often surrounded by a fluid,<sup>42</sup> such as air or water. The fluid may play an important role in the dynamics of the system, particularly in nature: at the beach, wind picks up the grains and builds dunes through a process known as saltation.<sup>36,5,6</sup>

One might expect that granular materials behave like a gas or fluid, on a larger scale. This expectation is not met for a variety of reasons. Granular interactions are inelastic. If a system starts with nonzero kinetic energy, it very rapidly loses that energy— in a finite length of time. In the process, clustering occurs, and the system becomes inhomogeneous.<sup>7</sup> Non-transient granular flow requires the constant input of energy, from gravity, shaking, or other sources. Often, the ergodic hypothesis of statistical mechanics fails: the system comes nowhere near sampling the possible microstates for given macroscopic parameters; ordinary thermodynamics does not work. One of the complications of many granular flows is that part of the system is in a frozen state while nearby regions are moving. The transition from static to moving occurs in a relatively narrow width of material known as a shear band.

In situations where the grains remain in contact for substantial times, stress chains form, as typified by Fig. 1. In this example, static stresses are applied at the triangular boundaries, and the stress is indicated by the brightness of the region via the photoelastic effect. In the figure, stress chains, propagate essentially from one boundary to another, suggesting spatial correlation over many tens of disks. The long range of the chains raises the question of the smallest length scale over which a continuum description is appropriate. The fact that grain configurations frequently change slowly over measurement times leads to interesting fluctuational effects. In an ordinary gas, the molecular flux is enormous, with a cumulative effect of a homogeneous pressure on typical temporal and spatial scales. In the granular case, the number of particles in contact with a surface is much smaller, and the grain positions can easily evolve on instrumentally resolvable times. There is generally not time during a measurement to produce an averaging of the fluctuations. Granular measurements typically show large scale temporal fluctuations which can be an appreciable fraction of the mean.

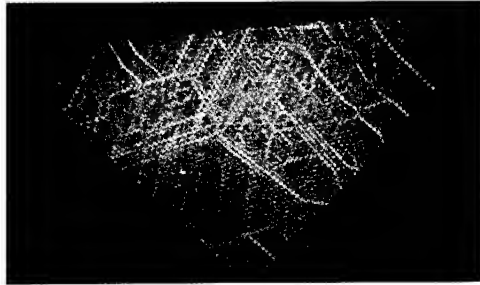


FIG. 1. Stress chains in a 2-D material. The grains are  $1/4$ in plastic disks cast from epoxy. Stress is applied from the three sides of the array, which is viewed through crossed polarizers.

An additional feature of granular materials is that the individual grains typically have a shape which need not be spherical. Under the force of gravity, or applied stress, the grains may exhibit long range orientational and/or packing effects associated with the grain shape.

Hence, it is hardly surprising that they exhibit a large and often surprising collection of phenomena. At the lowest level of temporal complexity are static or quasi-static phenomena. Granular materials can be solid-like because they can sustain weak shear stresses with essentially elastic deformation up to a point.<sup>3</sup> Unlike solids, noncohesive granular materials cannot sustain tension; in this case, they disintegrate. A heap of granular material can be stable, i.e. solid-like, as long as its inclination angle is not too steep. The conventional interpretation of this phenomena is one of Coulomb friction. Flow occurs in a thin avalanche area near the surface if the heap angle is too steep, until the heap is reduced to a lower angle.

With a steady source of energy, granular materials can exhibit a large variety of dynamical states including convection, wave phenomena, period doubling and temporal scale invariance. Sand piles have also been proposed and extensively studied as candidates for self-organized criticality.<sup>8</sup>

There are also many technical applications of granular materials, ranging from the commonplace transport of coal and grain to the high tech handling of pharmaceutical powders, fluidized beds, and the preparation of sinters for advanced materials. The total cost involved in the handling of these materials is enormous. A modest improvement in our understanding of their flow properties could lead to significant savings.

The current understanding of the statistical properties and dynamics of these materials lags far behind the understanding of the dynamics of conventional fluids. Current models, although useful and sophisticated, all show weaknesses which invite alternative models. In no case is there a model which is as firmly established as the Navier- Stokes equations of Newtonian fluid mechanics.

Models of granular flow typically fall into one of three different classes: continuum models based on plasticity theory,<sup>3</sup> kinetic theory,<sup>18</sup> and discrete particle models.<sup>33,34</sup> The first is appropriate for slowly deforming dense material, and is widely used in soil mechanics and engineering applications.<sup>9,10</sup> The second applies when the grains have more freedom of movement, and incorporates random motion through a granular temperature. The third circumvents difficult constitutive issues associated continuum models of granular dynamics

by adopting a microscopic description—i.e. at the level of individual grain interactions. The modeling can take various forms, including molecular dynamics (MD), a direct integration of Newton's equations, and cellular automata models.

Continuum models consist of a set of partial differential equations expressing conservation laws plus constitutive relations. An important feature of these models is dilatancy.<sup>11</sup> For dense granular materials to deform under shear, they must also dilate, an irreversible, hence plastic, process. Modern soil mechanics models, are based around the idea of plastic yield.<sup>9,3</sup> A relatively simple version is the rigid-plastic model. For moderate shearing, material is assumed to remain totally undeformed. When the shear is great enough to overcome the normal stress, the material deforms plastically. The locus of points giving the shear stress at which yield occurs versus the normal stress and density of the material defines the yield surface.

Analysis<sup>12</sup> of these models indicates that a uniformly deformed sample will typically be subject to instabilities having a characteristic time scale  $\tau$ , set by the flow speed,  $U$ , the size of the system,  $L$ , and a small parameter  $\beta$  characterizing the yield surface:  $\tau = L/(U\beta)$ . We have carried out two experiments measuring normal stress vs. time to identify this time scale, one for hoppers and the other for uniform shearing in a Couette geometry. In both cases, the predicted scale is absent. Instead, a large noisy fluctuating component dominates the measured time-dependence,<sup>14</sup> as in Fig. 2. For hopper flow, the power spectrum from the stress measurements is characterized reasonably well by a power law in the frequency:

$$P(\omega) \propto \omega^{-\alpha}. \quad (1)$$

with  $1.3 \leq \alpha \leq 2.3$ . A power law implies the absence of a characteristic time scale, and is typical of a self-affine process.<sup>15</sup> Experiments, of the stress for a sheared annular sample of material where  $L$  and  $U$  are more clearly defined than for hopper flow, also yield spectra which show no signs of the predicted  $\tau$ .

The important feature in these experiments is a large fluctuating component which is absent in the continuum models. A related observation has been obtained by Jaeger et al. in sound propagation measurements.<sup>16</sup> The frequency response of the system was very complex, and highly sensitive to very small changes in the particle contacts. Both the nearly frozen character of granular materials and the associated phenomena of stress chains play a role in these observations.

For faster lower density flows, correlations may have a shorter range, and some of flows become more like those of a conventional fluid. Current models envisage this kind of situation as a dense gas.<sup>18</sup> Fluctuations are modelled as a granular temperature,  $T_g$ . However, in a typical flow,<sup>19,2,20,21,23,24,26</sup> such as a chute flow—an approximately steady avalanche, Couette flow, or shaker-induced flow, different parts of the system will exist in both gas-like and frozen states. Even when the kinetic picture is thought to apply, the fluctuating components can be comparable to the mean values.

The dynamics of granular materials can also be strongly affected by the shape of the grains. The importance of particle shape is demonstrated in a set of experiments<sup>28</sup> which characterized the density of sand flowing in a thin hopper. The experiments produced digitized x-ray images of the flow at the rate of 10 frames/s. For nonspherical particles, such as rough sand, the experiments show low density propagating waves (dark regions), as in Fig. 3. Similar structures have been observed previously,<sup>27</sup> but the propagation of the waves was not captured. No waves occur if the grains are smooth sand or spherical particles, whereas they do occur for rough sand, i.e. for grains with asperities. The key point is not the difference in friction between grain types, which is small, but rather, the rotational hindrance.

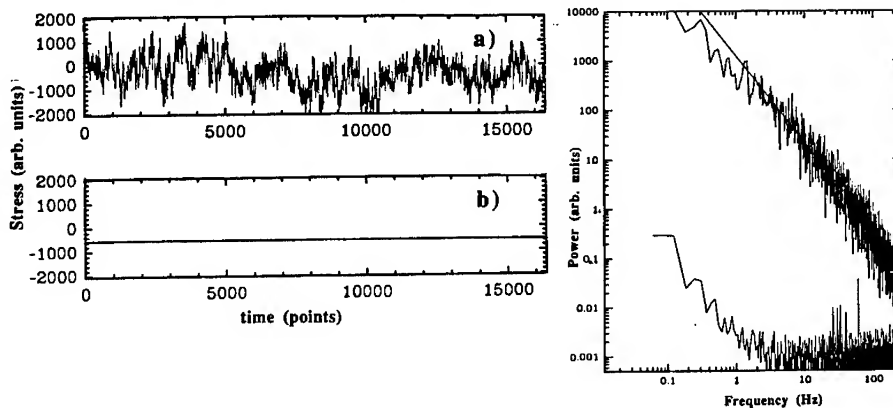


FIG. 2. Time series (left, a) and resulting power spectrum (right, upper data) for stress at the sidewall of a hopper during the outflow of sand. For comparison, the stress in the absence of flow (left, b) and the resulting measure of instrumental noise (right, lower data) are also given. On the scale of the figure, the no-flow time series looks like a straight line.

The role of grain shape and rotational hindrance is particularly important for materials consisting of long thin grains, such as grass seed or rice. Then, there is significant coupling between rotational and translation motion.<sup>29</sup>

Hopper flows obtain energy through gravity. Another simple way to provide a sustained input of energy to a granular flow is by vibration.<sup>30</sup> When the characteristic acceleration of the shaking exceeds  $g$ , the acceleration of gravity, a host of interesting dynamical states can occur, including convective flow, parametric and traveling waves, bubbling, and highly turbulent flow.

Some of the earliest reported observations on shaken granular material were by Faraday.<sup>31</sup> More recently, Savage<sup>32</sup> studied convection driven by a flexible metal sheet. Rajchenbach and Evesque<sup>20</sup> showed that a uniformly vibrated container of glass spheres with vertical displacement  $z = a \cos(\omega t)$  begins to convect when  $\Gamma \equiv a\omega^2/g$  slightly exceeds 1. Douady et al.<sup>21</sup> found that in thin layers a subharmonic instability can occur leading to parametric standing waves at half the shaking frequency. When an open container is used, as in the experiments of Umbanhower et al.,<sup>22</sup> wave patterns reminiscent of convection patterns occur.

Traveling wave states also exist, as reported by Pak and Behringer,<sup>24</sup> who found that the relevant parameters which describe their onset are  $\Gamma$  and  $E = A^2\omega^2/gd$ . Pak et al. also found<sup>25</sup> that when a granular system is strongly shaken, it can exhibit bubbling.

Three different phenomena may contribute to convection, inhomogeneity in the shaking,<sup>32</sup> wall friction,<sup>33,23</sup> and the presence of gas,<sup>31,26</sup> which can be trapped and compressed during part of each cycle of the shaker producing extra lift. We have recently carried out experiments<sup>26</sup> where the pressure was fixed at  $10^{-3}\text{Torr} \leq P \leq 1000\text{Torr}$ . The heaping for partial diameters  $0.01\text{cm} < d < 0.1\text{cm}$ , is unaffected until  $P$  is lowered to a few tens of Torr. But as  $P$  is decreased further, the heaping is dramatically reduced, as seen in Fig. 4 which shows the height of the heap relative to the base of the shaker, vs.  $P$ .

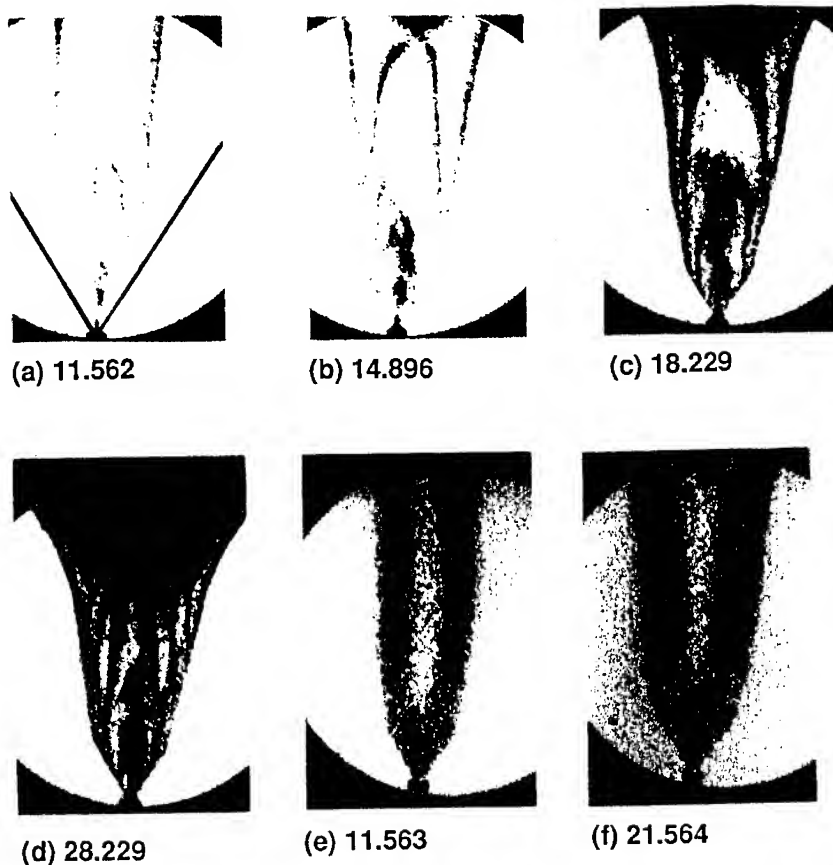


FIG. 3. Density images obtained with real time x-ray fluoroscopy. In all cases, the hopper was 1.27cm thick. Images a-d show the propagating density structures (dark is low density) which occur in rough faceted materials. The opening angles are  $\theta = 66.8^\circ$ ,  $25^\circ$ , and  $40^\circ$  respectively, for the group a-d, a and b. Images e-f show that these structures disappear when nearly spherical sand is used. In this case  $\theta = 66.8^\circ$ . The numbers on the figures indicate the time.

Molecular dynamics (MD), direct numerical simulations of discrete particles by integration of Newton's equations of motions (or an approximation of them) have also been used extensively for studies of granular flow.<sup>34,43,33</sup> These models typically assume spherical particles of radius  $r$  which are in free flight until they begin to overlap. Then, a force begins to push the particles apart which depends on the overlap  $2r - |\mathbf{r}_i - \mathbf{r}_j|$ , where  $\mathbf{r}_i$  is the vector position of particle  $i$ . The repulsive force for spheres increases as the  $3/2$  power of the overlap (the Hertzian force), but a linear repulsive force law is often assumed. The dissipative forces are typically modelled by velocity-dependent normal forces and frictional tangential forces. MD can yield local information on quantities such as mass flow and stress which are difficult to obtain experimentally. Here, I will focus on those calculations which

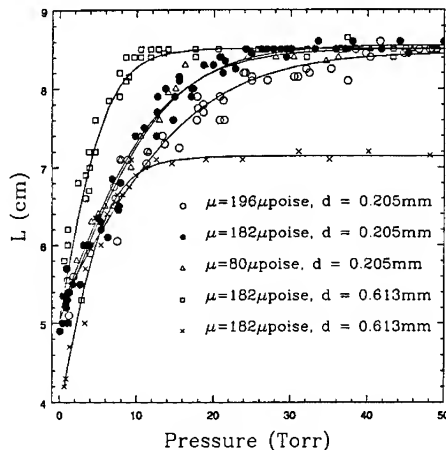


FIG. 4. Heap height,  $L$ , versus pressure for various grain sizes and gas viscosities.

pertain to shaking.

Taguchi, Gallas et al. and Thompson have shown<sup>33</sup> that a two-dimensional granular layer will undergo convection under vertical vibration. Several results from these calculations are interesting. The average mass current shows a relatively sharp transition to convection at  $\Gamma \simeq 1$  with two well defined rolls, as seen in experiments. In this case, convection is attributed to interactions with the side walls.<sup>33</sup> Fluidization also occurs. However, there is little indication of heaping, presumably because these models do not include gas effects.

Granular material also exhibit interesting mixing and segregation phenomena. Segregation by size can occur if there is a distribution of grain sizes.<sup>35,40</sup> Typically, larger particles rise to the top, even if they are heavier than the smaller particles. Important mechanisms for segregation include geometric effects (small particles fall more easily into the "cracks") and convection.

Recently, Metcalfe et al.<sup>44</sup> have considered experiments and models for the reverse process of mixing of granular materials. They have considered 2D flows in closed containers, such as cylinders, subject to uniform rotation. As the cylinder is rotated, avalanches occur on the upper surface of the material which cause mixing through two distinct mechanisms: rapid stirring of the material during an avalanche, and a geometric effect associated with the mixing of succeeding chunks of avalanche material. Two interesting results of these experiments and models are 1) that there is an ideal filling fraction for the most efficient mixing, and 2) that the shape of the 2D container is not particularly an important factor.

From the previous discussion, two points are clear: first, granular flows are strikingly different from their Newtonian counterparts, and second, we are far from a detailed understanding of these flows. In fact, in many cases, we are at the level of determining of the relevant parameters.

It is possible to identify several reasons which lead to the unusual behavior of granular materials. Two intertwined effects are 1) the long range correlations associated with stress networks, and 2) the relatively frozen and slowly evolving nature of these materials. One of several important questions is on what scale a dense granular medium can be approximated by a continuum. The characteristic scales may exceed tens to hundreds of grain diameters. Also, of importance is the role of particle shape. The current models clearly fall short of a truly accurate description of granular flows. Granular assemblies fall into an unusual regime between microscopic and continuum. As a consequence, answers to the questions posed above will require significant insights. The payoffs for answering these questions are significant: safer and more efficient handling of enormous amounts of granular solids.

## ACKNOWLEDGMENTS

This work has been supported under NSF grants DMR-9321791 and DMS-9201034.

## References

- <sup>1</sup>For a review see H.M. Jaeger and S. R. Nagel, *Science* **255**, 1523-1531 (1992).
- <sup>2</sup>C. S. Campbell, *Ann. Rev. Fluid Mech.* **22** 57-92 (1990).
- <sup>3</sup>For a recent review see R. Jackson, "Some Mathematical and Physical Aspects of Continuum Models for the Motion of Granular Materials", in *The Theory of Dispersed Multiphase Flow*, R. Meyer ed., Academic Press (1983).
- <sup>4</sup>For a review see R. P. Behringer, *Nonlinear Science Today*, **3**, 1 (1993).
- <sup>5</sup>R. A. Bagnold, *The Physics of Blown Sand and Desert Dunes*, Chapman and Hall, London, 1954.
- <sup>6</sup>B. T. Werner and D. T. Gillespie, preprint, (1993).
- <sup>7</sup>S. McNamara and W. R. Young, *Phys. Fluids A* **4** 496-504 (1992); *Phys. Fluids A* **5** 34-45 (1993).
- <sup>8</sup>P. Bak, C. Tang, and K. Wiesenfeld, *Phys. Rev. Lett.* **59**, 381-384 (1987). H. M. Jaeger, C. Liu, and S. R. Nagel, *Phys. Rev. Lett.* **62**, 40-43 (1989). G. Held et al. *Phys. Rev. Lett.* **65**, 1120-1123 (1990).
- <sup>9</sup>A. N. Schofield and C. P. Wroth, *Critical State Soil Mechanics*, McGrawHill Publishing Co. 1968.
- <sup>10</sup>A. W. Jenike, *Bulletin of the University of Utah Engineering Experiment Station* No. 108, (1961) and No. 123 (1964, seventh printing 1976).
- <sup>11</sup>O. Reynolds, *Phil. Mag.* **20** 469-481 (1885).
- <sup>12</sup>D. G. Schaeffer, *J. Diff. Eq.* **66**, 19 (1987). E. B. Pitman and D. G. Schaeffer, *Comm. Pure Appl. Math.* **40**, 421 (1987). D. G. Schaeffer, M. Shearer, and E. B. Pitman, *SIAM J. Appl Math.* **50**, 33-47 (1990).
- <sup>13</sup>A. Hettler and I. Vardoulakis, *Géotechnique* **34**, 183-197 (1984).



- <sup>14</sup>G. W. Baxter, R. Leone and R. P. Behringer, *Europhysics Lett.* **21**, 569-574 (1993).
- <sup>15</sup>B. B. Mandelbrot and J. R. Wallis, *Water Resour. Res. Ser.* **4** 909-918 (1968). *Jens Feder Fractals*, Plenum, New York, 1988.
- <sup>16</sup>C.-h. Liu and S. R. Nagel, *Phys. Rev. Lett.* **68** 2301-2304 (1992).
- <sup>17</sup>A. Drescher and G. De Josselin De Jong, *J. Mech. Phys. Solids* **20** 337-351 (1972). T. Travers, D. Bideau, A. Gervois, J. P. Troadec and J. C. Messenger, *J. Phys. A.* **19**, L1033-L1038 (1986).
- <sup>18</sup>P. K. Haff, *J. Fluid Mech.* **134**, 401-430 (1983). S. Ogawa in *Proceedings US-Japan Seminar on Continuum-Mechanical and Statistical Approaches in the Mechanics of Granular Materials*, S. C. Cowin and M. Satake eds, Gakujutsu Bunkai Fukyukai, Tokyo, Japan, 1978. J. T. Jenkins and S. B. Savage, *J. Fluid Mech.* **130**, 186-202 (1983).
- <sup>19</sup>T. G. Drake, *J. Geophys. Research* **95**, 8681 (1990).
- <sup>20</sup>P. Evesque and J. Rajchenbach, *Phys. Rev. Letters* **62**, 44 (1989).
- <sup>21</sup>S. Douady, S. Fauve and C. Laroche, *Europhysics Lett.* **8**, 621-627 (1989).
- <sup>22</sup>F. Melo, P. Umbanhower, and H. Swinney, *Phys. Rev. Lett.* **72**, 172 (1994).
- <sup>23</sup>E. Clement, J. Duran, and J. Rajchenbach, *Phys. Rev. Lett.* **69**, 1189-1192 (1992).
- <sup>24</sup>H. K. Pak and R. P. Behringer, *Phys. Rev. Lett.* **71**, 1832 (1993); in the *Proceedings of the First International Conference on chaos*, p. 91, ed. H. Lee (1993).
- <sup>25</sup>H.K. Pak and R.P. Behringer, *Nature* **371**, 231 (1994).
- <sup>26</sup>H.K. Pak, E. Van Doorn, and R.P. Behringer, to be published.
- <sup>27</sup>R. L. Michalowski, *Powder Tech.*, **39**, 29 (1984); A. Drescher, T.W. Cousens, and P.L. Bransby, *Géotechnique* **28**, 27 (1978).
- <sup>28</sup>G. W. Baxter, R. P. Behringer, T. Faggert and G. A. Johnson, *Phys. Rev. Lett.* **62**, 2825-2828 (1989); in *Two Phase Flows and Waves*, D. D. Joseph and D. G. Schaefer eds, pp. 1-29, Springer, 1990;
- <sup>29</sup>G. W. Baxter and R. P. Behringer, *Phys. Rev. A* **42**, 1017-1020 (1990); *Physica D* **51**, 465-471 (1991).
- <sup>30</sup>P. Evesque, *Shaking Powders and Grains*, *Contemporary Physics* **33**, 245-261 (1992).
- <sup>31</sup>M. Faraday, *Phil. Trans. R. Soc. Lond.* **121**, 299 (1831).
- <sup>32</sup>S. B. Savage, *J. Fluid Mech.* **194**, 457-478 (1988).
- <sup>33</sup>Y.-h. Taguchi, *Phys. Rev. Lett.* **69** 1367 (1992). J. A. C. Gallas, H. J. Herrmann, and S. Sokolowski, *Phys. Rev. Lett.* **69**, 1371-1374 (1992). P. A. Thompson, *Computer simulations in Condensed Matter Physics VI*, D. P. Landau, K. K. Mond, and H. B. Schuttler eds. Springer, 1993.

- <sup>34</sup>P. A. Cundall and O. D. L. Strack, *Géotechnique* **29**, 47 (1979). P. K. Haff and B. T. Werner, *Powder Tech.* **48**, 239-245 (1986). O. R. Walton and R. L. Braun, *J. Rheology* **30**, 949-980 (1986). Y. Zhang and C. S. Campbell, *J. Fluid Mech.* **237**, 541 (1992). P. A. Thompson and G. S. Grest, *Phys. Rev. Lett.* **67**, 1751-1754 (1991).
- <sup>35</sup>A. Rosato, K. J. Strandburg, F. Prinz, and R. H. Swendsen, *Phys. Rev. Lett.* **58**, 1038-1040 (1987).
- <sup>36</sup>R. S. Anderson and P. K. Haff, *Science* **241** 820-823 (1988); P. K. Haff, *Booming dunes*, *American Scientist* **74** 376-381 (1986).
- <sup>37</sup>J. E. S. Socolar, *Europhysics Lett.* **18**, 39-44 (1992). R. Jullien and P. Meakin, *Nature* **344**, 425-427 (1990).
- <sup>38</sup>A. Mehta, *Physica A* **186** 121-153 (1992).
- <sup>39</sup>J. Guckenheimer and P. Holmes, *Nonlinear Oscillations, Dynamical Systems, and Bifurcations of Vector Fields*, pp 102-116, Springer-Verlag, 1983.
- <sup>40</sup>J.B.Knight, H. M. Jaeger, and S. R. Nagel, *Phys. Rev. Lett.* **70**, 3728-3731 (1993).
- <sup>41</sup>*Nature* **361**, 142-145 (1993).
- <sup>42</sup>R. A. Bagnold, *Roy. Soc. London Ser. A* **225** 49-64 (1954).
- <sup>43</sup>H. J. Hermann, *Physica A* **191**, 263-276 (1992).
- <sup>44</sup>G. Metcalfe, T. Shinbrot, and J. Ottino, to be published.

## SEDIMENTATION TO FORM ROUGH, QUASI-ONE-DIMENSIONAL INTERFACES

JAMES V. MAHER AND M. LEVENT KURNAZ

University of Pittsburgh, Department of Physics and Astronomy, Pittsburgh, PA 15260

Sedimentation can result in the growth of rough interfaces. Although sedimentation has been widely investigated in various areas of geology and engineering, the rough interface aspect of sedimentation is still unstudied. Since hydrodynamic forces are in principle long range, rough interfaces formed through sedimentation provide a significantly different growth situation for comparison with other studies of apparently similar final interfaces. This leads us to the question of the possible existence of universal phenomena in sedimentation and if there are universal phenomena, can one use noise plus a simple growth law to explain them?

In the sedimentation experiment discussed in this paper all measurements have been performed with closed cells. The walls of these cells are of 1/4" float glass, and these are held 1mm apart by sealed side frames of precision machined plexiglass. To examine the effects of viscosity each cell was filled with one of three different viscous liquids. A very large number ( $\sim 40,000$ ) of 0.06cm diameter monodisperse silica spheres [1] were also placed in the cells before they were closed; these particles filled approximately 1% - 3% of the volume of the cells. The various cell sizes used and corresponding liquids are given in Table 1. One typical cell is shown in Figure 1. The cell can be rotated about a horizontal

Table 1: The various cell sizes used in the sedimentation experiment and corresponding liquids.

| Cell | Size         | Filling liquid      | $\alpha_s$      | $\alpha_t$      | $\beta$         |
|------|--------------|---------------------|-----------------|-----------------|-----------------|
| A    | 40cm x 40cm  | Glycerin (1300cps)  | $0.80 \pm 0.05$ | $0.93 \pm 0.03$ | $0.47 \pm 0.13$ |
| B    | 40cm x 40cm  | Heavy oil ( 180cps) | $0.76 \pm 0.07$ | $0.90 \pm 0.06$ | $0.43 \pm 0.18$ |
| C    | 40cm x 40cm  | Light oil ( 50cps)  | $0.72 \pm 0.03$ | $0.93 \pm 0.04$ | $0.46 \pm 0.03$ |
| D    | 40cm x 20cm  | Heavy oil ( 180cps) | $0.79 \pm 0.04$ | $0.94 \pm 0.04$ | $0.60 \pm 0.02$ |
| E    | 120cm x 30cm | Heavy oil ( 180cps) | $0.85 \pm 0.06$ | $0.97 \pm 0.03$ | $0.66 \pm 0.10$ |

axis perpendicular to the gap direction. When the cell is rotated, the particles which had been at rest at the bottom must fall through the oil. Although there is convection in the cell at large scales during the flow, as particles join the interface they tend to settle gently on a vertical line with no obvious lateral movement as they approach the surface. After hitting the interface they roll to the nearest local minimum which is no more than one particle diameter away from the impact point.

We concentrated our efforts mainly on analyzing the final surface and its formation. Particle density fluctuations in the fluid above the interface could also be determined from the intensity distribution in the digitized photographs. For each cell type we have measured several time series in which patterns were measured at regular intervals from the earliest completely-covering array until the last of the particles settled down. We have also

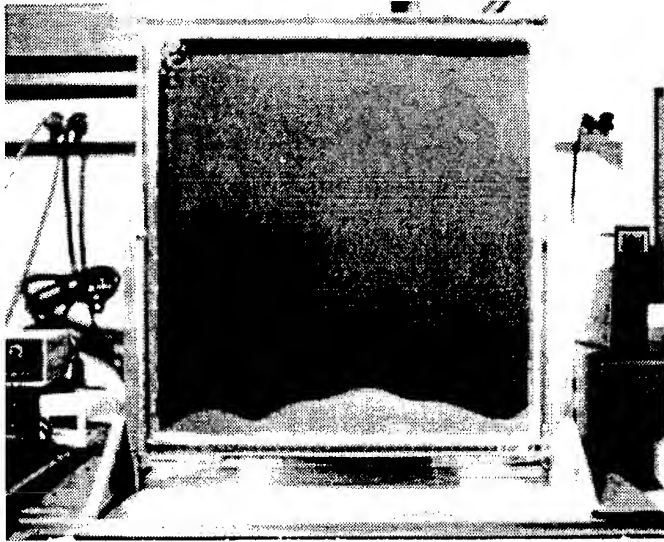


Figure 1: An example of a typical cell with dimensions of 40 cm by 40 cm and a gap of 1 mm.

measured numerous independent runs in which we measured only the final configuration of the settled particles.

The first obvious question about the global behaviour of the settling particles is whether the final configuration of particles might depend in some very important way on the initial configuration of particles at the top of the cell. We found that, if we tilted and shook the cell to force an initial configuration of particles which was very atypical, then the system required approximately four resettlings of the particles before the atypical configuration's features were completely obliterated. However, if the initial configuration was not prepared to be atypical, no obvious correlation between initial and final configurations could be discerned by eye as can be seen in Figure 2.

In an attempt to make this insight quantitative and to look for subtler correlations, we defined a mean absolute difference function [2] between initial and later configurations to be

$$\Delta h_n = \frac{1}{N} \sum_{x_i} |h_n(x_i) - h_1(x_i)| \quad (1)$$

where  $n$  is the number of the configurations in the sequence,  $h_n(x_i)$  is the height of the interface at horizontal position  $x_i$  after the  $n^{\text{th}}$  run and  $N$  is the number of surface sites  $x_i$ . Figure 3 shows this function for 50 sedimentation runs following a very atypical configuration in which the particles formed a triangle on one side of the cell. Figure 4 shows data from most of the same runs, but the sixth run from Figure 3 is used as the initial configuration and compared with all subsequent runs. No obvious correlations appear once the triangular configuration is forgotten by the system.

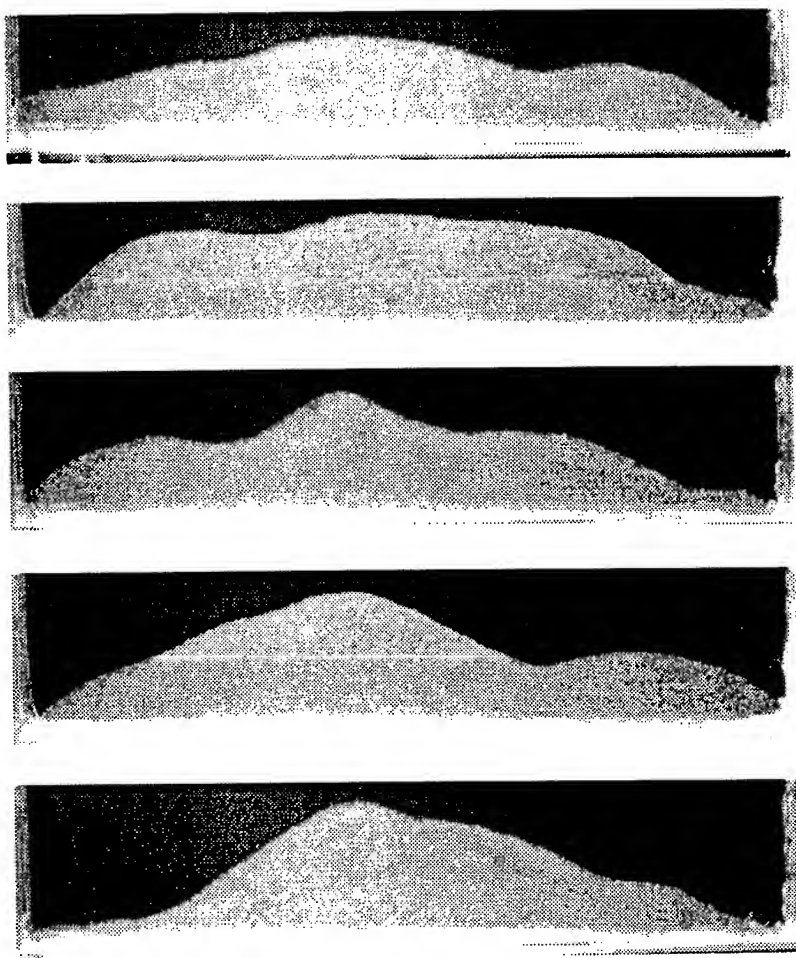


Figure 2: Evolution of a typical initial configuration.

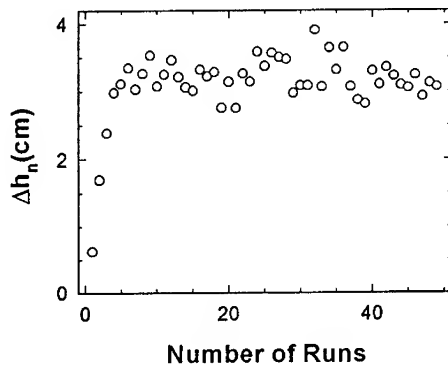


Figure 3: Mean absolute difference function defined in the text using an atypical triangular initial configuration for the first run.

The set of final configurations of all the runs from all the cell types can be used to define the roughness of the interface with great accuracy. We define the rms thickness of the interface to be

$$W(L, t) = \left[ \frac{1}{N} \sum_{i=1}^N \tilde{h}(x_i, t)^2 \right]^{\frac{1}{2}} \quad (2)$$

where

$$\tilde{h}(x_i, t) = h(x_i, t) - \bar{h}(t) \quad (3)$$

and

$$\bar{h}(t) = \frac{1}{N} \sum_{i=1}^N h(x_i, t). \quad (4)$$

It is not at all clear that our system is in a scaling regime, nor is it obvious that scaling ideas should apply to sedimentation, but one important tool we have to report our data and investigate the roughness of the surfaces formed is given by the scaling ansatz for rough interface growth [3]. If we follow this ansatz, we expect

$$W(L, t) = L^\alpha f(t/L^{\alpha/\beta}) \quad (5)$$

where the exponents  $\alpha$  and  $\beta$  are the static and dynamic scaling exponents. The function  $f(t/L^{\alpha/\beta})$  is expected to have an asymptotic form such that

$$W(L, t) \sim t^\beta \text{ for } t \ll L^{\alpha/\beta} \text{ and } W(L, t) \sim L^\alpha \text{ for } t \gg L^{\alpha/\beta} \quad (6)$$

Figure 5 shows a typical example of  $W(L)$  at late times for cell type A. There are clearly two domains of roughness. At small length scales ( $L \leq 1\text{cm}$ ), there is roughly a

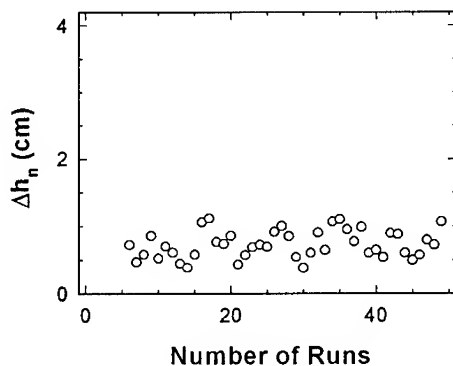


Figure 4: Mean absolute difference function defined in the text using a typical initial configuration for the first run.

decade in  $L$  wherein the data appear to follow a power law whose exponent is  $\alpha_s = 0.747$  for this final state. At longer length scales, ( $L \geq 1\text{cm}$ ), there is roughly a decade over which a different exponent can be identified. The value of this exponent  $\alpha_l$  in Figure 5 is 0.950. As can be seen from Table 1, which shows average exponents for all runs in each kind of cell, similar kinds of behavior are observed with all of the other cells.

While the roughness of the final-state interface is robust, the dynamics by which the growing interface develops appears to be subject to significant fluctuations. In an attempt to extend the analysis to observe early stages of the developing interface, time series of measurements were performed for various flow realizations. An example of this can be seen in Figure 6, where we show the interfacial thickness  $W(L, t)$  for three different times in the same run. In Figure 7 we show the two roughness exponents for all times in the same time series.

We have also investigated the effect of obtaining data from different parts of the final interface, i.e., closer to the walls or from the middle. For this purpose we have divided the interface into smaller boxes of width 10 cm. These boxes were from 0 cm to 10 cm, from 5cm to 15 cm, from 10 cm to 20 cm etc.. Figure 8 shows this analysis for the average of six runs from the set of 46 final runs for cell type A. The fluctuation in the exponents is of the order of the fluctuations from one run to the next.

In the hope of extracting more information from the growth dynamics, we have also constructed the height-height correlation function

$$c(L, t) = \langle [\tilde{h}(x', t') - \tilde{h}(x' + L, t' + t)]^2 \rangle_{x', t'} \quad (7)$$

Using the scaling ansatz of Family and Vicsek [4] we expect  $c(L, 0) \sim L^{2\alpha}$  for  $L$  significantly less than the length of the cell and  $c(0, t) \sim t^{2\beta}$  for short time differences.

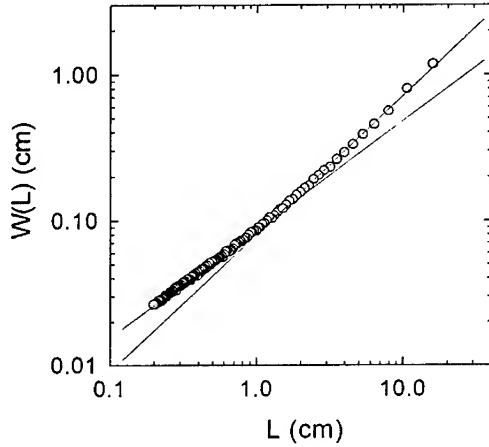


Figure 5: Roughness function  $W(L,t)$  at the end of a typical run.

In Figure 9 we show  $c(0,t)$  vs.  $t$  for one time series of cell type A obtained using Equation 7. The value of  $\beta$  determined from Figure 9 is  $0.61 \pm 0.05$ . Table 1 lists  $\beta$  values for all the time series runs of different cell types. As can be seen in the uncertainties from the table, the value of  $\beta$  fluctuates significantly from run to run, but over all of the runs we obtain an average of  $\beta = 0.52 \pm 0.10$ . It was not possible to use Equation 6 to extract reliable values of  $\beta$  from the roughness functions because the analysis is too sensitive to even small temporal variations in  $\alpha$ .

The question we are trying to answer is which, if either, regime is the scaling regime. To be able to answer these questions possible wall effects and long-range hydrodynamic forces must be investigated. We can control the dynamics by varying the viscosity and by varying the aspect ratio. While in principle, changing the viscosity and changing the aspect ratio can be argued to be equivalent, cooperative screening effects in this system are very likely to separate the two effects. By changing the viscosity and the aspect ratio we found that the short- and long-lengthscale roughness exponents remained unchanged. The crossover regime at about  $L = 1\text{cm}$  did not change either.

In an attempt to quantify the noise in the problem we have constructed a spatio-temporal fluctuation function [5].

$$\eta(x, t_1) = \frac{\tilde{h}(x, t_2) - \tilde{h}(x, t_1)}{\tilde{h}(t_2) - \tilde{h}(t_1)} \quad (8)$$

where  $t_2$  is larger than  $t_1$  by a specified small amount  $\delta t$ .

An example of the spatial correlation function of  $\eta(x, t)$  is shown in Figure 10. The



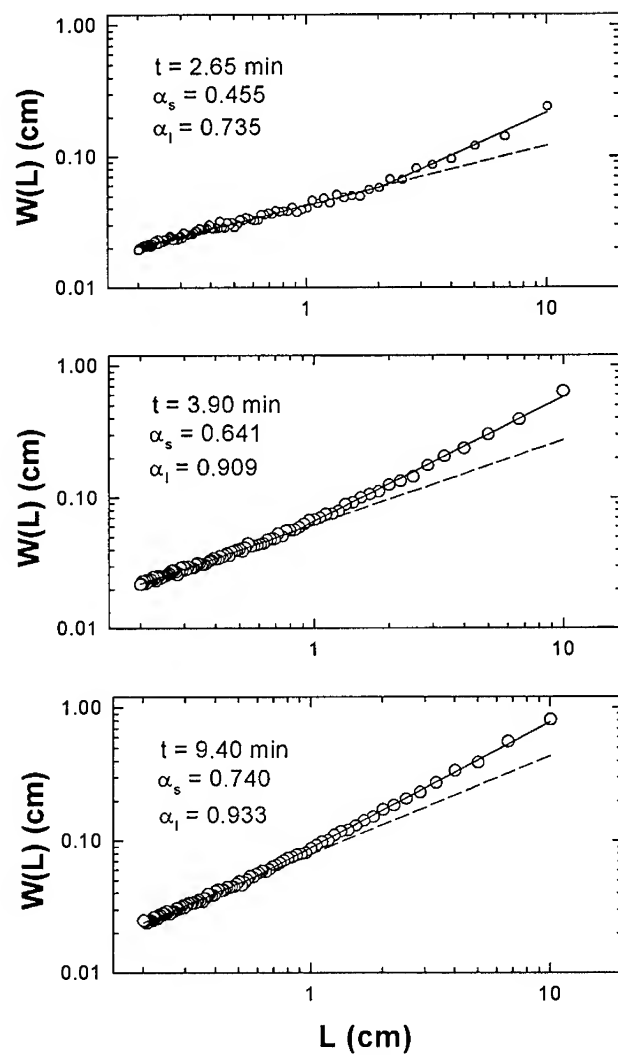


Figure 6: Roughness function  $W(L,t)$  is shown for three values of time in one typical time series for a cell type E.

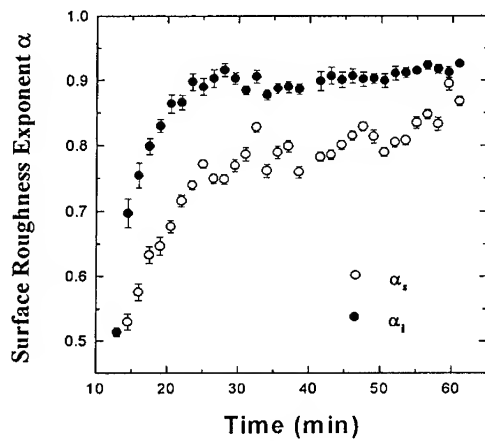


Figure 7: The time evolution of the two exponents  $\alpha_s$  and  $\alpha_l$  for a typical time series for cell type A.

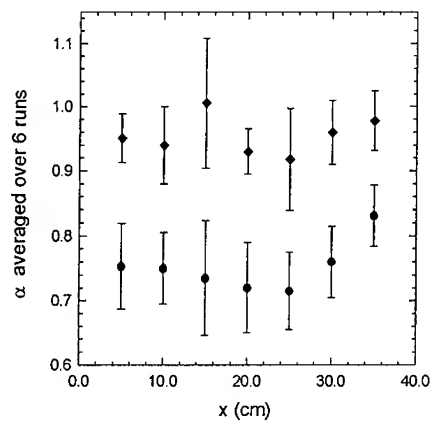


Figure 8: Roughness exponents  $\alpha_s$  and  $\alpha_l$  calculated from the data from different parts of the cell in the same run. This figure shows the average final frame behaviour over six runs arbitrarily selected from a pool of 46 runs for cell type A. All of the values correspond to analyses of 10 cm intervals with the center point of each interval shown as position  $x$  in the cell.

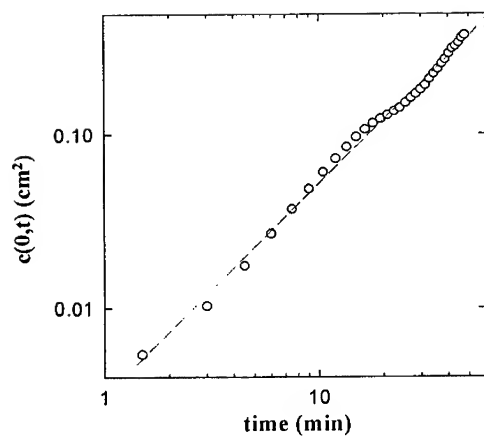


Figure 9:  $c(0,t)$  vs.  $t$  for one time series for cell type A.

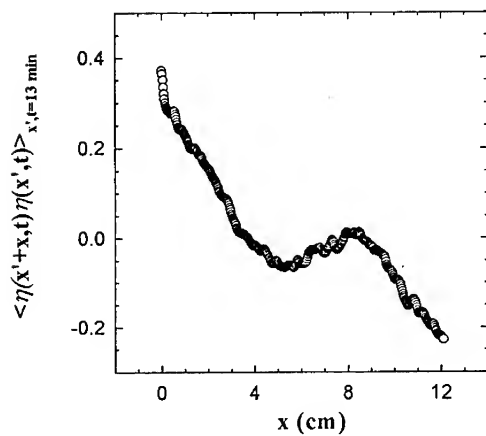


Figure 10: Spatial correlation function of spatio-temporal fluctuation function  $\eta(x,t)$  for arbitrarily chosen  $t = 13 \text{ min}$  in one time series of cell type A.

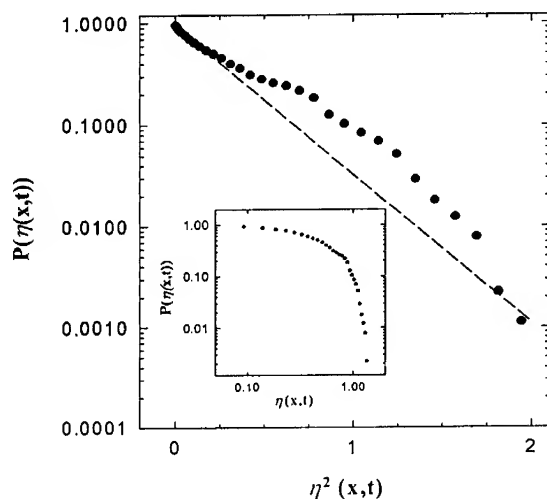


Figure 11: Probability distribution function of spatio-temporal fluctuation function  $\eta(x, t)$  for arbitrarily chosen  $t = 13 \text{ min}$  in one time series of cell type A.

noise falls off at short length scales with a characteristic distance of approximately 2cm and is anti correlated at large length scales ( $\geq 1\text{cm}$ ). The probability distribution of fluctuations is shown in Figure 11 vs  $\eta^2$ . If the noise were pure Gaussian, the data in Figure 11 would fall on a straight line. While the data do not fall on a line, they definitely do not follow a power law (see inset to Figure 11) and might be considered to be Gaussian with some superimposed long range distribution.

Surface roughness is robust against changes in control parameters of fluid flow which suggests that the roughness is apparently a universal behavior. But this leads us to the fact that there cannot be two asymptotic regimes, so if the large  $L$  regime is asymptotic, then we should examine the correlations in the fluid flow and look to the hydrodynamics for an explanation. If the small  $L$  regime is asymptotic, then a simple growth law plus noise might be appropriate to explain the results we obtained. If the latter explanation is adopted, it raises the same question raised by several rough interface growth experiments that the roughness exponents are not those expected from the KPZ dynamics [6] with Gaussian noise [2, 7, 8].

We appreciate helpful discussions with F. Family and D. Jasnow. We are grateful to D. Bideau for giving us samples of monodisperse silica particles. This work is supported by the U.S. D.O.E. on grant # DE-FG02-84ER45131.

## References

- [1] D. Bideau, private communication.
- [2] J. G. Amar and F. Family, Phys. Rev. E **47**, 1595 (1993).
- [3] F. Family and T. Vicsek, J. Phys. A: Math. Gen. **18**, 75 (1985).
- [4] F. Family, Physica A **168**, 561 (1990).
- [5] V. K. Horvath, F. Family, and T. Vicsek, Phys. Rev. Lett. **67**, 3207 (1991).
- [6] M. Kardar, G. Parisi, and Y. Zhang, Phys.Rev.Lett. **56**, 889 (1986).
- [7] E. Medina, T. Hwa, M. Kardar, and Y. C. Zhang, Phys. Rev. A **39**, 3053 (1989).
- [8] J. G. Amar, P. M. Lam, and F. Family, Phys. Rev. A **43**, 4548 (1991).

## DYNAMICS OF GRANULAR MATERIALS: FLOWS, RELAXATION AND CONVECTION

Daniel C. Hong and Su Yue

*Physics, Lewis Laboratory, Lehigh University, Bethlehem, Pennsylvania 18015*

Douglas A. Kurtze

*Department of Physics, North Dakota State University, Fargo, North Dakota 58105*

### Abstract

Using the diffusing void model of granular flows, we study the dynamic response of granular materials, in particular, the relaxation of granular pile, pipe flow of granular materials, and the convection of granular media in a two dimensional box subjected to vibrations. We first study the relaxation of a one dimensional granular pile of height  $L$  in a confined geometry under repeated tapping within the context of the diffusing void model. The reduction of height as a function of the number of taps is proportional to the accumulated void density at the top layer. The relaxation process is characterized by the two dynamic exponents  $z$  and  $z'$  which describe the time dependence of the height reduction,  $\Delta h(t) \approx t^z$  and the total relaxation time,  $T(L) \approx L^{z'}$ . While the governing equation is nonlinear, we find numerically that  $z=z'=1$ , which is robust against perturbations and independent of the initial void distributions. We then show that the existence of a steady state traveling wave solution is responsible for such a linear behavior. Next, we examine the case where each void is able to maintain its overall topology as a round object that can subject itself to compression. In this regime, the governing equations for voids reduce to traffic equations and numerical solutions reveal that a cluster of voids arrives at the top periodically, which is manifested by the appearance of periodic solutions in the density at the top. In this case, the relaxation proceeds via a stick-slip process and the reduction of the height is sudden and discontinuous. We then carry out the long wave analysis to demonstrate the existence of the KdV solitons in the traffic equations. Finally, we show our preliminary studies on granular convection in a box. We observe the appearance of two rolls when the control parameter exceeds the critical value, which then undergoes bifurcations to four rolls.

### 1. Introduction

One of the difficulties in studying the dynamic response of granular assembly using the plasticity model lies in our inability to derive the precise relation between the stress and the rate of strain. For this reason, plasticity model often predicts instability which is not real. Recently attention has focused on the large scale computer simulations such as Molecular Dynamics(MD) and/or cellular automata. At the level of MD, the primary difference between fluid and granular materials seem to be the *density* and, in the author's opinion, the hard-sphere gas in the very dense limit should exhibit most of the unique features of granular dynamics. The diffusing void model(DVM) [1] was proposed to trace the stochastic movement of voids in a very dense granular medium under gravity. This model has been shown to produce most of the unique features of the *granular flow* patterns in a confined geometry in the slow limit.(For studies on granular flow, see ref.1-4) The model is based on the assumption recognized previously by Litwinyszyn, Mullins [2] and others [3] that the flow of granular particles in a confined geometry is caused by the upward motion of voids resulting from the escape of granular particles through an orifice. But the

sharp departure of our approach lies in our recognition that the cascading process at the surface and the motion of grains at or near the boundary and obstacles are intrinsically nonlinear and hence the equation of motion must be nonlinear [4]. The purpose of this work is to extend the DVM further to study the *dynamic response* of the granular assembly. We are particularly interested in understanding nonlinear dynamical behaviors displayed by the granular materials, in particular: (a) relaxation of granular pile under repeated tapping, (b) existence of density waves in granular pipe flows, and (b) granular convection when grains are subjected to vibrations. Our long term goals are: (a) development of a minimal model suitable for investigating the collective dynamics of granular assembly, (b) study of the origin and its full dynamics of these complex, non-equilibrium and collective phenomena based on minimal models, (c) search for a common paradigm underlying failure dynamics such as granular dynamics, avalanche, crack propagation in dynamics fracture, and dynamics of peeling.

## II. Granular Relaxation Under Tapping

If a vertical column of granular materials is repeatedly tapped, the grains become more ordered and the minute voids inside the pile will move upward until they meet the sea of voids (empty space), which results in the reduction of the height. Hence, in this picture, the reduction of the height,  $\Delta h(t) = h_0 - h(t)$  with  $h_0 = L$  the initial height and  $h(t)$  the height at time  $t$ , will be proportional to the accumulated void density at the top layer:

$$\Delta h(t) \approx \rho_{acc} = \int_{h_0}^{h(t)} dz \rho(z, t) \sim t^z, \quad (1)$$

where we have defined the dynamic exponent  $z$  to characterize the relaxation process. A variable of particular relevance in experiments might be the saturation time  $T$ , beyond which the height saturates and the reduction of height no longer results in by tapping. We might define the second dynamic exponent,  $z'$ , to characterize this process,

$$T(L) \sim L^{z'}, \quad (2)$$

Note that since the dynamics is initiated by tapping, the time  $t$  is expected to be linearly proportional to the number of taps. The dynamics equation of motion for the void density has been derived in [5], which reads;

$$\frac{\partial \rho}{\partial t} = -\frac{\partial}{\partial z} [V_0 \rho (1 - \rho)] + D \frac{\partial}{\partial z} \left( \rho \frac{\partial \rho}{\partial z} \right), \quad (3)$$

Since Eq. (3) is intrinsically nonlinear, in what follows we first pursue numerical solutions and then present one particular solution to the similar but a slightly different one.

## III. Numerical Solutions

Numerical results with an initially random distribution with a mean value 0.5 is displayed in Fig.1. The imposed boundary conditions are:  $\rho(L, t) = 1$  and  $\rho(0, t) = 1$ .  $\Delta h(t)$  as a function of time  $t$  is evidently linear for all five different values of  $L$ :  $L = 1000, 3000, 5000, 7000$ , and  $9000$ , yielding the dynamic exponent  $z=1$ . The slope is proportional to the initial average density in the pile,  $\langle \rho_0 \rangle$ . We have also measured the total relaxation time,  $T(L)$ , as a function of  $t$  and found that it is also linear. (Fig.1b), yielding the second dynamic exponent  $z'=1$ .

Experimentally, it has been recognized that a loosely packed horizontal plane is often hard to remove when preparing the granular systems. In order to mimic this situation in our model, we select one layer, say  $z = z_0$ , and let the density at that layer remain fixed:  $\rho(z_0, t) = \rho_0$ . If  $\rho_0 \gg 0$ , this effectively models a case where a thin layer of void source is placed at  $z = z_0$ . If  $\rho_0 \ll 1$ , then we might say a barrier is placed at  $z = z_0$ . If we let the density at  $z_0$  evolve according to the dynamic equation, then we would not expect any substantial effect of this layer to the relaxation process. (Note the distribution is random) Physically, fixing the density at a particular point means that we are placing a (weak) source or sink at  $z = z_0$ . For the case with  $\rho_0 = 0.05 \ll 1$ , the relaxation process still remains linear, but the coefficient  $\beta$  crosses over to a different value. We have measured the crossover time,  $\tau_c$ , as a function of the distance from the top layer to the barrier and found that it still exhibits the linear behavior. If we put a source term at  $z_0$  with  $\rho(z_0) > 0.5$ , there exists no crossover time and the relaxation proceeds impressively linear all the way up to the total relaxation time. One might ask whether such linear behavior persists for different initial conditions. We have considered two cases with, (i) linear distribution with and without noise, and (ii) Boltzmann distribution and we have found that the linear relaxation persists.

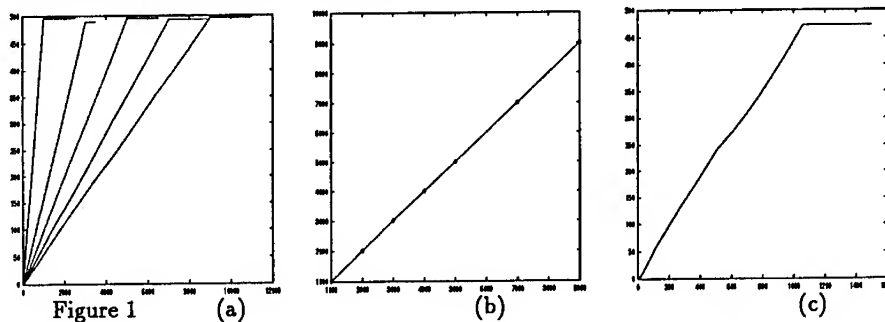


Fig. 1 (a) Reduction of the height  $\Delta h(t)$  as a function of time  $t$  with the random initial distribution. Clockwise from the left,  $L=1000, 3000, 5000, 7000$ , and  $9000$ . The relaxation is linear in  $t$ ;  $\Delta h(t) \approx \beta t^z$  with  $z=1$  and  $\beta \approx \langle \rho_0 \rangle$ . (b) Total relaxation time  $T(L)$  as a function of  $L$ . The slope is one. (c) Relaxation of a pile in the presence of a barrier of a fixed density  $\rho_{z_0}(t) = 0.05 \ll 1$ . The relaxation crosses over after all the voids above the barrier have diffused out, but the slope remains one.

We now search for the origin of the linear behavior by examining the steady state solution of eq.(3). Since the asymptotic behavior is determined mainly by the first term of (3), modifying the second term by a pure diffusion term should not change the physics. In this case, eq.(3) assumes the traveling wave solution of the form:  $\rho(x, t) = \rho(x - vt)$ :

$$\rho(x, t) = -(v - V_0)/2V_0 + Q \cdot \tanh(V_0/D \cdot Q(x - vt)), \quad (4)$$

where

$$Q = (\rho_{\infty} + \rho_{-\infty})/2; v = V_0[1 - (\rho_{-\infty} + \rho_{\infty})], \quad (5)$$

In the language of dynamical systems theory, eq.(4) is the trajectory that moves from the unstable fixed point at  $x = -\infty$  to the stable one at  $x = \infty$ . It is tempting to suggest that if we include the threshold condition to the dynamic equation (3), then there might exist



no  $v$  that satisfies the solvability condition, which might lead to a different universality class. The above result is for an infinite system. For a finite system, it can be shown that the total density inside the pile is not conserved and the interface advances.

There is one simulation where such a linear behavior has been observed in the context of the segregation of grains. The authors of ref.[6] carried out the Molecular Dynamics simulations for the segregation of two different sizes of grains under shaking and they have reported that the upward displacement of the larger one is linear in time. It remains to be seen whether real experiments would reveal such a linear behavior.

For future studies, we want to point out the missing pieces in our study of granular relaxation. First, we have assumed that the upward velocity  $V_z$  is proportional to  $1 - \rho h(z + \Delta z)$  with  $\Delta z$  constant. But it is in fact a dynamical variable. Hence, we should write a separate equation for  $\Delta z$ . Second, we have not taken into account the threshold condition. When the grain density is small, grains are locked, while it has to expand before making a move. One might need to introduce a hopping mechanism for a void from site to site with position and density dependent deep potential barriers. Finally, in our studies, we have assumed that the strength of the shaking is in such a way that it may destroy the local equilibrium to initiate the dynamic motion, but it may not be large enough to destroy the whole system. Specific assumption was that grains relax sufficiently fast between the successive tappings. Relaxation under arbitrary strength with arbitrary time steps will require substantial modification of the present model. We will report the effects of such modifications in our future studies.

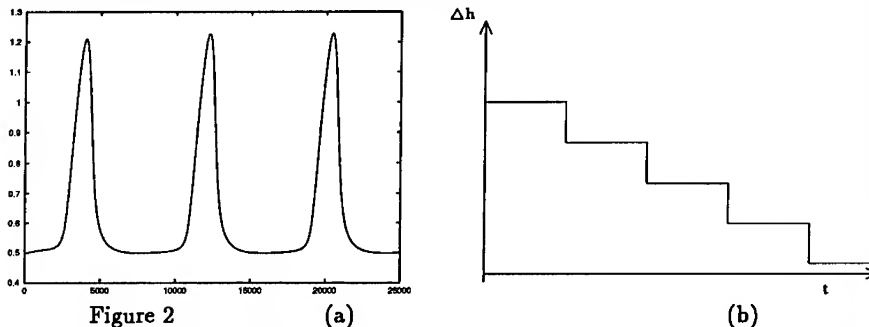


Fig. 2. (a) The density at the top obtained from the traffic equation (6) with a source and a sink. Note the appearance of the periodic solution. (b) Schematic picture of the stick-slip relaxation. Enough voids, accumulated near the top, form a shock or a pulse which collectively breaks the energy barrier and results in a sudden reduction in the height

#### IV. Stick-Slip Relaxation and Its Relation to the Traffic Problem

Suppose now the grains are very rough. Then the void size distribution produced by such rough grains presumably remains fairly uniform and each void is expected to be a robust object. In such cases, it would be more appropriate to write down the *time dependent* equation by taking into account fluctuations in the speed of the void;

$$\frac{\partial V_z}{\partial t} + V_z \frac{\partial V_z}{\partial z} = \gamma [V(\rho) - V_z] - \frac{c_0^2}{\rho} \frac{\partial \rho}{\partial z}. \quad (6)$$

where  $V(\rho) = \frac{\alpha}{1+\beta\rho^2}$  with  $\alpha$  and  $\beta$  being constants. Note that with the identification of  $\rho$

and  $V_x$  as the density and the speed of cars in a highway, respectively, Eq. (6) along with the continuity equation are precisely those used in the traffic problem [7].

Figure 2 displays the numerically obtained density at the top as a function of time, for  $\alpha = 1.2$ ,  $\beta = 4.2$ , and the source density  $\epsilon = 0.6$ , for which case the solution becomes unstable. Note the appearance of the periodic solution, which is a clear indication that clusters of voids in the form of shocks or pulses arrive at the top periodically. Hence, in the regime where the traffic equation makes more sense than the diffusing void equation, we anticipate that the reduction of the height of granular pile will be sudden and discontinuous, which we term the stick-slip relaxation. Slow relaxation observed in [8] requires more studies.

## V. Traffic jams, granular flow, and soliton selection

In this section, we demonstrate the existence of soliton modes in the traffic equation. The need for a rigorous nonlinear analysis of the traffic equations was in part motivated by the observation made in the previous section that beyond the onset of instability, the arrival of voids at the top is not continuous, but a localized cluster of voids arrives periodically, causing the height to decrease discontinuously. In addition, in a recent studies of traffic equations, it was found that homogeneous traffic flow can be unstable [9,10], with localized regions of high density and low average velocity spontaneously appearing. These pulses preserve their shape and move with constant speed; they correspond to the "phantom" traffic jams which appear on highways for no apparent reason.

We note that traffic equations essentially describe the flow of conserved but fluctuating physical quantities, such as cars on a highway or voids in a granular medium. They might equally well describe the migration of people, animals, or electronic messages. Hence, the appearance of localized pulses in an initially homogeneous flow is an interesting discovery which requires further investigation.

Details of our calculations can be found in ref.[12]. The long wave analysis has revealed that the density perturbation in the traffic equations satisfies the dynamical equation:

$$\frac{\partial \hat{\rho}}{\partial T} - \mu\tau|V'| \frac{\partial^3 \hat{\rho}}{\partial X^3} + [2V' + \rho_h V''] \hat{\rho} \frac{\partial \hat{\rho}}{\partial X} = -\epsilon R[\rho] \quad (7)$$

where  $X = \epsilon x$ ,  $T = \epsilon t$ , and all derivatives are evaluated at  $\rho_c$ . Note that in obtaining eq.(xx) we have implemented the scalings by writing

$$\rho(x, t) = \rho_h + \epsilon^2 \hat{\rho}(\epsilon x, \epsilon^3 t), v(x, t) = v_h + \epsilon^2 \hat{v}(\epsilon x, \epsilon^3 t) \quad (8)$$

where  $\epsilon$  is a small parameter measuring the distance from the onset of instability. The leading order in eq.(7) is the Korteweg-deVries equation, which is a classic integrable nonlinear evolution equation which is known to lead to solitons [13].

The one-soliton solution of the leading order of (7) is

$$\hat{\rho} = S(X, T; k) \equiv A \operatorname{sech}^2 k(X + uT), \quad (9)$$

where  $k$  is a free parameter and

$$u = 4\mu\tau|V'|k^2, \quad A = -\frac{12\mu\tau|V'|}{2V' + \rho_h V''} k^2. \quad (10)$$

If the denominator in the expression for  $A$  is negative, then the soliton represents a local increase in traffic density, with a concomitant decrease in speed – a traffic jam. On the other hand, if it is positive then it represents a local rarefaction of traffic density and increase of speed. The function  $c(\rho)$  is plotted in Fig. 1 of ref.[12]; for the parameter values used there, traffic jams appear near  $\rho_{c1}$  and rarefactions near  $\rho_{c2}$ .

To account for the effect of the order- $\epsilon$  correction on the right hand side of (7), we must allow for the possibility that it could cause a slow change in the parameter  $k$  of the unperturbed soliton. Thus we write

$$\hat{\rho} = S(X, T; k(T_1)) + \epsilon \hat{\rho}_3, \quad (11)$$

where  $T_1 \equiv \epsilon T$  is a slow time variable. Substituting this into (7) then leads to

$$\frac{\partial S}{\partial k} \frac{dk}{dT_1} + \left[ \frac{\partial}{\partial T} - \mu \tau |V'| \frac{\partial^3}{\partial X^3} + (2V' + \rho_h V'') \frac{\partial}{\partial X} \right] \hat{\rho}_3 = \text{RHS}, \quad (12)$$

where "RHS" stands for the right hand side of (7) without the factor  $\epsilon$  and with  $\hat{\rho}$  replaced by  $S$ . Multiplying (12) by  $S$ , integrating over all  $X$ , and averaging over  $T$  annihilates the term involving  $\hat{\rho}_3$  [14], and so leaves us with an evolution equation for  $k$ :

$$\frac{dk}{dT_1} = \frac{8\tau\rho_h}{15} \alpha k^3 - \frac{64}{105} \mu \tau^2 \rho_h |V'| \frac{4|V'|^2 + 7\rho_h |V'|V'' + 6c_0^2 L''}{2|V'| - \rho_h V''} k^5. \quad (13)$$

From this we see that when the coefficient of  $k^5$  is negative and  $\alpha$  is negative,  $k$  decreases to zero (so that the soliton amplitude vanishes), while for positive  $\alpha$ ,  $k$  tends to the nontrivial zero of the right side of (13). We then find that the velocity of the selected soliton is

$$\frac{7}{2} \frac{2|V'| - \rho_h V''}{4|V'|^2 + 7|V'|V'' + 6c_0^2 L''} \alpha, \quad (14)$$

and the amplitude of the density perturbation is

$$\frac{21}{2} \frac{\alpha}{4|V'|^2 + 7|V'|V'' + 6c_0^2 L''}. \quad (15)$$

The amplitude of the perturbation of the vehicle velocity, according to (7), is this multiplied by  $-|V'|$ . It is noteworthy that these results are independent of the "diffusion coefficient"  $\mu$ , although the width  $k$  of the selected soliton does depend on it (being proportional to  $\mu^{-1/2}$ ).

It is also possible for the coefficient of  $k^5$  in (12) to be positive. In this case there is a *subcritical* instability: for negative  $\alpha$ ,  $k$  decreases to zero if it initially is less than the zero of the right side of (13), otherwise it grows. The final form of the traffic jam would be something larger than assumed in the scalings (8) used to derive (10). This is the case for the parameters used by Kerner and Konhäuser; in their work, subcritical instabilities were observed at both  $\rho_{c1}$  and  $\rho_{c2}$ , leading to traffic jams in the former case and rarefactions in the latter.

We emphasize the role played by the correction term on the right hand side of (7). This destroys the integrability of the evolution equation for the traffic density. Without

this correction, a continuous range of soliton solutions would exist, and solitons which collided would pass through each other and maintain their separate identities. With it, a unique soliton solution is selected, and multiple solitons could merge. This last point is a subject of ongoing research. We have also found that applying a similar perturbation analysis to the periodic, cnoidal solutions of the KdV equation leads to selection of the amplitude of the solution, but not of the wavelength; thus periodic arrays of traffic jams could arise with any period.

We now briefly discuss the physical relevance of the existence of this soliton mode in the context of granular dynamics. In an effectively one dimensional granular assembly, the propagation of disturbance in the form of solitons might be associated with the sudden appearance of local ordering, perhaps hexagonal, which generates a massive voids. Such massive voids then move collectively until they disappear at the top layer to the air. The appearance of density waves [15,16] and clogging [17] in a pipe flow of granular materials might be a strong indication of such soliton modes in granular dynamics. Such soliton modes perhaps might be of relevance in understanding of unusual sound propagation through granular media [18].

## VI. Granular Convection in a Two Dimensional Box Subjected to Vibrations

In this section, we present our preliminary results for the granular convection in a two dimensional box that is subjected to vibrations. The equations of motion are as follows:

$$\partial_t \rho + \partial_x(\rho v_x) + \partial_y(\rho v_y) = 0 \quad (16)$$

$$\partial_t v_x + v_x \partial_x v_x + v_y \partial_y v_x = -\partial_x \rho / \rho + \mu(\partial_x^2 v_x + \partial_y^2 v_x) \quad (17)$$

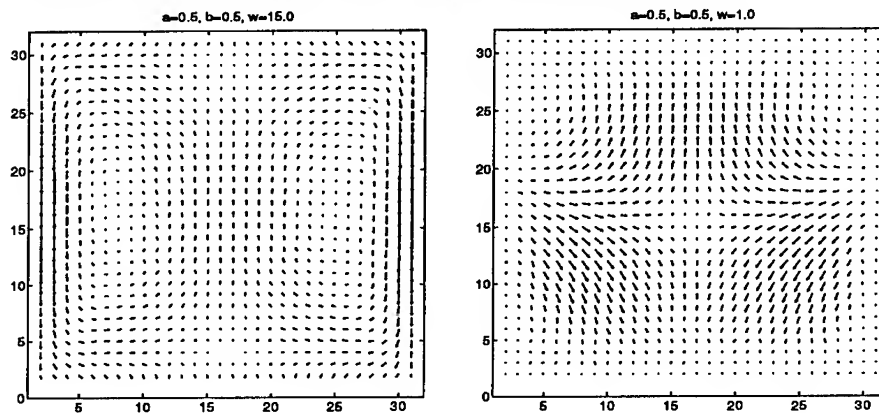
$$\partial_t v_y + v_x \partial_x v_y + v_y \partial_y v_y = V(\rho, t) - v_y - \partial_y \rho / \rho + \mu(\partial_x^2 v_y + \partial_y^2 v_y) \quad (18)$$

where  $V(\rho, t)$  is given by

$$V(\rho, t) = V_0(\rho)(1 - \Gamma \sin(\omega t)) \quad (19)$$

where  $V_0(\rho)$  is the same as in eq.(6) the control parameter  $\Gamma = A\omega^2/g$ . Eq.(19) effectively models the vibrations. The boundary conditions imposed at the wall is the non-slip boundary conditions, i.e,  $v_\perp = 0$  and the tangential component of the velocity  $v_\parallel = 0$ . We have applied different boundary conditions, but the main features obtained in this paper do not change. Numerical results are shown in Fig.(3) for different parameters. We are currently carrying out the linear stability analysis to sort out the mechanism for the instability and various bifurcations phenomena, which will be reported in future work.

Fig.3 Convection patterns obtained by eqs.(17)-(19). (a) Convection with two rolls. (b) Convection with four rolls. For both cases, the control parameter  $\Gamma > 1$ .



## References

- [1] H.S. Caram and D.C. Hong, Phys. Rev. Lett. **67**, 828 (1991); Mod. Phys. Lett. B **6**, 11 (1992).
- [2] J. Litwinyshyn, Bull. Acad. Polon. Sci. Ser. Sci. Tech. **11**, 593 (1962); W.W. Mullins, J. Appl. Phys. **43**, 867 (1974).
- [3] R. Neddermann, T. Davier, and D. Horton, Powder Tech. **25**, 215 (1980); R. Neddermann, U. Tuzun, and G.T. Houlsby, Chem. Eng. Sci. **37**, 1597 (1982).
- [4] M.Y. Choi, D.C. Hong, and Y.W. Kim, Phys. Rev. E **47**, 137 (1993); J.K. Rudra and D.C. Hong, Phys. Rev. E **47**, R1459 (1993).
- [5] D. Hong, S. Yue, J. Rudra, M. Choi and Y. Kim, "Granular relaxation under tapping and the traffic problem" (preprint).
- [6] R. Jullien, P. Meakin, and A. Pavlovitch, Phys. Rev. Lett. **69**, 640 (1993).
- [7] R. D. Kühne, in *Highway Capacity and Level of Service*, edited by U. Brannolte (Balkema, Rotterdam, 1991) p.211.
- [8] H. Jaeger, J. Knight, C. Liu, and S. Nagel, "What is shaking in the sandbox?", MRS Bulletin, Vol. XIX, No. 5, 25 (1994).
- [9] W. Leutzbach, *Introduction to the Theory of Traffic Flow* (Springer, Berlin, 1988) and references therein.
- [10] R. Kühne, in *Highway Capacity and Level of Service*, edited by U. Brannolte (Balkema, Rotterdam, 1991), p. 211.
- [11] B.S. Kerner and P. Konhäuser, Phys. Rev. E **48**, R2335 (1993); Phys. Rev. E **50**, 54 (1994).
- [12] D. A. Kurtze and D. C. Hong, "Traffic jams, granular flow and soliton selection, preprint (1994).
- [13] See, e.g., P. Drazin, *Solitons* (Cambridge, New York, 1985).
- [14] E. Ott and R.N. Sudan, Phys. Fluids **12**, 2388 (1969).
- [15] J. Lee and M. Leibig, J. Phys. I France, **4**, 507 (1994).
- [16] E. Ehrichs, H. M. Jaeger, G. Karczmar, J. Knight, V. Kuperman, and S. Nagel, "Granular convection observed by magnetic resonance imaging," (Preprint).
- [17] T. Poschel, J. Phys. I France, **4**, 499 (1994).
- [18] C. Liu and S. Nagel, Phys. Rev. Lett., **68**, 2301 (1992).

## DIRECT OBSERVATION OF SIZE SEGREGATION : CONVECTION AND ARCHING EFFECT

J.DURAN, T.MAZOZI, E.CLEMENT AND J.RAJCHENBACH

Laboratoire d'Acoustique et d'Optique de la Matière Condensée, Université Pierre et Marie Curie, 4 place Jussieu, 75252 PARIS, FRANCE.

### ABSTRACT

We report an experimental study of the ascent of a large disc imbedded in a 2D packing of small beads vertically vibrated. Two distinct mechanisms leading to size segregation are observed *in situ*. At high acceleration, the convection process associated with surface trapping is predominates. At low acceleration, we examine the effect of the size ratio on the dynamics of the segregation which is either intermittent or continuous. This is due to the successive formation and destruction of arches.

### INTRODUCTION

Vibrational size segregation, often referred to as the "Brazil nut problem" has been recently the focus of several computer simulations as well as experimental observations [1-4] displaying apparently conflicting results. Briefly stated, the existence of a size threshold for size segregation, as well as the up motion velocity dependence on the size ratio ( $\Phi = R/r$ ,  $R$  and  $r$  being respectively the radius of the intruder and of the particles in the granulate) seemed to be in conflict with existing experiments reported in literature or simulations.

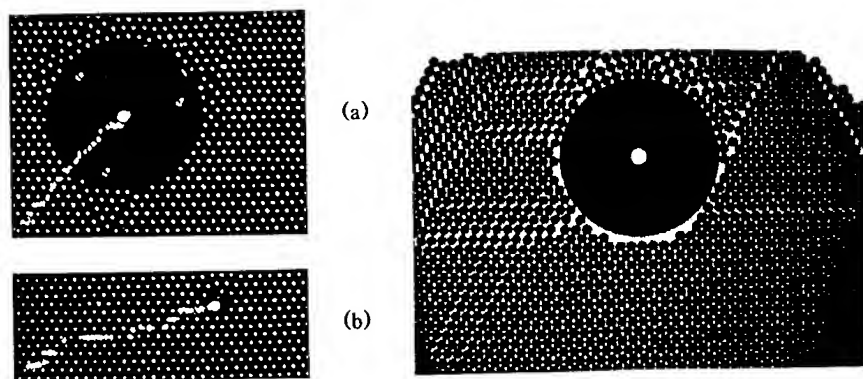


Fig 1 (right) Experimental observation of the continuous upward motion, under vibrations, of a large disc (a :  $\Phi=16$ ) and of the intermittent ascent of a small disc (b :  $\Phi=2$ ) in a vibrated set of monodisperse aluminum beads. In (a) the acceleration is 10% above threshold while it is 20% above threshold in (b). The horizontal time scale is about one hour for both (a) and (b). Fig 1 (left) displays a stroboscopic view of the behavior of the vibrated cocktail. We identified the small reversible and short duration cracks as the motor of the fluctuations of the relative positions of the intruder and the environment, responsible for the vertical ascent via arching effects [5].

We have shown elsewhere [5] that under low amplitude of excitation which means slightly above the gravitational acceleration, there exists a size threshold  $\Phi_c$  (12.9 in 2D and 2.8 in 3D) which determines the mode of ascent of the intruding disc in an assembly of smaller spheres. In short, small discs such as  $\Phi < \Phi_c$  will (and do) climb up intermittently, their motion being discretized by the granularity of the particulate, whereas larger intruders ( $\Phi > \Phi_c$ ) can move up continuously via permanent arching effects. (Fig. 1)

#### SIZE SEGREGATION VIA CONVECTION OR(AND) ARCHING EFFECT ?

Along the same line and keeping within the limit of this paper we report here the experimental observation that vibrational segregation can occur via *two distinct processes (namely convection and arching effects)* depending on the excitation amplitude of the container.

In the spirit of our previous experiments in the field of model granular materials, we restricted our experiments to 2D geometry which allows via image processing (CPP i.e. computer posed photograph) a direct observation of the relative motion of solid particles in a granulate and, in particular, to follow the up-motion of an intruding particle which can be chosen of a different size. Fig.2a shows a typical 2D container built for observing the two distinct regimes leading to size segregation. The cell is made of two rectangular glass plates (10x15 cm<sup>2</sup>) separated by rectangular plastic wedges, the width of which is adapted to accommodate, as accurately and freely as possible, the monodisperse set of 1.5 mm-diameter aluminum beads. The beads we use are oxidized aluminum beads (no segregation nor convection was ever observed for a set of polished aluminum beads) which have high solid friction coefficient and high momentum loss on collision. The experiments have been made using an excitation frequency of 15 Hz. Again, the excitation amplitude is indicated via the reduced acceleration parameter  $\Gamma$  (real acceleration divided by  $g$  the gravitational acceleration). At the beginning of the experiment, the intruding aluminum disc (1mm thick, radius  $R$ ) is inserted among the assembly of small beads (spheres with a diameter  $2r = 1.5\text{mm}$ ) at 1.5 cm above the bottom of the container.

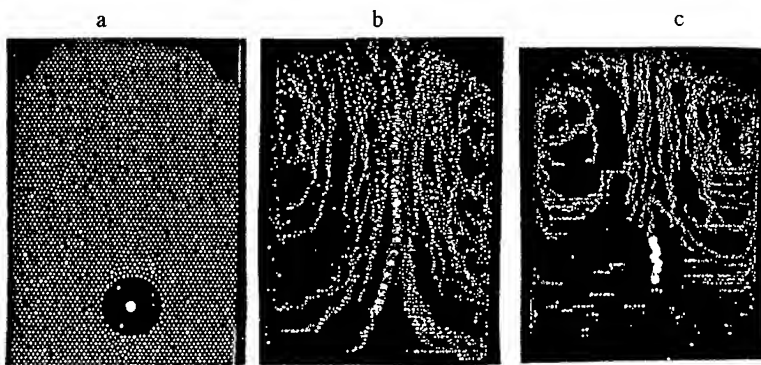


Fig.2 a) Single snapshot of the 2D container filled with aluminum beads, shiny markers and intruding disc at the beginning of the segregation experiment.

b) High amplitude excitation: (CPP). The convection driven ascent of the intruder is indicated by the large white trail in the middle of the two convective rolls. Here  $\Phi = 5.3$ ,  $\Gamma = 2$  at 15Hz.

c) Low amplitude excitation : (CPP during 10mn) The arching effect driven ascent of the intruder is clearly observed through the horizontal white trails left by the markers below the large disc. Here  $\Phi = 12.9$ ,  $\Gamma = 1.25$  at 15Hz.

The pile is prepared to match as much as possible a triangular lattice (except around the intruder which induces local perturbations in the array). In order to provide a quasi 2D free motion of the intruder between the two frontal windows of the cell, three equidistant steel 1.5 mm diameter beads are pinned in the outer ring of the circular disc. The intruder is painted in black with a white dot decorating its center.

Here we limit our description to the direct visualization of the trajectories of the small beads and of the larger disc. Note that a recent extension of the present work is devoted to the experimental analysis of the dynamic of the ascent of the intruder among the particulate [5]. Prior to vibration, we dispersed test beads among the assembly of corrugated aluminum beads. These test beads are about 1% in number, they are made of steel with the same diameter 1.5mm, and look more shiny compared to the aluminum ones. The stroboscopic flashing light is locked on the vibration such that positions are recorded for the same height of the container. Using an image processing device, we selectively record the test beads and the intruder positions. As in the preceding section, accumulation of such pictures bring up computer posed photographs (CPP) as reported in Fig.2b and 2c where we observe that exciting the cell at an acceleration larger than the gravitational acceleration induces internal motions in the pile. We recall that in the absence of intruder, the convection rolls spring up at the upper lateral corners of the granulate and when the excitation acceleration  $\Gamma$  is increased they expand in size towards the center of the cell [6]. Compared to our earlier observations, the introduction of a larger disc among an assembly of monodisperse beads produces several new and different characteristic features. We observe that, depending on the excitation amplitude, two different regimes are clearly distinguished:

i) At relatively large accelerations, i.e. when  $\Gamma \geq 1.5$ , and in agreement with recently reported experiments [7], we observe a global convective motions of all the particles in the cell. The CPP of such an experiment at  $\Phi = 9$ , is displayed on Fig 2b. Note that the trajectories of the small beads evidence convection rolls taking place *below* the intruding disc and carrying the bigger particle *at the same speed which is independent of the diameter ratio  $\Phi$* . In agreement with [7], we observed that the probability of being convected downwards at one of the lateral walls, when the surface is reached, strongly depends on the diameter ratio.

ii) Fig.2c is the CPP of an experiment performed at a lower acceleration  $\Gamma = 1.25$  and for a diameter ratio  $\Phi = 13$ . Without intruder, the convection rolls would be confined in the upper left and right corners of the cell. Here, two important features should be noticed. First, the extension of the convection rolls is much larger than without intruder. The roll localization starts just *above* the intruder and the roll size is progressively reduced when the bigger particle rises. A second characteristic feature is that the upward ascent of the intruder is accompanied by several *horizontal* block re-arrangements which are directly visualized via the horizontal tracks of the markers. Remark that in Fig.2c, the intruder is not carried upward in a convective motion of the surrounding particles, *since no upwards trail is present in the underlying environment*. This experiment was repeated at successive stages of the intruder ascent. It shows that once the intruder has left a lower region, no internal motion is any more evidenced. Moreover, and this feature definitely separates from the above mentioned convection motor, the ascent velocity strongly depends on the diameter ratio  $\Phi$  [8]. Thus, it is clear that segregation *can occur without a convection motor* and that an intruding particle creates in its surrounding, its own field of internal motion.



## REFERENCES

1. G.C.Barker, A.H.Mehta and M.J.Grimson, Phys.Rev.Lett. **70**, 2194, 1993.
2. R.Jullien, P.Meakin and A.Pavlovitch, Phys.Rev.Lett. **70**, 2195, 1993.
3. K.Ahmad and J.J.Smalley Powder Tech., **8**, 69, 1973.
4. A.Rosato, F.Prinz, K.J.Standburg and R.H.Swendsen, Powder Technol **49**,59,1986; Phys.Rev.Lett. **58**, 1038, 1987.
5. J.Duran, J.Rajchenbach and E.Clement, Phys.Rev.Lett. **70**, 2431, 1993
6. E.Clement, J.Duran and J.Rajchenbach, Phys.Rev.Lett. **69**, 1189, 1992, 1970.
- 7 J.B.Knight, H.M.Jaeger, Phys.Rev.Lett. **70**, 3728, 1993.
- 8 J.Duran, T.Mazoz, E.Clement and J.Rajchenbach, Phys.Rev.E,**50**,1994.(in press)

## INTERACTION LAWS AND THE DETACHMENT EFFECT IN GRANULAR MEDIA

S. LUDING<sup>\*/\*\*</sup>, E. CLÉMENT<sup>\*\*</sup>, A. BLUMEN<sup>\*</sup>, J. RAJCHENBACH<sup>\*\*</sup>, AND J. DURAN<sup>\*\*</sup>

<sup>\*</sup>Theoretische Polymerphysik, Universität Freiburg, Rheinstraße 12, D-79104 FREIBURG, GERMANY.

<sup>\*\*</sup>Laboratoire d'Acoustique et d'Optique de la Matière Condensée, Université Pierre et Marie Curie 4, place Jussieu, 75005 PARIS, FRANCE.

### Abstract

We study granular materials using both event driven (ED) and molecular dynamics (MD) methods. In the MD simulations we implement linear as well as nonlinear forces and also hysteretic interactions. For multiple collisions the two methods show differences: MD calculations lead to weak, whereas ED methods result in rather strong dissipation, as determined through an effective restitution coefficient.

### Introduction and Background

Recent years have seen much effort in understanding granulates, which are assemblies of solid, possibly nonuniform, particles, interacting via contact forces. Summaries of the present knowledge on granular media are given in Refs.[1-2]. These materials display size-segregation, heap formation under vibration and bulk dilatation, as well as density wave formation and 'decompaction' [3]; their fluid-like properties include convection rolls, surface fluidization, and surface waves.

Probing the dynamics of granular particles on scales comparable to their dimensions is difficult. Advances have been made by investigating model systems, such as assemblies of relatively large spheres. Here the binary interactions are quite well understood, both experimentally [4] and theoretically [4,5]; however, multiparticle interactions have been often neglected. Using binary interactions, numerical simulations [6] allow to study the dynamics of many particle systems and by this complement the experimental findings and the analytical approaches [7]; numerically one uses molecular dynamics (MD) [8-10] as well as event-driven (ED) algorithms [11-13].

The MD techniques often involve ad-hoc microscopic assumptions, such as linear [9] or non-linear [10] interactions between the spheres. Evidently the specific contact laws which depict the microscopic situation are fundamental [14,15]; here a major advance are the recently proposed hysteretic interaction laws [14] which lead directly to dissipation. Event-driven (ED) procedures are another means to simulate granulates see e.g. Lubachevsky [11]. Using ED simulations the "cooling" of one-dimensional (1D) granular media was investigated [12] and the ED method was extended to handle the occurrence of connected clusters in 1D [13]. Moreover arrays of spheres under vibration were described using both MD and ED methods [12,13,15,16].

We have shown that MD calculations may display anomalously low energy losses [15], due to the interactions used; the effect may subsist even in the limit of very 'hard' interactions. Then the spheres may separate completely, so that we called the effect "detachment" [15]. Detachment is different from the decompaction evidenced in 2D dissipative granular systems [3]: Decompaction is due to the friction with the walls, whereas detachment follows from the

elastic forces assumed. In fact detachment disappears in ED simulations.

In this note we report MD simulations using different interactions (linear, non-linear and hysteretic) and compare the results with corresponding ED simulations. The basic difference between ED and MD methods is the contact time  $t_c$ . In ED the time  $t_c$  in which colliding particles are in contact is ideally zero. This is quite different from MD, for which  $t_c$  does not vanish and in fact turns out to be quite significant.

## Simulations

We follow the 1D dynamics of a column of  $N$  spheres; these are numbered from below starting with  $i = 1$ . For the immobile bottom plate we set  $i = 0$ . Due to the 1D aspect, the order of the spheres never changes and we can even dispense with accounting for their diameter  $d$ . This fact permits to use diameter-independent coordinates  $z_i(t)$ ; these are related to the diameter dependent coordinates  $h_i(t)$  through  $z_i(t) = h_i(t) - (i-1)d - d/2$ .

We start with a short description of the ED procedures, which follow a sequence of events. Between events Newton's equation of motion for each object is solved analytically. An object is a sphere or the bottom plate; an event is defined for a sphere by a sudden change in momentum, i.e. a collision. Each object  $i$  follows its own undisturbed trajectory between events, because dissipation occurs only upon collisions. The times between collisions are determined through a sequential procedure, see Refs.[12,13]. We note that ED simulations take care of the energy loss in collisions through restitution coefficients  $\epsilon$ ; furthermore, this is the only way energy losses are accounted for. In the center of mass reference frame of two identical colliding particles, the incoming velocities are  $+V$  and  $-V$  and the outgoing velocities are  $-\epsilon V$  and  $+\epsilon V$ . A similar form also holds for collisions with the bottom plate, which is assumed to have infinite mass. Sphere 1 in the reference frame of the plate has a velocity  $V$  just before the collision and the velocity  $-\epsilon_p V$  after the collision. A detailed description of the procedure may be found in Refs.[12,13].

Distinct from ED simulations, where one defines a collision matrix in the system's frame of reference, MD calculations are based on elastic and dissipative forces. In our MD procedure we use a fifth order predictor-corrector algorithm [6] for the integration of the equations of motion.

In MD two particles (or a particle and a wall) interact when their relative distance  $r_{ij}$  is smaller than the sum of their radii (the radius of the particle). Here  $r_{ij} = |\mathbf{r}_{ij}|$  and  $\mathbf{r}_{ij}$  points from the center of  $i$  to the center of  $j$ . In a 1D model only forces in the normal direction,  $\mathbf{n}_{ij} = \mathbf{r}_{ij}/r_{ij}$  matter. Thus two forces are active in the regime  $d > r_{ij}$ ; first, an elastic restoration force:

$$f_{el}^{(i)} = -Kx^{1+\beta} \quad (1)$$

where  $K$  is the spring constant and  $x$  is the (positive) penetration depth  $x = d - r_{ij}$ . Second, a frictional force in the normal direction:

$$f_n^{(i)} = -D_n m_n [\mathbf{v}_{ij} \cdot \mathbf{n}_{ij}] x^\gamma \quad (2)$$

where  $\mathbf{v}_{ij}$  is the relative velocity of particles  $i$  and  $j$ ,  $D_n$  is the normal dissipation parameter and the normalized mass is  $m_n = 2m_{red} = 2m_i m_j / (m_i + m_j)$ . The parameters  $\beta$  and  $\gamma$  fix the non-

linearity of the forces; thus  $\beta = \gamma = 0$  leads to a linear spring-dashpot (LSD) interaction. From Eqs.(1) and (2) and for LSD the contact time  $t_c = \pi/\sqrt{K/m_{\text{red}} - D_n^2}$  and the restitution coefficient  $\epsilon = \exp(-D_n t_c)$  follow, see Ref.[15]. Note that for LSD interactions  $t_c$  and  $\epsilon$  are velocity independent.

Non-linear forces offer a more general way to mimic collisions. Thus Hertz' model for the interaction of two spheres [5] corresponds to  $\beta = 1/2$ . For non-linear forces the contact time and the restitution coefficient become velocity dependent, see Ref.[15] for details.

An alternative way to introduce dissipation is to use different forces for loading and unloading [14]. In detail, we use a spring constant  $K_1$  for loading and a larger spring constant  $K_2$  for unloading:

$$f_{\text{el}}^{(i)} = \begin{cases} -K_1 x & \text{for loading} \\ -K_2 (x - x_0) & \text{for unloading} \end{cases} \quad (3)$$

This behavior models energy loss due to plastic deformation, with the penetration depth  $x$  and a finite penetration  $x_0 = (1-\epsilon^2)x_{\text{max}}$  at which the contact force vanishes during unloading.  $\epsilon = \sqrt{K_1/K_2}$  is the momentum restitution coefficient and  $x_0$  is defined through the continuity of the forces at maximum penetration, i.e.  $K_1 x_{\text{max}} = K_2 (x_{\text{max}} - x_0)$ . In Fig.1 we give a schematic plot of the elastic force during the contact of two spheres. During loading the force increases linearly with slope  $K_1$  as a function of  $x$  until  $x_{\text{max}}$  is reached. Unloading follows the larger slope, i.e.  $K_2$ , until the force equals zero at a finite penetration  $x_0$ . We define the contact time  $t_c$  to be the time when the force vanishes, i.e. the time at which again  $x = x_0$ . When no additional force is active, the penetration decreases and the spheres separate after a time  $x_0/v(t_c)$ , where  $v(t_c)$  is the velocity at time  $t_c$ . If for example another sphere hits one of the two original spheres, reloading for  $0 < x' < x_0$  may take place with a force  $K_2(x-x')$  until the original loading curve is reached; further reloading follows then the original loading curve. However, this is not the only way to model plastic deformation, see Ref. [14] for extensive details. For the simple hysteretic force, Eq.(3),  $t_c$  and  $\epsilon$  can be computed [14]; in implicit form one has  $K_1 = m_{\text{red}} \pi^2 (1+\epsilon)^2 / (4t_c^2)$  and  $K_2 = K_1/\epsilon^2$ .

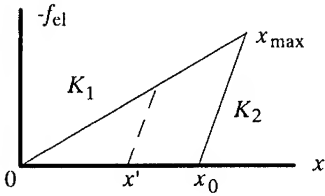


Fig.1:  
The elastic force, Eq.(3), plotted as a function of the penetration  $x$ . On contact two spheres load from 0 to  $x_{\text{max}}$  and then unload to  $x_0$ . Reloading may take place from  $x'$  to the original loading curve.

## Multiparticle collisions

We are now interested in the behavior of a column of spheres in 1D. We neglect gravitational effects and analyze the collision of the column with a static boundary. This situation is interesting, since it allows us to compare the MD results, obtained using different interactions, with those obtained by ED methods [12,13].

We introduce the effective restitution coefficient for many particle collisions through  $\epsilon_{\text{eff}} = \sqrt{E_f/E_0}$ , where  $E_0$  and  $E_f$  denote the kinetic energies of the particles relative to the

bottom plate before and after the collision, respectively, i.e.  $E = \frac{m}{2} \sum_{i=1}^N v_i^2$ .

In Fig.2 we display  $\epsilon_{\text{eff}}$  obtained from MD and ED simulations. The results depend on the initial separation  $s_0$  between the spheres, the initial velocity  $v_0$  and the contact time  $t_c$ . We rescale the axes so that the ratio of the mean time between events  $s_0/v_0$  to the contact time  $t_c$  shows up, i.e. we plot  $\epsilon_{\text{eff}}$  vs.  $\sigma = s_0/(v_0 t_c)$ . In Fig.2 we have  $N = 10$ ,  $\epsilon = 0.9$ ,  $t_c = 8.4 \times 10^{-6}$  s, and as the initial velocity  $v_0 = 0.5$  m/s; furthermore,  $s_0$  varies between  $10^{-9}$  and  $3.2 \times 10^{-3}$  m. In Fig.2 we find that the results of the linear spring-dashpot interaction (LSD) and of the hysteretic interaction model (HYS) agree qualitatively. Two features are prominent: first, when  $\sigma \ll 1$  the energy loss is small, i.e.  $\epsilon < \epsilon_{\text{eff}} \approx 1$  for LSD and  $\epsilon_{\text{eff}} \approx \epsilon$  for HYS. This fact leads to large interparticle distances after the collision with the bottom plate, a phenomenon which we call detachment. Second, for  $\sigma \gg 1$  the  $\epsilon$  values are lower and the energy loss turns out to be independent of  $\sigma$  [right side of Fig.2]. We note that the ED procedure [the dashed line in Fig.2] leads to  $\epsilon_{\text{eff}} \approx 0.341 \pm 0.002$ , a result practically independent of  $s_0$  and  $v_0$ . While for  $\sigma \gg 1$ , the ED and MD results agree with each other, there are large differences for  $\sigma \ll 1$ .

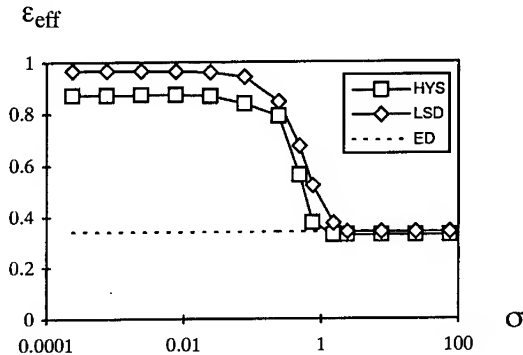


Fig.2: Linear-logarithmic plot of the effective restitution coefficient  $\epsilon_{\text{eff}}$  as a function of  $\sigma = s_0/v_0 t_c$  for different interaction models, see text for details. The calculations involve  $N = 10$  particles with  $\epsilon = 0.9$ , colliding with a fixed boundary.

Now we study the dependence of  $\epsilon_{\text{eff}}$  on the number of particles which hit the wall. In Fig.3 we plot  $\epsilon_{\text{eff}}$  as a function of  $N$  for  $s_0 = 0$ ,  $v_0 = 0.5 \text{ ms}^{-1}$ ,  $d = 1 \text{ mm}$  and for different interaction laws.

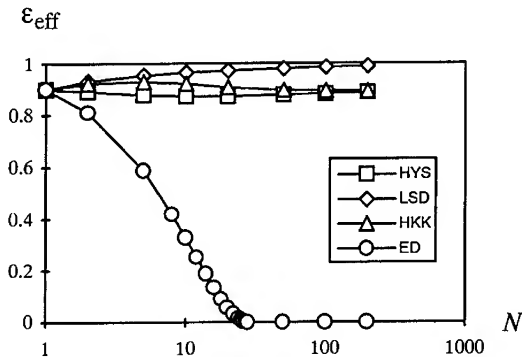


Fig.3: The effective restitution coefficient  $\epsilon_{\text{eff}}$ , plotted as a function of  $N$  for  $s_0 = 0$  and  $v_0 = 0.5 \text{ m/s}$ . We use the Hooke interaction ( $\beta = \gamma = 0$ , LSD), the Hertz-Kuwabara-Kono interaction ( $\beta = \gamma = 1/2$ , HKK), the hysteretic interaction Eq.(3) (HYS) and the ED method, see text for details.

Using the linear interaction law with  $\beta = \gamma = 0$ ,  $K/m_{\text{red}} = 8 \times 10^{10} \text{ s}^{-2}$ , and  $D_n = 9.48 \times 10^3 \text{ s}^{-1}$  we find that  $\epsilon_{\text{eff}}$  increases with  $N$ . Using the Hertz-Kuwabara-Kono (HKK) interaction, i.e.  $\beta = \gamma = 1/2$ , with  $K/m_{\text{red}} = 2 \times 10^{12} \text{ s}^{-2} \text{ m}^{-1/2}$ , and  $D_n = 3.5 \times 10^4 \text{ s}^{-1} \text{ m}^{-1/2}$  we find that  $\epsilon_{\text{eff}}$  varies little as a function of  $N$ . A hysteretic interaction with  $K_1/m_{\text{red}} = 1.78 \times 10^{11} \text{ s}^{-2}$ , and  $K_2/m_{\text{red}} = 2.2 \times 10^{11} \text{ s}^{-2}$ , agrees rather well with  $\epsilon_{\text{eff}}$  found using the HKK ( $\beta = \gamma = 1/2$ ) law. The detachment effect is weaker for non-linear interactions or for hysteretic interactions when compared to the simple LSD model; nonetheless all  $\epsilon_{\text{eff}}$  MD results differ from the ED ones, for which  $\epsilon_{\text{eff}}$  is close to zero for  $N(1 - \epsilon)$  large [13].

The difference between ED and MD results is also apparent from the *relative* kinetic energy  $E_{\text{rel}}$ , also called 'granular temperature' [7];  $E_{\text{rel}}$  is defined through  $E_{\text{rel}} = \frac{m}{2} \sum_{i=1}^N (v_i - v_{\text{cm}})^2$  where  $v_{\text{cm}}$  is the velocity of the center of mass of the assembly of spheres.

In Fig.4 we plot  $1 - E_{\text{rel}}/E_f$  where  $E_{\text{rel}}$  is the relative energy and  $E_f$  is the kinetic energy after collision. The parameters of the simulations are the same as the ones used in Fig.3.

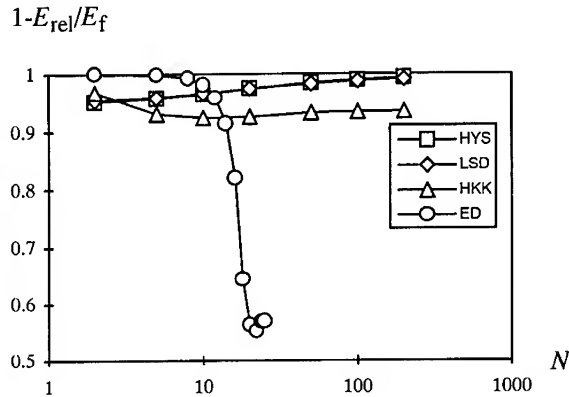


Fig.4:  
 $1 - E_{\text{rel}}/E_f$  plotted as a function of  $N$ . The parameters are as in Fig.3.

## Discussion and Conclusions

For MD simulations we introduced various microscopic interaction laws and compared the results with the outcome of ED simulations. The basic difference between ED and MD methods is the time  $t_c$ , during which particles are in contact. In ED  $t_c$  is implicitly zero, whereas for MD  $t_c$  depends on the interaction laws and parameters used. Thus a large spring constant leads, in general, to a small  $t_c$ . We found that MD calculations underestimate the energy dissipation when the number of spheres in contact is large. The effect is most obvious for linear interactions but also holds for non-linear interactions and for hysteretic models. Even in the case of very high dissipation, i.e.  $N = 10$  and  $\epsilon = 0.6$ , detachment occurs in MD calculations, whereas ED simulations lead to an  $\epsilon_{\text{eff}}$  which virtually vanishes, i.e. to a clustered column after collision.

The occurrence of an anomalously low energy dissipation in MD depends on the ratio  $\sigma$  between the time of free flight and  $t_c$ . MD simulations underestimate the energy dissipation and lead to large fluctuations for  $\sigma \ll 1$ . On the other hand, we find that for  $\sigma \gg 1$  the results of MD and ED simulations agree with each other.

We close this work on a cautionary note about computer simulations: a careful comparison

of the numerical outcome with experimental benchmarks, as well as a critical evaluation of the parameters used in simulations is required. From our side we view the question of the validity of the simulation methods and of the relevance of the interactions used as being still open in the case of multiparticle contacts.

#### Acknowledgements

LAOMC is an U. R. A. of the CNRS and this work was supported by a special grant A. T. P. "Matière en grain". The support of the Deutsche Forschungsgemeinschaft (SFB 60), of the Fonds der Chemischen Industrie, of the 'Forschungszentrum Jülich' (support of CRAY time), and of the PROCOPE scientific collaboration programme is acknowledged. In addition, we thank O. R. Walton for helpful discussions.

#### References

1. *Disorder and Granular Media*, D. Bideau and A. Hansen eds., (Elsevier Sci. Publ., Amsterdam 1993).
2. H. M. Jaeger, S. R. Nagel, *Science* **255**, 1523 (1992); H. M. Jaeger, J. B. Knight, C.-h. Liu, S. R. Nagel, *MRS Bulletin*, Vol. XIX, No.5, 25 (1994).
3. J. Duran, T. Mazozi, E. Clément, J. Rajchenbach, (to be published in *Phys. Rev. E*, 1994).
4. S. F. Foerster, M. Y. Louge, H. Chang, and K. Allia, *Phys. Fluids* **6**, 1108 (1994).
5. L. D. Landau, E. M. Lifschitz, *Band VII Elastizitätstheorie* (Akademie Verlag, Berlin, 1989); W. Goldsmith, *IMPACT The Theory and Physical Behaviour of Colliding Solids*, (Edward Arnold, Publishers, London, 1964); G. Kuwabara and K. Kono, *Jpn. J. Appl. Phys.* **26**, 1230 (1987).
6. M. P. Allen and D. J. Tildesley, *Computer Simulation of Liquids* (Oxford University Press, Oxford, 1987).
7. S. B. Savage, *J. Fluid Mech.* **92**, 53 (1979);
8. P. A. Cundall and O. D. L. Strack, *Geotechnique* **29**, 47 (1979).
9. J. A. C. Gallas, H. J. Herrmann, S. Sokolowski, *Phys. Rev. Lett.* **69**, 1371 (1992); Yi Zhang and C. S. Campbell, *J. Fluid Mech.* **237**, 541 (1992); D. C. Hong, J. A. McLennan, *Physica A* **187**, 159 (1992); Y-h. Taguchi, *Phys. Rev. Lett.* **69**, 1367 (1992).
10. G. H. Ristow, *Intern. J. Modern Phys. C* **3**, 1281 (1993); J. Lee, *J. Phys. A* **27**, L257 (1994).
11. B. D. Lubachevsky, *J. Comput. Phys.* **94**, 255 (1991).
12. B. Bernu and R. Mazighi, *J. Phys. A* **23**, 5745 (1990); S. McNamara, W. R. Young, *Phys. Fluids A* **4**, 496 (1992); S. McNamara, W. R. Young, *Phys. Fluids A* **5**, 34 (1993); R. Mazighi, B. Bernu, and F. Deylon, (to be published in *Phys. Rev. E*, 1994).
13. E. Clément, S. Luding, A. Blumen, J. Rajchenbach and J. Duran, *Internat. J. Modern Phys. B* **7**, 1807 (1993); S. Luding, E. Clément, A. Blumen, J. Rajchenbach and J. Duran, *Phys. Rev. E* **49**, 1634 (1994).
14. M. H. Sadd, Q. Tai, A. Shukla, *Intern. J. Non-Lin. Mech.* **28**, 251 (1993); C. Y. Zhu, A. Shukla, M. H. Sadd, *J. Appl. Mech.* **58**, 341 (1991); O. R. Walton, *Acta Mechanica* **63**, 947 (1986). O. R. Walton, R. L. Braun, *J. Rheology* **30**, 949 (1986).
15. S. Luding, E. Clément, A. Blumen, J. Rajchenbach and J. Duran, (to be published, *Phys. Rev. E*, Nov. 1994); S. Luding, E. Clément, A. Blumen, J. Rajchenbach and J. Duran, *Phys. Rev. E* **50**, R1762 (1994).
16. S. Luding, H. J. Herrmann, and A. Blumen, *Phys. Rev. E* **50**, 3100 (1994).

## 1D EXCITED GRANULAR MEDIA: CLUSTERING AND EQUATION OF STATE

D.R.M. WILLIAMS\* AND F.C. MACKINTOSH\*\*

\* Institute of Advanced Studies, Research School of Physical Sciences and Engineering, The Australian National University, Canberra, and Institute for Theoretical Physics, University of California at Santa Barbara, CA, 93106 and Department of Physics, University of Michigan, Ann Arbor MI 48109-1120.

\*\*Department of Physics, University of Michigan, Ann Arbor MI 48109-1120 and Institute for Theoretical Physics, University of California at Santa Barbara, CA, 93106.

### ABSTRACT

We study a one-dimensional granular system, excited by white noise, with inelastic interactions between the particles. When the coefficient of restitution,  $\eta$ , is one, the particles are totally uncorrelated. As  $\eta$  decreases the particles cluster. A computer simulation of the system shows equilibrium clustering with a power law particle-particle correlation function. This correlation function is independent of the average kinetic energy of the particles but depends strongly on  $\eta$ . We give simple analytical arguments to describe this clustering. We also present an "equation of state" for the particles, which relates the noise amplitude to the particle density and the average particle speed.

### 1. INTRODUCTION

In recent years there has been renewed interest in the phenomenon of particle clustering in granular materials and dissipative gases [1-5]. Such clustering is often observed when granular media are sheared. In general clustering is driven by inelastic collisions. When two particles collide inelastically they dissipate energy. Since the density of a particle at any point is proportional to the inverse of the particle speed, clustering results. Thus clustering occurs even in the absence of any other forces between the particles. There have been several studies of systems which show "inelastic collapse". In these systems the particles are started with some random velocities and then evolve in time according to Newtonian mechanics. The novel feature of the collapse is that for coefficients of restitution  $\eta$  below a critical value  $\eta_c$  the kinetic energy is dissipated in a finite time. For  $\eta > \eta_c$  the kinetic energy dissipates gradually.

In this paper we study a system which has a continuous input of energy as well as dissipative collisions. Thus, for large coefficients of restitution the system eventually settles down to some "steady-state" which looks at least superficially like a gas with some effective forces between the particles. The dissipative interactions mean that in general the structure function  $g(x)$  is no longer a constant (as it would be for an ideal gas), but shows a peak near the origin. Only in the limit  $\eta \rightarrow 1$  does the structure function become uniform. As  $\eta$  decreases  $g(x)$  becomes more and more sharply peaked about  $x = 0$ . The system we study is one-dimensional and has a continuous rate of energy input. This system has one advantage over the more usual problem where a granular material is sheared between two plates. This is that the energy input to each particle is well-controlled, and we do not need to worry about spatial gradients across the system. The simulation might model for instance a system of particles confined to a line on a vibrating plane.

### 2. THE MODEL

We have  $N$  particles of unit mass,  $m = 1$ , confined to a line of length  $L = 1$  (figure 1). We use periodic boundary conditions, so that the system of particles lie on a circle of unit radius. The coefficient of restitution is  $\eta$ , so that when two particles  $i$  and  $j$  collide the final (primed) velocities are given in terms of the initial (unprimed) velocities by



$$v'_i = \frac{1}{2}(1 - \eta)v_i + \frac{1}{2}(1 + \eta)v_j \quad (1)$$



**Figure 1:** A snapshot of a system of particles. Periodic boundary conditions are used, and the particles are points. In general clusters seem to form even for the perfectly elastic limit,  $\eta \rightarrow 1$ . However in this limit the correlation function is a constant. For small values of  $\eta$  the clusters become more pronounced.

The main difference between this and previous studies of dissipative gases is that each individual particle is “heated” at a constant rate. This is done by adding a random amount to the velocity of each particle during a time-step  $\Delta t$ . Thus we write the usual Langevin equation

$$v_i(t + \Delta t) = v_i(t) + \sqrt{r}\sqrt{\Delta t}f(t), \quad (2)$$

where  $f(t)$  is a random number chosen uniformly between  $-1/2$  and  $1/2$  and  $r$  is a number proportional to the heating rate. After the velocities are adjusted the system is transferred to the centre of mass frame, so that  $v_i \rightarrow v_i - \bar{v}$ , where  $\bar{v}$  is the average velocity of all the particles in the system. The algorithm (2) ensures that the velocities undergo a random walk, whilst the transfer to the centre of mass frame ensures that the particle speeds do not increase indefinitely. It should be emphasized that this transfer step is for convenience only, since the properties of collisions do not depend on the absolute speeds, only on the relative speeds. Before the heating step the kinetic energy of the system is

$$K = \frac{1}{2}m \sum_{i=1}^N v_i^2 \quad (3)$$

and after heating it is

$$K' = \frac{1}{2}m \sum_{i=1}^N (v_i + \delta v_i)^2 = K + m \sum_{i=1}^N v_i \delta v_i + \frac{1}{2}m \sum_{i=1}^N (\delta v_i)^2 \quad (4)$$

where  $\delta v_i = \sqrt{r}\sqrt{\Delta t}f(t)$ . The term  $m \sum_{i=1}^N v_i \delta v_i$  vanishes on average, by symmetry, and the term  $\frac{1}{2}m \sum_{i=1}^N (\delta v_i)^2$  is, on average  $\frac{1}{2}mrtN\langle f^2 \rangle = \frac{1}{24}mrtN$ . Hence our identification of  $r$  with the heating rate. It is convenient to introduce a quantity  $\Omega \equiv \frac{1}{24}mr$ , which is the energy input per unit time per particle.

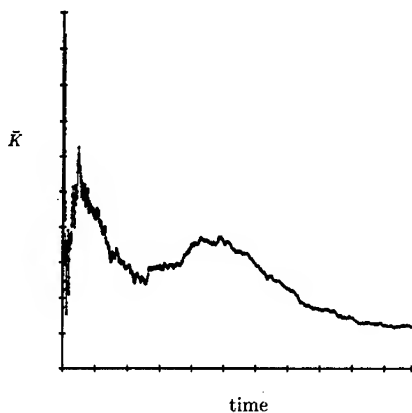


**Figure 2:** The approach of the system to equilibrium for  $N = 10$ . The particles are initially too hot but rapidly reach equilibrium. Here we have plotted the running time average of the kinetic energy per particle versus the logarithm of the time.

### 3. THE EQUATION OF STATE

Provided  $\eta < 1$ , this system, started with some initial random speeds, eventually reaches a steady-state configuration (figure 2). Of interest is the "equation of state", i.e. the relation between the heating rate, the number of particles, the system size, and the kinetic energy of the particles. One possible approximation to the equation of state can be derived as follows. Let us ignore correlations between the particles. The average distance a particle must move between collisions is  $L/(2N)$ . Then, for particles which have some average speed  $v$ , the time between a collision (for each particle) is  $t = (L/(2N))v^{-1}$ . Since there are  $N/2$  pairs of particles the rate of collisions is  $\approx (N/2)t^{-1} = vL^{-1}N^2$ . During each collision an amount of energy  $(1 - \eta^2)mv^2$  is dissipated. Thus the rate of energy dissipation is

$$W = v^3(1 - \eta^2)mL^{-1}N^2. \quad (5)$$

However, the rate of energy input is  $\Omega N$ . In the steady-state these must be equal. Thus we find an equation of state

$$v^3(1 - \eta^2)\rho = \Omega \quad (6)$$

or

$$(2K/m)^{3/2}(1 - \eta^2)\rho = \Omega, \quad (7)$$

where  $K$  is the kinetic energy per particle.

We can use this to obtain the force on a wall placed at the boundary of a finite system. We assume that the particles undergo perfectly elastic collisions with the wall. The time averaged force  $F$  exerted by the particles is the “pressure” for a 1D gas. The current of particles hitting the wall is  $J = Nv/L$ . Each particle imparts momentum  $2mv$  to the wall. Thus the time-averaged force is  $F = \rho v^2$ . Thus the relation between the force and the density is

$$F = \Omega^{2/3} \rho^{1/3} (1 - \eta^2)^{-2/3}. \quad (8)$$

This is very different from the result for an ideal gas where the pressure is proportional to the first power of the density.

We can compare our equation of state (6) to the simulation results. We do not expect that the numerical coefficients are accurate, since we have used a “mean-field” type argument, and assumed differences in velocities are equal to average velocities. We can however test the various proportionalities in (6). The first prediction is that  $K^{3/2} \propto (1 - \eta^2)^{-1}$ . These two quantities are plotted in figure 3. We see a very linear relation, except for small values of  $\eta$  where correlations between the particles become important. Second, we test that  $K^{3/2} \propto \rho^{-1}$ , i.e. that the cube of the velocity is inversely proportional to the density (figure 4). Here the data are somewhat noisy, but the agreement is still reasonable. Finally we test that  $K^{3/2}$  is proportional to the heating rate (figure 5). Again the agreement is good.

#### 4. THE DENSITY CORRELATION FUNCTION

We select a particle and ask what is the density of particles at distance  $x$  from it,  $g(x)$ . For an ideal gas of point particles the answer is  $g(x) = \text{a constant}$ . For a gas which has some attractive potential  $U(x)$  acting between the particles the answer is more complicated, but in general  $g(x)$  will be peaked about  $x = 0$  and will decay to a constant as  $x \rightarrow \infty$ . For the dissipative gas discussed here we find  $g(x)$  shows a peak at the origin, even though we have no potential acting between the particles. This peak is caused by the dissipation effect discussed above, and can be thought of as an equilibrium version of the collapse and clustering seen in cooling gases [1-5]. As  $\eta \rightarrow 1$  the structure becomes small as  $g(x)$  approaches a constant. However, as  $\eta$  becomes small,  $g(x)$  becomes very sharply peaked. Some characteristic results are shown in figure 6. We find that the correlation function depends only on the density and on  $\eta$  and is independent of the heating rate. At least for small  $x$ , where the finite size of the system has little effect,  $g(x)$  can be approximated by a power law  $g(x) \sim x^{-\alpha(\eta)}$ . Here  $\alpha(\eta)$  is a function of  $\eta$ . For  $\eta \rightarrow 1$ ,  $\alpha \rightarrow 0$ . For small  $\eta$ ,  $\alpha$  appears to approach  $1/3$ . This result can be understood as follows. When  $\eta$  is small the collisions between particles are almost perfectly inelastic and the particles lose almost all of their energy. The particles only move away from each other because of the random kicks induced by the heating. Thus we can consider a single particle moving away from a wall and subject to its velocity undergoing a random walk. We thus have  $\langle |v(t)|^2 \rangle \sim t$ . Hence  $v \sim t^{1/2}$  and the distance traveled from the wall in time  $t$  is  $x \sim \int_0^t v(t') dt' \sim t^{3/2} \sim v^3$ . The density of a particle at any point is just the inverse of the time it spends in that region i.e.  $v^{-1}$ , thus  $g(x) \sim v^{-1} \sim x^{-1/3}$ , and  $\alpha = 1/3$ .

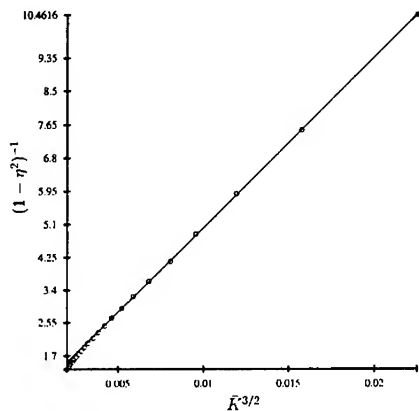


**Figure 3:** A test of the equation of state (6). Here we have plotted  $(1 - \eta^2)^{-1}$  versus  $K^{3/2}$  where  $K$  is the kinetic energy per particle. As predicted by theory (6) the relation is close to linear. The circles are points from the computer simulation, and the line is a line of best fit.

**Figure 4:** The cube of the average speed versus the inverse density for a system of 10 particles. The theory (6) predicts a linear relation. The circles are points from the computer simulation, and the line is a line of best fit.

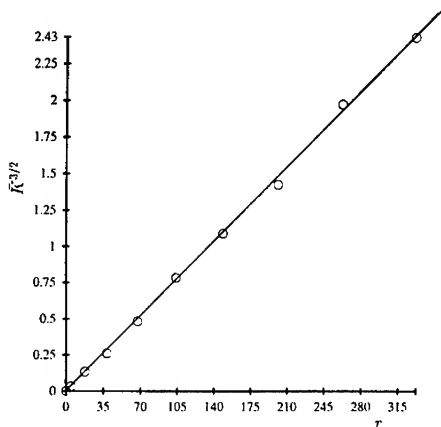
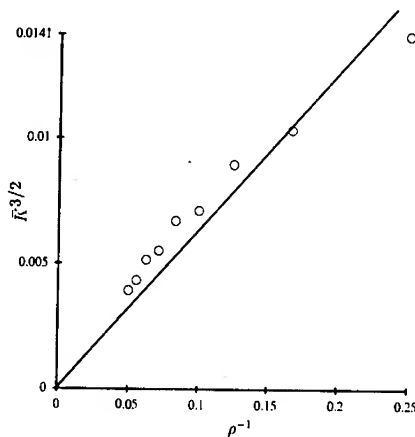


**Figure 5:** The cube of the average speed versus the heating rate  $r$  for a system of 10 particles. The relation is very close to linear, as predicted by the theory (6). The circles are points from the computer simulation, and the line is a line of best fit.

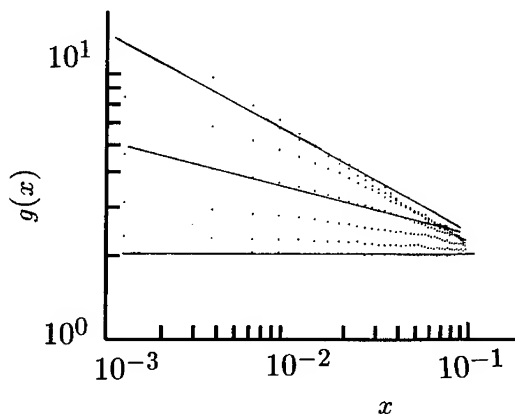


**Figure 6:** A log-log plot of the density correlation function  $g(x)$  versus distance between the particles  $x$ . The three lines shown, are (from bottom to top)  $\eta = 0.95$ ,  $\eta = 0.65$  and  $\eta = 0.45$ . Here  $N = 10$ . The line for  $\eta = 0.45$  has a slope very close to that expected for a perfectly inelastic system ( $-1/3$ ).

## 5. CONCLUSION

In this paper we have discussed a simple one dimensional model of an excited dissipative gas. The system shows clustering and can be described by a simple equation of state. It behaves in some respects like a gas of particles with a fictitious potential between the particles. We have presented results for a small number of particles  $N = 10$ . However, similar results are found for much larger numbers of particles, and in fact even for  $N = 2$  the behaviour is very much the same.

F.C.M was funded by NSF PHY8904035, DMR-92-5744 and by a PRF grant. D.R.M.W was funded by NSF PHY89-04035, DNR-91-17249, DMR-92-57544, by a QEII research fellowship, and by a PRF grant.

## REFERENCES

- [1] I. Goldhirsch and G. Zanetti, *Phys. Rev. Lett.* **70**, 1619 (1993).
- [2] B. Bernu and R. Mazighi, *J. Phys. A* **23**, 5745 (1990).
- [3] M.A. Hopkins and M.Y. Louge, *Phys. Fluids A* **3**, 47 (1991).
- [4] S. McNamara and W.R. Young, *Phys. Fluids A* **4**, 496 (1992).
- [5] S. Luding, E. Clément, A. Blumen, J. Rajchenbach and J. Duran, *Phys. Rev. E* **49**, 1634 (1994).

## REVERSIBLE AXIAL SEGREGATION IN ROTATING GRANULAR MEDIA

K. M. HILL, L. YARUSSO, and J. KAKALIOS

The University of Minnesota, School of Physics and Astronomy, Minneapolis, MN 55455

### ABSTRACT

Binary mixtures of granular media having differing diameters are combined in a horizontal cylinder and rotated like a drum mixer about its long axis. Within a few minutes of rotation at 15 rpm axial segregation occurs and the mixture separates into relatively pure alternating bands of the individual components along the axis of rotation. We describe an experimental system whereby the mixed state can be restored by changing the speed of rotation. The sensitivity of the reversible axial segregation effect to systematic variations of the glass bead diameter is reported. Measurements of the dynamic angle of repose of the mixed and segregated phases support an explanation for the reversible axial segregation effect involving the competition between axial drift and diffusion currents, leading to a diffusion equation with a negative effective diffusion coefficient.

### INTRODUCTION

While extensively studied by engineers,<sup>1-10</sup> granular materials have recently attracted the renewed attention of physicists,<sup>11-13</sup> due in part to a suggestion by Bak, Tang and Wiesenfeld.<sup>14</sup> These authors suggested that fractal geometries and  $1/f$  noise may arise from the dynamics of self-organized critical (SOC) states, and their paradigm system was the self-organization of a sandpile at its critical angle of repose. While experimental measurements have not found  $1/f$  dynamics in sandpile avalanches, the SOC model has had a real and significant impact by motivating physicists to study the dynamics and properties of granular materials. A striking property of granular systems is mass or size segregation when a homogeneous mixture of granular media of different sizes or masses is shaken or rotated.<sup>1-9,15-19</sup> If a cylinder partially filled with a binary mixture of granular media is tipped on its side so that its axis of symmetry is horizontal and rotated like a drum about that axis, the individual species will segregate into alternating bands of relatively pure single concentrations along the axis of rotation.<sup>4-7,17,18</sup> While this effect is well-known, we have recently described observations of a reversible segregation effect<sup>19</sup> wherein the mixed state can be restored by changing the speed of horizontal rotation. In this paper we report measurements of the axial segregation effect when the diameter of the glass beads is systematically varied from  $\sim 5$  mm to  $\sim 0.5$  mm. Measurements of the dynamic angle of repose for the different mixed and segregated phases is also described. These results are discussed in terms of a model whereby the difference between the dynamic angle of repose of the mixed phase and of one of the homogeneous phases determines the sign of the effective axial diffusion coefficient and thus the behavior of the mixture at each speed.

### EXPERIMENTAL TECHNIQUES AND RESULTS

Our experimental setup (similar to that employed in Ref. 20) is shown in Figure 1. A Plexiglas hollow cylinder 5 inches in diameter and 2 ft long has Plexiglas end plates bolted onto either end. A bolt is attached to the outside of each plate, coaxial to the cylinder, which rests on a ball bearing mount. One of these bolts has an additional flange at its other end connected by a belt to a 1/17 hp motor. The motor is not shown in Figure 1, but its mount can be seen near the bottom left hand corner of the photographs. For each run the cylinder was one third filled with a 50/50 binary mixture of either glass beads of two different diameters, each approximately uniform in size, or of glass beads of one diameter and sand. The glass beads ranged in diameter from about .7 to 4.8 mm, and the sand was very irregularly shaped with average distance across each grain of about .4 mm. The mixture used in Figures 1(a) and (b) is of glass beads of

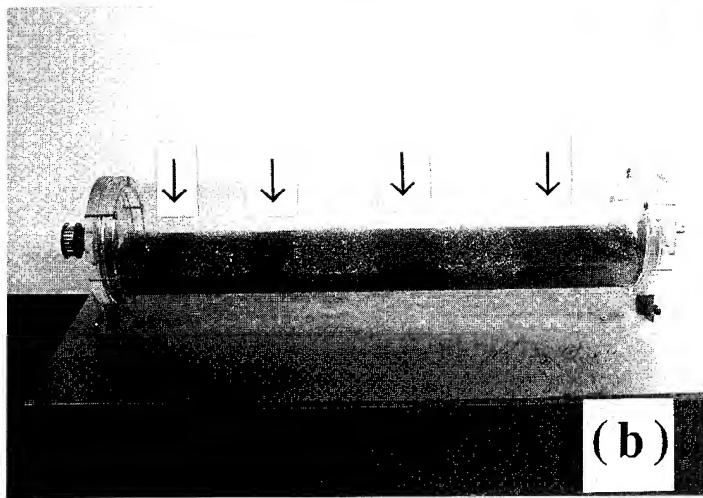
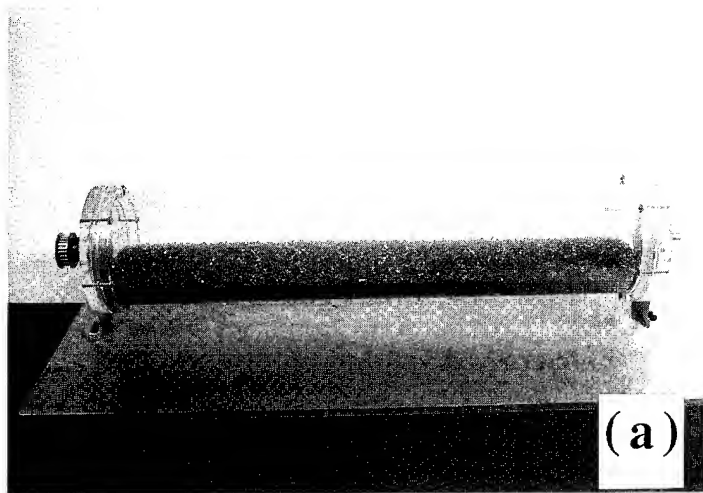


Fig. 1: Photographs of the horizontal rotating cylinder described in the text. The cylinder is  $1/3$  filled with a 50/50 mixture of large ( $d \sim 3$  mm) and small ( $d \sim 0.7$  mm) glass beads. The initial homogeneous mixed state is shown in photo (a). After rotation about the long axis for 15 min at 14 rpm, the large and small glass beads have segregated out into alternating bands, as shown in photo (b).

diameters 2.8 mm and .7 mm. The smaller beads are dyed black to improve the contrast in the photographs, though the phenomenon is not affected by the dye. The cylinder was leveled using shims, though again the results did not depend on precise leveling. For the run pictured in Figure 1, the homogeneous mixture of beads shown in Figure 1a was initially rotated in the cylinder at 14 rpm. After approximately 15 minutes, unmistakable alternating bands of large and small glass beads have evolved, as shown in Fig.1(b). The motor speed was then decreased to 5 rpm. After approximately one hour, the bands had disappeared, and the mixture had returned to a homogeneous state similar to that shown in Fig. 1(a). When the speed of the motor was returned to 14 rpm, the segregated state returned as well, though the widths and locations of the bands differed from that displayed in fig. 1(b).

We have investigated the dynamics of the axial segregation effect when the diameter of the glass beads used is systematically varied from 0.4 to 4.8 mm. The behavior of the different mixtures are summarized in Table 1. Binary mixtures of glass beads or beads and sand exhibit either a reversible axial segregation, a segregation effect which is not reversible at slower rotation speeds, or no segregation effect at all. Since most mixtures that segregated showed signs of initial segregation within the first few minutes of rotation, those mixtures that hadn't shown any sign of segregation within the first few hours were considered to not segregate. Similarly, since it took on the order of a few hours for the mixtures, once segregated, to completely remix at slower rotation speeds, we rotated the cylinder for over 24 hours before concluding that those mixtures that had segregated bands would not remix at other speeds. While Table 1 indicates a general trend towards the occurrence of reversible axial segregation as the ratio  $\beta$  of the larger bead diameter to the smaller increases, there are clear exceptions. For example, a mixture of large and small beads ( $\beta \sim 3.2$ ) shows a non-reversible segregation effect, while larger and smaller  $\beta$  values exhibit a reversible segregation. It is well known that the dynamic angle of repose of a granular material depends on many factors, including the particle size, mass, surface roughness, humidity, and kinetic friction between particles and between particles and the walls of the cylinder. Evidently other factors in addition to the diameter ratio influence the segregation behavior of a granular mixture.

**Table 1. Behaviors of different binary mixtures of granular media**  
 $\beta$  = diameter ratio, not applicable for the irregularly shaped sand.

| type and size (mm) | sand                       | x-small                                    | small                                      | medium                                 | large                          |
|--------------------|----------------------------|--|--|--|--------------------------------|
| sand 0.42+-08      | X                          | X  | X  | X                                      | X                              |
| x-small 0.70+-06   | non-reversible segregation | X  | X  | X                                      | X                              |
| small 0.97+-07     | not performed              | not performed<br>$\beta=1.39$              | X  | X                                      | X                              |
| medium 1.24+-08    | non-reversible segregation | non-reversible segregation<br>$\beta=1.77$ | non-reversible segregation<br>$\beta=1.28$ | X                                      | X                              |
| large 3.11+-20     | no segregation             | reversible segregation<br>$\beta=4.44$     | non-reversible segregation<br>$\beta=3.21$ | reversible segregation<br>$\beta=2.51$ | X                              |
| jumbo 4.84+-10     | no segregation             | reversible segregation<br>$\beta=6.91$     | reversible segregation<br>$\beta=4.99$     | reversible segregation<br>$\beta=3.90$ | no segregation<br>$\beta=1.56$ |

While the location and size of the bands vary from run to run for the segregated state, there are reproducible features at the beginning and end of each run. Upon beginning rotation, small beads almost immediately move toward the axis of rotation to form a radially segregated state. The radial segregation has been reported previously<sup>5-7</sup> and is most likely due to the variation in compactivity below the avalanching surface of the rotating drum.<sup>22</sup> The initial formation of segregated bands occurs adjacent to the end plates. Varying the cylinder length confirms that this is a boundary effect. Band development in the interior of the cylinder appears



to arise from concentration fluctuations along the axis. The initial pattern of bands is neither reproducible nor stable when the system is rotated for an extended period of time (on the order of a few hours at 15 rpm), rather the bands evolve to a reproducible final state of one central band of large beads with bands of small beads adjacent on either side and narrow bands of large beads at both end plates. The evolution of the bands involves a complicated process and will be described in more detail in a later publication.

The transition from concentration fluctuations to segregated band formation can be understood using a model based upon proposals by Donald and Roseman,<sup>5</sup> Bridgwater, Sharpe and Stocker,<sup>8</sup> deGennes, Savage,<sup>21</sup> and others.<sup>7,17</sup> The larger the dynamic angle of repose of a material, the higher the beads will maintain contact with the back of the cylinder before avalanching. If the dynamic angle of repose of the mixed phase  $\phi_m$  is significantly larger than that of at least one of the segregated phases (for example the large beads), then an axial fluctuation in density will lead to a fluctuation in height. Since some of the small beads have already segregated into the radial mode, the large beads are pushed to the avalanching top surface. If the monodisperse large glass beads have a lower dynamic angle of repose than the mixed phase, large beads will move to the lowest point on the slope, segregating out of the mixture. Assuming that the larger component has the lower angle of repose, we can write this axial drift current  $j_{\text{drift}}$  of the large beads out of the mixed phase as proportional to the gradient of the larger bead concentration  $C_L$

$$j_{\text{drift}} = \beta \partial C_L / \partial x \quad (1)$$

where the constant of proportionality  $\beta$  must vary monotonically with the bead height and hence with the difference in the dynamic angle of repose  $\Delta\phi = \phi_m - \phi_L$ . Particularly, when  $\Delta\phi = 0$ , then  $\beta = 0$ . If  $\Delta\phi$  increases, so should the tendency for segregation, i.e.  $j_{\text{drift}}$  should increase as well. In addition to the tendency to segregate, random collisions between the beads will lead to remixing. This can be expressed in terms of the normal Fickian diffusion current

$$j_{\text{diff}} = -D \partial C_L / \partial x \quad (2)$$

where  $D$  is the diffusion coefficient for the larger component. The total current should be a sum of the diffusion and drift currents:  $j = j_{\text{diff}} + j_{\text{drift}}$ . Thus, the rate of growth of the segregated phase  $C_L$  is given by the continuity equation

$$\partial C_L / \partial t = -\partial j / \partial x = \partial [(D - \beta) \partial C_L / \partial x] / \partial x, \quad (3)$$

This is similar to the traditional diffusion equation, with the normal Fickian diffusion coefficient replaced by an effective diffusion coefficient,  $D_{\text{eff}} = D - \beta$ . If  $D_{\text{eff}} < 0$ , concentration fluctuations of segregated regions would be enhanced, leading to band formation.

According to this model, at rotation speeds for which a mixture segregates into bands,  $\Delta\phi$  must be large enough so that  $\beta > D$  and  $D_{\text{eff}} < 0$ . Alternatively,  $\Delta\phi$  should be small or zero at lower speeds, so that  $\beta \sim 0$  and  $D_{\text{eff}} = D$  when the bands remix or no segregation occurs. To test this explanation, we measured the dynamic angle of repose for the different mixtures described in Table 1 and for each homogeneous state as a function of rotation speed. The end of the cylinder was photographed along the horizontal axis of rotation and the angle that the freely flowing surface made with a fixed horizontal marker was determined. In addition to the error associated with measuring a moving surface, the avalanching surface does not form a perfect plane, due to centrifugal forces and wall friction which give the flowing surface an s-shaped contour at high rotation speeds.<sup>23</sup> Thus the values of  $\phi$  reported are the averaged values of multiple measurements.

Measurements of the dynamic angle of repose as a function of rotation speed for the mixed phase and a homogeneous phase of the larger diameter glass beads for three different binary mixtures of granular media are shown in fig. 2-4. Figure 2 is a plot of  $\phi$  for a mixture of large ( $d \sim 3$  mm) and small ( $d \sim 0.7$  mm) glass beads which axially segregated at high speeds and remixed at lower speeds. There is a large difference between  $\phi$  of the mixture and the monodisperse large beads at higher speeds for which segregation occurs, while at lower speeds, where there was remixing, there was little or no difference of  $\phi$  between the two phases. Figure 3 is for a mixture of glass beads ( $d \sim 1.2$  mm) and sand ( $d \sim 0.4$  mm) which segregates at all speeds and does not remix when the rotation speed is changed. As expected,  $\phi$  of the mixed

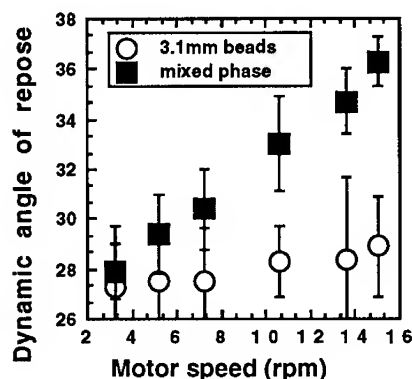


FIG. 2: Plot of dynamic angle of repose against rotation speed for the mixed phase (0.7 mm and 3 mm diameter glass beads) and monodisperse large beads, which exhibit a reversible axial segregation.

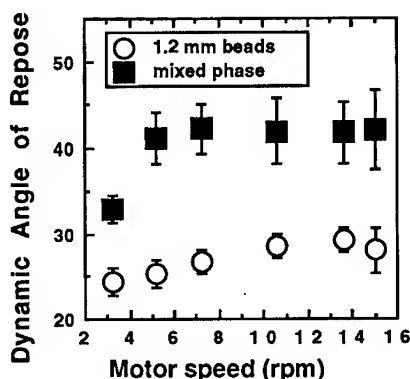


Fig. 3: Plot of dynamic angle of repose against rotation speed for the mixed phase (1.2 mm and 0.4 mm diameter glass beads) and monodisperse medium beads which exhibit a non-reversible axial segregation.

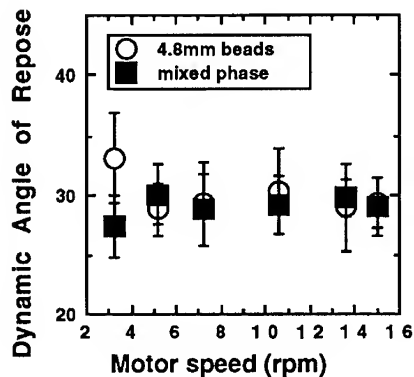


Fig. 4: Plot of dynamic angle of repose against rotation speed for the mixed phase (4.8 mm and 3 mm diameter glass beads) and monodisperse large beads, which exhibit no segregation at any rotation speed.

phase is larger than that of the monodisperse glass bead phase at all speeds. Figure 4 is a plot of the dynamic angle of repose  $\phi_m$  for a mixture of jumbo and large beads which does not segregate into bands at any rotation speed. In this case,  $\phi_m$  is equivalent to  $\phi$  of each monodisperse phase. Since  $\Delta\phi \sim 0$  at all speeds, then  $\beta \sim 0$  and  $D_{eff} = D$ , and there is no drift current to separate the mixed materials. These measurements are entirely consistent with the model described above, that is, axial segregation occurs when there is a large difference between  $\phi$  of the mixed phase compared to the segregated phase, and in order for a reversible segregation effect to be observed  $\Delta\phi \sim 0$  at small but finite rotation speeds. The measurements of  $\phi$  were obtained from photographs along the end of the cylinder, which raises the issue of whether the conditions of the different phases are different at the end plates than in the middle of the cylinder. Measurements of the height of the granular material at different points along the back wall of the cylinder found that the height shift was small and roughly constant for all mixtures and monodisperse phases at all rotation speeds.

We benefited from helpful comments from J. Knight, M. Hamermesh and S. F. Edwards. This work was supported by NSF DMR-9057722, the Xerox Corp. and the University of Minnesota.

## REFERENCES

1. M. H. Cooke, D. J. Stephens and J. Bridgwater, *Powder Tech.* **15**, 1 (1976).
2. L. T. Fan and Yi-Ming Chen, *Powder Tech.* **61**, 255 (1990).
3. James L. Olsen and Edward G. Rippie, *J. Pharmaceutical Sci.* **53**, 147 (1964).
4. Y. Oyama, *Bull. Inst. Phys. Chem. Res. (Tokyo)*, Rep. **5**, 600 (1939).
5. M. B. Donald and B. Roseman, *British Chem. Eng.* **7**, 749 (1962); B. Roseman and M. B. Donald, *British Chem. Eng.* **7**, 823 (1962).
6. J. Bridgwater, *Powder Tech.* **15**, 215 (1976).
7. S. Das Gupta, D. V. Khakhar and S. K. Bhatia, *Powder Tech.* **67**, 145 (1991); *Chemical Eng. Sci.* **46**, 1513 (1991).
8. J. Bridgwater, N. W. Sharpe and D. C. Stocker, *Trans. Instn. Chem. Engrs.* **47**, T114 (1969).
9. H. E. Rose, *Trans. Instn. Chem. Engrs.* **37**, 47 (1959).
10. S. J. Rao, S. K. Bhatia and D. V. Khakhar, *Powder Tech.* **67**, 153 (1991).
11. *Physics of Granular Media*, ed. by D. Bideau and A. Hansen (North-Holland, Amsterdam, 1993).
12. *Disorder and Granular Media*, ed. by D. Bideau and A. Hansen (North-Holland, Amsterdam, 1993).
13. *Granular Matter, An Interdisciplinary Approach*, ed. by Anita Mehta (Springer-Verlag, New York, 1994).
14. P. Bak, C. Tang and K. Wiesenfeld, *Phys. Rev. Lett.* **59**, 381 (1987); *Phys. Rev. A* **38**, 364 (1988); Chao Tang and Per Bak, *Phys., Rev. Lett.* **60**, 2347 (1988).
15. H. M. Jaeger and Sidney R. Nagel, *Science* **255**, 1523 (1992).
16. James B. Knight, H. M. Jaeger, and Sidney R. Nagel, *Phys. Rev. Lett.* **70**, 3728 (1993).
17. O. Zik, Dov Levine, S. G. Lipson, S. Shtrikman, and J. Stavans, *Phys. Rev. Lett.* **67**, 145 (1991).
18. M. Nakagawa, *Chem. Eng. Sci.* (in press).
19. K. M. Hill and J. Kakalios, *Phys. Rev. E* **49**, R3610 (1994).
20. S. Fauve, C. Laroche, and S. Douady, in *Physics of Granular Media*, edited by Daniel Bideau and John Dodds (Nova Science, Commack, NY, 1991), p.277.
21. Stuart B. Savage, in *Disorder and Granular Media*, edited by D. Bideau and A. Hansen (North-Holland, Amsterdam, 1993), p.255.
22. S. F. Edwards and Anita Mehta, *J. Phys. (Paris)* **50**, 2489 (1989); Anita Mehta and S. F. Edwards, *Physica A* **157**, 1091 (1989); **168**, 714 (1990).
23. Jean Rajchenbach, *Phys. Rev. Lett.* **65**, 2221 (1990).

## MIXING OF A GRANULAR MATERIAL IN A BIDIMENSIONAL ROTATING DRUM

ERIC CLEMENT, JEAN RAJCHENBACH AND JACQUES DURAN

Laboratoire A.O.M.C. - URA 800 - Université Pierre et Marie Curie, 4, pl. Jussieu - B86, 75005, FRANCE.

### ABSTRACT

We report experimental measurements on mixing properties in bidimensional rotating drum. Using an image processing device, we follow the trajectories of tracer particles in a mono-disperse assembly of beads. Tracer particles with different size ratios exhibit a violent segregation effect: a smaller particle has a tendency to stay in the centre and a larger one will rather dwell on the edges. Furthermore, for a tracer of identical size, we evidence a specific dispersion property where the centre and the edges are competing attractors of the mixing dynamics.

### INTRODUCTION

A very remarkable property of non cohesive granular materials is the empirical tendency towards demixion displayed by powders of different nature. These segregation properties have been known for a long time now and intervene, in a prejudicial way, in numerous industrial processes when the making of an homogeneous mixture is of utmost importance [1]. So far, very little on the physics of powder mixing, has been fundamentally elucidated, but all studies have shown that segregation is indeed a complex property which may result from several different and parallel processes. Size segregation of powders mixed in an half-filled and rotating cylinder has been reported for a long time ago [2]. Several parallel processes have been evidenced (see for example a review article by Cooke et al. [3]; and ref. therein). In three dimensional devices, simultaneous axial and longitudinal segregation routes are present [4,5]. Particle percolation has been invoked to be responsible of axial segregation [6], and longitudinal segregation, occurring in a long cylinder, is currently related to differential surface flow properties [7,8]. In this paper we are interested in studying the mixing properties of a model powder confined in a bidimensional rotating drum. One advantage of a 2D geometry, besides visualisation facilities, is that the dispersion properties of the surface flow are clearly separated from the parallel process present in 3D, which is the filtration of the smaller particles in the voids of the porous network made by the large particles. Also, in this geometry, we do not have the surface instability generated by the flow in the direction parallel to the axis of rotation. Our work deals essentially with the study of one tracer particle in the field of other identical grains and constitutes a first attempt to extract the very basic phenomenology. It should be seen as a complementary study made in this geometry, were several particles of different sizes are mixed together [9] and a strong segregation shows up after several rounds. Note that recently, computer simulations based either on a molecular dynamics algorithm [10] or a sequential piling algorithm [11] have been proposed to describe, the mixing of grains in this geometry.

## II. DESCRIPTION OF THE EXPERIMENT

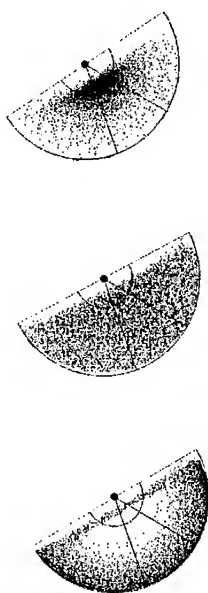
We use a cylinder partially filled with a powder and rotated at a constant velocity by a step by step motor. This configuration is a simple way to generate surface flow and shearing [12]. The model granular medium is a mono-disperse assembly of metallic beads displayed in a single layer array and confined vertically between a metallic boundary and a front glass window. They provide a real advantage to allow for direct visualisation, but we also insist on the fact that extrapolation of a 2D phenomenology to general 3D behaviour is not straightforward and should always requires a cautious discussion. Metallic bearing balls have been chosen for the good control of sphericity as well as the control of mechanical parameters (solid friction, restitution coefficient). In the present experiment the beads have a  $d = 1.5 \text{ mm}$  diameter and the cylinder inner diameter is  $D = 160 \text{ mm}$ . The beads are made of steel with an elasticity coefficient of  $\epsilon = .9$  and a friction coefficient  $f = .1$ . In order to avoid collective sliding of the granular assembly, an monolayer of beads is glued on the inner periphery of the cylinder.

A low rotation speed, the assembly of beads performs a solid rotation and the free surface slope is continuously increased until a surface avalanche starts. Then, the particles which are part of this surface flux undergo important relative motions. After the avalanche stops, the whole system is again part of the collective solid rotation. In all the experiments presented here, we work at a low rotation velocity (2 deg/s) and we stay in the avalanche regime. Studies have shown that this regime could be characterised by a typical time between avalanche [13, 14] but with a distribution rather broad in 2D [15,16]. Thus, this intermittent sequence of avalanches performs some mixing of the granular assembly and in this report, we focus on the description of this effect. For this purpose, we place in the granular assembly a test particle of the same material. For test particles larger than  $1.5 \text{ mm}$ , we use a disk slightly narrower than the width of the cell. For a test particle smaller than  $1.5 \text{ mm}$  we use a metallic bead. The beads and the cylinder have undertaken a chemical surface treatment which has darken their surface aspect. The test particle is still bright and can be selected preferentially through the image analysis routine. The whole experimental display is monitored using a CCD video camera linked to a computer device automatically performing the image analysis routine. As a function of time (every 5s roughly), we record the position of the centre of the test particle. From the statistical analysis of those trajectories, we extracted two major features that should be of general relevance, namely a size segregation effect as well as the presence of attracting regions for the dispersion dynamics.

## III. EVIDENCE FOR SIZE SEGREGATION

In Fig.1a, 1b, 1c, we show the accumulation pictures of all the locations occupied by the centre of the test particle during 12000 samplings. The diameters of the test particles are respectively  $D = 1\text{mm}$ ,  $D = 1.5 \text{ mm}$ ,  $D = 2\text{mm}$ . Note that the position is recorded every 5s. On the top of each accumulation picture we display the 1st iteration map of the dynamical process monitoring the event of a new passage in an angular sector  $\Delta\alpha = 40^\circ$  taken around the perpendicular axis to the mean flow direction and within the radii  $R_1$  and  $R_2$  (see picture 1). The minimum radius  $R_1$  corresponds to an exclusion of the surface flow region and the maximum radius  $R_2$  corresponds to the inner cylinder radius. This surface is called region S. The Curves displayed in Fig 2 correspond to the measurement of the presence probability  $P(r)$  in region S. In the three cases, the coarse-graining distance is  $\Delta r = 3d$ . The behaviour of the exploration curves are strikingly different for the three particle radii considered. Clearly, the

smaller particle is attracted to the centre and the larger one to the edge. Note that for a particle of identical size we observe an homogeneous exploration of all the granular medium.



(c)

Fig 1 - Distribution of the tracer centers for three different size ratios:  $\Phi = \Delta/d$ . Fig. 1 (a),  $\Phi = .66$ ; Fig. 1 (b),  $\Phi = 1$ ; Fig. 13 (c),  $\Phi = 1.33$ .

This size segregation confirms the results of a preliminary report made on 3 mm steel beads but with an aspect ratio for the cylinder size that was four times smaller [17]. In first approximation, the probability curves of fig 2 are fitted to an exponential decay  $P(r) \approx \exp(-\alpha r)$  and we evidence that segregation can be characterised by a typical segregation length  $\lambda = 1/\alpha$ , with a change of sign indicating an attractor preference.

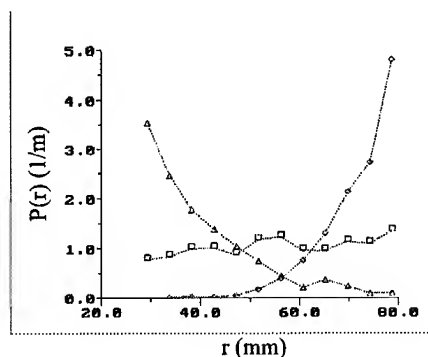


Fig 2. Presence probability  $P(r)$  as a function of  $r$  the distance to the centre in region S. Triangles ( $\Delta$ ):  $\Delta = 1 \text{ mm}$ ; squares ( $\square$ ):  $\Delta = 1.5 \text{ mm}$ ; diamonds ( $\diamond$ ):  $\Delta = 2 \text{ mm}$ .

#### IV STUDY OF THE DISPERSION PROPERTIES IN A MONO-DISPERSE ASSEMBLY OF SPHERES

Now we focus on the dispersion property of an identical sphere in a monodisperse assembly of beads. In view of figure 2, one could argue that a rotating cylinder device is at least a good mixer for identical particles since the final outcome of the presence density distribution looks homogeneous. Note that such a flat distribution for  $P(r)$  could also be obtained by a random redistribution of the test particle along the radius caused by the avalanche process. Here we point out that even for a similar size particle, the dispersion provided by the avalanche is in fact a complex mechanism. In the following we look at a stochastic description of the trajectories redistribution extracted from the map of Fig.1. We measure the conditionnal probabilities  $\Pi(r/r_0)$ , which are the probability, having performed a

solid rotation trajectory at a radius  $r_0$  in the domain S, to perform during the next passage in S, a trajectory with a radius  $r$ . This probability distribution is a indication of the attraction capability of a spatial position. In figure 3a, 3b, 3c we display the joint probabilities  $\Pi(r/r_0)$ , calculated in three different origins  $r_0$ : in 3a  $r_0$  is taken in the central region, in 3b  $r_0$  is taken in the intermediate region between the centre and the edge and the last picture is for  $r_0$  taken in the vicinity of the edge. The size of the coarse graining box is  $\Delta r = 3 \cdot d$ . We see clearly that the centre and the edge are prominent attractors for the trajectories, with a redistribution length comparable to the size of

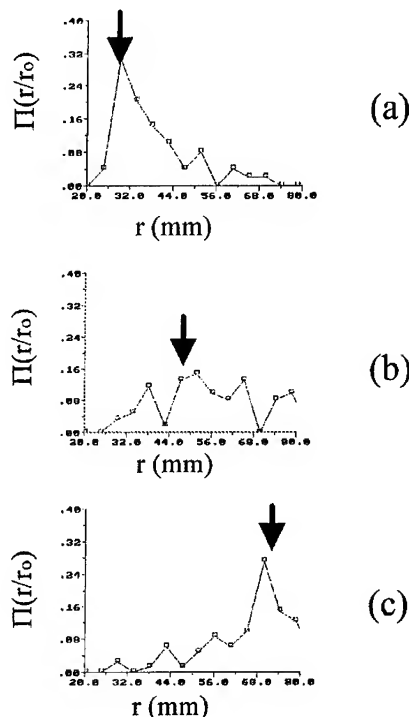


Fig 3. Joint probabilities of reinjection  $\Pi(r/r_0)$  for a test particle  $\Delta = 1.5 \text{ mm}$  at three different injection radii  $r_0$ . Fig. 3a:  $r_0 = 30 \text{ mm}$ , Fig. 3b:  $r_0 = 48 \text{ mm}$ , Fig. 3c:  $r_0 = 72 \text{ mm}$ . The injection position  $r_0$  is indicated by an arrow.

the cylinder. Note the important point that the intermediate region achieves more or less a *random redistribution* of the trajectories. So, although the memory of an initial position is lost after two or three rounds in the cylinder, there still is a strong memory of the injection radius in a *single* avalanche. This memory effect is probably due to the recurrence of a flow lines pattern. Thus, we evidenced clearly the existence of two competing regions and the mixing in fact due to the relative strength of the attraction power of the centre, compared to the attraction power of the edge. Also, an important fact is that for this cylinder, the size of the typical jump between successive trajectories is of the order of the size of the cylinder. This evidence is in favour of mixing and opposes a long time localisation in the vicinity of the attractors. A major point for future investigations will be to understand whether this tendency is confirmed when the size of the cylinder is increased and/or if a typical localisation length shows up which could be different from the cylinder size.

In the case of other tracer sizes, we observe similarly a bimodal attractive behaviour but the relative influence of the corresponding attractor is more pronounced and has a tendency to eat up the central region. Our experimental data did not allow us to go beyond this qualitative statement.

## V DISCUSSION AND PROSPECTIVE

This paper reports on experimental facts associated to the mixing properties in a bidimensional rotating cylinder. We do not propose any fundamental explanation for the phenomenon but we rather try to focus on the prominent experimental facts which should orient future experimental

and theoretical investigations. We evidence clearly a segregation mechanism of a single tracer particle based on the size ratio. A large particle is pushed to the edges and the small one will rather stay in the centre. We measured a segregation length dependent of the aspect ratio. Furthermore, we look at the redistribution probability for the trajectories of a single particle of the same size and we clearly see the presence of two competing regions: the centre of the cylinder and the edge which have a tendency to attract the trajectory distributions. Thus, the size segregation mechanism can be seen as a more pronounced influence of one attractor compared to the other. This phenomenology is really reminiscent of a stochastic bistability transition with a control parameter being the size ratio. Nevertheless here, the non trivial point is the importance of the fluctuations, i.e. the reinjection steps, which are in this experiment, of the size of the system. The stochastic phenomenological description of the experiment should not hide the fact that the origin of the phenomenon is rooted in the dispersion properties due to the geometry and the shearing action of the surface flow. These important questions are left for future work.

## REFERENCES

1. S.S.Weidenbaum, *Mixing of Solids*, Advance in Chemical Engineering, ed. by T.B.Drew and J.W.Hoopes, **2**, 211 (1959).
2. Y.Oyama, Bull.Inst.Phys.Chem.Res. Tokyo, **18**, 600 (1939).
3. M.H.Cooke, D.J.Stephens and J.Bridgewater, Powder Technology **15**, 1 (1976).
4. S.Das Gupta, D.V.Khakar and S.K.Bathia, Chem. Eng. Science **46**, 1513 (1991).
5. M.Nakagawa, Chem.Eng.Sci.-Shorter Com., **49**, 2544 (1994).
6. J.Bridgewater, N.W.Sharpe, D.C.Stocker, Trans.Instn.Chem.Engrs, **47**, 114 (1969).
7. O.Zik, D.Levine, S.G.Lipson, S.Shtirkman and J.Stavans, Phys.Rev.Lett *to be published* (1994).
8. K.M.Hill and J.Kaliakos, Phys.Rev.E **49**, 3610 (1994).
9. F.Cantelaube et D.Bideau., *preprint* (1994).
10. G.Bauman, I.Janosi and D.Wolf, Europhys.Lett **24**, 203 (1994).
11. G.Ristow, *preprint* (1994).
12. J.Rajchenbach, Phys.Rev.Lett **65**, 2221 (1990).
13. P.Evesque and J.Rajchenbach, C.R. Acad. Scien. (Paris) 307, Serie II, 223 (1988).
14. H.M.Jaeger, C.h.Liu and S.R.Nagel, Phys.Rev.lett. **62**,40, (1989).
15. Morales-Gamboa et al. Phys.Rev.E **47**, 2229 (1993)
16. F. Cantelaube., Y. Limon-Duparemeur, D. Bideau and G Ristow, *to appear in J.de Physique I* (1994).
17. E. Clément, J. Duran and J. Rajchenbach, *in Compte Rendus du 11° Congrès de la Société Française de Mécanique*, Vol.4, p.327 (1993).



## SUPERSONIC RUPTURE PULSES IN AN EARTHQUAKE MODEL

MICHAEL LEIBIG

The Institute for Theoretical Physics, The University of California Santa Barbara, Santa Barbara, CA 93019

*In this work, I study the supersonic rupture pulse in a two dimensional elastic sheet. There is a friction force acting at the edge of the sheet which is composed of a term that depends on the local displacement at the edge and a viscous dissipation term. I consider the case where the sheet is driven forward by a force acting in the bulk, but is held back by the interfacial friction. I present the equations which describe such a system and then look for solutions which describe a slip pulse propagating through a region which is uniformly stressed. Such a pulse will allow the entire interface to move forward and partially relieve the stress. I present the integral equation that such a pulse solution must satisfy, and then discuss the behavior observed in numerical solutions of this equation.*

The quite remarkable Burridge-Knopoff model has rekindled many physicists' interest in the problem of earthquake dynamics [1,2]. Much of the work in this area has centered around numerical simulation of simple models to determine which of them captures the essential features of earthquakes [3,4]. Debate continues concerning the proper functional form for the force at the simulated tectonic plate interface and how much of the actual geological structure ought to be included in simulations [4-6].

Quite separate from questions about the direct analogy between these numerical simulations and actual fault activity is the issue of understanding the dynamics of what is happening in the computer models themselves. There has been interesting work involving the predictability of these models and whether or not by studying the past activity in a simulation it is possible to determine when the next catastrophic large "earthquake" event is about to occur [7].

One of the barriers to answering these and related questions about these simulations is the lack of analytical results concerning the behavior seen in these models. One of the difficulties with doing analytic work on the simplest block-and-spring Burridge-Knopoff type models is that there is no well-defined continuum limit, and the behavior is dependent on the smallest scale of discretization [2,8,9]. In an effort to solve the problem of a well-defined continuum limit, a small viscous damping force can be added to the friction force law which smoothes out the discontinuities and allows for a continuum description. Numerical and analytical studies of a one dimensional model which included this viscosity yielded interesting results [9]. The rupture pulses were observed to travel supersonically. This does not violate causality in the system because the one dimensional interface is tied to a perfectly rigid rod which transmits information instantaneously throughout the system. The speed of these supersonic pulses was also seen to depend on how hard the system was driven.

This paper presents a study of this viscous-damping rupture model for the case of a two dimensional sheet. The interface at which the friction is acting is still one dimensional, but stress can now be transmitted through the bulk of the material. This work is more than just a trivial extension of a series of results which have been completely understood in one dimension. The addition of the second dimension allows for the separation of the elastic behavior in the bulk from the frictional force at the interface. Thus, different mathematical tools are available which allow for a more extensive analytical treatment.

I begin with the equation of motion for the displacements  $u(x, y, t)$  in the bulk of the elastic sheet

$$\ddot{u}(x, y, t) = \nabla^2 u(x, y, t) - (u(x, y, t) - \Delta), \quad (1)$$

where dots indicate derivatives with respect to time and I have performed a trivial change of scale to get rid of some uninteresting material parameters. The second term on the right-hand side of Eq. (1) provides the driving for the system, with  $\Delta$  the natural displacement to which the system equilibrates in the absence of (or far from) the friction at the interface. This choice of a form for the driving is quite different from the more physical driving which happens at the boundaries. It seems unlikely, although possible, that the overall behavior is sensitive to this choice for the driving force.

Because Eq. (1) is a scalar equation, I am also making the simplifying assumption that the vector character of the stresses and strains are not important. Equation (1) can also be viewed as describing the normal strains on a flat plate. This equation is also the starting point for a study of fracture in mode III [10].

The behavior of the frictional force is captured in the boundary conditions at the interface. The traction at the interface can be written as

$$\left. \frac{\partial u(x, y, t)}{\partial y} \right|_{y=0} = f(u(x, 0, t)) - \eta \left. \frac{\partial^2 u(x, y, t)}{\partial y^2} \right|_{y=0}, \quad (2)$$

where  $f(u(x, 0, t))$  is the frictional force which depends only on the local displacement at the interface and  $\eta$  is a small parameter. The second term on the right-hand side of (2) is the viscous damping force mentioned above.

I choose a velocity dependent frictional force of the form

$$f(u(x, 0, t)) = \begin{cases} (-\infty, 1) & \text{if } \dot{u}(x, 0, t) = 0, \\ 1 - \alpha \dot{u}(x, 0, t) & \text{if } 0 < \dot{u}(x, 0, t) < 1/\alpha \text{ and } \ddot{u}(x, 0, t) > 0, \\ \sigma - \alpha \dot{u}(x, 0, t) & \text{if } 0 < \dot{u}(x, 0, t) < 1/\alpha \text{ and } \ddot{u}(x, 0, t) < 0, \\ 0 & \text{otherwise,} \end{cases} \quad (3)$$

where  $\sigma \leq 1$  is the frictional force as the velocity approaches zero during deceleration and  $\alpha$  determines how quickly as a function of velocity this state dependent friction force disappears. Earlier studies using this type of velocity weakening friction have not allowed for a difference between the force during acceleration and deceleration, taking the special

case  $\sigma = 1$  [9]. I have been unable to find a solution for the special case  $\sigma = 1$ , and it may be true that an asymmetry in this force is necessary to produce supersonic solutions using this type of friction law.

This friction law also has the somewhat unattractive characteristic that it is multi-valued function for  $\dot{u}(x, 0, t) = 0$ . However, the value for the local frictional force at each point where the velocity vanishes can be fixed by requiring that

$$\dot{u}(x, 0, t) \geq 0 \quad \text{for all } x. \quad (4)$$

Equations (1 - 4) represent the complete specification of the model. There are three remaining material parameters: the coefficient for the viscous damping,  $\eta$ , and two parameters to characterize frictional force,  $\alpha$  and  $\sigma$ . The final parameter, which may be varied externally, is the driving force,  $\Delta$ .

Having described the model, I want to look for steady-state pulses traveling at constant velocity  $v$ . I consider the simplest case of a pulse which is propagating through a region which is uniformly stuck at  $u(x, 0, t) = 0$ . If the pulse travels at a uniform speed, then in the region behind the pulse there is a constant value for  $u(x, 0, t)$ . The amount of stress relieved by the slip pulse is the difference between the displacement which precedes and follows the pulse.

The first step in the analysis is to transform to a reference frame moving with the velocity  $v$  in which the propagating rupture is a stationary feature. I choose to let the pulse travel in the negative  $x$  direction. The most convenient change of variables for the supersonic propagation is  $\beta\xi = x + vt$ , where  $\beta^2 = v^2 - 1$  and the leading edge of the pulse is located at  $\xi = 0$ . (For subsonic propagation, the correct choice for  $\beta$  is  $\beta^2 = 1 - v^2$ , but the analysis proceeds similarly.) With this transformation and letting  $U(\xi, y) = u(x, y, t)$ , Eq. (1) becomes

$$\frac{\partial^2 U(\xi, y)}{\partial y^2} - \frac{\partial^2 U(\xi, y)}{\partial \xi^2} - (U(\xi, y) - \Delta) = 0. \quad (5)$$

Because the pulse is a stationary object in the new coordinate system, the frictional force can now be described by the value that it takes in different regions of the interface. Equation (3) is rewritten as

$$\frac{\partial U(\xi, y)}{\partial y} \Big|_{y=0} = \begin{cases} \psi_-(\xi) & \text{if } \xi < 0, \\ F(U(\xi)) - \nu U'''(\xi) & \text{if } 0 < \xi < l, \\ \psi_+(\xi) & \text{if } \xi > l, \end{cases} \quad (6)$$

where  $l$  is the length of the propagating pulse,  $U(\xi) = U(\xi, 0)$ ,  $\nu = \eta v / \beta^3$ , and primes signify derivatives with respect to the variable  $\xi$  in the moving frame. The function  $\psi_-(\xi)$  is the static frictional force which holds the surface in place in front of the pulse, and  $\psi_+(\xi)$  is the corresponding force which follows in the wake of the pulse. For the choice of a velocity weakening friction, the function  $F(U(\xi))$ , takes the form

$$F(U(\xi)) = \begin{cases} 1 - \gamma U'(\xi) & \text{if } U'(\xi) < 1/\gamma \text{ and } U''(\xi) > 0, \\ \sigma - \gamma U'(\xi) & \text{if } U'(\xi) < 1/\gamma \text{ and } U''(\xi) < 0, \\ 0 & \text{otherwise,} \end{cases} \quad (7)$$

where  $\gamma = \alpha v / \beta$ .

The form of Eqs. (5) and (6) are exactly the same as those studied by Langer and Nakanishi in connection with a one dimensional fracture model [10]. By using a Weiner-Hopf technique, they are able to solve these equations with the assumption that the forces  $F(U(\xi))$  and  $\psi_+(\xi)$  are known. Their solution for the pulse profile,  $U(\xi)$ , can be written most conveniently in a "Green's function" form

$$U'(\xi_0) = - \left( \int_0^l d\xi_1 G_0(\xi_0, \xi_1) F'(U(\xi_0)) + G_1(\xi_0) \int_l^\infty d\xi_1 e^{-p_0 \xi_1} \psi'_+(\xi_1) \right). \quad (8)$$

where  $G_0(\xi_0, \xi_1)$  and  $G_1(\xi_0)$  are known functions, and  $p_0 > 0$  is a constant which is related to the parameter  $\nu$ .

The reason that this equation can be solved is that it has a very weak dependence on  $\psi_+(\xi_1)$ . This function only enters the expression inside an integral which has no dependence on  $\xi_0$ . Therefore, the complete form of the function need not be known, only the value of this single integral.

Additionally, this weak dependence on this trailing force occurs only for supersonic pulses. In the case of subsonic rupture, one must know the complete functional form of  $\psi_+(\xi)$  in order to solve for the pulse profile. As a result that problem is significantly more difficult.

Finally, the Langer-Nakanishi solution requires continuity in the frictional force at the interface. In order to have continuity at the leading edge of the pulse ( $\xi = 0$ ), the driving force must satisfy the condition.

$$\Delta = \sigma e^{-p_0 l} + p_0 \int_0^l d\xi e^{-p_0 \xi} F(U(\xi)) + \int_0^\infty d\xi \psi_+(\xi) e^{-p_0 l}. \quad (9)$$

Again, there is the same weak dependence on the trailing frictional force, which allows for a relatively simple evaluation of this expression. In order to achieve continuity in the friction force at the trailing edge of the rupture ( $\xi = l$ ), the pulse profile must also satisfy the conditions  $U'(l) = U''(l) = 0$ .

Although there is this significant simplification in the supersonic case, Eqs. (8) and (9) are the limit of the analytical progress that has been made. I will forgo a discussion of the technique used to generate numerical solutions to these equations, and merely present the results.

Figure 1 shows velocity pulse profiles with fixed values for the physical parameters of the model, but for differing values of the driving force. The interesting trends to notice are that the local velocities in the pulse are becoming smaller with increased driving, while the pulse width is becoming larger. However, it must be remembered that this is in the moving frame, which has a velocity dependent change of scale. Taking into account this "boost," the former trend is robust, but in the latter case the pulses are actually becoming narrower as the driving increases.

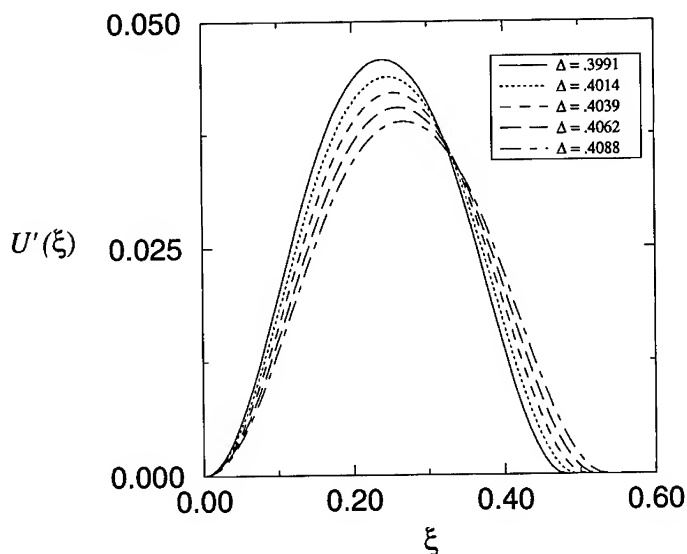


FIG. 1. Velocity pulse profiles for different values of driving force;  $\eta = .000143$ ,  $\alpha = 3.0$ ,  $\sigma = .999$

Figure 2 shows the velocity of these pulses as a function of driving. Note that the velocity of the pulse is becoming slower with increased driving. This is a somewhat disturbing trend. It is certainly counter-intuitive and is contrary to what is seen in numerical simulations of these models. This is somewhat similar to the behavior in the velocity weakening friction law itself in which a decrease in velocity means a larger friction force. Thus, the pulses found by using these parameters may actually be unstable and would not be observed in a direct simulation using these friction laws.

However, these results are for the case of a very weak viscous force. This pathological behavior may arise because the value for the viscous force at the leading edge of the pulse is given by  $\eta v U'''(0)/\sqrt{v^2 - 1} = 1 - \Delta$ . The only way that this can be satisfied with such a small value for  $\eta$  is with a pulse which has velocity very near 1. By moving away from the sound speed, the behavior might be quite different. A study of the pulse behavior for different regions of the parameter space is under way.

Finally, it is worth noting that efforts to find a solution for the case  $\sigma = 1$  were unsuccessful. If one views a glass as half full, this may indicate that an asymmetry in the force applied at the leading and trailing edge of the pulse is necessary in order to get a solution. If one sees a glass as half empty, it may indicate that supersonic pulse propagation may not be a particularly robust behavior in these systems.

The goal of this paper is two-fold. The first is to present the basic formalism which allows for the study of supersonic pulses in simple rupture models. The formalism is quite

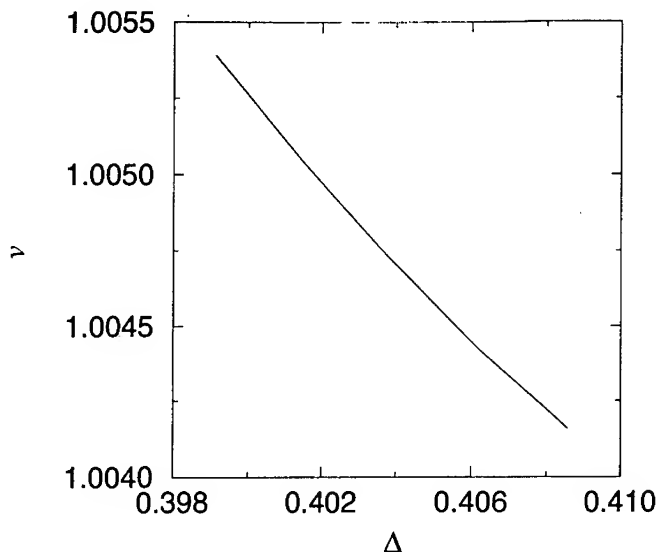


FIG. 2. Pulse speed as a function of driving force;  $\eta = .000143$ ,  $\alpha = 3.0$ ,  $\sigma = .999$

general and allows for a wide variety of local friction laws. The second goal is to present the results of an investigation into a particular model for the local friction at the interface. The model is a slight generalization of a force law that has been used in several numerical simulations [2,8,9] and I have shown that supersonic pulses do indeed represent possible solutions of the equations.

The author would like to express his extreme gratitude to Jim Langer for his guidance and assistance on this project. Much thanks also goes to Fong Liu for his enlightened remarks.

#### REFERENCES

- [1] R. Burridge, and L. Knopoff, *Bull. Seis. Soc. Am.* **57**, 3411 (1967).
- [2] J.M. Carlson, and J.S. Langer, *Phys. Rev. A* **40**, 6470 (1989).
- [3] K. Chen, P. Bak, and S.P. Obukhov, *Phys. Rev. A* **43**, 625 (1991); J.M. Carlson, J.S. Langer, B.E. Shaw and C. Tang, *Phys. Rev. A* **44**, 884 (1991); Z. Olami, H.J.S. Feder and K. Christensen, *Phys. Rev. Lett.* **68**, 1244 (1992); M. de Sousa Vieira, G.L. Vasconcelos and S.R. Nagel, *Phys. Rev. E* **47** 2221 (1993).
- [4] J.R. Rice, *J. Geo. Res.* **98**, 9885 (1993).
- [5] A. Lachenbruch, *J. Geo. Res.* **85**, 6097 (1980).
- [6] B.E. Shaw (unpublished).
- [7] S. Pepke and J.M. Carlson, *Phys. Rev. E* **50**, 236 (1994).
- [8] J.S. Langer and C. Tang, *Phys. Rev. Lett.* **67**, 1043 (1991).
- [9] C.R. Myers and J.S. Langer, *Phys. Rev. E* **47**, 3048 (1993).
- [10] J.S. Langer and H. Nakanishi, *Phys. Rev. E* **48**, 439 (1993).

## EXPERIMENTS IN MODEL GRANULAR MEDIA : A STUDY OF GRAVITY FLOWS

J. RAJCHENBACH, E. CLEMENT AND J. DURAN

Laboratoire d'Acoustique et d'Optique de la Matière Condensée, Université Pierre et Marie Curie,  
4 place Jussieu, 75005 PARIS, FRANCE.

### ABSTRACT

We study the flow under gravity of a granular model system submitted to shear in a rotating cylinder. The system is confined in a vertical 2D geometry which allows visualisation of the bulk and direct measurements of the velocity and density fields. We establish the existence of scaling properties displayed by velocity and density profiles for a large range of different flow rates.

### INTRODUCTION

Granular media consisting of assemblies of non-cohesive particles intervene in numerous practical domains of engineering and fabrication processes (soil mechanics, pharmacology, concrete, food industry, etc...). They display a large number of unusual properties (like strain localisation, segregation, non-Newtonian flows, spontaneous heaping etc..) [1] [2]. All those properties are weakly understood and remains a challenge for both engineers and physicists. Contrasting with atomic systems, for which equilibrium statistical mechanics and linear response theory provide a basis for the passage from a microscopic to a macroscopic viewpoint, the particles are here so large that fluctuations of thermal origin are irrelevant and all classical methods of statistical mechanics fail. Concerning granular flows, it has been known for a long time that they do not obey hydrodynamics laws and one of the most open questions is to obtain constitutive relations describing momentum and energy transport. For example, we know that, in opposition with Bernoulli's law, the discharge rate of an hourglass does not depend on the height in the upper vessel, and exhibits funnel behaviour. Furthermore, a gravity flow on an incline displays several regimes of flow and a transition between an intermittent regime to a continuous one [3]. Two major steps for the understanding of granular flows are due to Reynolds [4] and Bagnold [5]. The seminal concept of "dilatancy threshold" was proposed in 1885 by Reynolds who expressed the simple idea that a powder can flow from rest only if, it has been dilated below a given density threshold in order to overcome the large stress resistance due to the grain entanglement. Much later, Bagnold proposed that, for a rapidly flowing powder, a collision regime exists where the collision frequency, which sets the rate of momentum losses, scales like the velocity gradient between layers of flowing particles. As a consequence, the shear stress is proportional to the velocity gradient and is bound to diverge in the proximity of the dilatancy threshold, according to :

$$\sigma_{xz} = F(\rho) (\text{grad} v)^2 \quad (1)$$

where  $F(\rho)$  sets the divergence in the vicinity of the dilatancy threshold. More recently, several theories attempted to go beyond this elementary picture by using *a la Boltzmann* collision theories [6] [7], which attempt to describe the lower density collision regime. These theories have brought some rational to Bagnold's arguments and have elucidated some dependence as a function of micro mechanical parameters such as inelasticity of the grains, but still, there is no clear vision of the influence of the solid friction and the role of the boundaries, nor full understanding of the cross-over with the regime of higher density flows. Furthermore, considering the difficulties to make measurements inside the bulk, there are very little experimental studies probing quantitatively this

behaviour [8] 9] [10]. In our experiments we deal with bidimensional model system of grains, consequently we are able to get *in situ* velocity measurements and we test the existence of some general flowing behaviour.

## EXPERIMENTAL RESULTS

In the experiment reported here, we use a rotating cylinder which is a device initially designed by Franklin and Johanson [11]: it is an hollow duralumin cylinder (20 cm diameter) with glass windows, rotating around its horizontal axis at a constant speed  $\Omega$ . The rotating cylinder is a very convenient set-up to accumulate data over long time, because the heap is continuously supplied with new particles upstream. In the present case, the container is partly filled with monodisperse metal spheres ( $d=1.5$  mm) confined between two vertical boundaries separated by one bead diameter. The rotation speed is driven by a quartz clock, and is varied from 5 to 20 r.p.m which correspond to the steady continuous flow regime.

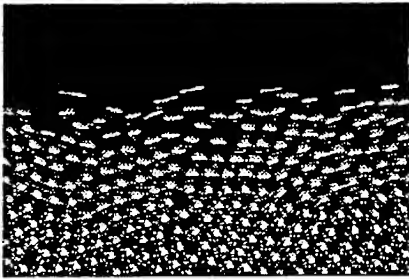


Figure 1. Bidimensional flow of steel spheres ( $d = 1.5$  mm). White trails correspond to the beads displacement during the opening time of the shutter. ( $\Delta t = 1/250$  s).

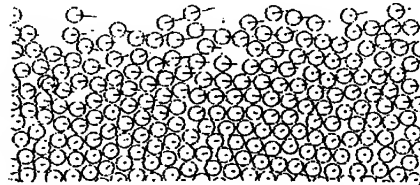


Figure 2. Computer reconstructed image corresponding to Fig.1

On Fig.1 we present a zoomed snapshot of the central region of the rotating cylinder. Each photo looks like a collection of bright trails due to the displacement of each grain during the opening time of the shutter. The inclined flow compares well with a flow of particles on an inclined plane, provided that the flux of matter and of momentum, brought up by the rotation process, is negligible in comparison to the surface gravity flow. This condition seems to be satisfied on the photos, since for this range of shutter time, the bottom bed of beads looks motionless. In the region where particles have attained their limiting velocity, the balance between shear stress and gravity yields:

$$\sigma_{xz} = (mg \sin \theta / d^2) \int_z^{+\infty} \rho(h) dh \quad (2).$$

The shear stress  $\sigma_{xz}$  integrates all mechanisms leading to loss of momentum, which namely are the diffusion of momentum due to collisions, the solid friction and the inelasticity. On Fig.2 we show a computer reconstructed image of the photo presented in Fig.1. We designed computer routines suited to analyse images of the flow and calculate displacement and density fields.



Now we present the results of a standard analysis where, for a fixed position in the laboratory reference frame and for a given rotation velocity, we average velocities and volume fractions over hundreds of snapshots. Fig.3 and Fig. 4, display the volume fraction profiles and the velocity profiles obtained for typical flow rate magnitudes corresponding to 500 particles/s (case a), 800 particles/s (case b) and 1500 particles (case c)/s. Note that the flux is externally driven by adjusting the rotation speed of the drum. Comparing Fig.3. and Fig.4, we notice that the flowing layer has a finite thickness (typically around 10 beads diameter) which depends on the flux. The motion appears frozen for volume concentrations of the order of  $\rho_c \approx 0.8$ , which is clearly smaller than the volume concentration of the 2D triangular compact lattice ( $\rho_{\max} = 0.91$ ). This gives an experimental approximation of the Reynolds dilatancy threshold. Furthermore, a remarkable feature is that, *in the average*, the velocity gradient looks weakly dependent on the flowing layer depth, and is roughly of same order of magnitude:  $\nabla V \approx 24 \text{ s}^{-1}$ .

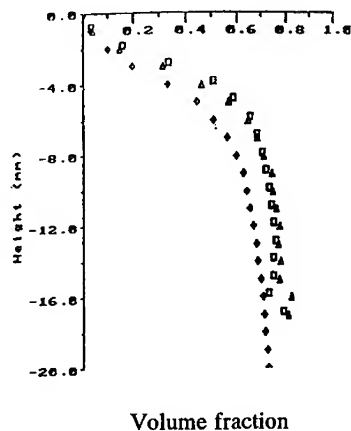
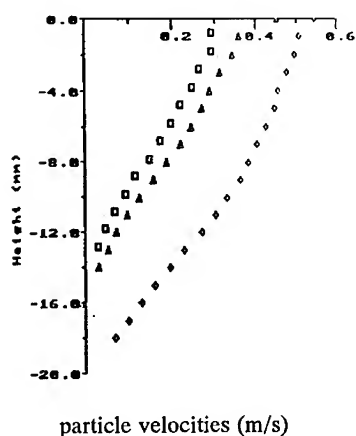


Figure 3 . Velocity profile of the 2d flow of steel beads ( $d = 1.5 \text{ mm}$ ) (averaged on 100 snapshots) [□ (case a), Δ (case b), ◇ (case c), see text.]

Figure 4 Corresponding volume fraction profiles (same experimental conditions)

We claim that the previous analysis has a major drawback. The averaging procedure ignores that for 2D experiments, fluctuations are of large amplitudes. Consequently, the standard averaging procedure mixes spatial domains with different physical significance and may smooth out essential pieces of information. Now we describe an alternative analysis procedure based on the hypothesis that every snapshot represents some mechanical steady state controlled by three variables:  $\nabla V$  the velocity gradient,  $J$  the particle flux,  $\theta$  the instantaneous flowing angle and  $\rho_c$  the maximum volume fraction of the flowing layer. These parameters are not necessarily independent but can be measured independently for each snapshot. There is also an implicit hypothesis on the existence of a time scale separations between the process controlling the shearing and the process controlling the fluctuations. For each picture,  $\nabla V$ ,  $J$  and  $\theta$  are measured as well as  $z_c$  the maximal depth of the flowing layer.

A flow depth scale  $H$  is computed:  $H = [J/\nabla V/\rho_c]^{1/2}$ . On fig 5 and 6 we display the rescaled velocity and density profiles for a large collection of snapshots at three rotation velocities.

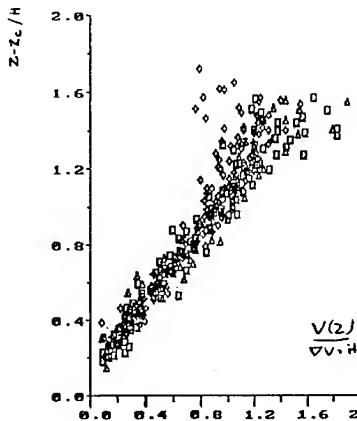


Figure 5: Rescaled velocity profile

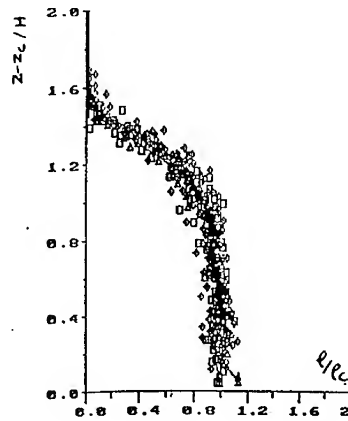


Figure 6: Corresponding rescaled volume fraction.

We observe a *data collapse* in favour of generic flow laws of the type:

$$V(z) = \nabla V (z-z_c) \quad (3a)$$

and

$$\rho(z) = \rho_c \Phi[(z-z_c)/H] \quad (3b)$$

where  $\Phi$  is an "universal" profile function. This flow structure seems to characterise a shearing regime for which the momentum transfer picture is to be established.

#### REFERENCES :

- 1 Jaeger, H.M. and Nagel, S.R. *Science*, **255**: 1523 (1992)
- 2 Rajchenbach, J., Clément, E., Duran J. and Mazozi T. in *Scale Invariance, Interfaces and non-equilibrium dynamics*, A. McKane Editor, Plenum, New York (1994)
- 3 Rajchenbach, J. *Phys. Rev. Lett.* **65** : 2221 (1990).
- 4 Reynolds, O. *Phil. Mag. Ser. 5*, **20** : 469 (1885)
- 5 Bagnold, R.A. *Proc. Roy. Soc. A* **225** : 49 (1954)
- 6 Jenkins J.T. and Savage S.B. *J. Fluid. Mech.* **130**, 187, (1983),
- 7 Lun C.K.K. Savage S.B., Jeffrey D.J., and Chepuriniy N., *J. Fluid. Mech.* **140**, 223, (1984),
- 8 Savage, S.B. *J. Fluid. Mech.* **92** : 53 (1979).
- 9 Hanes, D.M. and Inman, D.L. *J. Fluid Mech.* **50** : 357 (1985).
- 10 Drake, T.G. *J. of Geoph. Res.* **95**, B6 : 8681 (1990).
- 11 Franklin, F.C. and Johanson, L.N. *Chem. Eng. Sci.* **4**, 119 (1959)

## Author Index

- Amar, Jacques G., 149  
 Angulo, Rafael F., 131  
 Araujo, Mariela, 237  
 Araujo, Y. Carolina, 255  
 Argoul, F., 43  
 Armstrong, R., 417  
 Arneodo, A., 43
- Ball, Robin C., 367  
 Barabási, A.-L., 299  
 Behringer, R.P., 461  
 Ben-Jacob, Eshel, 405  
 Blumen, A., 495  
 Blumenfeld, Raphael, 53, 367  
 Bouchaud, Elisabeth, 83  
 Bouchaud, Jean-Philippe, 347  
 Brouers, F., 231, 423  
 Bushnell, L.T., 13
- Caponetti, E., 429  
 Card, Jill P., 113  
 Carns, T., 311  
 Chachaty, C., 215  
 Chassaing, E., 177  
 Chazalviel, J.-N., 169, 183  
 Chechetkina, Elena A., 397  
 Chin, Y.H., 355  
 Chopra, K.L., 195  
 Clement, Eric, 491, 495, 513, 525  
 Cohen, Inon, 405  
 Cohen, Richard J., 435  
 Credo, Grace M., 441  
 Cuerno, R., 299  
 Curtis, Corrine L., 441  
 Cziráok, Andras, 405
- Deltour, R., 423  
 Dickinson, J.T., 95  
 Doyama, Masao, 119, 385  
 Dumitrascu, M., 373  
 Dunin-Borkowski, R.E., 317  
 Duran, Jacques, 491, 495, 513, 525
- Family, Fereydoon, 149  
 Fishmeister, H., 141  
 Fleury, V., 169, 183  
 Floriano, M.A., 429
- Giversen, T., 113  
 Glebovsky, V., 141  
 Glicksman, M.E., 13  
 Golubović, Leonardo, 107  
 González, Agustín E., 447  
 Gonzalez, Hada Y., 255  
 Gumbsch, P., 141
- Hakizabera, P., 423  
 Halsey, Thomas C., 23  
 Hentschel, H.G.E., 33
- Hill, K.M., 507  
 Hinojosa, M., 125  
 Hiwatari, Y., 337  
 Hong, Daniel C., 483  
 Huang, J.W., 293  
 Huang, S., 311  
 Huttel, Y., 177  
 Hyde, J.M., 113
- Inglefield, P.T., 355  
 Inoue, Tomoyasu, 323  
 Itagaki, Kazuhiko, 379  
 Iwamoto, Atsushi, 159, 329  
 Iwasaki, Hiroshi, 159, 329
- Ji, Nina, 379  
 Jones, Alan A., 355
- Kakalios, J., 507  
 Kao, Y.H., 311  
 Kaufman, H., 73  
 Kim, W., 417  
 Kogure, Yoshiaki, 385  
 Korb, J.-P., 215  
 Koss, M.B., 13  
 Kouchi, O., 385  
 Kuech, T.F., 293  
 Kuhn, A., 43  
 Kurnaz, M. Levent, 471  
 Kurtze, Douglas A., 483
- Lacombe, J.C., 13  
 Lagally, M.G., 293  
 Langford, S.C., 95  
 Leibig, Michael, 519  
 Lemieux, G.E., 379  
 Li, N.F., 453  
 Li, W.H., 453  
 Lloyd, S.J., 317  
 Lu, Toh-Ming, 283  
 Luding, S., 495
- MacKintosh, F.C., 501  
 Maher, James V., 471  
 Mandelbrot, B.B., 73  
 Markel, V.A., 417  
 Mathur, B.K., 195  
 Matsui, J., 337  
 Mazozi, T., 491  
 McGill, T.C., 305  
 Medina, Ernesto, 131  
 Mehrabi, Alireza, 203  
 Miles, R.J., 305  
 Ming, Z.H., 311  
 Muzy, J.F., 43
- Nayak, S., 293  
 Ngo, Tue T., 273  
 Niwa, Y., 119

Odagaki, T., 337  
 Ohsuna, Tetsu, 323  
 Ortiz, U., 125  
 Oshnian, V.G., 249  
  
 Pencea, St.C., 373  
 Peredera, Anatoli, 107  
 Pettersson, P.O., 305  
 Pietronero, L., 67  
 Pipitone, Giuseppe, 429  
  
 Rajchenbach, Jean, 491, 495, 513, 525  
 Ramírez-Santiago, Guillermo, 447  
 Rao, M.V.H., 195  
 Rassamdana, Hossein, 203  
 Redwing, J.M., 293  
 Riedle, J., 141  
 Ritchie, Jason E., 441  
 Rodríguez, R., 125  
 Rosso, M., 177, 183  
 Russ, S., 243  
  
 Sahimi, Muhammad, 203  
 Sailor, Michael J., 441  
 Sander, Leonard M., 3  
 Sapoval, B., 177, 225, 243  
 Sarychev, A.K., 231  
 Satoh, Masataka, 323  
 Schmidt, Paul W., 429  
 Scudiero, Louis, 95  
 Semenov, V., 141  
 Shalaev, Vladimir, 417  
 Sherman, Derin A., 435  
 Shochet, Ofer, 405  
 Smilauer, Pavel, 263  
 Somekh, R.E., 317  
 Soo, Y.L., 311  
  
 Srinivas, V., 195  
 Stechel, E.B., 417  
 Stobbs, W.M., 317  
 Sudoh, Koichi, 159, 329  
  
 Tabeshfar, Kamran, 137  
 Takayama, T., 119  
 Tenenbaum, Adam, 405  
 Timan, S.A., 249  
 Toledo, Pedro G., 255  
 Tong, William M., 273  
 Triolo, R., 429  
 Tsukahara, H., 119  
  
 Vespignani, A., 73, 67  
 Vicsek, Tamas, 405  
 Vvedensky, Dimitri, 263  
  
 Wang, Gwo-Ching, 283  
 Wang, K.L., 311  
 Williams, D.R.M., 501  
 Williams, R. Stanley, 273  
 Winsa, E.A., 13  
  
 Xiao, Rong-Fu, 61  
  
 Yamamoto, Yasuhiro, 323  
 Yang, Hong-Ning, 283  
 Yarusso, L., 507  
 Yoshinobu, Tatsuo, 159, 329  
 Yu, Z.B., 453  
 Yue, Su, 483  
  
 Zapperi, S., 67  
 Zhang, C., 355  
 Zhu, Yao Hua, 391

## Subject Index

- 3D-islanding, 273
- a shear band, 461
- a-Si, 329
- active membranes, 225
- adhesion, 113
- AFM, 293, 305, 329
- ageing, 391
- aggregates, 429
- aging, 347
- AISI 316L steel, 125
- anharmonicity, 385
- anti-persistence, 203
- antibody, 435
- atomic force microscopy, 159, 293, 323, 329
- Au/Ru(0001), 149
- bacterial patterns, 405
- ballistic model, 373
- bending plastic deformation, 119
- bidimensional, 513
- branched growth, 23
- Brownian motion, 203
- Burridge-Knopoff model, 519
- CaF<sub>2</sub>, 305
- carbon tetrabromide, 61
- CB, 423
- CeO<sub>2</sub>(110)/Si(100), 323
- characterization, 367
- cleavage plane, 141
- clustering, 501
- coal slag, 453
- coherent medium approximation, 337
- colloidal
  - aggregation, 23, 373, 435
  - clusters, 447
- computer simulation, 119
- conducting polymer, 441
- conductor-insulator composites, 231
- convection, 13, 483
- cooperative strategies, 405
- copper, 119, 159
  - aggregates, 177
- correlations, 367
- crossover scaling, 149
- crack, 397
  - front, 141
  - plane, 141
  - propagation, 83
- creation of dislocations, 119
- critical
  - island size, 149
  - path analysis, 131
- cross-linked, 215
- crossover, 83
- crystal
  - growth, 13
- crystallographic orientation, 141
- damping, 243
- deformation, 95
- dendrite, 13, 61
- dendritic, 13
  - growth, 73
- deposits, 177
- detachment effect, 495
- dielectric breakdown model, 33
- diffraction, 283
- diffusing void model, 483
- Diffusion Limited Aggregation (DLA), 73
- diffusion, 237
  - equation, 507
  - limited cluster aggregation, 373
- diffusion-limited, 447
  - aggregates, 43
  - aggregation, 23, 373, 429
- dilatancy threshold, 525
- dislocations, 119
- disordered
  - aggregate, 379
  - heterogeneous media elastic properties, 249
- dissipative gases, 501
- distribution, 215
- DLA, 73, 183, 373
- dynamic
  - angle, 507
  - scaling, 159, 263, 273, 283, 435
- dynamical systems, 67
- dynamics, 215, 299, 461
- EAM, 385
- earthquake dynamics, 519
- elastic
  - anomaly, 317
  - constants, 385
- electrochemical deposition, 159, 183
- electrodeposition, 23, 177
- electroless deposition, 43
- electron beam, 305
- electropolymerization, 441
- environment, 107
- epitaxial growth, 263
- equation state, 501
- equilibrium, 435
- fabrication processes, 525
- faceted structure, 323
- facets, 61
- far from equilibrium dynamic growth, 283
- fatigue cracking, 137
- Fe/Cu(100), 149
- FEM, 249
- Fibonacci hierarchical ordering, 43
- five-fold symmetry, 43
- fluctuations, 461
- food industry, 525

- fractal, 67, 113, 149, 159, 183, 215, 255, 397
  - aggregates, 429
  - aggregation, 447
  - dimension, 53, 125
  - distribution, 215
  - geometry, 125
  - nanocomposites, 417
  - structures, 73
  - surface, 273
- fractals, 61, 203
- fracture, 95, 141, 305, 397
  - characteristics, 137
- Fresnel contrast, 317
- friction, 519
- fullerene C<sub>60</sub>, 61
- fuse networks, 131
- Gaussian noise, 203
- genome cybernetics, 405
- GIXS, 311
- glass, 355, 397
  - transition, 337, 355
- gradient, 215
- grain boundaries, 125
- granular
  - flows, 483
  - material, 461, 495, 513
  - materials, 501
  - media, 507, 525
  - model, 525
- gravity flows, 525
- grazing-incidence x-ray scattering (GIXS), 311
- growth, 53
  - law, 471
  - morphologies, 61
- Hamiltonian, 53
- Hele-Shaw cells, 169
- hierarchical patterns, 367
- homoeptaxy, 263
- hot corrosion mechanism, 453
- hydrodynamic equations, 33
- impedance, 177
- inelastic collapse, 501
- instability, 263
- interaction laws, 495
- interface, 53
  - roughness, 283, 311
- interfacial
  - curvature and growth probability, 33
  - failure, 95
- intergranular fracture, 107
- ion
  - bombardment, 299
  - sputtering, 299
- iron powder, 137
- iron-copper, 317
  - multilayers, 317
  - sintered compacts, 137
- irregular, 243
- irreversible growth, 73
- island
  - morphology, 149
  - nucleation, 273
- island-size distribution scaling functions, 149
- Ivantsov, 13
- KdV solitons, 483
- kinetic, 435
  - Monte Carlo, 149
  - roughening, 263
- Langevin equation, 237, 273
- Laplace equation, 3
- Laplacian field, 53
- laser scanning, 379
- Lévy distributions, 203
- light transmission, 379
- linear stability analysis, 3
- many-body, 53
- MBE, 305, 311
- metal-ceramic composites, 95
- metrics, 113
- microcavity nucleation, 107
- microgravity, 13
- microstructure, 83, 137
- molecular
  - beam epitaxy, 293, 299, 311
  - crystals, 61
  - dynamics, 119
    - simulation, 337, 385
- monodisperse nanoparticles, 273
- morphological evolution, 323
- morphologies, 183
- morphology, 367, 441
  - of the aggregates, 177
- MOVPE, 293
- multifractal dimensions, 23
- multiple collisions, 495
- n-body potential, 385
- nickel thin films, 195
- NMR, 355
- non-
  - linear response, 225
  - stationary dynamics, 347
  - universality, 423
- nonlocal velocity, 33
- nonstationary local slope, 283
- nuclear paramagnetic relaxation, 215
- numerical information, 379
- oil reservoir, 203
- optical processes in nanostructured
  - fractal composites, 417
- oscillations in logarithmic coordinates, 367
- Pacs numbers: 46.10, 05.40, 64.75, 491
- Pacs: 05.40, 46.10, 47.50, 83.70, 525
- pattern formation, 23, 183

- percolation, 249, 513
  - clusters, 243
  - theory, 231
  - threshold, 423
- pharmacology, 525
- phase transformation, 391
- phonon dispersion, 385
- planar film, 273
- poly(3-methylthiophene), 441
- poly-Si, 329
- polyaniline, 441
- polycrystals, 107
- polymercarbon black (CB) composites, 423
- pore sizes, 215
- porous media, 203, 255
- potassium sulfate, 453
- powders, 513
- precracks, 141
- pressure sensitive adhesives, 95
- probability distribution, 237
- profilometry, 113
- proton-pulsed-field, 215
- quantum
  - tunneling, 231
  - wires, 293
- quasi-static fracture, 83
- random
  - advection, 237
  - walk, 373
- re-entrant oscillations, 263
- real glasses, 347
- reflection high energy electron
  - diffraction, 323
- relaxation, 355, 483
- renormalization group, 67
- repose, 507
- resin, 215
- restitution coefficient, 495
- reversible axial segregation, 507
- RHEED, 293
- Richardson plots, 125
- ripple structure, 299
- rotating cylinder, 525
- rough interfaces, 471
- roughening, 299
- roughness, 159
  - index  $\zeta$ , 83
- rupture, 131
  - pulses, 519
- sandpile, 67
  - avalanches, 507
  - models, 67
- scalar fluctuations, 237
- scaling, 13, 255, 299, 329, 447
  - behavior, 311
  - law, 231, 299
  - of rough surfaces, 299
- sedimentation, 471
- self organized criticality, 67
- self-
  - affine, 203, 273
    - correlation length, 83
    - fractal, 83, 283, 329
    - surface, 195
  - organized critical state, 263
  - similar electrodes, 225
- silicon, 305
  - nitride, 453
- single crystal, 323
- sintering, 137
- size segregation, 507
- slow dynamics, 337
- small-angle
  - scattering, 429
  - x-ray scattering, 215
- snow packs, 379
- SOC, 67
- soil mechanics, 525
- solid-on-solid model, 263
- spin-glasses, 347
- stationary local slope, 283
- statistical-mechanical analysis, 53
- Stefan problem, 3
- step-edge barriers, 263
- STM, 195, 293
- stochastic nonlinear equation, 299
- Stokes equation, 169
- Stranski-Krastanov, 273
- stress chains, 461
- stretched exponential, 347, 355
- structural fractal analysis, 43
- structure
  - factor, 447
  - scaling, 447
- submonolayer epitaxial growth, 149
- super-alloys, 107
- supercooled fluid phase, 337
- superlattices, 293
- surface, 113
  - diffusion, 273
  - flow, 513
  - morphology, 305
  - roughness, 329
- textures, 113
- the dynamic scaling, 423
- theory, 53
- thermal crystallization, 3
- thin-film, 255
- three-dimensional information, 379
- tracer particles, 513
- traffic equations, 483
- transport, 255
  - of a scalar, 237
- trapping diffusion model, 337
- traps, 347
- traveling wave solution, 483
- tree-like, 177
- two-length-scale, 429
- velocity attractor and repeller points, 33
- vibrations, 243

viscosity, 215  
viscous fingering, 23  
Vogel-Fulcher temperature, 337  
Volmer-Weber, 273  
  
W single crystals, 141  
wavelet transform microscope, 43

weakened bonds, 397  
wetting phase, 255  
  
x-ray  
  diffraction, 311  
  photoelectron spectroscopy, 305  
  
Zn-Al alloy, 391